Transactions of the ASME®

Transactions of the ASME, Journal of Turbomachinery (ISSN 0889-504X) is published quarterly (Jan., Apr., July, Oct.) by The American Society of Mechanical Engineers, Three Park Avenue, New York, NY 10016. Periodicals postage paid at New York, NY and additional mailing offices. POSTMASTER: Send address changes to Transactions of the ASME, Journal of Turbomachinery, c/o THE AMERICAN SOCIETY OF MECHANICAL ENGINEERS, 22 Law Drive, Box 2300, Fairfield, NJ 07007-2300.
CHANGES OF ADDRESS must be received at Society headquarters seven weeks before they are to be effective. Please send old label and new address.
STATEMENT from By-Laws. The Society shall not be responsible for statements or opinions advanced in papers or ... printed in its publications (B7.1, Par. 3).

INDEXED by Applied Mechanics Reviews and Engineering Information, Inc. Canadian Goods & Services Tax Registration #126148048

Journal of Turbomachinery

Published Quarterly by The American Society of Mechanical Engineers

VOLUME 124 • NUMBER 2 • APRIL 2002

(**Contents continued on inside back cover**)

This journal is printed on acid-free paper, which exceeds the ANSI Z39.48-1992 specification for permanence of paper and library materials. ♾™
♻ 85% recycled content, including 10% post-consumer fibers.

Journal of Turbomachinery **Volume 124, Number 2** **APRIL 2002**

Pressure and Suction Surfaces Redesign for High-Lift Low-Pressure Turbines

P. González
e-mail: Paloma.gonzalez@itp.es

I. Ulizar

R. Vázquez

ITP, Industria de Turbo Propulsores,
Madrid, Spain

H. P. Hodson
Whittle Laboratory,
Cambridge University,
Cambridge, U.K.
e-mail: hph@eng.cam.ac.uk

Nowadays there is a big effort toward improving the low-pressure turbine efficiency even to the extent of penalizing other relevant design parameters. LP turbine efficiency influences SFC more than other modules in the engine. Most of the research has been oriented to reduce profile losses, modifying the suction surface, the pressure surface, or the three-dimensional regions of the flow. To date, the pressure surface has received very little attention. The dependence of the profile losses on the behavior of both pressure and suction surfaces has been investigated for the case of a high-lift design that is representative of a modern civil engine LP turbine. The experimental work described in this paper consists of two different sets of experiments: the first one concluded an improved pressure surface definition, and the second set was oriented to achieve further improvement in losses modifying the profile suction surface. Three profiles were designed and tested over a range of conditions. The first profile is a thin-solid design. This profile has a large pressure side separation bubble extending from near the leading edge to midchord. The second profile is a hollow design with the same suction surface as the first one, but avoiding pressure surface separation. The third one is also a hollow design with the same pressure surface as the second profile, but more aft loaded suction surface. The study is part of a wider ongoing research program covering the effects of the different design parameters on losses. The paper describes the experiments conducted in a low-speed linear cascade facility. It gathers together steady and unsteady loss measurements by wake traverse and surface pressure distributions for all the profiles. It is shown that thick profiles generate only around 90 percent of the losses of a thin-solid profile with the same suction surface. The results support the idea of an optimum axial position for the peak Mach number. Caution is recommended, as profile aft loading would not be a completely secure method for reducing losses. [DOI: 10.1115/1.1452747]

Introduction

The modern civil aero-engine LP turbines consist of several stages. As a result, besides the turbine efficiency which has a high influence in SFC, the weight and manufacturing cost are also important parameters to be considered in the design process. The weight of the LP turbine represents over 20 percent of the engine weight, and the cost could be up to 15 percent of the whole engine total cost. In order to optimize the LP turbine reducing both weight and cost maintaining the efficiency level, the number of aerofoils has been reduced in recent years increasing lift coefficient, leading to the so-called ''high-lift'' profiles. This change in design philosophy is supported by computational studies and experimental evidences [1,2] and it has been introduced into the latest LP turbines for civil applications [1–10].

Profile losses are greatly dependent on the development of the blade surface boundary layer. Due to the large aspect ratios existing in LP turbines, the profile loss is by far the largest percentage of the total loss, accounting for about 80 percent of the total loss according to [1]. Furthermore, reducing the 2-D losses to 90 percent of their former value can raise the efficiency of the LP turbine by approximately 0.5 percent. Therefore, it is important to be able to predict such changes as accurately as possible in order to control the loss generated.

Nowadays, there are two dominant profile design options in use in engines, either thin solid or thick hollow aerofoils. Hollow aerofoils are lighter, more efficient, more robust mechanically but around 30 percent more expensive because of the increased manufacturing complexity. Thin solid profiles are present in the current LP turbines but former LP turbines using hollow aerofoils have accumulated around 100 million h of successful operation over the last 30 yr.

The current profile design establishes the position of the peak Mach number around 60 percent of the suction surface length [1,3]. Some research [2,8] suggest that, for higher lift applications, there is a chance of reducing profile losses by moving aft the peak Mach number.

The first objective of this study is an attempt to define the differences between thin solid and thick hollow aerofoils discovering by which mechanisms and by how much the thickening of the profile influences the aerodynamic behavior of the aerofoil. The other important target is to give good quality experimental evidence to the fact that losses can be reduced aft loading the profile.

This paper describes the experiments conducted in a low-speed linear cascade in order to reduce profile losses and to develop an improved profile for a LP turbine.

Experimental Setup

The experimental work was conducted in low-speed cascade wind tunnels in the Whittle Laboratory, University of Cambridge. Figure 1 shows the test section for steady-state measurements and Fig. 2 shows the bar rig facility used for unsteady measurements.

The bars in the bar rig facility are driven by a variable-speed d-c motor. The bar speed is continuously monitored during the experiment.

To achieve a realistic simulation of wake-blade interactions, several parameters must be correctly matched [9,11]. The correct kinematics of the interaction is achieved by matching the velocity triangles using 50 percent stage reaction. The reduced frequency

Contributed by the International Gas Turbine Institute and presented at the International Gas Turbine and Aeroengine Congress and Exhibition, New Orleans, Louisiana, June 4–7, 2001. Manuscript received by the IGTI, October 16, 2000. Paper No. 2001-GT-439. Review Chair: R. Natole.

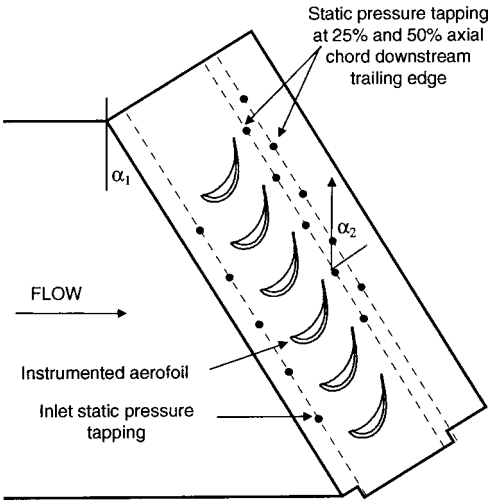

Fig. 1 Test section of the low-speed steady-state cascade

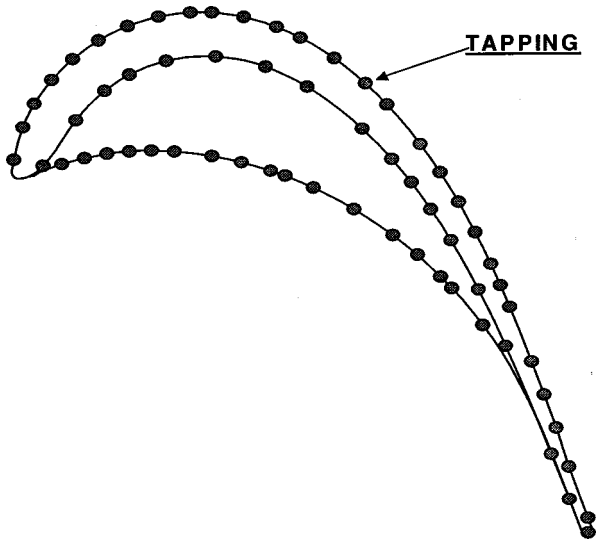

Fig. 3 Location of the tapping over the surface

in the experiments is set to the value in the real turbine and the diameter of the bars is adequate to simulate an upstream turbine blade with a representative wake defect. Bars diameter of 2 mm was used with a reduced frequency around the unity.

The cascade consists of six aerofoils (Fig. 1) with constant section. Three highly loaded profiles were tested. Each has the same lift coefficient ($\approx$1). Profile F is a thin solid high-lift profile following the current LP turbine design philosophy. Profile G is the redesign of profile F; it is a thick profile representative of a hollow blade. Profile G was designed by thickening profile F to the point that the pressure side bubble was suppressed. The pressure surface was not modified close to the leading edge and trailing edge so as not to modify the overall behavior of the profile. Both profile F and profile G have physically identical suction surfaces.

Profile G2 is a redesign of profile G by aft loading its suction surface without modifying pressure surface. The axial position of the peak Mach number was moved aft while back surface diffusion remains essentially constant.

For the purpose of testing, profile G was created by adding metal inserts to profile F to fill in the profile on the pressure side. Special attention was paid to the junction near to the leading edge so that the boundary layer was not tripped in this area. Profile G2 is a new cascade (new aerofoils and new endwalls).

Instrumentation. The instrumentation is the same for both tunnels.

The stagnation temperature at inlet to the cascade was measured using a thermocouple that was placed in the upstream plenum. The inlet stagnation pressure was measured upstream of the leading edge of the blades. A Pitot probe was placed at midpitch 33 percent C_{ax} upstream of each blade passage. Static pressure tappings were located in the same positions, but in the opposite sidewall. The average values of inlet static pressure and inlet stagnation pressure were determined using the values provided by the above instrumentation. Static pressure tappings were also placed at midpitch behind each blade passage at 25 percent C_{ax} and 50 percent C_{ax} downstream of the trailing edge plane.

One of the central two blades is instrumented with static pressure tappings at midspan. Figure 3 shows their location over the mid span section for profile F and profile G as the distribution is very similar for profile G2. The tappings were placed closer together on the suction side near to the leading edge in order to detect if a separation bubble is formed at positive incidence. Similarly, the tappings were placed closer together in the region of the separation bubble that was expected to form downstream of the throat on the suction surface in order to locate the separation and reattachment points.

Downstream of the cascade, a four-hole Neptune probe was used to measure the exit flow field. The probe was operated in a fixed orientation with its axis parallel to predicted flow direction. The local mean flow angle, static pressure and stagnation pressure were determined from the calibration of the probe. Integration of these local values was then carried out and a constant area mixing calculation was used to provide the mixed-out values of the cascade loss, exit flow angle and exit velocity. The traverse plane was located 25 percent C_{ax} downstream the trailing edge plane of the cascade.

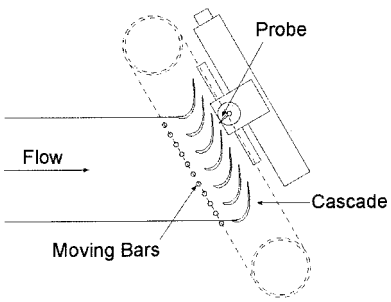

Fig. 2 Test section of the low-speed unsteady setup

Results and Discussion

Profiles F, G and G2 were tested over a range of chord based exit Reynolds numbers from 0.8×10^5 to 3.2×10^5 under steady-state flow conditions at design incidence. Profile G and profile G2 were also tested under unsteady conditions. Free stream turbulence was given by the characteristics of the tunnel, around 0.5 percent for all the experiments.

The unsteadiness was simulated using bars that were configured in such a way that represented a rotor blade row and the cascade, a stator blade row [9,11]. Only one reduced frequency that was representative of the turbine used as reference was tested.

The experiments were separated in two different sets: the first one was oriented to study the influence of the pressure surface geometric definition (profile F versus profile G) and the second one focused on the suction side configuration (profile G versus profile G2).

The static pressure data are presented in terms of the normalized velocity coefficient (V/V_2). The data are plotted against the

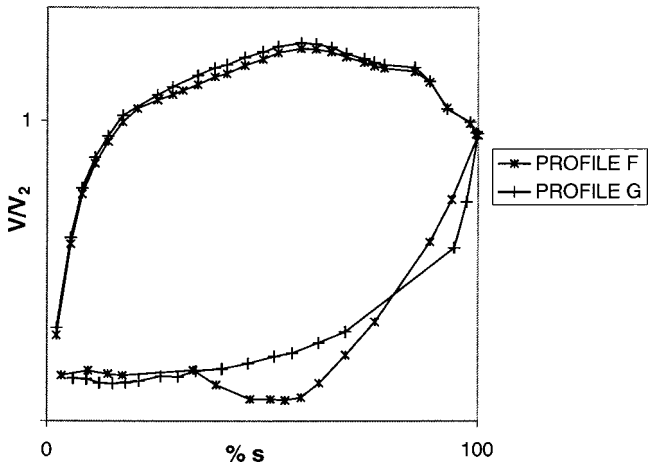

Fig. 4 Isentropic surface velocity distributions for profiles F and G at Re_d

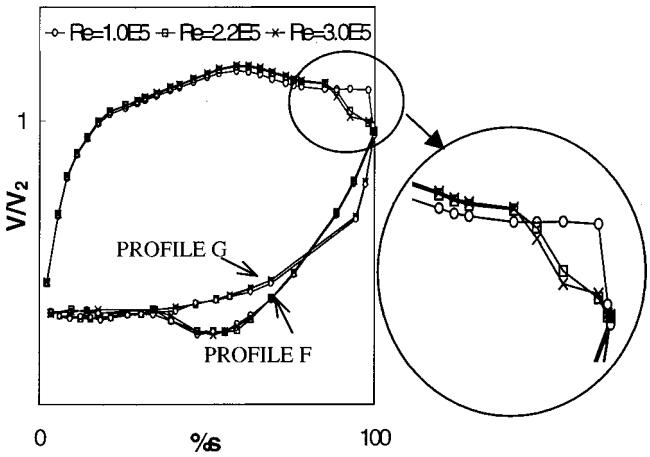

Fig. 5 Profiles F and G: isentropic surface velocity distributions at three Reynolds numbers

normalized surface length (percent s), since it is the development of the boundary layers that is of particular interest.

Profile F Versus Profile G. Both profiles were tested only under steady-state flow conditions to study the influence of the pressure surface definition on the overall behavior of the cascade.

Figure 4 presents the isentropic surface velocity distributions for profile F and profile G plotted against the percentage of surface length at the design representative Reynolds number ($Re_d \approx 2\times10^5$). The experimental results show that both profiles fulfil the high lift design criteria [2,3]; the leading portion of the suction surface has been carefully designed to avoid any possible separation and maximum Mach number is around 60 percent suction surface length; the strong deceleration on the suction surface leads to the formation of a laminar bubble. Transition occurs in the separated flow region compelling the flow to reattach before the trailing edge [5,12]. Figure 4 also shows that isentropic velocity distributions over the suction surface are practically the same for both profile F and profile G; there is a small increase in velocity for profile G due to the bigger blockage caused by the thickening of the profile on the pressure side. On the other hand, they are completely different on the pressure surface as it was intended: Profile F presents a pressure side bubble extended from close to the leading edge to around 60 percent of the axial chord while there is no pressure surface separation in profile G.

Figure 5 presents isentropic surface velocity distributions for both profile F and profile G at three chord-based exit Reynolds numbers. The distribution along the suction side has only been plotted for one profile as both distributions are very similar.

The Reynolds number affects the evolution of the boundary layer on the suction surface and in particular the characteristics of the suction side bubble. Increasing the Reynolds number reduces the length to transition and causes earlier reattachment of the separated shear layer. While the reattachment point varies its location, the separation point essentially remains constant. On the pressure surface, it seems that there is no noticeable effect of the Reynolds number on the behavior of the separation bubble. In all cases, separation has occurred before the first measurement point and reattachment appears to take place as the free stream flow begins to reaccelerate toward the trailing edge.

Figure 6 summarizes the loss data obtained for the two cascades; the variation of the profile loss coefficient (Y_{P03}) with the exit Reynolds number is shown together with its pitchwise variation downstream of the cascade at Re_d.

Both trend lines are almost parallel. As the Reynolds number is reduced, the stagnation pressure loss coefficients of both profiles increase, as is usually the case. Figure 4 shows that at the lowest Reynolds number tested the flow over the suction surface is already reattached by the trailing edge. As the Reynolds number is increased, the reattachment of the suction side separation bubble occurs further from the trailing edge and the losses are substantially lower. Figure 4 also shows that the laminar length of this separation bubble which appears as a plateau in the isentropic velocity distribution does not change very much between a Reynolds number of 2.2×10^5 and 3×10^5 and so stagnation pressure loss coefficients are almost constant.

The only physical difference between profile F and profile G is the shape of the pressure surface as shown in Fig. 3. Therefore, if there is any difference in the losses of the two profiles, it must be due to the pressure side behavior. It has already been noted that

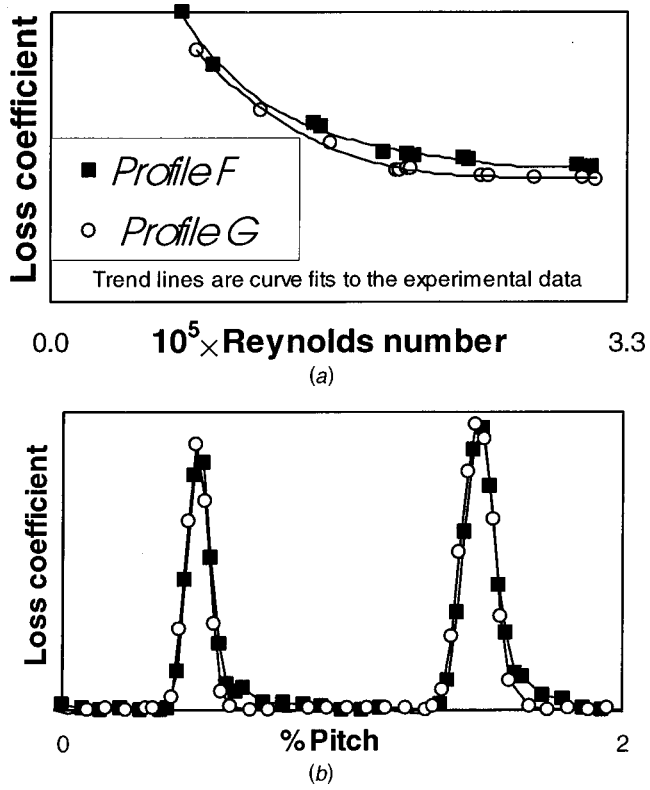

Fig. 6 (*a*) Profiles F and G variation of stagnation profile loss coefficient with Reynolds number; (*b*) profiles F and G stagnation pressure loss coefficient profile downstream the cascade at Re_d

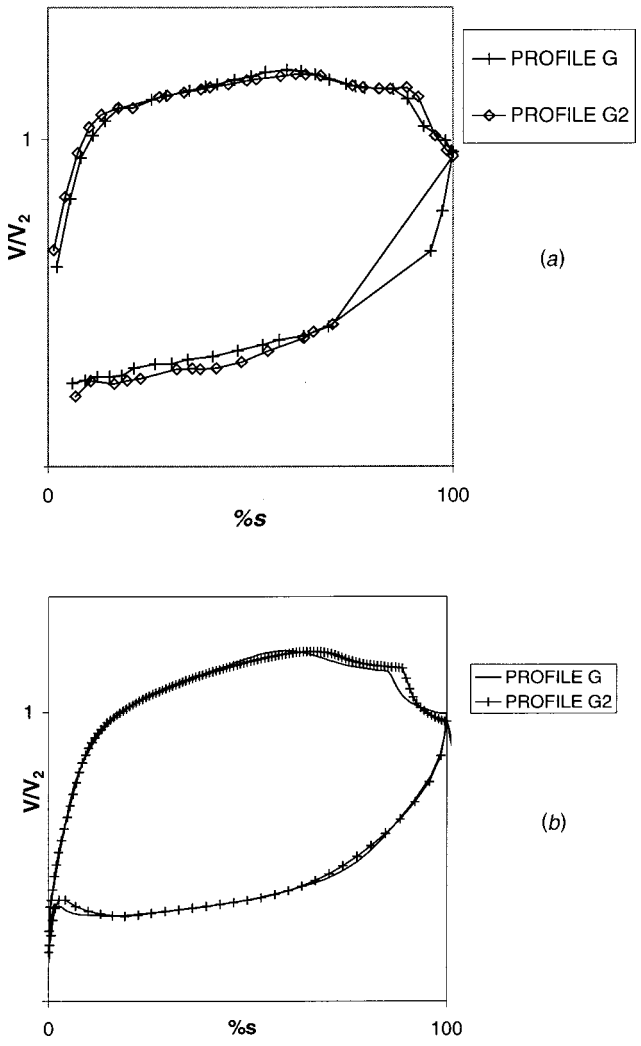

Fig. 7 Isentropic surface velocity distributions under steady flow conditions for profiles G and G2 at Re_d—(*a*) experimental data, (*b*) numerical predictions comparison

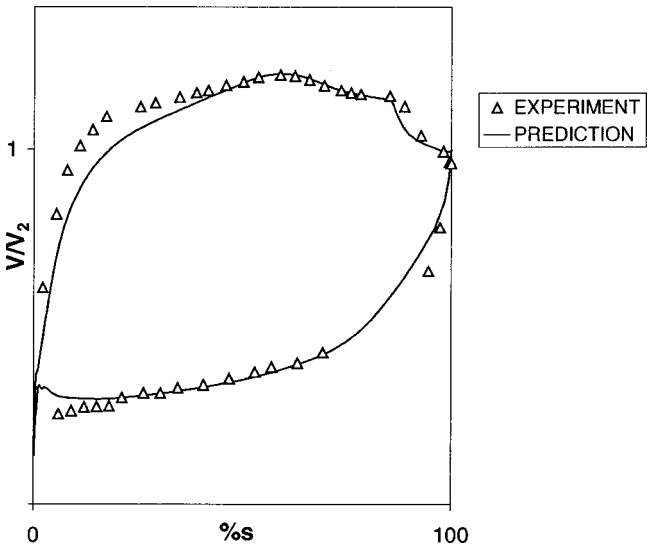

Fig. 8 Isentropic surface velocity distributions under steady flow conditions for profile G at Re_d: prediction versus experiments

the suction side velocity distributions are subtly different as a result of the different geometric definition and pressure side blockage. However, Fig. 6(*b*) shows that this is not the main reason for this. This plot shows how the stagnation pressure loss varies with pitchwise distance at the design Reynolds number. The wakes from the two central blades of the cascade are presented. The pressure side of each wake is to the right. The plot clearly shows that there is a so-called ''loss tail'' on the pressure side of the wake extending into the free stream in the case of profile F. An assessment of the losses in this region reveals that there are similar order to the differences in the loss coefficients of the two profiles. Figure 6(*a*) shows that the stagnation pressure loss coefficients of profile G are approximately 90 percent of those of profile F at a wide range of Re around the Re_d. For the lowest Re, this difference is reduced to 5 percent approximately. The very weak dependence on Reynolds number arises because, as Fig. 5 shows, changing the Reynolds number does not significantly alter the characteristics of the pressure side separation bubble.

Profile G versus Profile G2. Profiles G and G2 were tested over the same Reynolds number range as profile F under steady-state flow conditions and over a similar Reynolds number range under unsteady flow conditions to simulate the real turbine environment. The experiments were conducted in the bar rig facility; profile G experiments under steady state inlet flow conditions were redone due to the change of facility.

Figures 7, 8, 9, and 10 present the isentropic velocity distributions for profile G and profile G2 under steady and unsteady inlet flow conditions at Re_d. Experiments show that profile G2 fulfills the design intents as peak Mach number has moved aft without substantially modifying the diffusion of the profile. Figure 7(*b*) shows numerical predictions comparison [6]; based on the numerical prediction, a bigger movement of the peak Mach number was expected. Another difference between experiments and predictions is the size of the suction surface bubble; experiments show that the separation occurs fairly at the same position of surface length for both profiles, while predictions show a shift in the beginning of the laminar bubble.

The behavior of the front part of the profile has not been modified and pressure surface characteristics also remain constant.

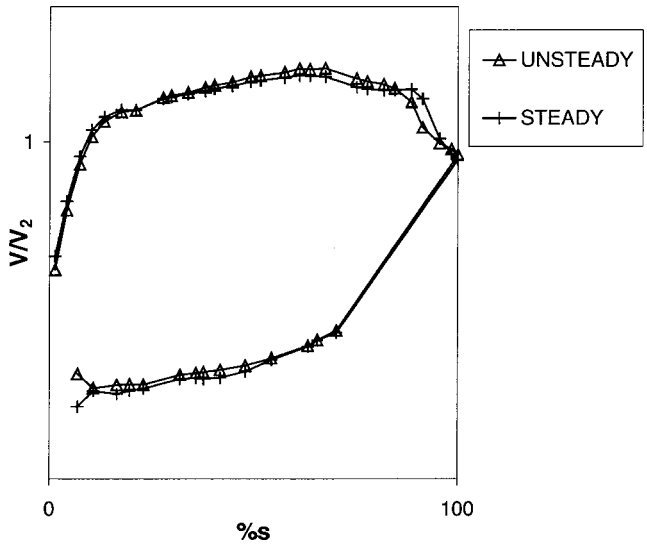

Fig. 9 Isentropic surface velocity distributions for profile G2 at Re_d: steady versus unsteady (reduced frequency ≈1, ϕ≈0.8) measurements

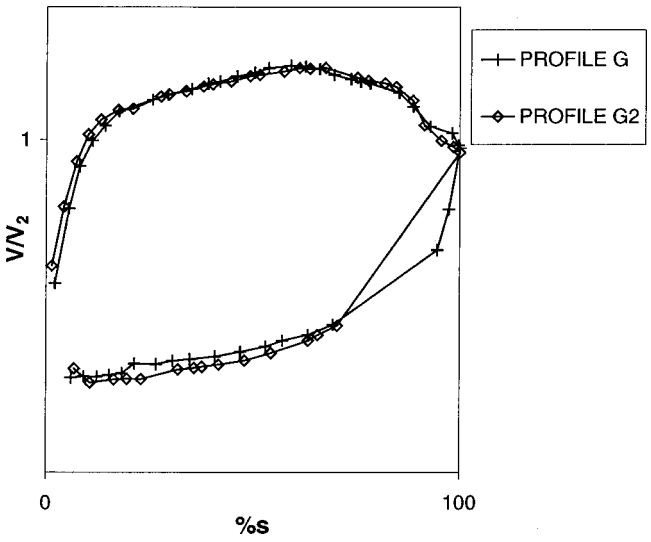

Fig. 10 Isentropic surface velocity distributions under unsteady flow conditions (reduced frequency ≈1, ϕ≈0.8) for profile G and profile G2 at Re_d

Comparing numerical prediction and experimental data (Fig. 8), it is shown that the profile is being tested at a certain positive incidence (around 7 deg). The existing gaps in the facility to allow the bars to pass in front of the cascade generate a positive incidence. It has been verified that this incidence is the same for both cascades. It can be avoided closing all gaps but this fact would not let the bars go through during the unsteady experiments.

The effect of the unsteadiness can be seen in Fig. 9. The unsteadiness causes the reattachment to occur earlier as transition to turbulent is also occurring earlier due to the incoming wakes.

Figure 10 shows a very little difference in suction side behavior between profile G and profile G2 for unsteady inlet flow conditions at Re_d. The difference in the position of the peak Mach number is still there, but the suction surface bubble is essentially equal for both profiles, not as in Fig. 7(*a*).

The behavior of the profiles at different Reynolds number follows the same trend both in steady and unsteady inlet flow conditions and it has already been shown in Fig. 6 for steady-state inlet flow conditions. The variation of the Reynolds number affects the suction surface behavior although pressure surface is only slightly affected. Figure 9 shows that unsteadiness is not affecting the pressure surface characteristics noticeably although there is no pressure surface separation for profiles G and G2; therefore, it is not accurate to say that unsteadiness does not affect pressure surface characteristics if there is any bubble. Figure 10 shows a detail of the isentropic surface velocity distributions for profile G and profile G2 at a low Reynolds number (10^5 approximately) under steady and unsteady inlet flow conditions.

Figure 11(*a*) shows that for profile G2 the flow seems not to reattach before the trailing edge. The shape of the isentropic velocity distribution changes: the peak Mach number moves forward and velocity ratio in the trailing edge is higher than 1. On the other hand, Fig. 11(*b*) shows the test data under unsteady flow conditions at the same Reynolds number. The flow is now reattached for both profiles and there is no significant difference between both profiles.

Figures 12(*a*), (*b*), and (*c*) summarize the loss data (Y_{P03}) for both profile G and profile G2. Figure 12(*a*) shows the steady-state measurements as Fig. 6(*a*) does for profile F and profile G. The trend of both distributions is very similar. Profile G2 has higher losses than profile G as it was expected due to the characteristics of the suction surface velocity distributions under steady-state flow conditions. For profile G2, suction surface bubble is bigger than in profile G and the flow reattaches later generating higher

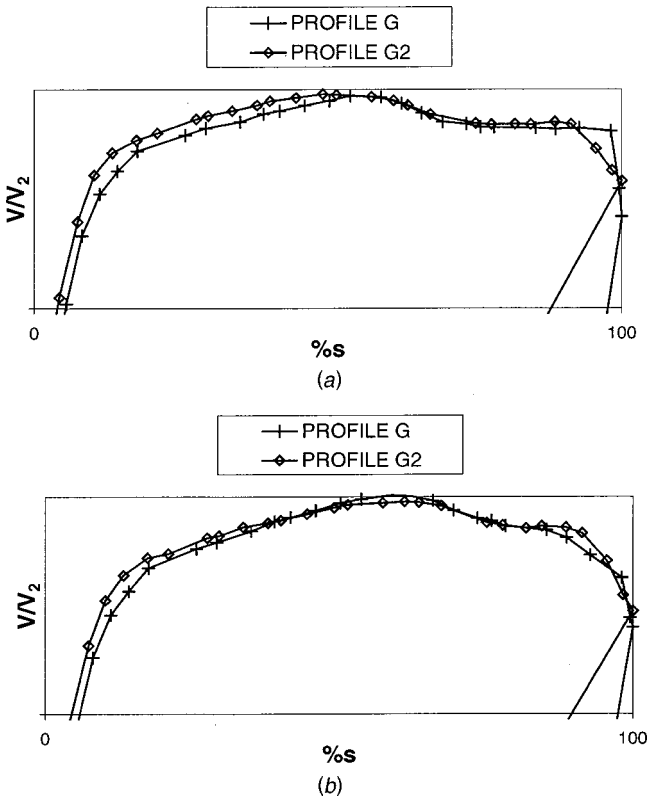

Fig. 11 Details of suction surface isentropic velocity distribution for profile G and G2 at a low Reynolds number (≈10^5)—(*a*) under steady, and (*b*) unsteady conditions

losses. Furthermore, if Reynolds number is low enough, the flow is separated at the trailing edge generating much higher losses.

Figure 12(*b*) shows the effect of the incoming wakes on the stagnation loss coefficient for profile G2. The plot is also applicable to profile G. Profile losses are reduced when the profile is under the effect of wakes.

Figure 12(*c*) shows the stagnation loss coefficient for profiles G and G2 under unsteady inlet flow conditions. This situation is the closest to the real turbine environment, although freestream turbulence level is much lower than in the real turbine. Losses for both profile G and profile G2 have been reduced from steady-state measurements due to the effect of the wakes. At Re_d, it is very difficult to establish which profile has higher losses. Profile G2 seems to be the worst one, with a bigger loss coefficient, but the difference between both profiles is so small that it is smaller than the measurements tolerances. At low Reynolds number, loss data are not coherent with the static pressure measurements; although the static pressure distributions over the surface are very similar for both profiles (Fig. 10(*b*)), loss coefficient is higher for profile G2 than for profile G. This result is still subject of study.

Conclusions

The suppression of the pressure surface separation by thickening the profile reduces the profile losses by approximately 10 percent. The thickening of the profile leads us to "hollow" aerofoils and must be done carefully: the global behavior of the profile and so the development of the suction surface boundary layer must not be affected by the pressure surface geometric definition.

Due to the large aspect ratios existing in LP turbines, the profile loss is around 80 percent of the total loss. If profile loss is reduced by 10 percent, a 0.5-percent improvement in efficiency is achieved.

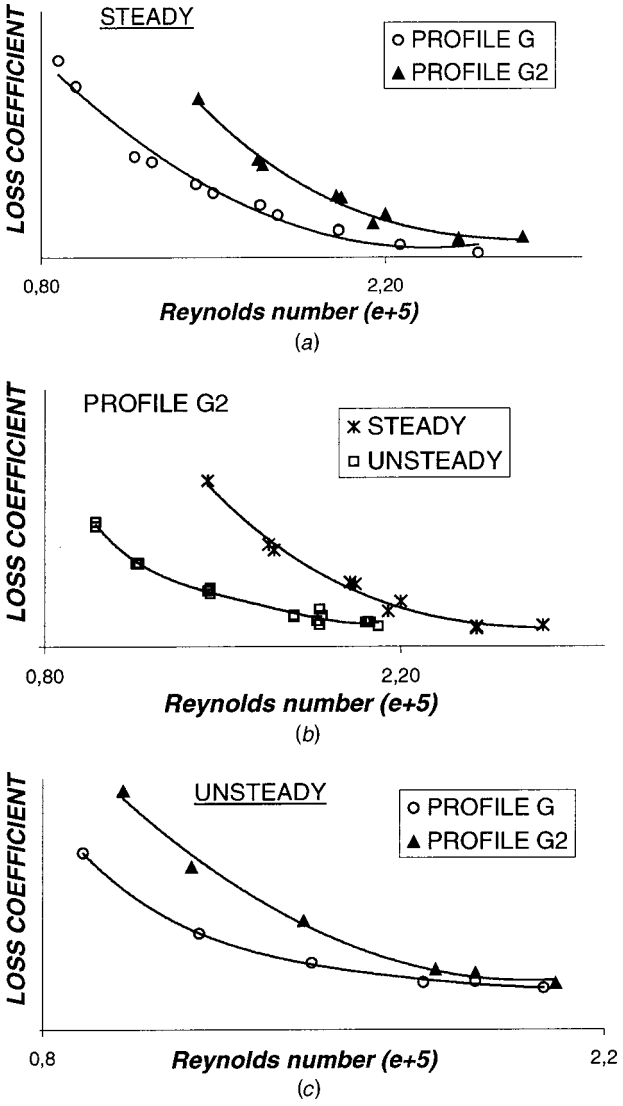

Fig. 12 (*a*) Steady-state measurements: variation of stagnation pressure loss coefficient with Reynolds; (*b*) profile G2: variation of stagnation pressure loss coefficient with Reynolds and unsteadiness; (*c*) unsteady measurements: variation of stagnation pressure loss coefficient with Reynolds

The search of the optimum peak Mach number position is not a straight forward study. If lift coefficient and back surface diffusion are not modified while the peak Mach number is moved towards the trailing edge the experiments conducted for profile G and profile G2 are not deciding. Although steady-state experiments show that the more aft-loaded profile has bigger losses as is expected, unsteady experiments do not allow us to decide which profile has lower profile losses. Further studies involving more drastic changes in suction surface velocity distributions are planned in order to clarify this effect.

Acknowledgments

The authors would like to thank all of the staff at the Whittle Laboratory for their help and ITP for its support to the project and the permission to publish this paper.

Nomenclature

α_1 = inlet flow angle
α_2 = outlet flow angle
C_{ax} = axial chord
I = incidence
LP = low pressure
Re = Reynolds no. based on true chord at exit conditions
Re_d = design Reynolds no. based on true chord at exit conditions
s = surface length
SFC = specific fuel consumption
V = local velocity
V_2 = exit velocity
ϕ = flow coefficient
$Y_{p03} = (P_{\text{total inlet}} - P_{\text{total mix-out}})/(P_{\text{total inlet}} - P_{\text{static mix-out}})$

References

[1] Curtis, E. M., Hodson, H. P., Banieghbal, M. R., Howell, R. J., and Harvey, N. W., 1997, "Development of Blade Profiles for Low Pressure Turbine Applications," ASME J. Turbomach., **119**, July.
[2] Howell, R. J., Ramesh, O. N., Hodson, H. P., Harvey, N. W., and Schulte, V., 2000, "High Lift and Aft Loaded Profiles for Low Pressure Turbines," ASME Paper No 2000-GT-0261, ASME Turbo Expo 2000, Munich, May.
[3] Cobley, K., Coleman, N., Siden, G., and Arndt, N., 1997, "Design of New Three Stage Low Pressure Turbine for the BMW Rolls-Royce BR715 Turbofan Engine," ASME Paper No. 97-GT-419, Orlando, FL, June.
[4] Denton, J. D. 1999, "State of the Art and Future of Turbine Technology," Proc. International Gas Turbine Congress, Kobe. pp. 27–37.
[5] Engber, M., and Fottner, L., 1995, "The Effect of Incoming Wakes in Boundary Later Transition of a Highly Loaded Turbine Cascade," Paper No. 21, AGARD Conference. Loss Mechanisms and Unsteady Flows in Turbomachinery, Derby, May.
[6] Giles, M., and Drela, M., 1985, "Two Dimensional Transonic Aerodynamic Design Method," AIAA J., **25**, No 9, pp. 127–134.
[7] Harvey, N. W., Schulte, V., Howell, R. J., and Hodson, H. P., 1999, "The Role of Research in the Aerodynamic Design of an Advanced Low Pressure Turbine," 3rd European Conf. on Turbomachinery, IMechE, London, Mar.
[8] Howell, R. J., 1999, "Wake-Separation Bubble Interactions in Low Reynolds Number Turbomachinery," Ph.D. dissertation, Cambridge University, Cambridge, UK.
[9] Schulte, V., and Hodson, H. P., 1998, "Unsteady Wake-Induced Boundary Layer Transition in High Lift LP Turbines," ASME J. Turbomach., **120**, Jan.
[10] Ulizar, I., and González, P., "Aerodynamic Design of a New Five Stage Low Pressure Turbine for the Rolls Royce Trent 500 Turbofan," accepted for publ., ASME J. Turbomach.
[11] Banieghbal, M. R., Curtis, E. M., Denton, J. D., Hodson, H. P., Huntsman, J., and Schulte, V., 1995, "Wake Passing in LP Turbines," Paper No. 23, AGARD Conference. Loss Mechanisms and Unsteady Flows in Turbomachinery, Derby, May.
[12] Hatman, A., and Wang, T., 1998, "A Prediction Model for Separated-Flow Transition," ASME Paper No. 98-GT-237, Stockholm, June.

Computational Design and Experimental Evaluation of Using a Leading Edge Fillet on a Gas Turbine Vane

G. A. Zess[1]

K. A. Thole
e-mail: thole@vt.edu

Mechanical Engineering Department,
Virginia Polytechnic Institute
and State University,
Blacksburg, VA 24061

With the desire for increased power output for a gas turbine engine comes the continual push to achieve higher turbine inlet temperatures. Higher temperatures result in large thermal and mechanical stresses particularly along the nozzle guide vane. One critical region along a vane is the leading edge-endwall juncture. Based on the assumption that the approaching flow to this juncture is similar to a two-dimensional boundary layer, previous studies have shown that a horseshoe vortex forms. This vortex forms because of a radial total pressure gradient from the approaching boundary layer. This paper documents the computational design and experimental validation of a fillet placed at the leading edge-endwall juncture of a guide vane to eliminate the horseshoe vortex. The fillet design effectively accelerated the incoming boundary layer thereby mitigating the effect of the total pressure gradient. To verify the CFD studies used to design the leading edge fillet, flowfield measurements were performed in a large-scale, linear, vane cascade. The flowfield measurements were performed with a laser Doppler velocimeter in four planes orientated orthogonal to the vane. Good agreement between the CFD predictions and the experimental measurements verified the effectiveness of the leading edge fillet at eliminating the horseshoe vortex. The flow-field results showed that the turbulent kinetic energy levels were significantly reduced in the endwall region because of the absence of the unsteady horseshoe vortex. [DOI: 10.1115/1.1460914]

Introduction

Modern gas turbine engines are designed to have products exiting the combustor at temperatures well above the melting temperature of the first vane in the downstream turbine. If these temperatures are not properly accounted for, the additional thermal load experienced by the vane significantly reduces the vane life. The leading edge and endwall platforms of the vanes are areas where the thermal loads are the highest for two reasons. First, because the platform is affected by secondary flows it experiences increased heat transfer coefficients. Second, the vortical flows increase the transport of relatively hotter fluid from the mid-span toward the endwall.

Previous studies have shown that regions on the platform having the highest heat transfer coefficients correlate with regions having the most intense vortex action. Langston [1] was the first to illustrate a secondary flow model for an approaching two-dimensional boundary layer along the endwall. This flow model agrees well with the flow field that has been measured for the vane used in our study (Kang et al. [2], and Kang and Thole [3]). The secondary flows include a leading edge horseshoe vortex that splits into a suction side leg and a pressure side leg with the pressure side leg becoming indistinguishable as it quickly merges with the passage vortex. It is not surprising then that the leading edge endwall juncture is where the highest heat transfer occurs (Kang et al. [2]).

The focus of the study reported in this paper is to evaluate a relatively simple modification that can be made to the leading edge-endwall juncture with the specific goal of reducing the horseshoe vortex. The specific objectives of this paper are two-fold. The first objective is to determine whether placing a fillet in the endwall juncture region will reduce (or eliminate) the horseshoe vortex and then to determine the impact of that reduction on the development of the downstream passage vortex. The second objective is to determine the feasibility of using CFD to design a fillet by comparing computational predictions and experimental measurements.

Previous Studies

To create a method of horseshoe vortex reduction/elimination, it is first necessary to understand the reason for the formation of the vortex. Kubendran et al. [4], Eckerle and Langston [5], Pierce and Shin [6], and Praisner et al. [7] have all provided similar explanations. When an incoming boundary layer approaches a bluff body a total pressure gradient forms along the span direction (radial direction in a turbine) at the leading edge. The reason for this gradient is because as the velocity decreases toward the wall a lower total pressure occurs near the wall when considering the static pressure to be constant normal to the wall (typical boundary layer assumption). As the flow stagnates, the total pressure profile then becomes a static pressure gradient along the span. This spanwise pressure gradient causes the boundary layer fluid to be driven towards the endwall. As the flow turns back upstream, it rolls into a vortex or a system of vortices that wrap around the body and proceed well downstream.

There are few studies in the open literature reporting methods to reduce or eliminate the horseshoe vortex with all of these studies using symmetric airfoils except for Sauer et al. [13] who studied an asymmetric airfoil (turbine blade). Many of these past studies were directed toward wing/body intersections and submarine conning tower applications. Table 1 summarizes past fillet studies along with their respective fillet geometries and sizes based on

[1]Present address is United Technologies-Pratt & Whitney, East Hartford, CT 06108; e-mail: zessga@pweh.com

Contributed by the International Gas Turbine Institute and presented at the International Gas Turbine and Aeroengine Congress and Exhibition, New Orleans, Louisiana, June 4–7, 2001. Manuscript received by the IGTI, December 7, 2000. Paper No. 2001-GT-404. Review Chair: R. A. Natole.

Table 1 Previous studies using fillets

Investigator	Geometries	Fillet Length	Fillet Height
Kubendran and Harvey [8]	curved and linear fillets	0.14δ , 0.28δ	0.14δ
Kebendran, et al. [4]	curved and linear fillets	3.7δ , 7.4δ	3.7δ
Pierce, et al. [6]	triangular /corner fillet, fence	0.78δ	2.33δ
Sung and Lin [9]	linear fillet	1δ, 1.5δ, 2δ	1δ, 1.5δ
Sung, et al. [10]	linear fillet	2δ	1δ
Devenport, et al. [11]	strake (curved) fillet	4.35δ, 8.37δ	1.98δ, 3.81δ
Bernstein and Hamid [12]	asymmetric fillet	no data	no data
Sauer et al. [13]	bulb on a blade	1.7δ	no data

inlet boundary layer characteristics. Some of the results from these studies will be highlighted in the next paragraphs.

Pierce et al. [6] compared five different fillet geometries including two different sizes of circular corner fillets, an elliptical corner fillet, an upstream flow fence, and a large leading edge triangular fillet. Their results showed that only the leading edge triangular fillet successfully reduced the leading edge vortex. Flow field measurements for this geometry not only indicated a reduction in the vortex, but also a reduction of the total turbulent kinetic energy by approximately 20 percent.

Kubendran and Harvey [8] studied three fillet geometries including two fillets in which the height was linearly varying with streamwise distance and one fillet in which the height was a polynomial function (curved fillet). They reported that all three geometries were effective at reducing the horseshoe vortex. The authors also performed the experiments with the airfoil at different angles of attack reporting that at moderate angles of attack the fillets still reduced the overall drag. When a larger fillet was used at higher angle of attack, the flow downstream of the wing was adversely affected. These results led the authors to conclude that an optimum fillet size may be required to achieve an overall improvement in the flow when operating at an angle of attack.

Sung and Lin [9] performed a numerical investigation to determine how the size of fillets, when placed on both the leading and trailing edges of the airfoil, affected its performance. Their results indicated that a leading edge fillet needed to have a length longer than or equal to the height of the fillet to be effective. They reasoned that these proportions were required since the distance between the vortex core and the leading edge of the airfoil, in absence of a fillet, was greater than the distance between the vortex core and the endwall.

Sung et al. [10] performed similar computations in conjunction with experimental measurements on two separate airfoils with the same fairing geometry. The airfoils used were NACA 0020 and NACA 0012 airfoils, with the NACA 0020 having a more blunt leading edge and thus a stronger horseshoe vortex in the absence of the fairing. The fillet geometry used was the most effective one studied by Sung and Lin [9], which was one boundary layer thickness high and two boundary layer thicknesses long. From their results they inferred that one fillet geometry was effective in reducing the horseshoe vortex for two very different airfoils.

Devenport et al. [14] performed measurements to evaluate the effectiveness of a constant radius fillet around the entire airfoil and found it to be ineffective for two different inlet boundary layers thicknesses. In a later study, Devenport et al. [11] performed measurements on the same airfoil using what they termed a strake (curved fillet). Their results indicated that the leading edge separation associated with a horseshoe vortex was not present. Velocity measurements, however, indicated that the addition of the strake did not totally eliminate the formation of vortices in the juncture. The authors hypothesized that the vortices seen downstream of the airfoil formed off the symmetry plane. The results did show that the vortex legs were much smaller and closer together indicating a weaker vortex. Two boundary layer thicknesses were studied using the same fillet with the results being surprisingly similar for both cases. These results indicate that boundary layer thickness may not be the correct scaling parameter.

Sauer et al. [13] studied the effects of various sized leading edge "bulbs." The objective of the study was to intensify the suction side branch of the horseshoe vortex and, through an interaction of the stronger suction side branch with the passage vortex, weaken the passage vortex. While Sauer et al. did not make measurements inside the passage or at the leading edge, their detailed total pressure field measurements at the exit of the cascade indicated an interaction between the suction and passage vortices and ultimately a 50 percent reduction in aerodynamic losses for their best bulb design. They found that the best geometry was an asymmetric bulb that had a pronounced suction side and a less extended pressure side. Sauer et al. also found that their CFD results agreed qualitatively to their measurements.

As can be seen in the above review, leading edge fillets are promising for reducing the horseshoe vortex formed at the leading edge of a blunt body such as an airfoil. While there have been some detailed measurements at the exit of the airfoil passage indicating a change to the total pressure profile, there is currently no experimental data to verify the effectiveness of the fillet at the leading edge of a turbine vane. In addition, there has not been any comparison between experimental results and CFD predictions in this region.

Computational and Experimental Methodologies

The approach taken for this study encompassed both computational and experimental efforts to determine a fillet design that was effective in eliminating the leading edge horseshoe vortex. The computational effort involved simulating the flow field for several fillet designs (to be described in the next section) and then assessing the effectiveness of each at reducing the vortex. After a fillet design was obtained, which proved to be successful based on the computational results, a model of this geometry was constructed for testing in a large-scale, linear, turbine vane cascade. Flowfield measurements were made at several locations to determine whether in fact the fillet was successful and how well the predictions compared to the experimental results.

The CFD efforts that guided the design of the leading-edge fillet were performed using the commercial software Fluent 5 [15]. The computations were made using an unstructured, tetrahedral mesh, and were second-order accurate. To insure grid insensitivity, adaptions were made on velocity gradients. The insensitivity was judged on flowfield features and the mass-averaged total pressure loss through the vane passage. The final grid size for the filleted vane was 1.2 million cells. A RNG-kε model with nonequilibrium wall functions was used for the turbulence model. The close resemblance of the numerical simulations using the RNG-$k\varepsilon$ turbulence model with nonequilibrium wall functions by Hermanson and Thole [16] and experimental measurements performed by Kang and Thole [3] on the same turbine vane geometry validated the use of these models for the fillet simulations. Each case took approximately 96 h of computing timing time on four processors.

The computational domain consisted of one passage with the vane split at the dynamic stagnation point and the pressure and suction surfaces. All physical surfaces were modeled as no-slip walls while periodic conditions were applied along the remaining mesh surfaces. A velocity inlet boundary condition was placed 0.75C upstream of the vane stagnation and an outflow boundary condition was placed 1.5C downstream of the vane trailing edge directed along the exit flow angle of the vane. Since the turbine

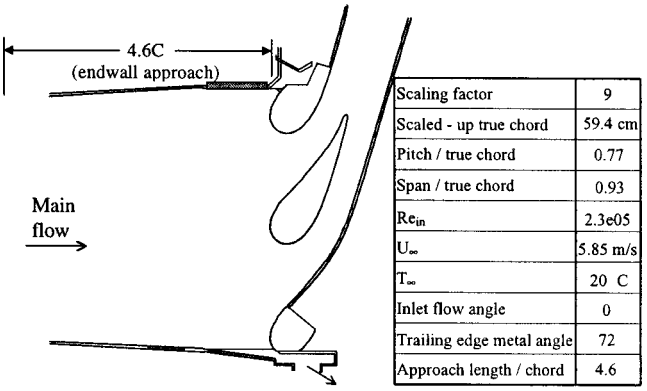

Scaling factor	9
Scaled - up true chord	59.4 cm
Pitch / true chord	0.77
Span / true chord	0.93
Re_{in}	2.3e05
U_∞	5.85 m/s
T_∞	20 C
Inlet flow angle	0
Trailing edge metal angle	72
Approach length / chord	4.6

Fig. 1 Schematic of the stator vane cascade

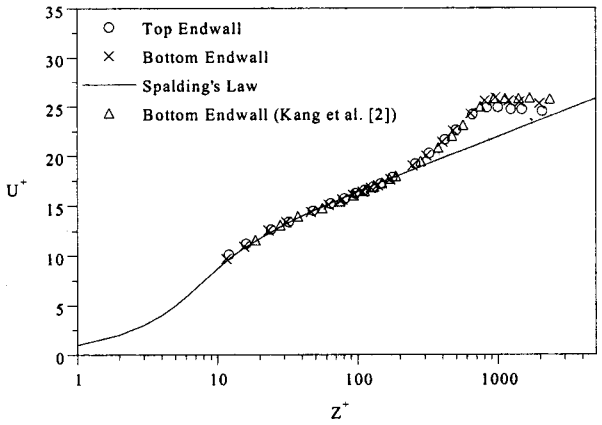

Fig. 3 Boundary layer profiles measured upstream of vane

vane is symmetric about its midspan, a symmetry boundary condition was applied at the midspan to minimize the size of the domain.

The details of the recirculating wind tunnel and design of the stator vane test section used in this study have been documented thoroughly in a number of previous studies including Kang et al. [2], Kang and Thole [3], and Radomsky and Thole [17,18]. To better achieve detailed flow-field measurements, the stator vane was scaled up by a factor of nine. Figure 1 depicts the corner test section of the wind tunnel as well as a description of the vane. The test section contained a central vane and two adjacent vane leading edges. These leading edges were installed to ensure proper modeling of the passage and secondary flows within the cascade. Attached to the outside leading edge was an adjustable flexible wall. The flexible wall was adjusted so that the geometry of the adjacent vane was matched. Downstream of where the adjacent vane ends, the flexible wall was adjusted so that the pressure distribution on the central vane was matched to a two-dimensional, inviscid, periodic CFD prediction for the vane at low speeds.

The inlet flow quality to the cascade has been previously reported by Kang et al. [2]. Particular care has been taken to insure equal flowrates in both passages to within 1 percent. The inlet turbulence for this study was 0.6 percent. The incident velocity was set to 5.85 m/s to match the inlet Reynolds number ($Re_{in} = 2.3\times10^5$) of that of the engine under operating conditions at an altitude of 9.1 km.

Figure 2 shows the position of the flow field planes measured and the nomenclature used in this study. In each plane the u, v, and w components of the velocity were measured using a laser Doppler velocimeter, where these components were the local velocities defined by the measurement planes. Note that these planes, except for the leading edge plane, were orthogonal to the vane surface. Orthogonal planes allowed the secondary flows to be analyzed. The planes were defined by finding a tangent line on the vane where the measurements were desired and creating a line normal to the tangent.

Since measurements were made on both the top and bottom endwalls, boundary layer measurements were characterized on both endwalls to ensure similarity of the incoming flow. Figure 3 shows the boundary layer measurements made one chord upstream of the vane leading edge and Table 2 summarizes the boundary layer characteristics. The figure shows the results plotted against the bottom boundary layer result of Kang et al. [2] and Spalding's law (White [19]) where the constants are 5.0 and 0.41. As can be seen, the top and bottom boundary layers exhibit the same boundary layer characteristics and closely match those measured by Kang et al. [3] and Kang and Thole [2]. Table 2 gives the boundary layer characteristics for the filleted and unfilleted experimental results. This agreement to the previous results is important since comparisons will be made to those unfilleted vane results.

A two-component, back-scatter, fiber optic laser Doppler velocimetry (LDV) system was used to measure the mean and turbulent flow fields in the turbine vane passage. The LDV system consisted of a 5W Coherent laser along with a TSI model 9201 Colorburst beam separator. A two-component laser probe, TSI model 9832, was used to transmit the laser beams and receive the scattered light. A fiber optic cable carried the velocity data to a TSI model IFA 755 Digital Burst Correlator where it was pro-

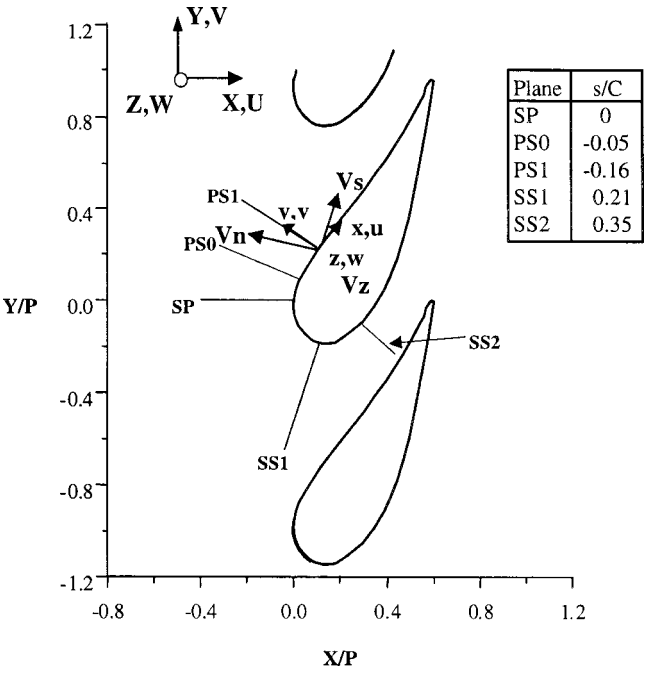

Plane	s/C
SP	0
PS0	-0.05
PS1	-0.16
SS1	0.21
SS2	0.35

Fig. 2 Measurement and computational plane locations

Table 2 Approaching boundary layer characteristics

	Re_{in} = 2.3e05, with fillet		2.5e05 no fillet (Kang, et al. [2])	
	Top	Bottom	Top	Bottom
δ_{99} (cm)	5.3	5.3	5	4.8
δ^* (cm)	0.89	1.06	1.06	0.92
θ (mm)	6.11	7.23	7.1	6.2
H	1.46	1.48	1.5	1.48
Re_θ	2874	3401	3340	2960
U (m/s)	6.29	6.27	7.33	7.45

Table 3 Uncertainty estimates

Value	Uncertainty Estimates	
Cp	4.7% for C_p = -9.5	4.2% for C_p = -22.7
Vs	2.0% near wall	
Vn	24.1% near wall	
Vz	2.9% near wall	
urms	2.8% near wall	6.8% at midspan
vrms	3.7% near wall	4.8% at midspan
wrms	1.3% near wall	2.9% at midspan

cessed. The Find™ software by TSI corrected the velocity for bias effects using residence time weighting. To map out the three-dimensional flowfield within the measurement planes, each location was measured twice with the two-component LDV. From a statistical analysis, we determined that 10,000 samples were needed for each component of the velocity. To allow optical access to measure the u and v components of velocity, a glass cover was placed over the vane test section. The *w*-component of the velocity was measured through glass windows located on the side of the test section.

Uncertainty estimates were calculated on the methods described by Moffat [20] with estimates of derived values being calculated using the sequential perturbation method. A 95 percent confidence interval was used for the precision uncertainty estimates. The uncertainties are given in Table 3 for each of the values reported in this paper.

Fillet Design and Fabrication

Nine different fillets were simulated computationally prior to experimentally testing a final fillet design. The CFD results from each of the fillets were assessed in terms of the effectiveness each had on the reduction of the horseshoe vortex as compared to the baseline CFD simulations for the unfilleted vane. The design of the fillet was first guided by the criteria set by Sung and Lin [9] in which the length of the fillet be greater than the height. A review of the literature on various fillet geometries for symmetric airfoils suggested that the fillet be at least one boundary layer thickness in height. Figure 4 presents the characteristics of the seven fillet designs computationally simulated (Zess and Thole [21]).

The initial fillet design was based on a 1/7th power law profile, similar to the velocity profile for a turbulent boundary layer. This profile represents the shape of the fillet approaching the stagnation plane, as illustrated in Fig. 4(*a*). This design indicated no reduction in the horseshoe vortex. Since a 1/4 power law profile also resulted in no reduction of the horseshoe vortex, the power law profile fillets were abandoned. Instead, a symmetric fillet about the stagnation line was designed to have a linear slope approaching the stagnation. After multiple trials, a fillet 1δ high and 2δ long was found to be effective at eliminating the horseshoe vortex. Further analysis of the flow around the fillet indicated that the flow was separating off the suction side of the fillet, producing yet another vortex. To eliminate the separation off the suction side of the fillet, the geometry of only the suction side was modified to eliminate the separation. The final fillet design was asymmetric having dimensions 1δ high and 2δ long. The final fillet design is illustrated in Fig. 4(*b*).

The asymmetric fillet design was then constructed and placed within the low-speed wind tunnel for experimental verification. Laminated Object Manufacturing (LOM) facilities at the Milwaukee School of Engineering Rapid Prototyping Laboratory were used to create two mirror imaged fillets (for the top and bottom endwalls). These fillets were installed at the leading edge of the central vane on both the top and bottom endwalls as well as on the adjacent airfoils (top and bottom endwalls also) to ensure periodic flow in both passages of the test section.

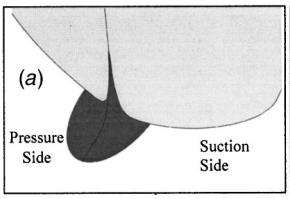

Height	Length	Description
1	1	1/7 profile
1	1	1/4 profile
1	2	elliptical, symmetric
1.5	2	elliptical, symmetric
1	1.5	elliptical, symmetric
1	1.5	elliptical, asymmetric
1	2	elliptical, asymetric

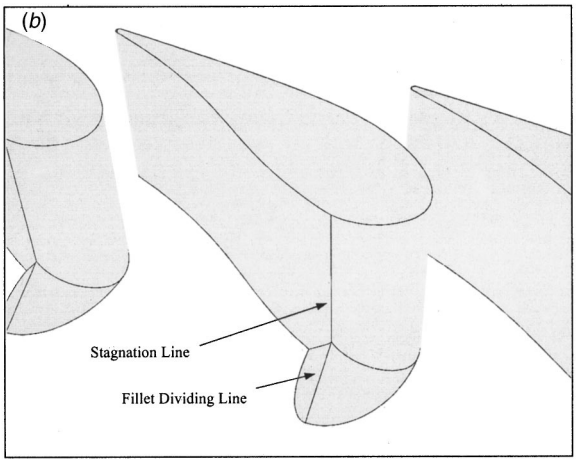

Fig. 4 Schematic illustrating an unsuccessful profile fillet (*a*) and the final fillet design (*b*) that was experimentally tested

For the remaining fillets (adjacent vanes), silicon molds of the two LOM fillets were made. The silicon molds were made by placing a fillet in a wooden box and covering half the fillet with modeling clay. Ultra-alloy silicon was poured over the exposed half of the fillet to form half the mold. After the first half of the mold cured, which required approximately 24 h, the clay was removed from the fillet. To allow air to be removed from the cavity of the silicon mold, a gating system was made by attaching straws to selected points of the fillet prior to pouring the second half of the mold. When the second half of the mold cured, the straws and fillet were removed and the mold was ready for use. A two-part polyurethane was poured into the mold cavity to form the fillets. When the polyurethane cured, the new fillet was removed from the mold and the gating system had to be broken off from the fillet. Because of the location of the adjacent vanes in the corner test section, the four extra fillets had to be cut nearly in half to fit in the correct positions. The fillets were then installed in the wind tunnel by placing a small amount of silicon adhesive between the fillet and the endwall and the fillet and the vane.

Experimental and Computational Results

The effectiveness of the fillet was determined through flow field measurements and predictions at various flow planes along the airfoil. These planes were normal to the airfoil (with the exception of the leading edge plane) and allowed the secondary flow field velocities to be clearly seen. Throughout this section of the paper, comparisons will be made between the flow field measurements with and without the fillet (previously made for this airfoil and reported by Kang et al. [2] and Kang and Thole [3]) and the computational results for the filleted vane.

The primary interest of this study was to discern any augmentations to the vortical patterns convecting through the turbine vane passage. To this purpose the flow planes were placed orthogonal to the vane with the velocity components being measured in this plane as was illustrated in Fig. 2. The velocity vectors of these vortices, which will be referred to as the secondary flow vectors, were determined by transforming the measured local velocities (u, v, and w in Fig. 2) into the mean flow direction based on that occurring at the midspan (V_s, V_n, and V_z). For this transforma-

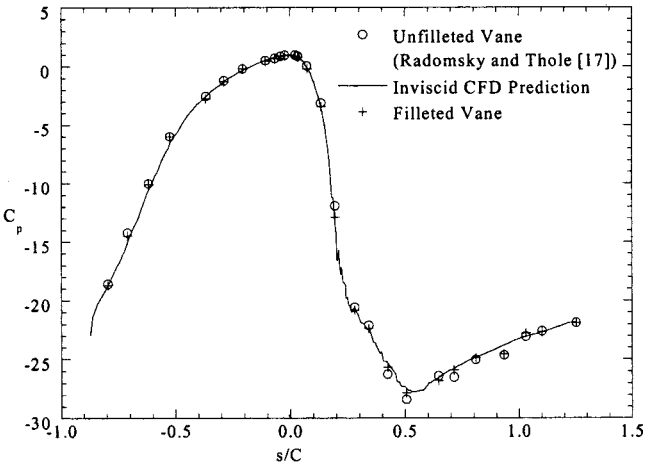

Fig. 5 Comparison of measured and computed static pressure distributions for the filleted and unfilleted vane

tion, the inviscid turning angle was calculated based on the measured velocities at the vane midspan with the relations between the secondary velocities and the midspan velocities given in the nomenclature of this paper. The secondary flow vectors are plotted using the components normal to the inviscid mean flow direction (V_n, V_z). In addition to the transformed velocities, contours of the secondary kinetic energy and turbulent kinetic energy are also presented.

Prior to measuring the flowfield, a comparison of the static pressure distribution at 40 percent of the span was made between the fillet and unfilleted geometry. Figure 5 shows a comparison for the vane with and without a fillet compared with the low speed, inviscid prediction for the unfilleted vane (note that the CFD prediction for the filleted geometry gave the same results). These

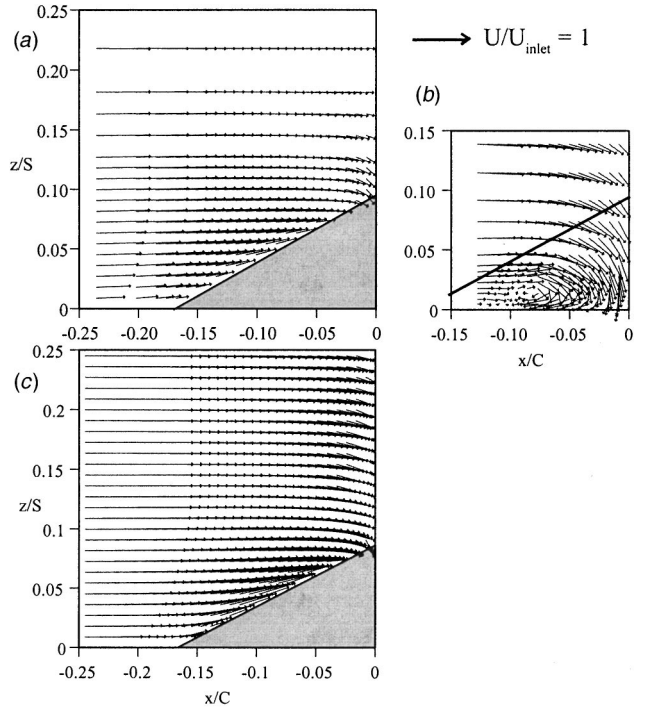

Fig. 6 Measured velocity vectors in plane SP for the (*a*) filleted, (*b*) unfilleted vane and (*c*) computed velocity vectors for the filleted vane

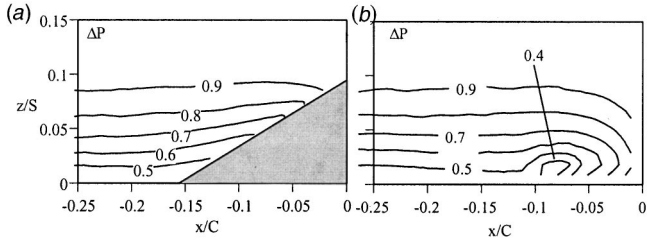

Fig. 7 Computed total pressure profiles in plane SP for the (*a*) filleted and (*b*) unfilleted vane

results indicated no alteration to the static pressure along the airfoil in adding the fillet in the leading edge region.

The Leading Edge Plane (Plane SP). Figures 6(*a*)–(*c*) depicts the measured velocity vectors, normalized by U_{inlet}, for the filleted and unfilleted vanes and the CFD predictions for the filleted vane, respectively. As can be seen, the addition of the fillet eliminated the vortex seen in this plane. As the flow approaches the vane, it does not separate from the endwall, but rather it accelerates up the fillet. Note that the line in Fig. 6(*b*) indicates the location of the fillet on the filleted vane. This line indicates that the core of the horseshoe vortex lies within the space that the fillet encompasses. A small downward flow along the vane surface and top of the fillet indicates that the flow is turning down the sides of the fillet. A comparison between the measurements and predictions indicate good agreement.

Figures 7(*a*) and (*b*) present computed total pressure contours for the filleted and unfilleted (Hermanson and Thole [16]) vanes. As was described previously for no fillet, there is a gradient of total pressure approaching the vane stagnation that drives the fluid down towards the endwall. By accelerating the flow, which happens in the case of the filleted vane, the downward force of the pressure gradient is overcome by the acceleration resulting in no horseshoe vortex formation. The total pressure profile for the filleted vane indicates no curling up of the contours. The contours are climbing up the fillet indicating that the flow is accelerating.

Figures 8(*a*) and (*b*) present the measured secondary kinetic energy contours in plane SP for the filleted and unfilleted vane. These secondary kinetic energy levels are a measure of the energy level of the secondary flows. As can be seen for this plane, the levels have been reduced by an order of magnitude due to the fillet. The secondary kinetic energy level contours along the fillet are a result of the flow being turned upward. Along the vane, in both the filleted and unfilleted cases, the secondary kinetic energy levels are due to the flow splitting at the stagnation location.

The most dramatic effects of the fillet are depicted in Figs. 9(*a*) and (*b*), which present the normalized turbulent kinetic energy levels for both the filleted and unfilleted geometries. There was no

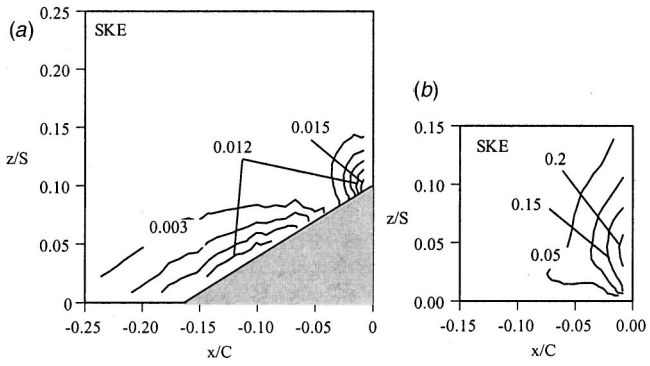

Fig. 8 Contours of measured secondary kinetic energy for (*a*) filleted and (*b*) unfilleted vane

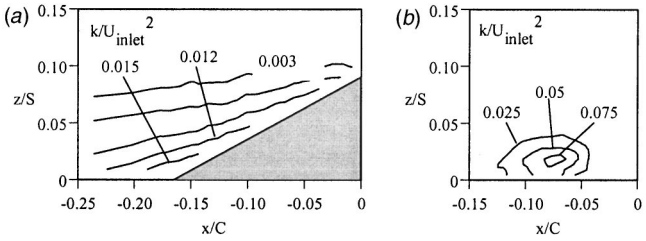

Fig. 9 Contours of measured secondary kinetic energy for (*a*) filleted and (*b*) unfilleted vane

indication of a vortex within the plane for the filleted case and the resulting contours were similar to a turbulent boundary layer. The peak in turbulent kinetic energy levels decreased for the filleted vane by nearly 80 percent. The results presented in this paper clearly show that by eliminating the horseshoe vortex the turbulent kinetic energy levels at all locations in the endwall region are reduced. This is important because the turbulent kinetic energy is a large contributor to aerodynamic losses in an airfoil passage (Gregory-Smith et al. [22]). Results previously reported by Radomsky and Thole [18]) have indicated that a large contributor to the high turbulent kinetic energy levels in the vortex regions are actually due to a vortex unsteadiness. The lower turbulent kinetic energy levels for the filleted vane as compared with the unfilleted vane indicate that the vortex is no longer present. Comparisons of turbulent kinetic energy between the CFD predictions and measurements did not indicate good agreement, which is to be expected given that it is believed that the vortex is highly unsteady.

Predicted streamlines for the filleted and unfilleted vanes are given in Figs. 10(*a*) and (*b*). The streamlines were released from a location that was 0–13 percent span and are colored by the normalized spanwise (w) component of velocity. Note that the position relative to the vane stagnation in the streamwise direction is slightly further upstream for the filleted vane ($x/C=-0.34$) as compared with the unfilleted vane ($x/C=-0.17$). It is evident that there is still a passage vortex that forms along the pressure side of the filleted vane, but the leading edge vortex does not seem to be present. Figure 10(*a*) also shows strong downward velocities along the suction side of the fillet. In contrasting Fig. 10(*a*) (the filleted vane) with Fig. 10(*b*) (the unfilleted vane), Fig. 10(*b*) clearly indicates a leading edge vortex with a stronger developing passage vortex.

Pressure Side Planes (PS0 and PS1). To verify the effect of the fillet on the development of the passage vortex, two downstream planes were compared. Plane PS0 was not measured in the unfilleted study of Kang and Thole [3] so the results of the experiment (Fig. 11(*a*)) will be compared to CFD results for both the filleted (Fig. 11(*b*)) and unfilleted (Figure 11*c*) cases. In comparing Figs. 11(*a*) and (*b*), there is good agreement between the measured and predicted secondary flows. Figure 11(*c*) shows that the passage vortex is definitely present in the CFD results for the unfilleted vane. The actual extent of the pressure side leg of the horseshoe vortex is hard to define in this plane because of its interaction with the cross and downflows, but is discernable by the flow turning away from the endwall. Figures 11(*a*) and (*b*), however, show that for the filleted vane there is a much different pattern. Because of the cross-passage pressure gradient, flow still travels along the endwall from the pressure side of the passage to the suction side. For the filleted vane there is no upward turning away from the endwall at this location indicating the disappearance of the pressure side leg of the horseshoe vortex at this location.

Figure 11(*d*) shows the normalized turbulent kinetic energy measured in plane PS0. The contours give no indication of a vortex and closely resemble a turbulent boundary layer. The magnitude of the peak turbulent kinetic energy has remained relatively constant from the plane SP to PS0.

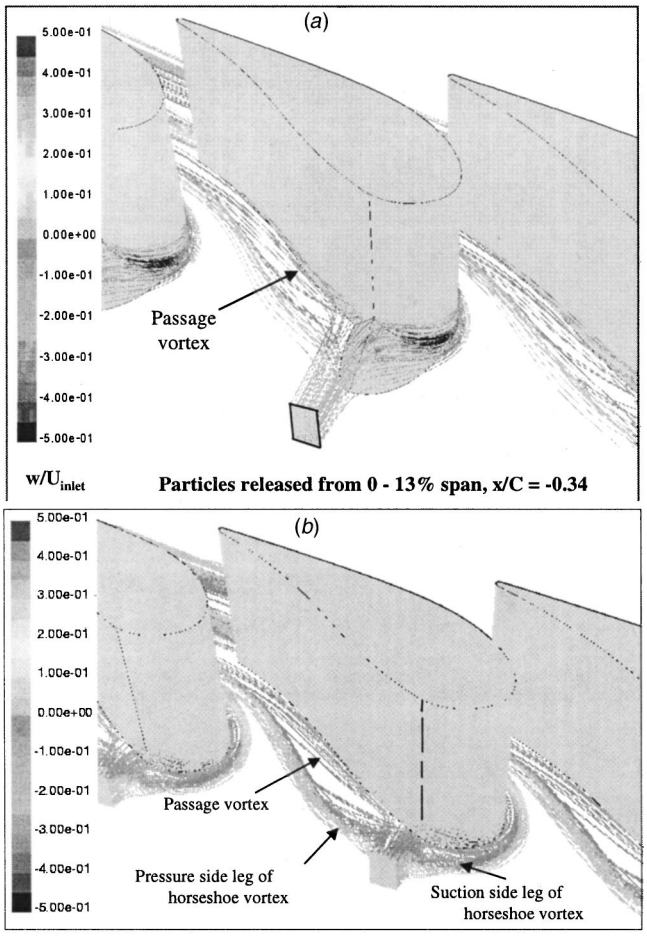

Fig. 10 Streamlines of a (*a*) filleted and (*b*) unfilleted vane

Moving farther down the pressure side of the vane to plane PS1, the measured secondary velocity vectors indicate a full passage vortex for the unfilleted vane (Fig. 12(*b*)), while the filleted vane shows the start of a passage vortex (Figs. 12(*a*) and (*c*)). The secondary velocity vectors for the filleted vane show that the vortex has not yet made a complete revolution within the measurement plane and the flow away from the endwall is relatively weak. For the unfilleted vane, the vortex does make a complete revolution and the flow away from the endwall is much stronger. The CFD results for the filleted vane shown in Fig. 12(*c*) indicates only a slight flow away from the endwall, as did the experiment.

The normalized turbulent kinetic energy levels for plane PS1 are shown in Figs. 12(*d*) and (*e*) for the filleted and unfilleted experimental results. The contours from the unfilleted experiment show a well-defined vortex core while the filleted results show much more uniform profiles in the pitch directions. The peak turbulent kinetic energy is decreased by nearly a factor of ten. In the filleted vane the largest fluctuations occur in the v-component of velocity, which is in contrast to the unfilleted vane where the largest fluctuations occur in the w-component of the velocity. Large fluctuations in the w-component (component normal to the endwall) indicate that for the unfilleted vane the unsteady vortex is bouncing to and from the wall.

Suction Side Plane (Plane SS1 and SS2). Measurements were performed along the suction side of the vane in Plane SS1. Figures 13(*a*)–(*e*) show the secondary velocity vectors for the experiments with and without the fillet for both measurements and

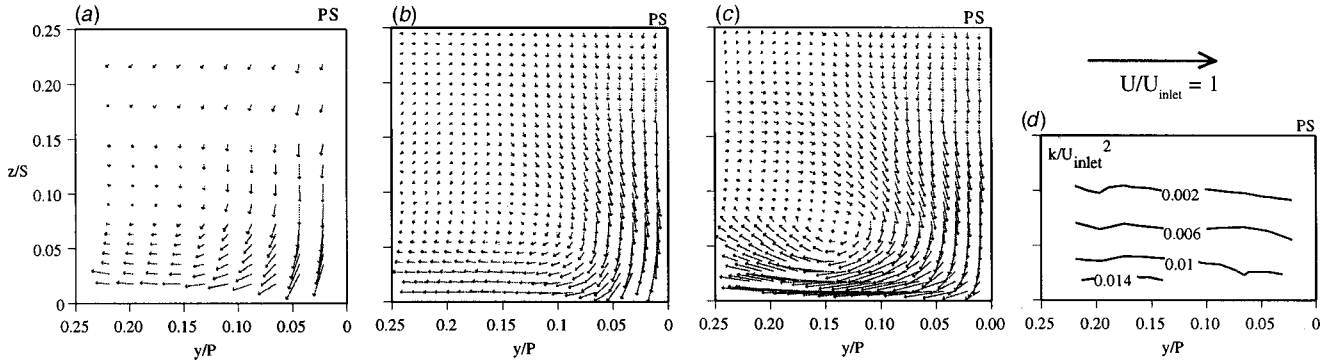

Fig. 11 Comparisons of secondary velocities in Plane PS0 for the (*a*) measured, and (*b*) computed filleted vane, and (*c*) computed unfilleted vane. Also shown are the measured turbulent kinetic energy levels for PS0 (*d*).

CFD predictions. Focusing on the region closest to the suction side-endwall corner, it can be seen that the secondary flows in this region for the filleted and unfilleted experiments are slightly different. The vortex in the corner region of the unfilleted vane (Fig. 13(*d*)) definitely shows an upward turn whereas in the measured and computed results for the filleted vane (Figs. 13(*a*) and (*c*)) there was only a downward velocity as the flow traveled down the suction side of the fillet. Another difference between the filleted and unfilleted experimental results is the stronger crossflow associated with the passage vortex in the unfilleted case. This stronger crossflow is consistent with the observations of plane PS1 where the crossflow component of the passage vortex was smaller in the filleted case.

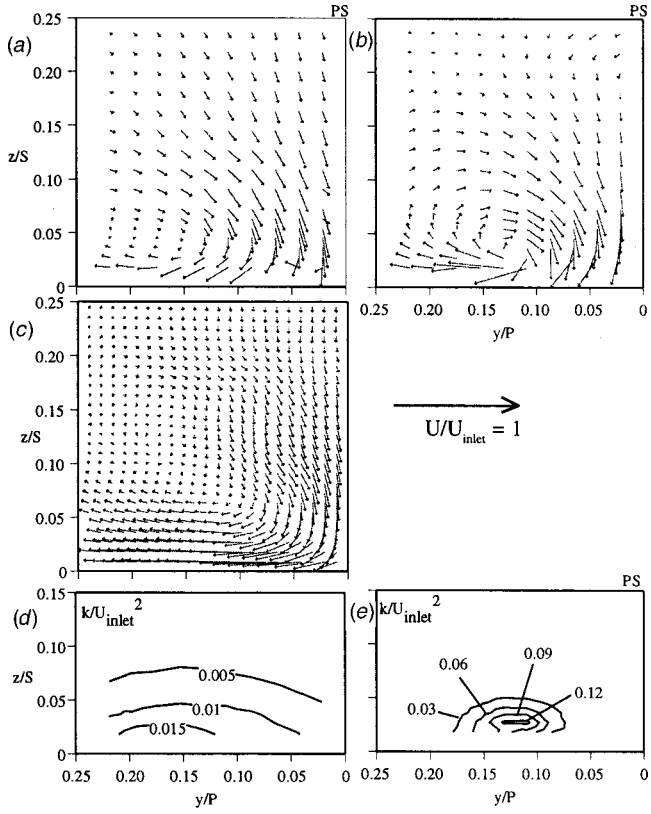

Fig. 12 Secondary velocity vectors measured for the (*a*) filleted, and (*b*) unfilleted vane compared with the (*c*) predicted for filleted vane in PS1. Contours of measured turbulent kinetic energy levels in Plane PS1 for the (*d*) filleted, and (*e*) unfilleted vane.

Figures 13(*b*) and (*d*) depict the turbulent kinetic energy for the filleted and unfilleted vanes. For the unfilleted vane the vortex structures can be seen by the regions of highest fluctuations coinciding with the vortex core of the suction side leg of the horseshoe vortex. For the filleted vane, the magnitude of the fluctuations in the suction side corner region was decreased by a factor of three. At this location, the passage vortex from the neighboring filleted vane has also progressed further downstream. Although the normal plane SS1 gives a skewed view of the neighboring vortex (since it is not normal to the neighboring vane), it can clearly be seen that even at this location, the turbulent kinetic energy levels are still lower for the filleted vane as compared to the unfilleted vane.

Further downstream at plane SS2, the computed secondary flows are presented in Figs. 14(*a*)–(*b*) for the filleted and unfilleted vanes. While a suction side vortex is present for both cases, it is much weaker for the filleted vane than for the unfilleted vane. In addition, the location of the passage vortex has shifted somewhat away from the endwall for the filleted vane. The predicted streamwise vorticity levels at this location are presented in Figs. 14(*c*)–(*d*) for both vanes. These levels indicate reduced levels in both the passage and suction corner vortices for the filleted vane as compared to the unfilleted vane.

Conclusions

Computational and experimental studies were performed on methods for reducing and/or eliminating the horseshoe vortex that forms at the leading edge of a gas turbine stator vane. A number of CFD simulations were made to design an effective fillet that resulted in a geometry that was one boundary layer thickness in height and two boundary layer thicknesses in length (protruding upstream of the vane). After the effective fillet geometry was designed, flow field measurements were made to verify its performance in a test section with a large-scale, linear vane cascade.

The flowfield results for a plane parallel to the inlet flow direction and located at the leading edge verified that the vortex was no longer present. The incoming boundary layer was accelerated as it traveled up the fillet surface resulting in no leading edge vortex formation. Near the top of the fillet, the flow did turn down the fillet sides, but the secondary kinetic energy levels associated with it decreased by nearly an order of magnitude over the levels measured without the fillet. The turbulent kinetic energy levels significantly decreased indicating that the fillet reduced the unsteadiness associated with the leading edge horseshoe vortex.

The results of the flow field measurements on the pressure side of the vane, just downstream of the stagnation region, also indicated the elimination of the horseshoe vortex and a delay in the development of the passage vortex. The turbulent kinetic energy levels appeared to be more consistent with wall-generated turbulence. Farther down the pressure side of the vane, the pitch and

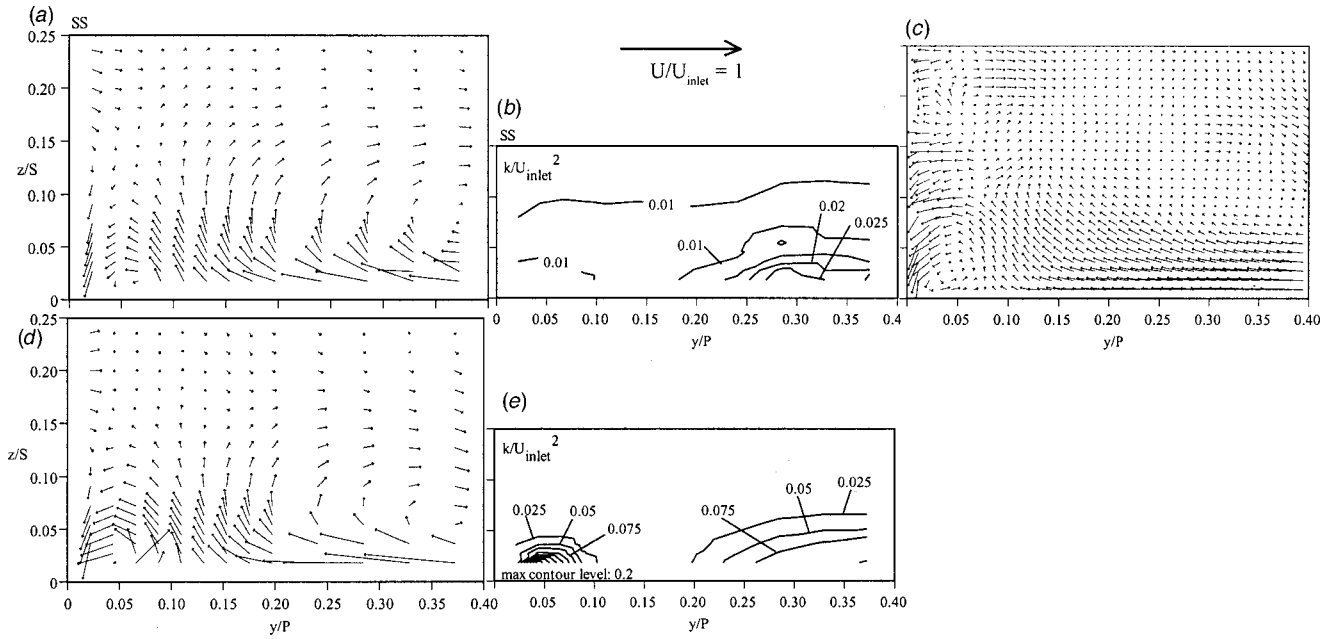

Fig. 13 Secondary velocity vectors in plane SS1 for measurements of the (*a*) filleted vane and computations of the (*c*) filleted vane and measurements of the (*d*) unfilleted vane. Contours of turbulent kinetic energy are shown for the (*b*) filleted and (*e*) unfilleted vanes.

span flows associated with the passage vortex were detected but were reduced with the addition of the fillet. This is in contrast to the unfilleted vane where the passage vortex was fully developed, making a complete rotation much earlier in the passage. The results presented in this paper indicate that the leading edge horseshoe vortex can be eliminated. The results of this study have shown significant reductions in the turbulent kinetic energy levels and in the streamwise vorticity levels both of which are large contributors to aerodynamic losses in a turbine vane passage.

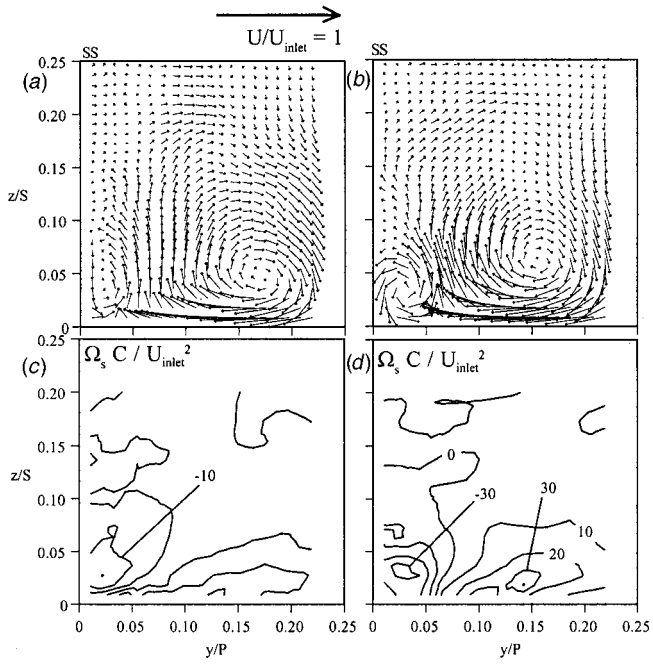

Fig. 14 Comparison of computed secondary flows (*a,b*) and vorticity (*c,d*) in plane SS2 for the filleted (*a,c*) and unfilleted (*b,d*) vane

Acknowledgments

The authors would like to acknowledge Pratt & Whitney for their support of this work with Fred Soechting and William Kvasnak serving as the contract monitors. The authors would also like to acknowledge the University of Wisconsin where G. A. Zess completed his MS degree.

Nomenclature

C = true chord of stator vane
Cp = static pressure coefficient, $(p-p_{\text{inlet}})/(P_o-p_{\text{inlet}})$
H = shape factor, δ^*/θ
k = turbulent kinetic energy, $k=1/2(u_{\text{rms}}^2+v_{\text{rms}}^2+w_{\text{rms}}^2)$
p = local static pressure
p_{inlet} = inlet static pressure
P_o = total inlet pressure
P = vane pitch
ΔP = normalized total pressure, $1-((P_{o,\text{ms}}-P_o)/(P_{o,\text{ms}}-p_{\text{inlet}}))$
Re_{in} = Reynolds no. defined as $\text{Re}_{\text{in}}=CU_{\text{inlet}}/\nu$
s = surface distance along vane measured from stagnation
S = span of vane
SKE = secondary kinetic energy, $(V_n^2+V_z^2)/(1/S)\int U_{\text{inlet}}^2 dz$
u_τ = shear velocity, $\sqrt{\tau_w/\rho}$
u^+ = velocity in inner coordinates, u/u
u,v,w = mean local velocity in local coordinate system
U,V,W = mean velocity in X, Y, Z directions
U_{inlet} = incident upstream velocity
V_s = streamwise velocity component, $u\cos\psi_{\text{ms}}+v\sin\psi_{\text{ms}}$
V_n = secondary velocity in pitch direction, $-u\sin\Psi_{\text{ms}}+v\cos\Psi_{\text{ms}}$
V_z = secondary velocity normal direction
x, y, z = local coordinates defined at measurement location
X, Y, Z = global coordinates defined from stagnation location
δ_{99} = boundary layer thickness

δ^* = displacement thickness
θ = momentum thickness
ρ = density
Ω_s = streamwise vorticity, $\Omega_x \cos(\Psi_{ms}) + \Omega_y \sin(\Psi_{ms})$
Ω_x, Ω_y = x and y vorticity components
τ_w = wall shear stress
ν = viscosity
Ψ_{ms} = inviscid mid-span turning angle, $\tan^{-1}(v_{ms}/u_{ms})$

Subscripts

in = inlet
ms = midspan values
rms = root mean square

Superscripts

$+$ = normalization using inner scaling coordinates

References

[1] Langston, L. S., 1980, ''Crossflows in a Turbine Cascade Passage,'' ASME J. Eng. Power, **102**, pp. 866–874.
[2] Kang, M., Kohli, A., and Thole, K. A., 1999, ''Heat Transfer And Flowfield Measurements in the Leading Edge Region of a Stator Vane Endwall,'' ASME J. Turbomach., **121**, pp. 558–568.
[3] Kang, M., and Thole, K. A., 2000, ''Flowfield Measurements in the Endwall Region of a Stator Vane,'' ASME J. Turbomach., **122**, pp. 458–466.
[4] Kubendran, L. R., Bar-Sever, A., and Harvey, W. D., 1988, ''Flow Control in a Wing/Fuselage Type Juncture,'' AIAA Pap., AIAA-88-0614.
[5] Eckerle, W. A., and Langston, L. S., 1987, ''Horseshoe Vortex Formation Around a Cylinder,'' ASME J. Turbomach., **109**, pp. 278–285.
[6] Pierce, F. J., and Shin, J., 1992, ''The Development of a Turbulent Junction Vortex System,'' ASME J. Fluids Eng., **114**, pp. 559–565.
[7] Praisner, T. J., Seal, C. V., Takmaz, L., and Smith, C. R., 1997, ''Spatial-Temporal Turbulent Flow-Field and Heat Transfer Behavior in End-Wall Junctions,'' Int. J. Heat Fluid Flow, **18**, pp. 142–151.
[8] Kubendran, L. R., and Harvey, W. D., 1985, ''Juncture Flow Control Using Leading-Edge Fillets,'' AIAA Pap., AIAA-85-4097.
[9] Sung, C.-H., and Lin, C.-W., 1988, ''Numerical Investigation on the Effect of Fairing on the Vortex Flows Around Airfoil/Flat—Plate Junctures,'' AIAA Pap., AIAA-88-0615.
[10] Sung, C.-H., Yang, C.-I., and Kubendran, L. R., 1988, ''Control of Horseshoe Vortex Juncture Flow Using a Fillet,'' Symp on Hydrodynamic Performance Enhancement for Marine Applications, Newport, RI.
[11] Devenport, W. J., Simpson, R. L., Dewitz, M. B., and Agarwal, N. K., 1991, ''Effects of a Strake on the Flow Past a Wing—Body Junction,'' AIAA Pap., AIAA-91-0252.
[12] Bernstein, L., and Hamid, S., 1995, ''On the Effect of a Strake-Like Junction Fillet on the Lift and Drag of a Wing,'' Aeronaut. J., Feb., pp. 39–52.
[13] Sauer, H., Mueller, R., and Vogeler, K., 2000, ''Reduction of Secondary Flow Losses in Turbine Cascades by Leading Edge Modifications at the Endwall,'' ASME Paper, 2000-GT-0473.
[14] Devenport, W. J., Agarwal, N. K., Dewitz, M. B., Simpson, R. L., and Poddar, K., 1990, ''Effects of a Fillet on the Flow Past a Wing—Body Junction,'' AIAA J., **28**, pp. 2017–2024.
[15] Fluent User's Guide, 1998, Version 5, Fluent Inc., NH.
[16] Hermanson, K., and Thole, K. A., 2000, ''Effect of Inlet Profiles on Endwall Secondary Flows,'' J. Propul. Power, **16**, pp 286–296.
[17] Radomsky, R., and Thole, K. A., 2000, ''Highly Turbulent Flowfield Measurements Around a Stator Vane,'' ASME J. Turbomach., **122**, pp. 255–262.
[18] Radomsky, R., and Thole, K. A., 2002, ''High Freestream Turbulence Effects in the Endwall Leading Edge Region,'' (ASME Paper 2000-6T-202), ASME J. Turbomach., **124**, pp. 107–118.
[19] White, F. M., 1974, *Viscous Fluid Flow*, McGraw-Hill, New York.
[20] Moffat, R. J., 1988, ''Describing the Uncertainties in Experimental Results,'' Exp. Therm. Fluid Sci., **1**, pp. 3–17.
[21] Zess, G. A., and Thole, K. A., 1999, ''Methods to Reduce the Leading Edge Horseshoe Vortex in a Gas Turbine Stator Vane,'' Report 99-3, University of Wisconsin.
[22] Gregory-Smith, D. G., Walsh, J. A., Graves, C. P., and Fulton, K. P., 1988, ''Turbulence Measurements and Secondary Flows in a Turbine Rotor Cascade,'' ASME J. Turbomach., **110**, pp. 479–485.

Midspan Flow-Field Measurements for Two Transonic Linear Turbine Cascades at Off-Design Conditions

D. B. M. Jouini

S. A. Sjolander
e-mail: ssjoland@mae.carleton.ca

Department of Mechanical and Aerospace Engineering,
Carleton University,
Ottawa, Ontario, K16 5B6, Canada

S. H. Moustapha
Pratt & Whitney Canada Inc.,
Longueuil, Quebec, Canada

The paper presents detailed midspan experimental results from two transonic linear turbine cascades. The blades for the two cascades were designed for the same service and differ mainly in their leading-edge geometries. One of the goals of the study was to investigate the influence of the leading-edge metal angle on the sensitivity of the blade to positive off-design incidence. Measurements were made for incidence values of −10.0, 0.0, +4.5, +10.0, and +14.5 deg relative to design incidence. The exit Mach numbers varied roughly from 0.5 to 1.2 and the Reynolds numbers from about 4×10^5 to 10^6. The measurements include the midspan losses, blade loadings and base pressures. In addition, the axial-velocity-density ratio (AVDR) was extracted for each operating point. The AVDR was found to vary from about 0.98 at −10.0 deg of incidence to about 1.27 at +14.5 deg. Thus, the data set also provides some evidence of the influence AVDR on axial turbine blade performance. Detailed experimental results for turbine blade performance at off-design incidence are very scarce in the open literature, particularly for transonic conditions. Among other things, the present results are intended to expand the database available in the open literature. To this end, the key aerodynamic results are presented in tabular form, along with the detailed geometry of the cascades. The results could be used in the development of new or improved correlations for use in the early stages of design. They could also be used to evaluate the ability of current CFD codes to capture reliably the variation in losses and other aerodynamic quantities with variations in blade incidence. [DOI: 10.1115/1.1458576]

Introduction

The aerodynamic design of turbine blades is one of the areas where improvements in blade performance over the range of operating conditions may lead to gains in turbine efficiency. The improvements in blade performance are measured in terms of reduction in blade losses. Thus, the goals of the blade designer are to produce blade shapes that have low losses at the design flow conditions and also to extend the envelope of the blade minimum losses to a wide range of blade operating conditions. These varying operating conditions include changes in operating Mach number, blade incidence, and blade Reynolds number.

Over the past decades, investigations in linear turbine cascades have led to the development of a number of correlations for blade losses and outlet flow angles. These correlations are intended to be used at an early stage of the design to account for the effects of some of the geometric and flow parameters on the aerodynamic performance of the blade design under consideration. Using the correlations, an initial machine geometry can be obtained and some optimization can be performed. Unfortunately, the existing correlations are largely limited to subsonic flow conditions. Also, transonic Mach number data is scarce in the open literature and the majority of the data are limited to the design incidence flow conditions. Hence, more data are needed in the transonic Mach number range, and in particular at off-design incidence. These data will help in the understanding of the flow physics and augment the data base available in the open literature so that improved loss and exit flow correlations at design and off-design incidence may be devised. They could also be used to evaluate the ability of existing CFD codes to capture reliably the variation in losses and other aerodynamic parameters with variation in blade incidence as a result of changes in blade designs.

A number of low-speed experimental studies have been carried out to investigate the effect of incidence on the performance of turbine cascades [1–3]. Profile and secondary losses correlations have been developed and improved over the years to include the induced incidence and leading edge geometry and to reflect recent trends in turbine design [4–7]. The effect of axial velocity density ratio (AVDR) has been investigated experimentally at low speed [1,2] and computationally at high speed [8]. The effects of compressibility on both profile and secondary losses, and the flow physics more generally, have also investigated by a number of researchers [9–12].

All of the above investigations have resulted in a better understanding of the flow field in turbine passages. However, there is still a lack of data on the performance of turbine blades of small aspect ratio (0.6 to 1.0) and high turning (100 to 130 deg) operating at varying incidences (up to ±30 deg relative to design), transonic Mach numbers (0.8 to 1.4) and down to very low Reynolds numbers (as low as 50,000).

The present work is part of a collaborative project between Pratt & Whitney Canada and Carleton University to address this lack of data. The ultimate objective is to develop improved design rules for small, low cost and efficient turbines. Krieger et al. [13] tested a realistic turbine stage in a cold flow rotating rig at various pressure ratios, speeds and Reynolds numbers. Jouini et al. [14] tested the mean section of the same turbine blade in a linear cascade in the Carleton University High Speed Wind Tunnel for various values of incidence angle and exit Mach number. This is the baseline cascade (designated HS1A) which was tested. A second cascade (designated HS1B) with a modified leading edge design was also tested. The modified geometry was designed by Pratt &

Contributed by the International Gas Turbine Institute and presented at the International Gas Turbine and Aeroengine Congress and Exhibition, New Orleans, Louisiana, June 4–7, 2001. Manuscript received by the IGTI, December 14, 2000. Paper No. 2001-GT-493. Review Chair: R. A. Natole.

Whitney Canada, and was intended to investigate one possible approach to reducing the sensitivity of the blade to off-design incidence. For completeness, some of the results from Jouini et al. [14] for HS1A are repeated here, along with the new results for HS1B. Together, these results expand the data base available in the open literature for transonic turbine aerodynamics at both design and off-design conditions. All of the key aerodynamic results are presented in tabular form, along with the detailed geometry of the cascades.

Experimental Apparatus and Procedures

High-Speed Wind Tunnel. All measurements were obtained using the Carleton University High Speed Wind Tunnel shown in Fig. 1 [15]. The wind tunnel is of the blow-down type and is used mainly for transonic turbine cascade research. The wind tunnel exhausts to the laboratory. It is equipped with an ejector-diffuser system to allow the cascade outlet pressure to be controlled independently of the blowing pressure. However, the ejector diffuser system was not used in the present measurements. Typical wind tunnel runtimes range from 15 to 30 s, depending on the blowing pressure and the Mach number level, and up to four runs per hour are possible. Typical blowing pressures are 2 to 3 bars and cascade exit Mach numbers as high as 1.5 can be achieved. The turbulence intensity in the test section is about 4 percent [16]. A more detailed description of the wind tunnel is given in Jeffries [17].

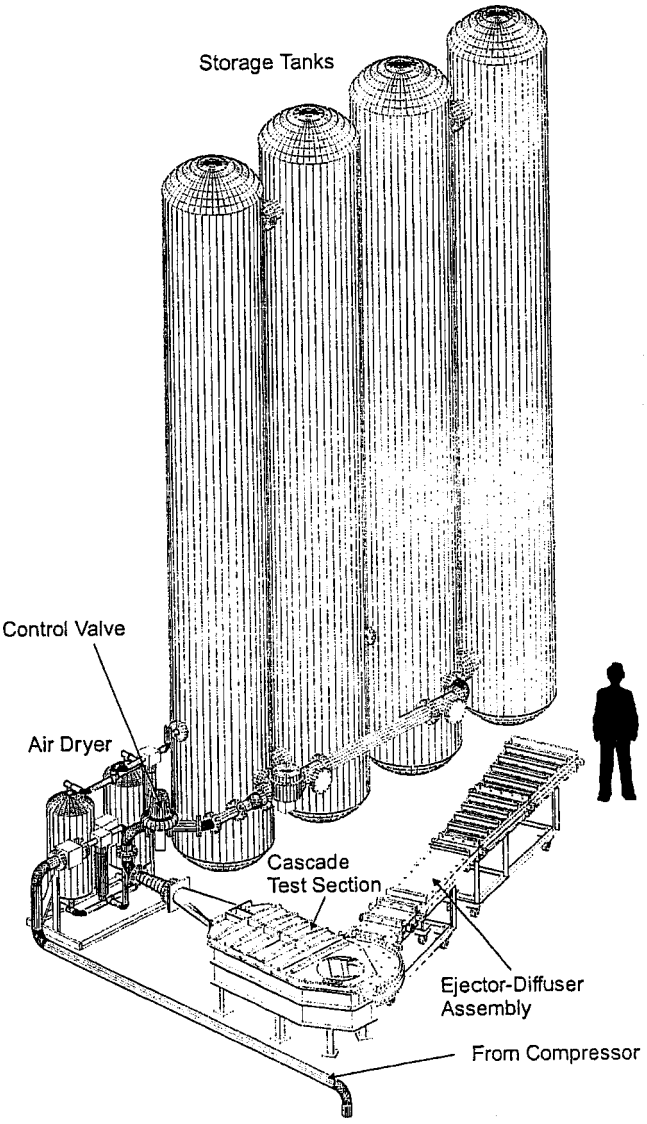

Fig. 1 Carleton University blowdown wind tunnel [15]

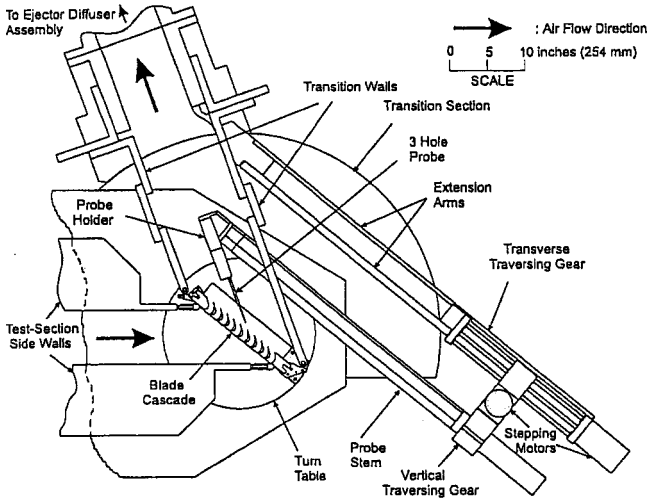

Fig. 2 Plan view of the cascade test section

Cascade Test Section and Test Cascade. A schematic diagram of the cascade test section is shown in Fig. 2. The test cascade is mounted on a turntable which allows variations in incidence of about ± 20 deg. The blade span is fixed at 61 mm. The geometry of the cascades used in this investigation is summarized in Figs. 3 and 4 and Tables 1(*a*) and (*b*). The baseline blade geometry, designated by HS1A, represents the midspan section of a high pressure turbine from a Pratt & Whitney Canada engine of recent design. The design incidence for HS1A blade is -4.5 deg. The second blade, designated by HS1B, represents a derivative of the HS1A blade and it differs mainly in the leading edge geometry. The design incidence for the HS1B blade is -15.0 deg. Both HS1A and HS1B blades were designed for the same service and as shown from Fig. 3, except for the differences in the leading edge metal angle, both blades have the same geometric parameters. Each cascade consists of seven blades and eight complete passages. Two of the blades in the middle of each cascade were instrumented with static taps at midspan. Table 2 summarizes the number and distribution of pressure taps for both cascades. The blades with suction surface taps also have a base-pressure tap on the trailing edge. The ratio of the diameter of the base-pressure tap to the trailing-edge thickness is 0.203.

The cascade were tested for exit Mach numbers from 0.5 to 1.2. The corresponding Reynolds numbers varied from approximately 4×10^5 to 10^6. Incidence values of $+14.5$, $+10$, $+4.5$, and 0 deg relative to design were examined for both blades. Only HS1A was examined at -10 deg since the interest is particularly in the behavior of HS1B at positive values of incidence.

Instrumentation and Experimental Procedures. All flowfield measurements were obtained using a three hole pressure probe. The probe tip has a width of 1.37 mm (0.054 in.) which is roughly 4.7 percent of the blade pitch, and a thickness of 0.46 mm (0.018 in.). Static pressures downstream of the cascade were also measured directly using a cylindrical static pressure probe. The probe tip has a cone angle of 15 deg and two static taps are located 180 deg apart at about 12 diameters from the tip. The static probe has a tip outer diameter of 1.02 mm (0.04 inch) which is approximately 3.5 percent of the blade pitch. Both probes were designed by Islam [18]. For loss calculations, the static pressures obtained with the static probe were combined with total pressures and exit flow angles obtained from the three hole probe. The losses quoted are the fully mixed-out values calculated using the

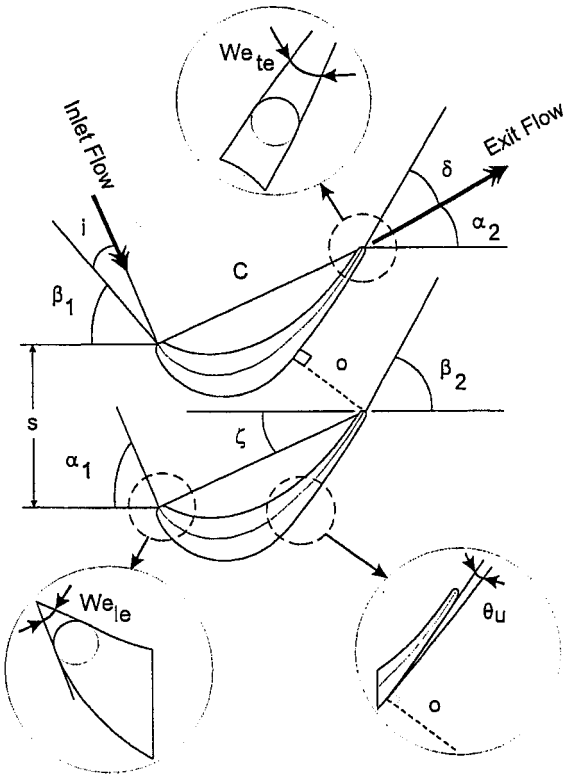

Cascade Parameters	HS1A	HS1B
Chord Length, C	40.0 mm	40.0 mm
Axial Chord, Cx	36.98	36.98
Blade Span, H	61.0 mm	61.0 mm
Blade Spacing, s	29.14	29.14
Trailing Edge Thickness, t	1.25 mm	1.25 mm
Aspect Ratio, H/C	1.525	1.525
Leading Metal Angle, β_1	50.5°	61.0°
Trailing Metal Angle, β_2	59.0°	59.0°
Leading Edge Wedge Angle, We_{te}	38.0°	38.0°
Trailing Edge Wedge Angle, We_{te}	6.0°	6.0°
Maximum Thickness-to-Chord Ratio	0.196	0.182
Design Incidence, i_{des}	-4.5°	-15.0°
Stagger Angle, ζ	25.1°	24.7°
Throat Opening, o	15.3 mm	15.3 mm
Unguided Turning, θ_u	11.5°	11.5°

Fig. 3 Summary of blades geometric parameters and nomenclature

procedures of Amecke and Šafařík [19]. Mixed values were also used where downstream parameters, such as the static or dynamic pressure, were needed in quantities such as the base pressure coefficient.

All pressures were measured using a 48-port Scanivalve system and a miniature, fast-response Kulite pressure transducer which is mounted in the Scanivalve housing. The outputs from the pressure transducer were recorded using a Hewlett-Packard high-speed

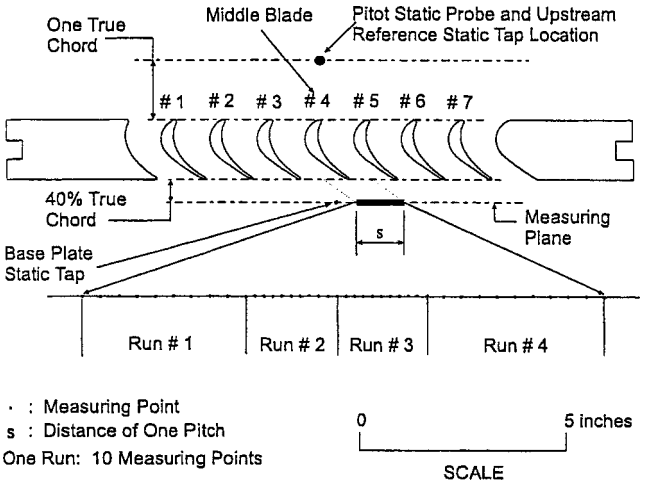

Fig. 4 Cascade blade row measurement locations

data acquisition system which was controlled by a microcomputer. Pressures were sampled for 0.1 s at a frequency of 2000 Hz based on investigations by Jeffries et al. [15].

The temperature in the storage tanks, and thus the total temperature T_{01} in the test section, typically starts at 13 to 20°C. The total temperature drops as the air in the tanks expands during a run. Therefore, T_{01} was measured upstream of the cascade during each run. Table 3 summarizes the temperature changes which were measured for several typical operating points. Also shown are the corresponding average Reynolds numbers and the variation in Reynolds number which corresponds to the variation in the total temperature. Finally, the estimated variations in the profile loss coefficients due to the Reynolds number variations are also given. These estimates are based on data for the variation in loss coefficient with Reynolds number which are presented later. As seen, the variation in the loss coefficient during the run is quite small compared with the mean value. The variation is also less than the estimated uncertainty in the loss coefficients due to all sources. It should also be mentioned that, for the loss calculations, the total temperature was assumed equal at the inlet and outlet planes of the cascade, even though a small amount of heat transfer would be occurring during a run. Jouini [20] has estimated in detail the total temperature variations which could occur across the cascade for different operating points. He also calculated the corresponding changes in the loss coefficients. The resulting uncertainty this introduces into the loss coefficients is less than the overall estimated uncertainty and is considered to be included in that overall value. Finally, it should be mentioned that several runs of the wind tunnel are made before a series of data runs are begun. These pre-runs are used to cool the cascade blades and the walls of the test section and thus reduce the heat transfer during the data runs.

The locations of the upstream and downstream traverse planes are indicated in Fig. 4. Downstream of the cascade, four runs are normally used to traverse the flow over one blade pitch. Measurements are made at a total of 40 points, with the spacing being halved for the 20 points which span the blade wake. Figure 5 shows sample total pressure distribution behind the three middle blades in the cascade at an incidence of +4.5 deg and for three Mach numbers. As shown, the wake profiles were very similar, indicating that there is good periodicity in the cascade flow. Static pressure and exit flow angle measurements, not presented here, behind the three middle blades also show similar wake profiles. The periodicity is somewhat poorer at high values of both positive and negative incidence at Mach numbers above 1.1. The measured flow quantities are estimated to have the following uncertainties: static pressures, ±2 percent of the local dynamic pressure; flow angles, ±0.5 deg; and exit Mach numbers, ±0.02. The estimated

Table 1 (*a*) HS1A Pratt & Whitney blade coordinates, (*b*) HS1B Pratt & Whitney blade coordinates

Suction Surface		Pressure Surface	
x (in)	y (in)	x (in)	y (in)
-0.26634	-0.01086	-0.26634	-0.01086
-0.26339	0.0005	-0.26339	-0.0213
-0.26044	0.00748	-0.26044	-0.02504
-0.25749	0.01379	-0.25749	-0.02746
-0.25454	0.01958	-0.25454	-0.0291
-0.25159	0.02494	-0.25159	-0.03015
-0.23684	0.04702	-0.23684	-0.02846
-0.22209	0.06397	-0.22209	-0.02021
-0.20734	0.0776	-0.20734	-0.01345
-0.19259	0.08881	-0.19259	-0.00798
-0.17784	0.09809	-0.17784	-0.00365
-0.16309	0.10576	-0.16309	-0.00032
-0.14834	0.11203	-0.14834	0.00208
-0.13359	0.11702	-0.1336	0.00362
-0.11884	0.12082	-0.11884	0.00434
-0.10409	0.12351	-0.10408	0.00428
-0.08934	0.1251	-0.08934	0.00346
-0.07459	0.12563	-0.07458	0.0019
-0.05984	0.1251	-0.05984	-0.00037
-0.04509	0.1235	-0.04509	-0.00336
-0.03034	0.1208	-0.03034	-0.00705
-0.01559	0.11697	-0.01559	-0.01142
-0.00084	0.11194	-0.00084	-0.01649
0.01391	0.10565	0.01391	-0.02224
0.02866	0.098	0.02866	-0.02869
0.04341	0.08886	0.04341	-0.03583
0.05816	0.0781	0.05816	-0.04367
0.07291	0.06559	0.07291	-0.05222
0.08766	0.05121	0.08766	-0.06147
0.10241	0.035	0.10241	-0.07145
0.11716	0.01724	0.11716	-0.08216
0.13191	-0.00154	0.13191	-0.09361
0.14666	-0.02097	0.14666	-0.10582
0.16141	-0.04084	0.16141	-0.11881
0.17617	-0.06099	0.17617	-0.1326
0.19091	-0.08128	0.19091	-0.1472
0.20566	-0.10169	0.20566	-0.16263
0.22042	-0.12223	0.22041	-0.17891
0.23516	-0.14294	0.23517	-0.19606
0.24991	-0.16394	0.24991	-0.21407
0.26466	-0.18538	0.26466	-0.23296
0.27941	-0.20749	0.27941	-0.25276
0.29416	-0.23059	0.29416	-0.27346
0.30006	-0.2402	0.30006	-0.282
0.30301	-0.2451	0.30301	-0.28633
0.30596	-0.25007	0.30596	-0.2906
0.30891	-0.25512	0.30891	-0.29302
0.31187	-0.26026	0.31186	-0.29406
0.31481	-0.26546	0.31481	-0.29416
0.31776	-0.27078	0.31776	-0.29334
0.32071	-0.2762	0.32072	-0.29131
0.32366	-0.28422	0.32366	-0.28422

Table 1 (*continued*)

Suction Surface		Pressure Surface	
x (in)	y (in)	x (in)	y (in)
-0.26003	-0.01896	-0.26003	-0.01896
-0.25708	-0.00325	-0.25709	-0.0294
-0.25414	0.00683	-0.25413	-0.03314
-0.25118	0.01511	-0.25118	-0.03556
-0.24824	0.02217	-0.24823	-0.0372
-0.24528	0.02845	-0.24528	-0.03826
-0.23053	0.05253	-0.23053	-0.03656
-0.21579	0.06982	-0.21578	-0.0249
-0.20104	0.08324	-0.20103	-0.01506
-0.18629	0.09399	-0.18628	-0.00726
-0.17154	0.10268	-0.17153	-0.00111
-0.15678	0.10969	-0.15678	0.00366
-0.14203	0.11524	-0.14203	0.00721
-0.12728	0.11948	-0.12728	0.00965
-0.11253	0.12253	-0.11254	0.01109
-0.09778	0.12445	-0.09778	0.01157
-0.08303	0.12528	-0.08303	0.01114
-0.06828	0.12505	-0.06827	0.00985
-0.05353	0.12376	-0.05353	0.00771
-0.03878	0.1214	-0.03878	0.00475
-0.02403	0.11796	-0.02403	0.00099
-0.00928	0.11339	-0.00928	-0.00356
0.00547	0.10763	0.00547	-0.00889
0.02022	0.10062	0.02022	-0.015
0.03497	0.09226	0.03497	-0.0219
0.04972	0.08244	0.04972	-0.02957
0.06446	0.07105	0.06447	-0.03803
0.07921	0.05799	0.07923	-0.04727
0.09396	0.04323	0.09397	-0.05729
0.10872	0.02683	0.10872	-0.0681
0.12347	0.00906	0.12347	-0.07971
0.13822	-0.00971	0.13822	-0.09211
0.15297	-0.02912	0.15297	-0.10532
0.16772	-0.04899	0.16772	-0.11935
0.18247	-0.06912	0.18247	-0.13419
0.19722	-0.08941	0.19722	-0.14986
0.21197	-0.10982	0.21197	-0.16634
0.22672	-0.13035	0.22672	-0.18362
0.24147	-0.15105	0.24147	-0.2017
0.25622	-0.17205	0.25622	-0.22054
0.27097	-0.1935	0.27097	-0.24015
0.28571	-0.2156	0.28572	-0.26046
0.30046	-0.23869	0.30047	-0.2815
0.30637	-0.2483	0.30637	-0.29009
0.30931	-0.2532	0.30932	-0.29443
0.31226	-0.25817	0.31226	-0.2987
0.31521	-0.26322	0.31521	-0.30113
0.31817	-0.26836	0.31816	-0.30216
0.32111	-0.27357	0.32111	-0.30226
0.32406	-0.27889	0.32406	-0.30145
0.32701	-0.28431	0.32702	-0.29941
0.32996	-0.29233	0.32996	-0.29233

uncertainty for the mixed-out total pressure loss coefficients is ± 0.005 for exit Mach numbers less than 0.5, ± 0.003 for Mach numbers from 0.5 to 0.85, ± 0.004 for Mach numbers between 0.85 and 1.1, and ± 0.005 for Mach numbers greater than 1.1. The estimated uncertainties are based on observed variations from blade to blade as well as repeatability runs made at a given operating point.

Results and Discussion

Axial Velocity Density Ratio (AVDR). Results are presented first for the axial velocity density ratio (AVDR) since the value of AVDR probably has an influence on most of the other results to be presented in the following sections. Physically, the AVDR is the ratio of the mass flow rates per unit area at inlet and outlet of the cascade. Thus, AVDR becomes a measure of the average contraction or expansion of the streamtube at the blade midspan. An AVDR of 1.0 is therefore a necessary, but not sufficient, condition for a two-dimensional midspan flow.

Figures 6(*a*) and (*b*) show the effects of both incidence and

Table 2 Blade static taps distribution and numbers

	HS1A	HS1B
Pressure Surface	19	17
Suction Surface	22	24
Base Pressure	1	1

Table 3 Typical variations in total temperature and Reynolds number during a run at design incidence

M_2	ΔT_{o1} (°C)	Average Re	$\pm\Delta$Re	$Y_t \pm \Delta Y_t$
0.55	7	500,000	5,500	0.0729 ± 0.0014
0.71	12	660,000	13,000	0.0666 ± 0.0002
1.14	19	1,040,000	97,000	0.0997 ± 0.0011

Mach number on the AVDR for HS1A and HS1B cascades respectively. As shown, the behavior of AVDR with Mach number for HS1B cascade is similar to the one observed for the HS1A cascade, with both showing relatively constant values with Mach number for a given incidence.

The variation of the AVDRs with incidence for both HS1B and HS1A cascades are summarized in Table 4 for an outlet Mach number near the design value of $M_2 = 1.05$. Table 4 shows that the AVDR values for the HS1B cascade are slightly higher than the ones for the HS1A cascade at the incidence values of 0.0 and +4.5 deg, and comparable at the incidence values of +10.0 and +14.5 deg. The differences in AVDR for HS1A and HS1B at low incidence are larger than the estimated uncertainty of ±0.02. Thus there seems to be some differing influence on AVDR for the two cascades at low incidence. At the incidence values of +10.0 and +14.5 deg, the differences in AVDR for HS1A and HS1B are within the estimated uncertainty of ±0.02. For a given value of incidence, comparable differences in AVDRs to the ones shown in Table 4 are also found between HS1A and HS1B at Mach numbers other than design.

There is little information available on the effects of AVDR on turbine cascade performance and the factors that influence AVDR. The effects which are thought to influence AVDR include the blade aspect ratio and the inlet endwall boundary layer thickness. However, these are very similar for HS1A and HS1B at all values of incidence. At the incidence values of 0.0 and +4.5 deg there

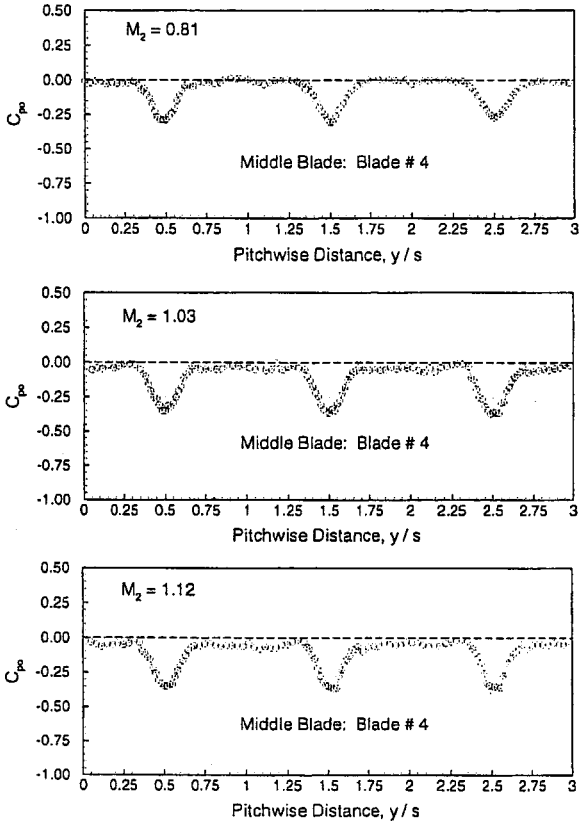

Fig. 5 Cascade downstream total pressure at off-design incidence, $i - i_{des} = 4.5$ deg, HS1A cascade

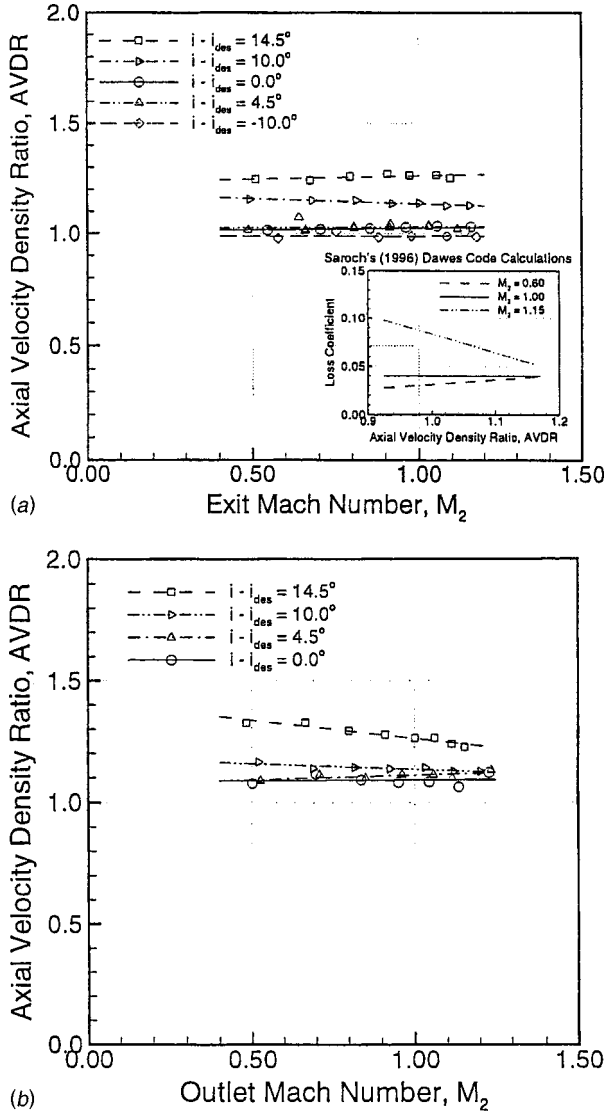

Fig. 6 Effects of incidence and Mach number on axial velocity density ratio (AVDR)—(*a*) HS1A cascade, (*b*) HS1B cascade

Table 4 A comparison between AVDRs for HS1A and HS1B cascades at near design Mach number (i.e., $M_2 = 1.05$) and off-design incidence

$i - i_{des}$	HS1A	HS1B
0.0°	1.034	1.083
4.5°	1.039	1.112
10.0°	1.126	1.141
14.5°	1.266	1.264

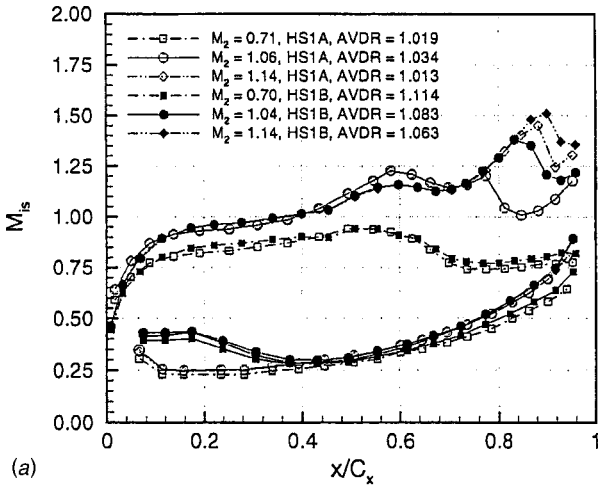

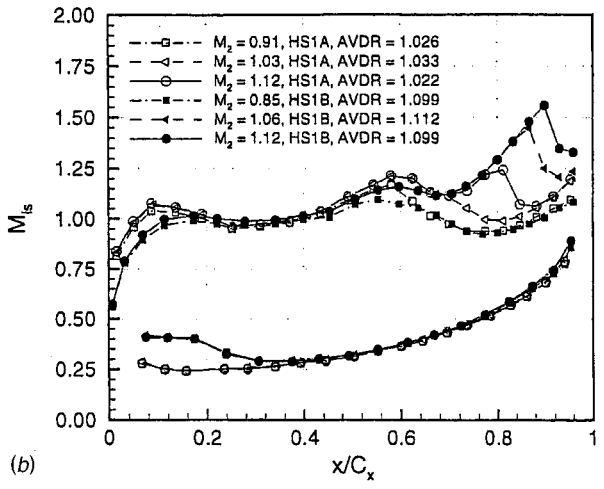

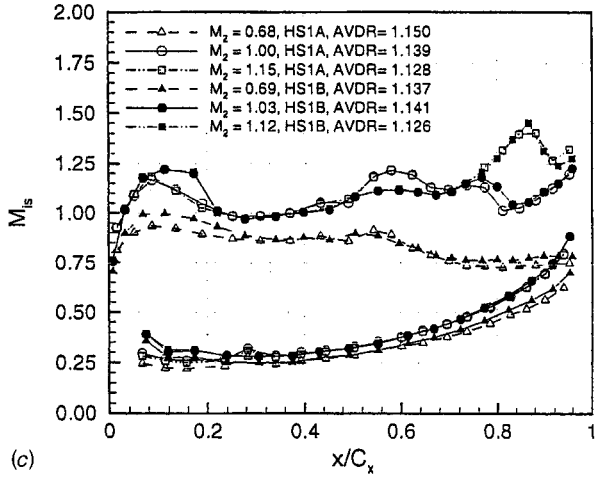

Fig. 7 Comparison of HS1A and HS1B blade loadings at (*a*) design incidence for various exit Mach numbers, (*b*) 4.5 deg off-design incidence, and for various exit Mach numbers, (*c*) 10.0 deg off-design incidence, and for various exit Mach numbers

are noticeable differences in blade loadings near the leading edge, as will be discussed in following section. The differences include the presence of an apparent separation bubble on the pressure side of HS1B. For these low incidence values the AVDRs for the HS1B cascade are higher than the ones for HS1A. At +10.0 and +14.5 deg incidence the loading distribution for the two blades

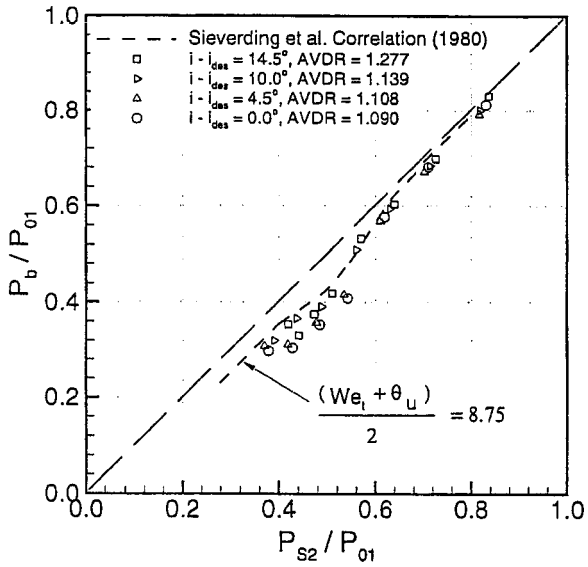

Fig. 8 Comparison of measured base pressure with Sieverding's et al. correlation, HS1B cascade

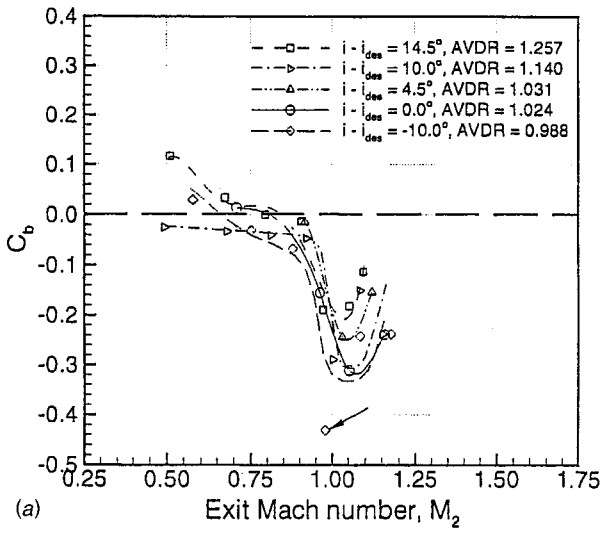

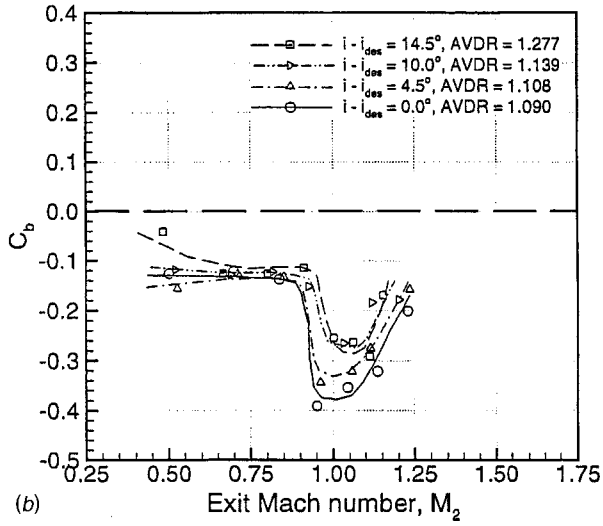

Fig. 9 Variation of Base Pressure Coefficient with Incidence and Mach Number—(*a*) HS1A cascade, (*b*) HS1B cascade

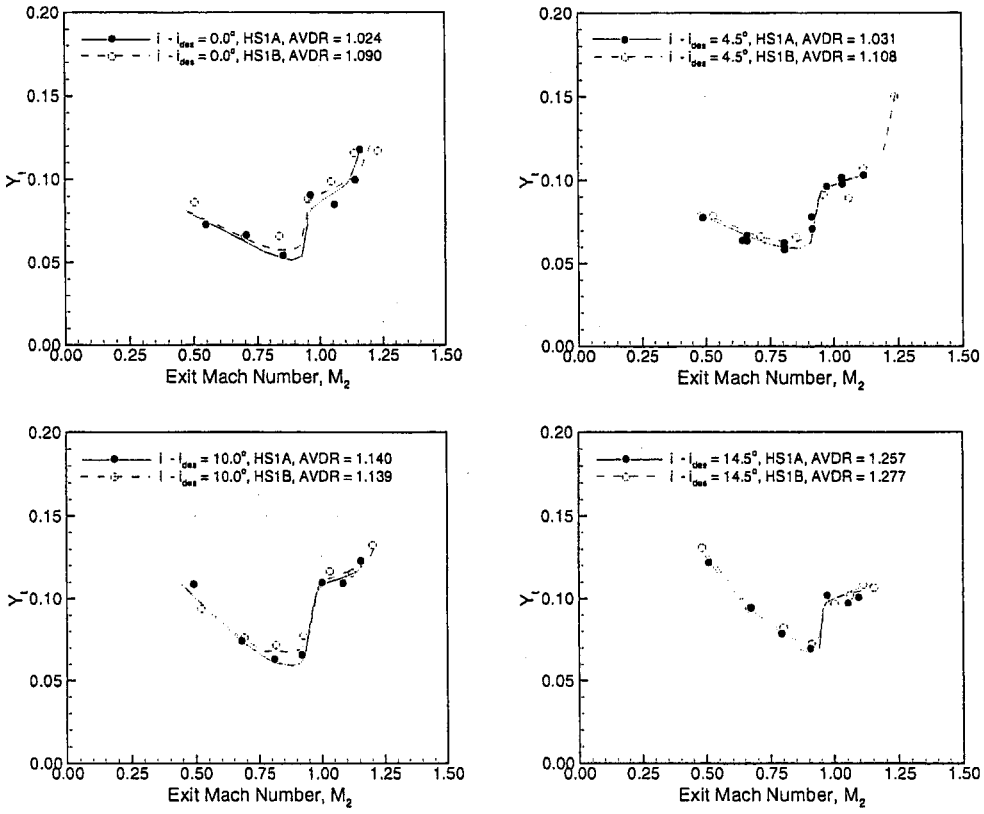

Fig. 10 A comparison between the profile losses for HS1A and HS1B cascades at all test flow conditions

are very similar with no sign of leading edge separation (e.g., Fig. 7(*c*)). For these high values of incidence, the AVDRs were also very similar. Thus, there may be some influence of the blade loading distribution on AVDR, or it may be influenced by the distribution of passage blockage associated with the blades and their surface flows. Additional experimental data on the effects of AVDR would be valuable for clarifying the physics. Computational studies using a Navier-Stokes solvers might also provide useful insights into the factors which influence AVDR.

Blade Loadings and Base Pressures. Figures 7(*a*) to (*c*) show a comparison between HS1A and HS1B blade loading distributions for the incidence values of 0.0, +4.5, and +10.0 deg. Each figure presents a comparison of blade loadings over a range of exit Mach numbers and for a fixed incidence. At design incidence, Fig. 7(*a*) shows that the blade loading on the suction surface is roughly the same for both blades at exit Mach numbers below the choking value, which is about 0.96. Figure 7(*a*) shows that for given exit Mach number (higher than 0.96) the shock impingement point on the aft part of the suction surface is different for the two blades: the impingement point for HS1B is located aft of the one for HS1A for a given exit Mach number. This change in the shock impingement point resulted in some change in the suction surface loading distribution in the vicinity of the trailing edge. With respect to the pressure side, Fig. 7(*a*) shows that the only difference in the loading distributions is in the vicinity of the leading edge. As noted earlier, the HS1B loading distribution shows signs of a separation bubble that extends over the first 20 percent axial chord. The HS1A loading distributions in the vicinity of the leading edge show no signs of separation.

The loading distributions for the two blades at +4.5 deg incidence are shown in Fig. 7(*b*). In this case, at Mach numbers higher than the choking value, there seem to be significant differences in the shock impingement points on the aft part of suction surface for the two blades. Thus, the loading distributions in the trailing edge region of the suction surface are also significantly different between the two blades. In addition, Fig. 7(*b*) shows that the loading distribution for the two blades in the vicinity of the suction side leading edge is different. The figure shows slightly higher peak Mach numbers for the HS1B blade in the first 10 percent axial chord. On the pressure side, the loading distribution for HS1B also suggests the presence of a separation bubble at the leading edge pressure side. From Figs. 7(*a*) and (*b*), the separation bubble at the +4.5 deg incidence appears to have the same extent as for the design case.

At +10.0 deg incidence, Fig. 7(*c*) shows that differences in loading distributions are now shifted toward the leading edge suction side. At subsonic exit Mach numbers the loading distributions show higher local peak Mach numbers for the HS1B blade in the first 20 percent axial chord. At Mach numbers higher than the choking value ($M_2 = 0.96$), both blade loadings show similar values of local peak Mach numbers in the vicinity of the leading edge suction side. However, the extent of the local peak Mach number region is greater for HS1B: three pressure taps for HS1B versus one tap for HS1A. For the pressure side, the loading distributions for the two blades are quite similar except for what appears to be a small pressure disturbance at the 15 percent axial chord shown by the HS1B pressure side loading distribution. This disturbance may be the sign of a small separation bubble. The HS1A and HS1B loading distributions at +14.5 deg incidence are similar to those shown for +10 deg in Fig. 7(*c*).

The base pressure for the HS1B cascade is plotted against Sieverding's et al. correlation in Fig. 8. The trend of the base pressure observed here is similar to the one for the HS1A cascade, not presented here. However, the values of base pressure for HS1B cascade are slightly lower. As found with the HS1A cascade, the measurements for HS1B cascade are in best agreement with the correlation for pressure ratios P_{s2}/P_{01} less than 0.55 (which corresponds to the chocking isentropic exit Mach

Table 5 (*a*) HS1A cascade performance data, (*b*) HS1B cascade performance data

M_2	P_{s2}/P_{01}	P_b/P_{01}	q_2/P_{01}	Re ± ΔRe	C_{bp}	Y_t	α_2	AVDR
HS1A Cascade, Off-Design Incidence, $i - i_{des} = -10.0°$								
0.58	0.788	0.793	0.184	52000 ± 6800	0.030	0.067	57.0	0.98
0.75	0.677	0.668	0.268	670000 ± 12000	-0.031	0.059	57.5	1.01
0.88	0.592	0.571	0.321	780000 ± 19000	-0.067	0.063	58.0	0.98
0.98	0.522	0.371	0.350	870000 ± 68000	-0.431	0.104	57.3	0.99
1.08	0.458	0.367	0.377	950000 ± 84000	-0.242	0.109	57.1	0.99
1.18	0.405	0.312	0.392	1020000 ± 135000	-0.238	0.124	56.3	0.99
HS1A Cascade, Design Incidence, $i - i_{des} = 0.0°$								
0.55	0.807	-	0.168	500000 ± 5400	-	0.073	56.7	1.02
0.71	0.704	0.707	0.247	660000 ± 13000	0.012	0.067	57.2	1.02
0.85	0.612	-	0.311	800000 ± 20000	-	0.054	57.7	1.02
0.96	0.535	0.481	0.346	880000 ± 50000	-0.156	0.091	57.1	1.03
1.06	0.479	0.365	0.374	970000 ± 79000	-0.304	0.085	57.0	1.03
1.14	0.429	0.323	0.389	1040000 ± 97000	-0.272	0.100	57.0	1.01
1.16	0.415	-	0.390	1060000 ± 126000	-	0.118	55.9	1.03
HS1A Cascade, Off-Design Incidence, $i - i_{des} = 4.5°$								
0.49	0.841	-	0.140	460000 ± 4000	-	0.078	56.4	1.02
0.64	0.749	-	0.215	600000 ± 8000	-	0.064	56.4	1.07
0.66	0.736	-	0.224	630000 ± 9000	-	0.064	56.6	1.02
0.81	0.641	-	0.291	780000 ± 16000	-	0.060	57.2	1.03
0.91	0.568	0.563	0.333	880000 ± 26000	-0.016	0.071	57.1	1.04
0.97	0.526	-	0.349	920000 ± 66000	-	0.097	56.8	1.05
1.03	0.490	0.403	0.366	980000 ± 90000	-0.241	0.098	56.7	1.04
1.12	0.440	0.378	0.385	1050000 ± 90000	-0.161	0.103	57.0	1.02
0.66	0.736	-	0.224	630000 ± 9000	-	0.067	57.0	1.01
0.81	0.641	-	0.292	770000 ± 14000	-	0.059	57.5	1.03
0.91	0.568	0.563	0.331	880000 ± 28000	-0.015	0.078	57.4	1.03
1.03	0.491	0.403	0.365	970000 ± 93000	-0.242	0.100	57.0	1.03
HS1A Cascade, Off-Design Incidence, $i - i_{des} = 10.0°$								
0.49	0.834	0.834	0.141	440000 ± 4000	-0.025	0.109	56.4	1.15
0.68	0.721	0.720	0.233	620000 ± 9700	-0.033	0.074	56.8	1.15
0.81	0.636	0.636	0.293	740000 ± 15000	-0.040	0.063	57.3	1.15
0.92	0.566	0.566	0.335	840000 ± 24000	-0.046	0.066	57.7	1.14
1.00	0.507	0.503	0.356	920000 ± 71000	-0.289	0.110	57.0	1.14
1.08	0.458	0.448	0.377	1000000 ± 98000	-0.150	0.109	57.1	1.13
1.15	0.416	0.405	0.389	1070000 ± 116000	-0.238	0.123	56.5	1.13
HS1A Cascade, Off-Design Incidence, $i - i_{des} = 14.5°$								
0.51	0.822	0.840	0.149	460000 ± 4800	0.117	0.122	55.8	1.25
0.67	0.722	0.730	0.229	620000 ± 7800	0.034	0.095	56.2	1.24
0.79	0.645	0.646	0.284	740000 ± 17000	0.000	0.079	56.6	1.26
0.91	0.574	0.569	0.330	870000 ± 24000	-0.013	0.070	56.9	1.27
0.97	0.526	0.460	0.348	940000 ± 45000	-0.189	0.102	56.7	1.26
1.05	0.478	0.411	0.371	1020000 ± 83000	-0.182	0.097	56.7	1.27
1.10	0.453	0.410	0.380	1050000 ± 104000	-0.113	0.101	56.9	1.25

number). At lower values of the pressure ratio, shock waves are present at the trailing edge and the correlation predicts somewhat higher values of base pressure than observed here. These discrepancies do not appear to be strongly related to the incidence, nor do they appear to be related to the effects of AVDR. They seem to be consistent with the discrepancies seen for the HS1A cascade. Similar discrepancies have been observed at design incidence by other investigators [21–23]. Denton [24] attributed these differences to the effects of trailing-edge blockage, which is not included as a correlating parameter in the Sieverding et al. correlation. It is not possible to confirm Denton's explanation from the present measurements. However, they do seem to support the suggestion that one or more important geometric parameters is missing from the Sieverding et al. correlation. It should also be noted that at high Mach numbers the base pressure varies considerably with the location on the trailing edge and the present single tap gives a somewhat limited picture of the base pressure behavior.

Figures 9(*a*) and (*b*) present the HS1A and HS1B cascade base pressure values in terms of the base pressure coefficient as a function of exit Mach number and incidence. As shown in the figures, C_b is generally negative and has a strong minimum around $M_2 = 1.0$. For both cascades, the highest value of C_b is found at the incidence value of +14.5 deg. The minimum C_b is seen to vary somewhat with incidence and AVDR, with the weakest minima occurring at high positive incidence and high AVDR.

When compared to the HS1A cascade, the C_b curves for the HS1B cascade are shifted downward to lower values for all incidence values. Denton and Xu [23] suggested that higher base pressure values are usually an indication of thicker trailing edge boundary layers relative to the trailing edge thickness. It is not possible to confirm that this is the explanation for the differences in C_b for HS1A and HS1B since no measurements were conducted on the blade boundary layers. Whatever the reasons for the differences in C_b, they have implications for the losses generated in the two cascades, as discussed in the next section.

Profile Losses. Figure 10 shows the variation of the total pressure loss coefficient Y_t with exit Mach number for the incidence values of 0.0, +4.5, +10.0, and +14.5 deg. Tables 5(*a*) and (*b*) list the loss coefficients for both cascades together with other aerodynamic parameters, such as AVDR, base pressure, and deviation angles.

The trend in loss coefficient shown in Fig. 10 is similar for the four incidence values and is consistent with the variation with Mach number found by Mee et al. [25] at design incidence. In all cases, the loss coefficient reached a minimum at the about $M_2 = 0.85$, after which the losses rose sharply through an exit Mach number of unity. From Fig. 10, it appears that the minimum losses occur at the point were the base pressure starts to decrease. From Denton [24], the contribution of the base pressure to profile loss coefficient, incompressible flow, is estimated at

Table 5 (*continued*)

M_2	P_{s2}/P_{01}	P_b/P_{01}	q_2/P_{01}	Re ± ΔRe	C_{bp}	Y_t	α_2	AVDR
HS1B Cascade, Design Incidence, $i - i_{des} = 0.0°$								
0.50	0.831	0.813	0.147	460000 ± 4000	-0.126	0.086	57.2	1.08
0.70	0.710	0.680	0.243	640000 ± 9600	-0.122	0.066	57.6	1.11
0.84	0.619	0.577	0.304	760000 ± 15000	-0.138	0.066	58.2	1.09
0.95	0.542	0.408	0.343	850000 ± 42000	-0.391	0.088	57.9	1.08
1.04	0.483	0.353	0.369	940000 ± 81000	-0.354	0.099	57.6	1.08
1.14	0.428	0.304	0.386	1010000 ± 113000	-0.321	0.116	57.5	1.06
1.23	0.378	0.297	0.400	1070000 ± 146000	-0.201	0.117	56.0	1.12
HS1B Cascade, Off-Design Incidence, $i - i_{des} = 4.5°$								
0.53	0.817	0.792	0.159	480000 ± 4400	-0.156	0.079	56.9	1.09
0.71	0.702	0.670	0.249	640000 ± 10000	-0.127	0.067	57.3	1.11
0.85	0.610	0.569	0.309	770000 ± 17000	-0.133	0.066	57.8	1.10
0.96	0.534	0.415	0.346	860000 ± 53000	-0.344	0.091	57.4	1.11
1.06	0.477	0.357	0.373	950000 ± 82000	-0.321	0.090	57.5	1.11
1.12	0.419	0.311	0.391	1020000 ± 106000	-0.276	0.107	57.1	1.10
1.24	0.370	0.307	0.396	1070000 ± 141000	-0.158	0.150	55.0	1.13
HS1B Cascade, Off-Design Incidence, $i - i_{des} = 10.0°$								
0.52	0.819	0.800	0.156	470000 ± 5000	-0.118	0.094	56.1	1.17
0.69	0.714	0.683	0.238	630000 ± 12000	-0.129	0.076	56.5	1.14
0.82	0.630	0.594	0.296	750000 ± 15000	-0.123	0.072	57.0	1.14
0.93	0.560	0.509	0.336	840000 ± 25000	-0.152	0.077	57.3	1.14
1.03	0.487	0.390	0.363	940000 ± 83000	-0.265	0.117	56.6	1.14
1.12	0.437	0.366	0.383	1010000 ± 94000	-0.184	0.116	56.8	1.13
1.20	0.390	0.319	0.394	1070000 ± 138000	-0.179	0.132	55.8	1.13
HS1B Cascade, Off-Design Incidence, $i - i_{des} = 14.5°$								
0.48	0.837	0.831	0.137	440000 ± 4000	-0.042	0.131	55.2	1.33
0.67	0.726	0.698	0.226	620000 ± 9000	-0.126	0.094	55.7	1.33
0.80	0.639	0.603	0.288	750000 ± 14000	-0.127	0.082	56.1	1.30
0.91	0.570	0.532	0.331	850000 ± 20000	-0.115	0.072	56.5	1.28
1.00	0.509	0.418	0.358	930000 ± 57000	-0.255	0.097	56.6	1.26
1.06	0.472	0.375	0.372	1000000 ± 90000	-0.263	0.102	56.3	1.26
1.11	0.442	0.330	0.383	1040000 ± 90000	-0.292	0.108	56.7	1.24
1.15	0.420	0.353	0.391	1080000 ± 86000	-0.170	0.107	56.8	1.23

$$\Delta Y_{te} = -C_b \frac{t}{o} \tag{1}$$

and at transonic conditions the effect would be expected to be even larger. For the present cascades the ratio of the trailing-edge thickness to the throat opening, t/o, is 0.08. Thus, from Eq. (1) and Fig. 10, at the minimum loss point ($M_2 = 0.85$) the difference in the base pressure coefficients contributes at least 0.008 to the difference in the loss coefficients. This is roughly 80 percent of the difference. The remainder is presumably due to small differences in the losses occurring in the blade boundary layers and the effects of AVDR, particularly at the incidence values of 0.0 and 4.5 deg.

At Mach numbers above the sonic condition, Fig. 10 shows that the losses for the two blades are very similar. The comparison between the loading distributions for the two blades, given in Figs. 7(*a*) to (*c*), shows regions with higher local Mach numbers for HS1B. As shown by Denton [24], the loss production in a boundary layer varies roughly with the cube of the edge velocity. This suggests that at these exit Mach numbers the local boundary layer losses for the HS1B cascade are somewhat higher than the ones for HS1A. There also appears to be an effect of AVDR on the HS1B losses. HS1B has somewhat higher AVDR than HS1A, particularly at the incidence values of 0.0 and +4.5 deg. These high values of AVDR seem to reduce the HS1B losses compared to HS1A values. Figure 10 shows that at +10.0 deg incidence and Mach numbers greater than 1.0, HS1B losses are slightly higher than the HS1A losses. At this incidence, HS1A and HS1B have the same AVDR and the increase in losses seen for HS1B appears to be mainly due to the loss production in the blade boundary layers.

Figure 11 shows the effect of incidence on profile losses at three representative Mach numbers. These curves are essentially a cross-plotting of the data from Fig. 10, using interpolated values of Y_t at the desired values of M_2. Within the uncertainties in the measurements, HS1A and HS1B gave very similar loss results at all conditions of M_2 and incidence, with HS1B giving perhaps slightly higher losses in the minimum loss region (M_2 about 0.85). The hope for the improvement in positive incidence behavior for HS1B clearly did not materialize.

Outlet Flow Angle. Figures 12(*a*) and (*b*) show the measured exit flow angles for HS1A and HS1B cascades respectively. As shown from the figures, for HS1B there seems to be a definite trend in the exit flow angle with increasing incidence which is not present for HS1A. Moreover, for a given incidence, the values of deviation seem to be somewhat higher for HS1B than HS1A. This raises the question of whether there is some trailing edge separa-

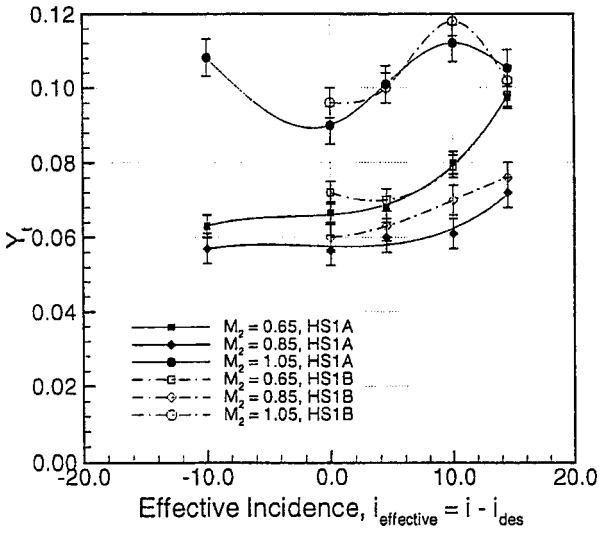

Fig. 11 Effects of off-design incidence on profile losses for both HS1A and HS1B cascades

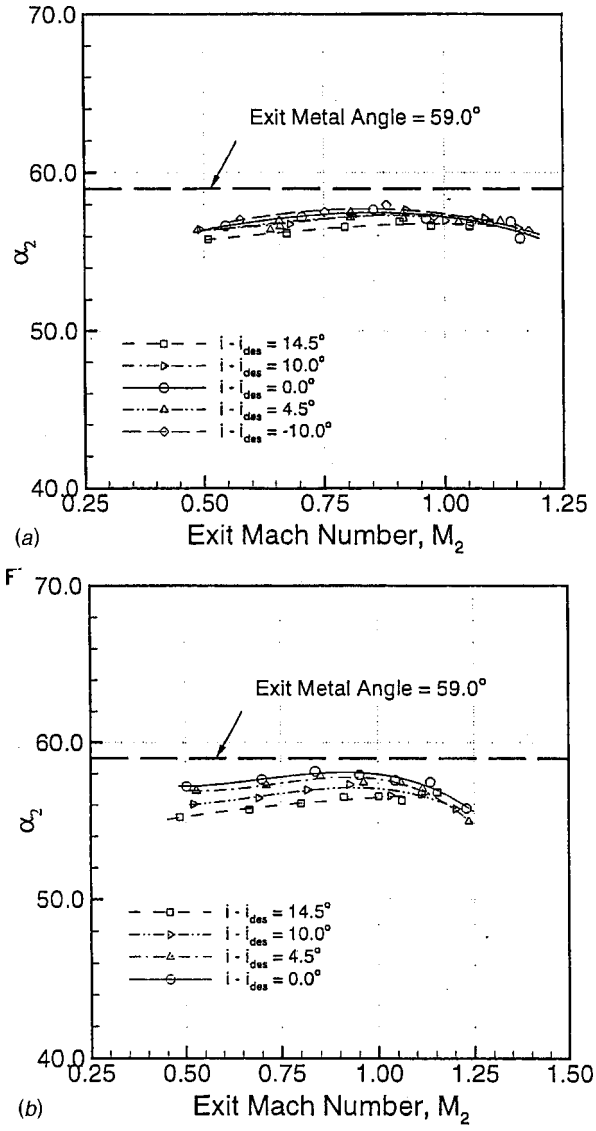

Fig. 12 Effects of incidence and Mach number on exit flow angle—(*a*) HS1A cascade, (*b*) HS1B cascade

tion present on HS1B. From the loading distributions for the two blades, there appear to be some differences in the loading distributions in the vicinity of the trailing edge. As shown in Figs. 7(*a*) to (*c*), the shock impingement point for HS1B is located aft of the one for HS1A for a given exit Mach number. However, there was no apparent evidence of separation present for HS1B. And if present, the separation may be at the trailing edge or there are not enough static taps on the suction side of the blade to capture it. Whatever the exact explanation, clearly the C_b and α_2 results both suggest that there are differences in the flows near the trailing edge for the two cascades. This is of course surprising considering their geometric similarity in this region.

Conclusions

Detailed measurements have been presented for the midspan aerodynamic performance of two transonic turbine cascades at off-design conditions. The blades tested differ mainly in the leading edge geometry. The baseline blade is of recent design and incorporates modern design philosophies for high pressure turbine blades. The modified blade has been designed to investigate one possible approach to reducing the sensitivity of the blade to off-design incidence.

The data cover a broad range of both incidence and exit Mach numbers. They provide a substantial addition to the data available in the open literature on the behavior of transonic turbine blades at off-design incidence. As such they could be used in the development of improved correlations for profile losses, base pressure behavior, and outlet flow angle. In addition, they could be used to investigate the ability of existing CFD codes to reliably compute the aerodynamic performance of turbine blades over the range of operating conditions.

Sieverding [26] recommended a minimum aspect ratio (H/C) of about 1.6 for two-dimensional, transonic testing of linear turbine cascades. This recommendation appears to be satisfactory for testing near the design incidence. However, for large values of off-design incidence the axial velocity density ratio in the present cascades deviated significantly from 1.0. For +14.5 deg in particular the AVDR reached about 1.26 and this apparently reduced the losses substantially below what they would have been for more nearly two-dimensional conditions. Based on the present results, an aspect ratio larger than 1.6 may be desirable for testing at off-design incidence.

Acknowledgment

Financial support for this study provided by the Natural Sciences and Engineering Research Council of Canada and Pratt & Whitney Canada Inc. is gratefully acknowledged.

Nomenclature

AVDR = axial velocity density ratio, $(=\int_0^1(\rho_2 C_{(ax)_2})_{MS}d(y/s)/\int_0^1(\rho_1 C_{(ax)_1})_{MS}d(y/s))$

AVR = axial velocity ratio, $(=\int_0^1(C_{(ax)_2})_{MS}d(y/s)/\int_0^1(C_{(ax)_1})_{MS}d(y/s))$

C = blade chord length or flow velocity

C_b = base pressure coefficient, $(=(P_b-P_{s2})/q_2)$

C_{P0} = total pressure coefficient, $(=(P_{02}-P_{01})/q_1)$

C_x = axial chord length

H = blade span

M = Mach no.

P_0 = total pressure

P_b = base pressure

P_{s2} = downstream static pressure

Re = Reynolds no., $(=(\rho C C_2)/\mu)$

T_{01} = inlet test section total temperature

ΔT_{01} = drop in inlet test section total temperature

We = wedge angle

Y_t = total pressure loss coefficient, $(=(P_{01}-P_{02})/q_2)$

$i_{\text{effective}}$ = effective incidence, in deg, $(=\alpha_1-(\alpha_1)_{des}=i-i_{des})$

o = throat opening

q = dynamic pressure, $(=1/2\rho C^2)$

x = axial distance

y = pitchwise location

s = pitch distance

t = trailing edge thickness

α = flow angle measured from axial direction, in degrees

β = blade metal angle measured from axial direction, in deg

δ = deviation angle, in deg, $(=\beta_2-\alpha_2)$

ζ = stagger angle measured from axial direction, in deg

μ = air dynamic viscosity

ρ = air density

θ_u = uncovered turning, in deg

Subscripts

1 = cascade inlet

2 = cascade outlet

ax = axial

des = design

is = isentropic
MS = mid-span
te = trailing edge
le = leading edge

References

[1] Goobie, S. M., Moustapha, S. H., and Sjolander, S. A., 1989, ''An Experimental Investigation of the Effect of Incidence on the Two-Dimensional Flow,'' Proc, IX International Symposium on Air Breathing Engines (ISABE), Sept., pp. 197–204.

[2] Rodger, P., Sjolander, S. A., and Moustapha, S. H., 1992, ''Establishing Two-Dimensional Flow in a Large-Scale Planar Turbine Cascade,'' AIAA Paper, No. 92-3066.

[3] Whitehouse, D. R., Moustapha, S. H., and Sjolander, S. A., 1993, ''The Effects of Axial Velocity Ratio, Turbulence Intensity, Incidence, and Leading Edge Geometry on the Mid-Span Performance of a Turbine Cascade,'' Can. Aeronautics Space J., **39**, No. 3, Sept., pp. 150–156.

[4] Benner, M. W., Sjolander, S. A., and Moustapha, S. H., 1997, ''Influence of Leading-Edge Geometry on Profile Losses in Turbines at Off-Design Incidence: Experimental Results and an Improved Correlation,'' ASME J. Turbomach., **119**, Apr., pp. 193–200.

[5] Moustapha, S. H., Kacker, S. C., and Tremblay, B., 1990, ''An Improved Incidence Losses Prediction Method for Turbine Airfoils,'' ASME J. Turbomach., **112**, Apr., pp. 267–276.

[6] Martelli, F., and Boretti, A., 1987, ''Development of an Experimental Correlation for Transonic Turbine Flow,'' ASME J. Turbomach., **109**, Apr., pp. 246–250.

[7] Kacker, S. C., and Okapuu, U., 1982, ''A Mean Line Prediction Method for Axial Flow Turbine Efficiency,'' ASME J. Turbomach., **104**, Jan., pp. 111–119.

[8] Saroch, M. F., 1996, ''Contributions to the Study of Turbomachinery: Part I—Design of a Fish-Tail Diffuser Test Section. Part II: Computations of the Effects of AVDR on Transonic Turbine Cascades,'' M. E. thesis, Department of Mechanical and Aerospace Engineering, Carleton University, Ottawa, Ontario, Canada, Jan.

[9] Graham, C. G., and Kost, F. H., 1979, ''Shock Boundary Layer Interaction on High Turning Transonic Turbine Cascade,'' ASME Paper No. 79-GT-37.

[10] Perdichizzi, A., 1990, ''Mach Number Effects on Secondary Flow Development of a Turbine Cascade,'' ASME J. Turbomach., **112**, Oct., pp. 643–651.

[11] Detemple-Laake, E., 1991, ''Detailed Measurements of the Flow Field in a Transonic Turbine Cascade,'' ASME Paper No. 91-GT-29.

[12] Moustapha, S. H., Carscallen, W. E., and McGeachy, J. D., 1993, ''Aerodynamic Performance of a Transonic Low Aspect Ratio Turbine Nozzle,'' ASME J. Turbomach., **115**, July, pp. 400–408.

[13] Krieger, M. W., Lavoie, J. P., Vlasic, E. P., and Moustapha, S. H., 1999, ''Off-Design Performance of a Single-Stage Transonic Turbine,'' ASME J. Turbomach., **121**, Apr., pp. 177–183.

[14] Jouini, D. B. M., Sjolander, S. A., and Moustapha, S. H., 2000, ''Aerodynamic Performance of a Transonic Turbine Cascade at Off-Design Conditions,'' ASME Paper No. 2000-GT-0482.

[15] Jeffries, M. S., Jouini, D., and Sjolander, S. A., 1997, ''Determining the Sampling Rates and Times in a High Speed Wind Tunnel,'' Proc., CASI 6th Symposium on Aerodynamics, Toronto, Canada, Apr.

[16] Corriveau, D., 1999, private communication, Carleton University, Ottawa, Canada.

[17] Jeffries, M. S., 2001, ''Initial Investigations of Transonic Turbine Aerodynamics using the Carleton University High-Speed Wind Tunnel,'' Ph.D. thesis, Department of Mechanical and Aerospace Engineering, Carleton University, Ottawa, Ontario, Canada, Jan.

[18] Islam, A. M. T., 1999, ''An Experimental and Computational Study of the Aerodynamics of Turbine Blades with Damage,'' Ph.D. thesis, Department of Mechanical and Aerospace Engineering, Carleton University, Ottawa, Ontario, Canada, Sept.

[19] Amecke, J., and Šafařík P., 1995, ''Data Reduction of Wake Flow Measurements with Injection of Other Gas,'' DLR-FB 95-32, DLR, Köln, Germany.

[20] Jouini, D. B. M., 2000, ''Experimental Investigation of Two Transonic Linear Turbine Cascades at Off-Design Conditions,'' Ph.D. thesis, Department of Mechanical and Aerospace Engineering, Carleton University, Ottawa, Ontario, Canada, July.

[21] Sieverding, C. H., Stanislas, M., and Snoeck, J., 1980, ''The Base Pressure Problem in Transonic Turbine Cascades,'' ASME J. Eng. Power, **102**, July, pp. 711–714.

[22] Xu, L., and Denton, J. D., 1980, ''The Base Pressure and Loss of a Family of Four Turbine Blades,'' ASME J. Turbomach., **110**, Jan., pp. 9–17.

[23] Denton, J. D., and Xu, L., 1990, ''The Trailing Edge Loss of Transonic Turbine Blades,'' ASME J. Turbomach., **112**, Apr., pp. 277–285.

[24] Denton, J. D., 1993, ''Loss Mechanisms in Turbomachines,'' ASME J. Turbomach., **115**, Oct., pp. 621–656.

[25] Mee, D. J., Baines, N. C., Oldfield, M. L. G., and Dickens, T. E., 1992, ''An Examination of the Contributions to Loss on a Transonic Turbine Blade in Cascade,'' ASME J. Turbomach., **114**, Jan., pp. 155–162.

[26] Sieverding, C. H., 1993, ''Advanced Methods for Cascade Testing,'' AGARDograph 328, AGARD-AG-328, Aug., pp. 22–34.

G. Medic
e-mail: gmedic@stanford.edu

P. A. Durbin
e-mail: durbin@vk.stanford.edu

Mechanical Engineering Department,
Stanford University,
Stanford, CA 94305-3030

Toward Improved Prediction of Heat Transfer on Turbine Blades

Reynolds averaged computations of turbulent flow in a transonic turbine passage are presented to illustrate a manner in which widely used turbulence models sometimes provide poor heat transfer predictions. It is shown that simple, physically and mathematically based constraints can substantially improve those predictions. [DOI: 10.1115/1.1458020]

1 Introduction

Three-dimensional numerical simulation of turbulent convective heat transfer is becoming a part of the complex procedure of gas turbine blade design and is slowly replacing simpler two-dimensional methods, mainly based on boundary layer computations and relying heavily on large experimental databases. However, many fundamental and practical developments are needed before full three-dimensional computational analysis becomes reliable.

In the present paper we discuss the effect of anomalous turbulent kinetic energy (k) production on predictions of two-equation turbulence closure models. This problem is known in the literature [1]; the term ''stagnation point anomaly'' has been used [2,3]. That terminology certainly does not do full justice to this fault. It seems that when a moderate level of turbulent energy is subjected to large rates of strain these models predict exorbitant growth of that energy. It is the large rate of strain, not the stagnation point, that is relevant. The strains occurring in the middle of a turbine passage are sufficient to cause the problem, as will be illustrated herein.

Two explicit proposals to cure the anomalous predicted levels of k are the methods of [4] and [2]. We will assess the ability of these cures to improve heat transfer predictions in turbomachinery flows. Both methods appear quite facile—they can be implemented by a few lines of computer code; but, we will demonstrate that the improvement to predictive accuracy can be quite substantial. Because of their role, these methods are sometimes called ''limiters,'' which is a term that will be used herein.

We have conducted a numerical study of an experimentally documented test case of [5–7] in order to assess different turbulence models. The present paper concerns the flow without film cooling, a companion paper addresses their film-cooling cases. Here the objective is to confirm the value of the limiters, applied to standard eddy-viscosity based turbulence models. This is done by comparison to measurements on the uncooled blade.

2 Turbulence Models and Numerics

In this analysis we are dealing with transonic compressible flow through a gas turbine blade cascade. The equations used to describe the flow are the Favre averaged, compressible Navier-Stokes equations with turbulence models that provide eddy viscosities. The effects of turbulence are taken into account through the constitutive model

$$\mathbf{R} = -\tfrac{2}{3}\rho k I + \mu_t[(\nabla U + \nabla U^T) - \tfrac{2}{3}(\nabla \cdot U)I]$$

$$\dot{\mathbf{q}}_\mathbf{t} = -\frac{\mu_t C_p}{\mathrm{Pr}_t}\nabla T \tag{1}$$

Contributed by the International Gas Turbine Institute for publication in the JOURNAL OF TURBOMACHINERY. Manuscript received by the IGTI, March 20, 2001; revised manuscript received October 15, 2001. Associate Editor: R. Bunker.

for the Reynolds stress and heat flux tensors. To predict the eddy viscosity μ_t the two-layer $k-\varepsilon$, the standard $k-\omega$ and the v^2-f models will be used (see Appendix). The heat flux was computed with a turbulent Prandtl number $\mathrm{Pr}_t = 0.9$.

2.1 Fixes for Anomalous Turbulent Energy. Excessive levels of turbulent kinetic energy are predicted by standard two-equation models in regions of large rate of strain. This was originally recognized in stagnation point flows [4], but it will be seen here that it is a more widespread anomaly. The following reviews two ideas to solve this problem.

Modification of Production. To understand the Kato and Launder [4] approach, consider the closed transport equation for turbulent kinetic energy

$$\partial_t(\rho k) + \nabla \cdot (\rho U k) = \rho P_k - \rho\varepsilon + \nabla \cdot ((\mu + \mu_t)\nabla k) \tag{2}$$

where the rate of energy production is given by

$$\rho P_k = R : \nabla U = -\tfrac{2}{3}\rho k(\nabla \cdot U) + 2\mu_t |S|^2 - \tfrac{2}{3}\mu_t(\nabla \cdot U)^2 \tag{3}$$

where $|S|^2 = S_{ij}S_{ji}$ with $S_{ij} = 1/2(\partial_j U_i + \partial_i U_j)$. In nondivergent flow $P_k = 2\nu_t|S|^2$. If one attributes excessive level of k to an over estimate of P_k, then one might look to modifying this term. As a pragmatic device to avoid the problem of spurious stagnation point build-up of turbulent kinetic energy, [4] replaced $|S|^2$ with $|S||\Omega|$ in (3). Here $\Omega_{ij} = 1/2(\partial_j U_i - \partial_i U_j)$ is the vorticity tensor and $|\Omega|$ is its magnitude.

This approach equates the rate of production to zero in irrotational flow ($|\Omega| = 0$); that eliminates the stagnation point problem, because the stagnation point flow is irrotational. While it is not correct that production vanishes in irrotational flow, it might be argued that for applications like heat transfer, the main interest is turbulence produced in the rotational boundary layer. Then little harm is done in replacing $|S|^2$ by $|S||\Omega|$. Difficulties could arise in rotating or swirling flows, where the dependence on $|\Omega|$ might incorrectly increase energy production.

A formal difficulty with setting $P_k = 2\nu_t|S||\Omega|$ is that P_k actually represents transfer of energy from the mean flow to turbulence. Therefore, it should be equal and opposite to a corresponding term in the mean flow energy equation. The term that derives from (1) is $2\nu_t|S|^2$; in other words, the Kato-Launder approach formally violates energy conservation.

Time-Scale Bound. Other perspectives on prediction of excessive levels of turbulent energy are easy to conceive: it could be due to underestimation of dissipation ε, or to over estimation of ν_t. A number of such ideas are subsumed by the idea of a time-scale bound, proposed in [2].

The eddy viscosity predicted by scalar equation turbulence models can be characterized by the form

$$\mu_t = C_\mu \rho u^2 T \tag{4}$$

where u^2 is the velocity scale and T is the turbulence time-scale. In $k-\varepsilon$ and $k-\omega$ models, $u^2 = k$ and in v^2-f model $u^2 = \overline{v^2}$. T equals k/ε, in $k-\varepsilon$ or v^2-f, and it equals $1/(C_\mu\omega)$ in $k-\omega$ [8].

T also appears in the source term $(C_{\varepsilon 1}\rho P_k - C_{\varepsilon 2}\rho\varepsilon)/T$ of the ε-equation. Also, production of turbulent energy can be stated as $P_k = C_\mu k|S|^2 T$.

A bound for the turbulent time scale T was derived in [2] from the condition that the eigenvalues of the Reynolds stress tensor in Eq. (1) should be non-negative—which is a sort of ''realizability'' constraint. The resulting inequality was expressed as a limit on the time-scale

$$T = \min\left[\frac{k}{\varepsilon}, \frac{\alpha}{\sqrt{6}C_\mu|S|}\right]$$

or

$$T = \min\left[\frac{1}{C_\mu\omega}, \frac{\alpha}{\sqrt{6}C_\mu|S|}\right] \tag{5}$$

For compressible flows S should be replaced by $S^* = S - 1/3(\nabla \cdot U)I$. A consequence of (5) is that P_k grows like $|S|$, rather than $|S|^2$ at large rates of strain; this is the theoretical behavior predicted by rapid distortion analysis (see [9]). The value of the coefficient α was selected as $\alpha = 0.6$ in [3] for the v^2-f model. The same value has been applied here to $k-\varepsilon$.

When this technique is invoked with the two-layer formulation, the limiter is applied only in the high Reynolds region. Near the wall the standard $k-l$ formulation, with prescribed l, is applied; the absence of a predictive equation for l obviates the need for a time-scale bound.

2.2 Numerical Method. For numerical solution of the flow equations, we have employed a commercial software package, STAR-CD. STAR-CD is an implicit finite volume solver that employs a variant of the well known SIMPLE method [10], with the turbulence model equations decoupled and solved sequentially. It can be used as a general-purpose convection-diffusion equation solver via user defined subroutines.

Particular turbulence models were programmed through these user defined subroutines. The complete $k-\omega$ and v^2-f models were programmed, while the built-in two-layer $k-\varepsilon$ model was used, with only the time-scale bound coded by a user routine; or in the case of Kato-Launder approach, the modified production term P_k. The bound (5) is usually considered part of the v^2-f formulation.

3 Assessment of Turbulence Models

The test case considered in this analysis is the VKI experiment by [5]. This represents a film-cooled gas turbine rotor blade: the present paper considers their data without film cooling; a companion paper addresses the cooled blade.

The blade chord length, c, equals 80 mm, with pitch-to-chord ratio equal to 0.67, and stagger angle of 38.5 deg. The flow through the cascade is transonic with the inflow conditions: $M_{in} = 0.25$, $Re_{c,in} = 8.5 \cdot 10^5$, $T_{0\infty} = 409.5$ K, and the exit Mach number $M_{ex,is} = 0.92$. The inflow angle is 30 deg and the wall temperature is $T_w = 298$ K. The geometry of the blade is described in more detail in [5].

The inflow turbulence intensity is $Tu_{in} = 5\%$, and the length scale $C_\mu^{3/4}k^{3/2}/\varepsilon$ was estimated as ≈ 1 cm. The presence of ambient turbulence at the entrance to the cascade is pertinent to the problem of the stagnation point anomaly; were Tu set to zero the anomaly would not be noticeable in the heat transfer predictions; but ambient turbulence is a fact of life in turbomachines.

3.1 Heat Transfer Coefficient. The following concentrates on the results that concern blade heat transfer: the surface isentropic Mach number, M_{is}; and the heat transfer coefficient, $h_t = \dot{q}_w/(T_{0\infty} - T_w)$. These quantities are presented with respect to curvilinear coordinate s (normalized by the blade chord c) with the origin at the stagnation point.

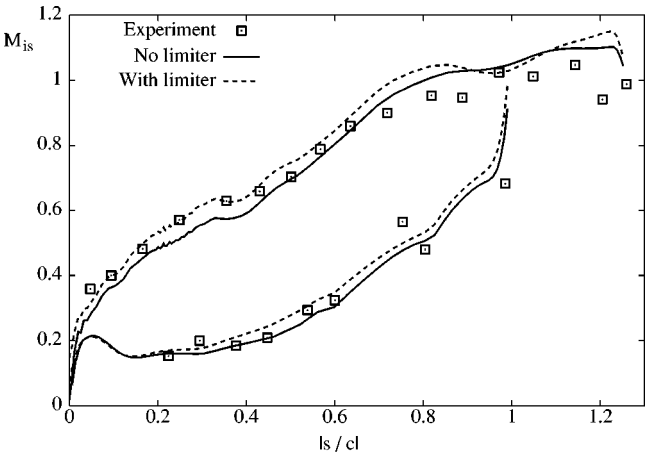

Fig. 1 Isentropic Mach number, M_{is}

The surface pressure distribution is not strongly affected by the choice of turbulence model; to avoid clutter, Fig. 1 only shows computations with $k-\varepsilon$. All the results obtained with limiters virtually coincide with the curve shown. Results obtained with the native $k-\varepsilon$ and $k-\omega$ models, without any limiters, are also almost coincident; they are slightly lower than the results with limiters. This might be understood by attributing the excessive k (or ν_T) levels produced by the native model with greater loss of mean flow energy.

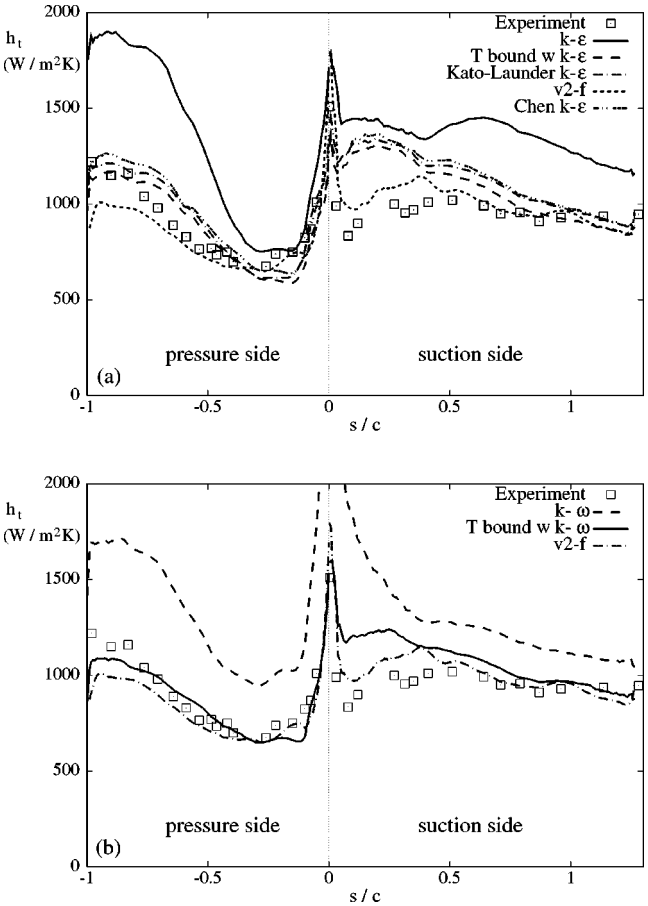

Fig. 2 Heat transfer coefficient h_t (W/m² K)—(*a*) $k-\varepsilon$ models, (*b*) $k-\omega$ models

However, significant differences among the various models are observed when comparing the surface heat transfer coefficients, h_t. These are presented in Fig. 2. The native $k-\varepsilon$ and $k-\omega$ models strongly overpredict the heat transfer coefficient. With either the Kato-Launder formulation, or the bound (5) on the turbulent time-scale, the level of heat transfer is reduced and seems to be predicted more correctly. Obviously, a vast improvement to the performance of $k-\varepsilon$ for some turbomachinery problems can be had quite simply.

Still, there are some discrepancies with the experimental data on the suction side, close to the leading edge of the blade, in the region $0<s/c<0.4$. This region might be a buffeted laminar flow, with transition to turbulence occurring within the region. The substantial overprediction of h_t might be caused partly by failure of the model to capture such processes. The two-layer formulation uses a turbulent length scale next to the wall; hence, it inherently cannot represent transitional regions. But the experimental data seem to imply that, at most, transition might have an influence for $s/c<0.1$—connections to transitional effects are mostly suggestive. Indeed, [5] note that their data for $s/c<0.2$ might have been affected by the film cooling holes, even though they were blocked off during these measurements. It will be shown below that both the limiters clean up the excessive levels of k, so the poor predictions near front of the suction surface are not a residue of the stagnation point anomaly either.

Figure 2 also includes a calculation with the Chen modification to $k-\varepsilon$, as defined in [10]. The same modification is discussed in [11], with the following rationale: the production term in the ε-equation is a dimensionally consistent analogy to that in the k-equation. This could be represented as $P_\varepsilon=F(P_k/\varepsilon)P_k/T$, for an arbitrary function F. The standard model is to make F constant: $F(P_k/\varepsilon)=C_{\varepsilon_1}$. Including the next term in a Taylor series makes F linear: $F(P_k/\varepsilon)=C_{\varepsilon_1}+C_{\varepsilon_3}P_k/\varepsilon$. A small value of $C_{\varepsilon_3}=0.25$ was selected by Chen and C_{ε_1} was reduced to 1.15 to avoid excessive levels of dissipation. The Chen model computation included in Fig. 2 has levels of k in the turbine passage that are similar to those obtained with the methods discussed in Section 2.1 (see Section 3.2).

Prakash [1] first noted that the Chen modification had the potential to prevent excessive growth of k, by increasing ε. He presented computations demonstrating its efficacy. Prakash also recommended clipping the linear term via $C_{\varepsilon_3}\min[3,P_k/\varepsilon]$. (A model that similarly boosts P_ε in highly strained flows is the RNG $k-\varepsilon$ model [10], but excessive levels of k were still seen with that model.)

Finally, the v^2-f model gives results which agree better with the suction side data. Overall, the qualitative distribution of h_t over the suction side looks better with this model. In other studies it has been found that this model produces a reasonable transition location (under zero pressure gradient); again, that property has some suggestive relevance to the improvement in the h_t predictions on the first half of the suction side. Nevertheless, a detailed examination of computed k fields did not show the existence of a transitional zone. Turbulent levels of k were seen in this region, similar to levels obtained with the other models.

Although the v^2-f predictions are much better than those by $k-\varepsilon$ on the *suction side*, it fails to recover to the right heat transfer level near the *pressure side* trailing edge, $s/c<-0.8$. It was suspected that this model might be tending toward relaminarization prematurely; a strongly accelerating pressure gradient can be seen in the lower curve of Fig. 1, beginning around $|s/c|=0.8$. However, here again, a close examination of the turbulent energy field did not confirm this hypothesis.

All models predict a sharp rise of h_t at the stagnation point ($s=0$). Experimental data show a similar behavior. The present geometry is not conducive to assessment of stagnation point heat transfer *per se*. The study by [3] focuses on the need for limiters in stagnation point heat transfer prediction.

Results with $k-\omega$ are similar, altogether, to those obtained with $k-\varepsilon$ model (Fig. 2). Introduction of the bound (5) on the turbulent time scale leads to a significant improvement. Mostly, results lie in between $k-\varepsilon$ and v^2-f.

3.2 Turbulent Kinetic Energy. The reason for the differences in heat transfer prediction obtained with different models must be related to the quantity which links turbulence equations to the mean flow and temperature—the turbulent eddy viscosity. For the present models eddy viscosity is related to the turbulent energy. In order to understand the improvement in heat transfer prediction we consider this quantity. Unfortunately, data for k are not available in the present transonic passage flow.

Examining the values of turbulent kinetic energy predicted in the center of the passage, shows that switching from standard $k-\varepsilon$ (or $k-\omega$) to one of the limiters, or to the v^2-f model, reduces k by a factor on the order of 30 times. This is illustrated in Figs. 3–8 by plotting the turbulent intensity $\mathrm{Tu}=\sqrt{2/3k}/|U|$ field.

The maximum value of intensity in the center of the passage goes from 23 percent, predicted with $k-\varepsilon$ model, to ~3.5 percent predicted with all other models. In other words, all the models except the native $k-\varepsilon$ and $k-\omega$ models predict a decrease of turbulence intensity relative to the inflow value of 5 percent; the latter predict a substantial increase.

The spatial distribution of intensity also differs. Because of the

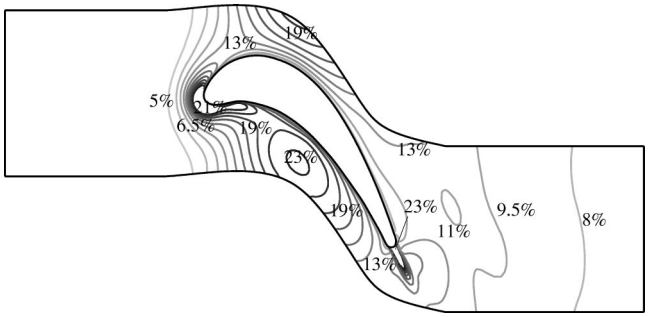

Fig. 3 Turbulence intensity, $k-\varepsilon$ model

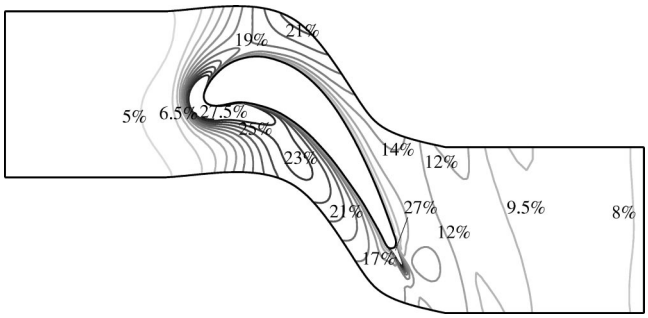

Fig. 4 Turbulence intensity, $k-\omega$ model

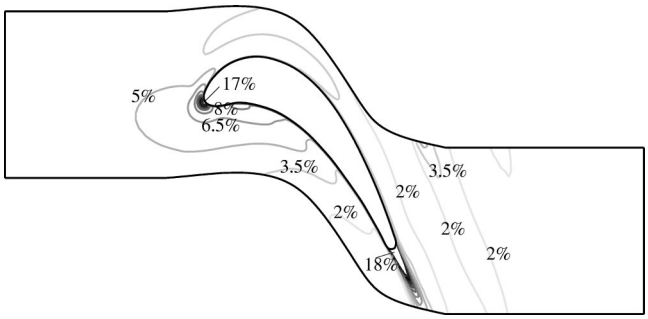

Fig. 5 Turbulence intensity, Kato-Launder $k-\varepsilon$ model

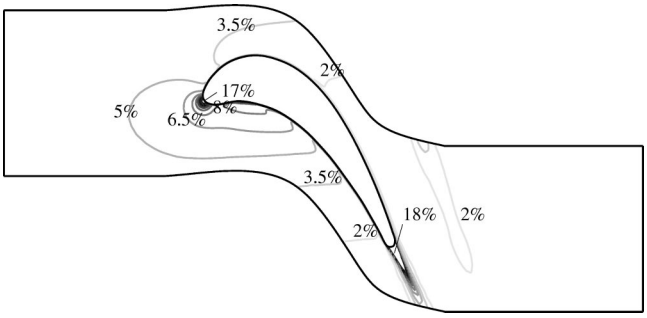

Fig. 6 Turbulence intensity, T bound with $k-\varepsilon$ model

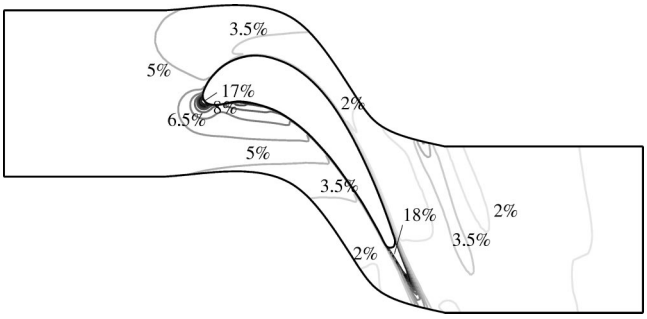

Fig. 7 Turbulence intensity, T bound with $k-\omega$ model

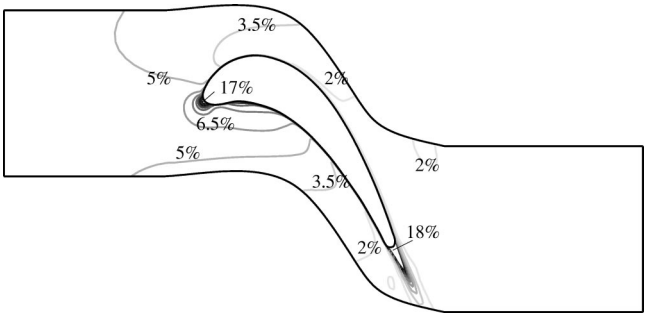

Fig. 8 Turbulence intensity, v^2-f model

normalization by $|U|$, Tu is high at the stagnation point and in the near wake in all of the figures. However, without limiters $k-\varepsilon$ and $k-\omega$ predict a pocket of high intensity below the pressure surface, while the other models show a monotonic decline of Tu through the passage. The bulge in the profile of h_t shown by the upper curve in Fig. 2 is not surprising in light of Fig. 3. That effect seems to be even more important in the case of $k-\omega$ model, which gives a peak value of 27.5 percent in the stagnation point region.

It might at first seem odd that the intensity *drops* in the strongly accelerating flow through the cascade passage. Indeed the turbulent energy rises from 37.5 to a maximum of 80 m^2/s^2 (in v^2-f computations, for instance), but the mean flow velocity increases more than $\sqrt{k}$, so that their ratio actually decreases. This behavior is qualitatively consistent with experiments in [12] and [13], and is also predicted by rapid distortion theory [9]. By contrast, $k-\varepsilon$ and $k-\omega$ with no limiters predict such an excessive increase of k that the turbulent intensity actually *increases*. The theory and limited data, just cited, argue strongly that this is unphysical.

In order to locate the regions where the standard $k-\varepsilon$ model violates the bound on the turbulent time scale, Figs. 9 and 10 present the ratio $T/T_{\lim}$, where $T=k/\varepsilon$ and $T_{\lim}=1/(\sqrt{6}C_\mu|S|)$. This ratio is plotted for two different values of the inflow turbulent dissipation rate ε. Where the ratio is greater than unity the limiter comes into play.

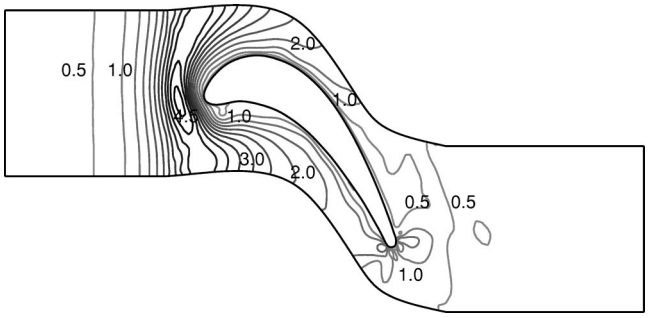

Fig. 9 $T/T_{\lim}$, $k-\varepsilon$ model, lower inflow value of ε, $l_\varepsilon = C_\mu^{3/4}k^{3/2}/\varepsilon = 0.01$ m

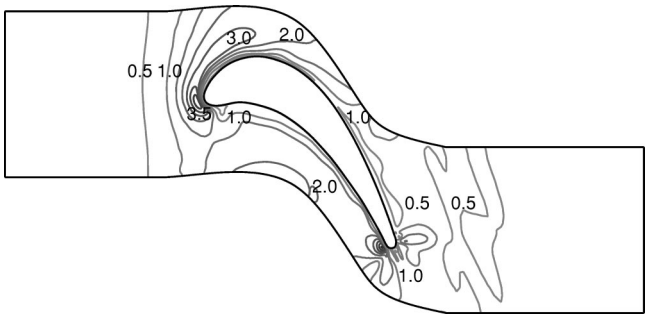

Fig. 10 $T/T_{\lim}$ $k-\varepsilon$ model, higher inflow value of ϵ, $l_\epsilon = C_\mu^{3/4}k^{3/2}/\epsilon = 0.001$ m model is used in any particular application

A higher level of inlet dissipation was used in Fig. 10. Such a device might be considered as an alternative method to reduce turbulent energy—cause it to decay before it reaches the blade. We consider this only because it has sometimes been noted that predictions can be improved by tuning the inlet conditions. While setting a higher value of inflow ε certainly does reduce the region where the time-scale inequality is violated, the stagnation point build-up of turbulent kinetic energy still presents a problem. Furthermore, increasing the inflow dissipation rate ε may lead to too strong decay of inflow turbulence, and therefore to the generation of flow conditions which differ from the actual situation of interest. With the limiter in place the model becomes much less sensitive to the inlet l_ε, since there is then no anomaly, even when l_ε is large.

In that sense, inclusion of the bound on turbulent time scale in the $k-\varepsilon$, or $k-\omega$, model represents a way to automatically preempt possible spurious predictions. Adjusting the inflow turbulence dissipation rate ε is not a generally applicable fix.

4 Conclusion

With the time-scale bound in place, rather good predictions are obtained using the two layer $k-\varepsilon$ model. This suggests that some of the failures reported in the literature may result from anomalous k production; an anomaly for which rather simple cures have been proposed.

We have shown herein that substantially improved heat transfer predictions can indeed be obtained by invoking these limiters. It should be emphasized that without the limiters, the excessive levels in the turbine passage are so high that they are actually the origin of over predictions of h_t—high levels of k near the stagnation point are not the only culprit.

Our objective in this paper has been to draw attention to an improvement that can be made to widely used turbulence models. Other considerations might determine which model is used in any particular application.

Appendix

Two-Layer Formulation of $k-\varepsilon$ Model. The two-layer method consists in patching together the $k-l$ and $k-\varepsilon$ models. The standard model equation for turbulent kinetic energy is

$$\partial_t(\rho k)+\nabla\cdot(\rho U k)=\rho P_k-\rho\varepsilon+\nabla\cdot((\mu+\mu_t)\nabla k) \tag{6}$$

where

$$\rho P_k=R:\nabla U=-\tfrac{2}{3}\rho k(\nabla\cdot U)+2\mu_t|S|^2-\tfrac{2}{3}\mu_t(\nabla\cdot U)^2 \tag{7}$$

with $S_{ij}=1/2(\partial_j U_i+\partial_i U_j)$ and μ_t being the eddy viscosity. It is used in both the $k-l$ and $k-\varepsilon$ formulations.

In the $k-\varepsilon$ model, Eq. (6) is supplemented by

$$\partial_t(\rho\varepsilon)+\nabla\cdot(\rho U\varepsilon)=\frac{C_{\varepsilon 1}\rho P_k-C_{\varepsilon 2}\rho\varepsilon}{T}+\nabla\cdot\left(\left(\mu+\frac{\mu_t}{\sigma_\varepsilon}\right)\nabla\varepsilon\right) \tag{8}$$

where the turbulence time-scale is $T=k/\varepsilon$ and the eddy viscosity is

$$\mu_t=C_\mu\rho kT \tag{9}$$

The standard model constants are

$$C_{\varepsilon 1}=1.44;\quad C_{\varepsilon 2}=1.92;\quad \sigma_\varepsilon=1.3;\quad C_\mu=0.09$$

In the $k-l$ model, the dissipation rate is represented by

$$\varepsilon=\frac{k^{3/2}}{l_\varepsilon} \tag{10}$$

and the eddy viscosity is

$$\mu_t=C_\mu\rho\sqrt{k}l_\nu \tag{11}$$

These supplement the k-equation (6). The VonDriest form for the length scales will be adopted here

$$l_\varepsilon=C_{ly}(1-e^{-R_y/A_\varepsilon});\quad l_\nu=C_l y(1-e^{-R_y/A_\nu}) \tag{12}$$

$R_y=y\rho\sqrt{k}/\mu$ is a wall-distance Reynolds number in which, for smooth walls, y is distance from the wall. The log-layer solution requires that $C_l=\kappa/C_\mu^{3/4}$ where κ is the VonKarman constant. The widely accepted value of $\kappa=0.41$ gives $C_l=2.5$. The requirement that $k\to\varepsilon y^2/2\nu$ as $y\to 0$ gives $A_\varepsilon=2C_l=5.0$. There is only one free constant, A_ν. The value $A_\nu=62.5$ was chosen for use with the two-layer formulation. This number gave very good agreement between C_f versus R_θ predictions and experiments for zero pressure gradient, flat plate boundary layers.

The two-layer formulation consists simply of using (11) and (10) near a wall, and switching abruptly to (9) and (8) at a patching point. The patching point is defined as the location where the damping function $1-e^{-R_y/A_\nu}$ equals 0.95; i.e., where $y=\log(20)A_\nu\nu/\sqrt{k}$. For solid walls, the boundary condition $k(0)=0$ is applied.

$k-\omega$ Model. In Wilcox's original $k-\omega$ model, the eddy viscosity is defined as $\mu_t=C_\mu\rho kT$, with turbulence time-scale $T=1/(C_\mu\omega)$; in other words, $\mu_t=\rho k/\omega$.

The original $k-\omega$ model equation for turbulent kinetic energy is

$$\partial_t(\rho k)+\nabla\cdot(\rho U k)=\rho P_k-C_\mu\rho\omega k+\nabla\cdot((\mu+\sigma_k\mu_t)\nabla k) \tag{13}$$

where

$$\rho P_k=R:\nabla U=-\tfrac{2}{3}\rho k(\nabla\cdot U)+2\mu_t|S|^2-\tfrac{2}{3}\mu_t(\nabla\cdot U)^2 \tag{14}$$

Equation (13) is supplemented by the equation for the specific dissipation rate ω

$$\partial_t(\rho\omega)+\nabla\cdot(\rho U\omega)=\frac{1}{T}\left(\frac{\gamma_1}{C_\mu k}\rho P_k-\frac{\beta_1}{C_\mu}\rho\omega\right)+\nabla\cdot(\mu+\sigma_\omega\mu_t)\nabla_\omega) \tag{15}$$

The original model constants are

$$\sigma_k=0.5;\quad \sigma_\omega=0.5;\quad \gamma_1=5/9;\quad \beta_1=0.075;\quad C_\mu=0.09$$

The boundary conditions for solid walls ($y\to 0$) are

$$k(0)=0,\quad \omega\to\frac{6\nu}{\beta_1 y^2} \tag{16}$$

v^2-f Model. The eddy viscosity is now defined as $\mu_t=C_\mu\rho\overline{v^2}T$, with the turbulence time-scale T

$$T=\min\left[\max\left[\frac{k}{\varepsilon},6\sqrt{\frac{\nu}{\varepsilon}}\right],\frac{\alpha k}{\sqrt{6}\,\overline{v^2}C_\mu|S|}\right] \tag{17}$$

with $\alpha=0.6$.

The equations for k and ε, (6) and (8), respectively, are supplemented with the equation for $\overline{v^2}$

$$\partial_t(\rho\overline{v^2})+\nabla\cdot(\rho U\overline{v^2})=\rho k f-\rho N\frac{\overline{v^2}}{k}\varepsilon+\nabla\cdot((\mu+\mu_t)\nabla\overline{v^2}) \tag{18}$$

with f representing the nonlocal effects

$$f-L^2\Delta f=(C_{f1}-1)\frac{2/3-\overline{v^2}/k}{T}+C_{f2}\frac{P_k}{k}+(N-1)\frac{\overline{v^2}}{kT} \tag{19}$$

where the turbulent length scale L is

$$L=C_L\max\left[\min\left[\frac{k^{3/2}}{\varepsilon},\frac{k^{3/2}}{\sqrt{6}\,\overline{v^2}C_\mu|S|}\right],C_\eta\frac{\nu^{3/4}}{\varepsilon^{1/4}}\right] \tag{20}$$

For solid walls, when $y\to 0$, this yields

$$k(0)=0;\quad \overline{v^2}(0)=0,\quad \varepsilon\to\frac{2\nu k}{y^2},\quad f\to-\frac{4(6-N)\nu^2\overline{v^2}}{\varepsilon y^4} \tag{21}$$

The original v^2-f model with $N=1$ was later modified (see [3], [14]) in order to avoid the numerical difficulties due to strong nonlinear coupling of turbulence variables through the boundary conditions (21) and the value of $N=6$ was chosen.

An additional modification was to eliminate the wall distance y from the equation for C_{e1} resulting in the following values of model constants used for the modified model:

$$C_\mu=0.22;\quad C_{\varepsilon 1}=1.4(1+0.050\sqrt{k/\overline{v^2}});\quad C_{\varepsilon 2}=1.9;$$
$$C_{f1}=1.4;\quad C_{f2}=0.3;\quad C_L=0.23;\quad C_\eta=70 \tag{22}$$

In this analysis we used this modified version of v^2-f model.

Acknowledgment

This work was sponsored by General Electric aircraft engines. We are grateful to Drs. Chander Prakash and Gary Steuber for private communications concerning their work at General Electric on excessive k production.

Nomenclature

M	=	Mach no.
$\mathrm{Re}_{c,\mathrm{in}}$	=	inflow Reynolds no. (based on chord length c)
T_o	=	total temperature
T_w	=	wall temperature
Tu	=	turbulence intensity $=\sqrt{2/3k}/\lvert U\rvert$
c	=	blade chord

h_t = heat transfer coefficient$=\dot{q}_w/(T_{o\infty}-T_w)$
$\dot{q}_w$ = wall heat flux rate
s = curvilinear coordinate

Subscripts

∞ = free stream
in = inflow
ex = exit
w = wall
o = total conditions
is = isentropic conditions

References

[1] Prakash, C., 1995, "Some Experiences With the Standard $k-\varepsilon$, RNG and Chen Turbulence Models," *National Turbulent Combustion Model Meeting, NASA Lewis*, July 27–28.

[2] Durbin, P. A., 1996, "On the $k-\varepsilon$ Stagnation Point Anomaly," Int. J. Heat Fluid Flow, **17**, pp. 89–90.

[3] Behnia, M., Parneix, S., Shabany, Y., and Durbin, P. A., 1999, "Numerical Study of Turbulent Heat Transfer in Confined and Unconfined Impinging Jets," Int. J. Heat Fluid Flow, **20**, pp. 1–9.

[4] Kato, M., and Launder, B. E., 1993, "Modelling Flow-Induced Oscillations in Turbulent Flow Around a Square Cylinder," ASME FED **157**, pp. 189–199.

[5] Camci, C., and Arts, T., 1985, "Short Duration Measurements and Numerical Simulation of Heat Transfer Along the Suction Side of a Film-Cooled Gas Turbine Blade," ASME J. Eng. Power, **107**, pp. 991–997.

[6] Camci, C., and Arts, T., 1985, "Experimental Heat Transfer Investigation Around the Film-Cooled Leading Edge of a High-Pressure Gas Turbine Rotor Blade," ASME J. Eng. Power, **107**, pp. 1016–1021.

[7] Camci, C., and Arts, T., 1990, "An Experimental Convective Heat Transfer Investigation Around a Film-Cooled Gas Turbine Blade," ASME J. Turbomach., **112**, pp. 497–503.

[8] Wilcox, D. C., 1993, *Turbulence Modeling for CFD*, DCW Industries, Inc., La Canada, CA.

[9] Durbin, P. A., and Pettersson Reif, B. A., 2001, *Statistical Theory and Modeling for Turbulent Flow*, John-Wiley & Sons, New York, NY.

[10] *STAR-CD Version 3.10—Methodology, 1999*, Computational Dynamics Limited.

[11] Durbin, P. A., 1990, "Turbulence Modeling Near Rigid Boundaries," *CTR Annual Research Briefs*, Stanford University, Stanford, CA.

[12] Radomsky, R. W., and Thole, K. A., 2000, "Flowfield Measurements for a Highly Turbulent Flow in a Stator Vane Passage," ASME J. Turbomach., **122**, pp. 255–262.

[13] Priddy, W. J., and Bayley, F. J., 1988, "Turbulence Measurements in Turbine Blade Passages and Implications for Heat Transfer," ASME J. Turbomach., **110**, pp. 73–79.

[14] Lien, F. S., and Kalitzin, G., 2001, "Computations of Transonic Flows With the v^2-f Turbulence Model," Int. J. Heat Fluid Flow, **22**, pp. 53–61.

G. Medic
e-mail: gmedic@stanford.edu

P. A. Durbin
e-mail: durbin@vk.stanford.edu

Mechanical Engineering Department,
Stanford University,
Stanford, CA 94305-3030

Toward Improved Film Cooling Prediction

Computations of flow and heat transfer for a film-cooled high pressure gas turbine rotor blade geometry are presented with an assessment of several turbulence models. Details of flow and temperature field predictions in the vicinity of cooling holes are examined. It is demonstrated that good predictions can be obtained when spurious turbulence energy production by the turbulence model is prevented. [DOI: 10.1115/1.1458021]

1 Introduction

In a companion paper [1], we demonstrated that the prediction of turbine blade heat transfer by two-equation turbulence closures could be greatly improved. In the absence of film cooling, the standard $k-\omega$ and two-layer $k-\epsilon$ models trend to overpredict the blade surface heat transfer coefficient, due mainly to the spurious production of turbulent energy under large rates of strain. This is a critical failing for turbomachinery applications—known, although not widely appreciated. It was demonstrated that this problem can be allayed by simple modifications of the native models. Either of the two cures proposed in [2] and [3] were found to give substantial improvement in predictions of heat transfer level. The term ''limiter'' can be used for this generic type of cure. In [1], the limiters improved heat transfer predictions by about 50 percent and reduced the excessive turbulent energy by a factor of about 30. It is known from theory and experiment that the level of k obtained with the limiters is far more plausible than without them.

The present paper extends the assessment to the problem of film cooling. Detailed computations of the flow through the film cooling hole and over the blade have previously met with limited success [4]. While the far-field full coverage film can be accurately computed, the near hole region is more difficult. Correct prediction of film-cooling heat transfer is directly related to the predicting how the jet mixes into the ambient cross-flow. Such predictions are strongly influenced by the choice of turbulence model.

Four configurations were studied in Camci and Arts [5–8], we will consider only two: suction side cooling and pressure side cooling, with different flow conditions. The overall flow is quite complex. It joins together the difficulties of computing the flow and associated heat transfer in a transonic cascade with the need for precise computations of the low speed flow in the cooling plenum and through the cooling holes. The velocity field in these holes is strongly non-uniform, with large secondary flow effects, see [4,9]. The cylindrical holes are conically shaped at the junction with the outer blade surface, adding the difficulty of accurately predicting diffuserlike geometries.

Computations of this test case have been presented in [10]. These authors used a simple algebraic turbulence model, without any detailed accounting for how the flow in the vicinity of the film cooling apparatus influences the turbulence. In the present paper, however, we find that predictions vary significantly with the different turbulence models, underlining the need to properly understand the coolant flow and its mixing with the mainstream.

Better understanding of the effects of hole geometry, and better predictions, especially of its influence on the local flow, could lead to the improvement of the hole geometry design process. More accurate computations might also make it possible to use predictive methods to optimize the positioning of cooling holes in the blade surface [11].

Contributed by the International Gas Turbine Institute for publication in the JOURNAL OF TURBOMACHINERY. Manuscript received by the IGTI, March 20, 2001; revised manuscript received Octoer 15, 2001. Associate Editor: R. Bunker.

2 Film Cooling

The same experiment of [6], addressed in the companion article, is computed here for two cases with film cooling. The first is a double row of staggered axial cooling holes on the suction side of the blade; the other has a single row of cooling holes along the pressure side. Detailed experimental results for various configurations are published in Camci and Arts [5–8]. An outline of the blade, with the location of the cooling holes and plenum shown, is presented in Fig. 1.

On the suction side there are two rows (S) of staggered axial holes located at $s/c=0.206$, 0.237, with s measured from the leading edge, LM, and $c=80$ mm. They have diameter $d=0.8$ mm at their base, and are conically flared, with a 10 deg angle of expansion below the exit. The row and hole spacings are, respectively, 2.5 and 2.6 mm. These holes are inclined at 37 and 43 deg with respect to the local blade surface. A single row of conically shaped, axial holes ($d=0.8$ mm, 10 deg angle of expansion, $s/c=-0.315$) is located on the pressure surface (P). The hole spacing is 2.6 mm. These holes are inclined at 35 deg with respect to the local blade surface. More detailed description of the hole geometry can be found in Camci and Arts [5–7].

The flow through the cascade is under the same conditions as when there is no cooling present: $M_{in}=0.25$, $Re_{cin}=8.5\cdot 10^5$, $Tu_{in}=5\%$, $T_{0\infty}=409.5$ K, inflow angle=30 deg, The exit Mach number is $M_{ex,is}=0.92$ and the wall temperature is $T_w=298$ K.

Several coolant inflow conditions were analyzed, both for the suction side and the pressure side cooling; notably, coolant temperatures T_c and blowing ratios $m=U_c\rho_c/(U_\infty\rho_\infty)$ were varied. Here, $U_c\rho_c$ is obtained from the mass flux and hole area, and $U_\infty\rho_\infty$ is found from local surface pressure, inlet total pressure and isentropic relations.

The experimental data are presented in the form of spanwise-averaged heat transfer coefficient h_t for a given wall temperature T_w (and not in the form of adiabatic effectiveness). Thus, we compare the heat transfer coefficient h_t with the computational predictions obtained with different turbulence models.

2.1 Numerical Procedure. For the process of numerical solution of flow equations, the turbulence models (modifications of two-layer $k-\epsilon$, standard and modified $k-\omega$ and v^2-f) were implemented into an implicit finite volume solver based on a variant of the well known SIMPLE method (see [12]), with the turbulence model equations decoupled and solved sequentially, for details see also [1].

Generation of a computational mesh for this flow presents a major challenge. We have opted for a multi-block, structured mesh having nonmatching (or non-conforming) interfaces. This

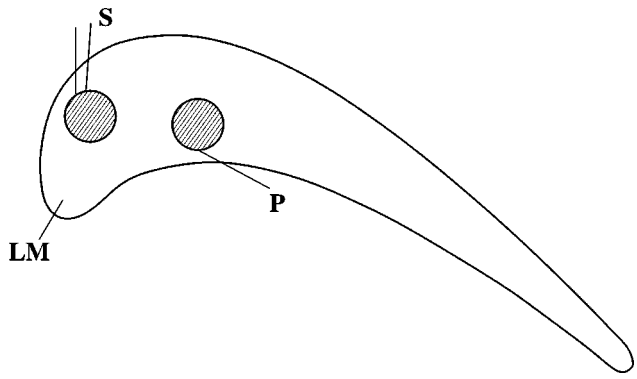

Fig. 1 Geometry of cooling holes

gives significant flexibility in generating generic mesh-blocks for different film cooling configurations—suction side cooling holes, pressure side holes, leading edge cooling, etc.

There are four non-matching mesh blocks: a plenum mesh; a mesh in the conical tubes; a portion of very fine outer O-mesh just above the cooling holes; and the rest of the outer O-mesh. Figures 2 and 3 are details of the grid near the cooling holes. It shows the higher resolution needed to capture the jet.

This topology, together with the mesh independence testing, lead to the final computational mesh of 750,000 vertices, with sufficiently fine resolution in the region of the holes.

Another matter of concern was specification of inflow boundary conditions for the coolant. The coolant plenum was included in the analysis, since the flow at the entrance to the cooling holes is far from being uniform and the length of the cooling tubes $L/D = 5-6$ implies that at the exit of the cooling tube the flow is not yet completely developed, see also [4] and [13]. Details of the flow field in the vicinity of the plenum-tube junction for the suction side holes are presented in Fig. 4. There is a low-momentum region at the inner wall of the tubes, induced by the turning of the flow into the cooling tubes. This leads to generation of high levels of turbulent kinetic energy at the boundary of that low momentum region inside the tubes. Such an effect can be seen in the v^2-f computations presented in Fig. 5.

To match experimental blowing ratios, it was necessary to iteratively adjust the plenum pressure. This is a computationally expensive procedure, but a good match to experimental conditions was obtained.

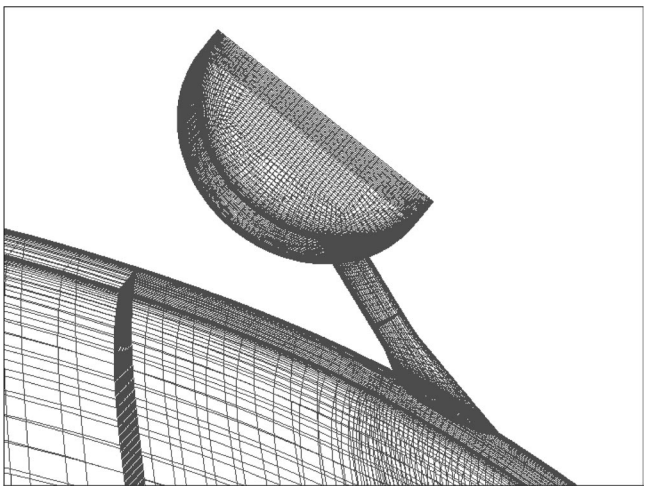

Fig. 3 Detail of the computational mesh, pressure side cooling holes

The appropriate boundary conditions for turbulence in the plenum are uncertain. To see whether this had any bearing on our results we have tested several levels of turbulence intensity, up to 20 percent. No significant effect on the film cooling predictions was observed since the flow in the plenum has very low velocity compared to the flow in the tubes, and the same goes for the value of turbulent kinetic energy when compared to the level of turbulent kinetic energy produced at the entrance of cooling tubes.

There was also some concern over the question of the appropriate inflow temperature to the plenum. For coolant temperatures, T_c, lower than the wall temperature, T_w, it was not clear whether heat transfer occurs in the plenum via conduction through the walls. To eliminate this uncertainty, we chose to consider the isothermal case, $T_c = T_w$, exclusively. A few calculations were done with $T_c = 0.7T_w$: they showed lower h_t near the exit of the cooling holes than the isothermal case. Experiments showed a smaller level of difference between the cold jet and isothermal cases, but the exit region is where preheating effects would be most significant.

In the results presented in [1] it was seen that the standard $k-\epsilon$ and $k-\omega$ models grossly overpredict the heat transfer coefficient h_t in the absence of film cooling. When either of the two

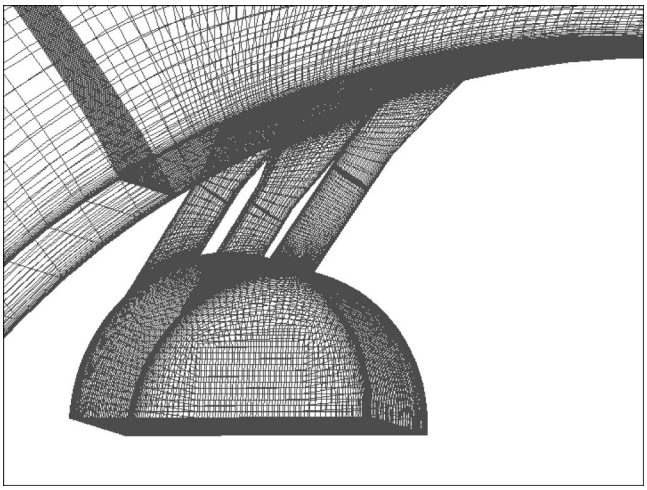

Fig. 2 Detail of the computational mesh, suction side cooling holes

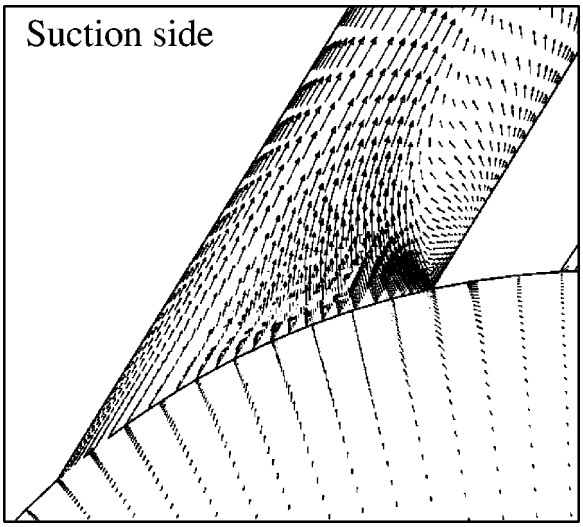

Fig. 4 Detail of velocity vectors in the plenum-tube junction region, computations with v^2-f model

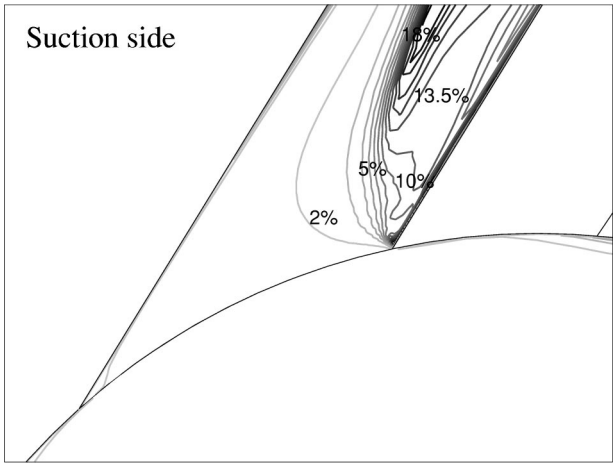

Fig. 5 Detail of turbulent intensity contours in the plenum-tube junction region, computations with v^2-f model

limiters were invoked, correct levels of heat transfer coefficient were predicted over most of the blade (with the primary exception in a zone on the suction side, near the leading edge).

This tendency was confirmed in the present cases with film cooling; the high values of turbulent viscosity in the passage predicted by the standard $k-\epsilon$ model led to overprediction of heat transfer coefficient downstream of cooling holes. For that reason, the majority of our comparisons of numerical solutions to experimental data on heat transfer will be for the $k-\epsilon$ model with a bound on turbulent time-scale and for the v^2-f model.

2.2 Suction Side Film Cooling. The coolant inflow conditions of Camci and Arts [5–7] for the suction side were blowing ratios in the range $m=0.45-1.0$, and temperatures in the range $T_c/T_w=0.6-1.0$. For the reason given in the foregoing, we will consider only the isothermal case, $T_c=T_w$. Since the numerical results for lower blowing ratios ($m=0.45$ and 0.60) tend to agree better with the experimental data, we will put more attention to detailed analysis of the flow field for the high blowing ratio, $m=1.0$; See Fig. 6.

As seen in Figs. 7 and 8, for lower blowing ratios the spanwise-averaged heat transfer coefficient h_t is predicted reasonably well, both with the $k-\epsilon$ model, invoking the bound on the turbulent time scale T, and with the v^2-f model. Near the hole the $k-\epsilon$ solution is in good agreement with data, while the v^2-f prediction is low.

However, for the high blowing ratio, $m=1.0$, Fig. 9 evidences are more significant discrepancies with the experimental data, especially in the vicinity of the film cooling holes. This figure presents results with four models that were assessed for the flow without cooling; the standard, two-layer $k-\epsilon$, the [2] modification to production, the time-scale limit [3], and v^2-f. Kato-Launder predictions of h_t are a bit higher than obtained with the time scale bound, and a bit higher than the data in the downstream region. The native $k-\epsilon$ model grossly overpredicts heat transfer

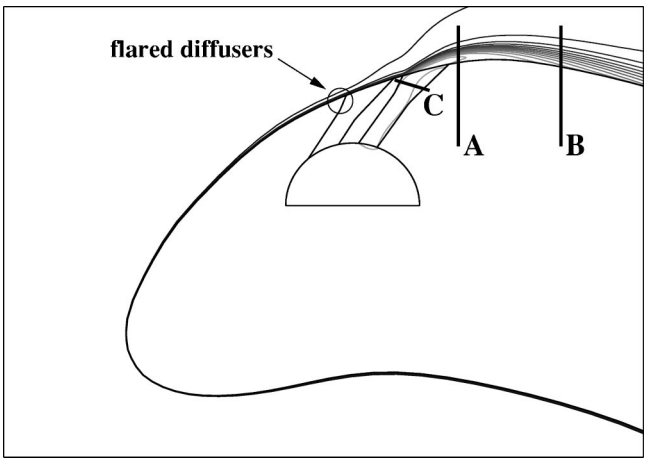

Fig. 6 Temperature and location of characteristic cross sections, $m=1.0$

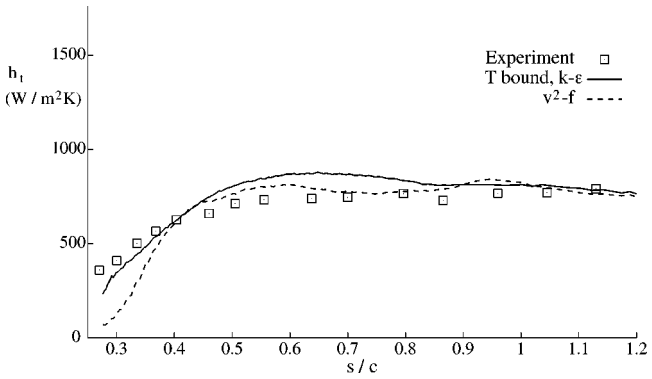

Fig. 7 Heat transfer coefficient, h_t (W/m²K), suction side cooling, $m=0.45$

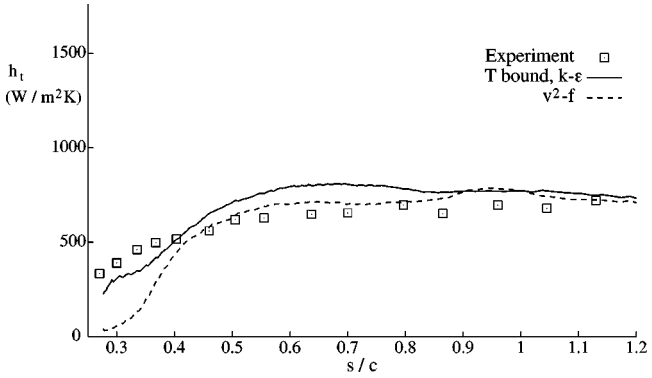

Fig. 8 Heat transfer coefficient, h_t (W/m²K), suction side cooling, $m=0.6$

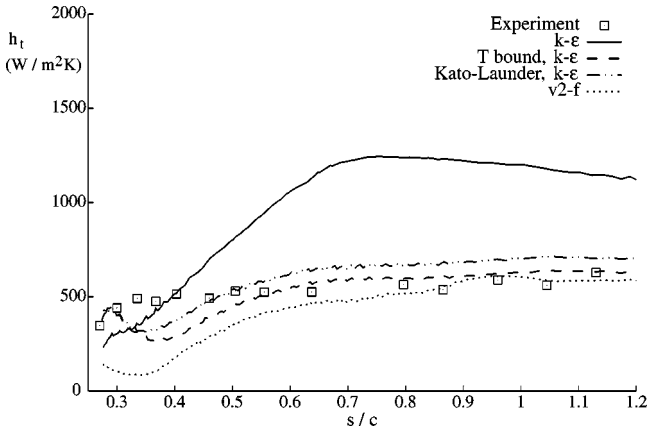

Fig. 9 Heat transfer coefficient, h_t (W/m²K), suction side cooling, $m=1.0$

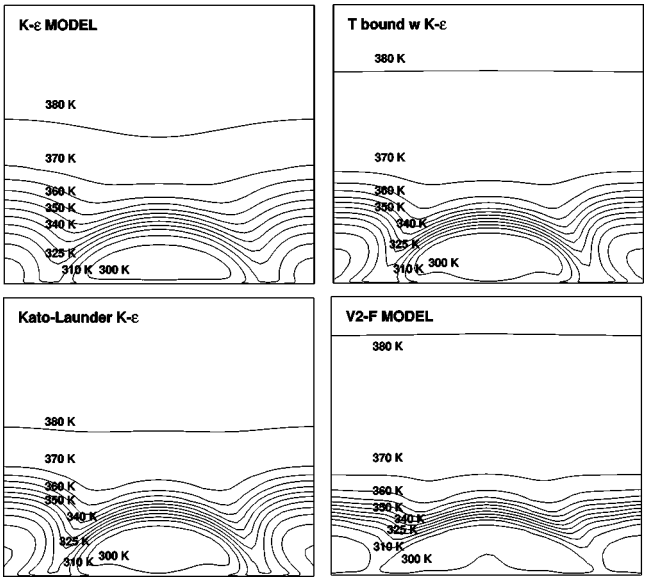

Fig. 10 Temperature contours computed with different turbulence models, cross section A, suction side cooling, high blowing ratio m=1.0

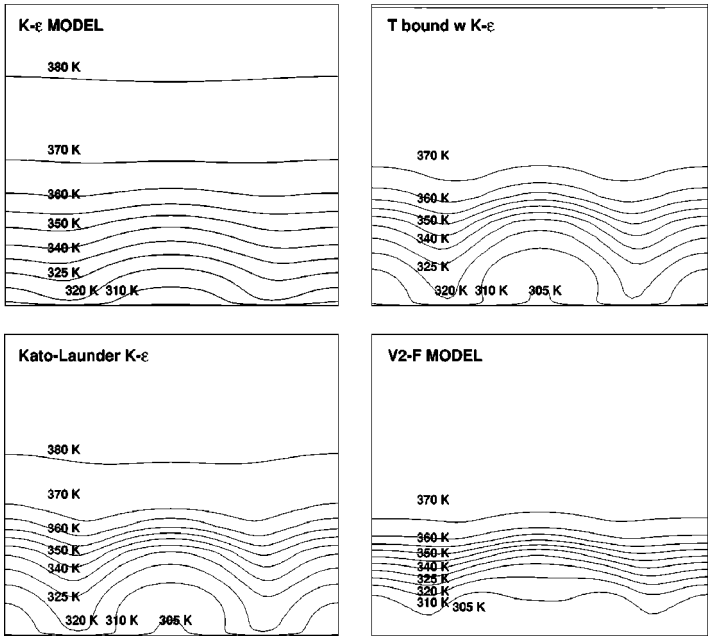

Fig. 11 Temperature contours computed with different models, cross section B, suction side cooling, high blowing ratio m=1.0

in the downstream region. This is due to excessive production of turbulence by the straining flow in the center of the passage. The excessive energy penetrates the boundary layer, leading to the increase of wall heat transfer (as in the case without cooling); the predictions h_t become completely erroneous.

Finally, the v^2-f model tends to predict the correct level of heat transfer coefficient downstream of the cooling holes, but not in the vicinity of the holes. There the level of cooling is overpredicted, resulting in lower values of h_t.

In order to better understand the computational predictions in the vicinity of the cooling holes, some relevant quantities were plotted in cross flow planes. Attention is focused on this blowing ratio of $m=1.0$. The following discusses fields of temperature, turbulence intensity, crossflow velocity and velocity magnitude, obtained with the various turbulence models. The locations of these characteristic cross-sections are shown in Fig. 6: axial sections (x=const) A and B are located at $s/c=0.28$ and 0.35, respectively; section C is located at 3/4 of the height of the second cooling tube.

Temperature contours in cross sections A and B are presented in Figs. 10 and 11. They reveal that the v^2-f model predicts the greatest spanwise spreading of the region of cold temperature, in the core of the cooling jet. All three $k-\epsilon$ results (standard, T bound, Kato-Launder) show less lateral spreading near the hole. The lateral spreading is due to a pair of counter-rotating, streamwise vortices that form on either side of the hole. Stronger spreading causes lower heat transfer because the jet shields the surface from the hot ambient.

Further downstream, in cross section (B), high turbulent viscosity is predicted by the standard $k-\epsilon$ model, leading to more diffusion. This causes high temperatures to penetrate from the freestream significantly closer to the blade surface than with other models.

Turbulence intensity contours in the same cross sections (Figs. 12 and 13) seem to be consistent with what was observed in the case without cooling [1]—the native $k-\epsilon$ model, with no limiters, strongly overpredicts turbulence levels.

Examining the velocity magnitude contours inside the second row of cooling holes (Fig. 14, which is a plane normal to the axis of the hole), we can see that the kidney-shaped core of the jet predicted with the v^2-f model seems to be slightly larger than with the other models. This larger high velocity region is probably a result of a weaker recirculation near the walls of this diffuser part of the tube.

It seems that differences in the magnitude of crossflow, as well in the high-velocity core of the jet, alter the extent of jet penetration into the mainstream and of the lateral spreading of cool fluid. These differences originate *inside* the hole. Their effect on turbulence production and the level of turbulent viscosity in the near wall region is equally important. The v^2-f model leads to a stronger interaction between the two rows of jets, and therefore to more spreading of coolant across the blade surface in the spanwise direction. $k-\epsilon$ predicts a higher near-wall eddy viscosity.

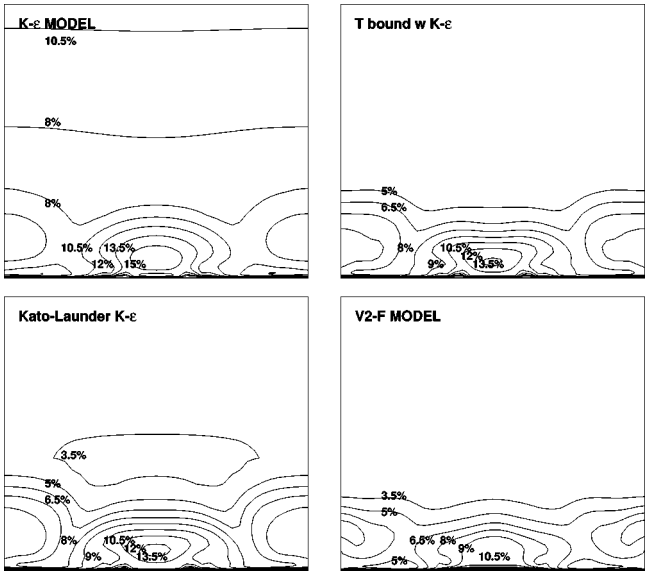

Fig. 12 Turbulence intensity computed with various models, cross section A, suction side cooling, high blowing ratio m=1.0

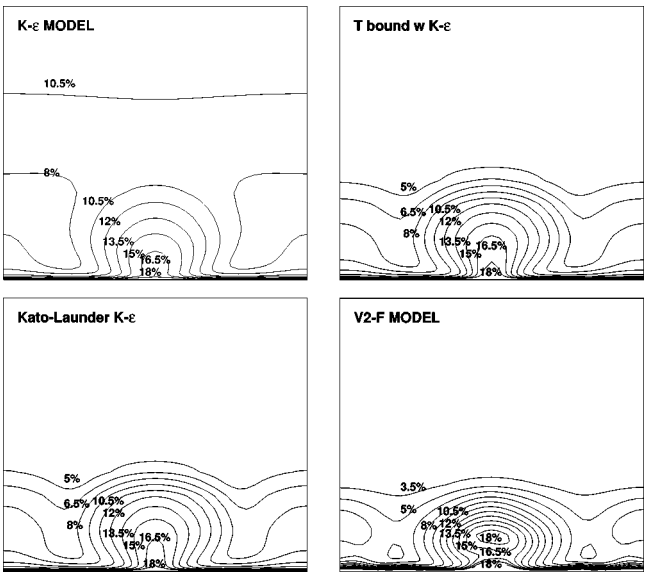

Fig. 13 Turbulence intensity computed with various models, cross section B, suction side cooling, high blowing ratio *m*=1.0

2.3 Pressure Side Film Cooling. The inflow boundary conditions for the coolant for the pressure side experiments of Camci [5] were blowing ratios in the range $m=1.75-4.25$ (see Fig. 15), and temperatures in the range $T_c/T_w=0.6-1.0$. As before, only the isothermal case $T_c=T_w$ will be considered; the experimental blowing ratios were 1.74, 3.28, and 4.23.

Similarly to the suction side cooling, lower blowing ratio cases are easier to compute. As can be seen from h_t predictions with $m=1.75$ in Fig. 16, solutions to the $k-\epsilon$ model with the bound on T invoked, agree reasonably well with the experimental measurements.

However, increasing the blowing ratio leads to the situation where the jet actually penetrates into the mainstream; see also [5]. As a consequence, a region of increased heat transfer occurs just downstream of cooling holes ($s/c\approx-0.35$ in Fig. 18)—near the holes without cooling h_t was about 20 percent lower. This phenomenon is difficult to compute accurately. The spanwise averaged heat transfer coefficient for $m=3.3$ and 4.25 is provided in Figs. 17 and 18, respectively.

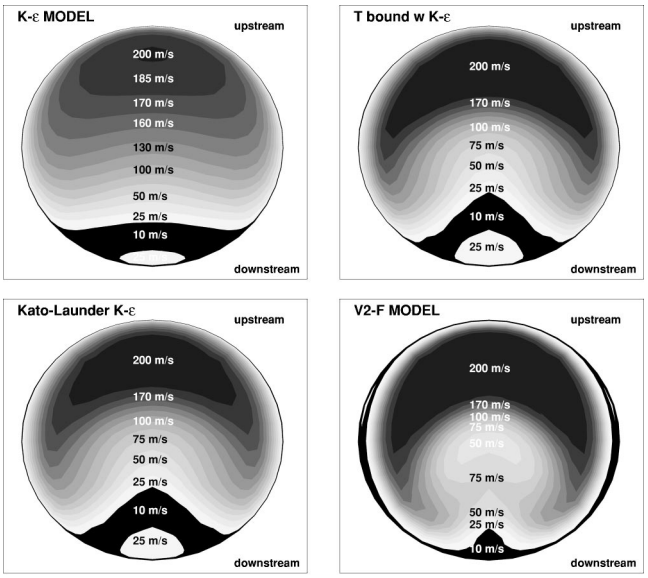

Fig. 14 Velocity magnitude with different models, cross section C, suction side cooling, high blowing ratio *m*=1.0 (cascade inflow $U_{inflow}=100$ m/s)

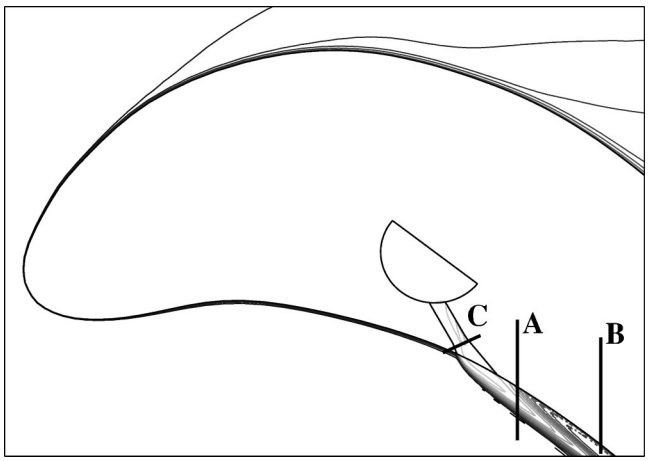

Fig. 15 Temperature and location of characteristic cross sections, *m*=4.25

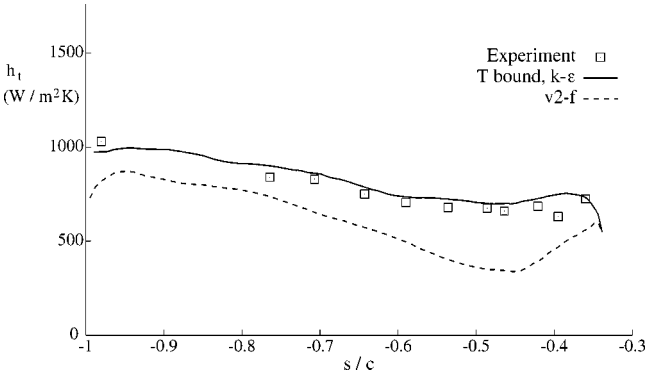

Fig. 16 Heat transfer coefficient, h_t (W/m²K), pressure side cooling, *m*=1.75

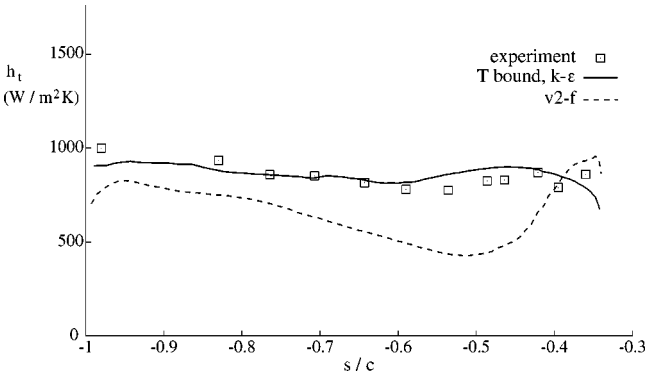

Fig. 17 Heat transfer coefficient, h_t (W/m²K), pressure side cooling, *m*=3.3

The predictions vary significantly in the vicinity of the cooling holes. The standard $k-\epsilon$ model gives predictions that are similar to the case of suction side cooling: further downstream the over estimation of turbulence level in the passage leads to an overprediction of wall heat transfer. (Note that the downstream direction in Figs. 16–18 is to the left, $s/c\rightarrow-1$.)

The v^2-f model does not recover to the right level. This is consistent with the results without film cooling in [1], where v^2

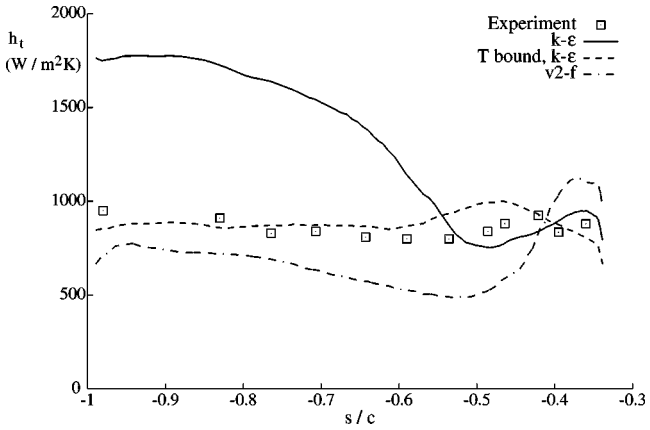

Fig. 18 Heat transfer coefficient, h_t (W/m^{2}K), pressure side cooling, m=4.25

$-f$ already tended to underpredict the heat transfer towards the rear of the pressure side. The main discrepancy is due to the baseline h_t, not to the film cooling, *per se*. On the other hand, the predictions with the $k-\epsilon$ model with the time-scale bound in place, seem to be in even better agreement with experiments than for suction side cooling. It is quite remarkable that this simple modification to the time-scale can improve predictions so substantially.

As for the suction side cooling, we will investigate the flow fields more closely for the high blowing ratio, m=4.25. Contour plots are provided at a few characteristic cross-sections, presented in Fig. 15. Axial sections (x=const) A and B are located at $s/c = -0.35$ and -0.45, respectively, section C is at 3/4 of the height of the cooling tube.

Comparing the computed temperature contours in cross-sections A and B (Figs. 19 and 20), one observes similar tendencies as for the suction side cooling. The core of the jet predicted by v^2-f model spreads more in the spanwise direction than with the other models. Figure 19 shows a temperature minimum well above the boundary layer, with higher temperatures penetrating under the jet; this is by contrast to Fig. 10, where the temperature minimum is adjacent to the surface. Thus, the jet is seen to have lifted from the wall at the blowing ratio m=4.25. Downstream, at section B, the elevated cold spot has largely dispersed, although it is still detectable in the modified $k-\epsilon$ solution (Fig. 20). Although the link between surface heat flux and the jet trajectory is somewhat circumstantial, it is generally believed that correct h_t predictions depend strongly on correct jet lift-off.

Finally, the velocity magnitude contours inside the tube, at cross section C, are presented in Fig. 21. Similar effects to the suction side case can be seen: slightly high velocity in the core of the jet predicted with the v^2-f model, and a slightly smaller low-speed region on the downstream side.

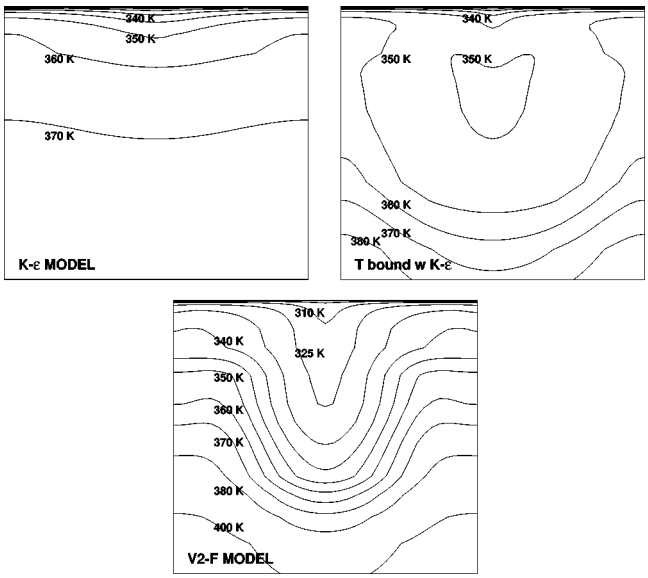

Fig. 20 Temperature contours computed with different models, cross section B, pressure side cooling, high blowing ratio m=4.25 (blade surface at the top)

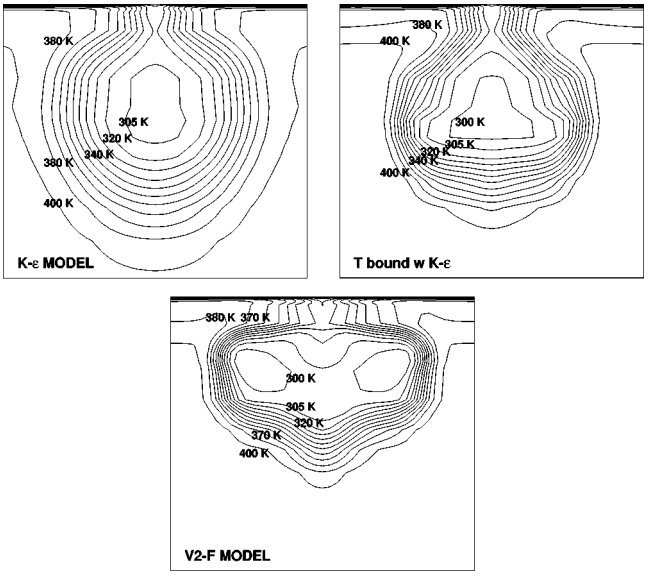

Fig. 19 Temperature contours computed with various turbulence models, cross section A, pressure side cooling, high blowing ratio m=4.25 (blade surface at the top)

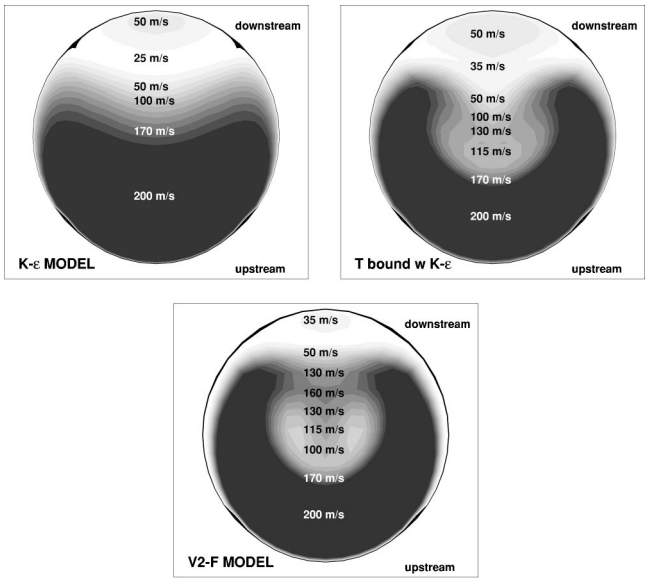

Fig. 21 Velocity magnitude with different models, cross section C, pressure side cooling, high blowing ratio m=4.25 (cascade inflow U_{inflow}=100 m/s)

3 Conclusions

In [1] and here, we have conducted detailed analysis of an experimentally documented test case. Turbulence models meant for practical, engineering flow computation have been used. Results were presented for the flow in the absence of, and with film cooling.

The most practically significant result of this study is that the native $k-\epsilon$ or $k-\omega$ models can give wildly unreasonable predictions of heat transfer in turbine passages. This fault is readily cured by invoking a bound on turbulent time scale. This *does not mean that the solution is clipped*; rather where a time-scale is needed, such as in the formula $\nu_t = C_\mu kT$, the bounded value is used. For instance, the $k-\omega$ eddy viscosity becomes

$$\nu_t = k \times \min\left[\frac{1}{\omega}, \frac{\alpha}{\sqrt{6}|S|}\right]$$

rather than $\nu_t = k/\omega$.

Numerical results for film cooling show that the $k-\epsilon$ model using the bound for turbulent time-scale T and the v^2-f model give satisfactory predictions of the overall heat transfer coefficient levels, except for high blowing ratios. On the suction side, they tend to overpredict the level of cooling in the vicinity of the film holes, that being true especially for v^2-f computations. On the pressure side the cooling jet penetrates into the mainstream, and it appears that the v^2-f model predicts stronger jet lateral spreading than the other models. This seems to originate inside the diffusing section of the cooling hole.

This analysis of film cooling represents a step in the direction of proper understanding of the effects of hole geometry and especially its influence on the local flow field, as well as better understanding of computational predictions using various turbulence models.

Acknowledgments

This work was sponsored by General Electric Aircraft Engines.

Nomenclature

- M = Mach no.
- $\mathrm{Re}_{c\mathrm{in}}$ = inflow Reynolds no. (based on chord length c)
- T_o = total temperature
- T_w = wall temperature
- T_c = coolant inflow temperature
- Tu = turbulence intensity $= \sqrt{2/3\,k}/|U|$
- c = blade chord
- h_t = heat transfer coefficient $= \dot{q}_w/(T_{o\infty} - T_w)$
- k = turbulent kinetic energy (per unit mass)
- m = blowing ratio $= U_c\rho_c/(U_\infty\rho_\infty)$, based on local free stream values
- $\dot{q}_w$ = wall heat flux rate
- s = curvilinear coordinate
- ϵ = rate of turbulent energy dissipation

Subscripts

- ∞ = free stream
- c = coolant inflow
- in = inflow
- ex = exit
- w = wall
- o = total conditions
- is = isentropic conditions

References

[1] Medic, G., and Durbin, P. A., 2002, "Toward Improved Prediction of Heat Transfer on Turbine Blades," ASME J. Turbomach., **124**, pp. 187–192.

[2] Launder, B. E., and Kato, M., 1993, Modelling Flow-Induced Oscillations in Turbulent Flow Around a Square Cylinder," ASME FED **157**, pp. 189–199.

[3] Durbin, P. A., 1996, "On the $k-\epsilon$ Stagnation Point Anomaly," Int. J. Heat Fluid Flow, **17**, pp. 89–90.

[4] Leylek, J. H., and Zerkle, R. D., 1994, "Discrete-Jet Film Cooling: A Comparison of Computational Results with Experiments," ASME J. Turbomach., **116**, pp. 358–368.

[5] Camci, C., 1985, *Theoretical and Experimental Investigation of Film Cooling Heat Transfer on a Gas Turbine Blade*, Ph.D. thesis, Von Karman Institute for Fluid Dynamics and University of Leuven, Belgium.

[6] Camci, C., and Arts, T., 1985a, "Short Duration Measurements and Numerical Simulation of Heat Transfer Along the Suction Side of a Film-Cooled Gas Turbine Blade," ASME J. Eng. Power, **107**, pp. 991–997.

[7] Camci, C., and Arts, T., 1985b, "Experimental Heat Transfer Investigation Around the Film-Cooled Leading Edge of a High-Pressure Gas Turbine Rotor Blade," ASME J. Eng. Power, **107**, pp. 1016–1021.

[8] Camci, C., and Arts, T., 1990, "An Experimental Convective Heat Transfer Investigation Around a Film-Cooled Gas Turbine Blade," ASME J. Turbomach., **112**, pp. 497–503.

[9] Walters, D. K., and Leylek, J. H., 2000, "A Detailed Analysis of Film Cooling Physics: Part I—Streamwise Injection With Cylindrical Holes," ASME J. Turbomach., **122**, pp. 102–112.

[10] Garg, V. K., and Gaugler, R. E., 1997, "Effect of Coolant Temperature and Mass Flow on Film Cooling of Turbine Blades," Int. J. Heat Mass Transf., **40**, 435–445.

[11] Friedrics, S., Hodson, H. P., and Dawes, W. N., 1999, "The Design of an Improved Endwall Film-Cooling Configuration," ASME J. Turbomach., **121**, pp. 772–780.

[12] STAR-CD Version 3.10—Methodology, 1999, Computational Dynamics Limited.

[13] Hale, C. A., Plesniak, M. W., and Ramadhyani, S., 2000, "Film Cooling Effectiveness for Short Film Cooling Holes Fed by a Narrow Plenum," ASME J. Turbomach., **122**, pp. 553–557.

Thermal Field and Flow Visualization Within the Stagnation Region of a Film-Cooled Turbine Vane

J. Michael Cutbirth[1]
e-mail: CutbirthJM@nswccd.navy.mil

David G. Bogard
e-mail: dbogard@mail.utexas.edu

Mechanical Engineering Department,
University of Texas at Austin,
Austin, TX 78712

To develop quality computational codes for the film cooling of a turbine vane, a detailed understanding is needed of the physical mechanisms of the mainstream-coolant interactions. In this study flow visualization, thermal profiles, and laser Doppler velocimetry measurements were used to define the thermal and velocity fields of the film cooled showerhead region of a turbine vane. The showerhead consisted of six rows of spanwise oriented coolant holes, and blowing ratios ranged from 0.5 to 2.0. Performances with low and high mainstream turbulence levels were tested. Coolant jets from the showerhead were completely separated from the surface even at relatively low blowing ratios. However, the interaction of the coolant jets from laterally adjacent holes created a barrier to the mainstream flow, resulting in relatively high adiabatic effectiveness.
[DOI: 10.1115/1.1451086]

Introduction

One of the most critical areas for turbine vane cooling, with respect to failure due to thermal loads, is of the leading edge of a turbine vane. The common approach to the protection of this region of the vane is to incorporate a dense array of discrete film cooling holes, typically referred to as the showerhead. Because of the high degree of coolant hole-to-hole interaction, this region cannot be reasonably approximated using simplified geometries with single and double rows of coolant holes. Furthermore, the location of the showerhead in terms of surface curvature and pressure gradient varies between vanes and blades. Consequently, the showerhead region of the vane, as studied by Polanka et al. [1] and Drost and Bölcs [2], is very different from leading edge cooling for blades as studied by Du et al. [3] and Takeishi et al. [4].

Previous turbine vane studies have concentrated on the lateral averaged adiabatic effectiveness and heat transfer coefficient, eg. Drost and Bölcs [2], and spatially resolved adiabatic effectiveness measurements, eg., Polanka et al. [1]. However, both the adiabatic effectiveness and heat transfer coefficient only offer a ''footprint'' of the film cooling jets. Therefore, while yielding results in overall film cooling performance, little insight is provided into the physical mechanisms involved in the coolant/mainstream interaction. Identification of these physical mechanisms is essential to the development of reliable computational codes.

To investigate the coolant/mainstream interaction, ''off-the-wall'' measurement techniques are required. These measurement techniques include the thermal and velocity fields as well as flow visualization providing visual snapshots of the coolant/mainstream interaction. Both thermal field measurements, such as Thole et al. [5] and Oke and Simon [6], and velocity field measurements, such as Pietrzyk et al. [7] and Sinha et al. [8], have been performed for various flat plate studies. However, similar measurements have not been previously made for the showerhead region.

Several turbine studies without film cooling have incorporated flow visualization as a measurement tool, such as Wang et al. [9] for the passage vortex, and Roy et al. [10] for the endwall flow through the turbine passage. However, only Schwarz et al. [11] incorporated this tool for a study of film cooling. In this study, flow visualization was used to evaluate the film cooling over a curved surface. No previous investigations have been performed using flow visualization on the showerhead region of a turbine vane.

The current study presents data using a combination of these ''off-the-wall'' techniques, i.e., thermal field, velocity field, and flow visualization, with adiabatic effectiveness measurements for the study of showerhead cooling of a turbine vane subjected to mainstream turbulence levels of $Tu_\infty = 0.5$ and 20 percent. The goal of this study was to determine details of the coolant jet interactions, and jet separation, that occur in the showerhead region. Also, the mechanisms of the increased dispersion of the coolant caused by the high mainstream turbulence. The thermal field, velocity field, and flow visualization results presented in this paper complement the velocity and turbulence field measurements for the same showerhead flow presented by Polanka et al. [12]. These details are essential for a thorough evaluation of CFD predictions of the showerhead region since currently the only information available is what might be considered the ''footprints'' of these coolant jet dynamics.

Facilities and Experimental Conditions

The test facility for this study consisted of a closed-loop, low-speed wind tunnel, driven by a 50-hp variable pitch fan. The test section, shown in Fig. 1, consisted of a simulated three-vane and two passage turbine vane cascade with outer by-pass passages and adjustable walls to assure proper flow about the center model test vane. A full description of the facility is given by Polanka [13].

The geometry of the airfoil was a large scale model of a first stage modern commercial inlet guide vane. The model vane had a chord length of 59.4 cm and a span length of 54.9 cm. The material of the test vane was a polyurethane foam that was selected for low conductivity, $k = 0.048$ W/m·K, and structural strength. The leading edge of the vane had a wall thickness of 1.37 cm. The coolant hole diameter and pitch were constant throughout the vane and were $d = 4.11$ mm and $p = 5.55d$, respectively. Spacing between rows in the showerhead was $s = 3.33d$.

The configuration of coolant holes in the showerhead is shown in Fig. 2. The showerhead region consisted of six rows of holes

[1]Currently at Naval Surface Warfare Center–Carderock Division, Memphis, TN 38113.

Contributed by the International Gas Turbine Institute and presented at the International Gas Turbine and Aeroengine Congress and Exhibition, New Orleans, Louisiana, June 4–7, 2001. Manuscript received by the IGTI, October 3, 2000. Paper No. 2001-GT-401. Review Chair: R. A. Natole.

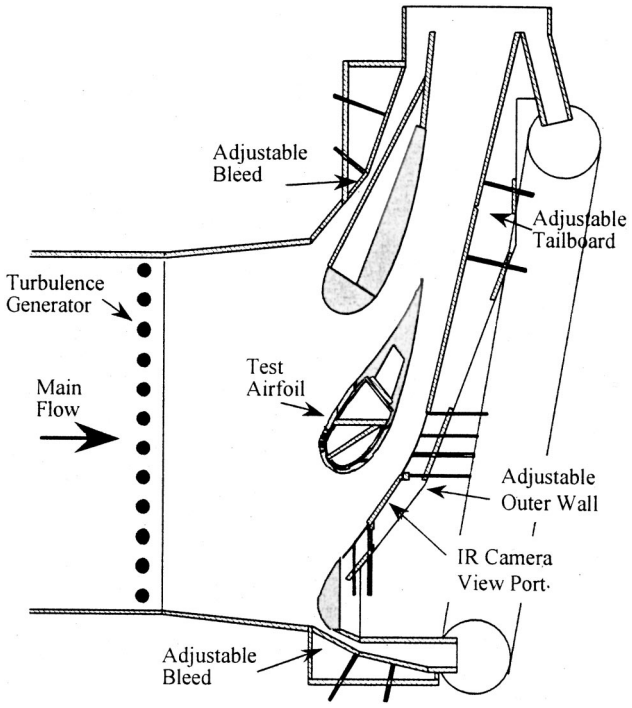

Fig. 1 Turbine vane test section

with staggered hole positions between rows. All measurements presented in this paper were done in the upper or central regions of the showerhead, i.e., no measurements are presented for the three-dimensional region near the bottom end-wall. For these measurements, the stagnation line of the flow was positioned at the center of the third row from the pressure side; this row is referred to as the stagnation row or Stag row. The two rows towards the pressure side from this stagnation row are referred to as the PS1 and PS2 rows. Each of the coolant holes in the upper and middle regions of the showerhead had an injection angle of $\phi=25$ deg, and were oriented laterally (downward, $-z$ direction) with a streamwise angle of $\theta=90$ deg.

To insure proper flow entering the coolant holes, the interior of the test airfoil included impingement plates consisting of 1-mm-thick stainless steel plates spaced 5.5 mm from the inner surface of the airfoil and molded to fit the contour of the turbine vane geometry. The impingement holes were 7.8 mm in diameter with a pitch of $5.55d$. The impingement holes were located between the entrances to the film cooling holes in line with the coolant rows.

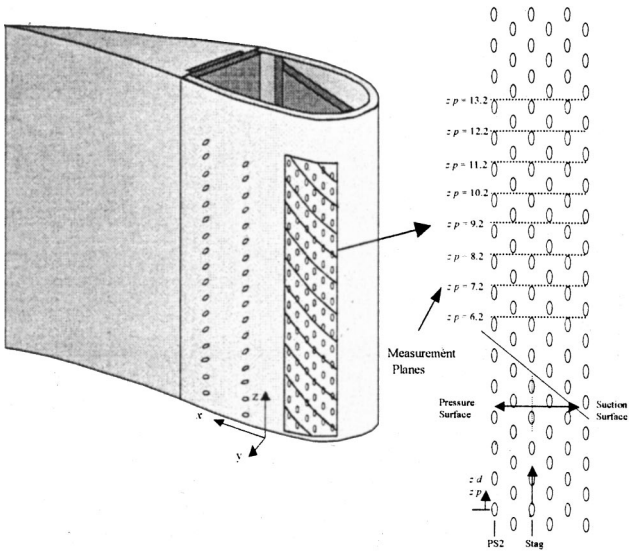

Fig. 2 Film cooling hole configuration and location of measurement planes (dashed lines)

To approximate the actual engine conditions for the adiabatic effectiveness measurements, the coolant temperature was cooled to 167 K while the mainstream temperature was maintained at ambient temperature, 300 K, yielding a density ratio of DR=1.8. To achieve this coolant temperature, a secondary flow loop, driven by an 8.5-hp centrifugal blower, passed air through a series of heat exchangers, with liquid nitrogen as the coolant. For the thermal field, velocity field, and flow visualization measurements, the coolant temperature was maintained at 250 K yielding a density ratio of DR=1.2. Cutbirth [14] showed that similar film cooling performance occurred for the two density ratio conditions when matching the mass flux ratio, M.

An infrared camera. Inframetrics 600L, was used to map the surface temperatures on the center vane model. A full description of this method is given by Witteveld et al. [15]. The resolution of the camera for these experiments was determined to be $0.6d \times 0.6d$, and the uncertainty of the surface temperatures were determined to be ± 1.0 K for $T_{aw}>220$ K and ± 2.6 K for $T_{aw}<220$ K. A hot-wire anemometer and laser Doppler velocimeter were used to measure the mainstream characteristics including the turbulence intensity, spectra, and integral time scale.

The adiabatic effectiveness, defined in Eq. (1), was calculated by using the surface temperature, coolant jet temperature, and the mainstream temperature as follows:

$$\eta \equiv \frac{(T_\infty - T_{aw})}{(T_\infty - T_c)} \tag{1}$$

The uncertainty in effectiveness (95 percent confidence interval) was $\delta\eta=\pm 0.02$ for $\eta>0.4$, $\delta\eta=\pm 0.01$ for $\eta<0.4$, and $\delta\overline{\eta}=\pm 0.01$ for all $\overline{\eta}$. The uncertainty of the blowing ratio was $\delta M_{sh}=\pm 0.03$.

Velocity measurements were performed using a three-component laser Doppler velocimeter constructed using TS1 components. For these measurements, collection was performed using side-scatter with 1-μm-dia titanium dioxide used as seed particles. Fluidized beds were used to seed the flow within the coolant line and mainstream.

The temperature probe used in this study consisted of twelve type E thermocouples suspended by two 1.5-mm-dia, $0.36d$, prongs. The prongs were spaced two pitches, 4.6 cm, $11.1d$, apart. The thermocouples were 80-μm-dia wire with 0.4-mm-dia Teflon insulation. The thermocouples were stripped bare for the center 2.0 mm of the probe, with a 1-mm overlap between the Constantan and Chromel wire, and tack welded. This yielded an array of 0.16-mm-dia, 1-mm-long temperature sensors. The thermal field data were normalized using Eq. (2)

$$\Theta \equiv \frac{(T_\infty - T)}{(T_\infty - T_c)} \tag{2}$$

The uncertainty in the measured Θ values (95 percent confidence interval) was $\Theta=\pm 0.01$.

For flow visualization, a 1-mm-thick laser sheet of light was used to illuminate titanium dioxide seed particles within the coolant flow. Imaging and recording of the flow visualization was performed using a commercial camcorder and VCR. The reduction of the data was performed using the NIH Image software's frame grabber and stepping the image frame by frame. This yielded instantaneous measurements of approximately 30 frames per second. For the time-averaged flow visualization images, eight images were used collected over a one second interval.

All experiments were conducted with a mainstream approach velocity of $U_\infty = 5.8$ m/s, which established a Reynolds number matching that of actual engine operation (Re, 1.2×10^6, based on chord length and exit velocity). These tests were run with low and high mainstream turbulence. The low mainstream turbulence level was $Tu_\infty \approx 0.5$ percent. The high mainstream turbulence generator, described by Cutbirth [14], consisted of 12 vertical, 3.8 cm diameter bars located 12.2 rod diameters upstream of the vane leading edge. At a position $x/C = 0.14$ upstream of the airfoil the turbulence intensity was $u_{\rm rms}/U_\infty = 0.20$, with an integral length scale of $\Lambda_f = 4.2$ cm or $\Lambda_f/d = 10$. At this position the mean velocity profile showed no indication of wakes from vertical bar grid [1], and the profiles of the three turbulence components were uniform within ± 10 percent [16].

Results

Several aspects of the showerhead injection process were examined. First was the ''build-up'' of coolant due to the lateral merging of coolant jets in the showerhead region. Coolant jet separation was then investigated for a range of blowing ratios. Particular attention was placed on examining the phenomenon of a dramatic increase in adiabatic effectiveness performance at a critical blowing ratio for the showerhead. Finally, the influence of very high level and large-scale mainstream turbulence was determined. Results from these studies follow.

Coolant Build-Up Effect. In a previous study of the showerhead adiabatic effectiveness for this vane, Polanka [13] showed a ''build-up'' of coolant as coolant jets directed downward combined with other coolant jets farther down the row of holes. Adiabatic effectiveness results indicated that a regular periodic condition between holes was not obtained until the 4th hole from the top, for low blowing ratio, or as far down as the 8th hole for high blowing ratio. One objective for this study was to determine how this ''build-up'' of coolant, which occurs moving down from the top holes in the showerhead array, alters the thermal field. Figures 3 and 4 present the thermal field measurements centered about the stagnation row of holes, Stag row, and the second row beyond the stagnation row on the pressure side, PS2 row, respectively, for a blowing ratio of $M_{\rm sh} = 1.5$. These figures show thermal field cross-sections in $x-y$ (streamwise-normal) planes each located at the top of a coolant hole.

Clearly evident in the thermal field cross sections for the Stag row shown in Fig. 3 are the cores of coolant jets displaced from the surface. The coolant jet evident above each hole actually originates from the hole adjacent to it. Consequently, in Fig. 3 we have indicated a jet number reflecting which hole from which the jet originated starting from the top of the row of holes. The thermal fields indicate an increasing Θ level, i.e., lower temperatures, from jets no. 3 through 6. Farther down the row of holes, the thermal field was essentially unchanged from jets no. 6 through 10. Interestingly, in the build-up region through jet no. 6, there was not only an increase in coolant surrounding the jet cores, but the maximum Θ level increases. This may be attributed to entrainment of colder fluid into the cores of the jets as the fluid surrounding the jet cores becomes colder with the build-up of coolant.

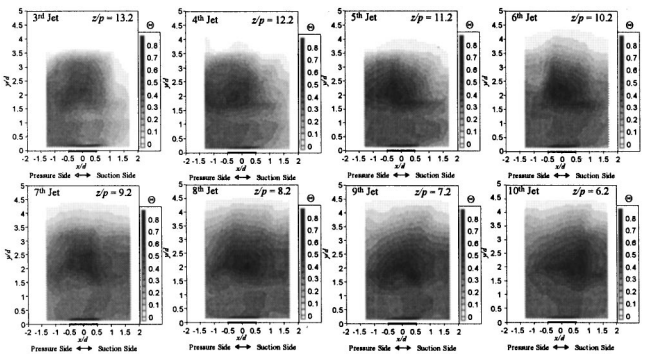

Fig. 3 Thermal profiles above the surface and along the Stag row of holes ($x/d = 0.0$) showing the build-up effect for $M_{\rm sh} = 1.5$

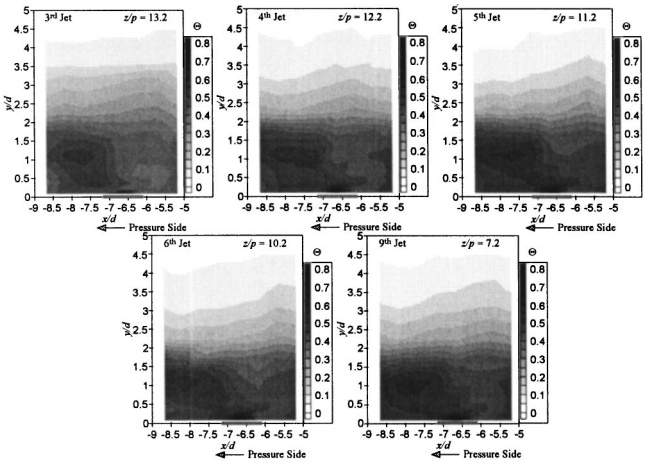

Fig. 4 Thermal profiles above the surface and along the PS2 row of holes showing the build-up effect for $M_{\rm sh} = 1.5$

Similar to the stagnation row of coolant holes, a trend of increasing Θ for jets farther down the row was observed for the PS2 coolant row (Fig. 4). This increase was observed for both the core of the coolant jet and the near-surface fluid, particularly upstream of the PS2 coolant row. A regular periodic pattern in the thermal field was obtained starting from jet no. 5.

Coolant Jet Separation. Jet separation is clearly indicated in Figs. 3 and 4, with the core of the coolant jet at $y/d = 2$ for the Stag row, and at $y/d = 1$ for the PS2 row. This separation of the coolant jet is also observed using the flow visualization. Visualizations of the first four holes in the Stag row are shown in Fig. 5 for blowing ratios of $M = 0.5$, 1.0, and 1.5. These visualizations indicate separation of the coolant jets occurs for all blowing ratios. Also, noticeable from the flow visualization is that the preceding jet is diluted well before the second successive jet. The thermal field cross sections centered about the Stag coolant row, Fig. 6, also showed that the location of the core of the coolant jet

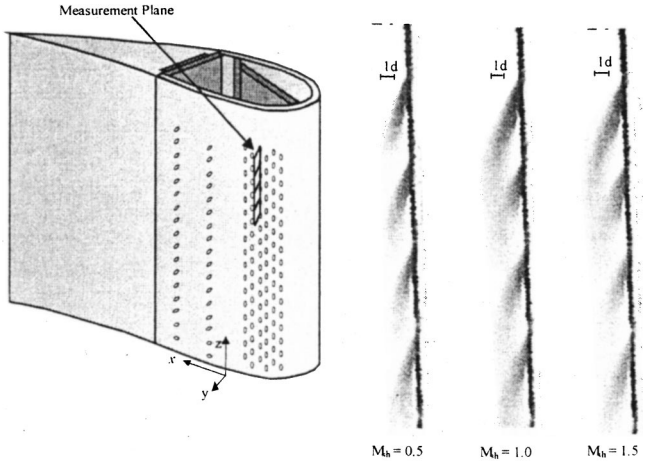

Fig. 5 Flow visualization of showerhead film cooling holes at $x/d = 0.0$ and with $Tu_\infty = 0.5$ percent. (images averaged over 1 second at 8 frames/s)

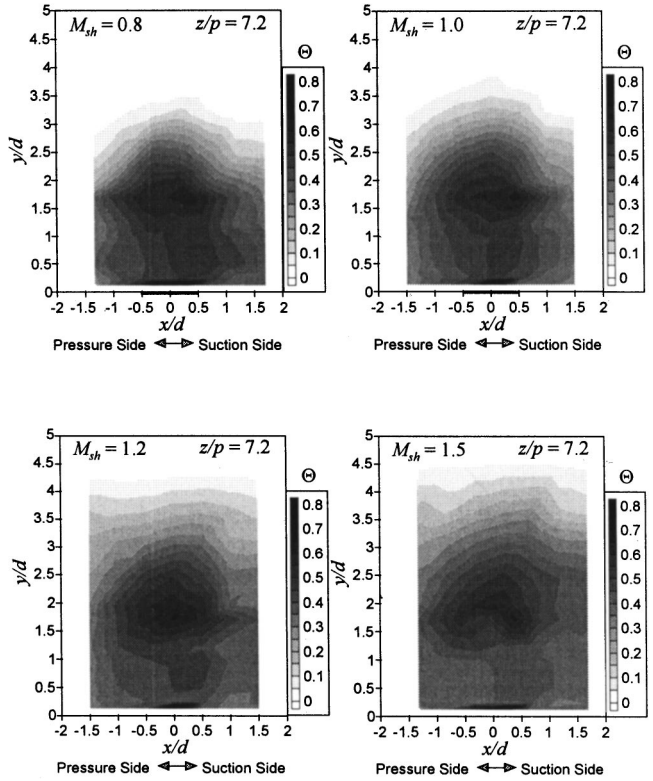

Fig. 6 Effect of the blowing ratio on the film cooling jet for the Stag row of holes ($x/d=0.0$). Profiles at $z/p=7.2$ and with $Tu_\infty=0.5$ percent.

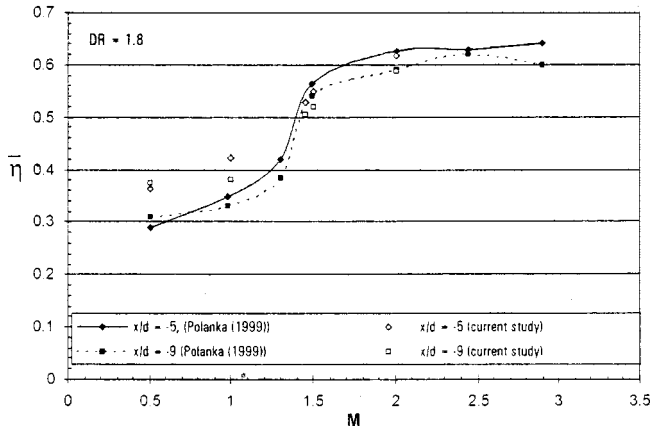

Fig. 7 Comparison of laterally averaged adiabatic effectiveness for the showerhead region with $Tu_\infty=0.5$ percent.

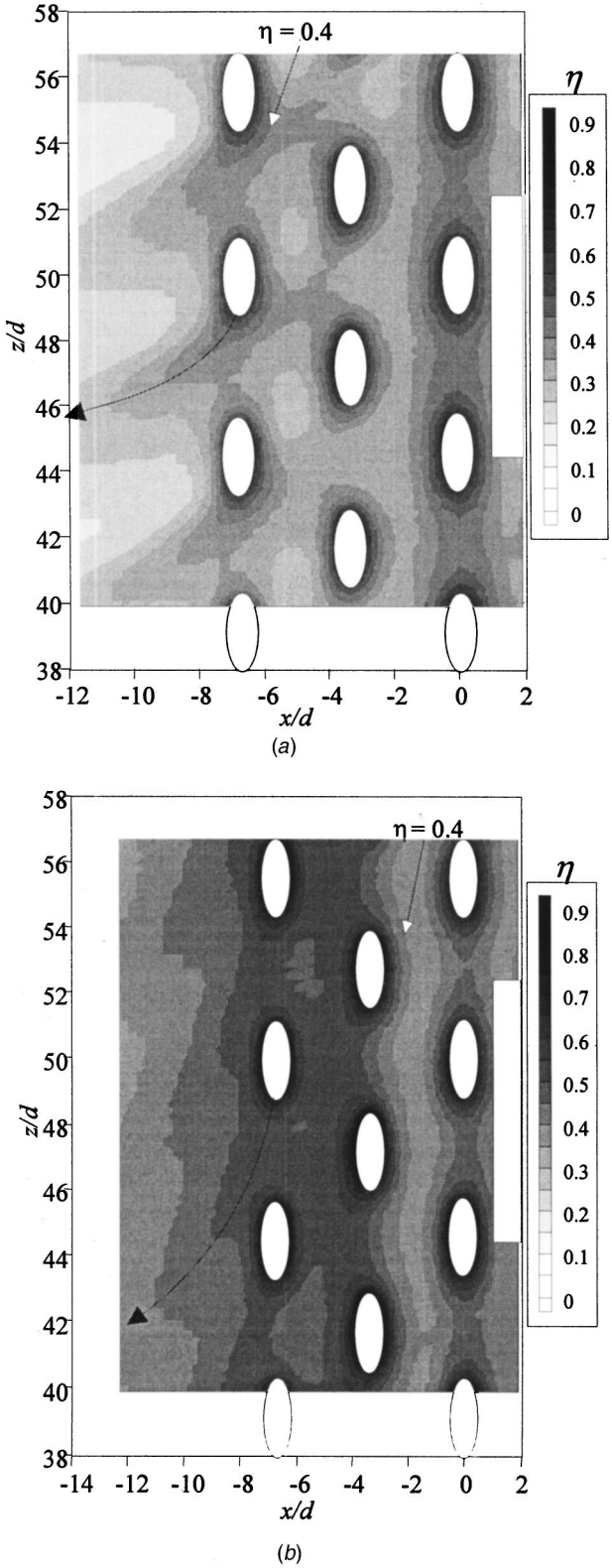

Fig. 8 Showerhead adiabatic effectiveness contours for $Tu_\infty=0.5$ percent, DR=1.8 and blowing ratios (*a*) $M_{sh}=1.0$, and (*b*) $M_{sh}=1.5$

was constant over a range of blowing ratios from $M=0.8$ to $M=1.5$. However, as the blowing ratio is increased, the overall thickness of the coolant layer (as defined by the $\Theta=0.05$ threshold level) increases from $y/d\approx3.5$ to $y/d\approx4.5$. Also as the blowing ratio was increased the coolant jet core became more dissociated from the surface.

The separation distance for the coolant jets along the stagnation row of holes was surprisingly large. However, this large separation is understandable when examining the velocity field approaching the stagnation line. The velocity field measurements presented in Polanka et al. [12] show that the mainstream velocity decelerated to less than 20 percent of the approach velocity when within $2d$ of the surface. Consequently, there is little counteraction to the coolant jets exiting the stagnation row of holes until beyond $y/d=2$. This is consistent with the flow visualizations shown in Fig. 5 which show the coolant jet continuing at the exit angle of 25 deg until beyond $y/d=1$. For the coolant jets from the

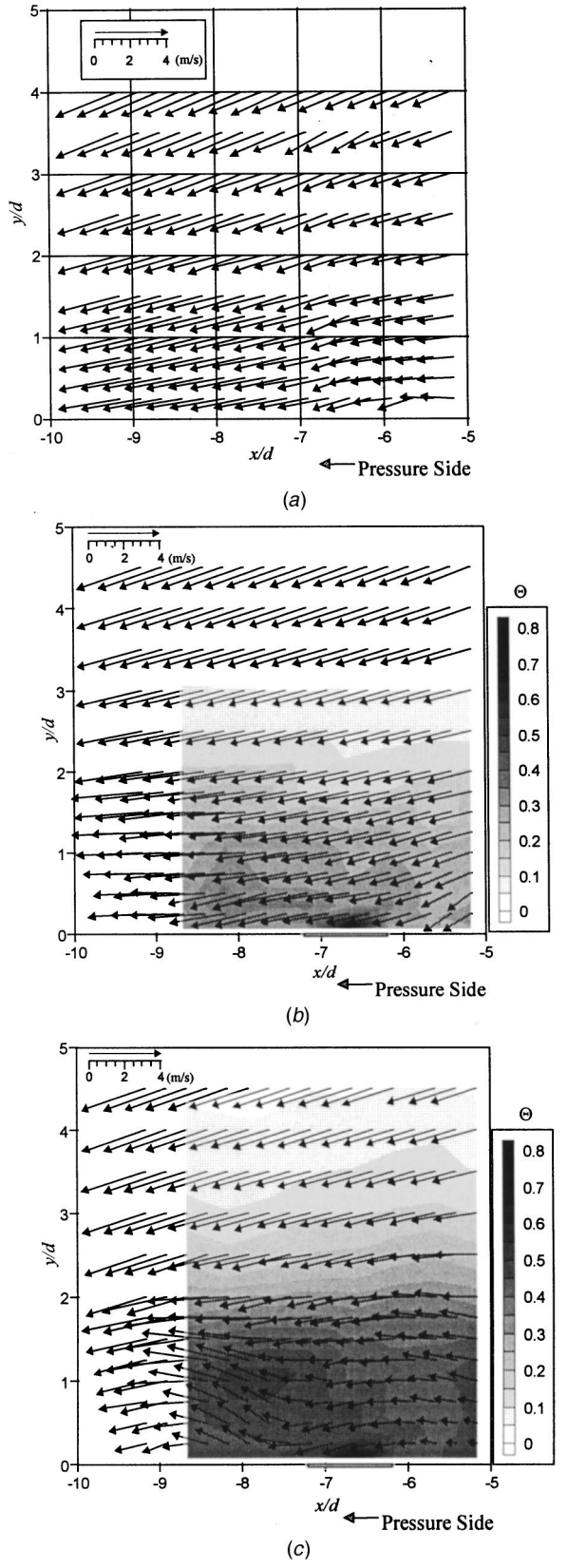

Fig. 9 Relationship of the thermal and velocity fields at $z/p=7.2$ for blowing ratios (*a*) $M_{sh}=0.0$, (*b*) $M_{sh}=1.0$, and (*c*) $M_{sh}=1.5$

PS2 row, the separation distance was only $y/d=1$, which is attributable to a stronger mainstream cross-flow at this location.

Jet-to-Jet Interaction Causing Increased Adiabatic Effectiveness. In an earlier study, Polanka et al. [1], a dramatic increase in adiabatic effectiveness in the showerhead region was found to occur at a critical blowing ratio of nominally $M_{sh}=1.5$. This sudden increase in adiabatic effectiveness is shown graphically in Fig. 7 in which the laterally averaged adiabatic effectiveness. $\overline{\eta}$, at $x/d=-5$ and -9 are presented as a function of blowing ratio. These positions $x/d=-5$ and -9 correspond to positions between the PS1 and PS2 rows, and $2d$ downstream of the last (PS2) row of holes in the showerhead, respectively. This figure also shows repeats of these measurements in the current study confirming that a large increase in $\overline{\eta}$ occurs as the blowing ratio increases from $M_{sh}=1.3$ to 1.5. (The differences between Polanka et al. [1] and current measurements at low M may be attributed to a sensitivity to precise location of the stagnation line along the stagnation row of holes.)

The basic reason for the sharp increase in adiabatic effectiveness with increasing blowing ratio is evident in the η contours shown in Figs. 8(*a*) and (*b*). These figures present the η contours for the showerhead for blowing ratios below and above the critical blowing ratio. Clearly evident is a large increase in η levels for $M_{sh}=1.5$ compared to $M_{sh}=1.0$. If the jet trajectories for the PS2 row of holes, at $x/d=-6.7$, for the two blowing conditions are compared, the reason for the ''step'' increase is identified. For the $M_{sh}=1.0$ blowing condition, the jet trajectory of a preceding hole is redirected downstream before it reaches the laterally adjacent coolant hole. This allows hot mainstream air to penetrate between the coolant holes. However, for the $M_{sh}=1.5$ blowing condition, the trajectory of the jet follows a path which comes close to intersecting the laterally adjacent coolant hole. Hence, for the higher blowing ratio there were no gaps between coolant jets, which prevented penetration of the mainstream.

Further details of the jet-to-jet interaction in the showerhead region were obtained using velocity field and thermal field measurements. The velocity and thermal fields centered about the PS2 row of holes and positioned at $z/p=7.2$, which is at the top of the coolant hole, are presented in Fig. 9 for blowing ratios of $M_{sh}=0$, 1.0, and 1.5. The velocity field with no blowing. Figure 9(*a*), shows that the coolant jets from the PS2 row were subjected primarily to a cross-flow of a magnitude approximately one-half the approach velocity. Consistent with the η contours discussed previously, the normalized thermal contours for $M_{sh}=1.0$ were generally $\Theta\approx0.3$ near the wall. This was substantially lower than the contour levels for $M_{sh}=1.5$ which were generally $\Theta\approx0.5$ near the wall.

Based on the η contours shown in Fig. 8, for $M_{sh}=1.5$ the coolant jet core from the hole above would be expected to inter-

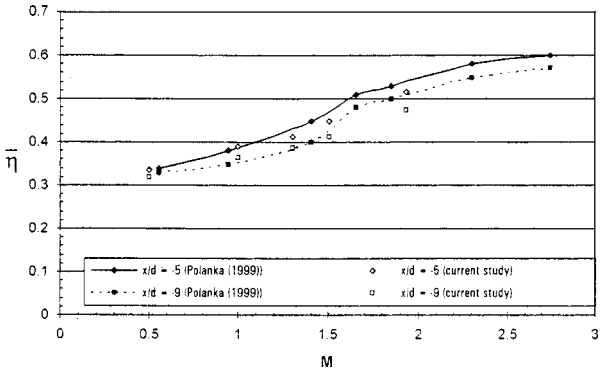

Fig. 10 Comparison of laterally averaged adiabatic effectiveness for the showerhead region with $Tu_\infty=20$ percent

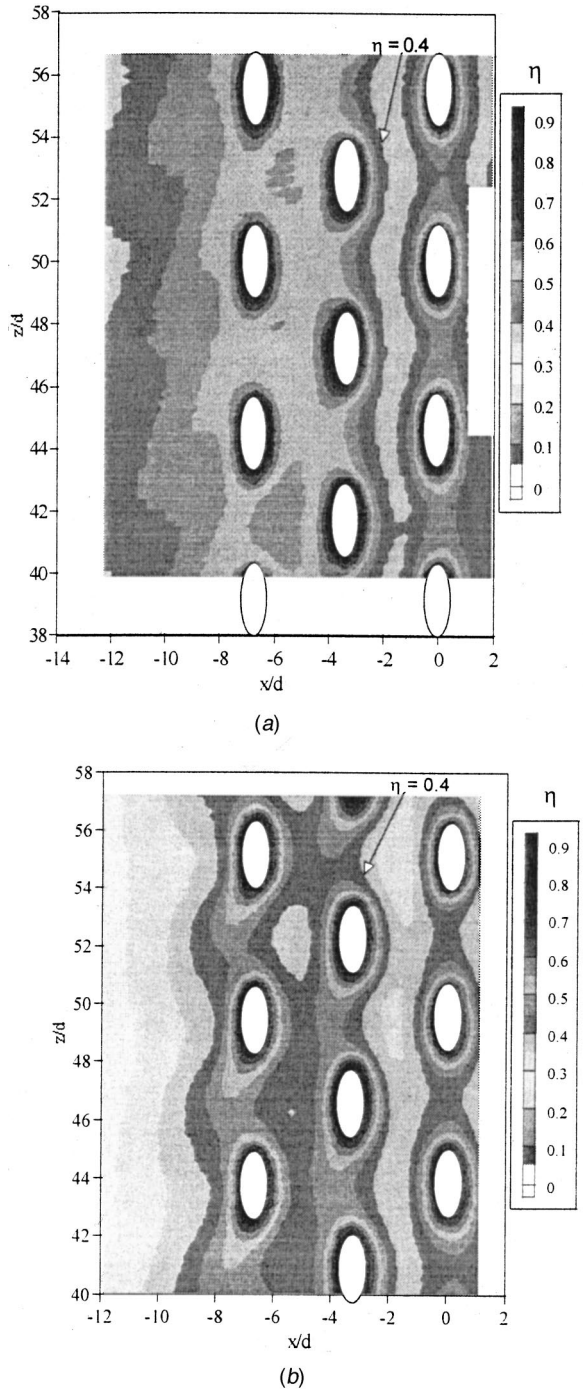

Fig. 11 Effect of mainstream turbulence level on adiabatic effectiveness contours for $M_{sh}=1.5$ and DR=1.8. (*a*) $Tu_\infty=0.5$ percent, and (*b*) $Tu_\infty=20$ percent

sect the plane of the thermal field at $x/d=8$, and this is consistent with the position the low temperature core evident in Fig. 9(*c*). The superimposed velocity field shows that this separated coolant jet core was still moving away from the wall. However, the η contours for $M_{sh}=1.0$ indicate that the coolant jet core did not intersect the plane of the thermal field shown in Fig. 9. Consequently, the low temperature peak evident in Fig. 9(*b*) should be interpreted as the edge of the coolant jet coming from the upper hole. This low temperature peak was quite close to the wall, $y/d=0.3$, indicating that the coolant jet does not have much separation for the lower blowing ratio of $M_{sh}=1.0$.

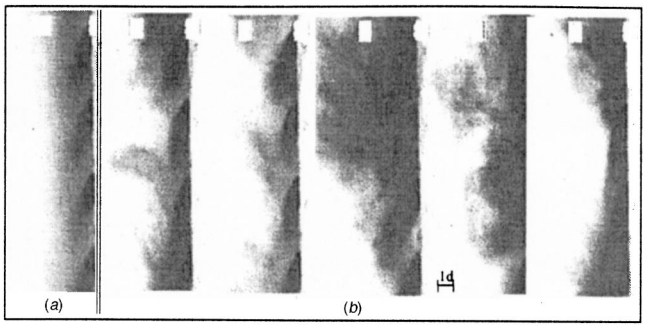

Fig. 12 Flow visualization of the Stag row ($x/d=0$) for $M_{sh}=1.5$ and $Tu_\infty=20$ percent—(*a*) time-averaged, and (*b*) instantaneous images

The increased adiabatic effectiveness for higher blowing ratios was hypothesized to be due to a blockage of the mainstream by the coolant jets. Measurements of the velocity field confirmed this blockage effect. Contrasting Figs. 9(*b*) and (*c*), the velocity field showed a strong inflow towards the wall for $M_{sh}=1.0$, while for $M_{sh}=1.5$ the flow was stagnated upstream of the coolant jet indicating a blocking by the coolant jet. With the mainstream blocked away from the wall, a larger concentration of coolant occurs resulting in greatly improved adiabatic effectiveness.

High Turbulence Effects. The variation of $\overline{\eta}$ with blowing ratio for high mainstream turbulence conditions, $Tu_\infty=20$ percent, are presented in Fig. 10, again at positions $x/d=-5$ and -9. The $\overline{\eta}$ values under high mainstream turbulence conditions were decreased compared to the low mainstream turbulence results (refer to Fig. 7). Furthermore, the $\overline{\eta}$ distribution had only a slight ''step'' increase in $\overline{\eta}$, and this increase occurred at a slightly higher blowing ratio, $M_{sh}=1.7$. Spatial details of the differences in adiabatic effectiveness with low and high mainstream turbulence are presented in Fig. 11. These spatial contours show that the high mainstream turbulence causes a general reduction in the levels of adiabatic effectiveness within the showerhead region, and a greater decay rate downstream of the showerhead.

Insight into the physical mechanisms involved in the increased dispersion by the high mainstream turbulence was obtained using flow visualization. Figure 12 shows a time-averaged image of the coolant distribution, and a sequence of instantaneous snapshot showing the time variation of the coolant distribution. Comparing the time-averaged image for the high mainstream turbulence, Fig. 12(*a*), with that for low mainstream turbulence, Fig. 5, the increased dispersion of coolant between the coolant jets is evident. More informative are the instantaneous snapshots of coolant distribution shown in Fig. 12(*b*). These snapshots show large elements of coolant fluid, often much larger than the jet diameter, being convected away from the wall. These images show that the increased dispersion by high mainstream turbulence is due to large scale break-up of coolant jets. In retrospect, considering that the integral length scale of the mainstream turbulence was $\Lambda_f=10d$, it is not surprising to find this break-up of the coolant jets by the mainstream turbulence.

Conclusions

This study was performed to provide more detailed measurements of the showerhead region than that given by previous adiabatic effectiveness measurements. These detailed measurements consisted of flow visualization, thermal profiles, and LDV measurements, yielding ''off-the-wall'' insight into the interaction of the mainstream and coolant flows.

Due to the spanwise orientation of the coolant holes and the near-stagnated mainstream flow within the showerhead, interaction among the coolant jets causes a build-up of coolant levels that continues up to six holes from the start of the row of holes. This

result is an important consideration for any experimental or computational study of showerhead cooling flows in showing that regular periodic conditions are established only after a large number of holes from the end of the row.

Coolant jets from the showerhead were found separated from the surface even at relatively low blowing ratios. Along the stagnation row the core of the coolant jets separated as much as $2d$ from the surface, while jets from the following rows had less separation. This separation is due to the lack of a strong mainstream flow near the surface in the stagnation region.

For low mainstream turbulence conditions, a ''step'' increase in effectiveness was seen for the showerhead region as the blowing ratio is increased between $M_{sh}=1.0$ and 1.5. The sudden increase in adiabatic effectiveness occurs when trajectories of coolant jets have a strong enough lateral component that they interact with the laterally adjacent coolant hole. The high level of adiabatic effectiveness is caused by the blockage of the mainstream from the surface of the turbine vane by the showerhead coolant. This blockage is created by the close proximity and the spanwise orientation of the coolant holes within showerhead. This blockage allows for the increased effectiveness level even though the coolant jets are separated from the surface of the vane.

The ''step'' increase in adiabatic effectiveness was reduced for the high mainstream turbulence condition as the mainstream was able to penetrate the coolant layer to the surface of the vane. Dispersion of the coolant jets by high mainstream turbulence was found to be due to large scale transport and break-up of the coolant jets.

Acknowledgments

We are most grateful to the sponsors of this work, Advanced Gas Turbine Systems Research Consortium and Pratt & Whitney. We would also like to thank Pratt & Whitney for supplying the turbine vane geometry, and Joel Wagner for review of this manuscript.

Nomenclature

C = chord length, 59.4 cm
d = coolant hole diameter, 4.11 mm
DR = density ratio, (ρ_c/ρ_∞)
k = thermal conductivity
M_{sh} = blowing ratio $(\rho_c \cdot U_c/\rho_\infty \cdot U_\infty)$
p = coolant hole-to-hole pitch, $5.6d$
s = spacing between rows of holes, $3.33d$
t = time
T = temperature
Tu = turbulence intensity (u_{rms}/U_∞)
U_c = average coolant velocity from showerhead holes
U_∞ = approach mainstream velocity
x,y,z = turbine vane surface coordinates
ϕ = injection angle wrt surface plane
$\underline{\eta}$ = adiabatic effectiveness $(T_\infty - T_{aw}/T_\infty - T_c)$
η = spanwise averaged adiabatic effectiveness
Λ_f = integral length scale
θ = streamwise injection angle
Θ = nondimensional temperature $(T_\infty - T/T_\infty - T_c)$
ρ = density

Subscripts

aw = adiabatic wall
c = coolant
∞ = approach condition

References

[1] Polanka, M. D., 1999, ''Detailed Film Cooling Effectiveness and Three Component Velocity Field Measurements on a First Stage Turbine Vane Subject to High Freestream Turbulence,'' Ph.D. dissertation, The University of Texas at Austin, Austin, TX.
[2] Drost, U., and Bölcs, A., 1999, ''Performance of a Turbine Airfoil with Multiple Film Cooling Stations Part 1: Heat Transfer and Film Cooling Effectiveness,'' ASME Paper No. 99-GT-171.
[3] Du, H., Han, J.-C., and Ekkad, S. V., 1997, ''Effect of Unsteady Wake on Detailed Heat Transfer Coefficient and Film Effectiveness Distributions for a Gas Turbine Blade,'' ASME Paper No. 97-GT-166.
[4] Takeishi, K., Aoki, S., Sato, T., and Tsukagoshi, K., 1992, ''Film Cooling on a Gas Turbine Rotor Blade,'' ASME J. Turbomach., **114**, pp. 828–834.
[5] Thole, K. A., Sinha, A. K., Bogard, D. G., and Crawford, M. E., 1992, ''Mean Temperature Measurements if Jets With a Crossflow for Gas Turbine Film Cooling Application,'' *Rotating Machinery Transport Phenomena*, J. H. Kim and W. J. Yang, eds., Hemisphere Pub. Corp., New York, NY, pp. 65–81.
[6] Oke, R. A., and Simon, I. W., 2000, ''Measurements in Film Cooling with Lateral Injection: Adiabatic Effectiveness Values and Temperature Fields,'' ASME Paper No. 2000-GT-597.
[7] Pietryzk, J. R., Bogar, D. G., and Crawford, M. E., 1990, ''Effect of Density Ratio on the Hydrodynamics of Film Cooling,'' ASME J. Turbomach., **112**, pp. 437–450.
[8] Sinha, A. K., Bogard, D. G., and Crawford, M. E., 1991, ''Gas Turbine Film Cooling: Flowfield due to a Second Row of Holes,'' ASME J. Turbomach., **113**, pp. 450–456.
[9] Wang, H. P., Olson, S. J., Goldstein, R. J., and Eckert, E. R. G., 1997, ''Flow Visualization in a Linear Turbine Cascade of High Performance Turbine Blades,'' ASME J. Turbomach., **119**, pp. 1–8.
[10] Roy, R. P., Squires, K. D., Gerendas, M., Song, S., Howe, W. J., and Ansari, A., 2000, ''Flow and Heat Transfer at the Hub Endwall of Inlet Vane Passages—Experiments and Simulations,'' ASME Paper No. 2000-GT-198.
[11] Schwarz, S. G., Goldstein, R. J., and Eckert, E. R. G., 1990, ''The Influence of Curvature on Film Cooling Performance,'' ASME Paper No. 90-GT-10.
[12] Polanka, M. D., Cutbirth, J. M., and Bogard, D. G., 2001, ''Three Component Velocity Field Measurements in the Stagnation Region of a Film Cooled Turbine Vane,'' ASME Paper No. 2001-GT-0402.
[13] Polanka, M. D., Witteveld, V. C., and Bogard, D. G., 1999, ''Film Cooling Effectiveness in the Showerhead Region of a Gas Turbine Vane Part I: Stagnation Region and Near-Pressure Side,'' ASME Paper No. 99-GT-48.
[14] Cutbirth, J. M., 2000, ''Turbulence and Three-Dimensional Effects on the Film Cooling of a Turbine Vane,'' Ph.D. dissertation, The University of Texas at Austin, Austin, TX.
[15] Witteveld, V. C., Polanka, M. D., and Bogard, D. G., 1999, ''Film Cooling Effectiveness in the Showerhead Region of a Gas Turbine Vane Part II: Stagnation Region and Near-Suction Side,'' ASME Paper No. 99-GT-49
[16] Ethridge, M. I., Cutbirth, J. M., and Bogard, D. G., 2000, ''Effects of Showerhead Cooling on Turbine Vane Suction Side Film Cooling Effectiveness,'' ASME IMECE Conference, Orlando, FL.

Modeling the Air-Cooled Gas Turbine: Part 1—General Thermodynamics

J. B. Young
e-mail: jby@eng.cam.ac.uk

R. C. Wilcock

Cambridge University Engineering Department,
Trumpington Street,
Cambridge, CB2 1PZ, United Kingdom

This paper is Part I of a study concerned with developing a formal framework for modeling air-cooled gas turbine cycles and deals with basic thermodynamic issues. Such cycles involve gas mixtures with varying composition which must be modeled realistically. A possible approach is to define just two components, air and gas, the latter being the products of stoichiometric combustion of the fuel with air. If these components can be represented as ideal gases, the entropy increase due to compositional mixing, although a true exergy loss, can be ignored for the purpose of performance prediction. This provides considerable simplification. Consideration of three idealized simple cycles shows that the introduction of cooling with an associated thermal mixing loss does not necessarily result in a loss of cycle efficiency. This is no longer true when real gas properties and turbomachinery losses are included. The analysis clarifies the role of the cooling losses and shows the importance of assessing performance in the context of the complete cycle. There is a strong case for representing the cooling losses in terms of irreversible entropy production as this provides a formalized framework, clarifies the modeling difficulties, and aids physical interpretation. Results are presented that show the effects on performance of varying cooling flowrates and cooling losses. A comparison between simple and reheat cycles highlights the rôle of the thermal mixing loss. Detailed modeling of the heat transfer and cooling losses is discussed in Part II of this paper.
[DOI: 10.1115/1.1415037]

1 Introduction

The cooling of gas turbine blades using air bled from the compressor has been standard practice in the gas turbine industry for 30 years. The technology was originally developed for aeroengines, but is now used routinely on machines specifically designed for electrical power generation. Currently (2000), the maximum combustor outlet temperature (COT) for a civil aeroengine is 1870 K at take-off (1550 K at cruise), and for an aeroderivative gas turbine for power generation it is 1780 K. The maximum COT of heavy-duty industrial machines is about 1700 K. The rotor inlet temperature (RIT) is often quoted as more indicative of performance than the COT. This is the mixed-out total temperature in a stationary frame of reference at exit from the first stage nozzle row and in air-cooled machines is 100–150 K less than the COT. The maximum allowable blade temperature depends on the material, stress levels and application. State-of-the-art values are 1370 K for aero-engines and aeroderivatives, and 1250 K for heavy-duty industrial machines.

Most manufacturers have undertaken extensive research programs on internal convection cooling and external film cooling (Lakshminarayana [1]). The main objective has been improved heat transfer performance, allowing higher turbine inlet temperatures and increased cycle efficiency. Unfortunately, increased cooling flowrates result in higher aerodynamic and thermodynamic losses, which offset the beneficial effect of increased turbine inlet temperatures. Cooling losses have been the subject of a few investigations (e.g., Day et al. [2]) but have not received the same attention as the heat transfer. Recently, MacArthur [3] and Horlock et al. [4] have suggested that, with current materials technology, further increases in COT might actually lead to a decrease in cycle efficiency.

As noted by Denton [5], the effects of blade cooling cannot be correctly assessed without consideration of the gas turbine cycle as a whole. Given the importance of cooling to gas turbine technology, it is therefore surprising that, with some notable exceptions (El-Masri [6,7], Chiesa et al. [8], Facchini et al. [9]), there have been few attempts to analyze the engine as a whole and identify the source and magnitude of the cooling losses. Indeed, most published works give few details, if any, of the cooling models used. Consideration soon shows, however, that it is surprisingly difficult to specify the losses in an unambiguous manner and much writing on turbine cooling is confused and imprecise in this respect. The present work is an attempt to clarify matters by providing a formal framework for analysis together with a more specific examination of heat transfer and loss models. Part I discusses the general thermodynamics of air-cooling, addressing some issues that have previously been neglected. Part II describes heat transfer and loss models that are sufficiently general for cycle calculations but that can be finetuned to provide the accuracy required for initial design work.

2 The Working Fluid

Gas turbine cycles with cooling involve gas mixtures with varying composition. A realistic analysis cannot avoid this complication, but it is important to adopt a model for the working fluid that will aid physical interpretation while maintaining computational accuracy. The traditional approach is to assume perfect gas behavior with different values of c_p and γ upstream and downstream of the combustor. This is unsatisfactory, however, not only because of the large temperature variations, but also because the gas composition in the turbine varies with the air/fuel ratio and the injection of coolant. For computer calculations, these problems are easily overcome by representing the gas as a semi-perfect mixture of its component species, N_2, O_2, CO_2, and H_2O. The semi-perfect gas assumption (i.e., temperature-dependent c_p and γ) gives good accuracy and is convenient for analytical work. Introducing a pressure dependence for c_p and γ via a more complex equation of state is an unnecessary complication that does little to improve accuracy and much to impede understanding.

Contributed by the International Gas Turbine Institute and presented at the 46th International Gas Turbine and Aeroengine Congress and Exhibition, New Orleans, Louisiana, June 4–7, 2001. Manuscript received by the International Gas Turbine Institute February 2001. Paper No. 2001-GT-385. Review Chair: R. Natole.

An attractive alternative approach, equally correct, is to recognize just two gaseous components, namely *air* and *gas*. *Air* (subscript *a*) is defined to be a mixture of 21 percent O_2 and 79 percent N_2 by volume, while *gas* (subscript *g*) is defined to be the products of complete stoichiometric combustion of a given fuel in air (not oxygen). For a specified fuel, the composition of *gas* remains constant throughout the cycle. Its properties (as a semi-perfect mixture of N_2, CO_2, and H_2O) can be established at the start of the calculation.

A two-component description implies that the working fluid can be represented anywhere as a mixture of *air* and *gas*. This model is therefore restricted to cycles involving complete oxidation of the fuel with negligible dissociation of the combustion products. Separation into more basic chemical constituents is not allowed and cycles involving coal gasification or CO_2 separation, for example, are excluded. Despite these constraints, the two-component formulation is very convenient for analyzing many types of gas turbine power plant. Furthermore, the model can be extended by adding extra components. Thus, for steam-injected gas turbines, the injected H_2O can be introduced as a third component that is treated separately from the H_2O in the component *gas*.

Adopting the two-component semi-perfect gas description, the changes in specific enthalpy and entropy of component *i* (*air* or *gas*) between states 1 and 2 are given by,

$$h_i(T_2)-h_i(T_1)=\int_{T_1}^{T_2} c_{pi}(T')\,dT' \tag{1a}$$

$$s_i(T_2,p_{i2})-s_i(T_1,p_{i1})=\int_{T_1}^{T_2}\frac{c_{pi}(T')}{T'}\,dT'-R_i\ln\left(\frac{p_{i2}}{p_{i1}}\right) \tag{1b}$$

By Dalton's law, the mixture static pressure is the sum of the partial pressures, $p=\Sigma p_i$. If x and y represent mass and mol fractions, respectively, the mixture specific enthalpy and entropy are given by,

$$h(T,x_i)=\sum_i x_i h_i(T) \tag{2a}$$

$$s(T,p,x_i)=\sum_i x_i s_i(T,p_i)=\sum_i x_i s_i(T,p)+s_{\mathrm{mix}} \tag{2b}$$

where s_{mix} is the specific entropy of compositional mixing,

$$s_{\mathrm{mix}}=-\sum_i x_i R_i\ln\left(\frac{p_i}{p}\right)=-\sum_i x_i R_i\ln y_i \tag{2c}$$

Clearly, s_{mix} depends only on the composition and hence remains constant so long as this does not change. It is zero for pure *air* and pure *gas*. If a four-component description were used, s_{mix} would still depend only on the composition but its value would be different. For equations of state involving pressure dependent c_p and γ, s_{mix} would be a function of temperature and pressure as well as composition.

3 Exergy Loss in Compositional Mixing

Figure 1(*a*) shows two low-velocity streams, both at pressure p and temperature T, mixing adiabatically. Stream 1 is pure *gas* with mass flowrate m_g and stream 2 is pure *air* with mass flowrate m_a. The downstream pressure is adjusted so that $p_3=p$. Neglecting changes in kinetic energy, the steady-flow energy equation is,

$$(m_g+m_a)[x_g h_g(T_3)+x_a h_a(T_3)]=m_g h_g(T)+m_a h_a(T) \tag{3a}$$

As $x_g=m_g/(m_g+m_a)$ and $x_a=m_a/(m_g+m_a)$, it follows that $T_3=T$. The rate of entropy creation by irreversible processes is,

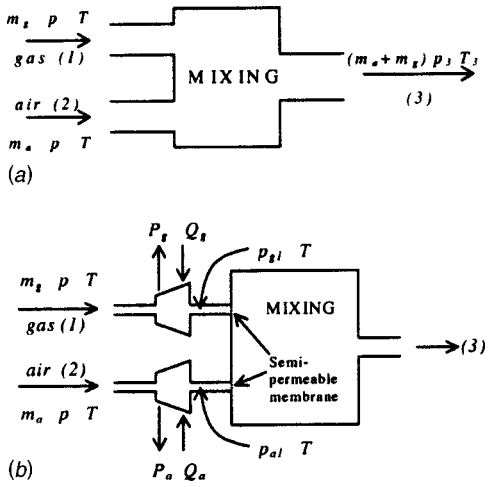

Fig. 1 (*a*) Irreversible mixing with entropy creation; (*b*) reversible mixing with zero entropy creation

$$\Delta\Sigma=(m_g+m_a)[x_g s_g(T_3,p_{g3})+x_a s_a(T_3,p_{a3})]-[m_g s_g(T,p)-m_a s_a(T,p)] \tag{3b}$$

Substituting Eq. (2*b*) then gives,

$$\Delta\Sigma=(m_g+m_a)s_{\mathrm{mix},3} \tag{3c}$$

where $s_{\mathrm{mix},3}$ is the specific entropy of mixing of the downstream flow. The result is easily generalized to multiple inlet and outlet streams.

Equation (3*c*) shows that entropy is created by the irreversible diffusional mixing of the *air* with the *gas*. If T is also the ambient temperature, then $T\Delta\Sigma$ represents a loss of useful power and should be included as such in an exergy analysis of the type advocated by Kotas [10]. It is worth examining, however, exactly how this loss might be avoided. One conceptually possible process is shown in Fig. 1(*b*). Each stream is expanded reversibly and isothermally in a turbine to its final mixture *partial* pressure and mixing then occurs reversibly through semi-permeable membranes. The entropy creation is now zero and the turbine power output is $T\Delta\Sigma$.

There may be other ways of avoiding the entropy creation $\Delta\Sigma$, but all such processes must involve *reversible* compositional mixing. This never happens in gas turbine plant and hence all *compositional* mixing losses are essentially unavoidable. Furthermore, the location in the cycle where the loss is incurred does not affect the *shaft* power output so long as all gas components are ideal. This can be seen by considering the reversible, adiabatic expansion of two *ideal* gases over a given pressure ratio. If the gases could have the same values of c_p and γ but were, nevertheless, distinguishable, the *shaft* power output would be independent of whether mixing took place before, during, or after the expansion. However, if the c_p and γ are pressure dependent, then so too is s_{mix} (because of the change of intermolecular potential energy during mixing). The entropy created during compositional mixing then varies with the pressure and the shaft power depends on the location where mixing takes place.

Assuming semi-perfect gas behavior, a rational approach is to accept the inevitability of compositional mixing losses and ignore them completely. This can easily be done by neglecting the s_{mix} term in Eq. (2*b*) and evaluating the mixture specific entropy as if each component existed alone at the mixture static pressure p. Thus,

$$s(T,p,x_i)=\sum_i x_i s_i(T,p) \tag{4}$$

This is the approach that will be adopted for the rest of the paper.

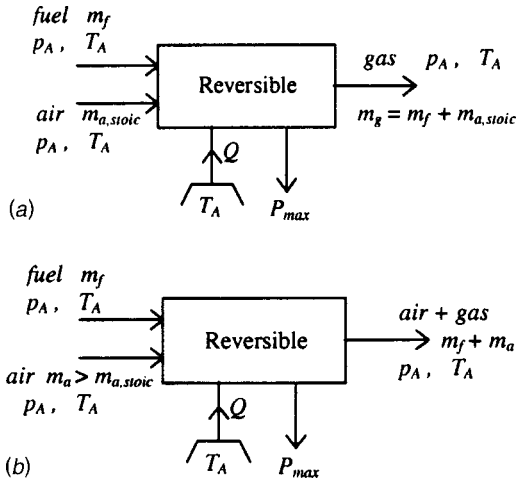

Fig. 2 (*a*) Ideal power plant with stoichiometric air supply; (*b*) ideal power plant with excess air supply

4 Ideal Gas Turbine Plant

Figure 2(*a*) shows an ideal gas turbine plant operating with a stoichiometric supply of fuel and air. All fluid streams enter or leave at ambient pressure p_A and temperature T_A. All processes are reversible including the heat transfer with the environment. Under these conditions, the maximum power output $P_{\max}$ is achieved and is given by the decrease in the steady flow availability function (or exergy). In terms of the two-component description, the exhaust stream is pure *gas* and,

$$P_{\max} = -m_f(\Delta H_A - T_A \Delta S_A) = -m_f \Delta G_A \tag{5a}$$

where ΔH_A and ΔS_A are defined by,

$$-m_f \Delta H_A = m_f h_{fA} + m_{a,\text{stoic}} h_{aA} - m_g h_{gA}$$

$$-m_f \Delta S_A = m_f s_{fA} + m_{a,\text{stoic}} s_{aA} - m_g s_{gA}$$

with $m_g = m_{a,\text{stoic}} + m_f$. The subscript A implies property evaluation at (T_A, p_A). If $T_A = 25°\text{C}$ and $p_A = 1$ bar, and if the properties of *gas* are established ignoring the entropy of mixing, then $\Delta G_A = \Delta G_0$ the standard Gibbs function change for the fuel. This, it will be recalled, corresponds to all chemical species entering and leaving *individually* at a pressure of 1 bar. If $T_A \neq 25°\text{C}$ or $p_A \neq 1$ bar, then $\Delta G_A \neq \Delta G_0$. $P_{\max}$ therefore varies with the ambient pressure and temperature.

In practice, all power plants operate with excess air as shown in Fig. 2(*b*). The maximum power output is still equal to the decrease in the steady-flow exergy but this is now given [using Eq. (2*b*)] by,

$$P_{\max} = -m_f \Delta G_A + (m_a + m_f) T_A s_{\text{mix},E} \tag{5b}$$

where $s_{\text{mix},E}$ is the specific entropy of mixing of the exhaust stream. Equation (5*b*) suggests that $P_{\max}$ increases with the air/fuel ratio but this is not so because the final term, representing the accumulated entropy of compositional mixing, is an unavoidable loss. In all practical situations $P_{\max}$ is still given by Eq. (5*a*).

The conclusions of sections 2–4 are important. They show that it is unnecessary to introduce compositional mixing losses and consideration of partial pressures so long as all component gases are ideal and all mixing processes occur irreversibly. For ambient conditions of 25°C and 1 bar, the relationship $P_{\max} = -m_f \Delta G_0$, widely thought of as a useful approximation, is actually exact for practical gas turbine power plant. A more complicated approach simply obscures the thermodynamics.

5 Exergy Analysis of Three Ideal Cycles

Figure 3 shows three cycles that are ideal in the sense that: (*i*) the compressor and turbine efficiencies are 100 percent, (*ii*) there are no total pressure losses in the combustor, (*iii*) the two components of the working fluid, although distinguishable, behave as *perfect* gases with the *same* values of c_p and γ. All three cycles have the same compressor pressure ratio, and the same *air* and *fuel* mass flowrates entering the combustor. The COT is therefore the same in all the cycles. As noted by Denton [5], the net power output and cycle efficiency are the same in all cases. This is surprising because the cycles of Figs. 3(*b*) and 3(*c*) include exergetic losses due to thermal mixing that are not present in the cycle of Fig. 3(*a*). The explanation is only revealed by an exergy analysis.

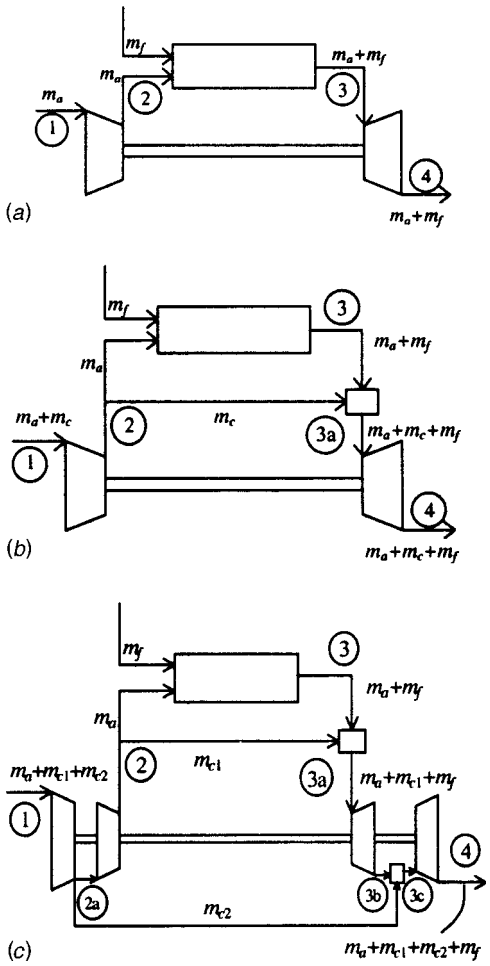

Fig. 3 (*a*) Ideal uncooled gas turbine; (*b*) ideal cooling of first stage stator; (*c*) ideal cooling of first stage stator and intermediate stage

The first and second laws of thermodynamics are applied in the usual way to the compressor (C), combustor (B), expander (T), mixer (M), and exhaust (E). Values of h and s are obtained by setting $c_{pa} = c_{pg} = \text{const}$ and $R_a = R_g = \text{const}$ in Eq. (1). The specific entropy of each component is evaluated at the local mixture pressure. As shown above, this is equivalent to ignoring compositional mixing losses and does not affect the shaft power.

The results are best presented in nondimensional form in terms of the parameters θ (dimensionless COT), τ (compressor isentropic temperature ratio) and ε (fuel/air ratio), defined by,

$$\theta = \frac{T_3}{T_1} \quad \tau = \frac{T_2}{T_1} = \left(\frac{p_2}{p_1}\right)^{\gamma - 1/\gamma} \quad \varepsilon = \frac{m_f}{m_a} \tag{6a}$$

Dimensionless versions of ΔG_A, ΔH_A, and ΔS_A are also defined by,

$$\Delta\bar{G}_A=\frac{\Delta G_A}{c_pT_1}\quad \Delta\bar{H}_A=\frac{\Delta H_A}{c_pT_1}\quad \Delta\bar{S}_A=\frac{\Delta S_A}{c_p} \tag{6b}$$

Power P and lost power I are nondimensionalized as follows:

$$\bar{P}=\frac{P}{m_ac_pT_1}\quad \bar{I}=\frac{I}{m_ac_pT_1} \tag{6c}$$

Consider first the basic gas turbine cycle without cooling shown in Fig. 3(*a*). Expressions for the dimensionless power and lost power of the individual components are given in Appendix 1. Combining these gives the following expressions for the net power and cycle efficiency (defined in terms of the lower heating value of the fuel):

$$\bar{P}=\bar{P}_T+\bar{P}_C=(1+\varepsilon)\theta\left(1-\frac{1}{\tau}\right)-(\tau-1) \tag{7a}$$

$$\eta_{ov}=\frac{\bar{P}_T+\bar{P}_C}{-\varepsilon\Delta\bar{H}_A}=\frac{(1+\varepsilon)\theta\left(1-\frac{1}{\tau}\right)-(\tau-1)}{(1+\varepsilon)(\theta-1)-(\tau-1)} \tag{7b}$$

The maximum available power is given by,

$$\bar{P}_{\max}=\bar{P}_T+\bar{P}_C+\bar{I}_B+\bar{I}_E=-\varepsilon\Delta\bar{G}_A \tag{7c}$$

in agreement with Eq. (5*a*).

Figure 3(*b*) shows a cycle where air is withdrawn at compressor exit, bypasses the combustor, and is mixed with the mainstream flow in the first turbine stage, upstream of the rotor. It is assumed that there is no change of total pressure during mixing, but this does not imply that the mixing process is ideal in the sense that there is no exergy loss. In Appendix 1 it is shown that the net output power and overall efficiency are still given by Eqs. (7*a*) and (7*b*) but the maximum available power is now given by

$$\bar{P}_{\max}=\bar{P}_T+\bar{P}_C+\bar{I}_B+\bar{I}_M+\bar{I}_E=-\varepsilon\Delta\bar{G}_A \tag{8}$$

Equation (8) shows that, although the maximum available power is unchanged, the loss distribution is different. The extra exergy loss due to the mixing of two fluids at different temperatures is exactly offset by the reduced exergy loss of the exhaust gas (which emerges at a lower temperature). However, although the net power output and overall efficiency remain the same, the compressor and turbine mass flowrates are both increased and the specific work output of the machine is therefore reduced.

Figure 3(*c*) shows a cycle with an extra cooling flow extracted part-way through the compressor. Assuming there is no total pressure loss in the second mixing process, it can be shown that the maximum available power, the net power output, and the overall efficiency are all unchanged. The breakdown of the maximum power is given by,

$$\bar{P}_{\max}=\bar{P}_T+\bar{P}_C+\bar{I}_B+\bar{I}_{M1}+\bar{I}_{M2}+\bar{I}_E=-\varepsilon\Delta\bar{G}_A \tag{9}$$

and the extra loss incurred during the second mixing process is exactly offset by a further decrease in the exhaust loss due to the reduced exit temperature. The specific work output is further reduced because of the increased air flowrate entering the compressor. The exergy analyses for the three cycles are shown graphically in Fig. 4 ($\tau=2.87$, $\theta=5$, $\Delta\bar{G}_A=\Delta\bar{H}_A=165$, $\phi=m_c/m_a=0.1$).

The entropy created during the mixing process of Fig. 3(*b*) (loosely termed the *thermal mixing loss*) is depicted graphically in Fig. 5. The mixture specific enthalpy is fixed by the first law of thermodynamics and the minimum mixture specific entropy by the second law:

$$(m_a+m_f+m_c)h_{03A}=m_ch_{02}+(m_a+m_f)h_{03} \tag{10a}$$

$$(m_a+m_f+m_c)s_{3A}\geq(m_a+m_f+m_c)s_{3AA}=m_cs_2+(m_a+m_f)s_3 \tag{10b}$$

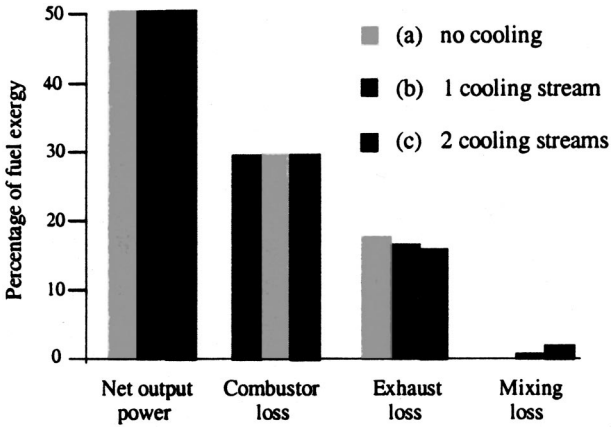

Fig. 4 Exergy analysis of the cycles of Fig. 3

The actual entropy created, $(m_a+m_f+m_3)(s_{3A}-s_{3AA})$, must be specified by a user-defined physical model. (This is true of all loss terms in calculations that do not use the momentum equation.) To specify a condition of zero total pressure loss and then to describe the consequent entropy increase as the *thermal mixing loss* is not strictly accurate. However, in Part II it will be shown that the entropy created during a (possibly high-speed) mixing process of different gases can be decomposed into components, one of which can be identified unambiguously as a thermal mixing loss.

The fact that all three cycles have the same power output and efficiency can be misleading, as it tends to suggest that the thermal mixing loss is unimportant. This is a commonly held belief, but it is important to realize that the above-described analysis applies only to simple cycle gas turbines. For gas turbines with reheat, regenerative heat exchangers, or bottoming cycles, the conclusions are quite different because, in each case, it is advantageous to overall cycle efficiency to maintain a high turbine exhaust gas temperature. (In the case of reheat, this statement refers to the HP rather than the LP turbine.) An extension of the analysis to a reheat cycle shows that ideal cooling of the HP turbine results in substantial changes to the power output and cycle efficiency. Cooling of the LP turbine using air bled from the compressor with zero pressure loss causes no further change, however. Such considerations highlight the importance of treating the thermal mixing loss and the exhaust loss separately rather than trying to offset one against the other.

More importantly, the numerical equivalence of the thermal mixing loss and the decrease in the exhaust loss, far from being a general result, is only true under special circumstances. It is not true, for example, if the turbine and compressor efficiencies are less than unity. This is easily shown by repeating the analysis, allowing for irreversibilities in the turbomachinery.

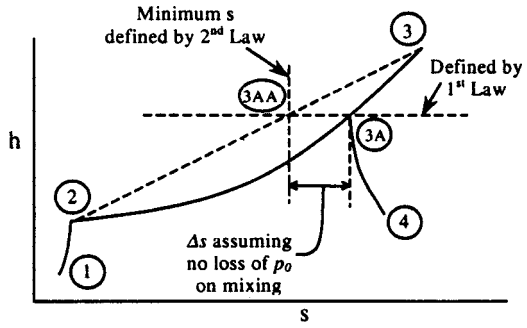

Fig. 5 Mixing of two streams at constant total pressure

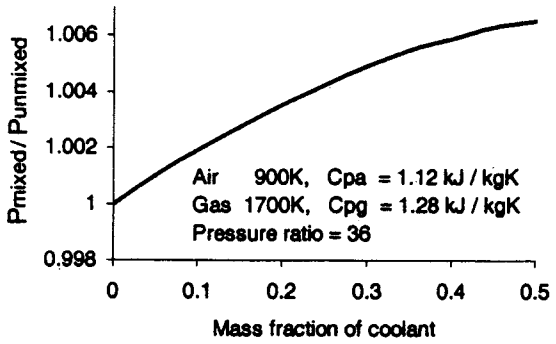

Fig. 6 Power output of mixed and unmixed expansions

Even with perfect turbomachinery, however, the result fails to hold if the gas composition varies. Consider, for example, the steady-flow expansion of *air* and *gas* (assumed now to be perfect gases with different c_p and γ) from the same initial temperature T_1 over a fixed pressure ratio. First, suppose the gases expand isentropically (but separately) before being mixed at constant total pressure. Second, suppose constant pressure mixing occurs first and is then followed by isentropic expansion. In both cases, the power output is given by,

$$P=(m_a c_{pa}+m_g c_{pg})(T_1-T_2) \tag{11}$$

but the final mixture temperature T_2 differs. Unlike a compositional mixing process, the location of a thermal mixing process involving two *different* gases does affect the shaft power output.

The difference in power output between mixed and unmixed expansions can be quite significant if the initial temperatures are radically different. The analysis for *perfect* gases with different c_p values but the same molar mass is presented in Appendix 2. (In gas turbines c_p of the combustion products is greater than c_p of the coolant although the specific gas constants are almost the same.)

Under these conditions, the power output from an adiabatic expansion of mixed gases is *always* greater than when they are unmixed (assuming fixed pressure ratio and polytropic efficiency). Figure 6 illustrates the magnitude of the effect for isentropic expansions of combustion products, a mixture of *air* and *gas*, and coolant, which is pure *air*, initially at 1700 K and 900 K, respectively.

Sometimes, the isentropic efficiency of a cooled turbine is defined as the ratio of the actual work output to the work output obtainable by separate isentropic expansions of the combustion gases and coolant over the same pressure ratio. Clearly, with this definition, efficiencies greater than unity are theoretically possible.

6 Specification of Cooling Flows and Losses

In order to calculate the performance of a cooled gas turbine, both the cooling flowrates and cooling losses must be defined. The cooling flowrates can either be specified as known input data or estimated using a combination of heat transfer theory and empirical data. The cooling losses are usually estimated from simplified theoretical models and added to a basic uncooled loss obtained from empirical correlations. Clearly, this is a gross simplification and results obtained from such modeling must be treated cautiously.

Any realistic model of the turbine must address the cooling of each blade row separately. Continuous cooling models, such as that proposed by El-Masri [6] (Part I), may be acceptable for initial cycle development work but are insufficiently specific to provide the accuracy required once some basic details of the turbine are known. A detailed set of cooling loss models describing the different aspects of entropy production within individual blade rows will be presented in Part II. Taking a global viewpoint at this stage, however, the following list represents sufficient information for calculating the cycle efficiency of a simple air-cooled gas turbine:

(i) The compressor pressure ratio and polytropic efficiency.
(ii) The cooling mass flowrates and their respective bleed pressures.
(iii) The calorific value and composition of the fuel.
(iv) The combustor outlet temperature and total pressure loss.
(v) The irreversible entropy increase between the turbine inlet streams (combustion products and coolant) and the exhaust.

Requirement (v) can be clarified by reference to Fig. 5. Assuming that all the cooling air is drawn from the compressor exit, the steady flow energy equation applied to the complete (adiabatic) turbine is,

$$\begin{aligned} P_T&=[m_c h_{02}+(m_a+m_f)h_{03}]-(m_a+m_f+m_c)h_{04}\\ &=(m_a+m_f+m_c)(h_{03A}-h_{04}) \end{aligned} \tag{12a}$$

If the cooling flowrate m_c is given, the only unknown is h_{04}, the specific total enthalpy at exhaust. This, however, is defined by the given exhaust total pressure and the entropy increase,

$$\begin{aligned} \Delta\Sigma&=(m_a+m_f+m_c)s_4-[m_c s_2+(m_a+m_f)s_3]\\ &=(m_a+m_f+m_c)(s_4-s_{3AA}) \end{aligned} \tag{12b}$$

If the losses are additive, $\Delta\Sigma$ can be decomposed into components representing a basic uncooled loss and a loss associated with cooling,

$$\Delta\Sigma=\Delta\Sigma_{\text{basic}}+\Delta\Sigma_{\text{cool}} \tag{12c}$$

The value of $\Delta\Sigma_{\text{basic}}$ for a turbine stage depends strongly on the stage pressure ratio and can be obtained from an uncooled efficiency, assumed known. The cooling losses, on the other hand, are essentially independent of the stage pressure ratios. Because of this, the common practice of describing the expansion in a cooled turbine by an *equivalent polytropic efficiency* is, in the opinion of the authors, inappropriate. It is also confusing because the efficiency in question, applying solely to the main turbine flow, excludes certain components of the cooling loss while including the effects of heat transfer to the blading (only part of which is associated with irreversible entropy creation). Most of the ambiguity that pervades the literature is traceable either to a lack of precision in defining cooling losses, or a confusion between reversible entropy change due to heat transfer and entropy production due to irreversible loss processes. The case is very strong, therefore, for representing the cooling losses unambiguously as a set of entropy creation terms summing to $\Delta\Sigma_{\text{cool}}$. This will form the philosophy of the approach in Part II.

For the present purposes $\Delta\Sigma_{\text{cool}}$ is split into just two additive components, $\Delta\Sigma_A$ and $\Delta\Sigma_B$. $\Delta\Sigma_A$ is defined by,

$$\Delta\Sigma_A=(m_a+m_f+m_c)(s_{3A}-s_{3AA}) \tag{12d}$$

and represents (at least approximately) the minimum unavoidable entropy creation due to the thermal mixing. $\Delta\Sigma_B$ represents all the other entropy creation terms associated with the cooling process (coolant throttling, dissipation of kinetic energy during mixing, etc.).

The detailed treatment in Part II suggests that these losses are each directly proportional to the coolant mass flowrate and hence,

$$\Delta\Sigma_B=K_B R_a m_2 \tag{12e}$$

where K_B is a loss coefficient rendered dimensionless by the introduction of the specific gas constant for air, R_a. Typical values of K_B probably lie in the range 0.1–0.3.

Treating K_B as a known parameter, Fig. 7 shows its effect on the performance of a simple cycle aeroderivative gas turbine with pressure ratio 36 and COT 1700 K. In such a machine, coolant

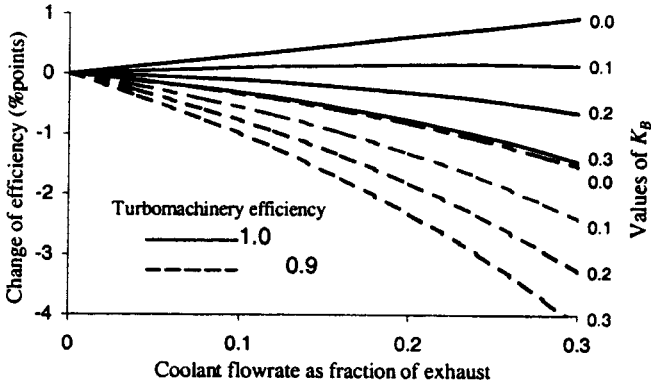

Fig. 7 Effect of coolant losses on the efficiency of a simple cycle GT

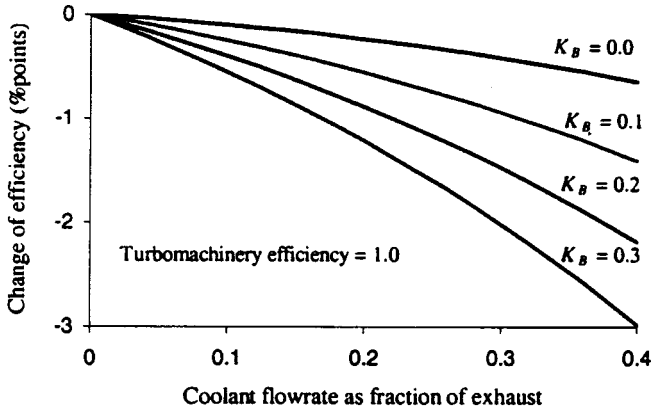

Fig. 8 Effect of coolant losses on the efficiency of a reheat GT

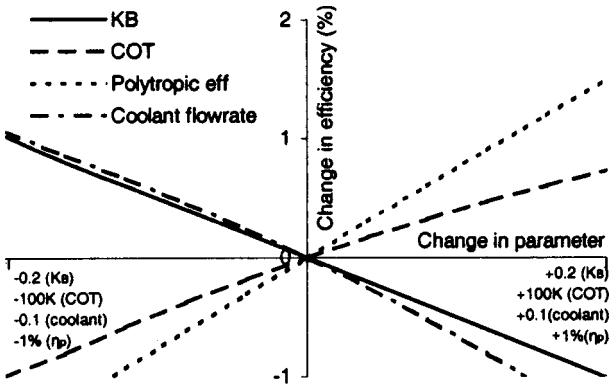

Fig. 9 The sensitivity of parameters in a simple cycle GT

injection would probably account for 20–25 percent of the exhaust flow. Figure 7 also shows the effect of nonisentropic turbomachinery as the cooling flowrate is varied. The increase in cycle efficiency for $K_B=0$, $\eta_C=\eta_T=1$ is due to the different c_p values of the coolant and combustion products as discussed previously. Clearly the value of K_B has a major effect on cycle efficiency.

The role of the *thermal mixing loss* is illustrated by considering a reheat gas turbine cycle. Accordingly, the simple cycle of Fig. 7 is modified by the addition of a second combustor also operating with COT 1700 K. The HP turbine pressure ratio is 2 and it is assumed that half the coolant is injected into the HP and half into the LP turbine. The results are shown in Fig. 8 for $\eta_C=\eta_T=1$. Comparison with Fig. 7 shows a more rapid drop in cycle efficiency with increasing coolant flowrate due to the deleterious effect of the thermal loss. The effect is particularly obvious for $K_B=0$ where the thermal loss represents the only contribution to the cooling loss.

Figure 9 is a sensitivity analysis showing the effect of changing various parameters in the simple cycle gas turbine of Fig. 7 operating with $\eta_C=\eta_T=0.9$, a coolant flow ratio of 0.2, and $K_B=0.2$. Keeping all other parameters constant, a 0.5 percent increase in cycle efficiency could be realized by: (*i*) an increase in COT of 65 K, (*ii*) a decrease in K_B of 0.1, (*iii*) a decrease in coolant flow ratio of 0.05, or (*iv*) an increase in the polytropic efficiencies of 0.35 percent.

7 Conclusions

This paper has explored the general principles involved in modeling the air-cooled gas turbine with a view to clarifying the thermodynamics and formalizing the approach. The conclusions are:

(i) The effect of cooling can only be assessed in the context of the complete cycle.
(ii) A two-component semi-perfect gas model of the working fluid provides an accurate and straightforward representation.
(iii) Compositional mixing losses do not affect the shaft power terms and can be neglected to considerable advantage. Component specific entropies must then be evaluated at the mixture rather than component partial pressure.
(iv) Exergy analysis of carefully selected ideal cycles can provide useful illumination of thermodynamic principles. This approach was used to clarify the rôle of the *thermal mixing loss*.
(v) For clarity and physical interpretation, it is extremely important that cooling losses should be modeled and incorporated in cycle calculations as entropy creation terms. The concept of an *equivalent cooled turbine efficiency* is unhelpful and confusing.
(vi) Blade cooling has a major impact on cycle efficiency and it is crucially important to establishing accurate prediction methods both for the required cooling flowrates and the cooling losses.

The final conclusion is particularly true at the present time as both MacArthur [3] and Horlock et al. [4] have stressed the fact that state-of-the-art gas turbines are operating at combustor outlet temperatures very near the point of maximum cycle efficiency.

Acknowledgments

The authors gratefully acknowledge numerous useful discussions with Sir John Horlock and other members of the Whittle Laboratory, Cambridge University. They are also indebted to Prof. T. V. Jones of the Osney Laboratory, Oxford University, and many members of Rolls Royce plc, particularly Mr. C. Freeman, Mr. P. Walsh, Mr. D. Watson, and Mr. B. Whinray. RCW was supported by an EPSRC studentship and Rolls-Royce CASE award.

Nomenclature

h = specific enthalpy
I = lost power
m = mass flowrate
P = power
p = pressure
s = specific entropy
T = temperature
x, y = mass, mol fraction
ε = fuel flowrate fraction
ϕ = cooling flowrate fraction
η_{ov} = plant overall efficiency (LHV)
θ = dimensionless temperature
τ = isentropic temperature ratio

Subscripts

A = ambient
a = air
f = fuel
g = gas
i = component i
mix = (entropy of) compositional mixing
stoic = stoichiometric
0 = total (as opposed to static) quantities

Appendix 1

Analysis of Ideal Cycles With and Without Cooling. Consider the uncooled gas turbine cycle shown in Fig. 3(*a*). In terms of the dimensionless parameters defined in Eq. (6), expressions for the dimensionless power and lost power of the individual components are,

$$\text{Compressor} \quad \overline{P}_C = (1-\tau) \tag{A1.1a}$$

$$\text{Turbine} \quad \overline{P}_T = (1+\varepsilon)\,\theta\left(1-\frac{1}{\tau}\right) \tag{A1.1b}$$

$$\text{Combustor} \quad \overline{I}_B = (1+\varepsilon)\ln\left(\frac{\theta}{\tau}\right)+\varepsilon\Delta\overline{S}_A \tag{A1.1c}$$

$$\text{Exhaust} \quad \overline{I}_E = (1+\varepsilon)\left(\frac{\theta}{\tau}-1\right)-(1+\varepsilon)\ln\left(\frac{\theta}{\tau}\right) \tag{A1.1d}$$

The steady flow energy equation for the combustor is,

$$-\varepsilon\Delta\overline{H}_A = (1+\varepsilon)(\theta-1)-(\tau-1) \tag{A1.1e}$$

On combination, Eq. (*A*1.1) gives Eq. (7) for the net power output, cycle efficiency, and maximum available power.

For the cooled cycle of Fig. 3(*b*), the combustor conditions are unchanged and hence Eqs. (*A*1.1*c*) and (*A*1.1*e*) still stand. Defining $\theta_A = T_{3A}/T_1$ and $\phi = m_c/m_a$ (where m_c is the coolant mass flowrate and m_a is the *combustor* air mass flowrate), the other power and lost power expressions are,

$$\text{Compressor} \quad \overline{P}_C = (1+\phi)(1-\tau) \tag{A1.2a}$$

$$\text{Turbine} \quad \overline{P}_T = (1+\varepsilon+\phi)\,\theta_A\left(1-\frac{1}{\tau}\right) \tag{A1.2b}$$

$$\text{Mixer} \quad \overline{I}_M = (1+\varepsilon+\phi)\ln\left(\frac{\theta_A}{\tau}\right)-(1+\varepsilon)\ln\left(\frac{\theta}{\tau}\right) \tag{A1.2c}$$

$$\text{Exhaust} \quad \overline{I}_E = (1+\varepsilon+\phi)\left(\frac{\theta_A}{\tau}-1\right)-(1+\varepsilon+\phi)\ln\left(\frac{\theta_A}{\tau}\right) \tag{A1.2d}$$

The energy equation applied to the mixer gives an expression for θ_A,

$$\theta_A = \frac{(1+\varepsilon)\,\theta+\phi\tau}{(1+\varepsilon+\phi)} \tag{A1.2e}$$

Combination of these equations shows that the net power output and cycle efficiency are still given by Eqs. (7*a*) and (7*b*) and the maximum available power is given by Eq. (8).

Appendix 2

Mixed and Unmixed Expansions of Different Perfect Gases. Consider the adiabatic steady-flow expansion of two perfect gases *a* and *b* (representing coolant and combustion products respectively) with the same pressure ratio $r = p_2/p_1 < 1$ and polytropic efficiency η. Let the initial temperatures be T_{1a} and T_{1b} ($T_{1b} > T_{1a}$) and the mass flowrates be m_a and m_b ($m_a + m_b = 1$). Assume $c_{pb} > c_{pa}$ but $R_b = R_a$.

If the gases expand without mixing, the power output is,

$$P_u = m_a c_{pa} T_{1a}(1-r^{\eta R/c_{pa}}) + m_b c_{pb} T_{1b}(1-r^{\eta R/c_{pb}}) \tag{A2.1a}$$

Conversely, if the gases are mixed at constant pressure before the expansion, the power output is,

$$P_m = (m_a c_{pa} T_{1a} + m_b c_{pb} T_{1b})(1-r^{\eta R/c_{pm}}) \tag{A2.1b}$$

where $c_{pm} = m_a c_{pa} + m_b c_{pb}$ is the mixture specific heat capacity. Thus,

$$P_m - P_u = r^{\eta R/c_{pm}}[m_a c_{pa} T_{1a}(r^{x_a}-1) + m_b c_{pb} T_{1b}(r^{x_b}-1)] \tag{A2.2}$$

where,

$$x_a = \frac{m_b \eta R(c_{pb}-c_{pa})}{c_{pa}c_{pm}} > 0 \qquad x_b = \frac{m_a \eta R(c_{pa}-c_{pb})}{c_{pb}c_{pm}} < 0$$

It is difficult to assess the sign of Eq. (*A*2.2), but clarification is possible by using the series expansion,

$$r^x = 1 + x\ln(r) + \frac{[x\ln(r)]^2}{2!} + \frac{[x\ln(r)]^3}{3!} + \ldots \tag{A2.3}$$

Substituting into Eq. (*A*2.2) and collecting terms then gives,

$$\frac{P_m - P_u}{A} = \ln(r)(T_{1a}-T_{ib}) + \frac{[\ln(r)]^2}{2!}(x_a T_{1a} - x_b T_{1b}) + \ldots \tag{A2.4}$$

where,

$$A = r^{\eta R/c_{pm}}\left[\frac{m_a m_b R(c_{pb}-c_{pa})}{c_{pm}}\right] > 0$$

The first two terms on the right-hand side dominate and are always positive. Hence $P_m > P_u$ and the power output in an adiabatic expansion with $c_{pb} > c_{pa}$ is *always* greater if the gases are premixed. Note that, if $T_{ib} = T_{1a}$ the first term disappears but the second term is still positive.

References

[1] Lakshminarayana, B., 1995, *Fluid Dynamics and Heat Transfer of Turbomachinery*, Wiley, New York, Chap. 7.
[2] Day, C. R. B., Oldfield, M. L. G., and Lock, G. D., 1999, "The Influence of Film Cooling on the Efficiency of an Annular Nozzle Guide Vane Cascade," ASME J. Turbomach., **121**, pp. 145–151.
[3] MacArthur, C. D., 1999, "Advanced Aero-Engine Turbine Technologies and Their Application to Industrial Gas Turbines," *Proc. 14th Int. Symp. on Air Breathing Engines*, Florence, Paper No. 99-7151.
[4] Horlock, J. H., Watson, D. T., and Jones, T. V., 2001, "Limitations on Gas Turbine Performance Imposed by Large Turbine Cooling Flows," ASME J. Eng. Gas Turbines Power, **123**, pp. 487–494.
[5] Denton, J. D., 1993, "Loss Mechanisms in Turbo-Machines," ASME J. Turbomach., **115**, pp. 621–656.
[6] El-Masri, M. A., 1985–6, "On Thermodynamics of Gas Turbine Cycles: Part I—Second Law Analysis of Combined Cycles," Part II—A Model for Expansion in Cooled Turbines," Part III—Thermodynamic Potential and Limitations of Cooled Reheat-Gas-Turbine Combined Cycles," ASME J. Eng. Gas Turbines Power, **107**, pp. 880–889; **108**, pp. 151–159; **108**, pp. 160–170.
[7] El-Masri, M. A., 1987, "Exergy Analysis of Combined Cycles: Part 1—Air-Cooled Brayton-Cycle Gas Turbines," ASME J. Eng. Gas Turbines Power, **109**, pp. 228–236.
[8] Chiesa, P., Consonni, S., Lozza, G., and Macchi, E., 1993, "Predicting the Ultimate Performance of Advanced Power Cycles Based on Very High Temperatures," ASME Paper No. 93-GT-223.
[9] Facchini, B., Fiaschi, D., and Manfrida, G., 2000, "Exergy Analysis of Combined Cycles Using Latest Generation Gas Turbines," ASME J. Eng. Gas Turbines Power, **122**, pp. 233–238.
[10] Kotas, T. J., 1985, *The Exergy Method of Thermal Plant Analysis*, Butterworths.

Modeling the Air-Cooled Gas Turbine: Part 2—Coolant Flows and Losses

J. B. Young
email: jby@eng.cam.ac.uk

R. C. Wilcock

Cambridge University Engineering Department,
Trumpington Street,
Cambridge, CB2 1PZ, United Kingdom

This paper is Part II of a study concerned with developing a formal framework for modeling air-cooled gas turbine cycles. It deals with the detailed specification of coolant flowrates and losses. For accurate performance assessment, it is necessary to divide the turbine expansion into individual stages with stator and rotor rows being treated separately. Particular care is needed when deriving the equations for the rotor, and it is shown how all required flow variables can be estimated from minimal data if design values are unavailable. Specification of the cooling flowrates is based on a modified Holland and Thake procedure, which can be formalized in terms of averaged parameters. Thermal barrier coatings can be included if present. The importance of allowing for fluctuations in combustor outlet temperature is stressed and procedures for dealing with end-wall and disk cooling are suggested. There is confusion in the literature concerning cooling losses, and it is shown how these may be defined and subdivided in a consistent way. The importance of representing losses in terms of irreversible entropy creation rather than total pressure loss is stressed. A set of models for the components of the cooling loss are presented and sample calculations are used to illustrate the division and magnitude of the loss. [DOI: 10.1115/1.1415038]

1 Introduction

This paper is Part II of a study concerned with developing a formal framework for modeling air-cooled gas turbine cycles and deals with the detailed specification of cooling flowrates and losses. A general discussion of the thermodynamics of air-cooling was presented in Part I (Young and Wilcock [1]).

Specification of the cooling flowrates and losses for performance predictions involve two essentially separate problems. In the detailed design of a turbine, the cooling flowrates are established by a complex procedure involving correlation of experimental results and semitheoretical calculations. For cycle calculations, this lengthy procedure must be condensed into a simplified scheme, which retains the essential features of the underlying physics and is valid over a range of operating conditions. In this paper, a modified version of the well-known scheme by Holland and Thake [2] is used. Most other theories (Horlock [3], El-Masri [4]) are restricted to a specific geometry or lack generality.

In Part I it was noted that the literature on cooling losses is often confused and that there is no definitive formal analysis available to provide a framework for development. Typically, cycle calculations seem to involve a rather random selection of losses drawn from a list that includes coolant–mainstream mixing, heat transfer through the blades, and coolant throttling. In Part I, a strong case was made for representing the cooling losses as additive entropy creation terms and this will be the approach pursued in Part II. Indeed, one of the main objectives is to provide a baseline set of well-defined expressions for the cooling losses that are sufficiently general for cycle calculations but that can be fine-tuned for more accurate design work.

The paper takes a deliberately detailed approach in specifying the cooling flows and losses but, in order to preserve continuity of the main text, most of the analysis has been relegated to the appendices. These, therefore, embody an important part of the development.

Contributed by the International Gas Turbine Institute and presented at the 46th International Gas Turbine and Aeroengine Congress and Exhibition, New Orleans, Louisiana, June 4–7, 2001. Manuscript received by the International Gas Turbine Institute February 2001. Paper No. 2001-GT-392. Review Chair: R. Natole.

2 The Cooled Turbine Stage

Any realistic model of a turbine must address the cooling of each blade row separately. Continuous expansion path cooling models (El-Masri [5]), may be acceptable for initial cycle development work but cannot provide the accuracy required once some basic details of the turbine layout are known. The information required to implement the calculation schemes described below is minimal, being little more than a knowledge of the number of stages, the stage pressure ratios or work requirements, and the uncooled stage efficiencies. These data can be obtained in a variety of ways ranging from informed guesswork to an elaborate flow analysis linked to the cooling calculations. A one-dimensional version of the latter based on mean blade angles and empirical loss coefficients is described by Kawaike et al. [6].

Figure 1 is a schematic diagram of a cooled gas turbine stage. Mass flowrate, specific total enthalpy (in a stationary frame of reference) and specific entropy are denoted by m, h_0, and s, respectively. The subscript g is appended to denote mainstream *gas* and c to denote *coolant*. Where necessary, subscripts sc, rc, or dc are used to differentiate between stator, rotor, and disk cooling. The flows crossing any reference plane may be nonuniform and it is understood that h_0 and s represent massflow-averaged values. Reference planes at stator inlet, stator outlet/rotor inlet, rotor outlet, and stage outlet are numbered 1, 2, 3, and 4, respectively.

The mass flowrate and composition of the mainstream changes from one plane to the next because of the addition of coolant. Coolant is drawn from the compressor at state k and enters the blade passages at state i. (The k and i states will generally be different for the stator and rotor blades.) For convection cooling, the coolant leaves from the end of the blade or the trailing edge (states b and t). For combined convection and film cooling, it exits through holes in the blade surfaces or endwalls (states f and e). For each type of flow, a massflow-averaged exit state can be defined. Thus, $h_{0c,f}$ and $s_{c,f}$ are values massflow-averaged over all film cooling holes. For each row, a mean massflow-averaged exit state x can be defined by,

$$m_c h_{0c,x} = m_{c,f} h_{0c,f} + m_{c,e} h_{0c,e} + m_{c,t} h_{0c,t} + m_{c,b} h_{0c,b} \quad (1a)$$

$$m_c s_{c,x} = m_{c,f} s_{c,f} + m_{c,e} s_{c,e} + m_{c,t} s_{c,t} + m_{c,b} s_{c,b} \quad (1b)$$

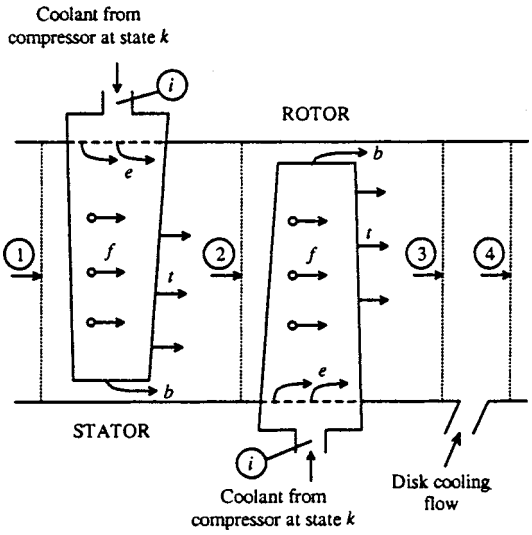

Fig. 1 Schematic diagram of a cooled gas turbine stage

where $m_c = m_{c,f} + m_{c,e} + m_{c,t} + m_{c,b}$. The cooling flows associated with each blade row can therefore be reduced to a single flow drawn from the compressor at state *k*, entering the blade passages at state *i* and exiting into the main flow path (before mixing) at state *x*.

Rotor disk cooling is treated separately. In the present work it is represented by a single injection after each rotor on the assumption that no useful shaft work is obtained from this cooling flow.

3 First Law Analysis

3.1 Stationary Blades. Figure 2 is a schematic diagram illustrating the simplified blade cooling model. Taken together, the mainstream and coolant flows are adiabatic and the steady-flow energy equation for the combination is,

$$m_{g,1}(h_{0g,1} - h_{0g,2}) + m_{sc}(h_{0sc,i} - h_{0g,2}) = 0 \qquad (2a)$$

Assuming adiabatic flow for the coolant between compressor bleed point and blade inlet, $h_{0sc,i} = h_{0sc,k}$, $h_{0g,1}$ and $h_{0sc,k}$ are known and hence $h_{0g,2}$ can be determined from Eq. (2*a*) once the coolant-to-mainstream mass flow ratio m_{sc}/m_{g1} is known.

Steady-flow energy equations can also be written separately for the external (mainstream) and internal (coolant) flows,

$$m_{g,1}(h_{0g,1} - h_{0g,2}) + m_{sc}(h_{0sc,x} - h_{0g,2}) = Q_s \qquad (2b)$$

$$m_{sc}(h_{0sc,i} - h_{0sc,x}) = -Q_s \qquad (2c)$$

where Q_s is the total rate of heat transfer through the blade surface (mainstream to coolant). Clearly, (2*a*)=(2*b*)+(2*c*).

3.2 Rotating Blades. The overall energy equation for the rotor is,

$$m_{g,2}(h_{0g,2} - h_{0g,3}) + m_{rc}(h_{0rc,i} - h_{0g,3}) = P \qquad (3a)$$

where $m_{g,2} = m_{g,1} + m_{sc}$ and *P* is the shaft power output. Assuming adiabatic flow between the compressor bleed point and blade inlet, $h_{0rc,i} = h_{0rc,k}$. For the final turbine stage on a spool, *P* is fixed by the compressor power requirement and $h_{0g,3}$ can be determined if $m_{rc}/m_{g,2}$ is known. The stage pressure ratio follows once the entropy creation due to the losses has been found. In other cases, the stage pressure ratio is specified, the losses are determined, and *P* and $h_{0g,3}$ follow.

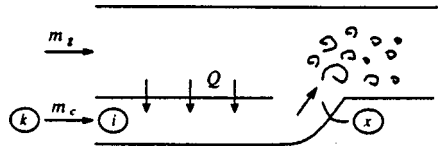

Fig. 2 Simplified blade cooling model

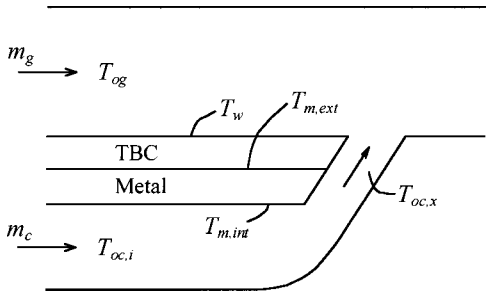

Fig. 3 Notation for the heat transfer model (stators and rotors)

The energy equations for the external and internal flows are,

$$m_{g,2}(h_{0g,2} - h_{0g,3}) + m_{rc}(h_{0rc,x} - h_{0g,3}) = P_{ext} + Q_r \qquad (3b)$$

$$m_{rc}(h_{0rc,i} - h_{0rc,x}) = P_{\text{int}} - Q_r \qquad (3c)$$

where P_{ext} and P_{int} are the external and internal contributions to the net power ($P = P_{ext} + P_{int}$). Introduction of the Euler turbine equation (see Appendix 1) results in energy equations expressed in terms of the specific rothalpy ($i = h_0 - UV_\theta$),

$$m_{g,2}(i_{g,2} - i_{g,3}) + m_{rc}(i_{rc,i} - i_{g,3}) = 0 \qquad (4a)$$

$$m_{g,2}(i_{g,2} - i_{g,3}) + m_{rc}(i_{rc,x} - i_{g,3}) = Q_r \qquad (4b)$$

$$m_{rc}(i_{rc,i} - i_{rc,x}) = -Q_r \qquad (4c)$$

The application of Eqs. (3) and (4) for the rotating blades requires detailed knowledge of the turbine (particularly the rotor inlet conditions), which may not be available. Simplification is possible, however, by expressing all the unknown quantities in terms of a *stage loading coefficient* ψ. This is defined in the usual way by,

$$\psi = \frac{P}{m_{g,3}U_{mean}^2} \qquad (5)$$

It is useful to recall that ψ can be related approximately to the *degree of reaction* ρ. Neglecting coolant addition, assuming constant axial velocity through the rotor and zero exit swirl from the stage, it can be shown that $\psi = 2(1-\rho)$. Thus, for impulse blading $\rho = 0$, $\psi \cong 2$, and for 50 percent reaction blading $\rho = 0.5$, $\psi \cong 1$. The rotor approximations are discussed in detail in Appendix 1.

3.3 Disk Cooling Flows. Disk cooling air is injected both before and after the rotor. The upstream injection does little work in the rotor, however, and it is expedient to combine the two flows into a single flow entering downstream. The energy equation between stations 3 and 4 is then,

$$m_{g,3}(h_{0g,3} - h_{0g,4}) + m_{dc}(h_{0dc,k} - h_{0g,4}) = 0 \qquad (6)$$

where $m_{g,3} = m_{g,2} + m_{rc}$ and m_{dc} is the mass flow rate of disk cooling air.

4 Calculation of the Cooling Flowrates

Application of Eqs. (2) and (3) in a performance calculation requires realistic values of the mass flow ratios $m_{sc}/m_{g,1}$ and $m_{rc}/m_{g,2}$. To obtain these, it is first necessary to estimate the minimum cooling flowrates required to maintain the blade temperatures within the safe operating range defined by the blade material properties. The procedure recommended is an extension of the method developed by Holland and Thake [2]. The notation is shown in Fig. 3. The internal and external surface metal tem-

peratures $T_{m,int}$ and $T_{m,ext}$ are assumed uniform over the blade. If a thermal barrier coating (TBC) is present, the outer temperature T_w differs from $T_{m,ext}$.

Details of the heat transfer model and cooling flowrate calculations are given in Appendix 2. The procedure for stator and rotor blades is the same except that the latter is carried out with respect to the rotating co-ordinate system. The calculations require the specification of a number of empirical parameters, notably the *internal flow cooling efficiency*, the *film cooling effectiveness*, and the metal and TBC *Biot numbers*. These parameters (defined in Appendix 2) reflect the level and sophistication of the cooling technology and are introduced in order to bypass the difficult problem of calculating the detailed flow behavior within the blade passages and in the external film. The other important empirical parameter, also defined in Appendix 2, is the *cooling flow factor* K_{cool}. This can be estimated from a knowledge of the blade geometry and the external flow Stanton number.

If the value of T_{0g} corresponding to the mass-averaged value of h_{0g} at blade inlet (absolute or relative as appropriate) is used in the heat transfer calculation procedure, the predicted cooling flowrates are invariably much lower than those found in real engines. This is because the design procedure must make allowance for the possibility of temperature fluctuations (hot spots) in the flow exiting the combustor. A simple way of doing this (Kawaike et al. [6]) is to replace T_{0g} by an estimated maximum temperature,

$$T_{0g}^{\max} = T_{0g} + K_{comb}\Delta T_{comb} \tag{7}$$

where ΔT_{comb} is the temperature rise through the combustor. K_{comb} (sometimes called the *combustion pattern factor*) is an empirical constant which depends on the type of combustor (aero or industrial) and the position of the blade row with respect to the combustor outlet.

The rotor disk cooling flows are more difficult to estimate than the blade cooling flows. Apart from cooling the rotor disks (which receive heat by conduction from the blades), the flows also prevent the ingestion of mainstream gas into the rotor disk cavities. In the present model, values of $m_{dc}/m_{g,3}$ are simply specified by the user.

As an example of the calculation of cooling flowrates, consider a single-stage turbine (without thermal barrier coatings) operating at the conditions given in Table 1. For the purpose of illustration, the stage polytropic efficiency is assumed to include the effects of the cooling losses. The cooling flow factor K_{cool} is based on $\mathrm{St}_g = 0.0015$ and $A_{surf}c_{pg}/A_g{*}c_{pc} = 30$ (see Appendix 2). Combustion pattern factors K_{comb} of 0.1 for the stator and 0.05 for the rotor were first used to calculate the cooling flowrates. Then, using these flowrates but taking $K_{comb} = 0$, the blade cooling effectiveness ε_0 and the metal temperatures $T_{m,ext}$ and $T_{m,int}$ were recalculated to give the values, representative of the mean flow conditions, presented in Table 1.

The coolant to mainstream flow ratios of 14.5 percent for the stator and 4.9 percent for the rotor are typical of those found in real engines. The sensitivity of the *total* stage cooling flowrate to changes in the operating conditions is shown in Fig. 4. Thus, a *decrease* of 1 percentage point in cooling flowrate corresponds to either: (*i*) a *decrease* in coolant supply temperature of 15°C, or (*ii*) a *decrease* in combustor outlet temperature of 32°C, or (*iii*) an *increase* in allowable blade temperature of 10°C, or (*iv*) an *increase* in film cooling effectiveness of 0.035, or (*v*) an *increase* in internal cooling efficiency of 0.08, or (*vi*) a *decrease* in metal Biot number of 0.08.

Table 1 Sample calculation of cooling flowrates

TURBINE DATA		
Combustor outlet temperature	$T_{0g,1}$	= 1700 K
Maximum metal temperature	$T_{m,ext}$	= 1100 K
Coolant supply temperature	$T_{0c,k}$	= 867 K
Turbine inlet total pressure	$p_{0g,1}$	= 34 bar
Coolant supply pressure	$p_{0c,k}$	= 34 bar
Stage pressure ratio	$p_{0g,1}/p_{0g,4}$	= 2.4
Stage loading coefficient	ψ	= 1.0
Stage polytropic efficiency	η_p	= 0.9
Combustion pattern factor (stator)	K_{comb}	= 0.1
Combustion pattern factor (rotor)	K_{comb}	= 0.05
Rotor swirl factor	K_{swirl}	= 0.5
Cooling flow factor (stator/rotor)	K_{cool}	= 0.045
Internal cooling efficiency (stator/rotor)	$\eta_{c,int}$	= 0.7
Film cooling effectiveness (stator/rotor)	ε_f	= 0.4
Metal Biot number (stator/rotor)	Bi_m	= 0.2
STATOR RESULTS		
Coolant/mainstream flowrate ratio	$m_{sc}/m_{g,1}$	= 0.145
Blade cooling effectiveness	ε_0	= 0.75
Rotor inlet temperature (absolute)	$T_{0g,2}$	= 1603 K
Coolant exit temperature	$T_{0c,x}$	= 969 K
External metal temperature	$T_{m,ext}$	= 1078 K
Internal metal temperature	$T_{m,int}$	= 1013 K
ROTOR RESULTS		
Coolant/mainstream flowrate ratio	$m_{rc}/m_{g,2}$	= 0.049
Blade cooling effectiveness	ε_0	= 0.58
Rotor inlet temperature (relative)	$T_{0g,2}$	= 1487 K
Coolant exit temperature (relative)	$T_{0c,x}$	= 966 K
External metal temperature	$T_{m,ext}$	= 1082 K
Internal metal temperature	$T_{m,int}$	= 1043 K

5 Second Law Analysis

5.1 Stationary Blades. With reference to Figs. 1 and 2, the second law of thermodynamics for the combined mainstream and coolant flows is,

$$\Delta\Sigma_s = \Delta\Sigma_{s,basic} + \Delta\Sigma_{s,cool} = m_{g,1}(s_{g,2} - s_{g,1}) + m_{sc}(s_{g,2} - s_{sc,k}) \tag{8a}$$

where $\Delta\Sigma_s$ is the total rate of entropy creation due to irreversibilities. (Because of irreversibilities between the compressor bleed point and the inlet to the internal blade passages, $s_{sc,i} > s_{sc,k}$ and this loss has been included in $\Delta\Sigma_s$.) $\Delta\Sigma_s$ is formally subdivided into $\Delta\Sigma_{s,basic}$ (the loss associated with uncooled operation) and $\Delta\Sigma_{s,cool}$ (the extra loss associated with cooling).

Second law statements can also be written for the external mainstream flow, the heat transfer through the TBC and metal, and the internal coolant flow. Thus,

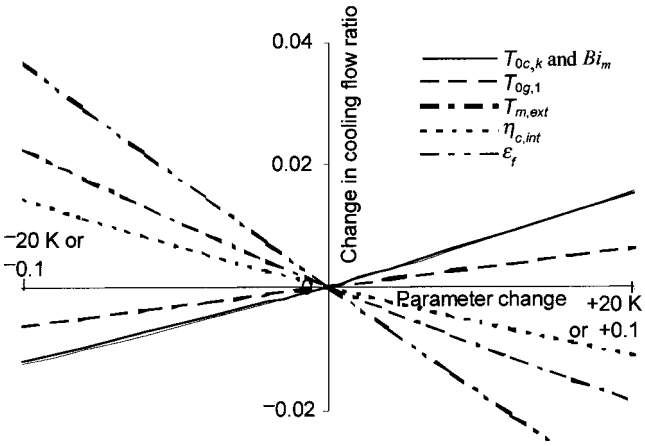

Fig. 4 Sensitivity of cooling flowrate to changes in operating conditions

$$\Delta\Sigma_{s,basic}+\Delta\Sigma_{s,ext}=m_{g,1}(s_{g,2}-s_{g,1})+m_{sc}(s_{g,2}-s_{sc,x})+\frac{Q_s}{T_{sw}} \tag{8b}$$

$$\Delta\Sigma_{s,tbc}=Q_s\left(\frac{1}{T_{sm,ext}}-\frac{1}{T_{sw}}\right) \tag{8c}$$

$$\Delta\Sigma_{s,met}=Q_s\left(\frac{1}{T_{sm,int}}-\frac{1}{T_{sm,ext}}\right) \tag{8d}$$

$$\Delta\Sigma_{s,int}=m_{cs}(s_{sc,x}-s_{sc,k})-\frac{Q_s}{T_{sm,int}} \tag{8e}$$

where subscripts sm and sw denote stator metal and external wall, respectively, and $\Delta\Sigma_{s,ext}$ refers solely to the cooling losses of the external flow. Adding Eqs. (8*b*)–(8*e*) and comparing with Eq. (8*a*) allows the cooling losses to be subdivided into four components,

$$\Delta\Sigma_{s,cool}=\Delta\Sigma_{s,ext}+\Delta\Sigma_{s,tbc}+\Delta\Sigma_{s,met}+\Delta\Sigma_{s,int} \tag{8f}$$

$\Delta\Sigma_{s,tbc}$ and $\Delta\Sigma_{s,met}$ can be calculated directly because Q_s, T_{sw}, $T_{sm,ext}$ and $T_{sm,int}$ are known from the heat transfer analysis. However, $\Delta\Sigma_{s,ext}$ and $\Delta\Sigma_{s,int}$ require separate empirical loss models. Then, $s_{g,2}$ can be found from Eq. (8*a*) and, with $h_{0g,2}$ known from the first law analysis and the gas composition from continuity, state 2 is completely specified.

If each $\Delta\Sigma$ term is multiplied by the *dead state temperature*, the resulting *lost power* term is identical to that which would arise from a formal exergy analysis. The introduction of exergy tends to cloud the issues, however, and it is felt that the straightforward second law analysis presented above provides a better physical interpretation.

5.2 Rotating Blades. The second law analysis for a rotor blade row is identical. Indeed, the entropy creation expressions can be obtained from Eq. (8) simply by an appropriate change of subscript. Thus,

$$\Delta\Sigma_r=\Delta\Sigma_{r,basic}+\Delta\Sigma_{r,cool}=m_{g,2}(s_{g,3}-s_{g,2})+m_{rc}(s_{g,3}-s_{rc,k}) \tag{9a}$$

$$\Delta\Sigma_{r,basic}+\Delta\Sigma_{r,ext}=m_{g,2}(s_{g,3}-s_{g,2})+m_{rc}(s_{g,3}-s_{rc,x})+\frac{Q_r}{T_{rw}} \tag{9b}$$

$$\Delta\Sigma_{r,tbc}=Q_r\left(\frac{1}{T_{rm,ext}}-\frac{1}{T_{rw}}\right) \tag{9c}$$

$$\Delta\Sigma_{r,met}=Q_r\left(\frac{1}{T_{rm,int}}-\frac{1}{T_{rm,ext}}\right) \tag{9d}$$

$$\Delta\Sigma_{r,int}=m_{rc}(s_{rc,x}-s_{rc,k})-\frac{Q_r}{T_{rm,int}} \tag{9e}$$

$$\Delta\Sigma_{r,cool}=\Delta\Sigma_{r,ext}+\Delta\Sigma_{r,tbc}+\Delta\Sigma_{r,met}+\Delta\Sigma_{r,int} \tag{9f}$$

5.3 Disk Cooling Flows. Applying the second law between planes 3 and 4 of Fig. 1 gives,

$$\Delta\Sigma_{dc}=m_{g,3}(s_{g,4}-s_{g,3})+m_{dc}(s_{g,4}-s_{dc,k}) \tag{10}$$

If $\Delta\Sigma_{dc}$ is specified by an empirical model, $s_{g,4}$ can be calculated from Eq. (10). Knowing $h_{0g,4}$ and the gas composition fixes state 4.

6 Specification of Losses

6.1 Basic (Uncooled) Loss. The *basic* rate of entropy creation is related to the uncooled stage polytropic efficiency η_{basic} (assumed known) by the expression,

$$\Delta\Sigma_{basic}=m_{g,1}R_g(1-\eta_{basic})\ln\left(\frac{p_{0g,1}}{p_{0g,4}}\right) \tag{11}$$

where p_{0g} and R_g are the mainstream total pressure and specific gas constant respectively. $\Delta\Sigma_{basic}$ is distributed between the stator and rotor in proportions deemed appropriate. It is a major assumption of the approach that $\Delta\Sigma_{basic}$ is unchanged by the presence of cooling.

6.2 Internal Friction and Heat Transfer Losses. Introducing Eq. (*A*2.1) for the heat transfer Q and assuming the coolant specific heat capacity c_{pc} to be temperature independent, Eqs. (8*e*) and (9*e*) can be written as a single equation,

$$\Delta\Sigma_{int}=m_c c_{pc}\left[\ln\left(\frac{T_{0c,x}}{T_{0c,k}}\right)-\left(\frac{T_{0c,x}-T_{0c,i}}{T_{m,int}}\right)\right]-m_c R_c\ln\left(\frac{p_{0c,x}}{p_{0c,k}}\right) \tag{12}$$

In Eq. (12), the coolant supply conditions $p_{0c,k}$ and $T_{0c,k}$ are expressed in the stationary frame of reference for both stator and rotor blade rows. For rotors, however, $T_{0c,i}$, $T_{0c,x}$ and $p_{0c,x}$, and must each be expressed in the rotating coordinate system.

There are two unknowns in Eq. (12), $\Delta\Sigma_{int}$ and $p_{0c,x}$. $\Delta\Sigma_{int}$ is the rate of entropy creation between the coolant supply and the blade exit holes, and $p_{0c,x}$ is the total pressure at these holes (absolute or relative as appropriate). One approach is to develop an expression for $\Delta\Sigma_{int}$ by modeling the friction and heat transfer losses. The internal flow is very complex, however, and it is actually easier to devise a method to specify $p_{0c,x}$. (This parallels the first law analysis in Appendix 2 where $h_{0c,x}$ was found by a suitable choice of $\eta_{c,int}$.)

Now, ignoring any streamline curvature effects, the coolant static pressure must equal the mainstream static pressure at the exit hole, $p_{c,x}=p_{g,x}$. If, in addition, some information about the coolant exit velocity is supplied, this is sufficient to fix $p_{0c,x}$. The most convenient parameter to specify is the coolant/mainstream momentum flux ratio,

$$I=\frac{\rho_{c,x}V_{c,x}^2}{\rho_{g,x}V_{g,x}^2}=\frac{\gamma_c M_{c,x}^2}{\gamma_g M_{g,x}^2} \tag{13a}$$

where V is velocity (absolute for a stator and relative for a rotor), and M is the corresponding Mach number. The coolant/mainstream total pressure ratio is then,

$$\frac{p_{0c,x}}{p_{0g,x}}=\frac{[1+0.5(\gamma_c-1)M_{c,x}^2]^{\gamma_c/(\gamma_c-1)}}{[1+0.5(\gamma_g-1)M_{g,x}^2]^{\gamma_g/(\gamma_g-1)}}=f(I,M_{g,x},\gamma_c,\gamma_g) \tag{13b}$$

$p_{0g,x}$ is approximately equal to the total pressure at blade inlet (absolute or relative as appropriate) and is therefore known. Thus, specifying I and $M_{g,x}$ allows the calculation of $p_{0c,x}$. $\Delta\Sigma_{int}$ then

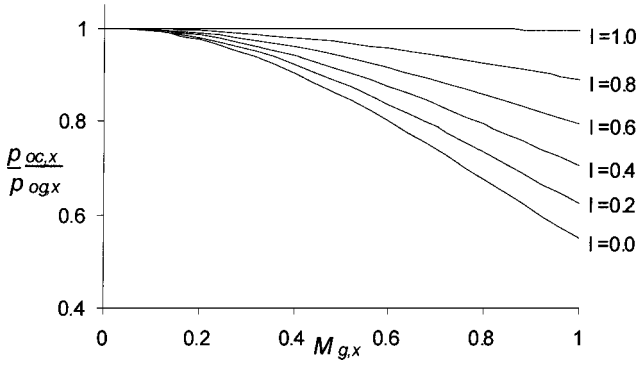

Fig. 5 Coolant/mainstream total pressure ratio as a function of mainstream Mach number and momentum flux ratio *I*

follows from Eq. (12). Figure 5 shows the variation of $p_{0c,x}/p_{0g,x}$ with mainstream Mach number $M_{g,x}$ for different values of the momentum flux ratio *I*.

This analysis shows that the internal losses are fixed by the pressure ratio $p_{0c,k}/p_{c,x}$, the coolant velocity at the exit hole and, to a lesser extent, the heat transfer to the coolant. Once these conditions are specified, no amount of redesign of the internal flow path will affect the loss. If, in practice, the exit velocity were higher than design, it would be necessary to introduce extra throttling somewhere along the flow path in order to achieve the chosen exit condition.

If desired, $\Delta\Sigma_{int}$ can (with minor approximation) be subdivided into contributions associated separately with heat transfer and fluid friction. The analysis, described in Appendix 3, is based on the one-dimensional control volume model illustrated in Fig. 6 and leads to,

$$\Delta\Sigma_{int,Q}=m_c c_{pc}\left[K_{int}\ln\left(\frac{T_{0c,x}}{T_{0c,i}}\right)-\left(\frac{T_{0c,x}-T_{0c,i}}{T_{m,int}}\right)\right] \quad (14a)$$

$$\Delta\Sigma_{int,F}=m_c c_{pc}\left[\ln\left(\frac{T_{0c,x}}{T_{0c,k}}\right)-K_{int}\ln\left(\frac{T_{0c,x}}{T_{0c,i}}\right)\right]-m_c R_c\ln\left(\frac{p_{0c,x}}{p_{0c,k}}\right) \quad (14b)$$

where K_{int} is defined by Eq. (*A*3.6). Clearly, addition of Eqs. (14*a*) and (14*b*) gives Eq. (12).

6.3 External Heat Transfer and Mixing Losses. The external losses result from: (*i*) boundary layer friction and heat transfer and, (*ii*) the mixing of the coolant with the mainstream. The friction loss is already accounted for in the basic loss of Eq. (11) and is assumed unchanged in the presence of cooling. The additional *cooling* losses are therefore the sum of the heat transfer and mixing losses,

$$\Delta\Sigma_{ext}=\Delta\Sigma_{ext,Q}+\Delta\Sigma_{mix} \quad (15)$$

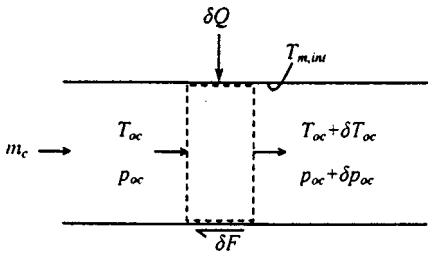

Fig. 6 Fluid friction and heat transfer in a one-dimensional flow

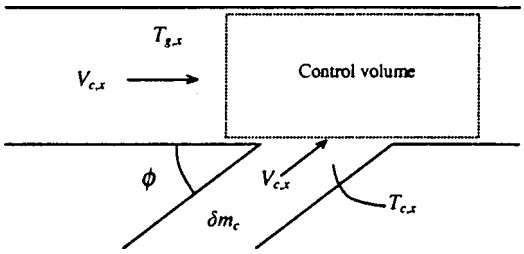

Fig. 7 Definition sketch for mixing analysis

$\Delta\Sigma_{ext,Q}$ can be estimated using the same approach as for the internal coolant flow (see Appendix 3). The resulting expression is,

$$\Delta\Sigma_{ext,Q}\cong\left(\frac{1}{T_w}-\frac{K_{ext}}{T_{0g}}\right)Q \quad (16)$$

where K_{ext} is defined by Eq. (*A*3.8).

The coolant-mainstream mixing loss is usually estimated using the method of Hartsell [7]. This is based on the Hawthorne–Shapiro theory of one-dimensional flow with mass addition and the result is usually expressed in terms of the change in mainstream total pressure. Change in p_0 is a measurable quantity but it can be misleading because, in a mixing process, it does not represent the irreversible loss. This has been the source of much confusion in the literature. In flows with mixing and heat transfer, it is important to work directly with expressions for the entropy creation rates.

The mixing process is shown in Fig. 7. It involves the injection of a differential coolant mass flowrate δm_c at *static* temperature $T_{c,x}$, velocity $V_{c,x}$, and angle ϕ, into the mainstream at local *static* temperature $T_{g,x}$ and velocity $V_{g,x}$. The differential analysis is general and is not restricted to mixing at either constant area or constant pressure. In Appendix 3 it is shown that the rate of entropy creation $\delta\Sigma_{mix}$ can be subdivided into separate contributions representing the dissipation of thermal energy and kinetic energy,

$$\delta\Sigma_{mix}=\delta\Sigma_{mix,Q}+\delta\Sigma_{mix,KE} \quad (17a)$$

$$\delta\Sigma_{mix,Q}=\delta m_c\int_{T_{c,x}}^{T_{g,x}}c_{pc}\left(\frac{1}{T}-\frac{1}{T_{g,x}}\right)dT \quad (17b)$$

$$\delta\Sigma_{mix,KE}=\delta m_c\left[\frac{(V_{g,x}-V_{c,x}\cos\phi)^2}{2T_{g,x}}+\frac{(V_{c,x}\sin\phi)^2}{2T_{g,x}}\right] \quad (17c)$$

Equation (17*b*) represents the thermal dissipation as the coolant mixes with the mainstream flow and their *static* temperatures equilibrate. Thus, $\Delta\Sigma_{mix,Q}$ multiplied by the mainstream temperature is exactly equal to the power that could theoretically be obtained from a Carnot engine coupled between the mainstream flow at constant temperature $T_{g,x}$ and the coolant, as the temperature of the latter increases from $T_{c,x}$ to $T_{g,x}$ due to the heat rejection from the engine. Equation (17*c*) represents the dissipation of bulk kinetic energy as the mainstream and coolant velocities equilibrate. The first term refers to velocity equilibration tangential to the blade surface. The second term shows that, subject to the assumptions of the theory, all the coolant kinetic energy normal to the blade surface is lost.

Following the discussion in Part I (Young and Wilcock [1]), the exergy loss arising from the diffusional mixing of the mainstream and coolant gases is ignored.

Integration of Eqs. (17*b*) and (17*c*) over the complete blade surface is difficult because of the variation of $T_{g,x}$ and $V_{g,x}$. One possible approach is described by Hartsell [7], but this requires comparatively detailed knowledge of the flow in the blade passage. If this is unavailable, it is necessary to adopt suitable average values and integrate approximately to give,

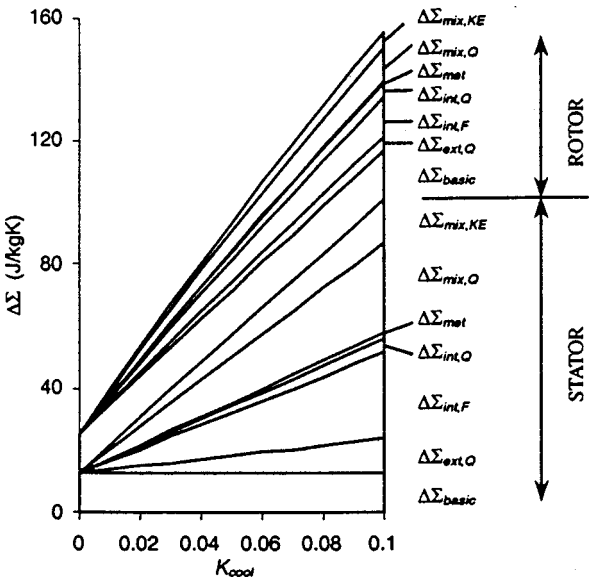

Fig. 8 Variation of cooling losses with cooling flowrate

$$\Delta\Sigma_{mix,Q} \cong m_c c_{pc}\left[\ln\left(\frac{T_{g,x}}{T_{c,x}}\right) - \left(1 - \frac{T_{c,x}}{T_{g,x}}\right)\right] \tag{18a}$$

$$\Delta\Sigma_{mix,KE} = m_c\left[\frac{(V_{g,x} - V_{c,x}\cos\phi)^2}{2T_{g,x}} + \frac{(V_{c,x}\sin\phi)^2}{2T_{g,x}}\right] \tag{18b}$$

6.4 Example: Cooling Loss Calculation. As an example, consider again the single stage turbine operating at the conditions shown in Table 1. The extra parameters required to estimate the losses were taken to be $K_{int}=1.01$, $K_{ext}=1.07$ and $\phi=30$ deg. Figure 8 shows how the stator and rotor losses vary with the cooling flow factor K_{cool} around its base value of 0.045. This corresponds to varying the coolant flowrate keeping the combustor flowrate constant. The magnitude of the cooling loss compared with the basic loss is particularly notable, indicating the possibility of improvements to cycle efficiency by careful design.

8 Conclusions

The paper has described a self-consistent approach for modeling the air-cooled gas turbine that is particularly suitable for thermodynamic cycle calculations. The procedure divides naturally into first law and second law analyses, which are almost independent. The former requires a heat transfer model to estimate the cooling flows and an extended Holland and Thake procedure is recommended. It is particularly important to acknowledge the nonuniformity of the combustor exit flow to avoid underestimating the cooling flowrates. Rotating blade rows also require careful consideration.

The second law analysis requires user-specified models for the cooling losses and it is strongly recommended that these are expressed in terms of irreversible entropy creation rates rather than loss of total pressure or modified stage efficiency. For flows with heat transfer, it is crucially important to distinguish clearly between reversible and irreversible entropy changes. Simple models have been proposed for each component of the loss and this allows the source and magnitude of the major cooling irreversibilities to be identified.

It is hoped that the analysis presented in this paper provides a firm foundation on which to proceed to improved and more accurate thermodynamic models of the air-cooled gas turbine.

Acknowledgments

The authors gratefully acknowledge numerous useful discussions with Sir John Horlock and other members of the Whittle Laboratory, Cambridge University. They are also indebted to Prof. T. V. Jones of the Osney Laboratory, Oxford University, and many members of Rolls Royce plc, particularly Mr. C. Freeman, Mr. P. Walsh, Mr. D. Watson, and Mr. B. Whinray. RCW was supported by an EPSRC studentship and Rolls-Royce CASE award.

Nomenclature

A = area
Bi = Biot number
h, i = specific enthalpy, rothalpy
m = mass flowrate
P = power
p = pressure
Q = heat transfer rate
St = Stanton number
s = specific entropy
t = thickness
T = temperature
U = blade speed
V = absolute flow velocity
α = heat transfer coefficient
ε_0 = blade cooling effectiveness
ε_f = film cooling effectiveness
η_c = internal flow cooling efficiency
λ = thermal conductivity
ψ = stage loading coefficient
$\Delta\Sigma$ = rate of entropy creation by irreversible processes

Subscripts

0 = total (as opposed to static) quantities
1, 2, 3, 4 = stator inlet, stator outlet/rotor inlet, rotor outlet, stage outlet
c, g = coolant, mainstream gas
i = coolant condition at inlet to blade passages
k = coolant condition at compressor bleed point
m = metal
w = wall (outer surface of blade)
x = coolant condition at exit from blade (before mixing)
r, s = rotor, stator (subscripts preceding c, m, w)
tbc = thermal barrier coating
* = blade throat

Appendix 1

Rotor Approximations. The Euler turbine equations are,

$$P = m_{g,2}[(UV_\theta)_{g,2} - (UV_\theta)_{g,3}] + m_{rc}[(UV_\theta)_{rc,i} - (UV_\theta)_{g,3}] \tag{A1.1a}$$

$$P_{ext} = m_{g,2}[(UV_\theta)_{g,2} - (UV_\theta)_{g,3}] + m_{rc}[(UV_\theta)_{rc,x} - (UV_\theta)_{g,3}] \tag{A1.1b}$$

$$P_{int} = m_{rc}[(UV_\theta)_{rc,i} - (UV_\theta)_{rc,x}] \tag{A1.1c}$$

where UV_θ is the massflow-averaged product of the blade speed U and the fluid absolute swirl velocity V_θ. Clearly $P = P_{ext} + P_{int}$.

Coolant Centrifuging Power Requirement. P_{int} represents the negative of the power required to increase the angular momentum of the coolant. This is *not* an irreversible power loss because, in principle, it is recoverable further downstream. P_{int} is given by Eq. (A1.1c) but the change in UV_θ of the coolant between passage inlet and outlet is unlikely to be known exactly.

It is assumed: (i) coolant enters the rotor with zero relative swirl $[(V_\theta)_{rc,i} = U_{rc,i}]$, ($ii$) the coolant relative swirl velocity at

exit from the rotor is zero $[(V_\theta)_{rc,x}=U_{rc,x}]$ and, (iii) $U_{rc,x}=U_{mean}$. Combining Eqs. (*A*1.1*c*) and (5) with a minor approximation then gives,

$$\frac{P_{int}}{P}\cong-\frac{1}{\psi}\frac{L}{R}\frac{m_{rc}}{m_{g,2}} \tag{A1.2}$$

where L/R is the ratio of blade length to mean blade radius. If $\psi=1$ and $L/R=0.2$ then $P_{int}/P\cong-0.2(m_{rc}/m_{g,2})$. Hence, for $m_{rc}/m_{g,2}=0.05$ about 1 percent of the gross power is used in centrifuging the coolant.

Coolant Centrifugal Temperature Change. Noting that $i=h_0^{rel}-U^2/2$, Eq. (4*c*) can be written,

$$-Q_r=m_{rc}\left[(h_{0rc,i}^{rel}-h_{0rc,x}^{rel})-\frac{(U_{rc,i}^2-U_{rc,x}^2)}{2}\right] \tag{A1.3}$$

The final term divided by c_{pc} represents the *centrifugal temperature change* and is typically 10–20°C. A typical value for $(T_{rc,i}-T_{rc,x})$ is 200°C. Given the approximate nature of the cooling model, it is expedient to neglect the centrifugal temperature change. Thus,

$$-Q_r\cong m_{rc}(h_{0rc,i}^{rel}-h_{0rc,x}^{rel}) \tag{A1.4}$$

Rotor Inlet Relative Total Enthalpy (Gas and Coolant). The heat transfer model requires a value of the *relative* total enthalpy of the mainstream gas at rotor inlet. This can be estimated from the stage inlet and outlet conditions and an assumed stage loading coefficient. First note that, without approximation,

$$h_{0g,2}^{rel}=h_{0g,2}+\frac{U_{mean}^2}{2}\left(1-\frac{2(V_\theta)_{g,2}}{U_{mean}}\right) \tag{A1.5}$$

where the enthalpies include the contribution from coolant injected in the stator. Assuming zero swirl at stage outlet and neglecting any cooling flow to the rotor, Eqs. (3*a*), (5), and (*A*1.1*a*) give,

$$\psi=\frac{(V_\theta)_{g,2}}{U_{mean}}=\frac{h_{0g,2}-h_{0g,3}}{U_{mean}^2} \tag{A1.6}$$

Combining Eqs. (*A*1.5) and (*A*1.6) gives the approximating expression,

$$h_{0g,2}^{rel}=\left(\frac{1}{2\psi}\right)h_{0g,2}+\left(1-\frac{1}{2\psi}\right)h_{0g,3} \tag{A1.7}$$

It is also necessary to relate the coolant relative total enthalpy at rotor inlet to the absolute value. The exact expression,

$$h_{0rc,i}-h_{0rc,i}^{rel}=(UV_\theta)_{rc,i}-\frac{U_{rc,i}^2}{2} \tag{A1.8}$$

shows that, if $(V_\theta)_{rc,i}>U_{rc,i}/2$, the relative total enthalpy of the coolant entering the rotor passage will be less than the absolute total enthalpy. From the rotor viewpoint, therefore, a considerable cooling effect is realized by a high coolant absolute swirl velocity $(V_\theta)_{rc,i}$. To this end, stationary swirl vanes are usually mounted upstream of the coolant inlet to the rotor and, in this way, it is possible to reduce the relative total temperature by as much as 100°C. For calculations, it is convenient to introduce a constant K_{swirl} (the *rotor swirl factor*) defined by $(V_\theta)_{rc,i}=K_{swirl}U_{rc,i}$. In practice, $0<K_{swirl}<2.5$. Using the definition of ψ, Eq. (*A*1.8) then becomes,

$$h_{0rc,i}-h_{0rc,i}^{rel}=\frac{(K_{swirl}-0.5)P}{\psi m_{g,3}} \tag{A1.9}$$

Appendix 2

Heat Transfer Calculations. The heat transfer rates are given by Eq. (2*c*) for stators and (*A*1.4) for rotors. Dropping the subscripts *s* and *r*,

$$Q\cong m_c c_{pc}(T_{0c,x}-T_{0c,i}) \tag{A2.1}$$

where T_{0c} denotes the coolant absolute total temperature for a stator and relative total temperature for a rotor. Calculation of $T_{0c,x}$ requires a knowledge of the mean internal heat transfer coefficient, which is difficult to predict accurately. The problem is bypassed by introducing an *internal flow cooling efficiency* $\eta_{c,int}$ defined by,

$$\eta_{c,int}=\frac{T_{0c,x}-T_{0c,i}}{T_{m,int}-T_{0c,i}} \tag{A2.2}$$

$\eta_{c,int}$ is treated as a known empirical parameter whose value (typically 0.6–0.8) reflects the level of the internal cooling technology.

In terms of the mainstream flow, Q can also be expressed by,

$$Q=\alpha_g A_{surf}(T_{aw}-T_w) \tag{A2.3}$$

where α_g is the mean external heat transfer coefficient and A_{surf} is the total cooled external surface area (including the endwalls). T_{aw} is the mean adiabatic wall temperature, which, in the absence of film cooling, equals the mainstream recovery temperature. This, in turn, is approximately equal to the inlet absolute total temperature for stators and the inlet relative total temperature for rotors, both of which will be denoted by T_{0g}. When film cooling is present, T_{aw} is related to T_{0g} and $T_{0c,x}$ by the mean *film cooling effectiveness* ε_f defined by,

$$\varepsilon_f=\frac{T_{0g}-T_{aw}}{T_{0g}-T_{0c,x}} \tag{A2.4}$$

ε_f is treated as a known empirical parameter whose value (typically 0.2–0.4) reflects the level of film cooling technology.

In terms of the heat conduction, Q can also be written,

$$Q=\frac{\lambda_{tbc}}{t_{tbc}}A_{surf}(T_w-T_{m,ext}) \tag{A2.5}$$

$$Q=\frac{\lambda_m}{t_m}A_{surf}(T_{m,ext}-T_{m,int}) \tag{A2.6}$$

where λ and t are the thermal conductivity and material thickness.

Using Eq. (*A*2.3) to eliminate Q from (*A*2.1), (*A*2.5) and (*A*2.6) gives equations for m_{c+} a dimensionless coolant mass flowrate, Bi_{tbc} a TBC Biot number, and Bi_m a metal Biot number:

$$m_{c+}=\frac{m_c c_{pc}}{\alpha_g A_{surf}}=\frac{T_{aw}-T_w}{T_{0c,x}-T_{0c,i}} \tag{A2.7}$$

$$\mathrm{Bi}_{tbc}=\frac{\alpha_g t_{tbc}}{\lambda_{tbc}}=\frac{T_w-T_{m,ext}}{T_{aw}-T_w} \tag{A2.8}$$

$$\mathrm{Bi}_m=\frac{\alpha_g t_m}{\lambda_m}=\frac{T_{m,ext}-T_{m,int}}{T_{aw}-T_w} \tag{A2.9}$$

Finally, the *blade cooling effectiveness* ε_0 is defined by,

$$\varepsilon_0=\frac{T_{0g}-T_{m,ext}}{T_{0g}-T_{0c,i}} \tag{A2.10}$$

ε_0 is fixed by the inlet total temperatures of the mainstream gas and coolant, and the desired external metal temperature.

Elimination of all temperature differences between Eqs. (*A*2.2), (*A*2.4) and (*A*2.7)–(*A*2.9) results in the following expression for m_{c+},

$$(1+\mathrm{Bi}_{tbc})m_{c+}=\frac{\varepsilon_0}{\eta_{c,ext}(1-\varepsilon_0)}-\varepsilon_f\left[\frac{1}{\eta_{c,ext}(1-\varepsilon_0)}-1\right] \tag{A2.11a}$$

where $\eta_{c,ext}$ is a cooling efficiency defined in terms of the external, rather than the internal, metal temperature,

$$\eta_{c,ext}=\frac{T_{0c,x}-T_{0c,i}}{T_{m,ext}-T_{0c,i}}=\frac{\eta_{c,int}}{1+m_{c+}\eta_{c,int}\mathrm{Bi}_m} \tag{A2.11b}$$

The first term of Eq. (*A*2.11*a*) gives the value of m_{c+} when internal convection is the only cooling mechanism. The second term gives the reduction when film cooling is also used. When a thermal barrier coating is present, m_{c+} is reduced by the factor $(1+\mathrm{Bi}_{tbc})$. Clearly m_{c+} can be determined once ε_0, $\eta_{c,int}$, ε_f, Bi_m, and Bi_{tbc} have been specified.

m_{c+} is now related to the actual coolant/mainstream mass flow ratio. Neglecting the coolant injected upstream of the throat,

$$m_g\cong\rho_{g*}V_{g*}A_{g*} \tag{A2.12}$$

where ρ_{g*}, V_{g*} and A_{g*} are the gas density, velocity, and flow cross-sectional area at the blade throat. Introducing Eq. (*A*2.7) gives,

$$\frac{m_c}{m_g}=\frac{A_{surf}}{A_{g*}}\frac{c_{pg}}{c_{pc}}\mathrm{St}_g m_{c+}=K_{cool}m_{c+} \tag{A2.13}$$

where $\mathrm{St}_g=\alpha_g/c_{pg}\rho_{g*}V_{g*}$ is a Stanton number based on the mean external heat transfer coefficient and the flow properties at the throat. Either α_g or St_g must be estimated from a suitable correlation. The *cooling flow factor* K_{cool} is defined by Eq. (*A*2.13).

Appendix 3

Entropy Creation

Internal Heat Transfer and Friction Losses. Figure 6 shows an idealized onedimensional coolant flow. The momentum, energy, and second law equations are,

$$m_c\left(\frac{\delta p_c}{\rho_c}+V_c\delta V_c\right)=-V_c\delta F \tag{A3.1a}$$

$$m_c(\delta h_c+V_c\delta V_c)=\delta Q \tag{A3.1b}$$

$$\delta\Sigma_{int}=m_c\delta s_c-\frac{\delta Q}{T_{m,int}} \tag{A3.1c}$$

Combining Eqs. (*A*3.1) and using $T_c\delta s_c=\delta h_c-\delta p_c/\rho_c$ gives,

$$\delta\Sigma_{int}=\left(\frac{1}{T_c}-\frac{1}{T_{m,int}}\right)\delta Q+\frac{V_c}{T_c}\delta F=\delta\Sigma_{int,Q}+\delta\Sigma_{int,F} \tag{A3.2}$$

This shows how $\delta\Sigma_{int}$ can be divided into two entropy creation terms, one associated with heat transfer and the other with fluid friction. Expressing δs_c in terms of changes in total temperature and pressure,

$$\delta s_c=c_{pc}\frac{\delta T_{0c}}{T_{0c}}-R_c\frac{\delta p_{0c}}{p_{0c}} \tag{A3.3}$$

and noting that $\delta Q=m_c c_{pc}\delta T_{0c}$, Eq. (*A*3.1*c*) can be written,

$$\delta\Sigma_{int}=\left(\frac{1}{T_{0c}}-\frac{1}{T_{m,int}}\right)m_c c_{pc}\delta T_{0c}-m_c R_c\frac{\delta p_{0c}}{p_{0c}} \tag{A3.4}$$

Taken together, Eqs. (*A*3.2) and (*A*3.4) give,

$$\delta\Sigma_{int,Q}=\left(\frac{1}{T_c}-\frac{1}{T_{m,int}}\right)\delta Q=\left(\frac{1}{T_c}-\frac{1}{T_{m,int}}\right)m_c c_{pc}\delta T_{0c} \tag{A3.5a}$$

$$\delta\Sigma_{int,F}=\frac{V_c}{T_c}\delta F=\left(\frac{1}{T_{0c}}-\frac{1}{T_c}\right)m_c c_{pc}\delta T_{0c}-m_c R_c\frac{\delta p_{0c}}{p_{0c}} \tag{A3.5b}$$

where R_c is the specific gas constant and T_c is the *static* temperature. Equations (*A*3.5) cannot be integrated analytically. One approximate method of attack is to write,

$$\frac{1}{T_c}=\left(1+\frac{\gamma_c-1}{2}M_c^2\right)\frac{1}{T_{0c}}=K_{int}\frac{1}{T_{0c}} \tag{A3.6}$$

and assume a constant mean value for the coolant Mach number M_c. Integration of Eqs. (*A*3.5) then gives Eqs. (14).

External Heat Transfer Loss. Rewriting Eq. (*A*3.5*a*) for the external flow,

$$\delta\Sigma_{ext,Q}\cong\left(\frac{1}{T_w}-\frac{1}{T_g}\right)\delta Q \tag{A3.7}$$

where T_g is the mainstream *static* temperature and δQ is the heat transfer to the blade. The variation of T_g is accommodated by writing,

$$\frac{1}{T_g}=\left(1+\frac{\gamma_g-1}{2}M_g^2\right)\frac{1}{T_{0g}}=K_{ext}\frac{1}{T_{0g}} \tag{A3.8}$$

and then assuming a constant mean value for the mainstream Mach number M_g. Integration of Eq. (*A*3.7) leads to Eq. (16).

External Mixing Process. The momentum and energy equations written for the control volume of Fig. 7 are (dropping the subscript *x*),

$$m_g\left(\frac{\delta p_g}{\rho_g}+V_g\delta V_g\right)+\delta m_c V_g(V_g-V_c\cos\phi)=0 \tag{A3.9a}$$

$$m_g(\delta h_g+V_g\delta V_g)+\delta m_c\left\{h_c(T_g)-h_c(T_c)+\frac{(V_g^2-V_c^2)}{2}\right\}=0 \tag{A3.9b}$$

The second law of thermodynamics is,

$$\delta\Sigma_{mix}=m_g\delta s_g+\delta m_c[s_c(T_g,p_g)-s_c(T_c,p_g)] \tag{A3.9c}$$

Combining Eqs. (*A*3.9) and using $T_g\delta s_g=\delta h_g-\delta p_g/\rho_g$ gives,

$$\delta\Sigma_{mix}=\delta m_c\left\{s_c(T_g,p_g)-s_c(T_c,p_g)-\frac{h_c(T_g)-h_c(T_c)}{T_g}\right\}+\delta m_c\left\{\frac{(V_g-V_c\cos\phi)^2}{2T_g}+\frac{(V_c\sin\phi)^2}{2T_g}\right\} \tag{A3.10}$$

For an ideal gas, Eq. (*A*3.10) is equivalent to Eq. (17).

References

[1] Young, J. B., and Wilcock, R. C., 2001, "Modelling the Air-Cooled Gas Turbine: Part I—General Thermodynamics," ASME J. Turbomach., this issue, **124**, pp. 207–213.

[2] Holland, M. J., and Thake, T. F., 1980, "Rotor Blade Cooling in High Pressure Turbines," J. Aircr., **17**, pp. 412–418.

[3] Horlock, J. H., 1966, *Axial Flow Turbines*, Chap. 8.3.

[4] El-Masri, M. A., 1986, "Prediction of Cooling Flow Requirements for Advanced Utility Gas Turbines: Part I: Analysis and Scaling of the Effectiveness Curve; Part II: Influence of Ceramic Thermal Barrier Coatings," ASME Papers No. 86-WA/HT-43 and 86-WA/HT-44.

[5] El-Masri, M. A., 1986, "On Thermodynamics of Gas Turbine Cycles: Part II—A Model for Expansion in Cooled Turbines," ASME J. Eng. Gas Turbines Power, **108**, pp. 151–159.

[6] Kawaike, K., Kobayishi, N., and Ikeguchi, T., 1984, "Effect of Blade Cooling System With Minimized Gas Temperature Dilution on Gas Turbine Performance," ASME J. Eng. Gas Turbines Power, **106**, pp. 766–764.

[7] Hartsell, J. E., 1972, "Prediction of Effects of Mass-Transfer Cooling on the Blade-Row Efficiency of Turbine Airfoils," AIAA 10th Aerospace Sciences Meeting, San Diego, Paper No. AIAA-72-11.

Discussion: "Modeling the Air-Cooled Gas Turbine" (Young, J. B., and Wilcock, R. C., 2002, ASME J. Turbomach., 124, No. 2, pp. 207–221)

J. H. Horlock
e-mail: j.h.horlock@talk21.com

The authors are to be commended for adding considerably to our understanding of the fluid mechanics and thermodynamics of turbine cooling.

I would pick out the following major contributions in the papers.

1 The breakdown of the entropy increases [or "irreversibilities" $\Sigma T_0 \Delta S$] is particularly enlightening. However, I would argue that an approach using Shapiro's influence coefficients (plus an important rider he gives in an additional equation for total entropy change) is not inconsistent with the approach in the papers—indeed the identity of the two may be shown formally. Shapiro/Hartsel determine T_0 and p_0 as the properties required to define the exit state. This is equivalent to the Young/Wilcock approach of finding T_0 from the steady flow energy equation and S at exit from the expressions for entropy change.

2 The Y/W concept of neglecting S_{mix} entirely throughout the cycle calculations is an invaluable generalization of the result of Horlock et al. [1]. They showed that the so-called "work of extraction and delivery" [WED], which appears in addition to $[-\Delta G_0]$ in the expression for fuel exergy, is equal to the sum of the changes in the entropy "partial pressure" terms arising (a) in the combustion process, and (b) in the discharge of the exhaust gases to atmosphere. Indeed, the HMY analysis may be formally extended to include turbine cooling effects, to fully justify the Y/W generalization. This reinforces the case for the "Haywood" expression for efficiency advocated by the authors.

3 The illustration in Fig. 6 of Paper 1, showing that a mixed expansion gives greater turbine work than parallel unmixed expansions, is also important. Note that it is true for real gas and air expansions but not for isentropic expansions of mainstream air and cooling air as in an air/standard analysis; Denton (see Horlock [2]). This result means that real gas effects in cycle calculations will become important as the maximum temperature is increased [and the air-fuel ratio is decreased]; the c_p and γ of the turbine gases then become considerably different from those of air. This has an effect on the optimum combustion temperature for maximum plant efficiency [see [3]] and will be the subject of a detailed future paper with the authors.

References

[1] Horlock, J. H., Manfrida, G., and Young, J. B., 2000, "Exergy Analysis of Modern Fossil-Fuel Power Plants," ASME J. Eng. Gas Turbines Power, **122**, pp. 1–17.
[2] Horlock, J. H., 2001, "Basic Thermodynamics of Turbine Cooling," ASME J. Turbomach., **123**, pp. 583–592.
[3] Horlock, J. H., Watson, D. T., and Jones, T. V., 2001, "Limitations on Gas Turbine Performance Imposed by Large Turbine Cooling Flows (ASME Paper 2000-GT-695)," ASME J. Eng. Gas Turbines Power, **123**, pp. 487–494.

Turbine Engine Performance Improvements—A Proactive Approach

Zane D. Gastineau
US Air Force,
AFRL/PRTA,
Wright-Patterson AFB, OH 45433-7251
e-mail: zane.gastineau@wpafb.af.mil

Turbine engine concepts for the future are placing ever increasing demands on the design engineer. These future systems are seeking to increase performance while at the same time reduce costs. However, traditional engine design methods use large margins in the design process of a specific component in order to guarantee proper operation throughout the flight envelope over the life of the engine. These margins in fact reduce engine performance and increase the costs. In this paper, active control will be presented as one potential means of achieving the requirements for future turbine engines. In addition, specific active control applications will be discussed. [DOI: 10.1115/1.1452246]

Introduction

The Controls and Accessories (C&A) group of the Air Force Research Laboratory (AFRL), Propulsion Directorate, Turbine Engine Division is an identified component area under the Integrated High Performance Turbine Engine Technology (IHPTET) program [1]. The goals of IHPTET have been defined to provide a doubling of propulsion capability over an established baseline. As such the objectives of the C&A group were defined to support the overall IHPTET goals and provide quantitative figures of merit for improvement. Because the C&A contribute significantly to the weight and costs of modern turbofan engines, weight reduction, production and maintenance cost reduction and margin reduction have been identified as component area objectives.

Engine company plans and government environmental requirements necessitate that tomorrow's advanced aircraft engines provide ultralow emissions and high efficiency at low cost, while maintaining current levels of reliability and operability. In terms of the turbine engine control system, the objective is to provide reliable and consistent operation throughout the flight envelope while not allowing the engine to damage itself. This is anticipated to continue to be the overall control system objective into the future. However, reliable and consistent control is becoming more difficult to achieve due to the additional demands that are placed on the propulsion system. It is clear from a comparison of Figs. 1 and 2 that the number of inputs and outputs on a typical turbine engine is growing. This suggests that the role the engine control system will play in the future is more demanding. In fact, the control system will be much more than a propulsion control, but will be an onboard management system balancing the propulsion control requirements, power distribution and management requirements and the health management system. This will require the marriage of many research disciplines in order to effectively build and demonstrate this new type of system as shown in Fig. 3.

Turbine engine component designs have historically incorporated large safety margins to account for uncertainties due to manufacturing tolerances, deterioration in service and variations in operation caused by sensing errors. These margins add weight, cost and reduce aerodynamic performance when added to a component. Now in order to further improve engine performance, these component margins are coming under increased scrutiny. However, when the margins are reduced, the risk of inducing both mechanical and flow instabilities increase. These instabilities are characterized by increased engine vibration or by rapid, unsteady fluctuations in velocity, temperature, and pressure in the flow. They disrupt surrounding flow fields and cause severe stress on engine components degrading engine performance. An approach to safely reduce these margins is using active control.

The paper is organized in the following manner. First, a discussion of what active control is and why it is important is given. Two active control technologies will then be described. This will be followed by a discussion on hardware and software implications for the turbine engine. The last section will discuss future directions for active control within the US Air Force.

Active Control

The traditional engine design process is based on a philosophy that each component can be designed and built independently and then brought back together to meet overall system functional requirements. Following this approach, the individual component designs are well established and possibly being built before the control system is ever considered, thus eliminating any benefit control system tailoring can offer to the component design. By considering active control methods early in the design process, turbine engine designs can capitalize on potential margin reductions that the control can offer.

Active control as used herein refers to dedicated feedback control loops around individual turbine engine modules (component) so that its performance (by some measure) can be optimized. This definition permits one to characterize the optimal performance of a component given its actual operating condition thereby minimizing off design losses. However, this will require closer coordination between the component and control system designers. Below is a brief description of active control technologies that are currently receiving a lot of attention by both university and government researchers.

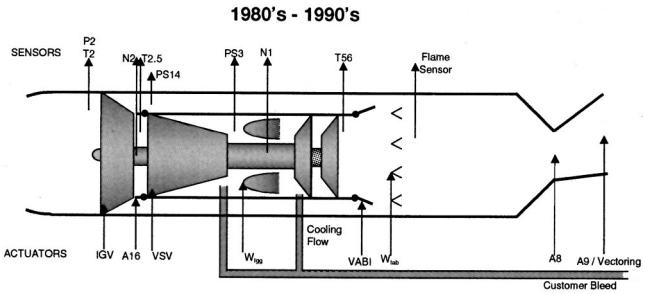

Fig. 1 Current control technology level

Contributed by the International Gas Turbine Institute and presented at the International Gas Turbine and Aeroengine Congress and Exhibition, New Orleans, Louisiana, June 4–7 2001. Manuscript received by the IGTI, January 3, 2001. Paper No. 2001-GT-371. Review Chair: R. Natole.

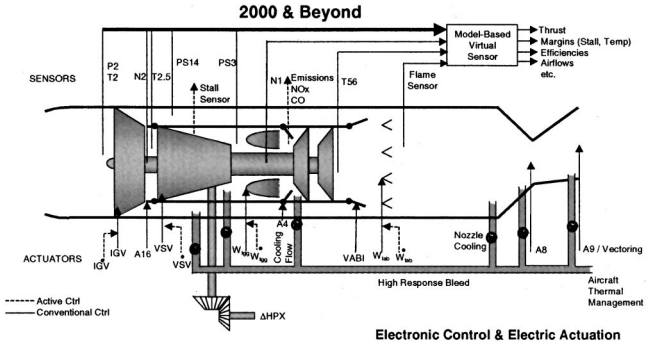

Fig. 2 Future control technology level

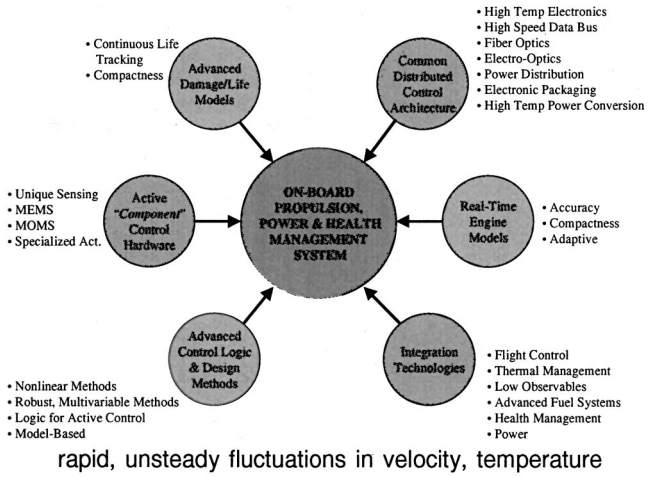

Fig. 3 Future control emphasis areas

Active Stability Control

Aircraft turbine engines operate in regimes limited by both rotating stall and surge. A good control design would allow operation close to compressor stability limits while preventing rotating stall and surge. The past decade has seen considerable research in the control of compressor stability. The interest in this area was initiated by the development of low-order nonlinear state-space model by Moore and Greitzer [2] and captures the nonlinear dynamics of the compression system through a bifurcation characteristic. Then, Nett and his group [3] showed that the control of rotating stall and surge using bifurcation theory developed by Abed et al. [4,5] was effective for implementation on industrial turbomachinery. A good overview of active stability control (ASC) work is given by Gu et al. [6]. Much of this work is based upon assumptions using low-speed compression systems and in many cases was successfully demonstrated on low-speed rigs. Although that is encouraging, questions still remained as to the relevance of the low-speed work to high speed compression systems. Other practical issued also remained, such as sensor locations, actuation capability, and reliability and system cost and weight. In order to address these concerns, the Air Force contracted with industry to investigate and determine the feasibility of ASC for large engine applications and accelerate the maturation of the most promising concepts [7].

In terms of the IHPTET program ASC is projected to have the benefits summarized in Table 1 [7]. To achieve stall-free operation in conventional engine systems, compressor designs require that stall pressure ratio capability exceed the steady-state and transient requirements by 10–30 percent as shown in Fig. 4. To achieve this extra capability extra stages of compression must be added to the compressor this increases weight and costs while adversely impacting the aerodynamic performance. Active stability control has the potential to reduce the required number of stages of compression, thereby reducing weight and costs.

Table 1 Projected active stability control benefits

IHPTET Metric	% Improvement
Thrust-to-Weight	2.0
Fuel Burn	1.5
Production Cost	0.5
Acquisition Cost	3.15
Operating Cost	1.0

One of the control objectives under the IHPTET program is 50 percent margin reduction. This margin refers to the excess stall pressure ratio that is used in every conventional compressor design. The excess stall pressure ratio consists of a stack-up of worst case effects due to transients, distortion, clearance, deterioration, variability and random effects. Through a combination of active stability control and stability management control, along with aerodynamic and mechanical design improvements, the overall required margin can be reduced by more than 50 percent, Fig. 5. Active stability control concepts provide operation at or beyond conventional stability limits and can be used to eliminate variability and random effects from the stack-ups. Stability management control refers to the direct control of the operating line and permits the reduction in the amount of margin carried for transient and distortion. Finally, elements of the stack-up associated with

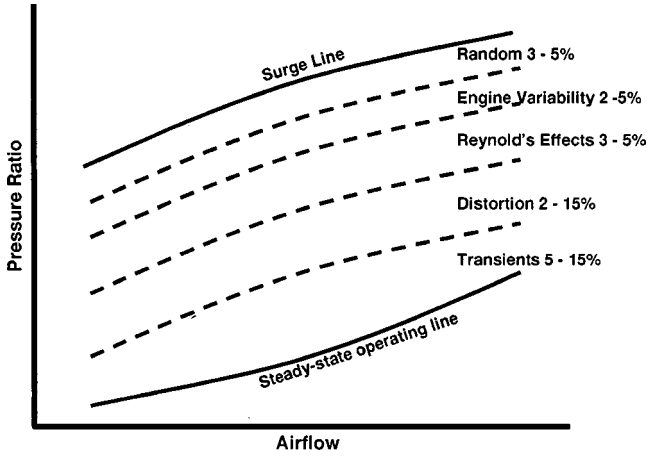

Fig. 4 Stability audit

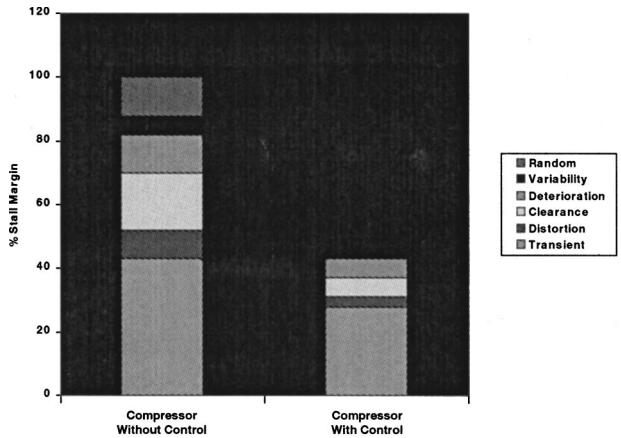

Fig. 5 Stability stackup

clearance and distortion can be reduced through improved mechanical and aerodynamic design. It is important to note that benefits due to other technologies such as an active clearance control system have not been considered here.

This demonstration of active stability control on an aircraft gas turbine engine requires the development of some key technologies. first the development of a flightweight, durable actuation system with adequate bandwidth to provide robust control is needed. Second, an appropriate sensing system needs to be defined, developed, and demonstrated. Third, the development and demonstration of control algorithms that are easy to integrate and adaptive to the changing operating conditions. Fourth, a multiprocessing capability is needed to account for the smaller execution time required for active control versus the main control laws. While progress is being made with the development of ASC algorithms, the need for flight-worthy hardware must be given more attention.

Active Combustion Control

Future advanced engines will require precise, reliable fuel control technologies in order to improve performance and operability. In terms of engine combustion systems, precision control and manipulation of fuel delivery will be needed to provide a smart, adaptive means to manage heat release, mixing, exit temperatures, and emissions. Several approaches have been investigated for active control of combustion instabilities [8]. Active control of combustion instabilities is a relatively new field, established to find solutions to the combustion stability problem in advanced propulsion systems. One of the first realizations was the need for a model capable of simulating the performance of the actively controlled system that could be used to guide the combustor design process [9].

Industry experience indicates that the operability, robustness and durability of high-performance combustion systems can be severely compromised by combustion instabilities leading to high development, operational, and maintenance costs. To eliminate or reduce the problems associated with these instabilities, current combustion system designers attempt to use passive techniques such as modifying the combustion process (increase pressure drop across fuel nozzles) in such a way as to reduce the forcing of the instability, increase the acoustic damping within the system, or modification of the combustor geometry to prevent excitation of unstable modes. These passive solutions generally require considerable investment of time and resources to produce solutions that are limited to a specific system or limited operating range. These limitations have stimulated research in active combustion control for large ranges of applicability and operating conditions. Research activities over the past decade have shown that actively controlled fuel modulation can significantly reduce and sometimes eliminate instabilities in laboratory combustors. Active combustion control in the literature has focused predominantly on the thermoacoustic instability due to the coupling between the heat release and acoustic behavior of the combustor. However, the control of the combustion process covers also pattern factor control (exit plane temperature profile) as well as emissions (NO_x/CO/UHC).

The demonstration of active combustion control on an aircraft gas turbine engine requires the development of three key technology areas as well as focused research in combustion. First, the development and demonstration of a flightweight, durable actuation system with adequate bandwidth to provide robust control is needed. Second, an appropriate sensing system needs to be defined, developed, and demonstrated. Third, the development and demonstration of control algorithms that are easy to integrate and adaptive to changing operating conditions. Fourth, the development of comprehensive dynamic combustion models is necessary to facilitate the control system design. Finally, multiprocessing capabilities must be developed to handle the significantly smaller execution time for active combustion control than what is required for the main control law. The development of these models is clearly on of the areas that needs the most attention due to the lack of understanding of the combustion process.

General Observations

Active control tends to focus on individual components, though system benefits are usually realized. This implies that system level improvements need to be recognized and become an integral part of future research goals. These benefits are usually due to margin reduction for a given component. While in some cases benefits can be realized for retrofit systems, the largest benefits are realized when active controls are designed into new-centerline engines.

In order to implement an active control system, multiple sensors and actuators will often be required. The sensors must survive in high-temperature environments and the actuators must have high response. In addition, the wiring of individual sensors and actuators to the control box may be impractical requiring the development of some level of smart actuators and sensors for implementation in a distributed control architecture.

Finally, active controls can compensate for errors or omissions in the design of the engine. They can also compensate for problems that occur due to in service degradation. To accomplish this, active controls often deal with parameters which are of diagnostic interest. Which facilitates the whole concept of managing the health of engine.

Summary

There are a number of technical challenges that must be met in order for active control to become a reality for aircraft turbine engines. The development of sensors that can survive in harsh environments. Highly distributed actuators employing microvalving may be needed for some applications. As well as high response actuators to suppress instabilities. Accurate physics-based models that capture the dynamics of interest are required to guide both the development of passive and active instability suppression methods. Simplified dynamic models are needed to provide or enhance the capability of the component under active control while maintaining full-envelope stability and operability margins.

It is clear that the implementation of active control approaches on an aircraft gas turbine engine is predominantly limited by the availability of high bandwidth actuators and high temperature sensors. Additional active-control areas are also limited by the lack of understanding of the physical phenomenon that is of interest. Currently, there is work being pursued to address the hardware limitations that exist. However, no design has been shown to be compact, lightweight, and reliable enough for aircraft engine applications. Therefore, the best place for demonstration of active control technologies will be on ground-based aero-derivative engines used for power generation or onboard turbine-powered ships.

Nomenclature

AFRL = Air Force Research Laboratory
A_8 = nozzle throat area, sq. in.
ACC = active combustion control
ASC = active stability control
C&A = controls and accessories
CO = carbon monoxide
HPX = horse power extraction
IGV = inlet guide vane
IHPTET = integrated high-performance turbine engine technology
N1 = compressor rotor speed, rpm
N2 = fan rotor speed, rpm
NO_x = nitrous oxide
P2 = fan rotor inlet pressure, psia
PS3 = static pressure at compressor discharge, psia

T56 = temperature at low-pressure turbine exit, R
UHC = unburned hydrocarbons
VSV = variable stator vane
w_f = fuel flow, lb/h

References

[1] Gastineau, Z. D., 2000, ''High Temperature Smart Actuator Development for Aircraft Turbine Engines,'' Proc. 5th International High Temperature Electronics Conference, Albuquerque, NM.

[2] Moore, F. K., and Greitzer, E. M., 1986, ''A Theory of Poststall Transients in Axial Compressors—Part I: Development of Equations,'' ASME J. Eng. Gas Turbines Power **108**, pp. 68–76.

[3] Evekar, K. M., Gysling, D. L., Nett, C.N., and Sharma, O. P., 1995, ''Integrated Control of Rotating Stall and Surge in Aeroengines,'' SPIE **2494**, pp. 21–34.

[4] Adomaitis, R. A., and Abed, E. H., 1992, ''Bifurcation Analysis of Nonuniform Flow Patterns in Axial-Flow Gas Compressors,'' 1st World Congress on Nonlinear Analysis.

[5] Abed, E. H., Houpt, P. K., and Hosny, W. M., 1993, ''Bifurcation Analysis of Surge and Rotating Stall in Axial Flow Compressors,'' ASME J. Turbomach. **115**, pp. 817–824.

[6] Gu, G., Sparks, A., and Banda, S. S., 1999, ''An Overview of Rotating Stall and Surge Control for Axial Flow Compressors,'' IEEE Trans. Control Syst. Technol. **7**, No. 6, pp. 639–647.

[7] Gallops, G. W., Thomsen, C. J., Darden, L. A., Tempelman, W. G., and Hill, B. H., 1999, ''Active Stability Control Program,'' AFRL-PR-WP-TR-1999-2043.

[8] Mcmanus, K. R., Poinsot, T., and Candel, S. M., 1993, ''A Review of Active Control of Combustion Instabilities,'' Prog. Energy Combust. Sci. **19**, No. 1, pp. 1–29.

[9] Mohanraj, R., Neumeier, Y., Zinn, B. T., 1997, ''A Combustor Model for Control Oriented Simulation of Combustion Instabilities,'' 35th Aerospace Sciences Meeting and Exhibit, Reno, NV, AIAA-97-0466.

A Review of Purge Air Designs for Aeroengine-Based Optical Pyrometers

Clive I. Kerr
e-mail: c.i.v.kerr.1998@cranfield.ac.uk

Paul C. Ivey

School of Mechanical Engineering,
Cranfield University,
Cranfield MK43 0AL, United Kingdom

With the advent of "power by the hour" type agreements within the civil aeroengine market, the application of engine monitoring system data has reached the level of strategic use for informed decision making in not only the aftermarket but increasingly in the contract negotiation stage. One of the key cost drivers in these dollar-per-hour contracts for the OEMs to analyze is the life and maintenance requirements of the turbine blades leading ultimately to blade life management. Such life management of key components is of critical importance to ensure that the economic and technical risks to both service provider and customer are minimized. The optical pyrometer, through providing a direct temperature measurement of the turbine blades, is a primary input for providing a more realistic assessment of the component's operating history associated with the use of life usage/remaining algorithms. However, the greatest concern with the in-service use of pyrometry is the issue of fouling since the pyrometer's lens is exposed to the turbine environment. The level of optical contamination is usually minimized by introducing purge air, bled from the compressor, down the sight tube to prevent both the build-up of contaminants on the exposed system optics and particles in the gas stream from coming in contact with the lens. This paper provides a review of purge air designs and the key methodologies for engine designers to be acquainted with when seeking to integrate the use of optical pyrometry systems in new engine concepts. [DOI: 10.1115/1.1458578]

Introduction

Optical pyrometers as used on gas turbine aeroengines conventionally have their sight tube assemblies mounted to project through to the turbine chamber in order to view the turbine blades. This therefore means that the pyrometer is open to the particle-laden gas stream of the turbine. In general a pyrometer has only one optical surface, namely the lens, exposed to this harsh environment and since the lens acts as the interface between the interior of the instrument and the exterior environment, particulates such as soot and sand can deposit on the lens acting as an interference filter by absorbing some of the thermal radiation from the blades. This will result in an output signal that is representative of a lower temperature than the actual blade temperature due to the measurement error introduced by the optical fouling. It is acknowledged that the optical contamination of the lens is the major source of error in the use of pyrometry temperature measurement in gas turbines; the other prime contributing factor being inaccurate evaluation of the target emissivity [1].

In controlling applications, fouling of the lens would permit higher turbine temperature operation resulting in blade temperatures in excess of their intended limits and thus shortening blade life. It is therefore essential to keep the pyrometer lens clean and so prevent contamination. This is accomplished by introducing purge air, bled from the compressor, down the sight tube to prevent any contaminants from depositing on the lens surface. According to Sellers et al. [2], the purge air arrangement is probably the most critical aspect of the pyrometer system for use in engine control with the success of the system being driven by the cleanliness of the lens' surface. Kirby [3] further reinforced this point by stating "lens contamination is of crucial importance since it constitutes a fail-dangerous error mode (erroneous low reading)." Furthermore, the frequency of cleaning the pyrometer will have direct impact on the level of engine maintenance through to on-wing and aircraft turnaround times.

Thus, the exposed lens surface of a pyrometer system must be maintained free from deposits if accurate temperature readings are to be maintained and the provision of a purge air system attempts to ensure this likelihood. However, it is not possible to completely eliminate fouling, nor may it ever be, since there will always be a degree of deposition and the resultant changes in lens transmission caused by the contamination will alter the pyrometer calibration, thus limiting the length of time for which the pyrometer can be used without maintenance or recalibration [4]. It must also be stressed that it is not just a simple matter of cleaning the lens during maintenance since the present purge designs can only satisfy the military requirements of a few hundred hours, which is completely unacceptable in the civil market where thousands of hours are required.

To further complicate the situation, each pyrometry application is different due to the function the pyrometer should undertake, the engine type and envelope size, so requiring a different approach to installation. Hence, a purge air system must be adapted for the given engine geometry being penetrated resulting in the specific design being initially studied for each installation. Atkinson and Guenard [5] even described the design of a purge system as "somewhat of a black art requiring a trial and error process to develop a system that works for a particular engine installation." One of the most critical aspects of developing a purge design is the imposed space restriction, dictated by envelope size, which can compromise the purge geometry, and hence its effectiveness.

Generic Purge Configurations

An optical pyrometer is generally cylindrically shaped and mounted in the gas turbine with its forward end projecting through an aperture in the engine casing. Barber [6] was the first to note that particulate deposition on the lens would be the "most likely source of trouble in operation," and it would therefore be necessary to purge the sight tube assembly with a comparatively clean airflow to both prevent the penetration of particles in the turbine

Contributed by the International Gas Turbine Institute and presented at the International Gas Turbine and Aeroengine Congress and Exhibition, New Orleans, Louisiana, June 4–7, 2001. Manuscript received by the IGTI, October 12, 2000. Paper No. 2001-GT-580. Review Chair: R. A. Natole.

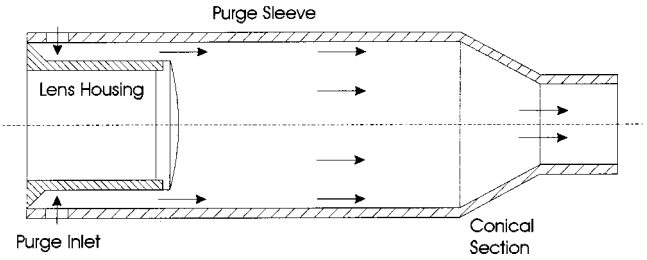

Fig. 1 Fundamental purge design

gas stream and any recirculation. The essence of the purge air system is to maintain a positive pressure flow through the sight tube to prevent combustion gases with suspended particles from entering the pyrometer and contaminating the lens.

The most fundamental purge design is to flow air, at right angle to the plane of the lens, down an elongated cylindrical tube in front of the lens housing—specifically, a tubular passageway having an open front end. The drag of the out-flowing purge air serves to stop most particles from flowing up through the sight aperture and contacting the lens. In general, the sight tube assembly consists of the lens housing, basically a tube that holds the lens in position, and a purge sleeve, which is another tube that fits in front of the lens housing and has a number of purge inlets for the tangential introduction of the purge air as illustrated in Fig. 1.

It should be noted that the purge inlets can be of any desired number sufficient to provide an adequate volume of purge flow and are generally circular in shape. The purge sleeve consists of both cylindrical and conical sections that define a funnel-shape. The resulting converging profile of the purge sleeve means that it functions as a nozzle so that the velocity of the purge airflow increases through the conical section in order to minimize any backflow within the sight tube that would otherwise draw particles in from the turbine chamber.

Air Scrubbing. The air scrubbing approach utilizes the layer attachment or Coanda effect whereby the purge airflow is directed over the lens surface so as to form a barrier to prevent any particulates penetrating the sight tube from coming into contact with the lens. As the purge air flows over the lens it tends to scrub across its surface and any particles on the lens will be re-entrained (Fig. 2). The purge must be controlled so as to maintain an adequate flow velocity to insure that any particles that are removed from the lens remain entrained and are carried outwardly away from the optics. An important advantage of this generic configuration is that the scrubbing action permits the removal of ignition phase deposits that may form during engine start-up [7]. Also, any particles that deposit as the aeroengine shuts down, due to gravitational settling for example, are then removed when the purge system begins to operate with engine start-up.

However, Hayden et al. [8] acknowledged two principal disadvantages with the scrubbing approach; firstly any particles in the purge air itself are brought to the lens thus increasing the likelihood of deposition. Secondly, although the scrubbing action can remove large particles the technique experiences difficulty in removing submicron particles or large sticky particles already deposited.

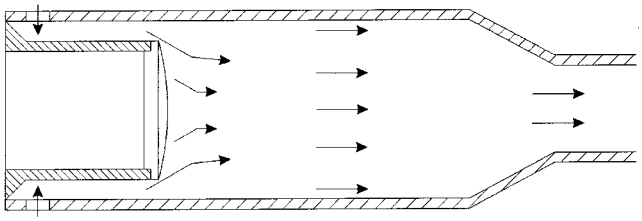

Fig. 2 Air scrubbing configuration

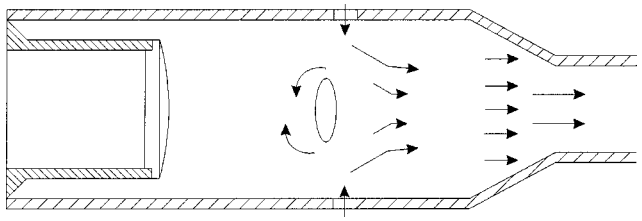

Fig. 3 Air curtain configuration

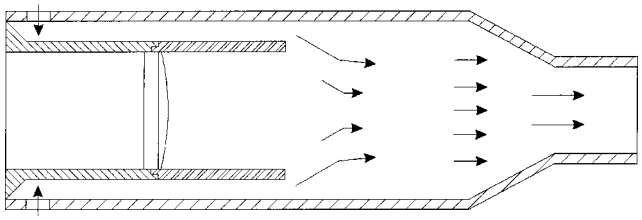

Fig. 4 Still tube configuration

Air Curtain. The second generic configuration is the air curtain approach where the design concept is to provide an airflow in front of the lens so establishing a barrier that prevents any contaminants from entering the sight tube, but unlike the air scrubbing system the purge air does not contact the lens. The air curtain can be formed either through purge inlets positioned forward of the lens, as shown in Fig. 3, or with the addition of a still tube extension in front of the lens (Fig. 4). The principal advantage of this type of system is the reduced probability of the lens being contaminated by any particles in the purge air itself since the airflow does not make direct contact with the lens. Although, two disadvantages do emerge from this approach, namely particles may become trapped and then accumulate in the dead air zone between the lens and air curtain [8]. Secondly, there is no mechanism for removing any particles that may settle on the surface of the lens after the aeroengine shuts down, excluding cleaning during routine maintenance.

Sources of Contamination

There are only two sources of lens fouling. Firstly and the most obvious being gas stream particles in the turbine chamber that enter through the sighting aperture and it is this source of contamination that the purge air system is employed to minimize, if not prevent. The second contributing factor to lens fouling is more subtle yet just as significant, the fact that the source of purge air is bled from the compressor means that particles are present in the purge airflow itself. Thus, in certain designs the purge air can actually be attributed to the cause of lens fouling rather than minimizing deposition as it was intended.

Turbine Chamber Penetration. A positive pressure flow is maintained through the sight tube to prevent particulates in the turbine gas stream from penetrating the sight tube and reaching the lens. Such particles typically have high inertia and thus the purge airflow must be adequate to redirect these contaminants back around and down the sight tube to re-enter the turbine chamber. The most significant particulate matter in the turbine gas stream is the suspended particulates that result from the combustion process, with soot being the major constituent. Of course, there are many other particles present such as those that have been ingested by the engine, for example sand, and particles from the engine itself through erosion of components.

Purge Air Deposition. The second source of contamination is the deposition of particles from the purge air and this source of error is sometimes easily overlooked especially in some air scrubbing systems. Compressor bleed air is used as the supply for the pyrometer purge system and it is usually particle-laden with particulates that originate from the surrounding atmosphere ingested by the engine. For example, any sand that reaches the pyrometer will probably be in the molten state and thus be sticky so that it adheres to the lens and will then further attract other particles increasing the accumulation. It is also this source of contamination that blocks the cooling channels of turbine blades that can eventually lead to blade overheating and reduced life. A simple solution is to remove the particles in the purge through the use of a filter; however, such items are not favored due to maintenance issues, weight and the fact that this is another component that must be added to the aeroengine together with the subsequent ramifications that may then emerge with its installation.

Proprietary Designs

Although there are only two generic configurations for pyrometer purge air systems, there are numerous adaptations that have been developed and implemented in order to improve the effectiveness of the basic designs or to overcome certain inherent weaknesses. In order to develop a greater appreciation and insight into lens purging, a survey of the design methodologies and proprietary techniques has been conducted. It is worthy to note that such proprietary designs are not only from the pyrometer companies themselves, but just as significantly from the end users, in this case, principally the gas turbine OEMs.

Symmetrical Scrubbing. For the air scrubbing configuration, Rosemount Aerospace [9] introduced the use of a flow tube or flow control sleeve, which controls or directs the purge, to further induce the airflow to scrub across the outer surface of the lens (Fig. 5). The application of the flow tube, with a number of tangential ports arranged around the circumference of the lens surface as shown in Fig. 6, is intended to increase the scrubbing action because an adequate air velocity will be passed across the lens to reentrain any deposited particles. However, the resultant symmetrical inward flow will produce a stagnation zone, or spot of no flow, on the lens because the radial flow is balanced. Thus, as noted by O'Brien and Myhre [10], particles will therefore tend to deposit and then accumulate at this dead air zone in the center of the lens. Rosemount also remarked that they found it very difficult to re-entrain submicron particles already deposited using this air scrubbing technology.

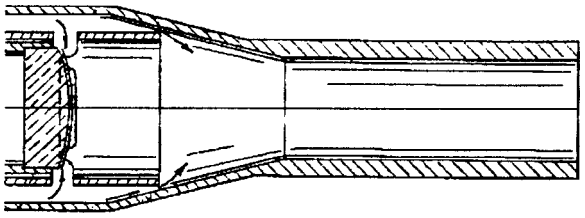

Fig. 5 Air scrubbing via flow tube (US 4,786,188)

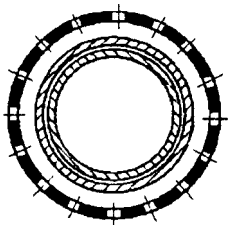

Fig. 6 Flow tube inlet arrangement (US 4,786,188)

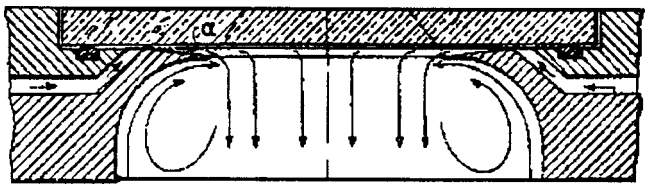

Fig. 7 Air scrubbing via protruding lip (US 4,240,691)

A similar design concept has been proposed by Holmqvist et al. [11] whereby a protruding lip, inclined to the lens, is positioned with a forward set of purge air inlets so that the airflow scrubs across the optics (Fig. 7). The narrow gap formed between the lip and lens is such that it causes the purge stream to be uniformly distributed around the entire rim in order that the airflow meets symmetrically in the opening. According to their design methodology, the edge of the lip facing the lens must not be greater than 15 deg so as to avoid turbulent flow during expansion along the edge and ensure that the purge air flows in a substantially laminar fashion. If this slope angle were to be larger than its recommended value, then the likelihood of particle deposition would be significantly increased since turbulent flow would develop. The edge itself is also made as sharp as possible in order to prevent turbulence. However, through their experimental testing of the design, Holmqvist et al. noticed that a layer of deposits formed at the lip of the edge. Their solution to this problem was to recommend that the velocity of the purge air be intermittently increased at given time intervals such that the length of time between consecutive increases in velocity is a function of the speed at which the layer builds up and its thickness. The difficulty of implementing this on an aeroengine installation is firstly, there is no available data on the build-up of the deposits, and secondly, the need to regulate purge velocity adds to system complexity.

Inertial Separation. Principally in air scrubbing designs, inertial separation techniques are employed to remove particles from the main flow of purge air prior to the flow actually contacting with the optics. This is usually achieved by causing an abrupt change in the direction of the airflow, before passage over the lens, such that the larger particles are separated, due to their high inertia, and thus do not impact and adhere to the outer surface of the lens. With proper design the process of entrained particles impinging against a surface can establish a division between suspended particles larger than a specific critical diameter that collect on the surface and those smaller particles that remain in the airflow [12].

Rosemount Aerospace makes ready use of inertial separation for pyrometer purge air systems. In their patent US 4,786,188, the purge inlets' axes are inclined to the longitudinal axes of the sight tube assembly, as illustrated in Fig. 8, in order to minimize direction change and turbulence as the purge air enters the unit. Particles within the purge air then impact on the outer surface of the flow tube. Rosemount found that the larger particles are deflected and carried along with the flow whereas the smaller particles with adhesive properties adhere to the tube. These smaller particles may then agglomerate and be later re-entrained by the flow as a

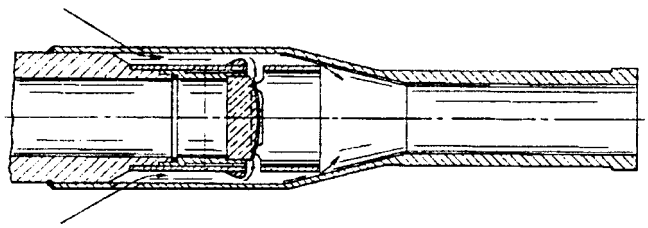

Fig. 8 Use of inertial separation (US 4,786,188)

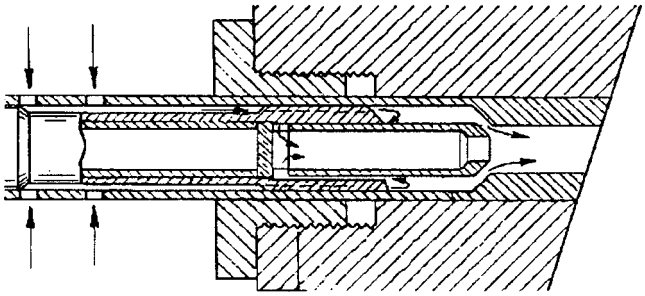

Fig. 9 180 deg inertial separator (US 4,786,188)

large particle forms. In this design, the flow tube has a number of openings in transverse alignment with the lens surface such that the main purge flow is across the optics and through the interior of the sleeve. It is this abrupt change in flow direction that causes inertial separation such that large particles, those greater than a few microns, are separated from the air before it enters the flow tube. The minor airflow between the purge sleeve and flow tube will then transport these larger particles through the sight-tube assembly into the turbine chamber. However, the smaller particles, those less than a few microns, will tend to remain entrained in the flow that scrubs the lens; although, according to Rosemount's patent, these smaller particles are not effectively deposited on the lens as they have insufficient momentum to penetrate the boundary layer of purge air formed at the lens' surface.

The inertial separation and air scrubbing effects incorporated within this design can be further enhanced by shaping an annular portion of the outer surface of the flow tube, just before the transverse openings, into an airfoil shape to produce a reaction force to induce a large flow across the lens [9]. In order to minimize any potential contamination from the purge air Myhre et al. [9] recommend an abrupt change in airflow of at least 90 deg prior to scrubbing. In a variation to their original design. Rosemount have also produced a separator with a 180-deg directional change of the purge air as shown in Fig. 9 [9].

However, there are a number of important disadvantages associated with the use of inertial impactors. Those stated by Biswas and Flagan [13] include:

- particle bounce from the collection surface upon impaction
- break-up of particles upon impaction
- blow-off or re-entrainment of collected particles
- wall losses

More importantly, the fact that particles smaller than a specific critical diameter still remain in the airflow and contact the lens does not lessen the difficulty of re-entraining submicron particles already deposited using this air scrubbing approach.

Swirl Components. In a different approach to improving the effectiveness of the basic air scrubbing configuration, Allied-Signal [14] introduced an air swirl component defined by an alternating series of merlons and crenels extending circumferentially around the lens housing a distance behind the lens (Fig. 10). Thus, the air entering the plenum from the purge inlets flows

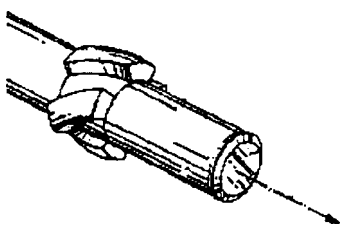

Fig. 10 Air swirl component (US 4,934,137)

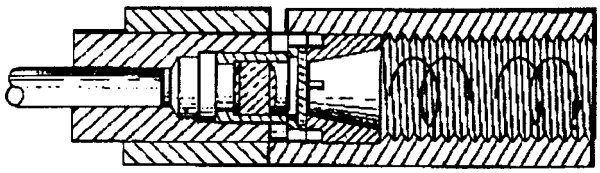

Fig. 11 Swirl system via gas nozzle (US 4,784,491)

downstream through the crenels and then over the lens. The resultant swirling flow not only scrubs the lens but also sweeps through the gap between the lens housing and the inner surface of the purge sleeve. The angle at which the air is redirected, i.e. the angle of the path defined by the crenels with respect to the pyrometer central axis, should not exceed 30 deg without encountering separation problems at the lens' surface.

GE have also utilized a swirl component in some of their designs [15]; however, their systems impart the swirl after the air has scrubbed across the lens. This use of swirled flow is to increase the allowable flow velocity of the purge air in order to minimize particle penetration and to divert such particles toward the sight tube walls. The means to impart the swirling motion to the air consists of a gas nozzle and its mount, which are positioned in front of the lens, such that after the scrubbing process the air flows through the holes of the nozzle mount and into the gas nozzle (Fig. 11). The result of this configuration is the establishment of a spiral motion in the purge as it flows at high velocity through these components and down the sight tube. Principally, the swirling motion imparted to the purge air means that it can be given higher velocity for the same flow rate and thus increase its ability to divert penetrating particles.

Also, the internal surface of the sight tube has relatively deep grooves, or screw threads, pitched in the direction of purge to support its rotation as it swirls along toward the outlet. Under the action of the centrifugal force caused by the rotation of the purge air, particles are turned toward the walls of the sight tube and deposited on the threaded channel walls with the grooves being angled to encourage the particles to bounce back out of the sight tube.

Swirling Vortex. GE further adapted the use of swirling flows to produce another form to the basic lens scrubbing configuration whereby the lens cleaning is achieved by directing purge air spirally inward over the lens surface [16]. Surrounding the lens housing is an annular chamber formed by the purge sleeve with an inlet tube through which bleed air is introduced into the annular chamber (Fig. 12). This annular chamber thus acts as a manifold to distribute the entering purge air to produce uniform circumferential airflow with its velocity being related to the mean diameter of the annular chamber. At one end of the annular chamber adjacent to the outer surface of lens is an annular gap that introduces the purge air along the outer perimeter of the lens.

The tangential component of the air results in a swirling or vortex flow shown in Fig. 13, which then scrubs across the lens as

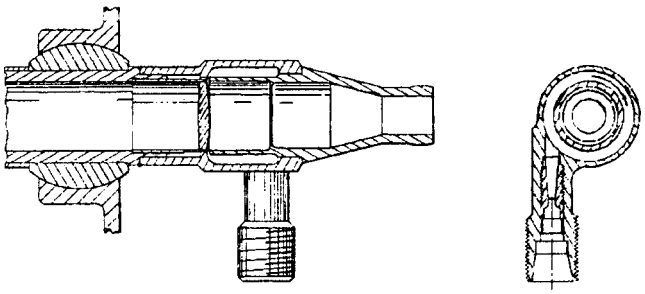

Fig. 12 Vortex purge system (US 4,738,528)

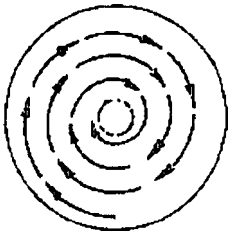

Fig. 13 Swirling vortex (US 4,738,528)

the airflow moves inwardly due to angular momentum. However, as noted by Craft [16], when the radius of the airflow is reduced as it moves radially inward, with increased velocity flow, at some critical distance from the center of the lens the vortex airflow terminates and moves axially outward along the axis of symmetry of the sighting tube. Thus, a stagnation zone develops at some radius from the axis of symmetry, and as a result particles are deposited at the center of the lens at the stagnation zone while an annular area of the lens surrounding the stagnation zone will be virtually clean.

Asymmetrical Scrubbing. To overcome the deposition of particles at the center of the lens or stagnation zone (due to symmetrical scrubbing and vortex flows) O'Brien and Myhre [10] modified the design to produce an asymmetric flow of purge air. The resultant shifting of the flow pattern across the lens avoids the development of a dead air zone and thus reduces the likelihood of particles being ejected from the flow and depositing. Their improvement was achieved through enhanced control of the airflow through the openings of the flow tube since these openings were made so that they were not symmetrical with respect to the central axis of the lens.

In one version of their design [10] the openings at the periphery of the lens comprises of two large ports and two smaller ports separated by support webs as illustrated in Fig. 14. The positioning of the support webs is such that the radial inward airflow from each of the openings is not opposed by an equally sized port directly opposite. In other words, the axes normal to the tangent plane at the center of each opening are not in common axis with another opening on the opposite side of the lens [10]. Effectively, this means that the airflow from each of the openings does not have a diametrically equal opposing flow since if the flows were balanced the central stagnation zone would develop where the opposing flows would merge. This asymmetrical flow therefore causes a shifting turbulent flow pattern that tends to move across the entire surface of the lens and can be controlled through both pressure and opening size.

However, even with the improvement in scrubbing with asymmetric flow Myhre et al. [17] later acknowledged that the support webs, which define the peripheral ports to the lens, also lead to the formation of low flow areas on the lens adjacent to their inside surfaces such that particles tended to accumulate. This effect of the support webs had not been initially recognized as an inhibiting

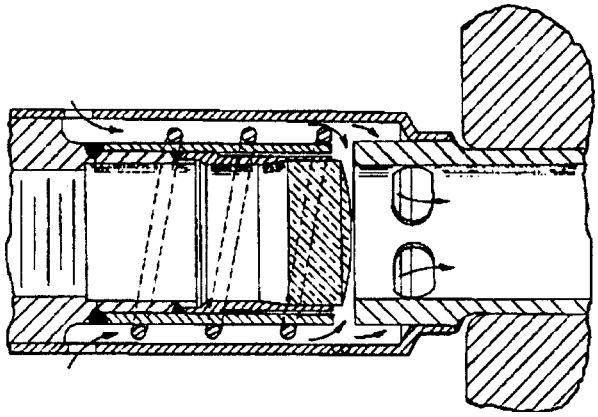

Fig. 15 Annular slotted flow tube (US 5,146,244)

factor in particle removal from the lens via air scrubbing. Their solution, as outlined in patent US 5,146,244, was the elimination of these webs with a continuous, open annular slot that extends the complete 360 deg around the lens shown in Fig. 15. The asymmetric flow pattern is now obtained by providing a swirling flow upstream, prior to the time the purge flow scrubs the lens, via a helical surface feature on the outer surface of the lens housing. Thus, the coils of the helix impart a helical flow to the purge that then scrubs across the lens. This axial turning of the airflow provides inertial separation, due to its centrifugal force since larger particles will then tend to move radially outward, and because of the tangential component of the air movement (once it is turned to flow across the lens (Fig. 16)), there is a shifting of the flow so eliminating any stagnation zone or other low flow areas that would cause particle accumulation.

Additionally, the near end of the flow tube has a series of secondary flow apertures positioned such that a part of the flow, called the secondary flow, exits through these openings so that the entrained inertially separated particles pass downstream away from the lens. It must be noted that the secondary flow is less in volume than the primary flow that scrubs across the lens and that the flow tube can be positioned in the desired location along the sight tube assembly in order to provide an adequate size of opening for the secondary flow.

Rosemount also developed a second form of this assembly whereby instead of using a helical surface, to impart the asymmetric flow, the end of the flow tube is inclined or tapered, with respect to the central axis of the sight tube, such that the upper portion of the slot is wider than at the bottom section [17]. This tapered slot, illustrated in Fig. 17, then provides the necessary asymmetric flow pattern that shifts laterally across the lens because the slot smoothly tapers from its maximum gap width at the upper section, and hence greater inlet flow, to the narrower gap at the bottom.

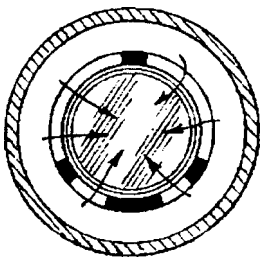

Fig. 14 Flow tube inlet arrangement for asymmetrical scrubbing (US 4,836,689)

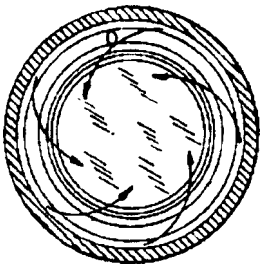

Fig. 16 Primary airflow through slotted flow tube (US 5,146,244)

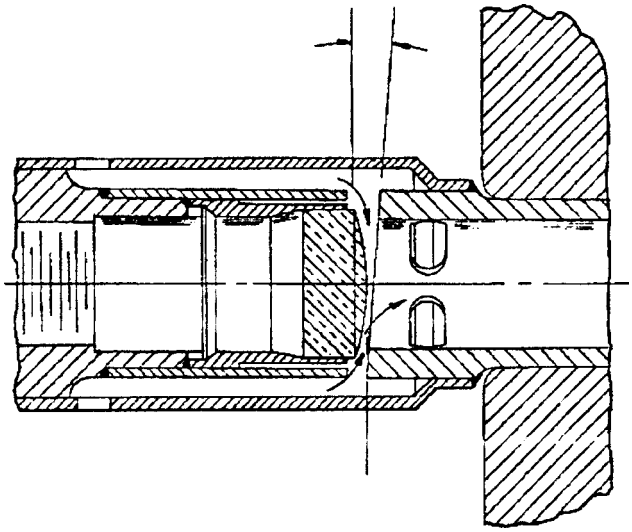

Fig. 17 Tapered flow tube (US 5,146,244)

Fluid Screens. Making the transition to the air curtain cofiguration for preventing lens fouling is the application of fluid screens, whereby the idea is not to scrub the lens, but instead to form a protective curtain of air to prevent particles from penetrating the sight tube. In the design proposed by Harley [18], an array of equal diameter purge inlets are inclined at an angle, preferably in the range of 25–30 deg, with an equal spacing between adjacent inlets as shown in Fig. 18. As the airflow enters through the inlets a conically shaped fluid screen is developed in front of the lens in order to prevent particle penetration from the turbine chamber (Fig. 19). It is recommended in patent US 4,306,835 that the angle of the fluid screen be preferably in the range of 50–60 deg.

Still Tubes. The fluid screen method for providing an air curtain can be greatly enhanced through the addition of a still tube in front of the lens. This tube has the opposite function to the flow tube used in air scrubbing designs since it establishes a still region in front of the lens to prevent any contaminants in the purge air itself from depositing on the optics. Smiths Industries utilized such a design through their patent GB 2,158,576 [19] where the lens is mounted in the lens housing that then has an addition tube, with a reduced diameter front portion, attached to its front end. An outer co-axial tube, or purge sleeve, is further fitted around the still tube to form an annular gas passageway—essentially, the

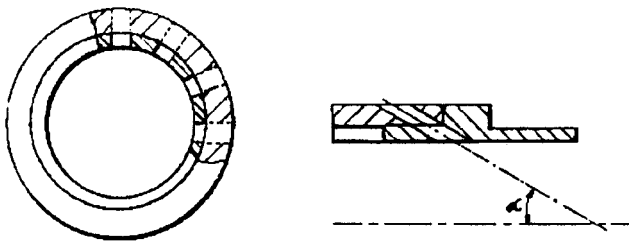

Fig. 18 Purge inlet arrangement for fluid screen (US 4,306,835)

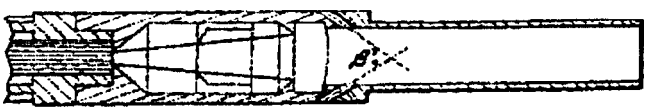

Fig. 19 Fluid screen (US 4,306,835)

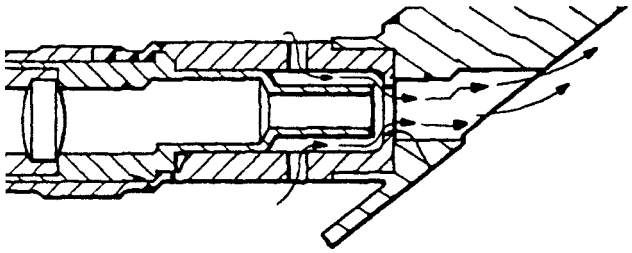

Fig. 20 Still tube system (GB 2,158,576)

purge system (Fig. 20). The bled air is introduced through the purge inlets, then flows along the annular passageway, across the front end of the still tube and finally exits the sight tube assembly into the turbine chamber.

According to Pointer and Masom [19], when sufficient purge flows across the end of the still tube it tends to draw air out, causing a slight reduction in pressure within the larger diameter rear portion, developing a substantially constant pressure environment within the tube. This establishes what Smiths Industries term ''a resonant column of gas'' within the sight tube such that there is substantially constant pressure at any point along the column, and therefore no overall mass transfer along the tube so minimizing particle deposition on the outer surface of the lens. The frequency of this resonant column is dependent on the dimensions of the still tube. In addition, the design of their still tube is such that at lower gas flows (insufficient to set up the resonant column), any turbulence in the purge flow at the tip of the tube is confined to the smaller-diameter portion, which in effect acts as a barrier.

Smiths also elaborated on a number of design rules for their purge system. The first of these relates to the six purge air inlet holes, which are equally distributed about the purge sleeve, allowing the entry of air from the engine by-pass duct to the rear of the annular passageway. The combined area of these six air inlets is significantly larger than the area of the smallest gap formed between the end of the still tube and the in-turned lip of the purge sleeve that defines the circular exit aperture for the purge flow. Secondly, the exit aperture of the sight tube assembly is larger than the internal diameter of the forward portion of the still tube, but smaller than its external diameter. The still tube has an internal diameter of about 12 mm at its rear portion and is stepped to an 8-mm diameter about halfway along its length by a conical section.

Typically air curtain purge systems with still tubes have only a single purge air entry inlet. However, the purge air may then undergo swirl after entry and result in a nonuniform velocity distribution together with the development of eddy flows inside the still tube. To prevent such a scenario Ridley and Fearnehough [20] of Land Infrared produced a modified still tube with the addition of extending vanes to produce a swirl reducing system as shown in Fig. 21. Their purge assembly has at least two axially spaced chambers, positioned about the purge sleeve, linked by a restrictive opening such that a pressure difference exists between the

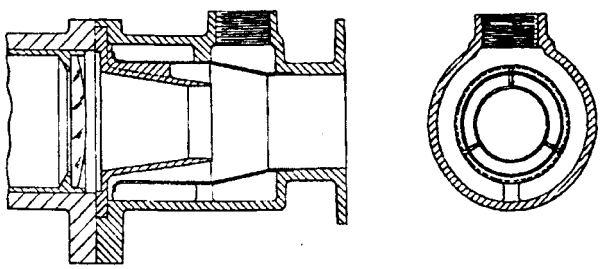

Fig. 21 Swirl reducing system via vanes (US 5,599,105)

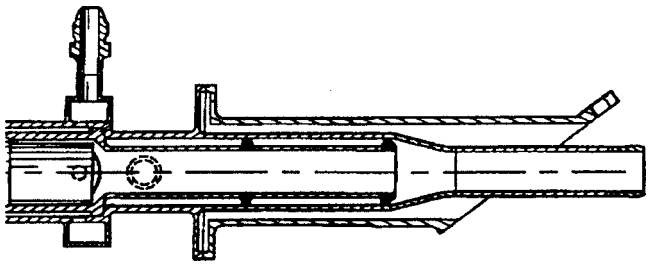

Fig. 22 Swirl reducing system via diffusers (US 5,421,652)

adjacent chambers. The upstream chamber is connected to the source of purge air and the downstream chamber opens into the purge passageway via the swirl reducing system. This swirl reducing system consists of a number of long vanes that extend along at least half the length of the still tube in order to straighten or remove the swirl of the purge airflow. The still tube, itself, will also need to be sufficient in length since it is provided to reduce eddy current velocities within its inner domain due to the purge flow at its outer end. Land also found that the eddy flows could be further suppressed if the still tube where tapered radially inward, in a direction away from the lens, and if a sharp lip was also provided to its outer end [20]. Kast and Prasad [21] of GE have also patented an air-straightening component for pyrometer purge systems that takes the form of a pair of diffusers being positioned midway along the sight tube and at its tip (Fig. 22).

Deflection Surfaces. Another approach that complements the use of purge air to prevent lens fouling, is the use of deflectors or lips employed at the end of the sight tube in order to deflect the cross flow of the combustion products in the turbine chamber. The Avcu Corporation has patented such a technique whereby the upstream edge of the sight tube functions as a lip, shown in Fig. 23, to minimize entry of particles into the pyrometer [18]. Their design is further aided by a secondary fluid screen, to supplement the primary screen at the lens, where purge air flows through an annular spacing between the turbine casing wall and sight tube.

Along a similar design process MacKay [14] proposed to bevel the turbine shroud at the sight tube aperture so to form a deflection surface to deflect particulates in the turbine gas stream (Fig. 24(*a*)). The entry of particulates into the sight tube is thus minimized by beveling or rounding the rim of the shroud where it surrounds the sighting tube aperture in a downstream portion in relation to the turbine stream. The radially inward-facing surface of the shroud defines a deflection surface from which particulates, which would otherwise penetrate the sighting tube, are deflected back into the turbine chamber. The angle between the deflection surface and the shroud, see Fig. 24(*b*), should be in the range 25–45 deg [14].

Optical Shutters. In further analysis of the particle penetration problem Suarez-Gonzalez and Kepple [22] noted that lens fouling was particularly acute during start-up or shutdown of the aeroengine since the pressure of the purging air is reduced and so insufficient to ensure that particle penetration of the sight tube is at least minimal. This problem was aggravated in certain Pratt & Whitney turbines because maintenance requirements forced the installation to be located in a region near the bottom of the turbine in order to allow easy access during scheduled servicing [2]. Such a location is of course prone to gravitation settling of particles.

A solution to this problem was developed by the United Technologies Corporation [22] through the addition of a shutter at the end of the sight tube that operates to seal the tube until the air pressure within the aeroengine exceeds a pre-selected threshold magnitude with the shutter remaining open as long as that threshold is exceeded. The shutter itself consists of a conventional helical spring attached to a movable piston as illustrated in Fig. 25.

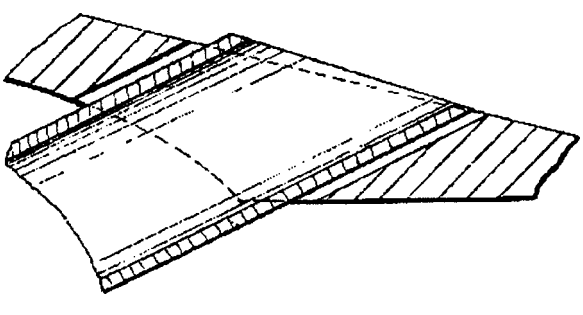

Fig. 23 Sight tube lip (US 4,306,835)

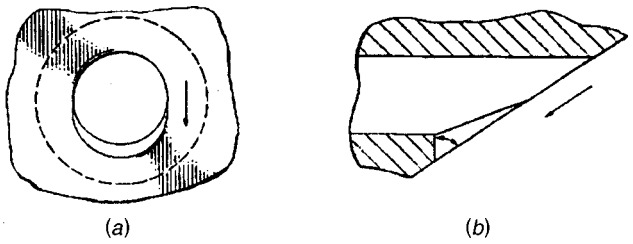

Fig. 24 Beveled sight tube aperture (US 4,934,137)

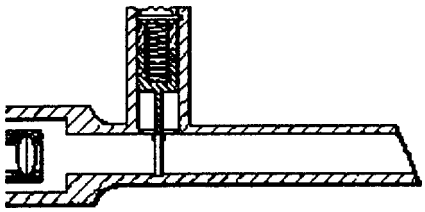

Fig. 25 Optical shutter (US 4,657,386)

Conclusion

Since each pyrometer installation is different for a given engine type, the basic configuration and dimensions of the system are modified to meet the envelope size requirements. This design process can potentially comprise the effectiveness of the unit's purge air system and thus have significant impact on the operational use of the optical pyrometer. In order to aid design re-use, this paper has provided an overview of pyrometer purge air systems applicable to gas turbine installations. This acts as the first step in allowing designers to understand the relationships between lens fouling and the pyrometer installation through having an appreciation of the practices already employed.

Acknowledgments

The authors would like to acknowledge the UK Engineering and Physical Sciences Research Council and Rolls-Royce plc as project sponsors, and to thank C. Bird and P. Loftus for the guidance received during the course of this study.

References

[1] De Lucia, M., and Lanfranchi, C., 1994, "An Infrared Pyrometry System for Monitoring Gas Turbine Blades: Development of a Computer Model and Experimental Results," ASME J. Eng. Gas Turbines Power, **116**, pp. 172–177.
[2] Sellers, R. R., Przirembel, H. R., Clevenger, D. H., and Lang, J. L., 1989, "The Use of Optical Pyrometers in Axial Flow Turbines," AIAA/ASME/SAE/ASEE 25th Joint Propulsion Conference, Monterey, July 10–12, AIAA-89-2692.
[3] Kirby, P. J., 1986, "Some Considerations Relating to Aero Engine Pyrometry," Advance Instrumentation for Aero Engine Components, The Propulsion and

Energetics Panel 67th Symposium, Philadelphia, May 19–23, 1986. AGARD-CP-399.
[4] Davinson, I., 1984, ''Detection of and Correction for Lens Contamination in Radiation Pyrometers, EIR 00862. Rolls-Royce Limited, Derby, England.
[5] Atkinson, W. H., and Guenard, R. N., 1978 ''Turbine Pyrometry in Aircraft Engines,'' IEEE/ERA Electro-78 Conference Record Session 33/3, Boston, MA, May 23–25.
[6] Barber, R., 1969, ''A Radiation Pyrometer Designed for Inflight Measurement of Turbine Blade Temperatures,'' National Air Transportation Meeting, New York, NY, April 21–24, SAE 690432.
[7] Berenblut, B. J., and Masom, R. A., 1982, ''Radiation Pyrometry for Gas Turbine Engines—An Introduction,'' Br. J. Non-Destr. Test., **24**(5), 268–269.
[8] Hayden, T., Myhre, D., Pui, D. Y. H., Kuehn, T. H., and Tsai, C. J., 1988, ''Evaluating Lens Purge Systems for Optical Sensors on Turbine Engines,'' AIAA/ASME/SAE/ASEE 24th Joint Propulsion Conference, Boston, MA, July 11–13, AIAA-88-3037.
[9] Myhre, D. C., Pui, D. Y. H., and Miller, L. V., 1988, ''Purge Air System for a Combustion Instrument,'' Rosemount, US 4,786,188.
[10] O'Brien, R. J., and Myhre, D. C., 1989, ''Asymmetric Purge Air System for Cleaning a Lens,'' Rosemount, US 4,836,689.
[11] Holmqvist, G., Kallon, S., and Jansson, B., 1980, ''Protective Device for Optical Elements,'' AGA Aktiebolag, US 4,240,691.
[12] De La Mora, J. F., Rao, N., and McMurry, P. H., 1990, ''Inertial Impaction of Fine Particles at Moderate Reynolds Numbers and in the Transonic Regime With a Thin-Plate Orifice Nozzle,'' J. Aerosol Sci., **21**(7), pp. 889–909.
[13] Biswas, P., and Flagan, R. C., 1988, ''The Particle Trap Impactor,'' J. Aerosol Sci., **19**(1), pp. 113–121.
[14] MacKay, C. G., 1990, ''Temperature Measurement in Turbine Engines,'' Allied-Signal Inc, US 4,934,137.
[15] Penney, C. M., and Lund, R. M., 1988, ''System to Protect Optics Against Dirty Environments,'' General Electric Company, US 4,784,491.
[16] Craft, D. W., 1988, ''Pyrometer Vortex Purge Air Cleaning System With Center Masked Pyrometer Lens,'' General Electric Company, US 4,738,528.
[17] Myhre, D. C., O'Brien, R. J., Pui, D. Y. H., and Tsai, C. J., 1992, ''Window Purging System for a Combustion Instrument,'' Rosemount, US 5,146,244.
[18] Harley, J. F., 1981, ''Air Purging for an Optical Pyrometer of a Gas Turbine Engine,'' Avcu Corporation, US 4,306,835.
[19] Pointer, J., and Masom, R. A., 1985, ''Radiation Pyrometer,'' Smiths Industries Public Limited Company, GB 2,158,576.
[20] Ridley, I. H., and Fearnehough, P., 1997, ''Purge Assembly,'' Land Instruments International Limited, US 5,599,105.
[21] Kast, H. B., and Prasad, M. E., 1995, ''Pyrometer Adapter,'' General Electric Company, US 5,421,652.
[22] Suarez-Gonzalez, E., and Kepple, D. A., 1987, ''In-flight Engine Control Optical Pyrometer,'' United Technologies Corporation, US 4,657,386.

An Argument for Enhancement of the Current Inlet Distortion Ground Test Practice for Aircraft Gas Turbine Engines[1]

Milt Davis
e-mail: milt.davis@arnold.af.mil

Alan Hale

Dave Beale

Sverdrup Technology, Inc.,
Arnold Engineering Development Center, AEDC,
Arnold Air Force Base, TN 37389

The current high-performance aircraft development programs, and the trends in research and development activities suggest a rapidly increasing level of aircraft subsystem integration, particularly between the airframe/inlet and the propulsion system. Traditionally, these subsystems have been designed, analyzed, and tested as isolated systems. The interaction between the subsystems is modeled primarily through evaluating inlet distortion in an inlet test and simulating this distortion in engine tests via screens or similar devices. For the current test methodology, the environment that is supplied by the inlet is simulated by the imposition of total pressure profiles at the aerodynamic interface plane (AIP). Unsteady or transient variation in total pressure is generally not considered to be important. In addition, angular flow, commonly called swirl, is also not considered important enough to be simulated. In the current paper, an overview of current techniques for inlet performance, distortion characterization, and engine distortion testing is presented. A numerical study was conducted on a single high-speed rotor to qualify potential effects on stability and performance and to support the concept that dynamic distortion and swirl may have large enough effects to affect the experimentally determined stability limit. This paper reports a numerical investigation using a 3-D compression system simulation that supports the enhancement of the existing methodology to include the effects of time-dependent distortion and swirl effects. Based upon both experimental and numerical evidence, AEDC has embarked on efforts to develop inlet simulator technologies directed toward future airframe-propulsion integration requirements. This paper presents issues that require advancements in the simulation of inlet distortion techniques for direct-connect turbine engine tests. [DOI: 10.1115/1.1451087]

Introduction

A primary objective of the Arnold Engineering Development Center (AEDC) test and evaluation (T&E) mission is centered on gas turbine engine propulsion issues. The advent of technologies for providing controlled flight at extremely high angles of attack and sideslip have enabled weapon system developers to consider supermaneuver and post-stall maneuver capabilities as combat tactics. As a result, future fighter aircraft may be required to execute maneuvers containing drastic and transient changes in flight conditions at the high power settings demanded by combat. Such maneuvers present the issue of the role that the distortion time history might play in the inlet-engine integration task. Large and transient changes in angle of attack can produce hysteresis, and therefore deviations, from the steady-state condition. As a result, future direct-connect engine or compressor tests may require distortion generators capable of producing a rapid sequence of distortion patterns to provide a time history corresponding to a transient maneuver.

Another type of inlet distortion that may appear in future operability and performance assessments involves flow angularity. The current total-pressure methodology neglects flow angularity as a separate distortion parameter. However, experience with a number of systems showed that flow angularity could affect both operability and performance (According to the unpublished S-16 document, *"Intake Flow Anularity: A Current Assessment of the Inlet/Engine Swirl Distortion Problem"*). In an aircraft inlet, flow angularity appears in the form of swirling flow. A rotation of the entire flow about the engine or compressor hub constitutes a bulk swirl and either increases or decreases engine performance depending on the direction of rotation with respect to the machine. Localized swirl, in the form of vortices appearing in various regions of the AIP, can affect surge margin. Engines lacking inlet guide vanes have demonstrated the highest sensitivity to inlet swirl. As examples, inlet swirl can originate at the aircraft forebody or it can be generated in S-shaped inlet diffuser ducts. Therefore, the advent of stealth systems, with blended inlets and S-ducts, may introduce requirements to address swirl in future engine compatibility tests.

Both inlet and engine ground and/or flight testing use a methodology developed by the S-16 committee of the Society of Automotive Engineers (SAE), the Aerospace Recommended Practice, ARP-1420 [1] and its companion document, the Aerospace Information Report, AIR-1419 [2] as guidelines for evaluating inlet and engine performance and operability with nonuniform inlet airflow. These documents are a recommended practice, derived by consensus of industry and government practices during the late 1970s and early 1980s. Over the last 25 yr, these consensus practices have become established methodologies.

This paper reviews what constitutes the current practice for evaluating engine and inlet compatibility issues and highlights the potential for increasing the information available from current testing through the fusing of computational modeling and simulation and experimental data to provide a numerical simulation of

[1]The research reported herein was performed by the Arnold Engineering Development Center (AEDC), Air Force Material Command. Work and analysis for this research were done by personnel of Sverdrup Technology, Inc., AEDC Group, technical services contractor. Further reproduction is authorized to satisfy the needs of the U.S. Government.

Contributed by the International Gas Turbine Institute and presented at the International Gas Turbine and Aeroengine Congress and Exhibition, New Orleans, Louisiana, June 4–7, 2001. Manuscript received by the IGTI, November 17, 2000. Paper No. 2001-GT-507. Review Chair: R. A. Natole.

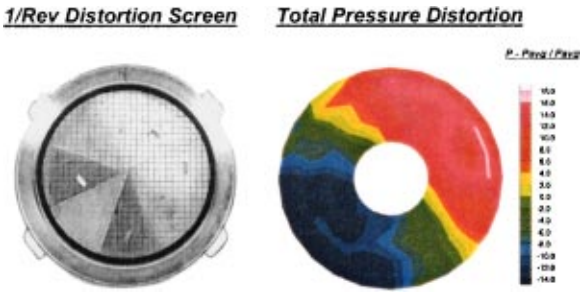

Fig. 1 Typical distortion screen and corresponding distortion pattern

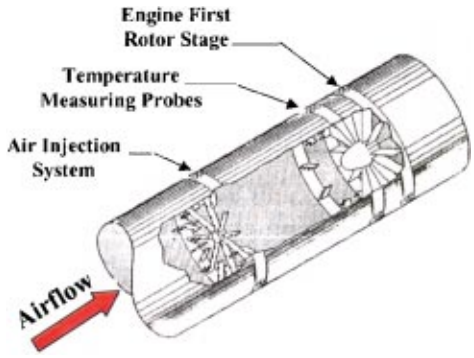

Fig. 2 Schematic of airjet distortion generator

the airframe-engine system. A previous paper [3] addressed the need and level of simulation technology that will be required for ground test facilities to provide a simulation capability for full inlet-engine compatibility evaluations. This paper specifically addresses the need for modifying the current ground test methodology to include the effects of dynamic distortion and swirl.

Current Distortion Test Practices

Keeping with one of the fundamental precepts of the recommended practice set forth in the ARP-1420, namely, that engine stability can be defined by tests using equivalent levels of steady-state distortion, the aircraft manufacturers, engine manufacturers and testing organizations have implemented testing procedures which reflect that premise.

By virtue of being available early in the air vehicle development cycle, the direct-connect method has become the workhorse for testing compressors or engines in distorted flows. The method can readily be applied to engine components such as individual fans or compressors as well as to complete engines. In the direct-connect test, the component or engine is connected directly to an air supply duct that provides conditioned air at a pressure, temperature, and Mach number commensurate with a given flight condition. Thus, the duct conditions correspond to the flow output by the inlet after the diffusion process. With respect to the freestream, these conditions often include lower Mach numbers, higher static pressure, and higher static temperature. So, in a sense, the supply duct functions as an inlet simulator taking the place of the actual inlet.

In the absence of the inlet and airframe, the direct-connect approach must rely on additional techniques to simulate the distortion produced by the inlet. A number of methods have been applied to simulate steady-state inlet distortion as well as various aspects of time-variant distortion. The two most widely used inlet distortion simulators are the distortion screen and the air jet distortion generator.

The distortion screen generates steady-state total-pressure patterns through flow blockage, a function of screen porosity and approach velocity. The screen consists of an assembly of various wire meshes with shape and porosity tailored according to the particular pattern of interest. When mounted forward of the compressor or engine and normal to the flow, the screen subjects the machine to distortion similar to that produced by the inlet. An example of a distortion screen appears in Fig. 1.

This particular screen produces a one-per-revolution, 180-deg circumferential pattern. As each screen produces a single distortion pattern, a particular test program may require a family of screen assemblies to satisfy inlet-engine compatibility verification objectives.

The air jet distortion generator [4] evolved as an approach to avoid the cost and cycle time needed to fabricate and install separate screens for each distortion pattern. The device uses the viscous mixing as a means of reducing the momentum in regions of the approaching flow. Forward-facing airjets exchange momentum with the approaching flow to effect pressure losses. An array of such jets, mounted on struts upstream of the test article, provides a means of spatially varying the pressure defects (Fig. 2).

By remotely adjusting the flow distribution among the jets, the tester can set desired distortion patterns without interrupting the test for hardware changes. Unlike the wind tunnel or flight test methods, the direct-connect method requires a-priori definition of the flow distortion patterns to set in the inlet simulator whether screen or air jet distortion generator. As the direct-connect approach finds wide application throughout the vehicle development cycle, the patterns fall into two general categories: 1) classical distortion patterns, and 2) composite or complex distortion patterns.

The so-called classical distortion patterns consist of standardized patterns that provide specific distortion features such as tip radial distortion, hub radial distortion, circumferential distortion with various multiple-per-rev specifications, or combinations. These patterns are generic in the sense that they do not necessarily correspond to a specific vehicle. The classical patterns generally find application earlier in the development cycle to establish the basic sensitivity characteristics of the engine or compression system. A discussion of the classical patterns and sensitivity tests appears in the AIR 1419.

The screen and air jet distortion generator devices provide only steady-state distortion patterns. However, historical wind tunnel test results have shown that the time-variant distortion or swirl can be significantly higher than steady state. Over the years, a number of devices have been developed in an effort to simulate time-variant distortion in direct-connect tests. Examples of such devices can be found in the random-frequency generator [5], the discrete-frequency generator [6], and planar-wave generator [7]. The random frequency generator devices generally used separated flow to produce fluctuations similar in nature to those encountered in an inlet duct. Discrete-frequency generators generally use a periodic pulsing of the flow to develop fluctuations at specific frequencies. These fluctuations may be produced by the air jet distortion generator with pulsed jets or by rotor-stator devices. However, these devices have yet to find general application.

To address time-variant distortion, the current methodology applies the following approach. The time-variant distortion measurements obtained in the wind tunnel, the distortion time history, is screened over the time recorded during the particular test point to identify peak levels of distortion. The wind tunnel data acquisition procedure must include a sufficient data record, typically 20 or 30 s, to capture peak distortion events. Experience has shown that turbomachines require a finite time, on the order of one revolution of the compression system, to respond to dynamic distortion events. Therefore, the screening process neglects time-dependent events lasting less than approximately one revolution and does not even begin to address the effects of swirl. The peak level of distortion is then applied in the direct-connect test using the screen or air jet distortion generator. The peak time-variant pattern becomes

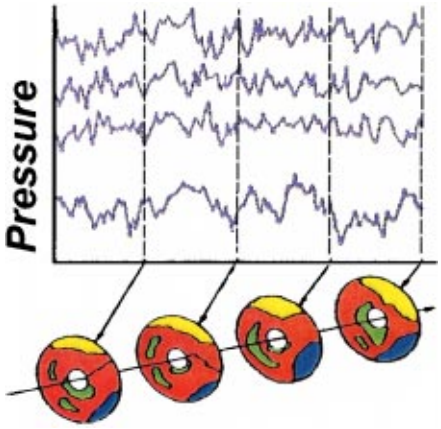

Fig. 3 Simulation of time-variant distortion with steady-state patterns

a steady-state pattern in the engine or compressor test neglecting the effects of time history. Figure 3 illustrates this approach.

The SAE methodology described thus far evolved over several decades and has been successfully applied to a number of systems up to current generation fighter aircraft.

Over the last several years the SAE S-16 committee has been in the process of evaluating time-dependent distortion (document on planar wave effects, [8]) and swirl. This paper reports a numerical investigation using a 3-D compression system simulation that supports the enhancement of the existing methodology to include the effects of time-dependent distortion and swirl effects.

Numerical Investigation

The following numerical investigation into the effects of time-dependent distortion and swirl was conducted using the AEDC generated 3-D compression system code known as TEACC (Turbine Engine Analysis Compressor Code) [9], and illustrated in Fig. 4.

The governing equations used in TEACC were developed by applying the conservation of mass, momentum, and energy. TEACC allows for circumferential and radial control volumes to interact directly with each other via the three-dimensional Euler equations with source terms representing a blade row. These source terms representing mass bleed, blade forces and shaft work are supplied by a streamline curvature code (a derivative of HTO300 by Hearsey) [10].

Rotor 1B [11] was chosen as the investigation vehicle because it offered simplicity in the number of stages (1 blade row), and it

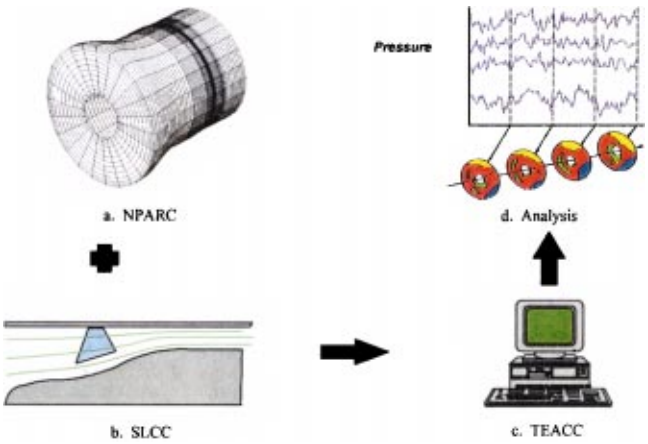

Fig. 4 Overall TEACC methodology

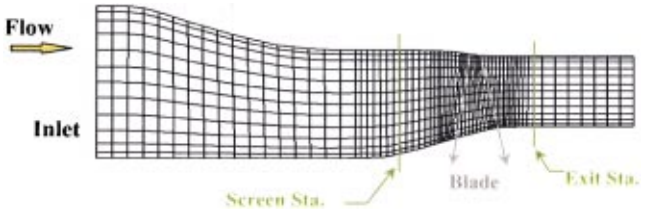

Fig. 5 Grid of Rotor 1B

represented a compression system with a thorough analysis of clean and distorted inlet. Rotor 1B is a high-performance transonic rotor similar to those found in modern high-speed aircraft. The rotor was designed with a multiple circular-arc blade shape which was applied over the top 40 percent of the blade while a double circular-arc construction was employed for the bottom 60 percent of the blade. With a hub-to-tip ratio at the rotor inlet of 0.5, the blade sections were long enough to require a mid-span damper to maintain structural integrity during operation. Rotor 1B consisted of 44 blades, producing a moderate solidity of 1.3 at the rotor tip.

Grid Development. TEACC requires a fixed three-dimensional grid on which to resolve the conservation equations. A grid of $(69\times13\times26)$ was constructed to model Rotor 1B, where the inlet and exit of the blade were defined as slanting lines in Fig. 5.

The grid was constructed with vertical grid lines in the vicinity of the screen to property model the experimental distortion screen. Grid lines were smoothly packed to reduce numerical losses through the bladed region where the flow was known to have strong gradients. A radial-circumferential view of this base grid is presented in Fig. 6, where a cylindrical right-handed coordinate system has been used with uniform circumferential segments.

An integer number of grid segments was constructed to conveniently model a 90-deg, one-per-revolution inlet distortion. Each segment was 15 deg in circumferential extent with a total of 24 segments within a circle (six segments in each quadrant).

Rotor 1B Steady Performance With Distortion. The information presented in this section was taken from a previous paper, [9], and re-presented to provide a baseline for the dynamic distortion and swirl investigations. Rotor 1B was tested with an inlet screen to quantify the effects of inlet flow distortion on its performance. Because the distortion data provided with Rotor 1B was based on a 90-deg, one-per-revolution screen, a simulation of the screen was used in the TEACC simulation. For this study, TEACC was compared at three different corrected speedlines for a distorted inlet.

A single screen with a 90-deg, one-per-revolution pattern was designed to give a classical circumferential inlet total pressure

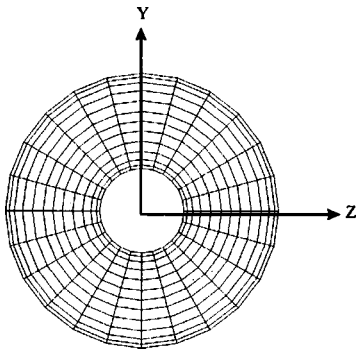

Fig. 6 Radial-circumferential view of 3-D grid for Rotor 1B

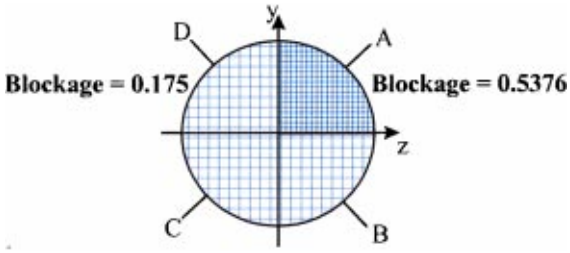

Fig. 7 Rotor 1B distortion screen definition

inlet distortion to Rotor 1B. At the 100-percent speed, the experimental data showed that the screen produced a total pressure loss of 15 percent from the clean inlet which was duplicated for the TEACC simulation. Investigations were conducted through the middle of the four circumferential quadrants where the experimental data was taken. The screen was located in quadrant A (Fig. 7). The compressor rotates clockwise, causing air to swirl in the direction of increasing quadrant letter (A, B, C, and D).

An overall total pressure ratio performance map for Rotor 1B is presented for three corrected speeds of 50, 70, and 100 percent. The clean speedlines are presented to give a proper orientation of the distorted data, with stall depicted for each speedline at its lowest corrected mass flow rate. A conservative, but simple, stalling criterion was imposed on the TEACC simulation. When any one of the circumferential segments acquired a corrected mass flow which exceeded stall for the clean inlet, the compressor was considered stalled. Likewise, the TEACC simulation was halted when any one of the circumferential segments exceeded the clean inlet data on the choked end of the speedlines. These two restrictions define the distortion calculation limits presented for each speed in Fig. 8.

For the two low-speed cases, the clean and distorted data lay close together. The extent in corrected mass flow rate is about the same for the simulation and the experimental distortion data. The maximum percent difference between TEACC results and experimental data at the lower speeds was approximately 2 percent. The 100-percent speed is more interesting because the experimental data presented a region where the compressor intermittently stalled or remained stable with the imposed inlet distortion screen. The TEACC simulation predicted the corrected mass flow rate differently from reported experimental data by a maximum of 3 percent. The TEACC simulation maps out a range of corrected mass flow which includes approximately the middle of the intermittent stall region.

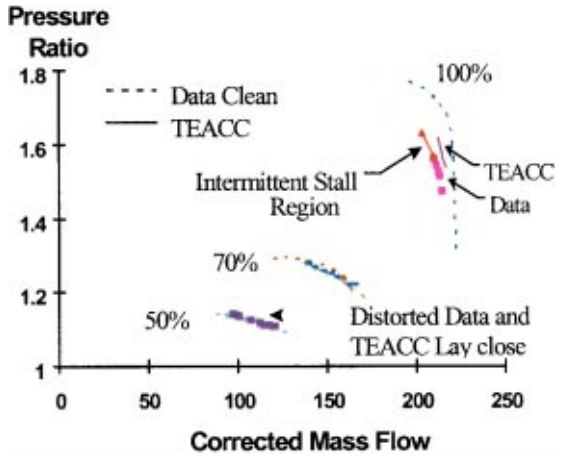

Fig. 8 Comparison of TEACC calculations with distortion to that observed experimentally

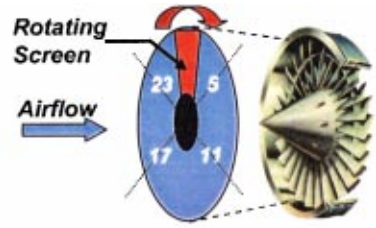

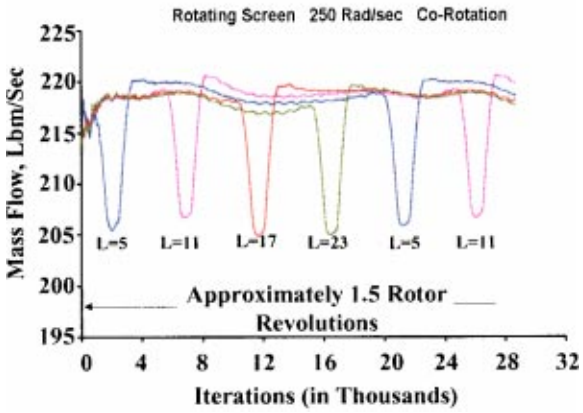

Fig. 9 Dynamic distortion generator concept and corresponding airflow reduction behind the screen

Dynamic Distortion Investigation. The numerical three-dimensional compressor code, TEACC, was modified for dynamic boundary conditions. That modification consisted of simulating a rotating screen, approximately one compressor diameter upstream, with a single one-per-revolution pattern. The rotating screen simulated the effect of an upstream rotating stall cell in an upstream compressor as illustrated in Fig. 9. This form of dynamic distortion was chosen since experimental rig data exists with that type of unsteady distortion for comparison purposes and reported in Longley et al. [12]. The approach adopted and reported in the ASME paper was to rotate a distortion screen upstream of several low-speed multistage compressors. The experimental facility used allowed the distortion screen to be rotated in either direction (co-or-counter-rotational) at various fractions of rotor speed. Comparisons were also made with calculations using a model developed by Hynes and Greitzer. This investigation, although not related to distortion produced by a typical inlet does provide insight into the effects of dynamic distortion. The measured mean flow coefficients at stall inception as a function of screen rotational speed for one of the compressors tested is presented in Fig. 10.

The stall flow coefficients with no distortion and the design flow coefficient are also indicated in the figure. Negative screen speeds correspond to distortion rotating in the direction opposite to the rotor rotation (counter-rotation). The authors made several observations. The most evident is that the speed at which the inlet distortion rotates has a major effect on the stability point, with co-rotation of the screen having a much larger impact than counter-rotation.

The change in the stall flow coefficient with co-rotation was a substantial fraction of the difference between the stall flow coefficient at zero distortion screen speed and the design flow, thus giving an indication of how much the stability margin is degraded by co-rotating distortion.

The screen rotational speed was controlled by the proper selection of the time step and the time spent at each of the 24 circumferential locations. The screen width can be set within the resolution of approximately 5 percent of the frontal area to 100 percent of the total area as determined by the specification of a porosity at specific grid points. For this illustration, two of the 24

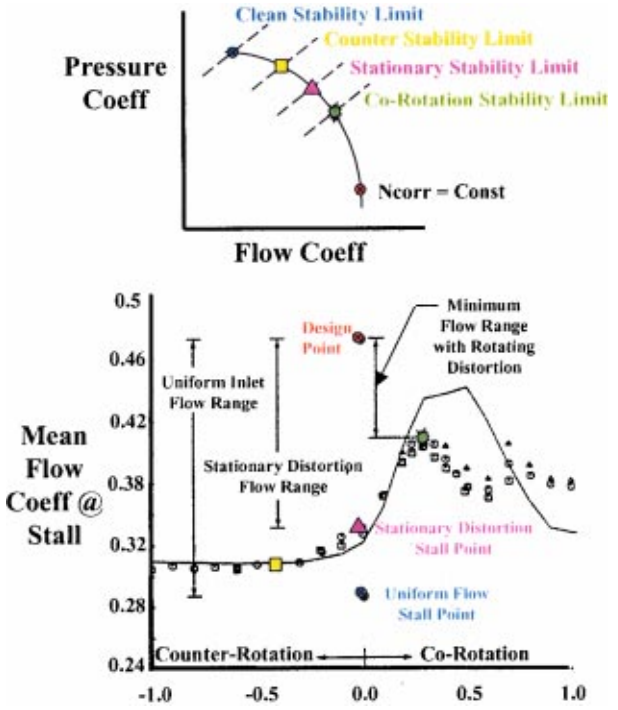

Fig. 10 Flow coefficient at stall versus distortion rotation rate [12]

circumferential grid segments were obstructed using the porous screen boundary condition. The potential exists for both co-rotation and counter-rotation in addition to a superposition of a swirl.

Early on in the analysis, it was discovered that unless the effect of the rotating screen on the fluid was modeled (i.e., the swirl generated by the rotation of a solid body), no difference was observed to that generated either by co or counter-rotation. That is to say, both co and counter-rotation produced the same result for the same rotational speed without the swirl component but were at a different level than the stationary case. Once a level of swirl was imposed in the direction of rotation, the calculations started providing results that were consistent with that observed by Longley. Thus, the results of this analysis are not only that of dynamic distortion but that mixed with swirl. The effect shows up in the determination of the stability limit and illustrated in Fig. 11.

Since TEACC was not equipped with a stall criterion, the effect of the rotating screen had to be inferred using an operating point away from stall. The rotating distortion was implemented at a nominal operating point, not near stall, and the change in airflow was compared to the non-distorted airflow at stall. In the counter-rotation case, the change in airflow was in a direction away from stall and in the co-rotation cases, the change in airflow was near to the stall point. This generalization, was the same as was observed in the actual experimental setup. Thus, we can conclude, that the TEACC model is giving qualitatively correct results.

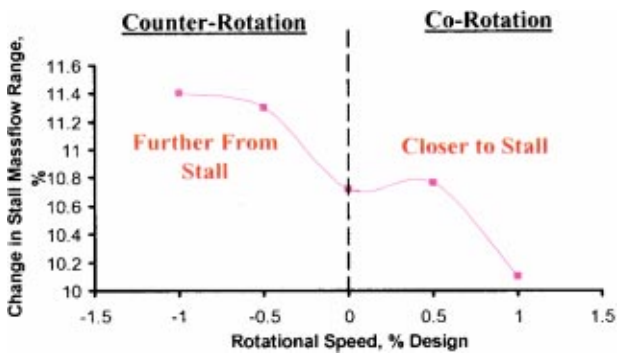

Fig. 11 Effect of rotating screen on Rotor 1B stability limit

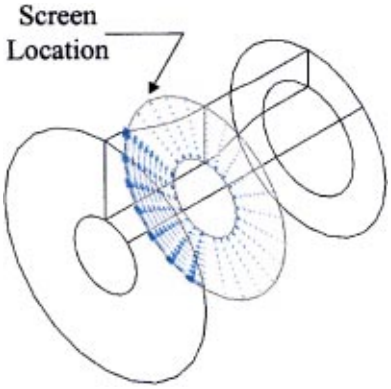

Fig. 12 Example of induced swirl at screen boundary location—co-rotation shown

Swirl Investigation. With the advent of stealth-type inlets which change the flow direction to hide the engine face, the engine compression system can be subjected to significant flow angularities as well as total pressure distortion at the aerodynamic interface plane (AIP). These flow angularities may have both radial and circumferential velocity components. Swirl is generally considered as being that portion of the flow vector which is directed circumferentially. Swirl can strongly affect the work of the downstream fan or compressor. It has been noted that engines without inlet guide vanes are especially susceptible to swirl effect and tend to exhibit a higher sensitivity to swirl than engines with IGVs. If the swirl is in a direction opposite to that of the compressor rotation, the blading in that area becomes highly loaded. On the other hand, if the swirl is in the direction of rotation, then the blades become unloaded and the stability margin is enhanced.

Swirl is produced when vorticity normal to the mean flow direction is turned in its own plane. It is convenient to identify swirl into different categories to characterize certain aspects of the flow. According to the unpublished S-16 document, ''*Intake Flow Anularity: A Current Assessment of the Inlet/Engine Swirl Distortion Problem*,'' swirl can be characterized as: 1) paired; 2) bulk; 3) downstream engine induced; 4) cross-flow induced; 5) externally generated vortices; and 6) wrapping swirl.

For this investigation, it was decided to investigate ''bulk'' swirl effects since it would be the easiest to implement as a boundary condition within the TEACC code. Bulk swirl is characterized as a nonzero circumferential average flow around the annulus.

For this investigation, a swirl component of approximately 26 ft/sec in a 90-deg segment, as illustrated in Fig. 12, was induced at the same boundary where the rotating screen had been placed in the earlier investigation.

Illustrated in Fig. 13 are steady solutions at a constant mass flow rate of 210 lbm/s with co-rotation and counter-rotation swirl of the same magnitude and in the same physical location. This particular flow point represents a compressor operating point at 100 percent corrected speed at somewhat of a benign condition (i.e., away from stall and away from choke). As was expected counter-rotation produced a more highly loaded blade.

To understand these findings, a more detailed analysis across the bladed region was performed. The swirl component of the flow field as presented in Fig. 14 can be analyzed to gain insight into the effects of the swirl on performance.

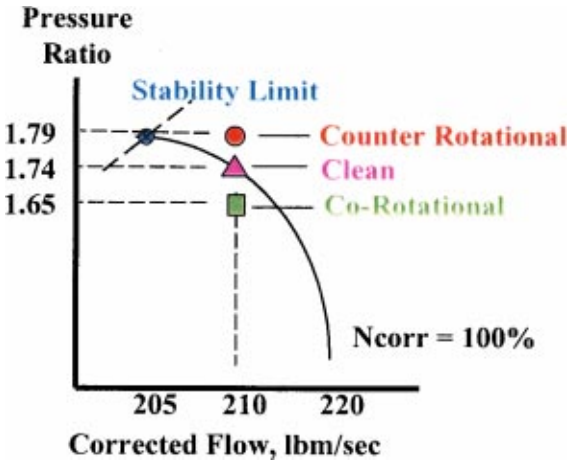

Fig. 13 Comparison of blade overall performance with swirl at a constant airflow rate

As was expected, the swirl component is attenuated as it passes through the rotor. For both the co-rotation and counter-rotation cases, the swirl becomes positive after passing through the rotor. However, for the counter-rotation case, the swirl component is smaller than the co-rotation in the vicinity of the implementation, which translated to higher pressure, and temperature rises in that area as illustrated in Fig. 15.

Although these results were obtained for a fairly benign operating point, one can infer the effect on a point nearer to the stability limit. Counter-rotating swirl does indeed increase the loading on the blade and is most pronounced in the tip region. If the tip proves to be the area where stall inception takes place, a likely scenario for many of today's transonic fans, stall can occur at a lower flow rate than for a clean inlet. On the other hand, co-rotation will unload the tip and may enhance the system's stability margin. Since the swirl is attenuated as it passes the first rotor, the effect on other rotors will be less pronounced. Thus, for a multi-stage fan, swirl will have its most impact on the first stage. Much of the effect of swirl will be taken out by the use of inlet guide vanes.

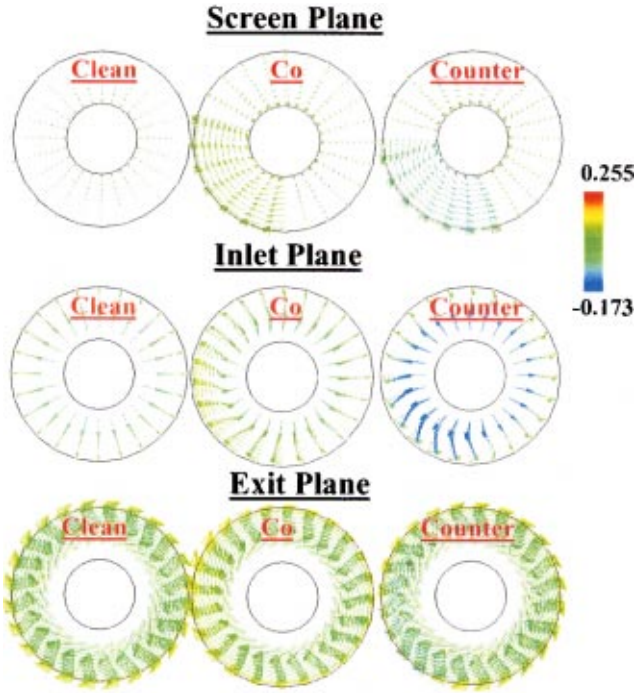

Fig. 14 Comparison of flowfield swirl before and after the rotor against the clean inlet for both co and counter-rotation swirl

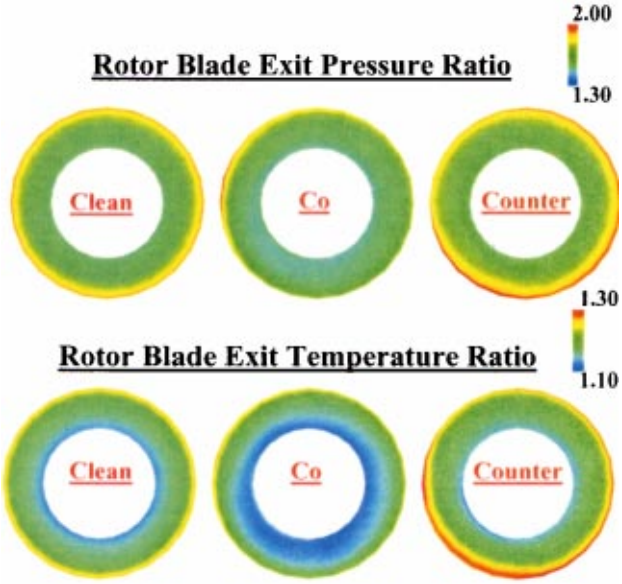

Fig. 15 Comparison of blade performance with co and counter-rotation present

What Does This All Mean? With the presence of swirl combined with total pressure distortion, the compression system may be subjected to a more severe problem than either phenomenon acting by itself. If the swirl is in a direction opposite to that of the compressor rotation, the swirl can load the fan and cause engine surge, even though the total pressure distortion is within perceived allowable limits. With the advent of S-shaped inlets, twin engine installations may display what is called a ''handed'' behavior. That is, engine performance and stability will depend on whether the bulk swirl is in the direction of or opposite to that of rotor rotation. In that situation, one engine may consistently surge during a particular maneuver, while the other engine remains stable. This phenomenon may also appear in a single engine installation, when the aircraft yaws to one side or the other.

Current Activities Toward Development of Test Hardware

AEDC has embarked on efforts to develop inlet simulator technologies directed toward future airframe-propulsion integration requirements. Currently, a transient total pressure distortion generator is in the concept development phase. Initial experiments have been completed to define the distortion developed by elements of the generator. Concepts have been identified for the simulation of bulk and local swirl. Efforts are underway to identify concepts for total temperature distortion generators. The inlet simulator development effort considers seven overall issues:

1 reduction of test cost and cycle time;
2 the evolution of advanced inlet systems;
3 the implementation of supermaneuverability;
4 in-flight weapon launches in aircraft featuring supercruise and stealth capabilities;
5 V/STOL aircraft operations in ground effect;
6 the advent of engines employing light-weight and highly loaded compressor stages; and
7 engine performance enhancement through surge margin reduction or active stall control.

Each of these issues demands advancements in the simulation of inlet distortion in the direct-connect test. Furthermore, planning

includes provisions for devices that will simulate distortion parameters of interest in the area of aeromechanics.

Summary

This paper has reviewed the state-of-the-art in engine inlet distortion testing procedures and an investigation into the potential effects of dynamic distortion and swirl on compression system stability was conducted to develop advocacy for enhancing the current distortion testing methodology. The S-16 committee of the Society of Automotive Engineers (SAE) is currently developing a recommended practice that deals with the effects of swirl on system behavior. The numerical investigation reported in this paper supports the experimental observations within the draft S-16 document on swirl and reported in references [13] and [14]. The dynamic distortion investigation produced results that are similar to that obtained by experimental means and reported in reference [12]. Further numerical investigations should now be conducted with a multi-stage compression system to verify the trends that have been observed during this investigation.

References

[1] SAE Aerospace Recommended Practice, 1978, ARP-1420, ''Gas Turbine Engine Inlet Flow Distortion Guidelines,'' Mar.

[2] SAE Aerospace Information Report, 1983, AIR-1419, ''Inlet Total-Pressure Distortion Considerations for Gas Turbine Engines,'' May.

[3] Davis, M. W., Jr., et al. 1999, ''A Proposal for Integration of Wind Tunnel and Engine Test Programs for the Evaluation of Airframe-Propulsion Compatibility Using Numerical Simulations,'' ASME Paper No. 99-GT-345.

[4] Overall, B. W., 1976, ''Evaluation of an Airjet Distortion Generator Used to Produce Steady-State Total-pressure Distortion at the Inlet of Turbine Engines,'' AEDC-TR-76-141.

[5] Brimelow, B., Collins, T. P., and G. A. Pfefferkorn, 1976, ''Engine Testing in a Dynamic Environment,'' AIAA Paper No. 74-1198.

[6] Lazalier, G. R., and J. T. Tate, 1970, ''Development of a Prototype Discrete Frequency, Total-pressure Fluctuation Generator for Jet Engine/Inlet Compatibility Investigation,'' Proc. Air Force Airframe Propulsion Compatibility Symposium, AFAPL-TR-69-103.

[7] Reynolds, G. G., et al., 1973, ''An Experimental Evaluation of Unsteady Flow Effects on an Axial Compressor—P^3 Generator Program,'' AFAPL-TR-73-43, July.

[8] SAE S-16 Committee, 1995, ARD50026, ''A Current Assessment of Planer Waves,'' Society of Automotive Engineers.

[9] Hale, A. A., and O'Brien, W. F., 1998, ''A Three-Dimensional Turbine Engine Analysis Compressor Code (TEACC) for Steady-State Inlet Distortion,'' ASME J. Turbomach., **120**, pp. 422–430.

[10] Hearsey, R. M., 1970, ''HTO300—A Computer Program for the Design and Analysis of Axial Turbomachinery.''

[11] Seyler, D. R., and Gestolow, J. P., 1967, ''Single Stage Experimental Evaluation of High Mach Number Compressor Rotor Blading—Part 2: Performance of Rotor 1B,'' NASA-CR-54582.

[12] Longley, J. P., et al., 1994, ''Effects of Rotating Inlet Distortion on Multistage Compressor Stability,'' ASME Paper 94-GT-220.

[13] Stocks, C. P., and Bissinger, N. C., 1981, ''The Design and Development of the Tornado Engine Air Intake,'' Paper No. 10 of AGARD CP-301.

[14] Ludwig, G., 1989, ''Tomahawk Engine/Inlet Compatibility Study for F107-WR-400/402 Engines,'' Williams International Report CMEP 5003-2025.

Mohammad Al-Qahtani

Yong-Jun Jang
Turbine Heat Transfer Laboratory,
Department of Mechanical Engineering,
Texas A&M University,
College Station, TX 77843

Hamn-Ching Chen
Ocean Engineering Program,
Department of Civil Engineering,
Texas A&M University,
College Station, TX 77843

Je-Chin Han
Turbine Heat Transfer Laboratory,
Department of Mechanical Engineering,
Texas A&M University,
College Station, TX 77843

Prediction of Flow and Heat Transfer in Rotating Two-Pass Rectangular Channels With 45-deg Rib Turbulators

Numerical predictions of three-dimensional flow and heat transfer are presented for a rotating two-pass rectangular channel with 45-deg rib turbulators and channel aspect ratio of 2:1. The rib height-to-hydraulic diameter ratio (e/D_h) is 0.094 and the rib-pitch-to-height ratio (P/e) is 10. Two channel orientations are studied: $\beta=90$ deg and 135 deg, corresponding to the mid-portion and the trailing edge regions of a turbine blade, respectively. The focus of this study is twofold; namely, to investigate the effect of the channel aspect ratio and the channel orientation on the nature of the flow and heat transfer enhancement. A multi-block Reynolds-averaged Navier-Stokes (RANS) method was employed in conjunction with a near-wall second-moment turbulence closure. In the present method, the convective transport equations for momentum, energy, and turbulence quantities are solved in curvilinear, body-fitted coordinates using the finite-analytic method. The numerical results compare reasonably well with experimental data for both stationary and rotating rectangular channels with rib turbulators at Reynolds number (Re) of 10,000, rotation number (Ro) of 0.11 and inlet coolant-to-wall density ratio ($\Delta\rho/\rho$) of 0.115. [DOI: 10.1115/1.1450568]

Introduction

Modern gas turbine blades are designed to operate at increasingly higher inlet temperatures to improve thermal efficiency. To maintain acceptable blade life, sophisticated cooling techniques such as film cooling, impingement cooling and convective internal cooling are essential. Rotation of turbine blade cooling passages gives rise to Coriolis and buoyancy forces that can significantly alter the local heat transfer in the internal coolant passages due to the development of cross stream (Coriolis) as well as radial (buoyant) secondary flows. Moreover, the heat transfer augmentation is usually achieved by using repeated ribs as turbulence promoters. The presence of these ribs leads to further complex flow fields such as flow separation, reattachment and secondary flow between the ribs, which produces a high turbulence level that leads to high heat transfer coefficients. The complex coupling of the Coriolis and buoyancy forces with flow separation/reattachment by ribs has prompted many investigators to study the flow and temperature fields generated in heated, rotating ribbed wall passages. Experimental studies on rib-roughened channels have been quite extensive (see Han and Park [1]; Ekkad and Han, [2] (for nonrotating channels); and Wagner et al., [3]; Johnson et al. [4,5]; Parsons et al. [6]; and Zhang et al. [7], (for rotating square channels with normal and angled ribs). Dutta and Han [8] investigated the local heat transfer coefficients in rotating smooth and ribbed two-pass square channels with three channel orientations. They found that a change in the channel orientation about the rotating frame causes a change in the secondary flow structure and the associated flow and turbulence distribution. Consequently, the heat transfer coefficient from the individual surfaces changes. Parson et al. [6] studied the effects of the model orientation on the local heat transfer coefficients in a rotating two-pass square channel with ribbed walls. They found that the effect of the Coriolis force and cross-stream flow were reduced as the channel orientation changes from the 90 to 135-deg orientation. Recently, Azad et al. [9] studied the effect of the channel orientation ($\beta=90$ and 135 deg from the direction of rotation) on two-pass rectangular channels for both smooth and 45-deg ribbed walls. For the smooth wall case, they found that the Nusselt number ratios for the first pass trailing and second pass leading surfaces with $\beta=135$ deg are lower than those with $\beta=90$ deg. Whereas, the Nusselt number ratios in the first pass leading and second pass trailing are higher compared to those with 90 deg. However, for the ribbed wall case, the channel orientation effect was less sensitive compared to the smooth wall case. Their study provided a data basis for the present work.

The earlier computational studies on internal coolant passages with ribs have mostly been restricted to two-dimensional flows (Liou et al. [10]). In recent years, a number of researchers have reported three-dimensional studies. Stephens et al. [11] and Rigby et al. [12], using a low-Reynolds number k-ω turbulence model, presented the numerical simulations for flow and heat transfer in a nonrotating straight duct with normal 90-deg ribs. Stephens et al. [13] investigated flow and heat transfer characteristics in a straight nonrotating duct with angled, rounded ribs on two opposite walls and provided important characteristics on the angled rib ducts (k-ω turbulence model). Stephens and Shih [14] and Shih et al. [15] investigated the effect of angled ribs on the heat transfer coefficients in a rotating two-passage duct using a low-Re number k-ω turbulence model. They studied the effects of Reynolds numbers, rotation numbers, and buoyancy parameters. Their comparison with Johnson's et al. [4] data revealed that the heat transfer coefficient was underpredicted for the stationary case. However, the results for the rotating case were not clearly verified.

Prakash and Zerkle [16], employing a high Reynolds number k-ε turbulence model with wall function, performed a numerical prediction of flow and heat transfer in a ribbed rectangular duct (90-deg rib) with and without rotation. However, their calculations used periodicity and neglected buoyancy effects. They suggested that a low Reynolds number model is necessary to simulate real gas turbine engine conditions and a Reynolds stress model is required to capture anisotropic effects. Bonhoff et al. [17] calculated

Contributed by the International Gas Turbine Institute and presented at the International Gas Turbine and Aeroengine Congress and Exhibition, New Orleans, Louisiana, June 4–7, 2001. Manuscript received by the IGTI, January 19, 2001. Paper No. 2001-GT-187. Review Chair: R. Natole.

the heat transfer coefficients and flow fields for rotating U-shaped coolant channels with angled ribs (45 deg). They used a Reynolds stress turbulence model with wall functions in the FLUENT CFD code. Their results show that the Nusselt number ratios of the rotating first pass leading and trailing surfaces are underpredicted compared to the experimental data. Using the periodicity of the flow, Iacovides [18] computed flow and temperature fields in a rotating straight duct with normal ribs. Two zonal models of turbulence were tested: a k-ε with a 1-equation model of k transport across the near-wall region and a low-Re differential stress model (DSM). He concluded that the DSM thermal computations were clearly superior to those of the k-ε/1-equation. Rigby et al. [19] presented numerical prediction of flow and heat transfer in a rotating ribbed (90-deg rib) coolant passage with a 180-deg turn. The computation was performed using a k-ω turbulence model, and the heat transfer coefficient was overpredicted in the stationary case and underpredicted in the rotating case compared to experimental data. Iacovides and Raisee [20] explored turbulence modeling issues related to the computation of flow and heat transfer in internal cooling passages of turbine blades with normal ribs (90 deg). They tested four turbulence models: a zonal k-ε, a low-Re k-ε, a zonal differential stress model (DSM), and a low-Re DSM. They found that zonal models underpredicted surface heat transfer coefficients because they ignored the effects of transport on the near-wall turbulence scale. The low-Re closures were found to reproduce the correct surface heat transfer coefficients. In their results, the low-Re DSM model reproduced the turbulence field more reasonably than the k-ε model.

Chen et al. [21,22] studied rotating two-pass square channel with smooth walls. They used two turbulence models: a two-layer k-ε isotropic eddy viscosity model and a near-wall second-moment closure model. The near-wall second-moment closure model produced accurate predictions in comparison with Wagner et al. [23] data. Using the same model, Jang et al. [24,25] studied flow and heat transfer behavior in a non-rotating two-pass square channel with 60-deg and 90-deg ribs, respectively. Their results were in good agreement with Ekkad and Han's [2] detailed heat transfer data which validated their code and demonstrated the second-moment closure model superiority in predicting flow and heat transfer characteristics in the ribbed duct. In a later study, Jang et al. [26] predicted flow and heat transfer in a rotating square channel with 45-deg angled ribs by the same second-moment closure model. Heat transfer coefficient prediction was well matched with Johnson et al. [4] data for both stationary and rotating case. This has affirmed the superiority of the second-moment closure model compared to simpler isotropic eddy viscosity turbulence models. This model solves each individual Reynolds stress component directly from their respective transport equation. The primary advantage of this model is that it resolves the near-wall flow all the way to the solid wall rather than using log-law assumption in the viscous sublayer. With this near-wall closure, surface data like heat transfer coefficients and friction coefficients can be evaluated directly from velocity and temperature gradient on the solid wall. In view of the success achieved in the earlier studies, it is desirable to extend the present second moment RANS method to study more sophisticated cooling channel configurations. Most of the previous studies investigated coolant channels that have square cross sections and are perpendicular to the axis of rotation. However, the orientation of the cooling channel in the leading and trailing edge regions of the turbine blade may be at an angle β from the direction of rotation and its cross section may not be square. It is not well known how this affects the flow field and heat transfer characteristics. In the present study, numerical predictions of the three-dimensional flow and heat transfer are presented for the rotating two-pass rectangular duct (aspect ratio is 2:1) with 45-deg angled ribs and 180-deg sharp turn are presented. Meanwhile, this study investigates the effects of the channel orientation ($\beta = 90$ and 135 deg) on the flow and heat transfer for the same geometry. In the present study, the

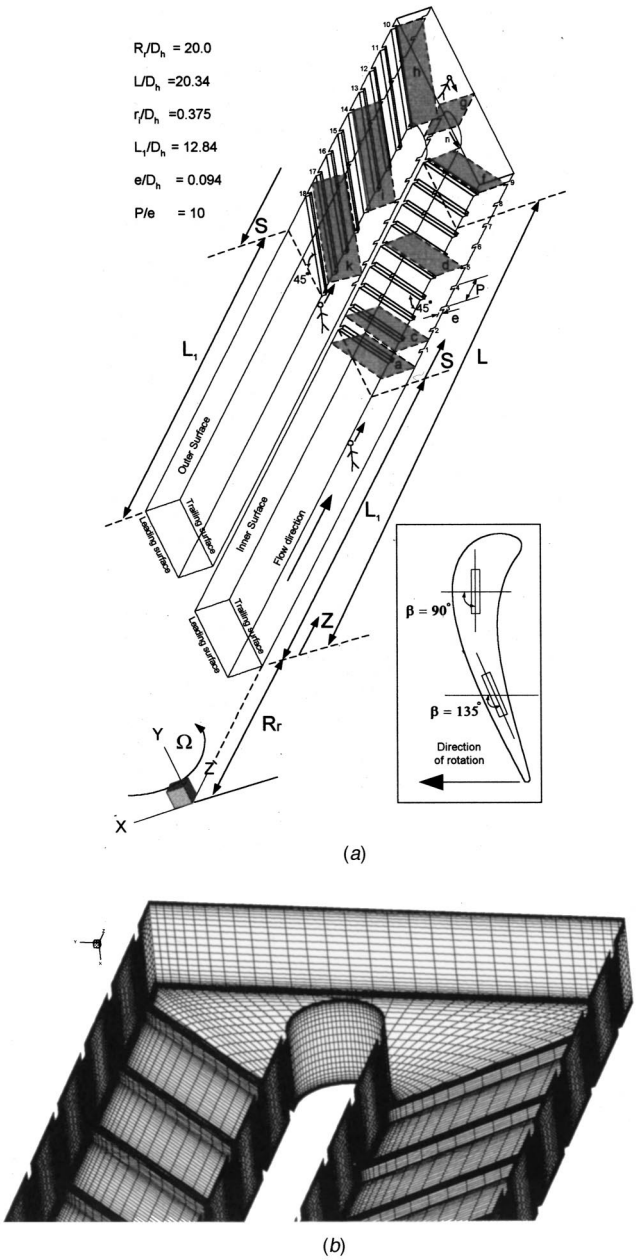

Fig. 1 (*a*) **Geometry,** (*b*) **numerical grid**

chimera RANS method of Chen et al. [21,22] was employed for the calculation of fluid flow and heat transfer in stationary and rotating ribbed channels. The numerical method and the governing equations of the turbulence model were described in detail by Chen et al. [21,22] and will not be repeated here.

Description of Problem

Calculation was performed for the two-pass rectangular channel with 45-deg ribbed walls as tested by Azad et al. [9]. The geometry and numerical grids around the sharp 180-deg turn are shown in Fig. 1. The axial stations (at which results are presented) and the way to view them are also shown in Fig. 1. The geometry consists of a U-shaped channel of rectangular cross section with channel aspect ratio of 2:1. The channel is made up of two straight passages and a 180-deg sharp turn. Two of the four side walls, in the rotational direction, are denoted as the leading and trailing surfaces, respectively, while the other two side walls are denoted

as the inner and outer surfaces. The channel hydraulic diameter, D_h, is 1.69 cm. The distance between the inlet of the duct and the axis of rotation (Y-axis) is given by $R_r/D_h=20.0$. The length of each of the first and second passages is given as $L/D_h=20.34$. Each passage consists of unheated smooth section and heated ribbed section. The length of the unheated smooth section is given by $L_1/D_h=12.84$. It extends from the inlet to the first rib in the first passage and from the exit to the last rib in the second passage. The arc length S is measured from the beginning of the ribbed section in the first passage (where heating starts) to the end of the ribbed section in the second passage (where heating ends). The radius of curvature of the 180-deg sharp turn is given as $r_i/D_h=0.375$. In the ribbed section, the leading and trailing surfaces for both the first and second passages are roughened with nine equally spaced ribs of square cross section. The rib height-to-hydraulic diameter ratio (e/D_h) is 0.094 and the rib-pitch-to-height ratio (P/e) is 10. All ribs are inclined at an angle $\alpha=45$ deg with respect to the flow. Two channel orientations are studied: $\beta=90$ deg corresponding to the midportion of a turbine blade and $\beta=135$ deg corresponding to the serpentine passages in the trailing edge region of a blade. In this study, the Reynolds number (Re) was fixed at 10,000. The inlet coolant-to-wall density ratio ($\Delta\rho/\rho$) was fixed at 0.115. Three cases were studied: 1) nonrotating channel (Ro=0.0), 2) rotating channel (Ro=0.11) with channel orientation angle, β, of 90 deg, and 3) rotating channel (Ro=0.11) with channel orientation angle, β, of 135 deg.

A uniform velocity profile was used at the inlet of the duct ($Z=0$). The unheated length (L_1) was long enough for the velocity profile to be fully developed turbulent profile before the heating start-point ($Z=L_1$). The flow was assumed to be parabolic at the exit of the duct (i.e., zero-gradient boundary conditions) for mean velocity and all turbulence quantities, while linear extrapolation was used for the pressure field. The coolant fluid at the inlet of the duct is air at uniform temperature $T=T_o$ (i.e., $\theta=(T-T_o)/(T_w-T_o)=0$). The wall temperature of the smooth section is kept constant at $T=T_o$ ($\theta=0$) while the wall temperature of the ribbed section, including the ribs, is kept constant at $T=T_w$ ($\theta=1$).

The Nusselt numbers presented here were normalized with a smooth tube correlation by Dittus-Boelter/McAdams (Rohsenow and Choi [27]) for the fully developed turbulent flow in a smooth stationary pipe

$$\mathrm{Nu}_o=0.023\,\mathrm{Re}^{0.8}\,\mathrm{Pr}^{0.4}$$

The present numerical grid was generated using an interactive gridding code GRIDGEN. It was divided into five overlapped Chimera grid blocks to facilitate the implementation of the near-wall turbulence model and the specification of boundary conditions. To provide adequate resolutions of the viscous sublayer and buffer layer adjacent to a solid surface, the minimum grid spacing in the near-wall region is maintained at 10^{-3} of the hydraulic diameter which corresponds to a wall coordinate y^+ of the order of 0.5. In all calculations, the root-mean-square (rms) and the maximum absolute errors for both the mean flow and turbulence quantities were monitored for each computational block to ensure complete convergence of the numerical solutions. A convergence criterion of 10^{-5} was used for the rms error.

The present grid uses $33\times41\times804$ grid points (804 in the streamwise direction and 33×41 in the cross-stream directions) with a total number of approximately 1,100,000 points. This choice is based on three systematic grid-refinement studies performed earlier for the prediction of flow and heat transfer in similar geometries. The geometry used in the first study (Jang et al. [25]) was a 90-deg ribbed two-pass square channel with nine ribs and a total grid points of 1,060,000 (Re=30,000). In the second study (Jang et al. [24]), a total of 1,020,000 grid points was used for a 60-deg ribbed two-pass square channel with nine ribs (Re=30,000). The total grid points in the third study (Jang et al. [26]) was 1,000,000 for a 45-deg ribbed one-pass square channel with 13 ribs (Re=25,000). The numerical grids used in these studies were shown to yield nearly grid-independent results. Also, their results were in close agreement with the experimental data. Note that the number of grid points used in the present rectangular configuration is comparable to the aforementioned geometries. In addition, the Reynolds number used in the present study (Re=10,000) is lower than the one used in the previous studies. Therefore, it is believed that the present grid will produce nearly grid-independent results with accurate resolution of the boundary layer profile and Nusselt number distribution.

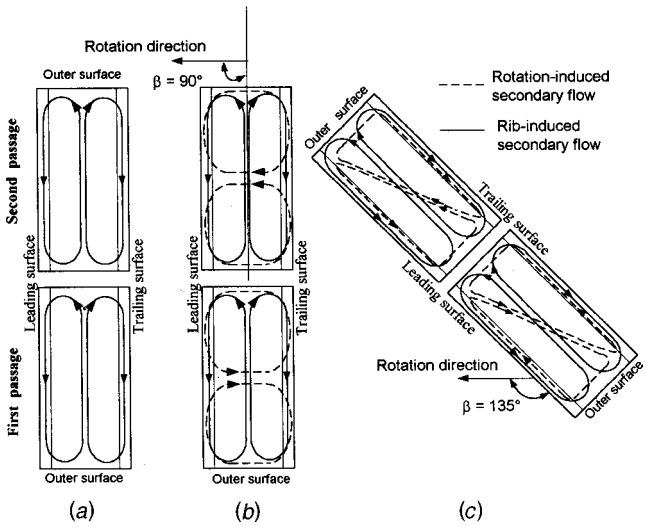

Fig. 2 Conceptual view of the secondary flow induced by angled ribs and rotation—(*a*) nonrotating, Ro=0, $\Delta\rho/\rho=0.115$; (*b*) rotating, Ro=0.11, $\Delta\rho/\rho=0.115$, $\beta=90$ deg; (*c*) rotating, Ro=0.11, $\Delta\rho/\rho=0.115$, $\beta=135$ deg

Results

This section presents the three-dimensional mean flow and temperature fields for the rotating rectangular duct with 45-deg angled ribs. Computations were performed for nonrotating (Ro=0.0) and rotating (Ro=0.11) cases with two channel orientations of $\beta=90$ and 135 deg at a Reynolds number of 10,000 and an inlet coolant-to-wall density ratio of 0.115.

Velocity and Temperature Fields. Before discussing the detailed computed velocity field, a general conceptual view about the secondary flow patterns induced by angled ribs and rotation is summarized and sketched in Fig. 2. The parallel angled ribs in the nonrotating duct (case 1, Fig. 2(*a*)) produce symmetric counter rotating vortices that impinge on the inner surface in the first passage and on the outer surface in the second passage. The Coriolis force in the 90-deg rotating duct (case 2, Fig. 2(*b*)) produces two additional counter-rotating vortices that push the cooler fluid from the core to the trailing surface in the first passage, and to the leading surface in the second passage. For the 135-deg rotating duct (case 3, Fig. 2(*c*)), the Coriolis force produces secondary flow that migrates diagonally away from the corner of the inner-leading surfaces toward the center of the channel in the first passage, and from the corner of the inner-trailing surfaces towards the center of the channel in the second passage.

For a nonrotating duct (case 1), Fig. 3 is a plot of the secondary flow in the inter-rib regions on a plane parallel to the leading and trailing surfaces and 1/10 rib height away from any of them. The 45-deg inclined ribs in the first passage (Fig. 3(*a*)) induce fast secondary flow that moves parallel to the ribs from the inner surface (where it is strongest) to the outer surfaces (where it is weakest). The situation is reversed in the second passage (Fig. 3(*b*)). The ribs induce secondary flow from the outer surface (where it is strongest) to the inner surface (where it is weakest). Note that this secondary flow pattern is the same in all inter-rib areas. The consequence of this fast secondary flow is explained in Fig. 4.

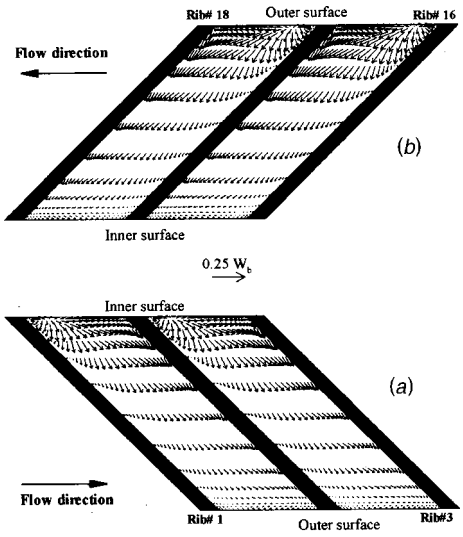

Fig. 3 Velocity vectors 1/10 rib height from the leading and trailing surfaces for nonrotating case (plotted every other vector)—(*a*) first pass, (*b*) second pass

Figure 4 is a plot of the calculated secondary flow vectors and constant temperature contours for the nonrotating case at several axial stations as shown in Figure 1. Figs. 4(*a*) through 4(*f*) (first passage) are viewed from upstream of the first passage, while Figures 4(*g*) through 4(*l*) (middle of the bend and second passage) are viewed from downstream of the second passage. The secondary flow field will be discussed first and then its effect on the temperature field. In the first passage, and as the fluid approaches the first rib (Fig. 4(*a*)), the rib-induced fast secondary flow discussed in Fig. 3(*a*) moves towards the outer surface and returns back to the inner surface along the centerline of the inclined cross-stream plane. In the same figure, one can also notice the early stages of two symmetric counter-rotating vortices, which shrink in size on the first rib (Fig. 4(*b*)), and by the midsection of ribs 1 and 2 (Fig. 4(*c*)) become two full symmetric counter-rotating vortices. Along the streamwise direction, the size of these two vortices oscillate from the largest in the middle of each inter-rib distance to the smallest on the ribs (Fig. 4(*d*)). This pattern keeps repeating until rib 8. However, midway between ribs 8 and 9 (Fig. 4(*e*)) the strength of those two vortices shifts towards the inner surface. On rib 9 (Fig. 4(*f*)), the secondary flow becomes a strong fluid motion from the outer to the inner surface due to the turn effects.

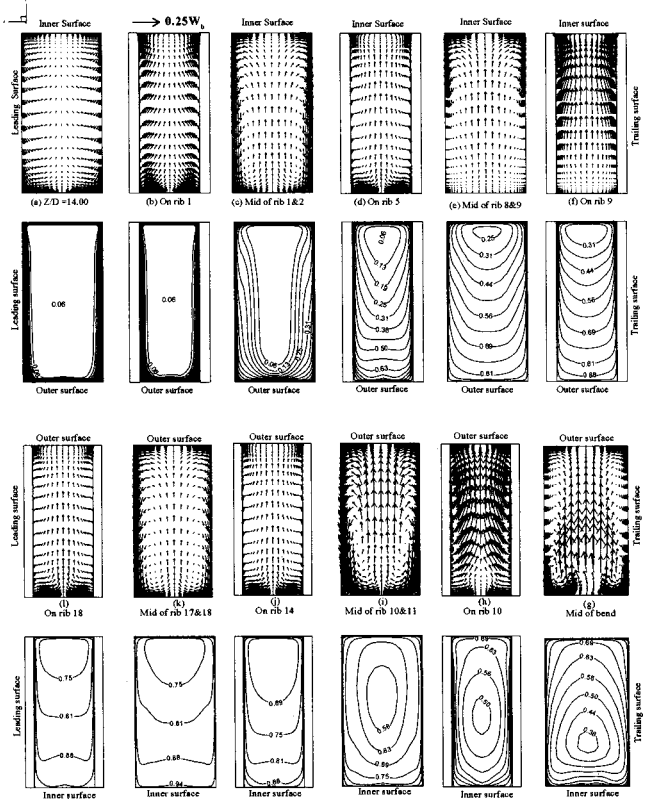

Fig. 4 Secondary flow and temperature $[\theta=(T-T_o)/(T_w-T_o)]$ for nonrotating duct, Ro=0.0

Upon entering the turn, the curvature induced secondary flow (which pushes fluid from the inner to outer surface) overcomes the rib induced secondary flow discussed in Fig. 4(*f*), and the direction of the secondary flow is reversed and becomes from the inner to outer surface. This happens in less than one hydraulic diameter after the ninth rib. As the fluid proceeds towards the center of the turn, we notice the gradual formation of two counter-rotating vortices that reach their full size by the center of the turn (Fig. 4(*g*)). The size of these two vortices begin to decrease gradually as the fluid approaches the second sharp corner and soon is mixed with the second passage rib-induced secondary flow (Fig. 4(*h*)) resulting in a complex secondary flow. In the second passage and as discussed in Fig. 3(*b*), the rib-induced fast flow is reversed in direction due to the opposite rib angle compared to the first passage. Here, Fig. 4(*i*) the rib-induced secondary flow moves from the outer to the inner surfaces and returns back to the outer surface along the centerline of the inclined cross-stream. As a result, two symmetric counter-rotating vortices are formed. The size of these two vortices oscillate in size from the smallest on each rib (Fig. 4(*j*)) to the largest in the midsection between each two ribs (Fig. 4(*k*)). This pattern keeps repeating until rib 18 (Fig. 4(*l*)). Due to the absence of the ribs, the secondary flow decreases gradually after rib 18 and vanishes almost completely $7D_h$ after rib 18.

The overall effect of this secondary flow structure on the temperature field will be discussed here, referring to the temperature contour plots in Fig. 4. In the first passage, the effect of the secondary flow is convecting the cooler fluid from the inner surface and along the ribbed surfaces towards the outer surface. It then moves back to the inner surface, which results in steep temperature gradients and high heat transfer coefficients on both the inner and ribbed surfaces as seen in the corresponding temperature contours. In the middle of the turn, the two counter-rotating vortices convect fluid from the core towards the outer surface, resulting in a steeper temperature gradient and thus a higher heat transfer coefficients on the outer surface. In the second passage, the secondary flow convects the cooler fluid from the outer surface and along the ribbed surfaces towards the inner surface. It then moves back to the outer surface resulting in steep temperature gradients and high heat transfer coefficients on both the outer and ribbed surfaces as seen in the corresponding temperature contours.

Figure 5 is a plot of the cross-stream velocity vectors and temperature contours for case 2 (Ro=0.11 and $\beta=90$ deg) at the same planes as in the nonrotating duct (case 1). A few hydraulic diameters before the first rib, the Coriolis force was found to produce two counter-rotating vortices that push the cooler fluid at the core towards the trailing surface and then returns along the inner and outer surfaces. As the flow approaches the first rib, this Coriolis force induced secondary flow starts to distort the secondary flow started by the inclined ribs. This effect can be clearly seen by comparing Figs. 5(*a*) through (*f*) with Figs. 4(*c*) through (*f*). From this comparison, the following conclusions can be drawn. The magnitude of the Coriolis force induced secondary flow is weaker than the rib induced secondary flow. In the midsections of each of two ribs, the rib-induced vortex near the leading surface is weakened while the other vortex near the trailing

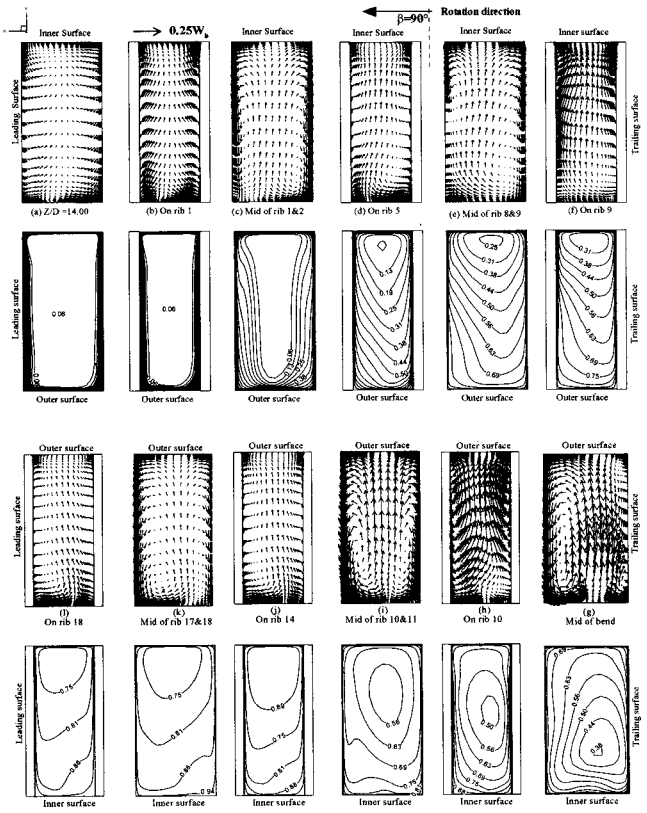

Fig. 5 Secondary flow and temperature $[\theta=(T-T_o)/(T_w-T_o)]$ for rotating duct, Ro=0.11 and $\beta=90$ deg

surface is strengthened (Fig. 5(*c*)). This pattern repeats itself until midway between ribs 8 and 9 (Fig. 5(*e*)), where the larger vortex near the trailing surface grows at the expense of the smaller vortex near the leading surface, which shrinks in size and moves toward the inner surface. On the ribs (Fig. 5(*d*)), both vortices shrink in size and get distorted significantly by the Coriolis force-induced secondary flow. This pattern repeats itself until rib 9, where the turn effect alters significantly the secondary flow structure, as seen in Fig. 5(*f*).

The general effect of the Coriolis force-induced secondary flow in the first passage is to distort the rib induced vortices. Consequently, the temperature contours are shifted toward the trailing surface, which affects the heat transfer coefficients from both the leading and trailing surfaces as seen from the corresponding temperature contour plot. Notice that, in the turn (Fig. 5(*g*)), the vortex near the leading surface grew considerably at the expense of the one next to the trailing surface, which was weakened and split into two small vortices near the two corners of the trailing surface. This results in pushing the cold fluid toward the outer and trailing surfaces as seen in the corresponding contour plot. This effect dominates until rib 10, which is the first rib in the second passage (Fig. 5(*h*)). After rib 11, the Coriolis force induced secondary flow (which pushes the cold fluid towards the leading surface) gradually overcomes the turn induced secondary flow (which pushes the cold fluid toward the trailing surface). This is shown clearly in the temperature contour plots of Figs. 5(*g*) through (*l*).

Figure 6 is a plot of the cross-stream velocity vectors and temperature contours for case 3 (Ro=0.11 and $\beta=135$ deg) at the same planes as in the rotating case. The discussion of this figure is based on comparing Fig. 6 (case 3: Ro=0.11 and $\beta=135$ deg) and Fig. 5 (case 2: Ro=0.11 and $\beta=90$ deg). A few hydraulic diameters before the first rib, the Coriolis force produces secondary flow that migrates diagonally away from the corner of the inner-leading surfaces toward the center of the channel. As the

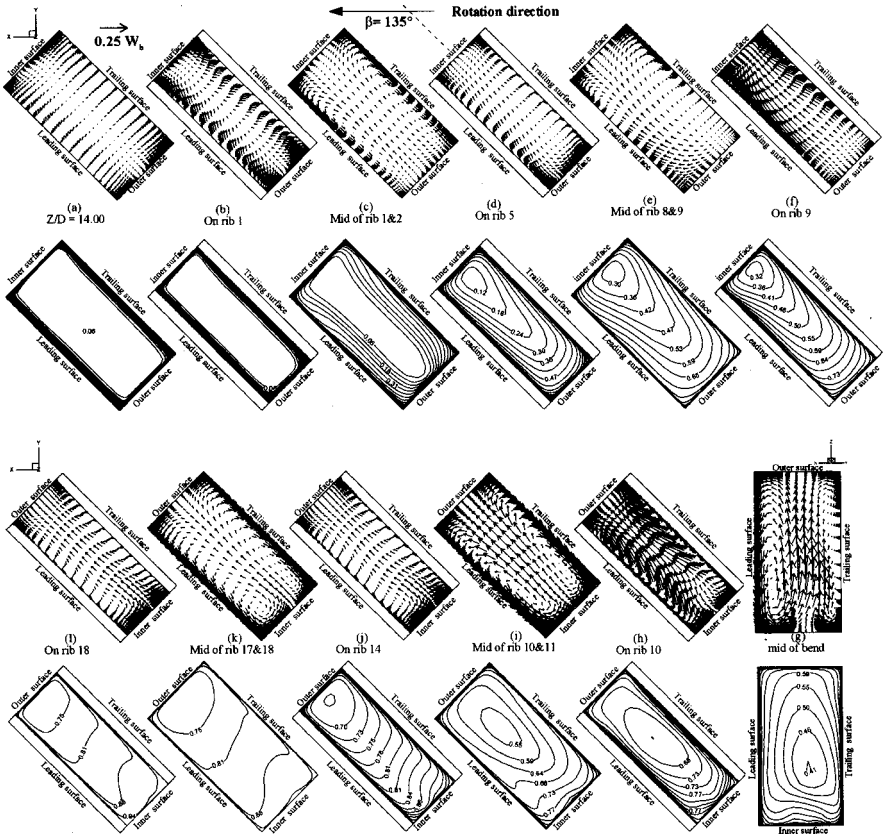

Fig. 6 Secondary flow and temperature $[\theta=(T-T_o)/(T_w-T_o)]$ for rotating duct, Ro=0.11 and $\beta=135$ deg

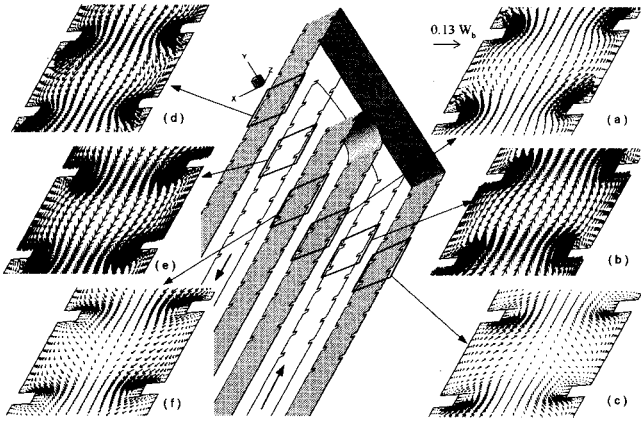

Fig. 7 Streamwise velocity vector distribution for nonrotating duct (case 1) at three planes: $0.002D_h$ below the inner surface, midway between the inner and outer surfaces and $0.002D_h$ above the outer surface

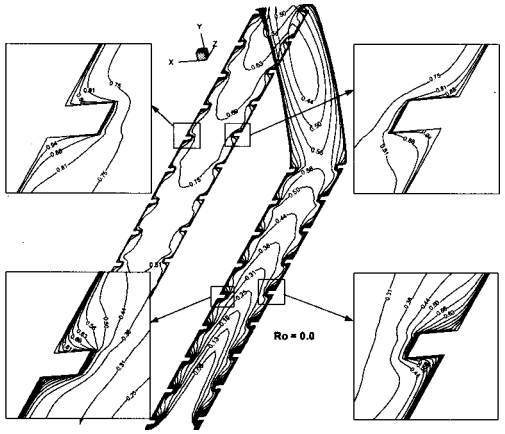

Fig. 8 Temperature contours midway between the inner and outer surfaces for case 1 (Ro=0.0)

flow approaches the first rib, this Coriolis force-induced secondary flow distorts the secondary flow started by the inclined ribs. This effect can be clearly seen by comparing Fig. 6(*a*) with Fig. 5(*a*). However, from rib 1 on, this rotation induced secondary flow is dominated by the rib-induced secondary flow. A careful comparison between the secondary flow fields of case 3 and case 2 (e.g., Fig. 6(*d*) with Fig. 5(*d*)) shows that the rotation induced secondary flow in case 3 ($\beta=135$ deg) changes the rib induced secondary flow compared to case 2($\beta=90$ deg). This change appears more clearly in the temperature field. By comparing the temperature contours in Fig. 6 (Ro=0.11 and $\beta=135$ deg) with Fig. 5 (Ro=0.11 and $\beta=90$ deg), we notice the following. In the first passage, the cooler fluid is pushed back toward the leading surface, reducing the steep temperature gradients on the trailing surface. The temperature contours do not change much in the bend (Fig. 6(*g*)). In the beginning of the second passage (Fig. 6(*h*)), the cooler fluid is pushed back slightly toward the leading surface, while the temperature field in the rest of the second passage is the same as in case 2.

Figure 7 is a plot of the streamwise velocity vector distribution for the nonrotating duct (case 1) at three planes: $0.002D_h$ below the inner surface, midway between the inner and outer surfaces, and $0.002D_h$ above the outer surface. A detailed investigation of the streamwise velocity field between the inner and outer surfaces revealed the following. In the first passage and near the inner surface (Fig. 7(*a*)), fairly large separation bubbles extend about 4 rib heights downstream of the rib followed by a reattachment region that separates once again about one rib height upstream of the next rib. The size of the separation bubble after the rib decreases as we move away from the inner surface (parallel to the rib), and no reattachment is found once we reach the midplane between the inner and outer surfaces (Fig. 7(*b*)). Moving further toward the outer surface, the flow separation resumes occurring only on top of the rib (Fig. 7(*c*)). The flow is able to reattach near the inner surface because the secondary flow boundary layer in this region is very thin. As we move toward the outer surface, the secondary flow boundary layer gets thicker. Hence, the mainstream flow can not reattach in these regions. In the second passage, the large separation bubbles are formed near the outer surface (Fig. 7(*d*)). The separation region extends to about 3.79 rib heights after the rib, followed by a reattachment region that separates again about one rib height before the next rib. Moving towards the inner surface, the size of the separation bubble decreases until no reattachment is found midway between the outer and inner surfaces (Fig. 7(*e*)). Separation resumes upon approaching the inner surface (Fig. 7(*f*)) and occurs only on the rib top. Moreover, in the first passage, velocity magnitude near the inner surface (Fig. 7(*a*)) is larger than the one near the outer surface (Fig. 7(*a*)). The reason is that the rib-induced secondary flow near the inner surface is much stronger than the one near the outer surface. For the same reason mentioned above; the second passage velocity magnitude near the outer surface (Fig. 7(*d*)) is larger than the one near the inner surface (Fig. 7(*f*)). It should be mentioned that in this figure, the apparent nonsymmetric velocity field between the leading and trailing sides is a result of the angled 3-D view. This was confirmed by orthogonal 2-D views (not shown).

Figure 8 shows the temperature contours for the nonrotating case midway between the inner and outer surfaces for the whole duct. In the first passage, a thin thermal boundary layer forms first near the leading and trailing surfaces. However, the periodic ribs disturb and break the viscous sublayer and create high level of turbulence in the near-wall region. The steeper temperature gradients can be seen on the rib tip (due to flow impingement) and between the two adjacent ribs (due to flow reattachment), but the smaller temperature gradients are found right before and after the rib (due to a separation bubble). A much higher temperature exists in the second passage due to the thermal boundary layer thickening.

Detailed Local Heat Transfer Coefficient Distribution. Figure 9(*a*) is a plot of the local Nusselt number ratio contours on both the leading and trailing surfaces for the nonrotating case. The entrance and exit regions were cut to focus on the ribs and turn effects. The highest Nusselt number ratios were obtained on the top of the ribs, and the lower Nusselt number ratios were obtained right before and after the ribs for the first and second passages, respectively. Between any two ribs in the first passage, the Nusselt number ratios are highest near the inner surface and decrease as we move towards the outer surface. This is due to the rib-induced secondary flow moving from the rib leading to the trailing side as shown in Fig. 3(*a*). Moreover, the Nusselt number ratios between the ribs increased gradually along the first passage until the flow approaches the seventh rib, where it decreases gradually until the ninth rib. Nusselt number ratios in the turn are higher in the region next to the divider wall tip while lower at the first corner. In the second passage (between any two ribs), the Nusselt number ratios are higher near the outer surface and decrease as we move toward the inner surface. Again, this is a result of the rib-induced secondary flow in the second passage shown in Fig. 3(*b*).

Figures 9(*b*) and (*c*) show the Nusselt number ratio contours on the leading side for case 2 (Ro=0.11 and $\beta=90$ deg) and case 3 (Ro=0.11 and $\beta=135$ deg), respectively. Comparing these figures with the nonrotating leading side (Fig. 9(*a*)), we notice that the Nusselt number ratios decrease in the first passage, in both

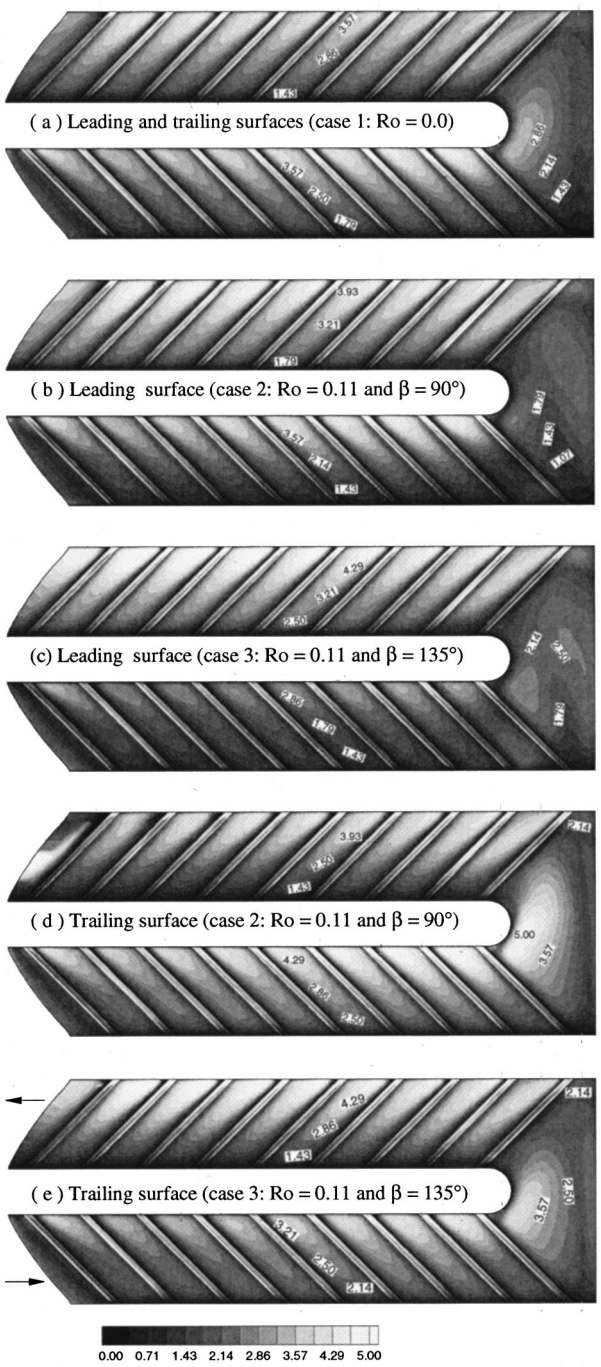

Fig. 9 Detailed Nusselt number ratio distribution

cases, with the decrease in case 3 being higher. In the second passage, the Nusselt number ratios in both cases increase with respect to case 1.

Figures 9(*d*) and (*e*) show the Nusselt number ratios contours on the trailing surface for case 2 (Ro=0.11 and β=90 deg) and case 3 (Ro=0.11 and β=135 deg), respectively. Comparing these figures with the nonrotating trailing side (Fig. 9(*a*)), we notice that the Nusselt number ratios increase in the first passage, for both cases, with the increase in case 2 being higher. In the second passage, the Nusselt number ratios in both cases decrease, with the decrease in case 2 being higher. The Nusselt number in the bend is much higher for both cases when compared to the nonrotating case.

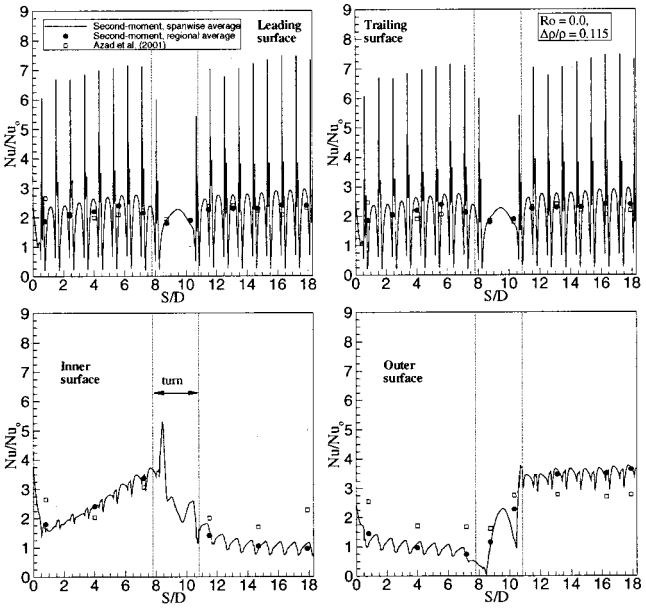

Fig. 10 Calculated and measured Nusselt number ratios; Ro =0.0, $\Delta\rho/\rho$=0.115

Spanwise-Averaged and Regional-Averaged Heat Transfer Coefficients and Comparison With Experimental Data. Comparisons were made with the experimental data of Azad et al. [9] in order to provide a thorough evaluation of the present second moment closure model. Figures 10 through 12 are plots of the spanwise-averaged and regional-averaged Nusselt number ratios (Nu/Nu_o) for each of the three cases (Ro=0.0, Ro=0.11 (β =90 deg), and Ro=0.11 (β=135 deg)). The Reynolds number and the inlet coolant-to-wall density ratio were held constant at values of 10,000, and 0.115, respectively. Note that the experimental regional-averaged Nusselt number in Azad et al. [9] is based on the projected area of each copper plate rather than the true heat transfer surface area which includes the 45-deg rib-increased area. However, the predicted regional-averaged Nusselt

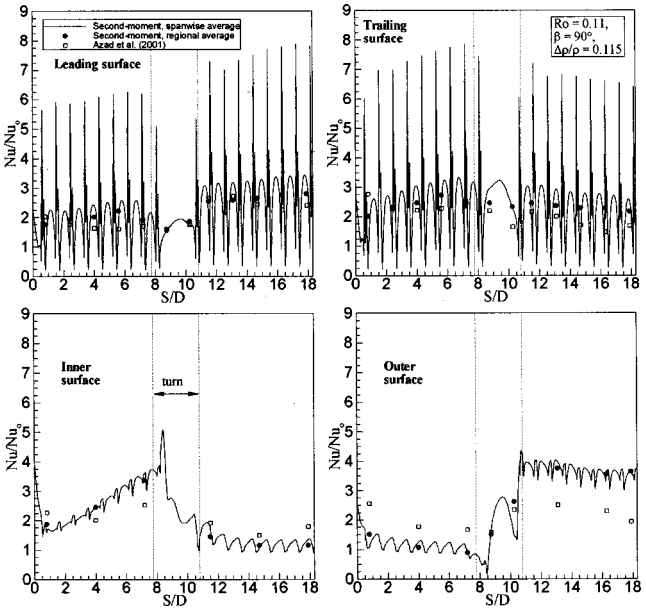

Fig. 11 Calculated and measured Nusselt number ratios; Ro =0.11, β=90 deg $\Delta\rho/\rho$=0.115

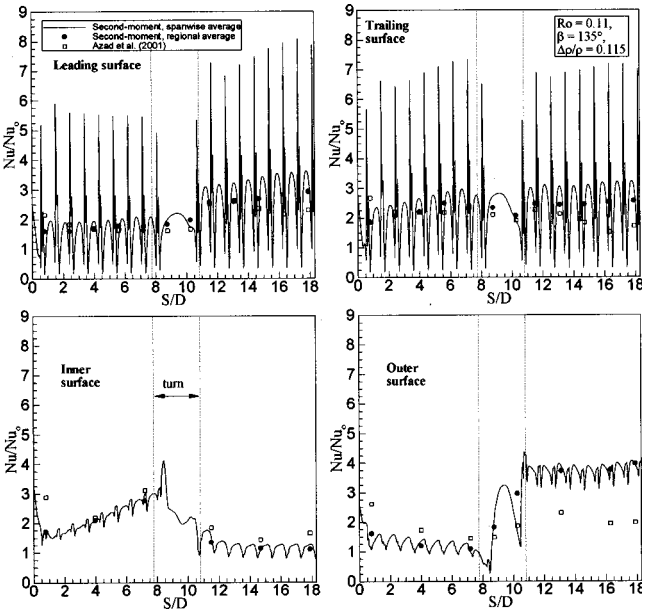

Fig. 12 Calculated and measured Nusselt number ratios; Ro $=0.11$, $\beta=135$ deg$\Delta\rho/\rho=0.115$

number is based on the true heat transfer area for the test surfaces with 45-deg ribs which is 1.25 times the projected area. Therefore, the experimental data were divided by 1.25 to reasonably compare with our regional-averaged Nusselt number, except for the inner and outer surfaces where there were no ribs.

In Fig. 10 (case 1), the spanwise-averaged Nusselt number distributions on the leading and trailing surfaces show periodic spikes. The higher spikes are caused by the flow impingement on the ribs, and the lower spikes are caused by the flow reattachment between the ribs. The Nusselt number ratios are lower just upstream and downstream of the ribs and higher in the regions between the ribs. The Nusselt number ratios increase until about the midsection between the seventh and eighth rib, which is similar to Jang's et al. [26] 45-deg-rib case in a square channel. This phenomenon is caused by the rib-induced secondary flow becoming stronger along the duct as discussed in Fig. 4 and also mentioned by Han and Park [1]. The Nusselt number distribution on the inner surface shows that (in the first passage) it increases all the way to rib 9 as a result of the secondary flow that pushes the cold fluid towards the inner surface. As was shown in Fig. 4, the direction of the secondary flow in the turn is reversed becoming from inner to outer surface, which results in sharp decrease of the Nusselt number on the inner wall. In the second passage, the Nusselt number values at the inner surface are low due to hot fluid coming from the outer and ribbed surfaces. For the same reasons discussed in the foregoing, the Nusselt number distribution on the outer surface is the opposite of the Nusselt number distribution on the inner surface.

Figure 11 (case 2: Ro $=0.11$, $\beta=90$ deg) shows that the heat transfer coefficients on the leading surface decreased approximately 8 percent in the first passage when compared to the stationary case, while increased approximately 14 percent in the second passage. The decrease and increase in heat transfer coefficients were due to the Coriolis force. On the trailing surface, the heat transfer increased approximately 12 percent in the first passage as compared to the stationary case while decreased by 5 percent in the rest of the second passage.

Figure 12 (Ro $=0.11$, $\beta=135$ deg) shows that the heat transfer coefficients on the leading surface decreased approximately 22 percent in the first passage when compared to the stationary case, while increased approximately 16 percent in the second passage. On the trailing surface, the heat transfer increased approximately 3 percent (in the first passage) and 7 percent (in the second passage) when compared to the stationary case. The reason why the Nusselt number ratios in case 3 ($\beta=135$ deg) decreased more in the first pass leading and trailing sides and increased more in the second pass leading and trailing sides compared to case 2 ($\beta=90$ deg) can be understood in light of the conceptual secondary flow diagram in Fig. 2.

The rotation-induced vortices in the 135-deg configuration move along the full face of the leading or trailing surfaces. However, the rotation induced vortices in the 90-deg configuration move along only one-half the face of the leading or trailing surfaces. With this in mind, we notice in Fig. 2 that the two secondary flows produced by rotation and angled ribs for the rotating 135-deg duct combine in the first passage to destructively (opposite direction) reduce heat transfer on both the leading surface (a 22-percent decrease compared to an 8 percent decrease in $\beta=90$ deg) and the trailing surface (a 3-percent increase compared to a 12-percent increase in $\beta=90$ deg). Moreover, they combine in the second passage to constructively (same direction) enhance heat transfer on both the leading surface (a 16-percent increase compared to a 14-percent increase in $\beta=90$ deg) and the trailing surface (a 7-percent increase compared to a 5-percent decrease in $\beta=90$ deg). On the other hand, the two secondary flows produced by rotation and angled ribs for the rotating 90-deg duct combine to (*i*) constructively (same direction) enhance heat transfer for only one half of each of the leading and trailing surfaces, and (*ii*) destructively (opposite direction) reduce heat transfer for the other half of each of the leading and trailing surfaces. The overall predicted Nusselt number behavior was relatively close to Azad et al. [9] data. However, the predicted Nusselt numbers on the outer surface and part of the trailing surface for the second-pass of the rotating case were overpredicted. This may be partly attributed to the fact that the predicted Nusselt number ratios are based on a uniform wall temperature boundary condition, while the experimental ones are based on a uniform wall heat flux boundary condition.

This computational study can be used to visualize the rib-induced, turn induced, and rotation induced secondary flows in the two-pass rectangular channels for both 90 and 135-deg orientations. This will help in designing better coolant passages which save coolant flow consumption and improve turbine efficiency. Moreover, this study reveals that the 135-deg orientation has a lower Nusselt number in the first pass leading and trailing sides compared to the 90-deg orientation. This should be taken into consideration by the internal cooling designer to prevent excessive heating should the design is based only on the 90-deg orientation assumptions.

Conclusions

A validated multi-block RANS method was employed to predict three-dimensional flow and heat transfer in a rotating two-pass rectangular channel (AR $=2:1$) roughened with 45-deg angled ribs on both the leading and trailing sides. Two channel orientations are studied: $\beta=90$ and 135-deg. The present near-wall second-moment closure model results were compared with the experimental data of Azad et al. [9]. It predicted fairly well the complex three-dimensional flow and heat transfer characteristics resulting from the angled ribs, sharp 180-deg turn, rotation, centrifugal buoyancy forces and channel orientation. The inclined ribs start two counter-rotating vortices that oscillate in size along the streamwise direction. For case 1, the secondary flow results in steep temperature gradients and high heat transfer coefficients on both the inner and ribbed surfaces (for the first passage) and on both the outer and ribbed surfaces (for the second passage). In the turn, the two counter-rotating vortices convect fluid from the core towards the outer surface, resulting in higher heat transfer coefficients on the outer surface. For case 2 ($\beta=90$ deg), rotation-induced cross-stream secondary flow distorts the rib-induced vortices and consequently, rotation shifts the temperature contours and affects the heat transfer coefficients from both the leading and

trailing surfaces. For case 3 ($\beta = 135$ deg), rotation-induced cross-stream secondary flow distorts the rib induced vortices. The rotation-induced vortices have more space (compared to case 2) either to combine constructively (same direction) or destructively (opposite direction) with the rib induced vortices and thus produce greater increase or decrease in the heat transfer coefficients.

Acknowledgments

The leading author, Mohammad Al-Qahtani, received a fellowship from King Fahd University; Saudi Arabia, for his Ph.D. study at Texas A&M University. This work was supported by the Texas Higher Education Coordination Board—Advanced Technology Program under grant number 999903-165. The computations were performed on the Cray J90 at the Texas A&M Supercomputer Center under a supercomputer research grant. The GRIDGEN software was supported by Pointwise Inc. The support of all of the above institutions is greatly appreciated.

Nomenclature

D_h, D = hydraulic diameter, m
e = rib height, m
h = heat transfer coefficient, W/m^2.K
k = thermal conductivity of coolant, W/m.K
Nu = local Nusselt number, hD/k
Nu_o = Nusselt number in fully developed turbulent nonrotating tube flow, hD/k
Pr = Prandtl number
Re = Reynolds number, $\rho W_b D_h/\mu$
r_i = inner radius of bend, m
Ro = rotation number, $\Omega D_h/W_b$
R_r = radius from axis of rotation, m
S = streamwise distance, m
T = local coolant temperature, SDC
T_o = coolant temperature at inlet, °C
T_w = wall temperature, °C
W_b = bulk velocity in streamwise direction, m/s
α = rib angle
β = angle of channel orientation measured from direction of rotation
ρ = density of coolant, kg/m^3
$\Delta\rho/\rho$ = inlet coolant-to-wall density ratio [based on ideal gas assumption], $(T_w - T_o)/T_w$
Ω = rotational speed, rad/s
θ = dimensionless temperature, $(T - T_o)/(T_w - T_o)$
μ = dynamic viscosity of coolant, N.s/m^2

References

[1] Han, J. C., and Park, J. S., 1988, ''Developing Heat Transfer in Rectangular Channel with Rib Turbulators,'' Int. J. Heat Mass Transf., **31**, No. 1, pp. 183–195.
[2] Ekkad, S. V., and Han, J. C., 1997, ''Detailed Heat Transfer Distributions in Two-pass square Channels with Rib Turbulators,'' Int. J. Heat Mass Transf., **40**, No. 11, pp. 2525–2537.
[3] Wagner, J. H., Johnson, B. V., Graziani, R. A., and Yeh, F. C., 1992, ''Heat Transfer in Rotating Serpentine Passages with Trips Normal to the Flow,'' ASME J. Turbomach., **114**, pp. 847–857.
[4] Johnson, B. V., Wagner, J. H., Steuber, G. D., and Yeh, F. C., 1994, ''Heat Transfer in Rotating serpentine Passage with Trips Skewed to the Flow,'' ASME J. Turbomach., **116**, pp. 113–123.
[5] Johnson, B. V., Wagner, J. H., Steuber, G. D., and Yeh, F. C., 1994, ''Heat Transfer in Rotating serpentine Passage with selected Model Orientations for Smooth or Skewed Trip Walls,'' ASME J. Turbomach., **116**, pp. 738–744.
[6] Parsons, J. A., Han, J. C., and Zhang, Y. M., 1995, ''Effects of Model Orientation and Wall Heating Condition on Local Heat Transfer in a Rotating Two-Pass Square Channel with Rib Turbulators,'' Int. J. Heat Mass Transf., **38**, No. 7, pp. 1151–1159.
[7] Zhang, Y. M., Han, J. C., Parsons, J. A., and Lee, C. P., 1995, ''Surface Heating Effect on Local Heat Transfer in a Rotating Two-pass Square Channel With 60 deg Angled Rib Turbulators,'' ASME J. Turbomach., **177**, pp. 272–280.
[8] Dutta, S., and Han, J. C., 1996, ''Local Heat Transfer in Rotating Smooth and Ribbed Two-Pass Square Channels with Three Channel Orientations,'' ASME J. Heat Transfer, **118**, pp. 578–584.
[9] Azad, GM S., Uddin, M. J., Han, J. C., Moon, H. K., and Glezer, B., 2001, ''Heat Transfer in Two-Pass Rectangular Rotating Channels with 45 deg Parallel and Crossed Rib Turbulators,'' submitted to the 2001 IGTI Conference to be held in New Orleans, LA.
[10] Liou, T. M., Hwang, J. J., and Chen, S. H., 1993, ''Simulation and Measurement of Enhanced Turbulent Heat Transfer in a Channel With Periodic Ribs on One Principal Wall,'' Int. J. Heat Mass Transf., **36**, pp. 507–517.
[11] Stephens, M. A., Shih, T. I-P., and Civinskas, K. C., 1995, ''Computation of Flow and Heat Transfer in a Rectangular Channel with Ribs,'' AIAA Paper 95-0180.
[12] Rigby, D. L., Steinthorsson, E., and Ameri, A. A., 1997, ''Numerical Prediction of Heat Transfer in a Channel with Ribs and Bleed,'' ASME Paper 97-GT-431.
[13] Stephens, M. A., Chyu, M. K., and Shih, T. I-P., 1996, ''Computation of Convective Heat Transfer in a Square Duct with Inclined Ribs of Rounded Cross Section,'' ASME Paper 96-WA/HT-12.
[14] Stephens, M. A., and Shih T. I-P., 1997, ''Computation of Compressible Flow and Heat Transfer in a Rotating Duct With Inclined Ribs a 180 deg Bend,'' ASME Paper 97-GT-192.
[15] Shih, T. I-P., Lin, Y.-L., Stephens, M. A., and Chyu, M. K., 1998, ''Flow and Heat Transfer in a Ribbed U-Duct under Typical Engine Conditions,'' ASME Paper 98-GT-213.
[16] Prakash, C., and Zerkle, R., 1995, ''Prediction of Turbulent Flow and Heat Transfer in a Ribbed Rectangular Duct With and Without Rotation,'' ASME J. Turbomach., **177**, pp. 255–264.
[17] Bonhoff, B., Tomm, U., Johnson, B. V., and Jennions, I., 1997, ''Heat Transfer Predictions For Rotating U-Shaped Coolant Channels With Skewed Ribs and with Smooth Walls,'' ASME 97-GT-162.
[18] Iacovides, H., 1998, ''Computation of Flow and Heat Transfer Through Rotating Ribbed Passage,'' Int. J. Heat Fluid Flow, **19**, pp. 393–400.
[19] Rigby, D. L., 1998, ''Prediction of Heat and Mass Transfer in a Rotating Ribbed Coolant Passage with a 180 Degree Turn,'' ASME Paper 98-GT-329.
[20] Iacovides, H., and Raisee, M., 1999, ''Recent Progress in the Computation of Flow and Heat Transfer in Internal Cooling Passages of Turbine Blades,'' Int. J. Heat Fluid Flow, **20**, pp. 320–328.
[21] Chen, H. C., Jang, Y. J., and Han, J. C., 2000, ''Computation of heat transfer in rotating two-pass square channels by a second-moment closure model,'' Int. J. Heat Mass Transf., **43**, No. 9, May, pp. 1603–1616.
[22] Chen, H. C., Jang, Y. J., and Han, J. C., 2000, ''Near-Wall Second-Moment Closure for Rotating Multi-pass Cooling Channels,'' Int. J. Heat Mass Transf., **14**, No. 2, pp. 201–209.
[23] Wagner, J. H., Johnson, B. V., and Kopper, F. C., 1991, ''Heat transfer in Rotating Serpentine Passage with Smooth Walls,'' ASME J. Turbomach., **113**, pp. 321–330.
[24] Jang, Y. J., Chen, H. C., and Han, J. C., 2000, ''Computation of Flow and Heat Transfer in Two-Pass Channels with 60° Ribs,'' AIAA Paper 2000-1036, 38th Aerospace Science Meeting & Exhibit, Reno, NV, January 10–13.
[25] Jang, Y. J., Chen, H. C., and Han, J. C., 2000, ''Numerical Prediction of the Flow and Heat Transfer in a Two-Pass Square Duct with 90° Ribs,'' 8th International Symposium on Transport Phenomena and Dynamics of Rotating Machinery (ISROMAC-8), Honolulu, HI, March 26–30, **1**, pp. 580–587.
[26] Jang, Y. J., Chen, H. C., and Han, J. C., 2000, ''Flow and Heat Transfer in a Rotating Square Channel with 45° Angled Ribs by Reynolds Stress Turbulence Model,'' ASME 2000-GT-0229.
[27] Rohsenow, W. M., and Choi, H., 1961, Heat, Mass and Momentum Transfer, Prentice-Hall Englewood Cliffs, NJ.

Heat Transfer in a Two-Pass Rectangular Rotating Channel With 45-deg Angled Rib Turbulators

Gm S. Azad

Mohammad J. Uddin

Je-Chin Han

Turbine Heat Transfer Laboratory,
Department of Mechanical Engineering,
Texas A&M University
College Station, TX 77843

Hee-Koo Moon

Boris Glezer

Solar Turbines,
San Diego, CA 92186

Experimental heat transfer results are presented in a two-pass rectangular channel (aspect ratio*=2:1) with smooth and ribbed surfaces for two channel orientations (90 and 135 deg to the direction of rotational plane). The rib turbulators are placed on the leading and trailing sides at an angle 45 deg to the main stream flow. Both 45-deg parallel and cross rib orientations are studied. The results are presented for stationary and rotating cases at three different Reynolds numbers of 5000, 10,000, and 25,000, the corresponding rotation numbers are 0.21, 0.11, and 0.04. The rib height to hydraulic diameter ratio (e/D) is 0.094; the rib pitch-to-height ratio (P/e) is 10 and the inlet wall-to-coolant density ratio ($\Delta\rho/\rho$) is maintained at 0.115 for all surfaces in the channel. Results show that the rotating ribbed wall heat transfer coefficients increase by a factor of 2 to 3 over the rotating smooth wall results. The heat transfer from the first pass trailing and second pass leading surfaces are enhanced by rotation. However, the first pass leading and the second pass trailing sides show a decrease in heat transfer with rotation. The result show that 45-deg parallel ribs produce a better heat transfer augmentation than 45-deg cross ribs, and a 90-deg channel orientation produces higher heat transfer effect over a 135-deg orientation.* [DOI: 10.1115/1.1450569]

Introduction

Thermal efficiency of a gas turbine engine can be improved by increasing the turbine inlet gas temperature. However, this causes an increase in heat load to the turbine components. Until now, no such suitable material is available that can withstand such high thermal stress in this hot operating environment. Therefore, standard metal blades with sophisticated cooling techniques such as film cooling and augmented internal cooling have been employed for turbine blades in order to maintain safe and long operation of the turbines under extreme operating conditions. Cooling air bled from suitable stages of the compressor section is fed to the root section of the rotating blade and subsequently flows through a series of internal passages in either a radial outward or inward direction depending on the complexity of the heat transfer duty required. Thus, it is subjected to the combined effect of Coriolis, buoyancy and centrifugal forces. In rotation, the Coriolis and buoyancy forces cause different heat transfer patterns from the leading and trailing surfaces. Coriolis force tends to create a secondary flow in planes perpendicular to the main flow direction, which encourages the migration of core region flow toward the trailing surface in the first pass and leading surface in the second pass. Angled ribs are also placed on leading and trailing surfaces to trip the boundary layer. These angle ribs not only trip the boundary layer, but also produce secondary flows, which enhance the surface heat transfer. These rib-induced secondary flows interact with the rotational secondary flows to create entirely different heat transfer phenomena. These secondary flows promote better heat transfer in the vicinity of the trailing surface compared to the leading surface in the first pass; while, the situation in the second pass is opposite. The intensity and nature of the secondary flow also depends on the coolant passage channel geometry. A rectangular channel would create a secondary flow pattern that is different from either in a square or a circular cross sectional channel. Thus, the heat transfer coefficient in a rectangular channel will be different than a square or a circular channel. However, most of the internal coolant passages toward the leading and trailing edges in a gas turbine blade are rectangular in shape due to the shape of the blade itself. The curved shape of a turbine blade as shown in Fig. 1 may prohibit the efficient use of square or circular cross sectional coolant flow passages. Thus, to maintain the integrity of a gas turbine blade, a rectangular coolant passage is of high importance, and in order to understand and improve internal cooling techniques, it is necessary to investigate the heat transfer coefficients in a rotating rectangular channel with different rib turbulators.

Numerous studies have been made both experimentally and numerically on the flow field and heat transfer in the internal coolant passage of gas turbine rotor blade. Most of these works deal with square channels. Han and Park [1] performed experimental studies on heat transfer characteristics in a non-rotating rib roughened rectangular channel. Han et al. [2] studied the effect of the rib angle orientation on heat transfer distributions and pressure drop in a non-rotating square channel with two opposite in-line ribbed walls. They found that the 60-deg (or 45-deg) V-shaped rib performs better than the 60-deg (or 45-deg) parallel rib and, subsequently, better than the 60-deg (or 45-deg) crossed rib and the 90-deg rib. The V-shaped rib produced the highest heat transfer augmentation, while the crossed rib had the lowest heat transfer enhancement. Ekkad and Han [3] performed a detailed study on heat transfer characteristics in a non-rotating square channels using liquid crystals techniques. Bonhoff et al. [4] and Schabacker et al. [5] studied the flow characteristics in non-rotating rib roughened channels. Tse and Steuber [6] investigated flow characteristics in rotating serpentine coolant passage with 45-deg angled ribs using LDV. Wagner et al. [7,8] conducted the most detailed experimental study to determine the effects of rotation (buoyancy and Coriolis forces) on the local heat transfer of a multi-pass square channel with smooth walls. They concluded that in the first pass of the coolant passage rotation created a thinner boundary layer on the

Contributed by the International Gas Turbine Institute and presented at the International Gas Turbine and Aeroengine Congress and Exhibition, New Orleans, Louisiana, June 4–7, 2001. Manuscript received by the IGTI, January 25, 2001. Paper No. 2001-GT-186. Review Chair: R. Natole.

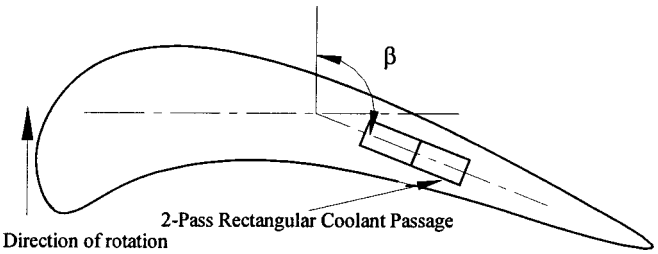

Fig. 1 Sketch of an internal coolant passage of a gas turbine blade

trailing surface and a thicker boundary layer on the leading surface, but in the second pass, the performance was different and opposite to the first pass. The leading surface Nusselt number ratios in the second pass were higher than the trailing surface Nusselt number ratios because of the reversal of the Coriolis force direction. Johnson et al. [9] performed the most thorough and systematic investigation of the effects of buoyancy and Coriolis forces on heat transfer coefficients distribution of four-pass square channels with trips angled to the flow (45-deg ribs). Fann et al. [10] reported local heat transfer in the rotating serpentine passage with ribbed surfaces. They found that both rotation and roughness configuration improved the local heat transfer, and 45-deg ribs performed the best in both the stationary and rotating cases.

Han et al. [11] investigated uneven wall temperature effect on local heat transfer in a rotating two-pass square channel with smooth walls. Zhang et al. [12] analyzed the heating condition effects in a duct with angled rib turbulators with rotation. They suggested that an uneven wall temperature had a significant impact on the local heat transfer coefficients. Parsons et al. [13] presented wall-heating effect on local heat transfer in a rotating two-pass square channel with orthogonal ribs. Johnson et al. [14] and Parsons et al. [15] studied the effects of channel orientation and wall heating condition on local heat transfer coefficient in a rotating two-pass square channel with ribbed walls. They found that the effects of the Coriolis force and cross-stream flow were reduced as the channel orientation changed from normal to an angled orientation. Dutta and Han [16] also investigated the local heat transfer coefficients in rotating smooth and ribbed two-pass square channels with three channel orientations. Dutta et al. [17] presented experimental heat transfer results for turbulent flows through a rotating two-pass rib-roughened triangular channel, with two channel orientations with respect to the direction of rotation. They also predicted numerically how the channel orientation affected the secondary flows in the triangular channel. Park et al. [18,19] conducted experiments to study the effect of rib size on the local heat (mass) transfer distribution for radial outward flow in a rotating channel with transverse ribs on the trailing and leading walls.

Most of the aforementioned studies dealt with square channels. However, to maintain the integrity of gas turbine blades, a rectangular coolant passage is of high importance. The curved shape of the turbine blade may prohibit the efficient use of square or circular cross sectional coolant flow channels. Very few experimental heat transfer data on a rectangular internal coolant passage are available in the literature. Taslim et al. [20,21] studied the heat transfer characteristics in rib-roughened square and rectangular orthogonal rotating channels. They used a liquid crystal technique to study the effect of rotation on heat transfer distributions on the walls. In Taslim et al. [20], the leading and the trailing walls of the test channel were roughened with staggered transverse ribs, while in Taslim et al. [21], the opposite walls were rib-roughened at 45 deg with respect to the main flow, in a criss-cross arrangement. They found that rotational effects were more pronounced in rib-roughened channels with a higher channel aspect ratio and a lower rib blockage ratio. They investigated heat transfer effects only in an orthogonally rotating single pass channel. However, they did not consider a two-pass channel and the effect of channel orientation. Prabhu and Vedula [22] investigated the pressure drop distribution in a rotating rectangular channel with transverse ribs on one wall. They conducted experiments for a rotation number up to 0.21 and rib pitch-to-height ratios of 3, 5, 7.5, and 10, and a rib height-to-hydraulic diameter ratio of 0.15. They found that a rib array with a pitch-to-height ratio of 5 caused the largest pressure drop.

Several questions still remain unsolved, that must be analyzed systematically: It is questionable whether 1) a rectangular channel provides the same heat-transfer performance as a square channel in a two-pass situation, 2) a channel orientation (orthogonal and nonorthogonal) affects heat transfer performance in a rectangular channel, and 3) a parallel or a cross rib provides a better heat transfer performance in a rectangular channel. These issues need to be determined for both nonrotating and rotating cases. This study helps answering the foregoing questions. Such experimental data are very important in the design of a gas turbine blade internal cooling passage system. The objective of this study is to investigate the effect of various angled rib configurations and channel orientations for a two-pass rotating and nonrotating rectangular channel.

Experimental Facility

The experimental test rig used by Parsons et al. [13,15] is used in this study. Regulated compressed air flows through an orifice meter and passes into the test section through a hollow rotating shaft and a hollow rotating arm, which is mounted perpendicular to the shaft. The test section is mounted inside the rotating arm. The air enters the test section and passes through both the first and second passages fabricated with segmented copper plates, and is exhausted into the atmosphere. Slip rings transfer thermocouple outputs to a data logger interfaced with a computer. Slip rings are also used to transfer the variac transformer outputs to wire resistance heaters uniformly cemented in grooves on the backside of the copper plates. An electric motor with an adjustable frequency controller rotates the shaft and arm of the test section. A digital photo tachometer measures the rotational speed of the rotating shaft

The test section has two passes. Each pass is 12.7 mm by 25.4 mm in cross section. The flow in the first pass is radially outward and the flow in the second pass in radially inward. To obtain local heat transfer coefficients, the duct is divided into twelve longitudinal sections, six sections in first pass and six in second pass. Each section has four copper plates on four walls of the channel. Thin teflon (1.59 mm) strips are inserted between copper plates to isolate from each other. These teflon strips work as insulation and reduce heat conduction from one plate to another and also along the longitudinal direction. A cross-sectional view of the test section is shown in Fig. 2. Each wall of the channel (total nine walls, four walls in each pass and an end cap) has an independent heater coil powered by an individual transformer. The power input of each heater is adjusted to maintain a uniform heat flux condition. The wall temperature for each test run is close to 65°C. The channel length-to-hydraulic diameter (L/D) ratio is 18, while each pass length-to-hydraulic diameter (L/D) ratio is 9, connected by a sharp 180-deg turn. The ratio of mean rotating arm radius to the channel hydraulic diameter (R/D) is 30. The entire test duct is surrounded by insulating teflon material and fits in a hollow cylindrical arm for structural rigidity. There is also an unheated teflon entrance channel that has the same cross section as the channel. The length of the unheated smooth section is twelve (12) hydraulic diameters. This serves to establish a hydrodynamically nearly fully developed flow at the entrance to the heated channel. The local wall temperature of the test section is measured by copper-constantan thermocouples attached to each copper plate. Each copper plate has a blind hole on the back side. The thermocouple is glued in the hole and comes out of the test section

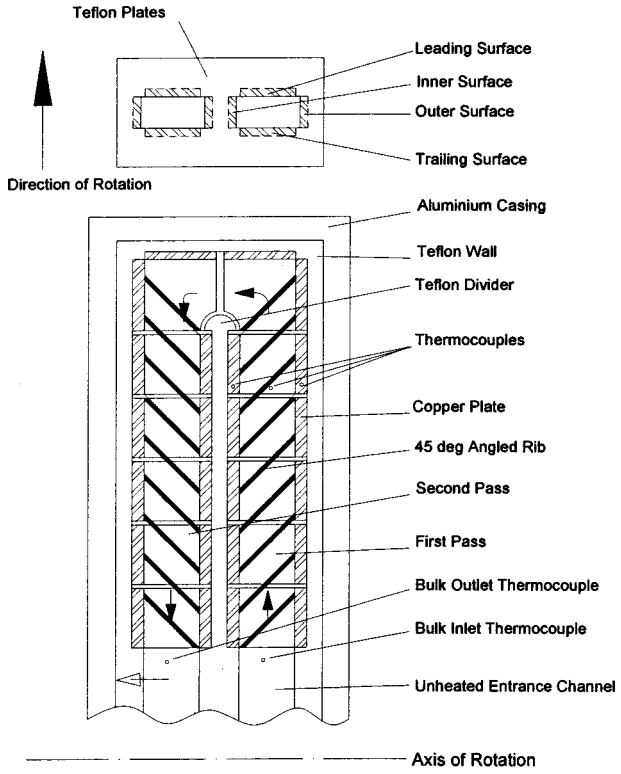

Fig. 2 Schematic of the two-pass test section

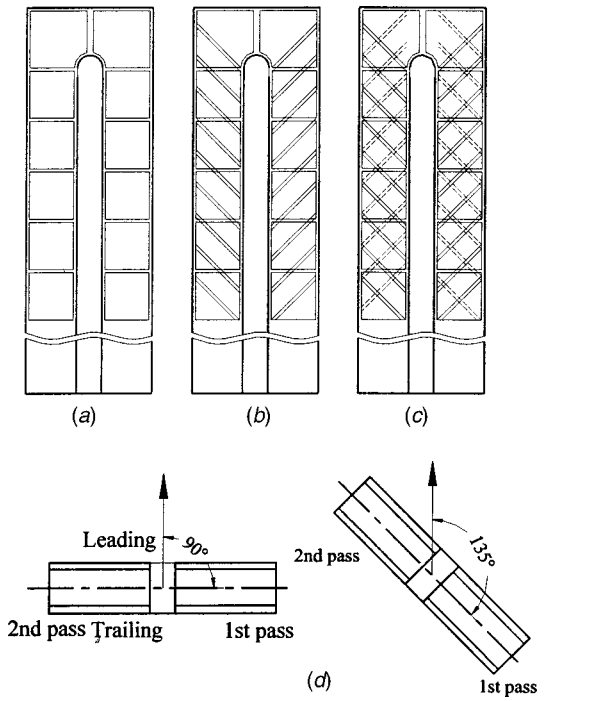

Fig. 3 Two-pass test section with (*a*) smooth walls, (*b*) 45-deg parallel ribs on leading and trailing surfaces, (*c*) 45-deg cross ribs on leading and trailing surfaces, (*d*) two different channel orientations

through the insulating teflon material. Thermocouples are also used to measure the inlet and outlet bulk air temperature.

Two different channel orientations with respect to the channel rotation direction and two different rib configurations in addition to the smooth case are investigated. Figure 3 shows a cut-away view of the two-pass test section for different cases studied here. Figure 3(*a*) shows the test section with smooth walls, 3(*b*) and 3(*c*) show test sections with 45 deg parallel and cross-ribbed walls, respectively. Figure 3(*d*) also shows two different channel orientations with respect to the direction of rotation. The channel is oriented at a 90 and 135-deg angle with respect to the direction of rotation. Copper ribs with a square cross section are glued on the leading and trailing surfaces of the duct in a 45-deg parallel and 45-deg cross fashion, as shown in Fig. 3. A thin layer of conductive glue is used so that it creates a negligible thermal insulation effect between the copper ribs and the copper plates. The rib increased surface area is 25 percent with respect to the smooth wall. The rib height-to-hydraulic diameter (e/D) ratio is 0.094 and the pitch-to-rib height (P/e) ratio is maintained at a value of 10. The pitch is measured along the length of the passage. The rib flow-attack-angle (the angle between the rib and coolant flow direction) is 45 deg. The experiments are conducted for three different Reynolds numbers: Re=5000, 10,000 and 25,000. The duct rotates at 550 rpm, resulting in rotation number of 0.21, 0.11 and 0.04.

Data Reduction

The local heat transfer coefficient is calculated from the local net heat transfer rate per unit surface area to the cooling air, the local wall temperature on each copper plate, and the local bulk mean air temperature as

$$h=(q-q_{\text{loss}})/[A(T_w-T_b)] \tag{1}$$

Local total heat transfer rate (q) is the electrical power dissipated by each heater, which is calculated from measured resistance and current ($q=I^2R$). The electrical power is also checked with the measured voltage drop across each heater ($q=VI$). The heat loss is determined experimentally by supplying electrical power to the test section until a steady state condition is achieved for a no flow (without any air flow) condition. This is done for several different power inputs to obtain a relation between the total heat loss from each surface and the corresponding surface temperature. The heat loss is experimentally determined for each stationary and rotating test case. The heat loss is about 5 percent of the total power input for non-rotating cases. However, it could be as high as 50 percent for a rotating low Reynolds number (Re=5000) case. The heat transfer surface area is increased due to the ribs. This rib increased area is about 25 percent of the total surface area. However, to present the results on a common basis, the heat transfer area used in Eq. (1) is always that of a smooth wall, i.e., the increased area due to the ribs is not included.

The local wall temperature in Eq. (1) is obtained from copper-constantan thermocouples in each copper plate. The individual electrical resistive heaters give a uniform heat flux heating condition. Therefore, the local bulk mean air temperature (T_b) used in Eq. (1) is determined assuming a linear air temperature rise along the test duct. The local bulk mean air temperature (T_b) is also calculated by an energy balance, as

$$T_{b,i}=T_{\text{in}}+\sum_i (q-q_{\text{loss}})/mc_p, \quad i=1,2,3,.....,12 \tag{2}$$

With the measured inlet air temperature, T_{in} and the accumulated net heat input from duct inlet to the ith copper segment, Eq. (2) calculated the bulk mean air temperature at each copper segment. Here m is mass flow rate and c_p is specific heat. The outlet bulk mean air temperature calculated in this way agreed with the measured values within 5 percent (i.e., an energy balance is achieved within 5 percent accuracy).

To separate the influence of the flow Reynolds number on the heat transfer coefficient, the local Nusselt number is normalized

by the Nusselt number for the fully developed turbulent flow in a smooth stationary circular pipe. This is correlated by Dittus-Boelter/McAdams or Rohsenow and Choi, as

$$\frac{\mathrm{Nu}}{\mathrm{Nu}_o} = \frac{hD}{k_{\mathrm{air}}} \frac{1}{(0.023\,\mathrm{Re}^{0.8}\,\mathrm{Pr}^{0.4})} \tag{3}$$

The Prandtl number, Pr, for air is 0.71. Air properties are taken based on the mean bulk air temperature.

The uncertainty of the local heat transfer coefficient depends on the uncertainties in the local wall and bulk temperature difference and the net heat input for each test run. The uncertainty increases with the decrease of the both local wall to air bulk temperature difference and the net heat input. Based on the method described by Kline and McClintock [23], the typical uncertainty in the Nusselt number is estimated to be less than 7 percent for Reynolds number larger than 5000. The maximum uncertainty, however, could be up to 20 percent for the lowest heat transfer coefficient at the lowest Reynolds number tested (Re=5000).

Results and Discussion

Experiments are conducted on a two-pass rectangular channel with smooth and ribbed surfaces. Two different rib configurations and a smooth surface case are investigated. Copper ribs with a square cross section are glued on the leading and trailing surfaces at a 45-deg angle of attack with the flow. In one case, the ribs are glued at a parallel and opposite orientation, while in the other case the ribs are glued at a cross orientation. The angled ribs are considered more effective in heat transfer augmentation than the ribs placed normal to the flow [2]. The angled ribs not only trip the boundary layer, but also produce secondary flows that enhance heat transfer from the surfaces. The test section rotating about an axis perpendicular to horizontal plane produces secondary flows due to centrifugal and buoyancy forces, which develop a new and different heat transfer pattern from the angled ribs or by rotation alone. A change in the channel orientation with respect to the direction of rotation causes a change in the secondary flow vortex and turbulence distribution. In each of the ribbed cases, the channel is oriented at two different angles and the heat transfer rate is measured. However, the frictional pressure losses are not measured in this study.

The discussion on secondary flow patterns induced by rotation, angled rib, or channel orientation is very important to explain the results. Figure 4 shows a conceptual view of the secondary flow patterns induced by these factors. Figure 4(*a*) shows the double cell secondary flow patterns induced by rotation only (smooth surface) for both channel orientations. Figure 4(*b*) shows the parallel rib-induced double-cell secondary flow patterns for both channel orientations. Similarly, Fig. 4(*c*) shows the cross rib induced single cell secondary flow patterns for both channel orientations. The rotation induced double cell counter rotating secondary flow as shown in Fig. 4(*a*) is generated by the Coriolis force that produce a cross-stream flow pattern. In the first pass of the channel, the fluid moves in a radially outward direction and the effect of Coriolis force directs the coolant from the core toward the trailing surface. However, in the second pass, the fluid moves in a radially inward direction and the Coriolis force directs the coolant toward the leading surface. When the channel is oriented at a 90-deg angle with respect to the direction of rotation, the secondary flow vortices are symmetric and directly act either on trailing (first pass) or leading (second pass) surface. However, at 135 deg channel orientation, the secondary flow vortices are asymmetric and migrate diagonally away from the corner region of the inner-leading surface toward the center in the first passage, and from the corner region of the inner-trailing surface toward the center in the second passage.

Angled ribs on the trailing and leading surfaces act as turbulence promoters. Angled parallel ribs create a symmetric counter rotating vortices parallel to the ribs that impinge on the inner surface in the first passage and on the outer surface in the second

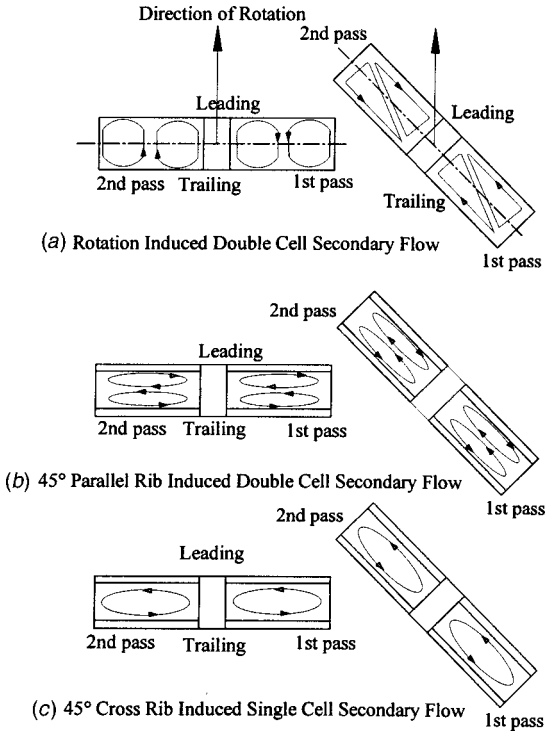

Fig. 4 A conceptual view of the secondary flow pattern

passage as shown in Fig. 4(*b*). This enhances heat transfer on both the leading and trailing surfaces when compared with the nonrotating smooth surface case. When this rib-roughened channel is rotated, the additional counter-rotating vortices as shown in Fig. 4(*a*), interacts with rib induced secondary flow. The general effect of the Coriolis force induced secondary flow in the first passage is to disturb the rib-induced vortices. This interaction continues to increase heat transfer on the first pass trailing and second pass leading surface, while decreasing heat transfer on the first pass leading and second pass trailing surface. Cross ribs create a single-cell secondary flow as shown in Fig. 4(*c*). The cross-rib-induced single-cell secondary flow is different compared to the parallel rib-induced double-cell secondary flow. The single cell secondary flow vortex does not mix well with the core flow (cold fluid) and merely restricts heat transfer because there is less temperature gradient left near the walls. Whereas, the double-cell secondary flow vortex provides more mixing between the center cold fluid and near-wall hot fluid. Thus, heat transfer enhancement for cross rib case is lower when compared with the parallel rib case. When rotation induced secondary flow as shown in Fig. 4(*a*), interacts with this cross-rib-induced secondary flow, the additional counter rotating vortices push the cooler fluid from the core to the trailing surface in the first passage, and to the leading surface in the second passage. Thus, heat transfer is enhanced in the first pass trailing and second pass leading surface, but decreased in the first pass leading and second pass trailing surface. Due to a 180- deg turn between the first and second pass, a secondary flow is generated. This curvature-induced secondary flow pushes fluid from the inner to outer surface. In the second pass, this curvature- induced secondary flow interacts with rib-induced and rotation-induced secondary flows. The conceptual view of the secondary flow patterns as shown in Figs. 4(*a*), (*b*), (*c*) will be useful to explain the heat transfer results. The detailed flow physics have been discussed in a companion numerical paper by Al-Qahtani et al. [24].

Smooth Case Results. Figure 5 presents the Nusselt number ratios for nonrotating and rotating smooth channels. The results are plotted separately for leading and trailing surfaces, and for

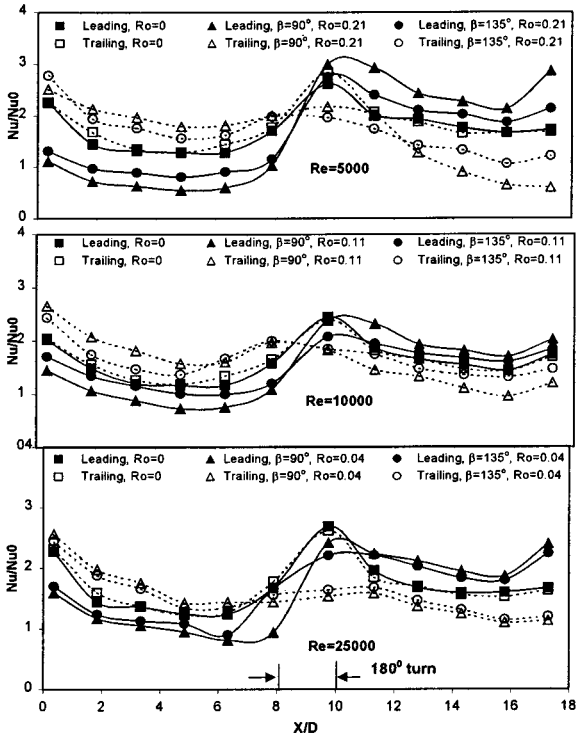

(*a*) Leading and Trailing Walls

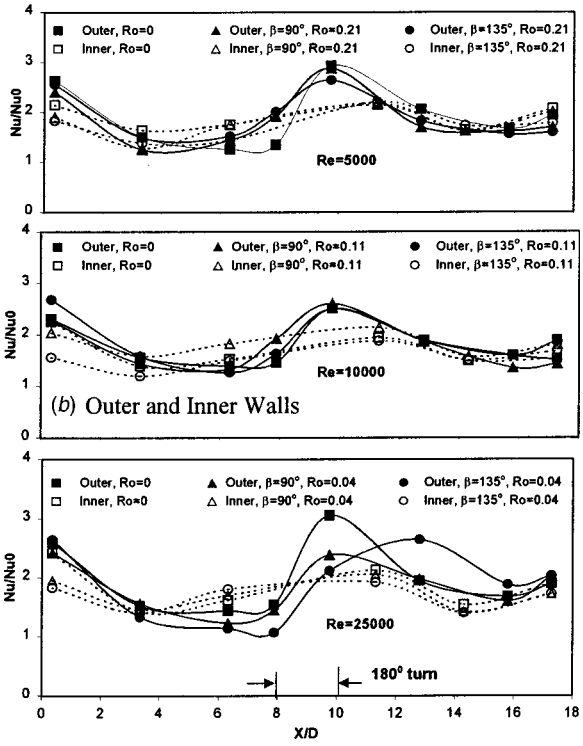

(*b*) Outer and Inner Walls

Fig. 5 Nusselt number ratio for smooth case

inner and outer walls at three different Reynolds numbers. Figure 5(*a*) shows the results for leading and trailing surfaces. The result shows that heat transfer ratio is higher near the inlet of the first pass due to thermal entrance effect. It then decreases, and again approaches asymptotically to the fully developed value. The heat transfer ratio in the bend and upstream of the second passage is high due to the additional secondary flow vortices induced by the curvature. Again, the Nusselt number ratio decreases gradually along the length of the channel in the second pass, and increases again at the exit end of the second pass due to a 90-deg turn in the exit flow direction. The Nusselt number ratios for both the leading and trailing surfaces are almost equal for nonrotating case. However, for rotating case, the trailing surface in the first pass has higher Nusselt number ratio than the leading surface, while in the second pass the trend is opposite. The difference in heat transfer between the rotating and nonrotating flow conditions is primarily attributed to the secondary flows associated with the Coriolis force as discussed in the earlier paragraph. This secondary flow effect is prominent on leading and trailing surfaces compared to the outer and inner side walls.

The rotation-induced Coriolis forces produce cross-stream flow patterns, which push the high-momentum cold fluid from the core towards the trailing surface, in the first pass, while towards the leading surface, in the second pass. Thus, the trailing surface heat transfer is higher than the leading surface in the first pass and similarly, the leading surface heat transfer is higher in the second pass. At a 90-deg channel orientation, this rotation induced secondary flow vortices push the core cold fluid toward either on trailing (first pass) or leading (second pass) surface. However, at 135-deg channel orientation, the secondary flow vortices migrate diagonally away from the corner region toward the center of the passage. In the first pass, it migrates diagonally away from the corner of the inner-leading surfaces toward the center of the passage, and in the second pass from the corner of the inner-trailing surfaces toward the center of the passage. Thus, the Nusselt number ratio on the first pass trailing and second pass leading surface is higher, and first pass leading and second pass trailing surface is lower in a 90-deg channel orientation when compared with the 135-deg channel orientation.

The heat transfer results are focused on the leading and trailing surfaces. These surfaces are important due to the flow of heat from the outside surface of the wall, which is directly exposed to hot combustion gasses. It is also of some interest to determine the heat transfer coefficient on the inner and outer surfaces of the duct. The results from these measurements appear in Fig. 5(*b*). The inner and outer surfaces for each pass show almost same order of heat transfer coefficient magnitude, except at the bend region. In the bend and immediately after the bend region, the Nusselt number ratio is higher at the outer surface when compared with the inner surface. This is due to the curvature-induced secondary flow vortices, as it push the fluid from the inner to the outer surface.

Ribbed Case With 45-deg Parallel Ribs. Figure 6 shows the Nusselt number ratio for 45-deg angled parallel ribs. The results show that the nonrotating Nusselt number ratios are much higher compared to the nonrotating smooth surface case. This is because of the rib induced secondary flow vortices as shown in Fig. 4(*b*). The results also show that rotation significantly increased the Nusselt number ratios on the first pass trailing surface and the second pass leading surface. The rotating Nusselt number ratios on the first pass trailing and second pass leading surface are much higher, but the first pass leading and second pass trailing are lower compared to the nonrotating case. This is because of the combined effect of the rib-induced secondary flow and the rotation-induced secondary flow vortices, as shown in Fig. 4. The results also show that the Nusselt number ratios on the leading and trailing surfaces with the 45-deg angled parallel ribs do not decrease significantly with X/D in the first passage as they did for the duct with smooth walls. The heat transfer coefficient at the entrance is high then it decreases to reach a minimum value at X/D around 4, and then again it increases to reach a higher value at X/D around 6.5, and then it decreases again in the downstream of the first pass. After the turn, the heat transfer coefficient starts increasing to a maximum value at X/D around 12.5, and then it decreases again with X/D. Downstream of the second pass, the heat transfer coefficient has the increasing trend due to a sharp 90-deg turn to the exit flow direction. An earlier study of a 60-deg parallel rib in a stationary

frame by Han et al. [2] also showed an increase in the Nusselt number downstream of the entrance. This behavior is attributable to the secondary flow-induced by the rib orientation as shown in Fig. 4(*b*). In the turn, the heat transfer coefficient is low because of the decay of turbulence as there is no rib. However, additional curvature-induced secondary flow vortices are generated in the bend region, which cause a higher Nusselt number after the bend region. It is believed that the flow pattern generated by the 45-deg parallel ribs contains a pair of counter rotating cells. These counter rotating cells have a greater mixing effect of the core cold fluid and the near-wall hot fluid which cause higher heat transfer.

For 135-deg channel orientation, the result also shows that rotation enhances the heat transfer in the first pass-trailing surface and second pass leading surfaces, whereas the heat transfer decreases in the first pass leading and the second pass trailing surfaces. Since in 135-deg orientation, the heat transfer surfaces are not orthogonal to the plane of rotation, the rotational effects are less significant when compared with 90-deg orientation, as shown in Fig. 4. The effect of Coriolis forces on the first pass trailing and second pass leading walls for 90-deg rotation is more since this force and cross-stream flows are normally incident on these destabilized surfaces. Thus greater differences between leading and trailing Nusselt number ratios in each pass are observed in 90-deg orientation. The Coriolis effect is also present in the 135-deg orientation but is reduced by being oblique at an angle to the first pass trailing and second pass leading walls. Hence differences in Nusselt number ratios between leading and trailing walls are not as significant for the 135-deg orientation as they are for the 90-deg orientation. In fact, unlike 90-deg orientation, the benefits of flow destabilization and drawbacks of flow stabilization are shared by more than one surface in 135-deg orientation. This sharing reduces the intensity of the corresponding effects in specified surfaces with a 135-deg orientation.

With an increase in rotation number (decrease in Reynolds number), the difference of Nusselt number ratios between leading and trailing surfaces increases, as shown in Fig. 6(*a*), but the distribution patterns remain similar to those pertaining to the stationary duct. The decrease in the first-pass leading and second-pass trailing surfaces from their stationary values are more than the increase in the first pass trailing and the second pass leading surface. Johnson et al. [9] observed similar behavior with 45-deg skewed ribs.

The results for the inner and outer surface show that the Nusselt number ratio for the outer surface decreases in the first pass, while it increases in the bend region and remains almost steady in the second pass. The Nusselt number ratios for the inner surface initially decreases in the first pass, then increases and again decreases through the bend region in the second pass. Finally, it increases towards the exit of the second pass due to a sharp 90-deg turn in the exit flow direction. The rib-induced secondary flow pushes the cold fluid towards the inner surface in the first pass causing a higher heat transfer rate on the inner wall. The direction of the secondary flow is reversed in the turn region (from inner to outer surface), which results a decrease of the Nusselt number on the inner wall. In the second pass, the inner wall Nusselt number values are lower due to hot fluid coming from the outer and ribbed surfaces. For the same reason discussed in the foregoing, the Nusselt number distributions on the outer surface is higher.

Ribbed Case With 45-deg Cross Ribs. Figure 7 shows the heat transfer results with cross ribs at three different Reynolds numbers. The results show that the nonrotating Nusselt number ratios, unlike parallel rib case decreases with increasing axial distance and increases in the bend region, and then decreases again in the second pass. The lower Nu/Nu_o ratios for the cross rib orientation as opposed to parallel rib may be caused due to a single-cell secondary flow vortex induced by cross ribs. The lower heat transfer coefficients obtained for cross rib as opposed to parallel rib are similar to those reported by Metzger and Vedula [25] in a straight triangular cross sectional channel with a transient heat transfer

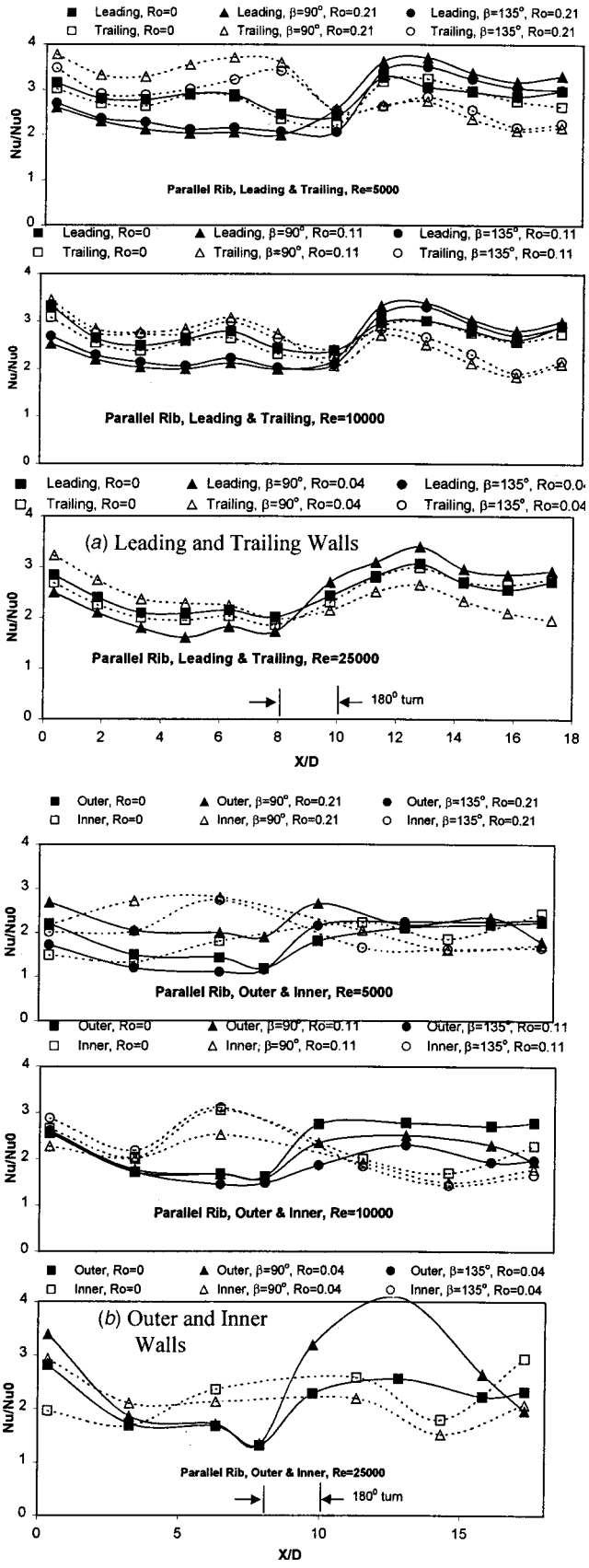

Fig. 6 Nusselt number ratio for 45-deg parallel rib case

method (paint-coated surface). Similar trend was reported in a previous study by Han et al. [2]. The flow pattern generated by the 45-deg cross ribs contains a single cell of secondary flow as shown in Fig. 4(*c*), whereas the 45-deg parallel rib contains a pair

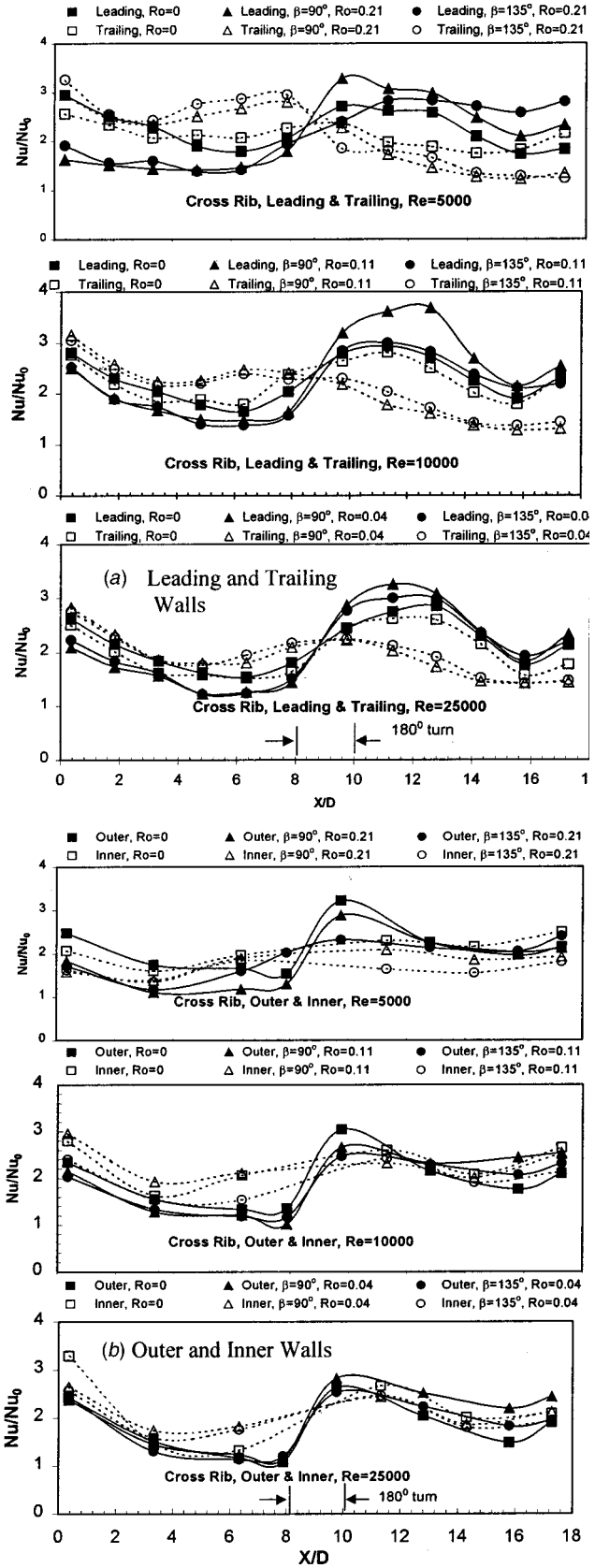

Fig. 7 Nusselt number ratio for 45-deg cross rib case

of counter-rotating cells. The single-cell vortex may not mix well with the core flow and reduce heat transfer because not much temperature gradient remained near the wall. The rotation-induced secondary flow vortex pushes the core cold fluid toward the trailing surface in the first pass and the leading surface in the second pass. Thus, it helps to increase the first pass trailing, and second pass leading surface heat transfer. An additional secondary flow vortex is generated in the bend region, which significantly affects the heat transfer in the second pass. The secondary flow vortex in the turn may grow considerably near the leading surface, causing a significantly high heat transfer in the second pass leading surface. This curvature-induced secondary flow vortex dominates for a certain distance in the second pass, however, the Coriolis and rib-induced vortex gradually diminishes the turn induced secondary flow vortex.

At a lower rotation number (higher Reynolds number), the inner surface produce higher Nusselt number ratio in the first pass when compared with the outer surface result, while in the second pass, both the inner and outer surface produce almost similar Nusselt number effect. However, at a high rotation number (Ro $=0.21$), the Nusselt number on the inner surface are much lower than the outer surface in the second pass. In the middle of the turn, the secondary flow vortex convects fluid from the core toward the outer surface resulting in a higher heat transfer coefficient on the outer surface. In the second passage, the secondary flow convects the cooler fluid from the outer surface and along the ribbed surfaces toward the inner surface, it then moves back to the outer surface resulting in a higher hear transfer coefficient.

Channel Averaged Nusselt Number Ratio. The channel averaged Nusselt number ratio on the leading and trailing surfaces are presented separately in Fig. 8 for both 90 and 135-deg channel orientations. The results are presented separately for first and second pass as a function of rotation number. Fig. 8(*a*) shows the averaged Nusselt number ratio for 90-deg channel orientation, while Fig. 8(*b*) for 135-deg channel orientation. In general, the results clearly show that for a 90-deg channel orientation, the Nusselt number ratio in the first pass trailing surface increases with an increase in rotation number, while it decreases in the first pass leading surface. However, in the second pass, the Nusselt number ratio on the leading surface increases with rotation number, while on the trailing surface it decreases. The Nusselt number ratios on the trailing surface are higher in the first pass and lower in the second pass compared with the leading surface at every rotation number. The parallel rib case produces highest heat transfer effect, because of rib induced double cell secondary flow vortices as shown in Fig. 4(*b*). Similarly, the cross rib enhances the non-rotating heat transfer more than a smooth case, because of a single cell secondary flow vortex as shown in Fig. 4(*c*). The rib-induced secondary flow effect is almost equal on the leading and trailing surface at a nonrotating (Ro $=0$) case as shown in Fig. 8 at Ro $=0$. Rotation induced secondary flow significantly enhances heat transfer in the first pass trailing and the second pass leading surface, while it reduces the heat transfer on first pass leading and second pass trailing surface. The decrease and increase in Nusselt numbers are due to the Coriolis force. This effect is larger at a higher rotation number. For a 135-deg channel orientation as shown in Fig. 8(*b*), the averaged Nusselt number trend is almost similar. However, variation exists between individual leading and trailing surface in each pass of the channel.

Conclusions

In order to achieve turbine blade durability goals modern gas turbine engines require combined cooling techniques such as blade film cooling and blade internal convective cooling. This study focuses on internal convective cooling of turbine rotor blades. The effects of Coriolis and buoyancy forces play important roles in rotating channel flow. Effects of ribs with different configurations and channel orientation on heat transfer are also studied. This work is helpful to understand and improve the internal cooling design of rotor blades especially for a rectangular channel (aspect ratio $=2:1$). The local heat transfer coefficient distribution in a rotating frame is different from that of a stationary frame. Heat transfer coefficient patterns in radial outward flow and radial inward flow conditions show different dependence on

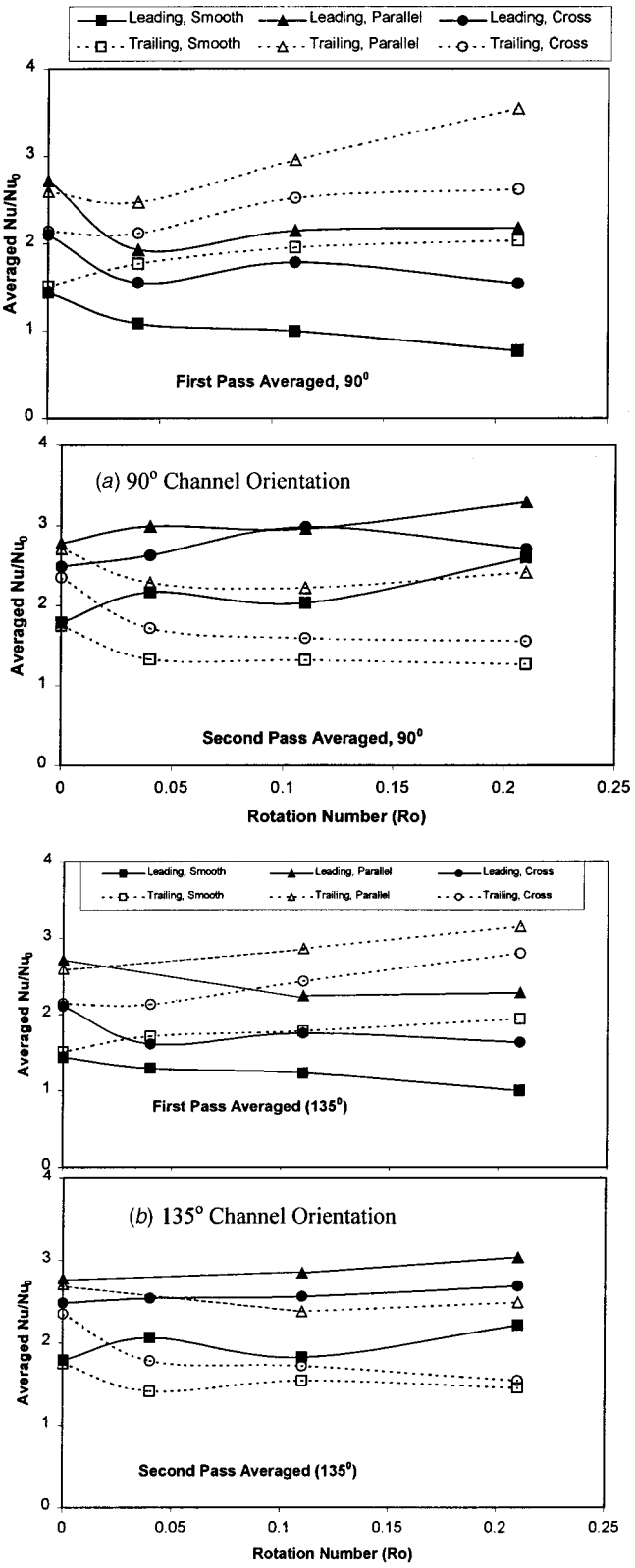

Fig. 8 Averaged Nusselt number ratio on leading and trailing surfaces

rotation. This is primarily due to the reversal of the Coriolis forces acting on the moving fluid in a rotating flow. The results in this study confirm a similar heat transfer effect in a two-pass rotating rectangular channel as is observed in a two-pass rotating square channel from the previous studies in the existing literature.

In general, the rib-roughened surfaces in a rectangular channel perform similarly to smooth surfaces with increasing rotational speed. However, the average heat transfer coefficient magnitude in a rectangular channel with ribbed wall is much higher than that of the smooth walls. Ribs placed at an angle to the bulk flow direction induce greater heat transfer enhancement. Comparative studies suggest that a 45-deg parallel rib configuration in a rectangular channel is more suitable to enhance heat transfer than a 45-deg cross configuration for both nonrotating and rotating cases. The effect of channel orientation on heat transfer shows that a 90-deg channel orientation has more effect on leading and trailing surfaces than a 135-deg orientation due to rotation. The difference in Nusselt number ratios between trailing and leading surfaces in a smooth channel is smaller in a 135-deg channel orientation than a 90-deg channel orientation. This Nusselt number difference is even reduced for ribbed channel cases.

Acknowledgment

This study was sponsored by Solar Turbines. The Solar technical team is Dr. Hee-Koo Moon and Dr. Boris Glezer. Their support is greatly appreciated.

Nomenclature

D = hydraulic diameter (m)
e = rib height (m)
h = heat transfer coefficient (W/m^2K)
k = thermal conductivity of coolant (W/mK)
L = length of the duct (m)
Nu = local Nusselt number, hD/k
Nu_o = Nusselt number in fully developed turbulent nonrotating tube flow without ribs
P = rib pitch (m)
Pr = Prandtl number
q''_{net} = net heat flux at wall (W/m^2)
R = rotating radius (m)
$\overline{R}$ = mean rotating radius (m)
Re = Reynolds number, $\rho VD/\mu$
Ro = rotation number, $\Omega D/V$
T_{bx} = local coolant temperature (°C)
T_i = coolant temperature at inlet (°C)
T_w = wall temperature (°C)
V = bulk velocity in streamwise direction (m/s)
X = distance measured along channel axis from start of heating (m)
β = angle of channel orientation
Ω = rotational speed (rad/s)
α = rib angle
μ = dynamic viscosity of coolant (Pa-s)
ρ = density of coolant (kg/m^3)
$\Delta\rho/\rho$ = coolant-to-wall density ratio, $(T_w - T_b)/T_w$

References

[1] Han, J. C., and Park, J. S., 1988, "Developing Heat Transfer in Rectangular Channel With Rib Turbulators," Int. J. Heat Mass Transf., **31**, No. 1, pp. 183–195.
[2] Han, J. C., Zhang, Y. M., and Lee, C. P., 1991, "Augmented Heat Transfer in Square Channels With Parallel, Crossed, and V-Shaped Angled Ribs," ASME J. Heat Transfer, **113**, pp. 590–596.
[3] Ekkad, S. V., and Han, J. C., 1997, "Detailed Heat Transfer Distribution in Two-Pass Square Channels With Rib Turbulators," Int. J. Heat Mass Transf. **40**, No. 11, pp. 2525–2537.
[4] Bonhoff, B., Parneix, S., Leusch, J., Johnson, B. V., Schabacker, J., and Bolcs, A., 1999, "Experimental and Numerical Study of Developed Flow and Heat Transfer in Coolant Channels With 45° Ribs," Int. J. Heat Fluid Flow, **20**, pp. 311–319.
[5] Schabacker, J., Boelcs, A., and Johnson, B. V., 1999, "PIV Investigation of the Flow Characteristics in an Internal Coolant Passage With 45° Rib Arrangement," ASME Paper 99-GT-120.
[6] Tse, D. G. N., and Steuber, G. D., 1997, "Flow in a Rotating Square Serpentine Coolant Passage With Skewed Trips," ASME Paper 97-GT-529.
[7] Wagner, J. H., Johnson, B. V., and Hajek, T. J., 1991a, "Heat Transfer in

Rotating Passage With Smooth Walls and Radial Outward Flow,'' ASME J. Turbomach., **113**, pp. 42–51.
[8] Wagner, J. H., Johnson, B. V., and Kooper, F. C., 1991b, ''Heat Transfer in Rotating Serpentine Passage With Smooth Walls,'' ASME J. Turbomach., **113**, pp. 321–330.
[9] Johnson, B. V., Wagner, J. H., Steuber, G. D., and Yeh, F. C., 1994, ''Heat Transfer in Rotating Serpentine Passage With Trips Skewed to the Flow,'' ASME J. Turbomach., **116**, pp. 113–123.
[10] Fann, S., Yang, W. J., and Zhang, N., 1994, ''Local Heat Transfer in a Rotating Serpentine Passage With Rib-Roughened Surfaces,'' Int. J. Heat Mass Transf. , **37**, No. 2, pp. 217–228.
[11] Han, J. C., Zhang, Y. M., and Kalkuehler, K., 1993, ''Uneven Wall Temperature Effect on Local Heat Transfer in a Rotating Two-Pass Square Channel With Smooth Walls,'' ASME J. Heat Transfer, **115**, pp. 912–920.
[12] Zhang, Y. M., Han, J. C., Parsons, J. A., and Lee, C. P., 1995, ''Surface Heating Effect on Local Heat Transfer in a Rotating Two-Pass Square Channel With 60° Angled Rib Turbulators,'' ASME J. Turbomach., **117**, pp. 272–280.
[13] Parsons, J. A., Han, J. C., and Zhang, Y. M., 1994, ''Wall Heating Effect on Local Heat Transfer in a Rotating Two-Pass Square Channel With 90° Rib Turbulators,'' Int. J. Heat Mass Transf., **37**, No. 9, pp. 1411–1420.
[14] Johnson, B. V., Wagner, J. H., Steuber, G. D., and Yeh, F. C., 1994b, ''Heat Transfer in Rotating Serpentine Passage With Selected Model Orientations for Smooth or Skewed Trip Walls,'' ASME J. Turbomach., **116**, pp. 738–744.
[15] Parsons, J. A., Han, J. C., and Zhang, Y. M., 1995, ''Effects of Model Orientation and Wall Heating Condition on Local Heat Transfer in a Rotating Two-Pass Square Channel With 90° Rib Turbulators,'' Int. J. Heat Mass Transf., **38**, No. 7, pp. 1151–1159.
[16] Dutta, S., and Han, J. C., 1996, ''Local Heat Transfer in Rotating Smooth and Ribbed Two- Pass Square Channels With Three Channel Orientations,'' ASME J. Heat Transfer, **118**, pp. 578–584.
[17] Dutta, S., and Han, J. C., and Lee, C. P., 1996, ''Local Heat Transfer in a Rotating Two-Pass Ribbed Triangular Duct With Two Model Orientations,'' Int. J. Heat Mass Transf., **39**, pp. 707–715.
[18] Park, C. W., Lau, S. C., and Kukreja, R. T., 1997, ''Effect of Rib Size on Heat (Mass) Transfer Distribution in a Rotating Channel,'' ASME Paper No. 97-AA-126.
[19] Park, C. W., Lau, S. C., and Kukreja, R. T., 1998, ''Heat (Mass) Transfer in a Rotating Channel With Ribs of Various Sizes on Two Walls,'' J. Thermophys. Heat Transfer, **12**, pp. 452–455.
[20] Taslim, M. E., Rahman, A., and Spring, S. D., 1991, ''An Experimental Investigation of Heat Transfer Coefficients in a Spanwise Rotating Channel With Two Opposite Rib-Roughened Walls,'' ASME J. Turbomach., **113**, pp. 75–82.
[21] Taslim, M. E., Bondi, L. A., and Kercher, D. M., 1991, ''An Experimental Investigation of Heat Transfer in an Orthogonally Rotating Channel Roughened With 45° Criss-Cross Ribs on Two Opposite Walls,'' ASME J. Turbomach., **113**, pp. 346–353.
[22] Prabhu, S. V., and Vedula, R. P., 1997, ''Pressure Drop Distribution in a Rotating Rectangular Channel With One Ribbed Surface,'' ASME Paper No. 97-AA-118.
[23] Kline, S. J., and McClintock, F. A., 1953, ''Describing Uncertainties in Single-Sample Experiments,'' Mech. Eng. (Am. Soc. Mech. Eng.), **75**, pp. 3–8.
[24] Al-Qahtani, M., Jang, Y., Chen, H. C., and Han, J. C., 2001, ''Prediction of Flow and Heat Transfer in Rotating Two-Pass Rectangular Channels with 45° Rib Turbulators,'' ASME Paper No. 2001-GT-187.
[25] Metzger, D. E., and Vedula, R. P., 1987, ''Heat Transfer in Triangular Channels With Angled Ribs on Two Walls,'' Exp. Heat Transfer, **1**, pp. 31–44.

Fluid Flow and Heat Transfer in a Rotating Two-Pass Square Duct With In-Line 90-deg Ribs

Tong-Miin Liou
Professor and Dean,
College of Engineering,
Feng Chia University,
Taichung, Taiwan, ROC
e-mail: tmliou@pme.nthu.edu.tw

Meng-Yu Chen
Graduate Student,
e-mail: d853708@oz.nthu.edu.tw

Meng-Hsiun Tsai
e-mail: g883703@oz.nthu.edu.tw

Department of Power Mechanical Engineering,
National Tsing Hua University,
Hsinchu, Taiwan, ROC

Laser-doppler velocimetry and transient thermochromic liquid crystal measurements are presented to understand local fluid flow and surface heat transfer distributions in a rotating ribbed duct with a 180 deg sharp turn. The in-line 90-deg ribs were arranged on the leading and trailing walls with rib height-to-hydraulic diameter ratio and pitch-to-height ratio of 0.136 and 10, respectively. The Reynolds number, based on duct hydraulic diameter and bulk mean velocity, was fixed at 1.0×10^4 whereas the rotational number varied from 0 to 0.2. Results are compared with those of the rotating smooth duct flow in terms of maximum streamwise mean velocities (U_{max}/U_b) and turbulence intensities (u'_{max}/U_b), skewness of mean velocity profiles, secondary flow pattern, turn-induced separation bubble, and turbulence anisotropy. Nusselt number ratio mappings are also provided on the leading and trailing walls. The relationships between the fluid flow and local heat transfer enhancement are also documented. It is found that the rotating ribbed duct flow provides higher U_{max}/U_b, u'_{max}/U_b, and stronger total averaged secondary flow and, hence heat transfer is enhanced. Comparisons with heat transfer data published by other research groups are also made. Furthermore, simple linear correlations between regional averaged Nusselt number ratio and rotation number are developed.
[DOI: 10.1115/1.1459079]

Introduction

To remove the heat load effectively from a rotating serpentine duct and achieve excellent cooling performance is a challenging issue for turbine blade designers. Among various cooling methods, the internal cooling technique is considered in this paper. Presentation of results is focused on the sparse fluid flow information complemented by local heat transfer data. The heat transfer measurements were performed by the transient liquid crystal thermometry which is seldom reported in open literature for a rotating two-pass square-sectioned duct with 90-deg ribs.

One of the reasons why extensive numerical studies of the fluid flow and heat transfer in rotating ribbed ducts with 180-deg sharp turns have not been possible to date is the lack of local flow field and surface heat transfer data. To provide detailed local information, non-intrusive measurement techniques are often needed. But the problem is that they are difficultly implemented under rotating conditions. In the following, the literature survey is only restricted to rotating channels.

Elfer [1] examined the rotational effect on fluid flow in a single-pass smooth-walled circular channel by using a laser two-focus method. Bons and Kerrebrock [2] used particle image velocimetry (PIV) to investigate the internal flow of a single-pass square-sectioned smooth duct for rotating number Ro up to 0.2. Because the effect of 180-deg turn has prominent influence on fluid flow and heat transfer in the serpentine channels, Liou and Chen [3] presented a set of laser-Doppler velocity (LDV) data for developing flows through a 180-deg straight-corner turn at Ro=0.082. Servouze [4] performed three-dimensional LDV measurements in a rotating two-pass channel with a 180 deg sharp turn. His results were mainly obtained at Re=5000 and Ro=0.33. Some results were obtained at Re=25000 and Ro=0.033 and 0.066. Recently, Chen and Liou [5] investigated rotating effect on fluid flow in a smooth duct with a 180-deg sharp turn for $Re=1\times10^4$ and Ro from 0 to 0.2. They found that both the skewness of streamwise mean velocity and magnitude of secondary flow velocity increased linearly, and turbulence intensity increased nonlinearly with increasing Ro. Their results also illustrated the reported spanwise heat transfer variation in the rotating channels, especially the high heat transfer enhancement on the leading wall in the turn. More importantly, they concluded that the direction and strength of the secondary flow with respect to the heat transfer wall were the most important fluid dynamic factors affecting the local heat transfer distributions inside a 180-deg sharp turn under both rotating and non-rotating conditions. All the foregoing fluid flow studies were performed for orthogonal rotation (rotation about an axis normal to that of the turn curvature) whereas Cheah et al. [6] and Hsieh et al. [7] applied LDV to fluid flow in a rotating two-pass channel for parallel rotation. In practical applications, the orthogonal rotation is used and ribs are often arranged on the channel wall to enhance the heat transfer. Tse and Steuber [8] investigated flow characteristics in a serpentine coolant passage with 45-deg ribs using LDV for orthogonal rotation. Up to date, detailed flow field measurements using nonintrusive LDV or PIV in an orthogonally rotating multi-pass ribbed channel with 180-deg sharp turns are still lacking.

Computationally, Prakash and Zerkle [9] suggested that a low Reynolds number model should be used to simulate practical gas turbine engine conditions and a Reynolds stress model is necessary to capture anisotropy turbulence effects. Iacovides and Raisee [10] explored four turbulence models to compute the fluid flow and heat transfer in internal cooling passages of turbine blades with 90-deg ribs. They concluded that the wall function approach is inappropriate and the simple isotropic eddy viscosity model fails to capture physically reasonable heat transfer and fluid flow behavior since the presence of ribs generally generates flow separation and anisotropic turbulence. Recently, Jang et al. [11] predicted flow and heat transfer in a rotating square channel with 45-deg ribs by the use of Reynolds stress turbulence model and showed that the secondary flow induced by the angled ribs, rotating buoyancy, and Coriolis forces produced strong anisotropic turbulent stresses and heat fluxes. These computations all reflect the necessity of detailed flow field information provided by experimental measurements.

Contributed by the International Gas Turbine Institute and presented at the International Gas Turbine and Aeroengine Congress and Exhibition, New Orleans, Louisiana, June 4–7, 2001; Manuscript received by the IGTI, January 18, 2001. Paper No. 2001-GT-185. Review Chair: R. A. Natole.

Wagner et al. [12] made thermocouple measurements in serpentine square passages with staggered 90-deg ribs on the leading and trailing surfaces. The ribs' H/D_H and Pi/H were fixed at 0.1 and 10, respectively. Flow parameters were $\mathrm{Re}=2.5\times10^3$ and Ro varying from 0 to 0.35. They showed that the maximum heat transfer coefficient increased up to 4.5 times (in contrast to 3.5 times for the rotating smooth-walled passages) from the stationary fully developed circular tube values, whereas the minimum heat transfer coefficients decreased to 80% of the stationary 90-deg ribbed wall results. When the 90-deg ribs were replaced by 45 deg ribs, Johnson et al. [13] found that the maximum heat transfer coefficient increased up to 5.0 times of the stationary tube values but the minimum heat transfer coefficient decreased to 40% of the stationary 45-deg ribbed wall values. Parsons et al. [14] performed thermocouple measurements to investigate wall heating effect on heat transfer in a rotating two-pass square channel with in-line 90-deg ribs for Re and Ro from 2.5×10^3 to 2.5×10^4 and 0 to 0.35, respectively. Zhang et al. [15] substituted in-line 60-deg ribs for the in-line 90-deg ribs of Parsons et al. [14] and examined the effect of rotation on heat transfer using thermocouples. In all cases the rotating ribbed wall heat transfer coefficients were two to three times higher than their corresponding rotating smooth-walled channel values.

All the above heat transfer results were based on thermocouple readings which gave actually regional averaged values. The steady-state liquid-crystal thermometry (SLCT) was used by Taslim et al. [16] and El-Husayni et al. [17] to obtain heat transfer data in rotating single pass channel with criss-cross 45-deg ribs and staggered 60 deg ribs, respectively. The former reported the averaged data (per rib interval) only and the latter both local and averaged data. Up to date, no SLCT measurements have been reported for rotating multi-pass ribbed channels. To overcome the problems of limited color play range and deteriorating characteristic of color play encountered in SLCT, the transient thermochromic liquid crystal thermometry (TLCT) was developed in past years but has only been used to obtain local heat transfer coefficient distribution in stationary two-pass smooth-walled (Liou, et al. [18]) and ribbed (Liou, et al. [19]) channels and in rotating two-pass smooth-walled channels (Liou et al. [20]).

Owing to the facts described above, the objective of this study is to acquire local fluid flow and surface heat transfer distributions in an orthogonally rotating two-pass square-sectioned duct with in-line 90 deg ribs mounted on the leading and trailing walls using LDV and TLCT, respectively. As pointed out previously, both LDV and TLCT have seldom been applied to such a difficult condition. The gathered information is compared with that of the rotating smooth duct flow and is believed to provide a better understanding of the relation between the fluid flow and heat transfer in a rotating internal cooling channel.

Experimental Facility and Conditions

The TLCT and LDV experimental setup is schematically depicted in Fig. 1. The principles of both TLCT and LDV have been well described in Liou et al. [19,20]; Chen et al. [5]. As shown in Fig. 2, the inlet air was heated by a rapid-response mesh heater 100 mm long. The hot air flowed radially outward in the first passage and radially inward in the second passage after making a 180-deg sharp turn. After being cooled by the colder duct walls. The cooled air from the test section was exhausted to ambient by a 2.2-kW turbo blower whose blowing flow rate was adjusted by a frequency inverter. During each experiment, the flow system was turned on first. After the rotating duct flow had attained a steady state to allow the development of the Coriolis forces in the test duct, the mesh heater was switched on to initiate the transient heat transfer test. A digital video camera and white fluorescent lamps fixed to the rotating test section (Fig. 1) were used to record the color change of the liquid crystal coating when the hot air passed through the test section. A two-channel thermocouple recorder measured the main flow temperatures at the upstream and downstream locations of the test section during the test. The junction-bead of the thermocouple was about 0.15-mm in diameter. All the data and power lines from the rotating part were connected to the stationary part via a 12-channel slip ring. The video and temperature data were then fed to a PC for post processing.

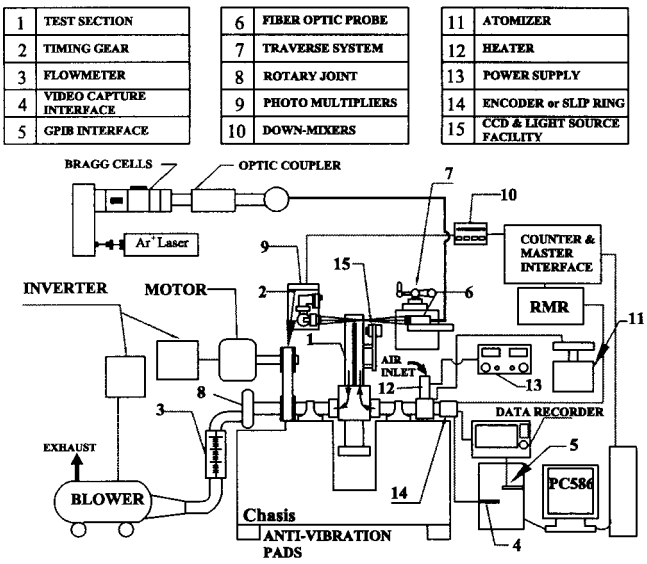

Fig. 1 Schematic drawing of the LDV and TLCT experimental system

The test section shown in Fig. 2 was made of acrylic sheets 20 mm thick for optical access. The hydraulic diameter of the square cross-sectional flow path was $D_H=22$ mm and the divider-wall thickness was 0.5 D_H. At the turn, the clearance between the tip of the divider wall and the duct outer wall was fixed at 1 D_H. The 90 deg transverse ribs were mounted on the leading and trailing walls and directly opposite (not staggered). One pair of ribs was installed at the divider wall tip in the turn and nine pairs of ribs in each pass. The rib height-to-hydraulic diameter ratio (H/D_H) and the rib pitch-to-height ratio (Pi/H) were 0.136 and 10, respectively, in each pass. The TLCT measurements were made in the region of $4D_H$ (or 3 rib pitch) upstream to 4 D_H downstream of the turn on the trailing and leading walls. The Reynolds number, based on the bulk mean velocity of 7.58 m/s and hydraulic diameter, was fixed at 1.0×10^4. The range of the rotation number examined was from 0 to 0.20 corresponding to the range of rotational speed from 0 to 660 rpm. These conditions were selected to compare with the stationary part reported by Liou and Chen [3].

The LDV measurements were performed in the region 2 rib pitches upstream to two rib pitches downstream of the turn along the longitudinal central plane of each pass, i.e., $Z^*=\pm0.5$. At each X station, the measurements were made at twelve or thirteen locations. The secondary-flow velocity vector mappings were made at a midturn cross section.

Methodology of Liquid Crystal Thermometry

A one-dimensional transient heat conduction analysis

$$\alpha\frac{\partial^2T}{\partial Y^2}=\frac{\partial T}{\partial t} \tag{1}$$

over a semi-infinite solid medium with a convective boundary condition and assumptions of constant property and heat transfer coefficient values

$$-k\frac{\partial T}{\partial Y}=h(T_w-T_b)\quad \text{at } Y=0$$

$$T(Y,0)=T_i\quad T(\infty,t)=T_i \tag{2}$$

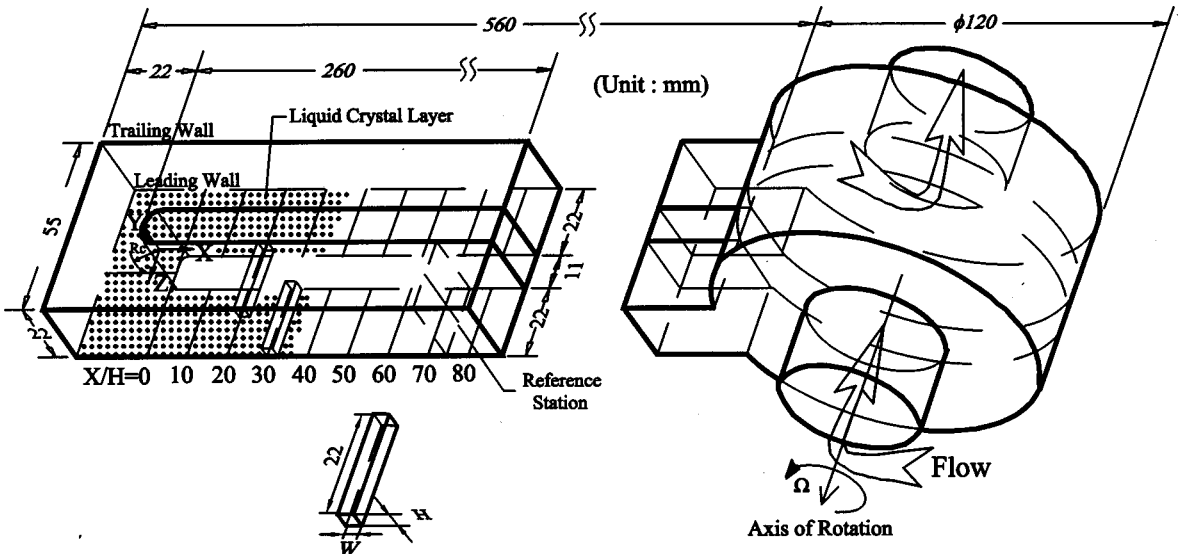

Fig. 2 Sketch of configuration, coordinate system, and dimensions of test section

gives the dimensionless wall temperature T_w for the test surface as below

$$\frac{T_w - T_i}{T_b - T_i} = 1 - \exp\left(\frac{h^2 \alpha_w t}{k_w^2}\right) \operatorname{erfc}\left(\frac{h\sqrt{\alpha_w t}}{k_w}\right) \tag{3}$$

Note that the semi-infinite wall is initially at a uniform temperature ($T = T_i$ at $t = 0$) and the surface of the wall is suddenly heated or cooled convectively with a fluid at a constant temperature or a bulk temperature T_b. When T_i, T_b, and the time, t, for T_w attaining the green point are given, the local heat transfer coefficient, h, over the test surface coated with liquid crystals can be calculated from Eq. (3). The green point is the temperature at which the liquid crystal appears green with the largest light intensity. The local bulk mean temperature $T_b(X)$ can be calculated by the interpolation of inlet and outlet coolant temperature. Due to the inability of performing an abrupt-change of the main air temperature during the transient test, the time history (Fig. 3) of the main stream air temperature is reproduced as a series of step functions. Using the Duhamel's superposition theorem, Eq. (3) can be rewritten as Eq. (4)

$$T_w - T_i = \sum_{j=1}^{N} \left[1 - \exp\left(\frac{h^2 \alpha_w (t - \tau_j)}{k_w^2}\right) \operatorname{erfc}\left(\frac{h\sqrt{\alpha_w (t - \tau_j)}}{k_w}\right)\right] [\Delta T_r] \tag{4}$$

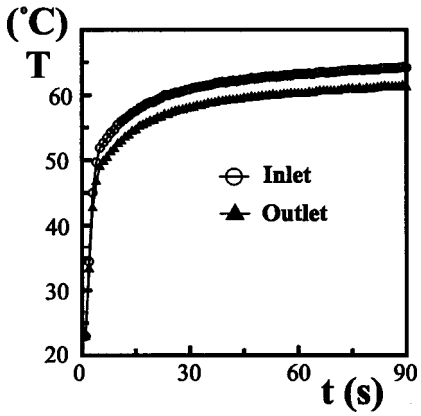

Fig. 3 Mainstream temperature variations during the transient test

where ΔT_r and τ_j are the temperature and time step changes from the recorded output. The local heat transfer coefficient at a given point on the measured region is thus actually obtained by solving Eq. (4).

Data Accuracy

The statistical errors in the mean velocity and turbulence intensity were less than 1.8 and 3.1 percent, respectively, for a 95% confidence level. More detailed uncertainty estimates and velocity bias correlations are included in Liou et al. [3]. For the range of atomizer pressure settling used, the saline solution was mixed to produce particles from 0.5 to 1.2 μm. This particle diameter range is able to follow turbulence frequencies exceeding 1 KHz (Durst et al. [21]).

The most proper uncertainty in obtaining heat transfer coefficient is estimated to be $\pm 10.3\%$ resulting from ± 3.5, ± 5.0, ± 5.0, ± 5.5, ± 1.5, ± 1.5, and $\pm 3.2\%$ uncertainty in time of color change, thermal diffusivity of wall, thermal conductivity of wall, bulk mean temperature of main stream, green-point temperature, initial temperature of wall, and buoyancy effect, respectively. Conduction losses are relatively small because the transient test period is short and the walls are made of insulating material (Bakelite, thermal conductivity = 0.23 W/mK). It should be mentioned that the total time for each transient test is typically in the range of 30 to 65 s. The time is smaller than 120 s for a test wall thickness of 22 mm. Thus, the semi-infinite solid assumption for the TLCT is valid for all tests. Radiation is negligible because the entire walls of the channel are heated by the mainstream at fairly uniform temperature.

It is inevitable to have the variation of buoyancy effect when the technique of TLCT is applied to evaluate the heat transfer of a rotating duct. However, there are experimental evidences to demonstrate that the effect of centripetal buoyancy on heat transfer depends on the surface condition of heated wall. In general, the more significant buoyancy effect was found in a smooth-walled duct relative to a duct fitted with transverse ribs [22]. As an illustrative example to quantify the buoyancy effect in a rotating duct fitted with 90-deg transverse ribs, the variations of buoyancy parameter in terms of $\beta(T_b - T_w)$ from 0.055 to 0.221 caused about 15% of Nusselt number variation when the rotating number and Reynolds number were, respectively, controlled at 0.2 and 8000 [23]. For the present investigation, the range of buoyancy parameter tested for a single experimental run was about 0.050 to 0.058. Thus, based on the measurements in [23] for a square duct fitted

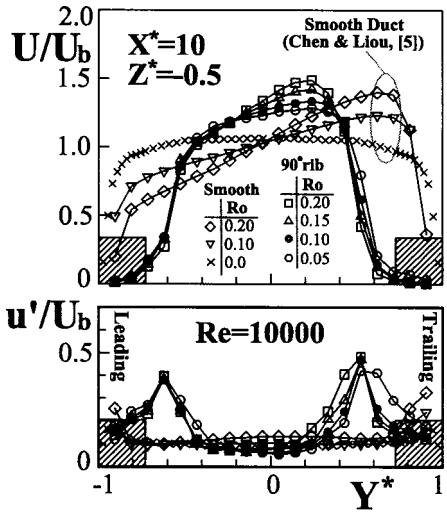

Fig. 4 Variation of streamwise mean velocity and turbulence intensity profiles with rotation number at reference station ($X/H=73$) of the first pass in the $Z^*=-0.5$ plane

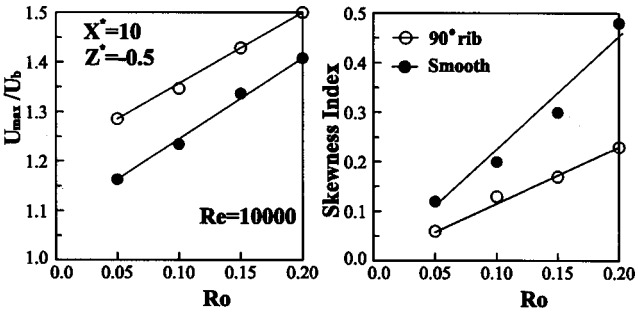

Fig. 5 Rotation effect on the U_{max}/U_b and skewness index of U profiles at the reference station in the first pass of the ribbed and smooth ducts

with 90-deg transverse ribs, the variation of Nusselt number due to the change of buoyancy level for each single test run of the present study is about ±3.2%. Even if the buoyancy effect was reversed from the scenario of gas turbine rotor blade when each single test was performed, the parametric range tested (e.g., $Ro \leqslant 0.2$, $0.050 < \beta(T_b - T_w) < 0.058$) by the present study should not cause considerable buoyancy interaction. Furthermore, for a steady state heat transfer test, it normally takes about 30 min for the wall and fluid temperature to become stable. In other words, the buoyancy interaction will require this time span to settle and provide its effect on heat transfer. A single test run using the technique of transient liquid crystal normally takes 30~65 s to complete. This period of time is far more less than the time span required for the buoyancy interaction to be well established. Thus, within the parametric range tested by the present study, the heat transfer data generated shall be able to reflect the rotational effects due to the negligible buoyancy variation during each single test run.

Results and Discussion

Flow Patterns at Inlet Reference Station. Figure 4 depicts the variation of streamwise mean X-component velocity and turbulence intensity profiles with Ro at $X/H=73$ (or $X^*=10$) station which is located in between the 8th and 9th rib pairs (Fig. 2) upstream of the turn in the first pass. This station corresponds to the inlet reference station reported by Chen and Liou [5] in their study of rotating effect on fluid flow in a smooth duct with a 180-deg sharp turn. It is observed that the skewness of U/U_b increases monotonically as Ro is increased from 0.05 to 0.20. The skewness indices, defined as $\int_{-1}^{1} Y^{*3}(U/U_b)dY^*/\sigma_{Y^*}^3$ in the present study, are 0.06, 0.13, 0.17, and 0.23 for Ro=0.05, 0.10, 0.15, and 0.20, respectively. The maximum U/U_b accelerated by the Coriolis force occur around $Y^*=0.24$ and are $1.28U_b$, $1.34U_b$, $1.42U_b$, and $1.49U_b$ for Ro=0.05, 0.10, 0.15, and 0.20, respectively. Figure 4 also includes the mean flow results in the corresponding smooth duct reported by Chen and Liou [5] for comparison. Their maximum U/U_b appear around $Y^*=0.60$ and are $1.23U_b$ and $1.40U_b$ for Ro=0.10 and 0.20, respectively. Their skewness indices are 0.20 and 0.48 for Ro=0.10 and 0.20, respectively. Figure 5 summarizes the rotation effect on U_{max}/U_b and skewness index of U profiles at the reference station for both rotating ribbed and smooth duct flows. It is seen that both U_{max}/U_b and skewness index of U profiles increase linearly with increasing Ro. The U_{max}/U_b of the rotating ribbed duct flow increases up to 1.10 times that of rotating smooth duct flow, while the skewness index decreases to 48% of the rotating smooth duct value. It is obvious from the foregoing comparison and Fig. 4 that the presence of in-line rib arrays decelerates the fluid flow for $|Y^*|>0.4$ due to the blockage of ribs, but accelerates the fluid flow for $|Y^*|<0.4$ due to mass conservation. For this reason, the present ribbed duct shifts the locations of U_{max}/U_b from $Y^*=0.6$ of the smooth duct case to $Y^*=0.24$ near the duct centerline and, in turn, results in less skewed U/U_b profiles. The velocity skewness in $Z^*=-0.5$ plane gradually increases with the development of the fluid flow in the rotating duct (not shown due to space limitation). When Ro is increased from 0.05 to 0.20, the turbulence intensity level only increases slightly, more notably near the trailing wall ($u'/U_b = 0.42 \sim 0.48$ at $Y^*=0.52$) than near the leading wall ($u'/U_b = 0.38 \sim 0.40$ at $Y^*=-0.62$) as a result of the movement of U_{max}/U_b toward the trailing wall and the increase of U_{max}/U_b with increasing Ro. It should be pointed out that the steeper mean velocity gradients resulting from ribs (or so called turbulators) lead to much higher peak turbulence intensities than the corresponding smooth wall case, as shown in Fig. 4. Quantitatively, the peak turbulence intensities for the ribbed duct case can attain values as high as 1.5 to 2.1 times and 1.6 to 2.5 times those of the smooth duct case near the trailing wall and leading wall, respectively, for the range of Ro examined. In summary, higher heat transfer augmentation can be expected from rotating ribbed duct compared to the rotating smooth duct.

Flow Development Around the Turn in Z^* Planes. As the flow proceeds toward the turn in the first pass, the flow patterns in terms of the mean velocity vector plots in $Z^*=-0.5$ plane are depicted in Fig. 6 for Ro=0.15. Near the turn, the slant impingement of fluid flow upon the trailing wall directed by the Coriolis force is clearly revealed. The corresponding heat transfer enhancement ($Nu/Nu_o>1$) and deterioration ($Nu/Nu_o<1$) on the trailing and leading walls of the first pass, respectively, are demonstrated by the contour plots of Nu/Nu_o calculated from the TLCT measurements in Fig. 7. The poor heat transfer immediately behind each rib (purple color in Fig. 7) is due to the presence of the rib-top separated recirculating zone behind each rib. Downstream of the rib-top separated bubble, the large area of heat augmentation results from flow reattachment. It should be pointed out that in order to compare with some of the ribbed data taken by thermocouples in the later section, the rib-top liquid crystal data have been removed from Fig. 7. The thermocouple measurements performed by previous researchers generally do not provide the rib-top data.

Inside the 180-deg sharp turn, the combined effects of curvature and rotation make the flow pattern in the region $-1<X^*<0$ (or $-10<X/H<0$) of $Z^*=-0.5$ plane assume a skewed Dean-type secondary flow (a more intact pattern will be revealed shortly on the midturn cross section), as shown in Fig. 6. Note that the LDV

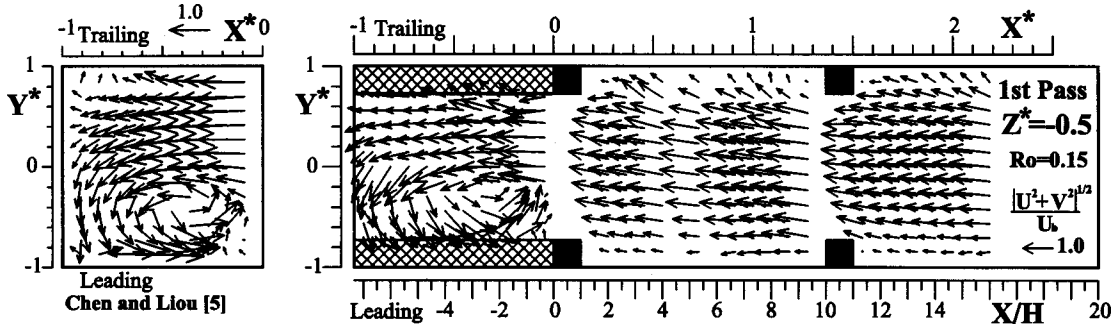

Fig. 6 Mean velocity vector plots around the turn in the first pass for Ro=0.15 and Re=1.0×10^4 (Coriolis forces point toward trailing wall)

measurements can be brought as close as 2~3 mm from the wall for the ribbed duct case and 1 mm for the smooth duct wall case. For this reason, the flow reversal part of the vortex on the trailing wall side squeezed by the Coriolis force was not measured. The presence of ribs displaces the center of dominant vortex slightly away from the leading wall, i.e., from $Y^*=-0.4$ of the smooth duct case (left diagram of Fig. 6) to $Y^*=-0.3$ of the ribbed duct case. Both ribbed and smooth duct flows have nearly the same value of maximum turbulent kinetic energy $0.3U_b^2$ ($K\equiv(u'^2+v'^2)/2$ defined in this paper, K contours not shown due to space limitation) in this cross-sectional plane.

The secondary flow structure inside the turn has intimate relationship with the corresponding heat transfer distribution. Figure 6 shows that the secondary flow impinges directly upon the duct tip ($X^*=-1$ or $X/H=-10$) and the heat transfer there is elevated as depicted in Fig. 7. The Dean vortices also collide with the most parts of leading and trailing walls except for $-2<X/H<0$ where the secondary flow vectors point away from the walls. The strength of impingement is stronger on the leading wall than on the trailing wall, as demonstrated by the Nu/Nu_0 contours in Fig. 7. This observation together with other secondary flow patterns to be shown shortly provide the rationale for the heat transfer augmentation inside the turn on the leading and trailing walls. The lower Nu/Nu_0 regions, $-2<X/H<0$, in Fig. 7 result from the aforementioned upwash flow more notably for the dominant vortex on the leading wall side.

The Dean vortices in the $Z^{**}=0$ cross-sectional plane, in between the in-line ribs as displayed in Fig. 8, are more intact within the measurement range. Attention should be given to the vortex on the trailing wall side which is further distorted into two small vortices by the Coriolis force and the decrease in the Y^* extent from $-1<Y^*<1$ to $-0.73<Y^*<0.73$. The centers of the three vortices indicated in Fig. 8 are located at ($X^*=-0.4$, $Y^*=-0.4$), (-0.75, 0.7), and (-0.15, 0.6). The dominant vortex occupies more than 90% area of the midturn cross section, and directs the major secondary flow to impinge and sweep the leading wall. This causes a greater heat transfer elevation on the leading wall than on the trailing wall, as evidenced from the regional averaged Nusselt number ratio in the area of region index 0 in Fig. 9. The values of Nu_{rg}/Nu_0 attain as high as 5.9 and 5.1 on the leading and trailing walls, respectively, for region index 0. Comparing the left diagram with the right diagram of Fig. 8, the regional averaged strength of secondary flow ($\sqrt{U^2+V^2}$) and maximum turbulent kinetic energy located at the dominant vortex center of the ribbed and smooth duct flows are ($0.81U_b$, $0.28U_b^2$) and ($0.73U_b$,$0.25U_b^2$), respectively. The comparison provides the rationale for the higher heat transfer augmentation in the midturn region (region index 0 in Fig. 9) attained by the ribbed duct (empty diamond, Fig. 9) compared to the smooth-walled duct (solid diamond, Fig. 9), $(Nu_{rg})_{rib}=1.7(Nu_{rg})_{smooth}$ and $2.2(Nu_{rg})_{smooth}$ on the leading and trailing walls, respectively.

In the rear part of the turn, the secondary flow patterns (Fig. 10) are much different because the flow has turned about 180 deg and is ready for flowing radially inward. The direction of Coriolis force is reversed. More fluid flow is now gathered near the leading wall in the region $-10<XH<0$ of the $Z^*=0.5$ plane (Fig. 10),

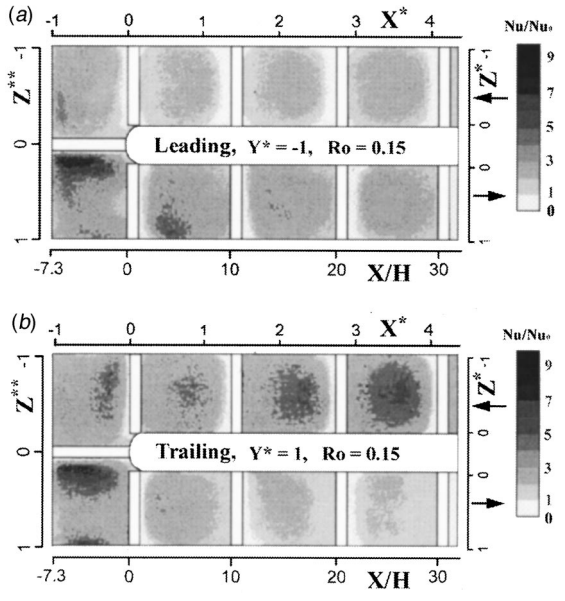

Fig. 7 Detailed local Nusselt number ratio distributions for Ro=0.15 and Re=10000 on the (*a*) leading wall, and (*b*) trailing wall

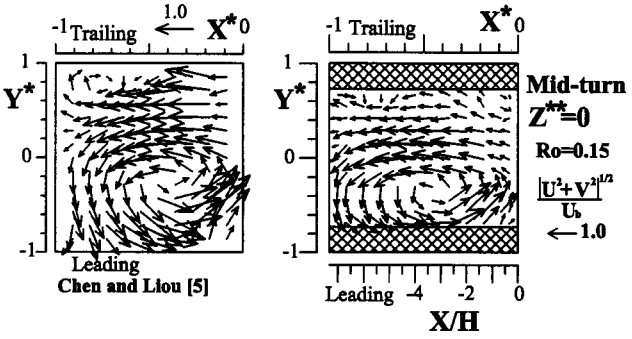

Fig. 8 Cross-stream secondary flow patterns in the midturn ($Z^{**}=0$) for Ro=0.15 and Re=1.0×10^4

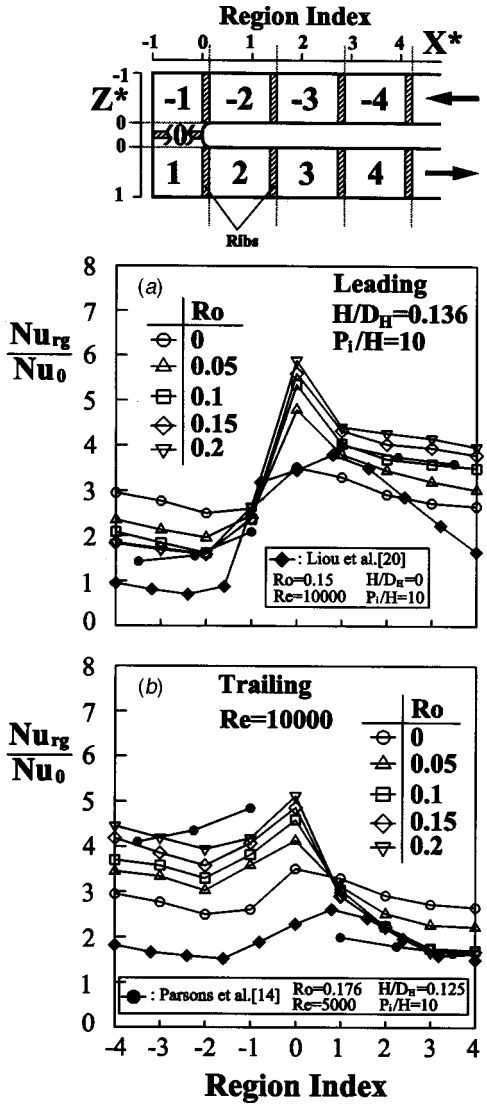

Fig. 9 Regional averaged Nusselt number ratio distribution for various rotation numbers on (*a*) leading wall, and (*b*) trailing wall

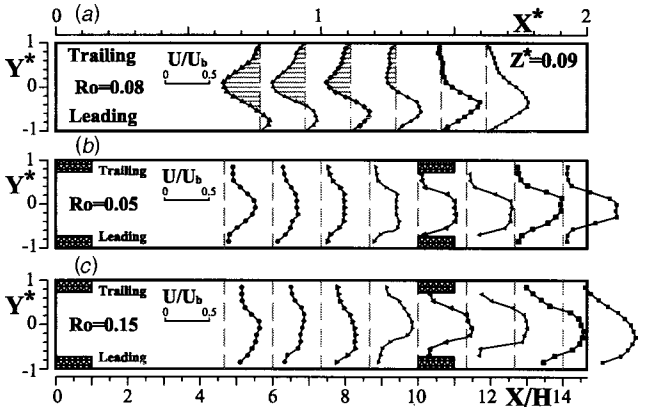

Fig. 11 Evolution of streamwise mean velocity profile immediately behind the 180-deg sharp turn in a longitudinal plane adjacent to the divider wall under rotating condition and Re=1×10^4 for (*a*) the smooth two-pass duct with Ro=0.08, (*b*) the ribbed duct with Ro=0.05, (*c*) the ribbed duct with Ro=0.15 (Coriolis forces point toward leading wall)

opposite to that in the region $-10<X/H<0$ of the $Z^*-0.5$ plane (Fig. 6). Thus, heat transfer promotion in the second pass is expected to be larger on the leading wall than on the trailing wall, as proved from comparisons between Figs. 7(*a*) and (*b*) as well as between Figs. 9(*a*) and (*b*).

Fluid Flow and Surface Heat Transfer. Attention is focused on the effect of 90-deg parallel ribs on the fluid flow and surface heat transfer characteristics immediately downstream of the 180-deg sharp turn and near the divider wall, an issue not being addressed previously for the case of duct rotation. Hence, additional LDV measurements were performed along a longitudinal plane $Z^*=0.09$ adjacent to the divider wall to examine the status of the well-known separation bubble normally taking place near the divider tip in the turn and reattaching on the divider wall in the second pass for the smooth duct case if the 90-deg parallel ribs are installed in the duct under rotating condition. Keep in mind that if the aforementioned separation bubble on the divider wall resulting from the sharp turn is present, the *x*-component mean velocity profiles on the $Z^*=0.09$ plane across the separation bubble should have negative values. Indeed, the negative velocities (shaded area up to $X/H=10.7$) shown in Fig. 11(*a*) for the smooth wall duct at Ro=0.08 indicate the occurrence of turn-induced separation bubble. Its shape skews toward the trailing wall since the Coriolis force directs most fluid toward the leading wall (left diagram of Fig. 10) and thus make the streamwise mean velocities near the leading wall positive (Fig. 11(*a*)). The low speed fluid flow in the turn-induced separation bubble generally leads to lesser heat transfer enhancement on the trailing wall near the divider (Liou et al. [20]).

At this stage, it is instructive to schematically draw in Fig. 12 a summary of flow patterns within the measurement range. Once the inline 90-deg ribs are installed in the duct, the positive *X*-component mean velocities depicted in Figs. 11(*b*) and 12

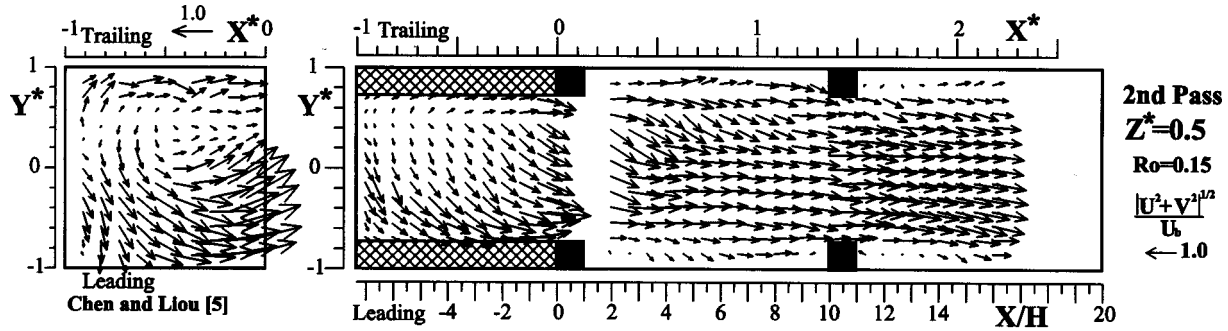

Fig. 10 Mean velocity vector plots around the turn in the second pass for Ro=0.15 and Re=1.0×10^4 (Coriolis forces point toward leading wall)

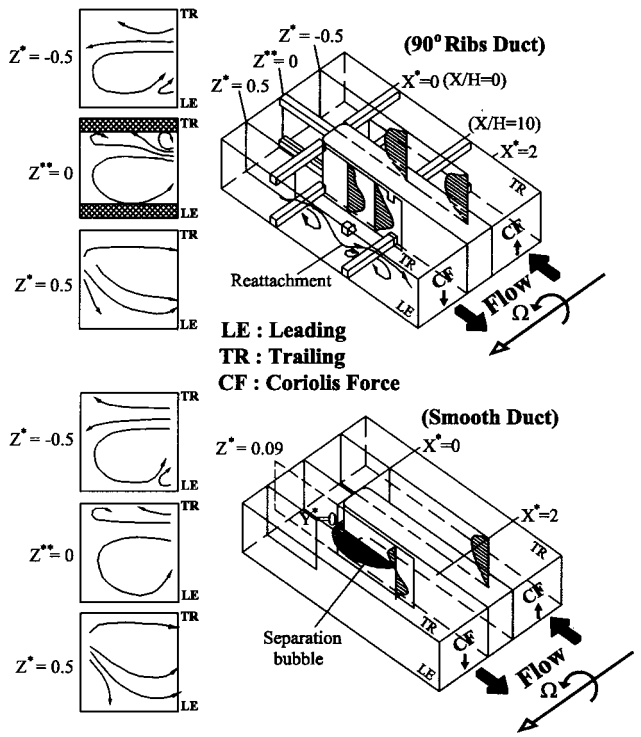

Fig. 12 A summary of flow patterns within the measurement range

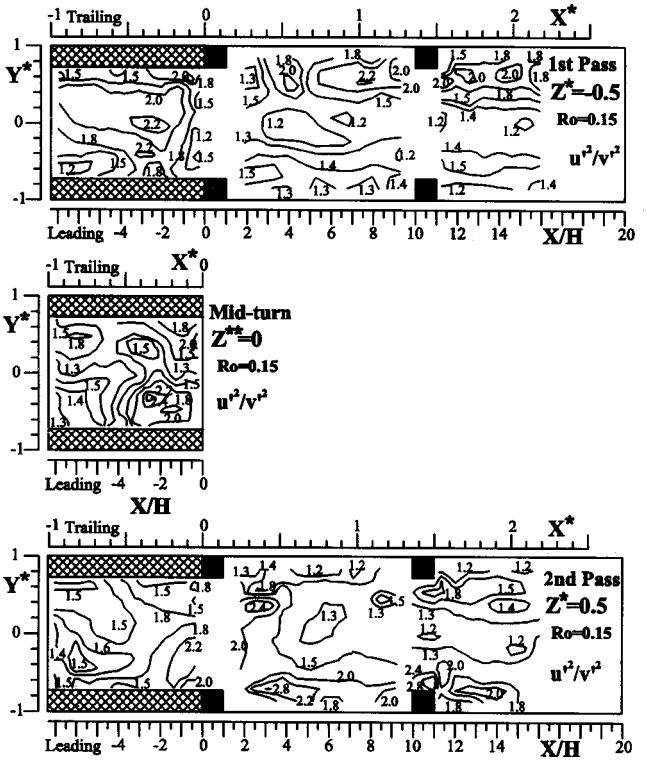

Fig. 13 Turbulence anisotropy in terms of u'^2/v'^2 contours in the first pass, turn region, and the second pass

clearly demonstrate the absence of turn-induced separation bubble within the range of measurements. It is attributed to the spatially periodic disruption of boundary layers on the leading and trailing walls by the ribs and contraction (or acceleration) into the rib gap to thin the boundary layers on the divider wall and outer side wall. These effects are particularly effective at the inlet of the 180-deg turn ($X/H=0$), the midturn ($Z^{**}=0$), the outlet of the turn ($X/H=0$), and the $X/H=10$ station in the second pass. It is worth pointing out that numerical prediction of flow and heat transfer in a stationary two-pass square channel with 90-deg parallel ribs employed on one wall performed by Jang et al. [24] also found the absence of the turn-induced separation bubble. It seems that duct rotation contributes little to the absence of turn-induced separation bubble. Conversely, the presence of periodic ribs which strip and thin the wall boundary layers has intimate relationship with the elimination of turn-induced flow separation. The jetlike profiles in Fig. 11(*b*) as a result of rib-induced flow contraction and expansion are further skewed by the Coriolis force. The degree of skewness and the *X*-component mean velocities in this plane ($Z^*=0.09$) increase with increasing Ro as can be realized by comparing Fig. 11(*c*) with Fig. 11(*b*). Without curvature-induced separation bubble for the ribbed duct case, the heat transfer augmentation immediately downstream of the 180-deg sharp turn near the divide wall is improved as shown in Figs. 7 and 9.

Turbulence Anisotropy. As mentioned in the Introduction, researchers who performed computations of the fluid flow and heat transfer in rotating internal cooling passages of turbine blade models (Prakash and Zerkle [9]; Iacovides and Raisee [10]; Jang et al. [24]) all pointed out the necessity of employing a turbulence model capable of capturing anisotropic turbulence effects. This is because the presence of ribs and sharp turns often generate anisotropic turbulence. Thus, experimental verification of the above statement would be valuable. Figure 13 shows the ratio of the Reynolds stress normal components in the first pass, 180-deg turn, and second pass as contours. In the first passage, the Coriolis force is directed toward the trailing wall such that the *U* profiles are also skewed toward the trailing wall. The high velocity gradients associated with skewed velocity profiles and rib generated shear layer on the trailing wall side result in high turbulence anisotropy, typically having values of 1.8~2.2. The situation is reversed in the second pass, typically having values of 1.8~2.8 on the leading wall side. In the 180-deg turn region, the turn and rib generated secondary flow leads to turbulence anisotropy of 1.3 to 2.4. As a comparison, Jang et al. [11] in their computations of flow and heat transfer in a stationary two-pass square channel with 90 deg ribs on one wall reported turbulence anisotropy, also in terms of the ratio of the Reynolds stress normal components, of 1 to 2, up to 2.3, and 1.5 to 2.9 in the first passage, turn region, and second passage, respectively.

Regional Averaged Nu Distribution. Figure 9 depicts that the presence of periodic ribs greatly enhances the regional averaged heat transfer over the entire serpentine passage, as supported by $Nu_{rg}/Nu_0>1$ over all region indexes for $Ro=0$ to 0.2 and by previous discussion from fluid dynamics point of view. In contrast, for a given value of Ro, say $Ro=0.15$, the level of Nu_{rg}/Nu_0 distribution for the smooth duct case ($H/D_H=0$, solid diamond in Fig. 9) is lower than that for the ribbed duct case (empty diamond in Fig. 9), except on the trailing wall of the second pass, and even lower than 1 on the leading wall (region indices: -4, -3 and -2 in Fig. 9(*a*)) of the first pass.

For the case of ribbed duct, the Nu_{rg}/Nu_0 on the leading wall in the first pass decreases with increasing rotation number (Fig. 9(*a*)) since the Coriolis force is directed toward the trailing wall and its strength increases with increasing Ro. The decrease is linear if Nu is normalized by its stationary counter part and averaged over the first pass, as shown in Fig. 14 where the data of Parsons et al. [14] is also included for comparison. Note that in Fig. 14 the $(Nu_p)_{rr}/(Nu_p)_{rs}$ data of the present work is actually averaged over the indices -2 to -4 coated by liquid crystal, while the data of Parsons et al. [14] is averaged over the length installed with thermocouples. Similar averages are applied to the second pass. A

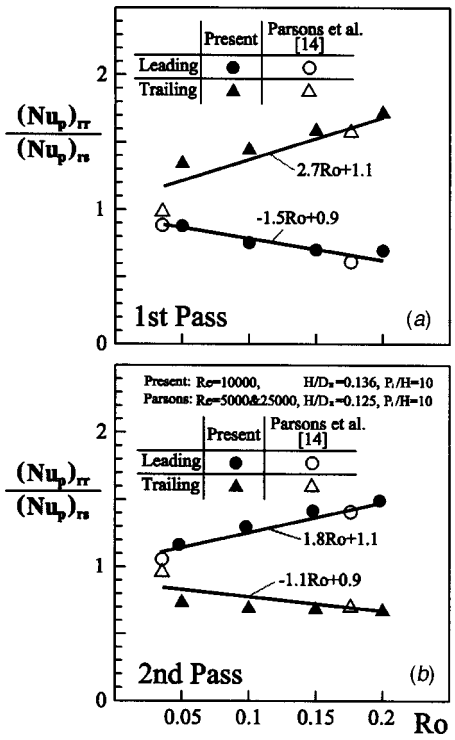

Fig. 14 Passage averaged Nusselt number ratio versus rotation number in (*a*) first pass, and (*b*) second pass for data from two research groups

simple linear equation, $(\mathrm{Nu}_p)_{rr}/(\mathrm{Nu}_p)_{rs} = -1.5\mathrm{Ro} + 0.9$, correlated the two sets of data is drawn in Fig. 14 for design reference. In general, Figs. 14 and 9 show that the two sets of data taken from two different research groups reveal similar trends on both leading and trailing walls of the first and second passes with some quantitative differences. The differences result from different rib heights H/D_H, lengths of average, Re, heating methods, etc.

The $\mathrm{Nu}_{rg}/\mathrm{Nu}_0$ on the leading wall in the second pass, (region indices 2 to 4, (Fig. 9(*a*)), however, increases as Ro is increased since the Coriolis force is now also directed toward the leading wall and its strength increases with increasing Ro. The increase is linear in terms of $(\mathrm{Nu}_p)_{rr}/(\mathrm{Nu}_p)_{rs}$ and can be correlated by the equation $(\mathrm{Nu}_p)_{rr}/(\mathrm{Nu}_p)_{rs} = 1.8\mathrm{Ro} + 1.1$ (Fig. 14(*b*)). Rotation affects the heat transfer enhancement on the trailing wall in the opposite way. The corresponding correlations are given in Fig. 14. As can be understood from previous discussion of flow characteristics, the heat transfer augmentation is the highest in the mid-turn region, around index 0 in Fig. 9, having $\mathrm{Nu}_{rg}/\mathrm{Nu}_0$ as high as 5.9. Wagner et al. [12] reported a maximum value 4.5 for H/D_H, Pi/H, Re, and Ro of 0.1, 10, 3.5×10^3, and 0 to 3.5, respectively, as mentioned in the Introduction. Hence, the comparison tends to suggest that H/D_H is a dominant factor in affecting heat transfer elevation.

Conclusions

Laser-doppler velocimetry and transient thermochromic liquid crystal thermography measurements have been performed in a rotating two-pass square-sectioned duct with 90-deg in-line ribs mounted on the leading and trailing walls. The heat transfer measurements using TLCT are unique in comparison with thermocouples and the steady-state liquid-crystal technique reported previously in open literature. The following conclusions can be drawn from the data presented:

1 Before the 180-deg sharp turn in the first passage the maximum streamwise mean velocity ($U_{\max}/U_b$) and turbulence intensity ($u'_{\max}/U_b$) of the rotating ribbed duct flow at the reference station increase up to 1.1 times and 2.5 times those of the rotating smooth duct flow, respectively, while the skewness of U profiles decreases to 40% of the rotating smooth duct value for the rotation number range examined. Both the $U_{\max}/U_b$ and skewness of U profiles increase linearly with increasing rotation number.

2 In the first half of the 180-deg turn, the cross-sectional flow is featured by a dominant streamwise vortex formed near the leading wall. As a result, most areas of the duct tip are directly encountered with flow impingement whereas two-thirds and one-third of the leading wall are experienced with downwash and upwash flow, respectively. Convective flow sweeps the trailing wall. All the above flow characteristics enhance the heat transfer in the corresponding regions except for the upwash flow which is detrimental to heat transfer elevation.

3 The secondary flow in the midturn cross section is characterized by the aforementioned dominant streamwise vortex on the leading wall side and two small and narrow streamwise vortices on the trailing wall side. The latter is different from one small and narrow streamwise vortex occurred in the smooth-walled duct flow. The total averaged strength of secondary flow and maximum turbulent kinetic energy in the mid-turn region of the ribbed duct flow increase up to 1.1 times those of the smooth duct flow.

4 In the rear half of the 180-deg turn, there is no more intact streamwise vortex. The duct tip and trailing wall are experienced with weak convective flow whereas the leading wall is confronted with downwash flow.

5 Downstream of the 180-deg turn, there exists no turn-induced separation bubble for the rotating ribbed duct case, a feature different from the rotating smooth-walled duct case and responsible for the improvement of heat transfer augmentation in the region immediately downstream of the turn and near the divider wall.

6 Turbulence anisotropy in terms of the ratio of Reynolds stress normal components is found to be rather high, having values of 1.2 to 2.2, 1.3 to 2.4, and 1.2 to 2.8 in the first pass, midturn, and second pass, respectively. The information provides a useful reference for numerical predictions of such flow fields.

7 Variations of regional and passage-averaged Nusselt number ratios with rotation number are found to be in reasonable agreement between the present TLCT and previous thermocouple results. Moreover, the passage averaged Nusselt number ratios on the leading and trailing walls of the first and second passes can be correlated as linear functions of rotation number.

Acknowledgment

Support for this work was partially provided by the National Science Council of the Republic of China under contract NSC 89-2212-E-007-135.

Nomenclature

A = half-width of duct [m]
B = half-height of duct [m]
C_p = specific heat [$\mathrm{Jkg^{-1}K^{-1}}$]
D_H = hydraulic diameter, 4AB/(A+B) [m]
h = heat transfer coefficient [$\mathrm{Wm^{-2}K^{-1}}$]
H = rib height [m]
k = turbulent kinetic energy, $(\overline{u^2}+\overline{v^2})/2$ [$\mathrm{m^2s^{-2}}$]
k_a = thermal conductivity of air [$\mathrm{Wm^{-1}K^{-1}}$]
k_w = thermal conductivity of wall [$\mathrm{Wm^{-1}K^{-1}}$]
Nu = local Nusselt no., $h \cdot D_H/k_a$
Nu_0 = Nusselt no. in fully developed tube flow $= 0.023 \cdot \mathrm{Re}^{0.8} \cdot \mathrm{Pr}^{0.4}$
Nu_p = passage-averaged Nusselt no.
Pi = rib pitch [m]
Pr = Prandtl no. of air, $\rho C_p \nu/k_a$
Re = Reynolds no., $U_b D_H/\nu$
Ro = rotation no., $\Omega D_H/U_b$
U = streamwise mean velocity [$\mathrm{ms^{-1}}$]

U_b = duct bulk mean velocity [ms^{-1}]
u = streamwise velocity fluctuation [ms^{-1}]
u' = rms value of streamwise velocity fluctuation, $\sqrt{u^2}$ [ms^{-1}]
V = transverse mean velocity [ms^{-1}]
v = transverse velocity fluctuation [ms^{-1}]
v' = rms value of transverse velocity fluctuation, $\sqrt{v^2}$ [ms^{-1}]
W = rib width [m]
W_1 = width of first-pass duct [m]
W_2 = width of second-pass duct [m]
W_d = divider thickness [m]
W_d^* = dimensionless divider thickness, $W_d/(W_1+W_2)$
X = streamwise coordinate, Fig. 2 [m]
X^* = normalized streamwise coordinate, X/D_H
Y = transverse coordinate, Fig. 2 [m]
Y^* = normalized transverse coordinate, Y/B
Z = spanwise coordinate, Fig. 2 [m]
Z^*, Z^{**}= normalized spanwise coordinate
(i) $X<0$, $Z^{**}=Z/(2A+W_d)$ (in turn)
(ii) $X\geqq 0$, $Z<0$, $Z^*=(Z+W_d/2)/2A$ (in first pass)
(iii) $X\geqq 0$, $Z>0$, $Z^*=(Z-W_d/2)/2A$ (in second pass)
α_w = thermal diffusivity of wall [m^2/s]
β = thermal expansion coefficient [1/K]
ρ = air density [kg/m^3]
σ = standard deviation
ν = kinematic viscosity [m^2/s]
Ω = rotating speed [rad s^{-1}]

Subscripts

b = bulk
rg = regional averaged
rr = ribbed duct with rotation
rs = ribbed duct without rotation
w = wall

References

[1] Elfer, M., 1993, "The Effect of Rotation and Buoyancy on Flow Development in a Rotating Circular Coolant Channel," *2nd International Symposium on Engineering Turbulence Modeling and Measurements*, May 31–June 2, Florence, Italy.
[2] Bons, J. P., and Kerrebrock, J. L., 1998, "Complementary Velocity and Heat Transfer Measurements in a Rotating Cooling Passage with Smooth Walls," ASME Paper No. 98-GT-464.
[3] Liou, T. M., and Chen, C. C., 1999, "LDV Study of Developing Flows through a Smooth Duct with 180-deg Straight-Corner Turn," Paper No. 97-GT-283, ASME J. Turbomach., **121**, pp. 167–174.
[4] Servouze, Y., 1998, "3D Laser Anemometry in a Rotating Cooling Channel," ASME Paper No. 98-GT-123.
[5] Chen, C. C., and Liou, T. M., 2000, "Rotating Effect on Fluid Flow in a Smooth Duct with a 180-Deg Sharp Turn," 45th ASME Int. Gas Turbine & Aeroengine Technical Congress, Munich, Germany. ASME Paper No. 2000-GT-228.
[6] Cheah, S. C., Iacovides, H., Jackson, D. C., Ji, H., and Launder, B. E., 1996, "LDA Investigation of the Flow Development through Rotating U-Ducts," ASME J. Turbomach., **118**, pp. 590–596.
[7] Hsieh, S. S., Chiang, M. H., and Chen, P. J., 1997, "Velocity Measurements and Local Heat Transfer in a Rotating Ribbed Two-Pass Square Channel with Uneven Wall Heat Flux," ASME Paper No. 97-GT-160.
[8] Tse, G. N., and Steuber, G. D., 1997, "Flow in a Rotating Square Serpentine Coolant Passage With Skewed Trips," ASME Paper No. 97-GT-529.
[9] Prakash, C., and Zerkle, R., 1995, "Prediction of Turbulent Flow and Heat Transfer in a Ribbed Rectangular Duct With and Without Rotation," ASME J. Turbomach., **177**, pp. 255–264.
[10] Iacovides, H., and Raisee, M., 1999, "Recent Progress in the Computation of Flow and Heat Transfer in Internal Cooling Passages of Turbine Blades," Int. J. Heat Mass Transf., **20**, pp. 320–328.
[11] Jang, Y. J. Chen, H. C., and Han, J. C., 2000, "Flow and Heat Transfer in a Rotating Square Channel with 45° Angled Ribs by Reynolds Stress Turbulence Mosel," 45th ASME Int. Gas Turbine & Aeroengine Technical Congress, Munich, Germany.
[12] Wagner, J. H., Johnson, B. V., Graziani, R. A., and Yeh, F. C., 1992, "Heat Transfer in Rotating Serpentine Passages with Trips Normal to the Flow," ASME J. Turbomach., **114**, pp. 847–857.
[13] Johnson, B. V., Wagner, J. H., Steuber, G. D., and Yeh, F. C., 1994, "Heat Transfer in Rotating Serpentine Passages with Trips Skewed to the Flow," ASME J. Turbomach., **116**, pp. 113–123.
[14] Parsons, J. A., Han, J. C., and Zhang, Y. M., 1994, "Wall Heating Effect on Local Heat Transfer in a Rotating Two-Pass Square Channel with 90° Rib Turbulators," Int. J. Heat Mass Transf., **37**, No. 9, pp. 1411–1420.
[15] Zhang, Y. M., Han, J. C., Parsons, J. A., 1993, "Surface Heating Effect on Local Heat Transfer in a Rotating Two-Pass Square Channel with 60° Angled Rib Turbulators," ASME J. Turbomach., **117**, pp. 272–280.
[16] Taslim, M. E., Rahman, A., and Spring, S. D., 1991, "An Experimental Investigation of Heat Transfer Coefficients in a Spanwise Rotating Channel with Two Opposite Rib-Roughened Walls," ASME J. Turbomach., **113**, pp. 75–82.
[17] El-Husayni, H. A., Taslim, M. E., and Kercher, D. M., 1994, "Experimental Heat Transfer Investigation of Stationary and Orthogonally Rotating Asymmetric and Symmetric Heated Smooth and Turbulated Channels," ASME J. Turbomach., **166**, pp. 124–132.
[18] Liou, T. M., Tzeng, Y. Y., and Chen, C. C., 1999, "Fluid Flow in a 180 deg Sharp Turning Duct With Different Divider Thickness," ASME J. Turbomach., **121**, pp. 569–576.
[19] Liou, T. M., Chen, C. C., and Tsai, T. W., 2000, "Heat Transfer and Fluid Flow in a Square Duct with 12 Different Shaped Vortex Generators," ASME J. Heat Transfer, **122**, pp. 327–335.
[20] Liou, T. M., Chen, C. C., and Chen, M. Y., 2001, "TLCT and LDV Measurements of Heat Transfer and Fluid Flow in a Rotating Sharp Turning Duct," Int. J. Heat Mass Transf., **44**, No 9, pp. 1777–1787.
[21] Durst, F., Melling, A., and Whitelaw, J. H., 1976, *Principles and Practice of Laser-Doppler Anemometry*, Academic Press, New York, NY.
[22] Chang, S. W., and Morris, W. D., 1998, "A Comparative Study of Heat Transfer Between Rotating Circular Smooth-Walled and Square Rib-Roughened Ducts With Cooling Application for Gas Turbine Rotor Blade," JSME Int. J., Ser. B, **41**, pp. 302–315.
[23] Chang, S. W., 1995, "An Experimental Study of Heat Transfer in the Cooling Passages of Gas Turbine Rotor Blades," doctoral dissertation, Department of Mechanical Engineering, University of Wales, Swansea, UK.
[24] Jang, Y. J., Chen, H. C., and Han, J. C., 2000, "Numerical Prediction of Flow and Heat Transfer in a Two-Pass Square Channel with 90° Ribs," Proc., 8th International Symposium on Transport Phenomena and Dynamics of Rotating Machinery, Honolulu, HI, **1**, pp. 580–587.

H. S. Wijesinghe
C. S. Tan
E. E. Covert

Gas Turbine Laboratory,
Department of Aeronautics and Astronautics,
Massachusetts Institute of Technology,
Cambridge, MA 02139

Aerodynamic Response of Turbomachinery Blade Rows to Convecting Density Wakes

A two-dimensional computational study was conducted to characterize the density wake induced force and moment fluctuations on a compressor blade row. The flow simulations indicate unsteady blade excitation generated by: (1) density wake fluid directed to the blade suction surface, (2) axial deflection of the blade passage shock wave position and (3) formation of a separation bubble on the blade suction surface. The blade force and moment fluctuation amplitudes are found to scale with the nondimensional density wake width w/c and a nondimensional density parameter ρ^*. [S0889-504X(00)01504-X]

Introduction and Background

Increased operational requirements and increased thrust-to-weight ratios have led to higher mean and fluctuating stresses in components of modern turbomachinery. This has increased the likelihood of encountering high cycle fatigue (HCF) failure in fan, compressor, and turbine blades. The U.S. Air Force in particular claims 50 percent of their total irrecoverable in-flight engine shutdowns can be traced to HCF failure. This clearly places a huge burden on maintaining a mission ready force and consequently the prevention of HCF failure in turbomachinery components has become an increasingly important issue. An additional implication is that it is difficult to extract general guidelines for HCF prevention because of the high dimensionality of the parameter space that must be explored. Further complexity is introduced by the diversity of local phenomena, e.g., tip leakage flows, unsteady shock motion, and local separation that are characteristic of turbomachinery flows. At a recent HCF workshop held at the MIT Gas Turbine Laboratory [1] it was noted that " . . . forced blade response is not currently predictable, and structural design and analysis for high cycle fatigue situations have not advanced beyond the early concepts of the fatigue limit, the Goodman diagram and Miner's rule."

The goal of the present study is to contribute to the aerodynamic forced response aspect of the HCF problem. While the influence of velocity and pressure disturbances on engine operation have been considered in great detail [2,3], the present study is focused on characterizing low-density (high-temperature) wakes. Density wakes can enter the engine from ground ingested hot air, steam ingestion during carrier launches, and exhaust gas ingestion from forward firing weapons [4]. The difference in temperature between the blades and the surrounding fluid can also generate density gradients, particularly in the downstream wakes of blades.

Marble [5] was first to recognize the technological relevance of density nonuniformities as a source for fluctuating blade loads. In his fundamental contribution he generalized classical nonstationary airfoil theory and the application of Kelvin's theorem to the situations of airfoils in nonuniform density fields. In such situations, the flow unsteadiness arises from vorticity generated by the interaction of the convected density field and the airfoil pressure field. Marble further shows that lift and moment on a flat plate airfoil can respond prior to intercept with a density nonuniformity.

Marble's seminal work on this topic motivated Ramer et al. [6] to implement inviscid, incompressible numerical simulations of sinusoidal and square wave density wake profiles convecting past a compressor blade row. The basic physical mechanism responsible for blade excitation in inviscid, incompressible flow is illustrated in Fig. 1. As the density wake moves through the blade row, the low-density fluid migrates toward the suction side (low-pressure side) of the blades. To satisfy mass conservation, the surrounding higher density fluid is displaced toward the pressure side of the blade. This relative motion of low and high-density fluids generates a pair of counterrotating vortices in the blade passage. The generation of vorticity in this manner by misaligned density gradients and pressure gradients is commonly referred to as "baroclinic torque." The blade pressure distribution is influenced by the impact of the low-density fluid on the blade surface and hence the blade force and moment coefficients change with time during passage of the density wake.

The present work extends Ramer's analysis to viscous, compressible flow regimes. This paper highlights the interaction of density wakes with shock waves and blade boundary layers. The technical approach is described first together with a summary of the nondimensional parameters used to characterize the density wake and force and moment fluctuations. This is followed by a discussion of the viscous flow simulation results and the physical mechanisms responsible for blade excitation during the passage of density wakes.

Technical Approach

Computational fluid dynamics (CFD) is the "tool" used to investigate the forces and moments induced by convecting density wakes. The present study is focused on two-dimensional unsteady flows and a single density wake convecting through a single compressor blade row geometry.[1] The compressor blade profile used is the General Electric, Low-Speed Research Compressor (LSRC) stator-B blade [7]. The density wakes considered convect along the axial direction and have density gradients also directed in this direction. Discussion is focused on low-density wakes (wake densities lower than free-stream density), which are more common in compressor blade passages. The density variation inside the wake is specified to be sinusoidal.

An unsteady, compressible, integrated Euler and Navier–Stokes solver was used to conduct the flow simulations. The key features of the flow solver are summarized below. For specific implementation details see Hoying [8].

1. Finite difference discretization.
2. Fourth-order spatial accuracy and third-order temporal accuracy.

Contributed by the International Gas Turbine Institute and presented at the 45th International Gas Turbine and Aeroengine Congress and Exhibition, Munich, Germany, May 8–11, 2000. Manuscript received by the International Gas Turbine Institute Feb. 2000. Paper No. 2000-GT-417. Review Chair: D. Ballal.

[1]While turbine blades are subjected to larger density nonuniformities (due to hot streaks from the combustor and from blade cooling), compressor blades are considered here since they are more susceptible to HCF failure.

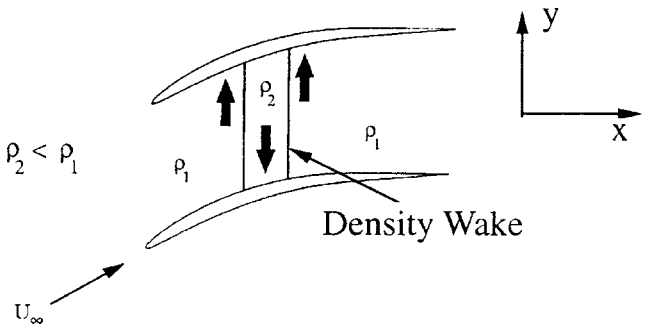

Fig. 1 Density wake convecting through a compressor blade row

3 Dispersion Relation Preserving (DRP) scheme [9].
4 $k-\varepsilon$ turbulence model.
5 Wall functions [10]
6 Nonreflecting inlet and exit boundary conditions [11].

The computational domain used in the solver is shown schematically in Fig. 2. The flow upstream and downstream of the blade row is assumed to be governed by the Euler equations. The flow in the blade passages surrounding the blades is assumed to be governed by the Navier–Stokes equations. This division helps to reduce the required computational resources since the solution of the more expensive Navier–Stokes equations is confined to a physically smaller region of the flow.

Additional computational savings are achieved by using wall functions to model the inner portion of the blade boundary layers. Wall functions allow the first near wall grid point to be located at $y^+ \approx 30-150$. This results in a considerable saving of the number of near-wall grid points. An adiabatic wall boundary condition is also applied at the blade surface.

Nonreflecting boundary conditions developed by Giles [11] are implemented at the inlet and exit boundaries of the computational domain to allow all outgoing modes of the solution to propagate through the boundaries with minimal reflection. Periodic boundary conditions are imposed along the side boundaries parallel to the axial flow direction.

Governing Nondimensional Parameters

The vorticity production due to misaligned density gradients and pressure gradients in two-dimensional, inviscid, incompressible flow can be expressed by the linearized relation

$$\left(\frac{\partial}{\partial t}+U\frac{\partial}{\partial x}\right)\overline{\omega}=\frac{1}{\rho^2}\nabla p\times\nabla\rho \tag{1}$$

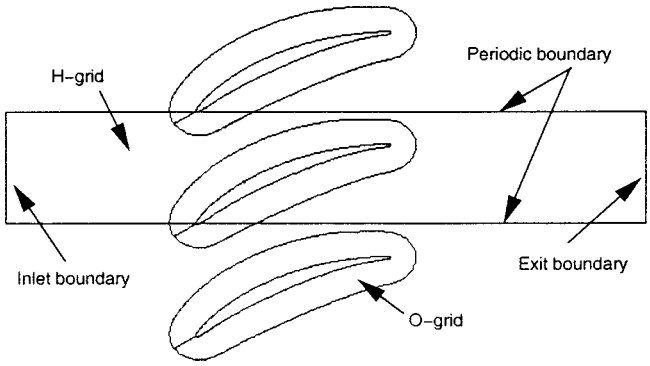

Fig. 2 Schematic of the computational domain and boundary conditions

If the density gradient ($\nabla\rho$) is large (zeroth order), the convected vorticity ω is of the same order as the pressure field [5].

Marble's linearized analysis provides a basic understanding of the parameters involved in this problem. In particular the density parameter

$$\rho^*=\frac{\rho_2-\rho_1}{\rho_2+\rho_1} \tag{2}$$

is shown to be a key parameter in the unsteady loading. Rewriting Eq. (1) using the density parameter ρ^* and the nondimensionalized vorticity $\overline{\omega}=\overline{\omega}c/U_\infty$ gives

$$\frac{D\overline{\omega}}{D\tau}=\frac{c^2}{wh}\rho^*\left[\frac{1}{\tilde{\rho}^2}(\tilde{\nabla}_w\tilde{\rho}\times\tilde{\nabla}_h\tilde{p})\right] \tag{3}$$

where

$$\tilde{p}=\frac{p}{(\rho_2-\rho_1)U_\infty^2}$$

$$\tau=\frac{U_\infty}{c}t$$

$$\overline{\rho}=\frac{\rho}{\rho_1+\rho_2}$$

$$\tilde{\nabla}_w=w\nabla$$

$$\tilde{\nabla}_h=h\nabla$$

Equation (3) suggests the nondimensional wake width w/c and nondimensional blade spacing h/c to be additional key parameters. The blade force and moment response due to passage of density wakes will be characterized in terms of the nondimensional parameters ρ^* and w/c. Variations in nondimensional blade spacing h/c are not investigated in this study.

Results From the Viscous Flow Simulations

The viscous flow simulations were conducted at Mach numbers ranging from $M_\infty=0.15$ to $M_\infty=0.87$ and Reynolds number $\mathrm{Re}(U_\infty,c)\approx 700{,}000$.[2] The mechanisms that contribute to density wake-induced blade excitation in these flow regimes are best described with reference to the time varying blade force and moment response profiles shown in Fig. 3. The force and moment profiles can be divided into three different regions defined by the position of the density wake. Table I lists the position of the density wake at selected times.

1 *Baseline response region*. This response corresponds to all times when the density wake is upstream of the compressor blade leading edge. The force and moment fluctuations observed here are a consequence of vortex shedding and will not be described in this context.

2 *Primary response region*. This response corresponds to when the density wake is within the compressor blade passage. The characteristic flow features here are the fluid flux directed to the blade surfaces and the associated counterrotating vortices [6]. For flow at $M_\infty=0.87$ deflection of the blade passage shock wave position is also observed.

3 *Secondary response region*. This response corresponds to all times after the density wake leaves the compressor blade row. A separation bubble is formed on the blade suction surface during this response.

Density Gradient–Blade Pressure Gradient Interaction. The primary response is attributed to the transport of low-density wake fluid to the blade suction surface. This transport can be seen in the disturbance velocity vectors plotted in Fig. 5. A pair of

[2]Typical for fan blade/IGV at sea level take-off conditions.

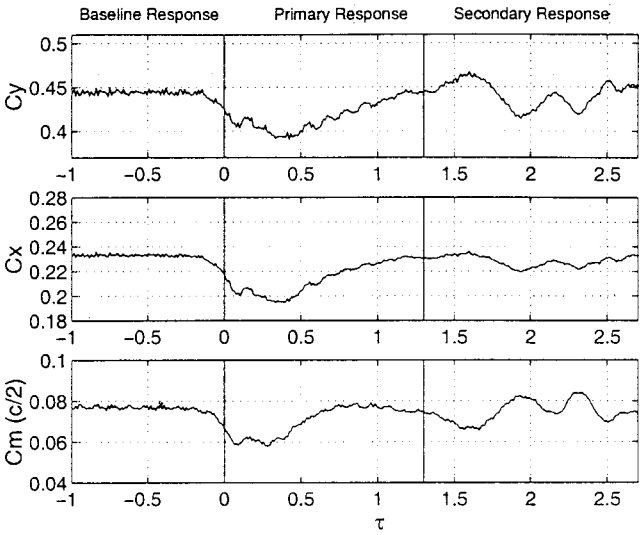

Fig. 3 Fluctuations in (1) azimuthal force coefficient, (2) axial force coefficient, and (3) moment coefficient (positive clockwise about the midchord) during passage of a density wake. Three distinct regions can be identifies in the response. $w/c=0.2$, $\rho^*=-0.333$, $M_\infty=0.15$.

Table 1 Location of the density wake at different times during passage through the compressor blade row. $w/c=0.2$, $\rho^*=-0.333$, $M_\infty=0.15$

Convective Time Scale (τ)	Location of density wake
0.0	wake l.e. intercepts blade l.e.
0.1	wake t.e. intercepts blade l.e.
1.3	wake t.e. passes blade t.e.

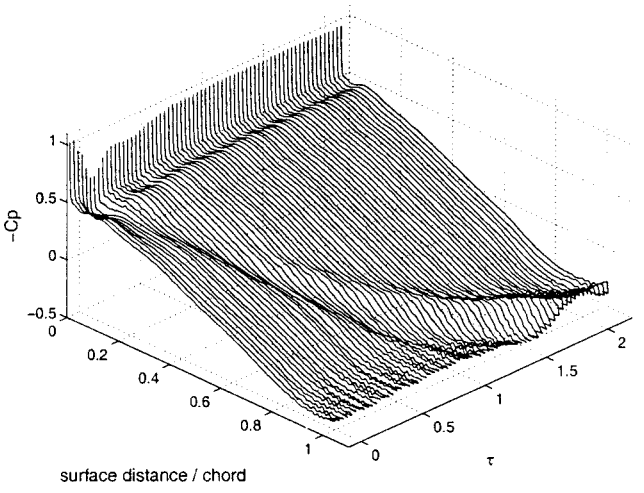

Fig. 4 Suction surface pressure distribution during passage of a density wake width, $w/c=0.2$ and $\rho^*=-0.333$

counterrotating vortices is also formed as the higher density freestream fluid is displaced toward the blade pressure surface. The impingement of the low-density fluid on the suction surface results in a local increase in the blade static pressure. This effect can be seen in the suction surface pressure distribution plotted in Fig. 4. As the density wake convects downstream, the static pressure

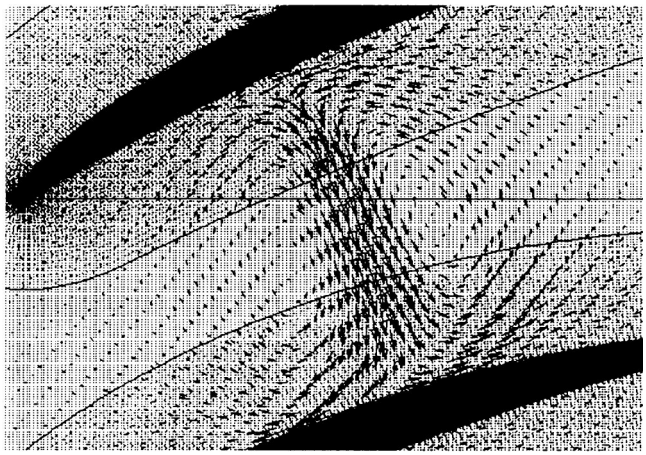

Fig. 5 Perturbation velocity vectors indicate a pair of counterrotating vortices in the blade passage; $w/c=0.2$, $\rho^*=-0.333$, $M_\infty=0.15$, $\tau=0.78$.

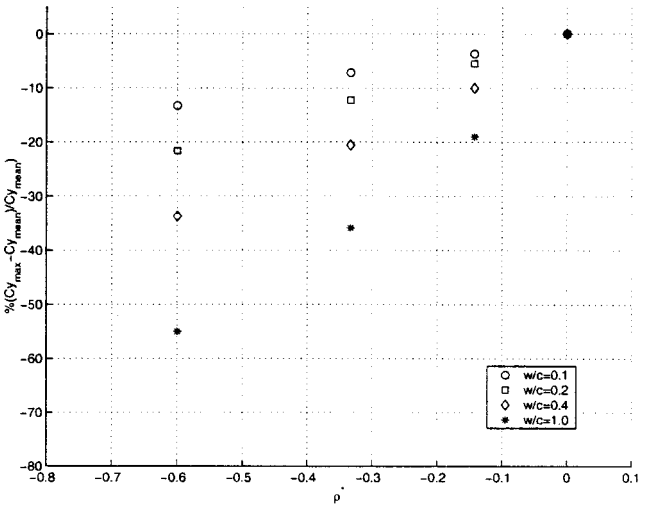

Fig. 6 Maximum fluctuation in the azimuthal force coefficient as functions of density wake width and density parameter; $M_\infty=0.15$

increase moves further aft along the blade suction surface. A corresponding decrease in static pressure occurs at the blade pressure surface due to the low pressure core of the counterrotating vortices. The net result is a local reduction in the static pressure difference across the blade and a decrease in the blade force and moment coefficients.

The magnitude of the force and moment fluctuations increases as the fluid flux to the blade surface increases. Hence larger wake widths w/c and larger density parameter ρ^* increase the magnitude of the blade force and moment fluctuations.[3] Figure 6 indicates these results for the azimuthal force coefficient for a range of wake widths and density parameters. For $w/c \leq 0.2$ the azimuthal force coefficient fluctuation scales linearly. Increasing nonlinearity is observed with increasing $|\rho^*|$ at larger wake widths.

Similar trends can be seen for the moment coefficient fluctuation and axial force coefficient fluctuation over the range of density wake widths $0.1 \leq w/c \leq 1.0$ and range of density parameters $-0.6 \leq \rho^* \leq 0.0$ considered.

[3]Larger $|\rho^*|$ is associated with larger density gradients hence stronger vorticity in the blade passage.

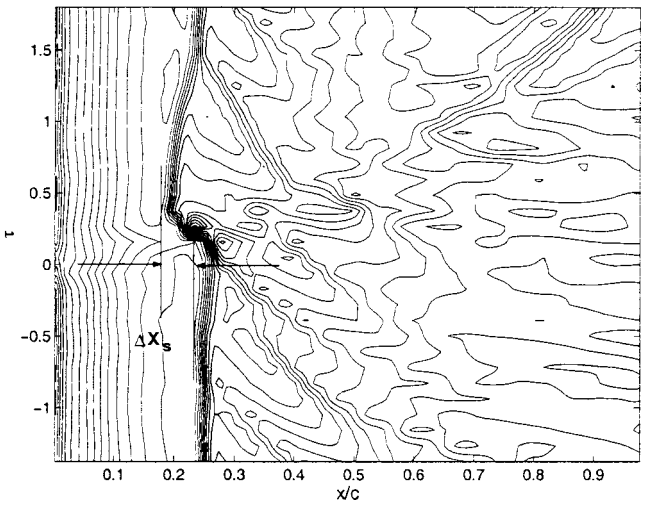

Fig. 7 Blade suction surface pressure contours show the upstream motion of the blade passage shock wave during passage of a density wake, $w/c=0.2$ and $\rho^*=-0.333$. The dark band initially at $x/c=0.25$ is the shock front. $M_\infty=0.87$.

Density Wake–Shock Wave Interaction. As the flow Mach number increases, the flux of density wake fluid to the blade suction surface continues to affect the blade force and moment fluctuations. At Mach number $M_\infty=0.87$ additional excitation occurs due to shock wave displacement induced by passage of the density wake. For steady flow at $M_\infty=0.87$ the shock wave is located $0.25c$ downstream of the blade leading edge, as shown in Fig. 7. During passage of a density wake $w/c=0.2$ and $\rho^*=-0.333$, the shock front is displaced upstream by approximately $0.05c$. The upstream motion of the shock wave is a consequence of the lower Mach number inside the density wake (due to the higher temperature and hence higher speed of sound). As the density wake convects further downstream the shock wave gradually returns to the steady position.

An additional excitation mechanism appears during passage of density wakes with larger density differences ($\rho^*\leq -0.6$). Figure 8 shows the time variation in blade suction surface pressure contours during passage of a density wake of width $w/c=0.4$ and $\rho^*=-0.6$. The shock front disappears at $\tau\approx 0.4$ as the density wake convects over the leading edge of the blade and reappears at $\tau\approx 1.2$ as the density wake convects farther downstream. This temporary suppression of the shock wave is also a consequence of the decrease in local flow Mach number within the density wake. In this case the reduction in local Mach number is such that supersonic flow over the blade leading edge ''switches'' to subsonic flow. The wider the density wake, the longer time the shock wave is suppressed.

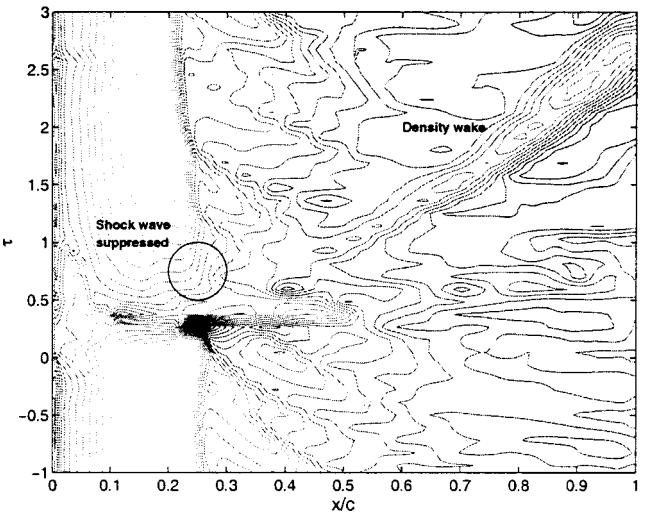

Fig. 8 Blade suction surface pressure contours show the temporary suppression of the blade passage shock wave during passage of a density wake, $w/c=0.4$ and $\rho^*=-0.6$. The dark band at $x/c=0.25$ is the shock front. $M_\infty=0.87$.

Table 2 Comparison of the maximum fluctuation in the azimuthal force coefficient and moment coefficient for the $M_\infty=0.87$ and $M_\infty=0.63$ simulations. Results for $M_\infty=0.63$ are shown in brackets.

w/c	ρ^*	% ΔCy	% ΔCm
0.1	-0.600	-28.0 (-14.4)	-47.3 (-30.1)
0.1	-0.333	-12.6 (-8.5)	-21.8 (-17.7)
0.1	-0.143	-6.4 (-3.7)	-16.2 (-7.9)
0.2	-0.600	-39.9 (-20.5)	-64.9 (-48.0)
0.2	-0.333	-19.9 (-13.2)	-30.2 (-30.7)
0.2	-0.143	-10.9 (-6.9)	-17.6 (-14.6)
0.4	-0.600	-49.8 (-33.0)	-75.6 (-71.1)
0.4	-0.333	-32.0 (-20.8)	-33.5 (-46.8)
0.4	-0.143	-17.6 (-11.6)	-10.3 (-22.9)

The quantitative effect of shock motion on the blade force and moment coefficients is seen by comparing the $M_\infty=0.63$ and $M_\infty=0.87$ simulation results in Table 2 (note the $M_\infty=0.63$ simulation does not contain blade passage shock waves). Table 2 shows the azimuthal force coefficient fluctuation magnitudes to differ by a factor 1.5–2.0 between the $M_\infty=0.63$ and $M_\infty=0.87$ simulations. The magnitude of the fluctuations also increase with $|\rho^*|$ and w/c, and similarly for the moment coefficient fluctuation magnitudes.

Density Wake–Boundary Layer Interaction. The blade force and moment continue to fluctuate after the density wake leaves the blade passage (Fig. 3). This fluctuation occurs due to the formation of a separation bubble on the blade suction surface. As the density wake convects through the blade passage, the fluid flux to the suction surface decelerates the boundary layer fluid upstream and increases the boundary layer thickness. As the density wake leaves the blade passage the decelerated boundary layer fluid accelerates and forms a convecting separation bubble. The separation bubble consists of a concentrated flow recirculation zone with a low pressure core region. A portion of the density wake fluid also remains ''trapped'' inside the bubble[4] as shown in Fig. 9.

In Fig. 10 the location of the blade separation point is plotted during passage of the density wake. The separation point is initially located at $0.94c$. As the separation bubble is formed the separation point moves upstream to $0.76c$ and reattaches at $0.84c$. The separation bubble then grows rapidly in the stream wise direction to a maximum length of approximately $0.20c$. After the separation bubble leaves the blade suction surface, continued fluctuation in the separation point occurs with an amplitude of $0.05c$. Comparison of Figs. 11 and 12 shows that the maximum upstream motion of the separation point correlates well with the maximum

[4]This trapped low density fluid corresponds to a high temperature ''spot'' which can influence the blade thermal stress distribution and hence also the life of the blade.

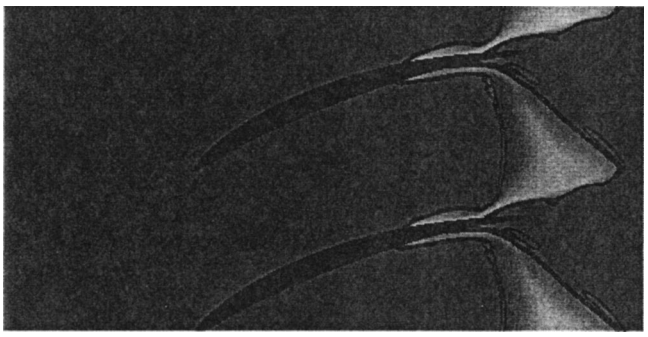

Fig. 9 Density contour image showing trapped density wake fluid at the blade trailing edge; $w/c=0.2$, $\rho^*=-0.333$, $M_\infty=0.15$, $\tau=1.28$

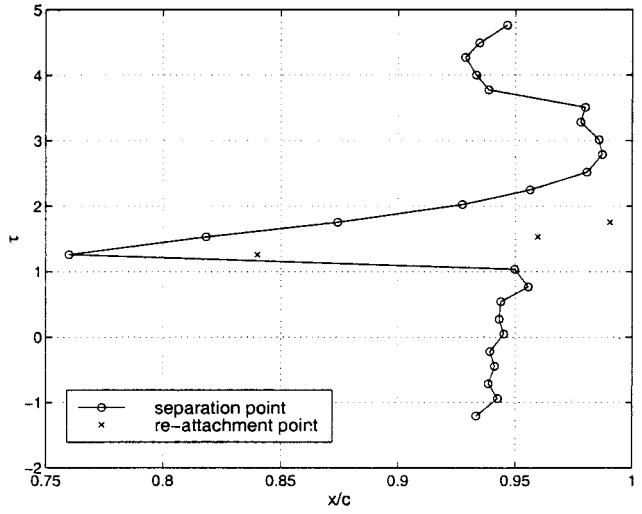

Fig. 10 Fluctuation of the suction surface flow separation and re-attachment points during passage of a density wake; $w/c=0.2$, $\rho^*=-0.333$, $M_\infty=0.15$.

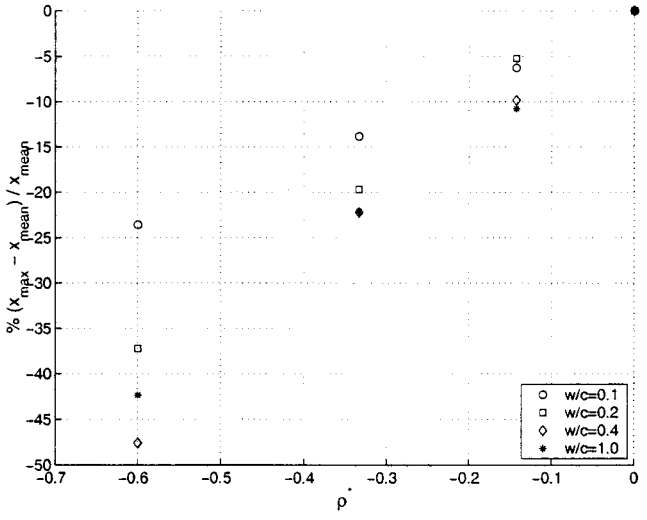

Fig. 11 Maximum change in the suction surface separation point from the mean baseline position as a function of wake width and density ratio; $M_\infty=0.15$.

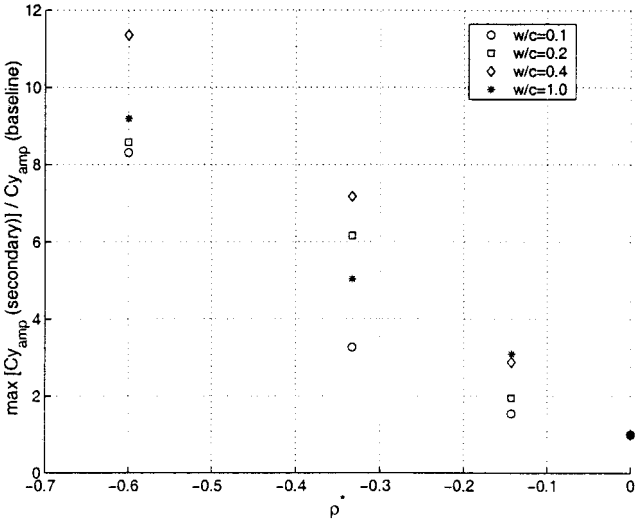

Fig. 12 Maximum fluctuation in the blade azimuthal force coefficient in the secondary response region as a function of wake width and density ratio; $M_\infty=0.15$ (amp=amplitude)

amplitude of the azimuthal force coefficient fluctuation. The maximum amplitude of the moment coefficient fluctuation also follows this same trend.

The amplitude of azimuthal force fluctuation during passage of wakes width $w/c=1.0$ is smaller than during passage of wakes width $w/c=0.4$ in the range $\rho^*\leq -0.333$. Examination of flow velocity vectors shows this reversal in trend to be attributed to the smaller streamwise extent (approximately $0.05c$) of the separation bubble formed on the suction surface.

Conclusions

The passage of low-density (high-temperature) wakes through a compressor blade row generates unsteady blade force and moment fluctuations, which are a potential new source for high cycle fatigue failure. The relative contribution of (1) baroclinic torque. (2) shock wave fluctuation, and (3) separation point fluctuation on the blade force and moment response is summarized in Table 3 for the case of a wake width $w/c=0.2$ and $\rho^*=-0.333$.

The following conclusions are reached in this study:

1 The density wake induced force and moment fluctuations scale with the nondimensional density wake width w/c and a nondimensional density parameter $\rho^*=(\rho_2-\rho_1)/(\rho_2+\rho_1)$ for a given compressor geometry.

2 The interaction of the wake density gradient and the blade pressure gradient generates a flux of density wake fluid to the blade suction surface (baroclinic torque). The impact of this low-density fluid on blade suction surface effects the blade pressure distribution and hence the blade force and moment fluctuation.

3 The density wake–blade passage shock wave interaction at higher Mach number ($M_\infty=0.87$) results in upstream motion of the shock front. This is a consequence of the lower Mach number within the density wake.

4 Temporary shock wave suppression is observed during passage of density wakes of width $w/c\geq 0.2$ and density parameter $\rho^*\leq -0.6$. The lower Mach number within the density wake ''switches'' the flow from supersonic to subsonic over the leading edge of the blade. The shock wave is re-established as the wake convects further downstream.

5 The fluid flux directed to the blade suction surface deflects the blade boundary layer to form a convecting separation bubble. The maximum upstream movement of the separation point scales

Table 3 Comparison of the contribution from various mechanisms to the azimuthal force coefficient fluctuation; $w/c=0.2$. $\rho^*=0.333$.

	Primary Response $\frac{Cy_{max}-Cy_{mean}}{Cy_{mean}}$		Secondary Resp. $max\left[\frac{Cy_{amp}(sec.)}{Cy_{amp}(base.)}\right]$
Flow	Baroclinic Torque	Shock fluctuation	Separation pt. fluctuation
Inviscid Incompressible	-10.0%	0.0	0.0
Viscous ($M_\infty = 0.15$)	-12.3%	0.0	6.2
Viscous ($M_\infty = 0.87$)	-12.3%	-7.6%	2.7

with the density wake width w/c and the density parameter ρ^*. The magnitude of the corresponding force and moment fluctuation also scales with these parameters.

Acknowledgments

The authors wish to acknowledge the assistance of Prof. Frank Marble of CalTech and Prof. Nick Cumpsty of Cambridge University for useful discussions and direction. This research has been supported by the Air Force Office of Scientific Research under grant number F49620-94-1-0202 with Major Brian Sanders as grant monitor and by the Wright Patterson Air Force Laboratory under grant number 153616 with Dr. Douglas Rabe as technical monitor.

Nomenclature

c = blade chord
h = blade spacing
p = static pressure
t = time
u = velocity in axial direction
v = velocity in azimuthal direction
w = wake width
x = axial direction coordinate
y = azimuthal direction coordinate
y^+ = boundary layer coordinate
Cm = moment coefficient about midchord (positive clockwise)
Cp = pressure coefficient
Cx = axial force coefficient
Cy = azimuthal force coefficient
M = Mach number
Re = Reynolds number
U = mean velocity
ρ = density
ρ^* = density parameter $=(\rho_2-\rho_1)/(\rho_2+\rho_1)$
τ = nondimensional time
ω = vorticity
1 = free-stream or value outside density wake
2 = peak value inside density wake
∞ = free-stream value or total value
$\tilde{(\ )}$ = nondimensionalized quantity
$\overline{(\ )}$ = mean quantity
Δ = difference operator
∇ = gradient operator

References

[1] *Basic Research Issues in Aerodynamics, Structural Dynamics and Control of High Cycle Fatigue*. Summary of a Workshop held at the Gas Turbine Laboratory, MIT, October 1995.
[2] Kerrebrock, J. L., and Mikolajczak, A. A., 1970, ''Intra-Stator Transport of Rotor Wakes and its Effect on Compressor Performance,'' ASME Paper No. 70-GT-39.
[3] Valkov, Theodore V., 1992, ''Control of Unsteady Flow in a Stator Blade Row Interacting With Upstream Moving Wakes.'' S. M. Thesis, Massachusetts Institute of Technology, Department of Aeronautics and Astronautics; also GTL Report No. 255, May.
[4] Platzer, M. F., 1978, ''Unsteady Flows In Turbomachines—A Review of Current Developments,'' AGARD CP-227, Paper 33.
[5] Marble, F. E., 1993, ''Response of a Thin Airfoil Encountering a Strong Density Discontinuity,'' ASME J. Fluids Eng., **115**, pp. 580–589.
[6] Ramer, B. E., Wijesinghe, H. S., Tan, C. S. and Covert, E. E., 1997, ''Aerodynamic Response of Turbomachinery Blade Rows to Convecting Density Wakes,'' *Proc. ASME Aerospace Division*, ASME AD-Vol. 55.
[7] Wisler, D. C., 1977, ''Core Compressor Exit Stage Study, Volume I—Design Report,'' NASA CR-135391, NASA Lewis Research Center, Dec.
[8] Hoying, D. A., 1996, ''Blade Passage Flow Structure Effects on Axial Compressor Rotating Stall Inception,'' Ph.D. thesis, Massachusetts Institute of Technology, Department of Aeronautics and Astronautics, Sept.
[9] Tam, C. K. W., and Webb, J. C., 1993, ''Dispersion-Relation-Preserving Finite Difference Schemes for Computational Acoustics,'' J. Comput. Phys., **107**, pp. 262–281.
[10] Chieng, C. C., and Launder, B. E., 1980, ''On the Calculation of Turbulent Heat Transport Downstream From an Abrupt Pipe Expansion,'' Numer. Heat Transfer, Part A, **3**, pp. 189–207.
[11] Giles, M. B., 1988, ''Non-Reflecting Boundary Conditions for the Euler Equations,'' CFDL-TR-88-1, Computational Fluid Dynamics Laboratory, Massachusetts Institute of Technology, Feb.

Dale E. Van Zante[1]
Mem. ASME
Iowa State University,
Ames, IA 50011
e-mail: dale.vanzante@slgrc.nasa.gov

John J. Adamczyk
Mem. ASME

Anthony J. Strazisar
Mem. ASME

NASA Glenn Research Center,
Cleveland, OH 44135

Theodore H. Okiishi
Mem. ASME
Iowa State University,
Ames, IA 50011

Wake Recovery Performance Benefit in a High-Speed Axial Compressor

Rotor wakes are an important source of loss in axial compressors. The decay rate of a rotor wake is largely due to both mixing (results in loss) and stretching (no loss accrual). Thus, the actual loss associated with rotor wake decay will vary in proportion to the amounts of mixing and stretching involved. This wake stretching process, referred to by Smith (1996) as recovery, is reversible and for a 2-D rotor wake leads to an inviscid reduction of the velocity deficit of the wake. It will be shown that for the rotor/stator spacing typical of core compressors, wake stretching is the dominant wake decay process within the stator with viscous mixing playing only a secondary role. A model for the rotor wake decay process is developed and used to quantify the viscous dissipation effects relative to those of inviscid wake stretching. The model is verified using laser anemometer measurements acquired in the wake of a transonic rotor operated alone and in a stage configuration at near peak efficiency and near stall operating conditions. Results from the wake decay model exhibit good agreement with the experimental data. Data from the model and laser anemometer measurements indicate that rotor wake straining (stretching) is the primary decay process in the stator passage. Some implications of these results on compressor stage design are discussed. [DOI: 10.1115/1.1445793]

Introduction

The unsteady process of rotor wake/stator blade row interaction has commonly been described using kinematic models of wake chopping and transport such as those discussed by Kerrebrock and Mikolajczak [1], and Tweedt et al. [2]. These papers considered wake transport solely as a mechanism that redistributes losses.

Additional mechanisms that act on rotor blade wakes in the stage environment are now receiving attention. Originally Smith [3] proposed one important mechanism, which he called wake recovery, that occurs in a downstream blade row and can be beneficial to performance. Wake recovery is the attenuation (or amplification) of the wake velocity profile by processes other than viscous dissipation occurring inside of a blade row. For a two-dimensional rotor wake passing through a compressor stator row, wake recovery leads to rotor wake decay through a reversible process. In this way, the loss due to wake decay by viscous mixing is not suffered.

Smith [3] was the first to propose a simple model for the rotor wake recovery mechanism. The model is based on the change in length of a rotor wake segment as it passes through a stator blade row. He later expanded on his ideas of wake stretching and developed a quantitative model of performance enhancement (Smith [4]) due to wake recovery. Smith [5] also provided circumstantial evidence that wake recovery benefits exist using data from a low-speed four stage research compressor that exhibited higher pressure rise and efficiency with closer axial blade spacing.

Several researchers have used numerical simulations to study wake recovery mechanisms. Adamczyk [6] showed that the wake recovery process is related to wake vorticity field kinematics and can be estimated from linear theory. He showed that for the 2-D, incompressible, inviscid case, the rotor wake recovery occurring in the stator row was directly related to the difference of disturbance (wake) kinetic energy flux entering and leaving the stator row. Also having a wake pass through a blade row prior to mixing the wake does reduce mixing loss. With the assumption of thin air foils at zero incidence and high reduced frequency, the model of Adamczyk reduces to the model of Smith.

Deregel and Tan [7] used a first of a kind 2-D time-accurate Navier Stokes simulation to study rotor wake recovery for a range of stator blade design parameters and found that mixing loss was reduced due to the inviscid stretching of the wakes in the stator passage. Pressure rise was also increased because of the reduction of disturbance kinetic energy from the inlet to outlet of the passage. Valkov [8] used a time-accurate RNS code to quantify the performance effect of unsteady flow mechanisms on a low-speed compressor stator. He found that wake stretching is the dominant rotor wake decay mechanism in the stator passage and leads to performance benefit.

Limited experimental data of wake decay in the multi-stage environment exist. Some early axial compressor stage measurements (Ding [9]), although limited in the number of axial and circumferential inter-blade measurement points, provided a first step in the experimental observation of rotor wake/stator blade row interactions in high-speed axial flow machines. Ding noted large flow acceleration and deflection within a short axial distance thus hinting at the strong wake/blade row interactions which occur in a close-coupled high-speed compressor stage. More extensive measurements of rotor wakes convecting through a stator row have been acquired in a low-speed axial compressor (Stauter [10]), a high-speed axial stage (Dunker [11]), a high-speed multi-stage compressor (Williams, [12]), and a transonic fan stage (Hathaway, [13]). However, none of these data have been analyzed from the viewpoint of rotor wake recovery or are of sufficient detail to do so.

The motivation for the current work comes from the hypothesis that the rotor wake chopping and transport by the stator row that occurs in a stage environment results in wake decay mainly by stretching of the rotor wakes. Thus, the actual loss due to rotor wake decay is less than expected. This paper will show that in the stator passage of a compressor stage wake decay is indeed mainly by wake stretching.

The first goal of this work is to provide a detailed experimental data set which illustrates the different rotor wake decay behavior in rotor alone (mixing only) and stage (mixing and stretching)

[1]Currently with NASA Glenn Research Center, Cleveland, OH 44135

Contributed by the International Gas Turbine Institute and presented at the International Gas Turbine and Aeroengine Congress and Exhibition, Orlando, Florida, June 2–5, 1997. Manuscript received by the IGTI, January 1997; revised manuscript received November 11, 2001. Paper No. 1997-GT-535. Review Chair: H. A. Kidd.

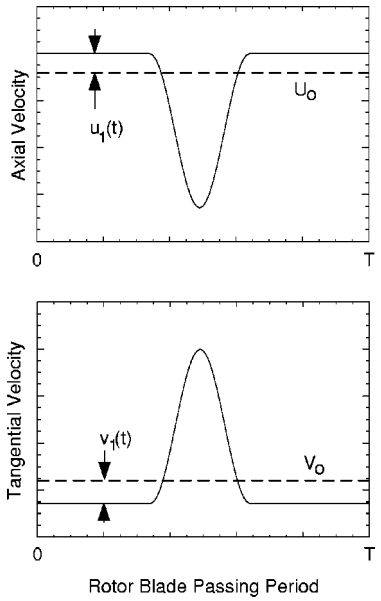

Fig. 1 Disturbance kinetic energy velocity components

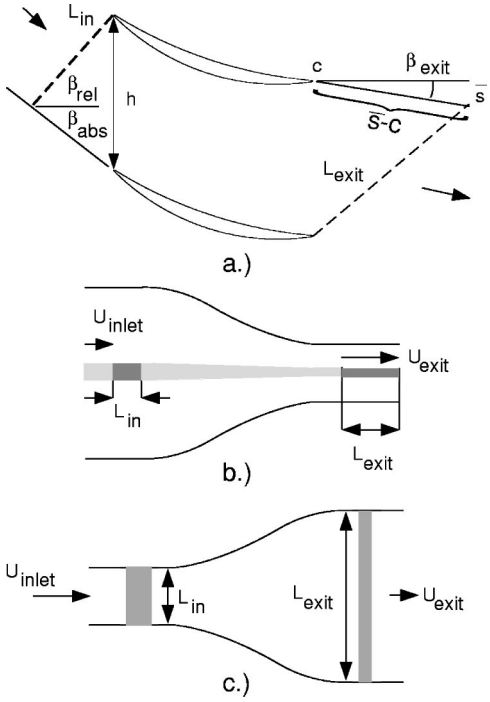

Fig. 2 Wake stretching situations

environments. Analysis of the experimental data identifies wake stretching as the primary rotor wake decay mechanism within the stator row. The second goal is to model the effects of wake stretching on rotor wake decay to allow more accurate prediction of wake decay and, therefore, loss production in a stage environment. Wake decay estimates from this simple model, which is based on the work of Hill et al. [14], are in reasonable agreement with the measured wake decay. This new wake decay model provides a simple method for predicting rotor wake decay due to both mixing and stretching by using only stator inlet and exit flow angles and an approximate rotor wake profile. It is thus useful for design. The rotor wake decay trends predicted by the model are used to suggest compressor design practices which can exploit the wake recovery process to reduce stage loss.

Wake Decay Model

A measure of rotor wake decay is the deterministic or periodic unsteadiness of the flow. The relationship between deterministic unsteadiness and rotor wake decay is discussed first. Next, the idea of wake recovery is considered. The link between wake recovery and wake stretching is stated and a method for estimating wake stretching is presented. Finally, equations to calculate the change in the rotor wake profile due to mixing and stretching are developed.

Relation of Deterministic Unsteadiness to Wake Decay. As suggested by Adamczyk [6], a measure of the deterministic unsteadiness of a flow can be defined as

$$K = \frac{1}{2} U_o A_y A_t (u_1^2 + \nu_1^2) \tag{1}$$

The definitions of u_1 and ν_1 are illustrated in Fig. 1. The time variation of these components define the wake profile. A_y is a pitchwise average operator and A_t is a time average operator. The difference in values of K at different axial locations is an indication of rotor wake decay over that axial distance.

Idea of Wake Recovery. Smith [3,4] offered the notion of wake recovery or wake decay by inviscid stretching with no loss accrual. Using the definition of K expressed in Eq. (1), we can relate wake decay to wake recovery with the expression

$$K_1 - K_2 = K_1 R + O(\Delta^3) \tag{2}$$

where K_1 and K_2 are evaluated at axial locations 1 and 2 which refer to the inlet and exit of the stator. R is Smith's recovery factor: i.e., $R=1$ means complete recovery of the wake by stretching with no loss accrual. With Eq. (2) it is possible to determine R by having values of K_1 and K_2 based on inviscid flow data. Alternatively, if R can be estimated by other means, the rotor wake decay, $K_1 - K_2$, due to stretching only can be obtained.

For this paper, the deterministic unsteadiness present at the stator midpitch location is considered representative of the entire pitch and the pitchwise operator, A_y, was dropped. To avoid confusion with the work of Adamczyk [6], the disturbance kinetic energy (DKE) is defined and used in this paper as a measure of the deterministic unsteadiness and thus wake decay.

$$\mathrm{DKE} = 0.5 U_o A_t (u_1^2 + \nu_1^2) \tag{3}$$

DKE is presented as a percentage of $0.5U_{tip}^3$ in all figures.

Determination of Wake Stretching. A wake passing through a stator passage is tilted and stretched due to stator circulation (loading) as shown in Fig. 2(*a*). Smith [3] proposed the wake recovery mechanism and found the following simple model for wake recovery which is based on wake lengths:

$$R = 1 - \left(\frac{L_{\mathrm{in}}}{L_{\mathrm{exit}}} \right)^2 \tag{4}$$

Also, Smith [3] proposed a simple method for estimating wake stretching based on inlet and exit velocity triangles. Adamczyk rediscovered Smith's result as the limit obtained from unsteady thin airfoil theory. The model as inspired by the work of Adamczyk [6] is

$$\frac{L_{\mathrm{exit}}}{L_{\mathrm{in}}} = \left. \frac{\sin(\beta_{rel} - \beta_{\mathrm{abs}})}{\cos\beta_{\mathrm{abs}}} \right|_{\mathrm{inlet}} \times \left[1 + \frac{2(\bar{s} - c)}{h} \sin(\beta_{\mathrm{exit}}) + \left(\frac{(\bar{s} - c)}{h} \right)^2 \right]^{1/2} \tag{5}$$

where

$$\frac{\bar{s}-c}{h}=\frac{\cos\beta_{\text{rel}}}{\sin(\beta_{\text{rel}}-\beta_{\text{abs}})}\left(\frac{\cos\beta_{\text{abs}}}{\cos\beta_{\text{exit}}}\right)-\frac{4(\tan\beta_{\text{abs}}-\tan\beta_{\text{exit}})}{(\cos\beta_{\text{abs}}+\cos\beta_{\text{exit}})^2}\cos\beta_{\text{exit}}(\cos\beta_{\text{abs}})^2 \quad (6)$$

See Fig. 2 for definitions of the terms. Angles are positive in the counterclockwise direction.

Equations (4)–(6) provide a method for estimating the kinematic contribution of wake stretching to the total rotor wake decay using only inlet and exit velocity triangles and blade geometry information.

Wake Profile Prediction. Inside the stator passage, wake stretching and viscous dissipation act concurrently on the rotor wake as it decays. A method for estimating the decay of the wake profile due to turbulent mixing and wake stretching is obtained from the work of Hill et al. [14] on turbulent wake decay in steady pressure gradients.

Hill et al. developed a decay model for 2-D incompressible turbulent wakes based on a constant eddy viscosity assumption. The model compared well with adverse pressure gradient wake decay measurements and was stated as being equally applicable to favorable pressure gradients. The model is extended to favorable pressure gradients as follows.

The wake stretching which occurs in a stator passage is analogous to the lengthening of a wake segment of constant mass as it passes axially through an acceleration (converging channel), as shown in Fig. 2(*b*) or convects through a diffuser as shown in Fig. 2(*c*). van de Wall [15] has proven analytically that situations (*b*) and (*c*) of Fig. 2 are mathematically equivalent given the 2-D incompressible assumptions. Note that the important parameter is the stretching of the wake by the mean flow field irrespective of how the mean flow field is constructed. Thus, stretching in flow situation 2(*b*) and (*a*) is similar.

For 2-D incompressible flow with shallow wakes, the wake length change ratio through channel (*b*) to first order is

$$\frac{L_{\text{exit}}}{L_{\text{in}}}=\frac{U_{\text{exit}}}{U_{\text{inlet}}} \quad (7)$$

By choosing the correct velocity ratio for a 2-D channel, the lengthening of a wake segment as it convects through that channel can be made to simulate rotor wake lengthening in a stator passage. This is done later in this paper.

The wake decay model taken from Hill et al.'s work can be framed in terms of

$$D=\frac{U-U_{\min}}{U} \quad (8)$$

where D is the relative wake depth, U is the average of the wake edge velocities (Nakayama [16]), and $U_{\min}$ is the wake center velocity. The wake depth, width, and velocity profile are given by

$$\frac{D}{D_o}=\left(\frac{U_o}{U}\right)^2\left[1+\frac{8\pi^2}{\pi^2-4}\left(\frac{\varepsilon}{U\theta}\right)\int_{x_o}\frac{U_o}{U}d\left(\frac{D_o^2x}{\theta_o}\right)\right]^{-1/2} \quad (9)$$

$$\frac{b}{b_o}=\left(\frac{U_o}{U}\right)^3\frac{\left(\frac{1}{D_o}-\frac{3}{4}\right)}{\left(\frac{1}{D_o}-\frac{3}{4}\frac{D}{D_o}\right)\frac{D}{D_o}} \quad (10)$$

$$\frac{U-u}{U}=D\frac{1}{2}\left[1+\cos\left(\pi\frac{y}{b}\right)\right] \quad (11)$$

Eq. 9 estimates the change in relative wake depth as a function of axial distance and velocity ratio which represents the free stream pressure gradient. Knowing the relative wake depth, the wake width can be computed from Eq. 10. The wake velocity profile is computed from Eq. (11). The grouping of terms containing eddy viscosity, $(\varepsilon/(U\theta))$, used in the model is constant with axial distance and equal to 0.044 [14].

Equations (5) through (11) represent the complete wake decay model which incorporates the effects of both wake stretching and viscous dissipation. The predicted wake decay from the model will be compared to measurements of rotor wake decay which were acquired downstream of a high-speed axial-compressor rotor alone and in a stage environment.

Test Compressor

The measurements were acquired in the NASA Glenn single-stage axial-flow compressor facility. The test stage consisted of NASA Rotor 35 and NASA Stator 37. The rotor had 36 blades, a hub-tip radius ratio of 0.70, an aspect ratio of 1.19, a tip solidity of 1.3, and an axial chord of 4.12 cm at the hub. The rotor tip clearance gap was 0.73 mm (0.029 in.). The stator had 46 blades, a tip solidity of 1.3, an aspect ratio of 1.26, and an axial chord of 3.57 cm at the hub. The gap/chord ratio for the stage varies from 18 percent at the hub to 31 percent at the tip based on rotor hub chord. The design and blade coordinates are found in Reid and Moore [17]. The original test stage consisted of Rotor 37 and Stator 37 with Stator 37 configured for optical access. At the beginning of the test program Rotor 37 was damaged from the implosion of an optical access window. Rotor 35, which used the same flowpath geometry, was substituted for Rotor 37. Because of the lower pressure ratio of Rotor 35, data were acquired at 80 percent of design speed to avoid choking problems in the stator. An average passage code analysis [18] was used to match the stator to the rotor at the lower operating speed. Based on this analysis, the stator stagger angle was decreased by 4 deg.

Data were taken with Rotor 35 alone at a tip speed of 363 m/s (80 percent design speed) at two operating conditions, near peak efficiency (PE) and near stall (NS). The stage data were acquired at conditions for which the rotor exit tip static pressures in the rotor only and stage configuration were matched. The rotor only and stage PE and NS operating points are shown in Fig. 3. The shaded symbols represent operating points at which laser doppler velocimeter data were acquired.

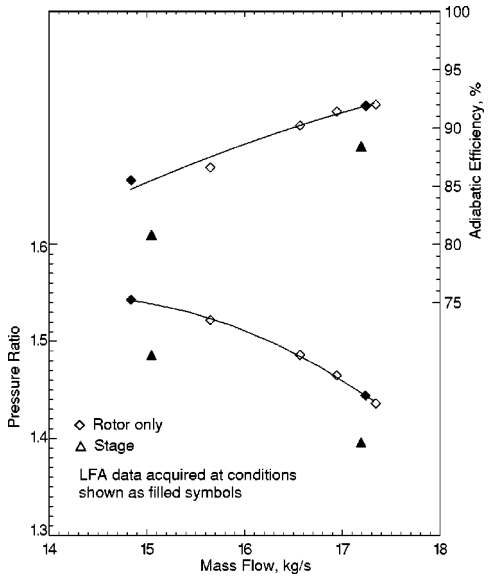

Fig. 3 Operating map for rotor alone and in the stage environment

Instrumentation and Measurement Techniques

Compressor massflow was measured using a calibrated orifice plate located far upstream of the compressor. Performance measurements were acquired using conventional static pressure and total pressure/temperature probes located upstream and downstream of the compressor. In the stage configuration, the downstream probes were traversed circumferentially across one stator pitch. At each span, the circumferential profiles of total temperature were mass averaged to obtain a radial profile. Similarly, the circumferential profiles of total pressure were energy averaged by converting them to their enthalpy equivalents and then mass averaged across the stator pitch. Similarly, overall performance was calculated by mass and energy averaging total temperature and total pressure, respectively, across the annulus [19]. Measurement uncertainties are: massflow ± 0.3 kg/s; flow angle ± 0.5 deg, total pressure ± 100 Pa, total temperature ± 0.6 K.

A large window, which conformed to the 3-D shroud contour, provided optical access to the flowfield from one rotor chord upstream of the rotor to one stator chord downstream of the stator. Laser doppler velocimeter (LDV) measurements were made at 75 percent span from the hub across one stator pitch; see Fig. 4. Detailed pitchwise surveys were acquired from the rotor trailing edge (TE) through 20 percent stator chord, at 50 percent stator chord, and at 90, 110, 120 percent stator chord. Typically there were 15 to 18 measurement locations in a pitchwise survey at each axial position. The 110 percent stator chord plane is the closest axial position to the STE where a complete pitchwise data survey was acquired and thus was used as the stator exit condition in calculations. Three streamwise surveys were done at 4.2, 50, and 87.5 percent of stator pitch (not percent gap). The axial locations at which rotor only data were acquired are also shown. The error in the LDV measurements is approximately ± 1.0 m/s for absolute velocity and ± 0.5 degrees in absolute flow angle.

The LDV was configured as a two-channel laser system which acquired axial and tangential velocities simultaneously. For each velocity measurement the rotor position was determined from a shaft angle encoder and the data placed into the window corresponding to that shaft angle position. There were 184 windows across one rotor blade pitch. Typically 40,000 to 60,000 individual velocity measurements were acquired for each survey point. Since the measurements were not evenly distributed over all of the windows, the total number of measurements were chosen so as to insure that there were a minimum of 30 measurements in any window. The LDV data are ensemble averaged using one rotor blade pitch as the time scale. See Strazisar et al. [20] for more detail on the LDV data acquisition and reduction technique.

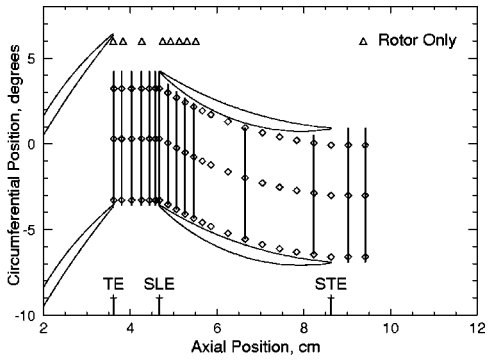

Fig. 4 LDV measurement locations for rotor and stage environment with axial locations of rotor trailing edge (TE), stator leading edge (SLE), and stator trailing edge (STE) at 75 percent span

Results

LDV Data Overview. The LDV data can be viewed as velocity versus spatial location for a particular rotor/stator orientation or as velocity versus rotor passing period for a particular location relative to the stator.

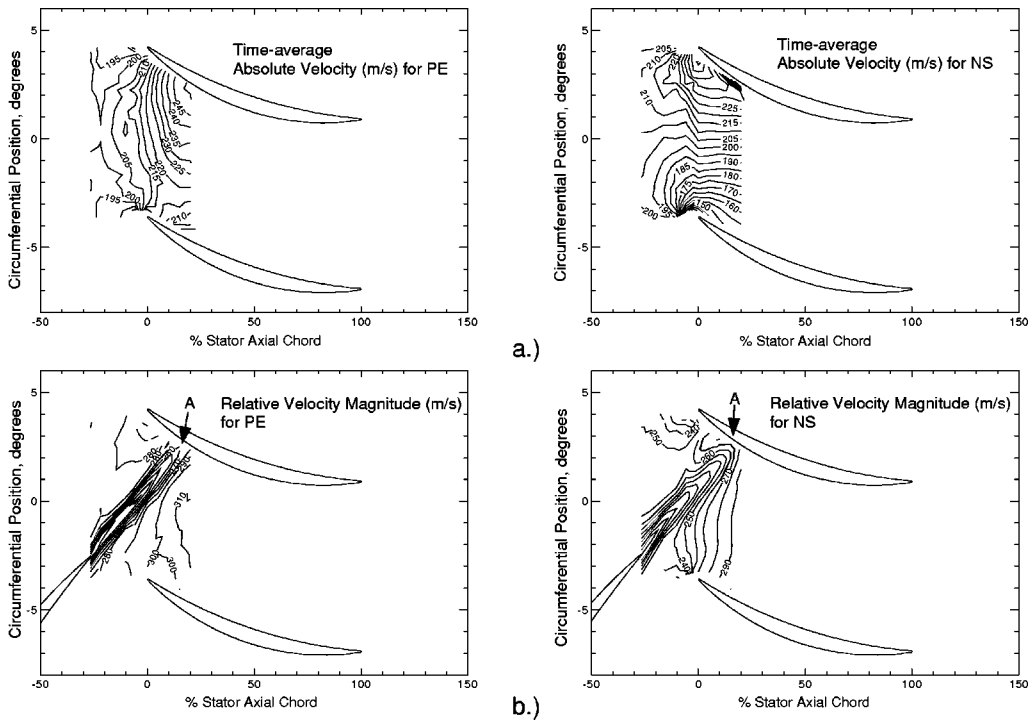

Fig. 5 Time average absolute velocity (m/s) and relative velocity magnitude (m/s) for a fixed rotor/stator position based on laser anemometer data at 75 percent span

Figure 5 shows examples of the LDV measurements from: (*a*) the time average velocity field, and (*b*) the flow field for a particular rotor/stator position for both peak efficiency and near stall. The measurements are only of sufficient spatial density from the rotor trailing edge to 20 percent stator chord to allow contour plotting of the wake for specific rotor/stator positions.

The time average absolute velocity field shows that the stator is aft loaded at the peak efficiency condition and front loaded at the near stall condition. This was confirmed by the Navier Stokes simulations described in the Appendix. In the near stall case, the front loading of the stator causes some rotation and stretching of the wake upstream of the stator leading edge plane.

Wake decay behavior in the stage environment was studied using the LDV measurements acquired at stator midpitch (diamond symbols at midpitch in Fig. 4) for a rotor passing period. This represents the deterministic unsteadiness that an observer at a fixed point relative to the stator would see. Rotor wake velocity profiles of this type are shown in the next section.

Wake Decay in the Rotor Only and Stage Environments. Figures 6 and 7 show rotor wake profiles at the stator leading edge and 120 percent stator chord axial locations for the rotor only and stage environments. Comparison of the width and depth of the wakes at the stator leading edge plane shows very similar character between the rotor only and stage cases for both operating conditions. At the 120 percent stator chord location the rotor only case still shows deterministic velocity fluctuations from the rotor wakes while the stage case does not show clearly identifiable rotor wakes exiting the stator passage.

The differing decay rates in the rotor only and stage environment are shown more quantitatively in Fig. 8 which compares the decay of DKE in the rotor only environment to the stage environment. If exponential decay is assumed, the slope of the curves is a direct comparison of decay rate. Note the DKE at the rotor trailing edge is not the same for rotor only and stage environments. However, the focus is on the comparisons of the decay rate and not the absolute level of DKE. Inside the stator passage the stage wake decay rate is greater than the rotor only decay rate. This leads to lower DKE at the stator exit in the stage environment. Because the rotor only results indicate the maximum decay due to viscous dissipation, another mechanism must be present to increase the wake decay rate in the stage environment.

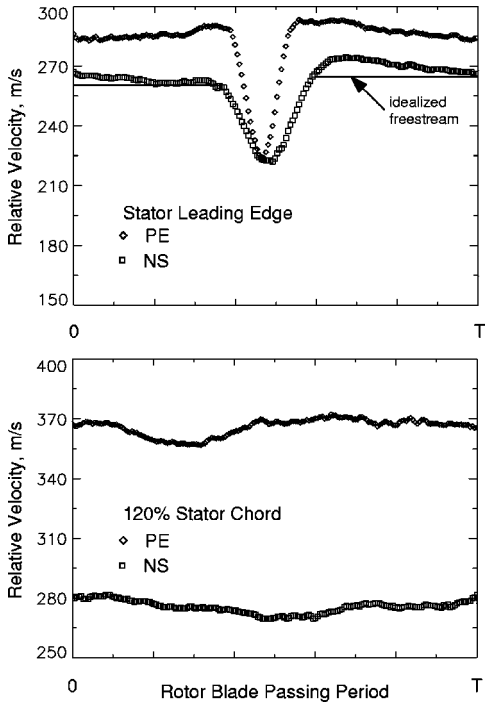

Fig. 7 Midpitch wake profiles for PE and NS at the stator leading edge and stator exit planes in the stage environment

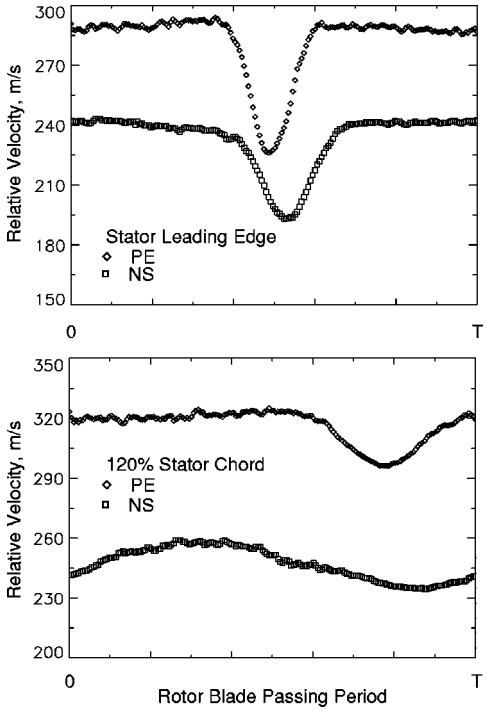

Fig. 6 Measured wakes in the rotor only environment at the stator leading edge and 120 percent stator chord planes from the PE and NS LFA data

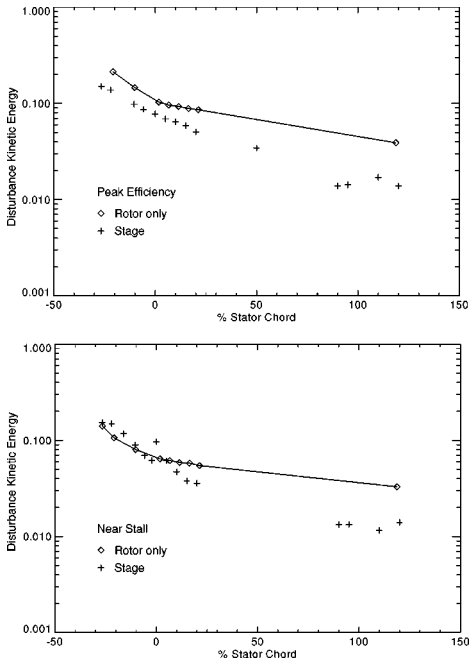

Fig. 8 Comparison of the DKE decay in the rotor only and pitch average DKE in the stage environment for the PE and NS LDV data

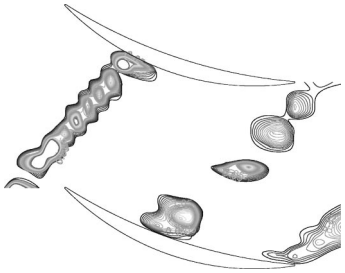

Fig. 9 Wake locations/orientation as shown by the number of measurements distribution

Measured Versus Calculated Wake Stretching. Smith's kinematic model of wake stretching and the wake decay model are based on 2-D incompressible flow assumptions and do not include the effects of either wake drift or radial transport. The validity of using the 2-D incompressible assumptions is discussed in the Appendix. For the results presented in this paper, wake drift and radial transport are not significant contributors to wake decay.

Some auxiliary LDV number of measurement data, which is compiled with the velocity data, proved useful to help identify the edges of the rotor wakes and to determine wake segment lengths. The number of data acquisitions per measurement window was not uniform with more measurements per window acquired in the rotor wake region than in the ''core flow'' region between wakes. Figure 9 shows an example of rotor wake locations at a particular rotor/stator position. With β_{exit} known and the wake orientation given by Fig. 9, it is simple to extrapolate the exit wake length as illustrated in cartoon form in Fig. 2(*a*).

Equation (5) provides a simple and adequate method for determining the wake lengths. Wake length ratios calculated with Eq. (5) are compared to length ratios obtained directly from experimental results in Table 1. Equation (5) does underpredict the wake stretching compared to the experimental data. Adding additional complexity to the wake stretching model might provide better agreement with experimental data. This is outside of the scope of this paper and is not pursued here.

From the inviscid models of Smith and Adamczyk, the recovery of the rotor wake is proportional to the wake inlet and exit length ratio, Eq. (4). A recovery of 1.0 (100 percent) means that the rotor wake has been completely mixed out in the stator passage by wake stretching only and the rotor wake defect has been completely recovered in a reversible way. The recovery calculated from experimentally measured wake length ratios is shown in Table 1. Using Eq. (4) and the measured wake lengths gives $R = 0.64$ and 0.78 for peak efficiency and near stall operating conditions. This can be interpreted as rotor wake decay due to the wake stretching mechanism. For comparison, the recovery due to wake stretching using wake length ratios as calculated from Eq. (5) is underpredicted by 10 percent for peak efficiency and 14 percent for near stall.

The total reduction in DKE from stator leading edge to stator trailing edge, as calculated from a fit to the experimental data of Fig. 8 is greater than that attributed to stretching only. The further decrease in DKE above that estimated due to stretching was due to viscous dissipation in the stator row. This comparison of the inviscid model recovery predicted from wake lengths to the total measured decrease in DKE strongly indicates that the primary decay mechanism in the stator passage might be wake stretching and that viscous dissipation appears to be of secondary importance. The stretching and viscous decay mechanisms act concurrently so the decay model is used to determine their relative contributions. In the subsequent discussion it will be shown that the wake decay model (Eqs. (7)–(11)) gives results in reasonable agreement with these preliminary findings.

Table 1 Comparison of wake length ratios measured from the LDV data and calculated using Eq. 5.

	Experiment		Model	
	measured	R	Eqn. 5	R
PE	1.67	0.64	1.52	0.57
NS	2.14	0.78	1.74	0.67

Wake Decay Calculations. The first step in the decay model calculation is to determine the initial conditions, U_o, D_o, b_o, and θ_o. These initial conditions are determined from a rotor wake profile measured at the stator leading edge axial location and midpitch circumferential location. The wake profiles are shown in Fig. 7. Note that the rotor relative velocity magnitude, as shown in the figure, was used for the calculations. van de Wall [15] in his numerical study of wake stretching used velocities in the absolute frame. In the present work the experimental data is not of sufficient spatial resolution through the entire stator passage to allow a rational transform into the absolute frame. Thus, the disturbance kinetic energy is defined in the relative frame, Eq. (13), and results from the model are presented in the relative frame, Fig. 10.

The stator midpitch location was chosen to minimize the wake gust/stator response interaction which is not included in the model. However, even at stator midpitch the LDV rotor wake velocity profiles contain the influences of both the rotor wake and the wake/blade interaction. To determine a relative wake depth from the LDV data the wake edge velocities must be determined. We considered the wake depth to be relatively unaffected, but the edges of the actual rotor wake were difficult to identify. The nonuniform measurement distribution across the wake was thus used to assist in locating the edges of the rotor wake in the velocity profiles. The velocity in the regions outside of the rotor wake was considered constant and was set equal to the corresponding wake edge velocity. This results in a ''idealized'' LDV rotor wake profile, see Fig. 7, for which the wake/blade interaction effects are minimized. The relative wake depth for the LDV data was then calculated from the average of the wake edge velocities and the minimum wake velocity.

The final setup step is to determine the relation of U_o/U with x distance. The flow turning determined from absolute flow angle data through the stator indicates that a linear change of U_o/U with x distance is a reasonable approximation to the wake stretching that occurs in the stator. A linear change of U_o/U in Eq. (9), was thus used in the model such that the velocity ratio at the stator exit was equal to the wake length ratio (see Eq. (7)) as determined from the experimental data.

The calculation procedure consists of numerically integrating Eq. (9) with x distance. The wake width is calculated at each integration step from Eq. (10) for viscous cases. For the inviscid case the exact analytic solution, $b/b_o = l_{\text{inlet}}/l_{\text{exit}}$ comes directly from Kelvin's theorem. Substituting Eq. (7) into the foregoing, the exact analytic solution is approximated as $b/b_o = U_o/U$ for $\varepsilon = 0$.

Equations (9) and (10) calculate results which are relative to the local freestream conditions and time scale. The local free stream conditions used in the model are meant to produce the correct strain field and are not representative of the convection velocity in the stator passage; therefore, the results must be related back to the initial free stream conditions and time scale. The relative wake depth, D, is multiplied by U/U_o to express the velocity deficit, $U\text{-}v_{\min}$, as a function of the initial free stream velocity. The wake width, b, is multiplied by U/U_o to adjust the time scale so the calculated wake width represents the correct fraction of a blade passing period consistent with b_o. This is necessary for computing the correct time average for Eq. (3). Because the exact solution for wake width and depth is known for the inviscid case, the foregoing relations can be verified using the inviscid case calculation.

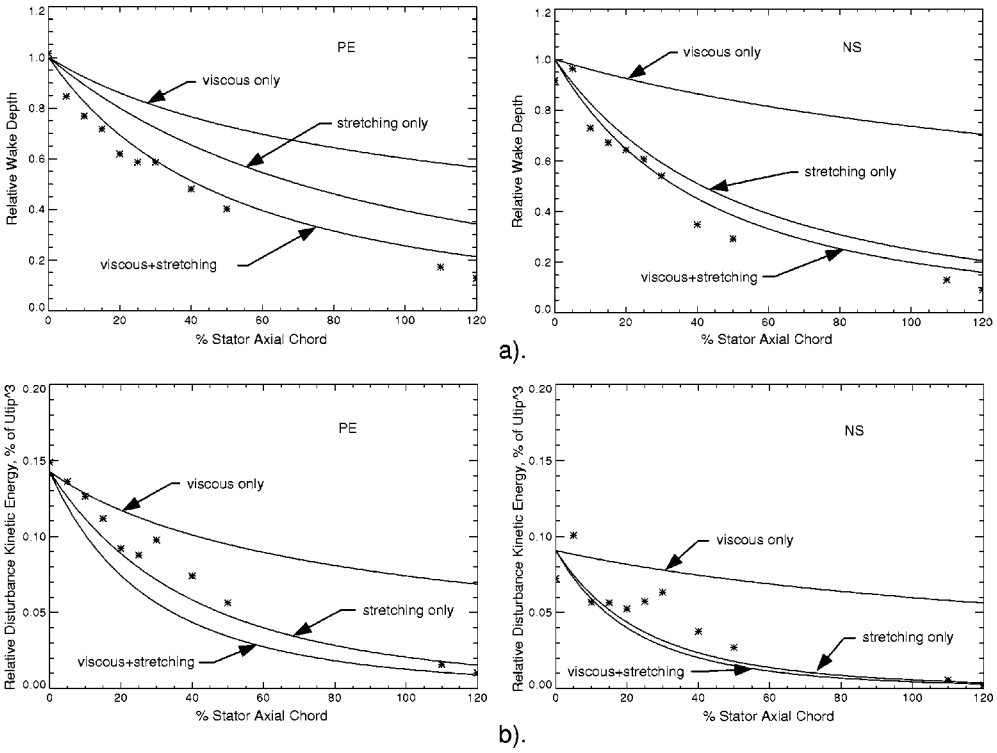

Fig. 10 Comparison of LDV data to wake decay model predictions for the PE and NS cases

Finally, the wake profiles are shifted so that

$$\int_0^T Vdt|_x = \int_0^T Vdt|_{\mathrm{SLE}} = \text{constant} \tag{12}$$

where V is the relative velocity magnitude. Equation (12) relates the free stream velocity used in the model back to a free stream velocity which is consistent with the initial condition. The relative disturbance kinetic energy is calculated from these profiles as

$$\mathrm{DKE_{REL}} = 0.5 V_o A_t (V - V_o)^2 \tag{13}$$

where V_o is the time average relative velocity magnitude. Change in $\mathrm{DKE_{REL}}$ represents the change of deterministic unsteadiness in the flowfield, and thus the change of the rotor wake. The $\mathrm{DKE_{REL}}$ for LDV data is calculated in a similar manner using the modified velocity profiles described previously.

A comparison between the wake model calculation and experimental (LDV) data at midpitch is shown in Fig. 10 in terms of (a) wake depth normalized by wake depth at the stator leading edge, and (b) relative disturbance kinetic energy. For the wake depth results: the curve labeled *viscous+stretching* is calculated from Eq. (9), the curve labeled *stretching only* is calculated from Eq. (9) with the eddy viscosity set to zero, the curve labeled *viscous only* is calculated from Eq. 9 with the velocity ratio set to 1.0.

Considering all of the assumptions, the predicted change in relative wake depth shows reasonable agreement with the LDV data as shown by the curve labeled *viscous+stretching* in of Fig. 10(*a*). The curves demonstrate that a process other than viscosity is at work. The *stretching only* curve shows that most of the wake depth change is due to wake stretching. For comparison, the curve *viscous only* shows how a rotor alone wake with the velocity profile shown in Fig. 7 at the stator leading edge would decay due to turbulent mixing alone. Not only is the rotor wake decay more rapid due to the presence of the stator, but the viscous contribution to wake decay is also greatly reduced.

The $\mathrm{DKE_{REL}}$ results are shown in Fig. 10(*b*). Differences between the model and the data are due to both poor wake width prediction by Eq. (10) and wake/blade interaction effects on the LDV wake profiles.

The wake decay model predicts a large reduction in $\mathrm{DKE_{REL}}$ across the stator with most of the reduction due to wake stretching. The *viscous only* curve shows the reduction in $\mathrm{DKE_{REL}}$ as if the rotor was operated alone.

The rotor wake decay model has been shown to explain differences between viscous produced wake decay and experimentally measured wake decay in the stator passage. The model indicates that wake stretching is the major contributor to rotor wake decay within the stator passage. The model can now be used to comment on the implications of the wake recovery process on stage design.

Design Implications

The combination of Eq. (5) for wake stretching and Eq. (9) for rotor wake decay, provides a simple method for predicting the benefit of rotor wake recovery in a stator row. The model is equally applicable to the recovery of stator wakes in a downstream rotor.

Assuming a 2-D incompressible flow, the wake decay model was used to perform a rotor wake decay audit based on the midpitch rotor wake profiles in the stage environment. The results are shown in Fig. 11. From the rotor trailing edge to stator leading edge, a significant amount of rotor wake decay occurred for both operating conditions, all of it due to viscous mixing, and thus resulting in loss (region labeled 1). Of the remaining rotor wake decay possible at the stator leading edge, most occurred by inviscid stretching of the rotor wake in the stator passage involving no loss (region labeled 2). Only small amounts of rotor wake mixing loss occurred in the stator passage because of viscous mixing (region labeled 3). This implies that using loss correlations based on isolated rotor or cascade data may be misleading for multistage design. Region 4 is mixing of any remaining velocity nonuniformity downstream of the stator.

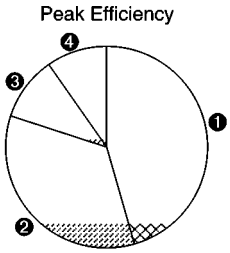

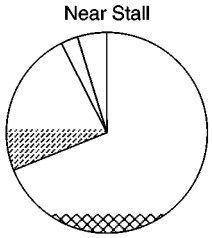

❶ Viscous loss from rotor trailing edge to stator leading edge
❷ Wake stretching in stator passage
❸ Viscous loss in stator passage
❹ Viscous loss downstream of stator

Fig. 11 Rotor wake decay audit

Since a significant amount of mixing loss occurs before the rotor wake enters the stator passage, closer axial spacing of blade rows to capture the rotor wake sooner could be beneficial. An efficiency gain due to closer axial spacing (7 versus 37 percent of chord) of 1.2 points was achieved in a four-stage low-speed compressor [5]. Of this efficiency gain, 0.52 points was attributed to wake recovery and the remainder attributed to other mechanisms, for example, tangential variations of total pressure caused by the downstream stator imposing nonuniform back pressure on the rotor ahead of it [21].

Additionally, capturing the rotor wake sooner assumes that the closer spacing would not cause increased losses in the rotor and/or stator due to potential field interactions or stronger wake/blade interactions. Regarding increased rotor losses, at 75 percent span in this stage, the stator velocity field impact on the rotor was small. The circumferential variation of the absolute velocity at the rotor trailing edge was 2.5 percent as measured by the LDV system at the near stall operating condition where the interaction was strongest. Because of the small interblade gap, no rotor performance measurements are possible in the stage configuration and nothing more definitive can be said about rotor performance at this time.

An effect similar to closer axial spacing could be achieved by reducing the viscous decay rate of the rotor wake. The viscous decay rate immediately downstream of the trailing edge is dependent on the shear velocity and the static pressure differences across the wake (the assumption of constant static pressure across the wake does not hold in this region). A small separation at the rotor trailing edge may reduce the shear velocity and static pressure difference and thus reduce the viscous mixing rate. This is speculative and needs further investigation.

By designing stages which use the wake recovery process to its full advantage, higher stage loading may be possible. As rotor blade loading is increased, profile loss, and thus rotor wake mixing loss, could also increase. However, in the stage environment a high percentage of the rotor wake decay could be recovered in the stator row. This recovery would offset some of the higher rotor profile losses, and thus might allow higher stage loading without incurring large efficiency penalties.

A higher percentage of mixing loss is recovered in the stator passage for the near stall case relative to the peak efficiency case due to less viscous contribution to mixing in the stator and more overall wake stretching. Front loaded stators (as in the near stall case) turn and stretch the wake sooner in the stator passage which further reduces the viscous decay contribution. Front loading also enhances the wake/blade response attenuation of the wake as shown at location A in Fig. 5. This attenuation occurs because the stator generates a pressure response to the presence of a rotor wake passing over the surface such that the correct boundary condition is maintained on the stator surface. This wake/blade response is also a reversible process.

Conclusions

A simple model has been developed to evaluate the relative contributions of viscous dissipation and inviscid stretching to the decay of a rotor wake in a stator row. The model requires only blade geometry, inlet and exit velocity triangles, and an assumed rotor wake profile as input and is simple enough to be useful as a design tool. Results from the model compared favorably with laser anemometer data. The model correctly predicts that, within the stator row, inviscid wake stretching is the dominant rotor wake decay mechanism as opposed to viscous dissipation.

Inviscid wake decay due to stretching provides a means of tailoring a compressor stage design to avoid some of the loss associated with the viscous decay of a rotor wake. This also implies that the use of rotor only or cascade loss correlations for multistage compressor design may be misleading. Examples of stage design features which influence the balance between viscous dissipation and wake stretching are:

- Axial Spacing of Blade Rows—In a compressor stage, a significant amount of rotor wake decay has already occurred by viscous dissipation before the wake enters the stator row. Some of this loss can be avoided by moving the stator row closer to the rotor trailing edge.
- Reduced Rotor Wake Shear—A reduction in the rotor wake shear will reduce the rotor wake viscous mixing in the axial gap between rotor and stator rows. Such a reduction might be achieved by designing for a small amount of separation within the rotor, thus broadening the wake width.
- Front Loading of Stators—Front loaded stator blades stretch the rotor wake inviscidly earlier in the stator passage and further reduce the already small amount of viscous dissipation involved in that row.

Acknowledgments

This work was done at the NASA Glenn Research Center under grant number NAG3-1302. We are grateful to Dr. Kenneth Suder for his assistance concerning the LDV system operation, to Mr. Jerry Wood for many helpful suggestions for data analysis, and to Dr. Alan van de Wall for his assistance with the wake recovery model.

Nomenclature

A_t = time average operator
A_y = pitchwise average operator
b, b_o = 1/2 wake width, initial 1/2 wake width
D, D_o = relative wake depth, initial relative wake depth
h = stator pitch
K = flux of kinetic energy of first-order unsteady velocity field
$L_{\text{in,exit}}$ = wake length
R = recovery parameter
$(\overline{s}-c)$ = distance, see Fig. 2
T = rotor blade passing period
U = free stream velocity
$U_{\text{inlet,exit}}$ = nozzle inlet and exit velocities
U_o, V_o = time average velocity, initial free stream velocity
u, v = axial and tangential velocity components

β_{abs} = absolute flow angle
β_{exit} = absolute flow angle at stator exit
β_{rel} = flow angle relative to rotor
Δ = perturbation parameter
ε = eddy viscosity
θ, θ_o = momentum thickness, initial momentum thickness

Appendix

Navier Stokes Computations. The kinematic model of wake stretching and the wake decay model are based on 2-D incompressible flow assumptions and do not include the effects of either wake drift or radial transport. 3-D time-accurate Navier Stokes simulations were therefore performed in order to generate a numerical database for use in developing the models, analyzing the experimental data, and assessing limitations in the models. The Navier Stokes simulations are mentioned here for completeness and are presented in more detail in Van Zante [22].

Three-dimensional time-averaged Navier Stokes simulations of the compressor stage operating at the peak efficiency and near stall conditions were first generated using the Average Passage code (Version 1.04) developed by Adamczyk [6]. 3-D, time-accurate, Reynolds-averaged Navier-Stokes simulations of the stator flow field were then generated using a code by Chen et al. [23]. The unsteady code uses a time-shifted non-uniform upstream boundary condition that simulates the relative movement of the incoming wake. The code used a Baldwin-Lomax turbulence model. The upstream boundary condition was obtained from the rotor flow field portion of the average passage simulation. The initial solution for the stator flow field was obtained from the stator portion of the average passage simulation. In all CFD simulations the stator count was increased from 46 to 48 to achieve a 3:4 rotor stator blade count in preparation for running a full stage unsteady simulation using the Chen/Adamczyk code. The grid size used was 101axial$\times$51radial$\times$43tangential nodes.

The massflow for the average passage simulations was matched to the experiment. The time-average absolute velocities from the LDV data and simulations agreed to within 5 percent. The wake kinematics predicted from the simulations agreed well with the experiment. Also, the unsteady behavior of the wakes in the simulations was qualitatively the same as for the LDV measurements. The simulations were therefore considered representative of the experimental observations and valid for use in interpreting the test data.

Nonmodeled Effects. Rotor wake drift in the stator row as described by Kerrebrock and Mikolajczak [1] is a result of the lower relative velocity of the wake fluid. Rotor wake fluid thus has a larger tangential velocity component than the free stream fluid and drifts toward the stator pressure surface. An estimate of the drift velocity from LDV data indicated that the maximum drift of a wake fluid particle as the wake convects through the stator passage would be less than 1/3 of the stator pitch toward the pressure surface. The entropy contours from the numerical simulations shown in Fig. 12 show that the high entropy rotor wake fluid particles extend across the stator pitch, even at the stator exit. Therefore, CFD predictions confirm that wake decay in the stator is not primarily due to the wake fluid drifting to the pressure surface of the stator.

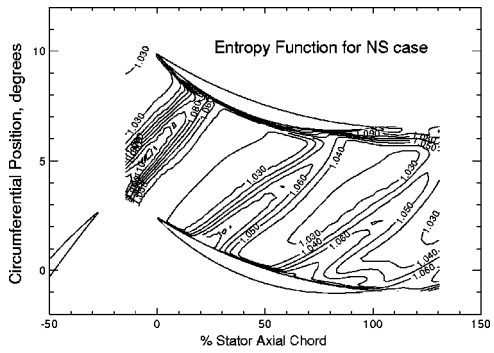

Fig. 12 Entropy contours showing the rotor wake locations for a fixed rotor/stator position from the near stall simulation

Radial velocities in the rotor wakes predicted by the CFD simulations were significant at the rotor trailing edge at 75 percent span, 12 and 27 percent of absolute velocity for peak efficiency and near stall cases, respectively. However, at the stator leading edge the radial velocities were reduced to 6 and 13 percent of absolute velocity for peak efficiency and near stall cases. The radial migration within the stator passage was 5.5 and 10.5 percent span for peak efficiency and near stall. Therefore, the flow field was considered sufficiently two dimensional in the core spans of the compressor stator such that calculating wake decay on a geometric 75 percent span stream surface was considered a reasonable approximation to following a wake fluid particle.

Because the LDV system only measures two velocity components, mixing loss calculations with the LDV data must be done by assuming 2-D incompressible flow. The unsteady simulations are used to estimate the error associated with these assumptions. The simple 2-D incompressible mixing loss calculations consistently underpredict the rotor wake mixing loss. The total mixing loss is small compared to the incoming kinetic energy, so the error incurred by the assumptions is small in absolute magnitude. More detail is included in Van Zante [22] and van de Wall [15].

Compressibility affects wake recovery in two ways. First, compressibility affects the mean flow velocities and it is the mean flow which determines the wake stretching. Both the LDV data and the simulation, of course, include this compressibility effect. The simple wake stretching model, which is based on an incompressible assumption, does well in predicting the wake stretching (see Table 1), and thus indicates that compressibility is a small effect. Secondly, wake recovery is affected because of the assumption that the circulation is constant for inviscid incompressible flow. For compressible viscous flow the circulation around a material segment of mass changes as [24]

$$\frac{d\Gamma}{dt} = \oint \left(-\frac{\nabla P}{\rho} + \frac{\nabla \cdot \tau}{\rho} \right) dr \tag{14}$$

This is a line integral that encloses the segment of mass. The first term on the right-hand side is zero if the density is only a function of the pressure. For a stator row where static temperature changes are small, this term should be small. The second term on the right-hand side is the divergence of the stress tensor and represents the viscous impact on circulation. Because the rotor wake has decayed significantly before entering the stator row, this term is expected to be small also except possibly near the blade surfaces. Further work is needed to better quantify these effects.

In summary, we conclude that wake drift, radial transport, and compressibility are not significant wake decay influences and evaluating mixing loss using 2-D incompressible assumptions will show the correct trends.

References

[1] Kerrebrock, J. L., and Mikolajczak, A. A., 1970, "Intra-Stator Transport of Rotor Wakes and Its Effect on Compressor Performance," ASME J. Eng. Power, pp. 359–368.
[2] Tweedt, D. L., Hathaway, M. D., and Okiishi, T. H., 1985, "Multistage Compressor Stator/Rotor Interaction," J Propul, **1**, No. 6, Nov-Dec., pp. 449–455.
[3] Smith, L. H., Jr., 1966, "Wake Dispersion in Turbomachines," J. Basic Eng., pp. 688–690.
[4] Smith, L. H., Jr., 1993, "Wake Ingestion Propulsion Benefit," J. Propul. Power, **9**, No. 1, Jan.-Feb., pp. 74–82.
[5] Smith, L. H., Jr., 1970, "Casing Boundary Layers in Multistage Axial-Flow Compressors," Flow Research in Blading, edited by L. S. Dzung, Elsevier Publishing Company, Amsterdam, 1970.
[6] Adamczyk, J. J., 1996, "Wake Mixing in Axial Flow Compressors," ASME Paper No. 96-GT-029.
[7] Deregel, P., and Tan, C. S., 1996, "Impact of Rotor Wakes on Steady-State

Axial Compressor Performance,'' ASME Paper No. 96-GT-253.
[8] Valkov, T. V., 1997, ''The Effect of Upstream Vortical Disturbances on the Time-Average Performance of Axial Compressor Stators,'' Ph.D. dissertation, Massachusetts Institute of Technology.
[9] Ding, K., 1982, ''Flow Measurements Using a Laser-Two-Focus Anemometer in a High-Speed Centrifugal and a Multistage Axial Compressor,'' presented at ASME Winter Annual Meeting, Phoenix, AZ, Nov.
[10] Stauter, R. C., Dring, R. P., and Carta, F. O., 1991, ''Temporally and Spatially Resolved Flow in a Two-Stage Axial Compressor: Part I—Experiment,'' ASME J. Turbomach., **113**, pp. 212–226.
[11] Dunker, R. J., 1983, ''Flow Measurements in the Stator Row of a Single-Stage Transonic Axial-Flow Compressor with Controlled Diffusion Stator Blades,'' AGARD CP-351, Viscous Effects in Turbomachines.
[12] Williams, M. C., 1988, ''Inter and Intrablade Row Laser Velocimetry Studies of Gas Turbine Compressor Flows,'' ASME J. Turbomach., **110**, pp. 369–376.
[13] Hathaway, M. D., 1986, ''Unsteady Flows in a Single-Stage Transonic Axial-Flow Fan Stator Row,'' NASA TM 88929, Dec., also, see ASME 87-GT-226 and 87-GT-227.
[14] Hill, P. G., Schaub, U. W., and Senoo, Y., 1963, ''Turbulent Wakes in Pressure Gradients,'' ASME J. Appl. Mech., pp. 518–524.
[15] van de Wall, Allan, G., Jaikrishnan, R., and Adamczyk, J. J., 2000, ''A Transport Model for the Deterministic Stresses Associated With Turbomachinery Blade Row Interactions,'' ASME J. Turbomach., **122**, pp. 593–603.
[16] Nakayama, A., 1987, ''Curvature and Pressure-Gradient Effects on a Small Defect Wake,'' J. Fluid Mech., **175**, pp. 215–246.
[17] Reid, L., and Moore, R. D., ''Design and Overall Performance of Four Highly Loaded, High-Speed Inlet Stages for an Advanced High-Pressure-Ratio Core Compressor,'' NASA TP 1337, October 1978.
[18] Adamczyk, J. J., 1985, ''Model Equation for Simulating Flows in Multistage Turbomachinery,'' ASME Paper No. 85-GT-226.
[19] Reid, L., and Moore, R. D., ''Performance of Single-Stage Axial-Flow Transonic Compressor With Rotor and Stator Aspect Ratios of 1.19 and 1.26, Respectively, and with Design Pressure Ratio of 1.82,'' NASA TP 1338, November 1978.
[20] Strazisar, A. J., Wood, J. R., Hathaway, M. D., and Suder, K., L., 1989, ''Laser Anemometer Measurements in a Transonic Axial-Flow Fan Rotor,'' NASA TP 2879.
[21] Smith, L. H., Jr., 1996, ''Discussion of ASME Paper No. 96-GT-029: Wake Mixing in Axial Flow Compressors,'' ASME Turbo Expo, Birmingham, England, June 10–13.
[22] Van Zante, D. E., 1997, ''Study of a Wake Recovery Mechanism in a High-Speed Axial Compressor Stage,'' Ph.D. dissertation, Iowa State University.
[23] Chen, J. P., Celestina, M. L., and Adamczyk, J. J., 1994, ''A New Procedure for Simulating Unsteady Flows Through Turbomachinery Blade Passages,'' ASME Paper No. 94-GT-151.
[24] Sherman, F. S., 1990, *Viscous Flow*, McGraw-Hill Publishing Company, New York, NY.

Single-Passage Analysis of Unsteady Flows Around Vibrating Blades of a Transonic Fan Under Inlet Distortion

H. D. Li
Senior Research Associate,
e-mail: Haidong.Li@durham.ac.uk

L. He
Professor in Thermo-Fluids,
e-mail: Li.He@durham.ac.uk

School of Engineering,
University of Durham,
U.K. DH1 3LE Durham

Computations of unsteady flows due to inlet distortion driven blade vibrations, characterized by long circumferential wavelengths, typically need to be carried out in multi-passage/whole-annulus domains. In the present work, a single-passage three-dimensional unsteady Navier-Stokes approach has been developed and applied to unsteady flows around vibrating blades of a transonic fan rotor (NASA Rotor-67) with inlet distortions. The phase-shifted periodic condition is applied using a Fourier series based method, "shape-correction," which enables a single-passage solution to unsteady flows under influences of multiple disturbances with arbitrary interblade phase angles. The computational study of the transonic fan illustrates that unsteady flow response to an inlet distortion varies greatly depending on its circumferential wavelength. The response to a long wavelength (whole-annulus) distortion is strongly nonlinear with a significant departure of its time-averaged flow from the steady state, while that at a short wavelength (two passages) behaves largely in a linear manner. Nevertheless, unsteady pressures due to blade vibration, though noticeably different under different inlet distortions, show a linear behavior. Thus, the nonlinearity of the flow response to inlet distortion appears to influence the aerodynamic damping predominantly by means of changing the time-averaged flow. Good agreements between single-passage solutions and multi-passage solutions are obtained for all the conditions considered, which clearly demonstrates the validity of the phase-shifted periodicity at a transonic nonlinear distorted flow condition. For the present cases, typical CPU time saving by a factor of 5–10 is achieved by the single-passage solutions. [DOI: 10.1115/1.1450567]

1 Introduction

In modern designs of gas turbine engines, advanced CFD modeling and noninstrusive measurement techniques have provided information essential for understanding complex steady flow physics. However, inlet distortion and its driven blade vibration are common problems for aero-engines during taking off or landing. Thus aerodynamic and aeromechanic responses of compressor/fan blades to nonuniform incoming flow conditions need to be assessed to ensure required aero-thermal performance as well as mechanical integrity. It is particularly of importance that blade stress levels due to forced responses can be evaluated at a design stage. Any redesigns to rectify vibration problems are time-consuming and expensive. Therefore, it is necessary to develop effective predictive methods, which can be used as design tools.

Many studies of inlet distortion effects and blade forced response have been carried out in the past both experimentally and numerically. Fleeter et al. [1] and Manwaring and Fleeter [2] carried out extensive experimental studies of unsteady loading of compressor blades under distortions, wakes and potential fields. Monsarrat [3] measured performance changes due to an inlet distortion. Bowditch and Coltrin [4] investigated the effects of distortion on compressor stability. On the computational side, Hah [5] analyzed an inlet distortion case with a length scale corresponding to only a few passages, which is useful for code validations and can give some useful information regarding high engine order blade forced responses. The most common pattern of inlet distortions has a circumferential length scale corresponding to the whole annulus. Computational studies of inlet distortion effects with long wavelengths, e.g., the work by Hirai [6], Marshall et al. [7] and Breard et al. [8] are typically very time-consuming, due to the need of using multiple passages/whole-annulus domains.

In the present work, a single-passage approach to three-dimensional unsteady Navier-Stokes calculations using a Fourier series based method (Shape-Correction), previously applied to 2-D Euler calculations [9], has been developed. The major advantage of the present single-passage method in comparison with other methods available, e.g., the direct store (Erdos et al. [10]) and the time-inclination (Giles [11]), is its ability to compute unsteady flows under multiple disturbances. The developed method is applied to analyze unsteady flows around oscillating blades of a transonic fan rotor influenced by inlet circumferential stagnation pressure distortion. Apart from verifying the present single-passage method and its implementation, there are several issues of interest. First, we would expect certain nonlinearity in an unsteady transonic flow under inlet distortion. It is then relevant to identify those parameters that might affect the nonlinearity. Also, as a general unsteady turbomachinery flow modeling issue, any case studies which can help to clarify the validity of the basic phase-shifted periodicity in a nonlinear transonic distorted flow would be useful. Finally, for blade aeroelasticity design and analysis, it is the conventional wisdom that aerodynamic damping characteristic behavior associated with blade flutter is by large linear, while unsteady forcing in blade forced response problems may be nonlinear. The question remains concerning whether or not the aerodynamic damping behavior would still be linear when the oscillating blade flow is subject to a distortion with a strong nonlinear effect. The present comparative studies also attempt to address these issues.

Contributed by the International Gas Turbine Institute and presented at the International Gas Turbine and Aeroengine Congress and Exhibition, New Orleans, Louisiana, June 4–7, 2001. Manuscript received by the IGTI, February 2001; revised manuscript received October 15, 2001. Paper No. 2001-GT-272. Review Chair: R. Natole.

2 Methodology

2.1 Flow Model. In simulations of unsteady turbomachinery flows with moving boundaries, an integral form of three-dimensional Navier-Stokes equations written in the absolute cylindrical coordinate system is usually used.

$$\frac{\partial}{\partial t}\int\int\int_{\delta V} U dV + \oint_{\delta A}\int [(F-Uu_{mg})n_x + (G-Uv_{mg})n_\theta + (H-Uw_{mg})n_r]\cdot dA = \int\int\int_{\delta V} S_i dV + \oint_{\delta A}\int [V_x n_x + V_\theta n_\theta + V_r n_r]\cdot dA \quad (1)$$

where U, F, G, and H are standard conservative variables and inviscid flux vectors. u_{mg}, v_{mg} and w_{mg} are mesh moving velocities due to blade vibration as well as rotation if the mesh is attached to a rotor. The extra inviscid flux terms Uu_{mg}, Uv_{mg} and Uw_{mg} count for the contribution to the fluxes due to grid movement. S_i is the inviscid source term. Full viscous stress terms (V_x, V_θ, and V_r) are adopted in the current work. The system equations are closed by the equation of state and the mixing length turbulence model by Baldwin and Lomax [12].

2.2 Discretization and Solution Methods. The foregoing governing equations are discretized in space using the cell-centered finite volume scheme, together with the blend second-order and fourth-order artificial dissipation [13] to damp numerical oscillations. Temporal integration of the discretized equations is carried out using the second-order four-step explicit Runge-Kutta scheme. A time-consistent multi-grid technique [14] has been adopted to speed up convergence procedure. In order to maintain temporal accuracy when using the multi-grid technique, the dual time-stepping scheme [15] is incorporated. It starts with an implicit backward temporal difference of the discretized equations

$$\frac{3}{2\Delta t}(U^{n+1}\Delta V^{n+1}) - \frac{2}{\Delta t}(U^n \Delta V^n) + \frac{1}{2\Delta t}(U^{n-1}\Delta V^{n-1}) = R^{n+1} \quad (2)$$

A pseudo-time τ is then introduced

$$\frac{\partial(U\Delta V^{n+1})}{\partial \tau} = R^{n+1} - \left(\frac{3}{2\Delta t}U^{n+1}\Delta V^{n+1} - \frac{2}{\Delta t}U^n\Delta V^n + \frac{1}{2\Delta t}U^{n-1}\Delta V^{n-1}\right) \quad (3)$$

Equation (3) is integrated in the pseudo-time using the four-step Runge-Kutta time-marching method with the multi-grid acceleration. When the left hand side of Eq. (3) is driven to zero, the second-order temporal accuracy is fully recovered, which is independent of the multi-grid acceleration technique.

2.3 Boundary Conditions. The computational domain consists of either a single passage or multiple passages with a blade being at the center of each passage. Compared to a blade-to-blade domain configuration, this middle-blade domain arrangement facilitates an easier implementation of the phase-shifted periodic boundary condition. The multi-passage domain requires the direct periodicity and is used here as the baseline option for validation purposes. On blade and end-wall surfaces, a logarithmic law is applied to determine the surface shear stress and the tangential velocity is left to slip. Compared to nonslip wall conditions, it needs fewer mesh points in the near wall region.

At the inlet, stagnation parameters and flow angles are specified. At the exit, pitchwise mean static pressure at each spanwise section is specified. The 1-D nonreflective procedure [16] has been implemented at both inlet and exit to shorten extension domains. In cases with inlet distortion, a sinusoidal pattern distortion of total pressure in the circumferential direction is superimposed on the specified mean stagnation pressure to generate nonuniform inlet conditions.

2.4 Shape-Correction Method. In a general situation with multiple periodic disturbances, suppose the number of unsteady disturbances of interest is N_{pt}; a flow variable at periodic boundaries can be expressed as

$$U(x,y,r,t) = U_0(x,y,r) + \sum_1^{N_{pt}} U_i(x,y,r,t) \quad (4)$$

where U_0 is the time-averaged part, U_i is the unsteady part induced by the ith unsteady disturbance and $y = r\theta$. Each unsteady part can be approximated by a set of Fourier series in time

$$U_i(x,y,r,t) = \sum_{n=1}^{Nfou} [A_{ni}(x,y,r)\sin(n\omega_i t) + B_{ni}(x,y,r)\cos(n\omega_i t)] \quad (5)$$

Accordingly, for any pair of mesh points at upper and lower periodic boundaries of a single passage domain, we have

$$U^L(x,y,r,t) = U_0(x,r) + \sum_{i=1}^{N_{pt}}\sum_{n=1}^{N_{fou}} [A_{ni}\sin(n\omega_i t) + B_{ni}\cos(n\omega_i t)]$$

$$U^U(x,y,r,t) = U_0(x,r) + \sum_{i=1}^{N_{pt}}\sum_{n=1}^{N_{fou}} [A_{ni}\sin(n(\omega_i t+\sigma_i)) + B_{ni}\cos(n(\omega_i t+\sigma_i))] \quad (6)$$

where σ_i is the inter-blade phase angle of the ith disturbance, A_{ni} and B_{ni} are corresponding nth-order Fourier coefficients of the disturbance i. Usually, the first five-order Fourier series are sufficient to capture periodic unsteadiness.

We should bear in mind that using the Fourier series to approximate unsteady flow variables doesn't include any linear assumptions of unsteady response. Since nonlinearity manifests itself in interaction between the time-averaged flow and various harmonics, nonlinear effects can be accommodated by the zero-order time-averaged components, and higher order Fourier components.

A particular issue arises here regarding how to update the Fourier coefficients for multiple disturbances. We know the beating period, which is the minimal common multiple of all the disturbances' periods, could be much longer than the period of each disturbance. Therefore, if we only update the coefficients once every beating period, the solution would have a very slow convergence rate for situations with very low beating frequencies. In order to avoid this difficulty and to update the Fourier coefficients as frequently as possible, we adopt a partial-substitution technique. That is, the coefficients are evaluated through the following formula:

$$A_{ni} = \frac{\omega_i}{\pi}\sum_1^{N_{pi}} (U-R_i)\sin(n\omega_i t)\Delta t$$

$$B_{ni} = \frac{\omega_i}{\pi}\sum_1^{N_{pi}} (U-R_i)\cos(n\omega_i t)\Delta t \quad (7)$$

where $R_i = \Sigma_{j\neq i}^{N_{pt}}\Sigma_{n=1}^{N_{fou}}[A_{nj}\sin(n\omega_j t) + B_{nj}\cos(n\omega_j t)]$ is the unsteady contribution of all disturbances except that from the ith disturbance. At every time step, the flow variables at periodic boundaries are corrected using the stored Fourier coefficients and the current solution. For each unsteady disturbance, new values of the coefficients as well as the time-averaged part can be obtained after one period of the disturbance under consideration, when the part-substitution (Eq. (7)) is used.

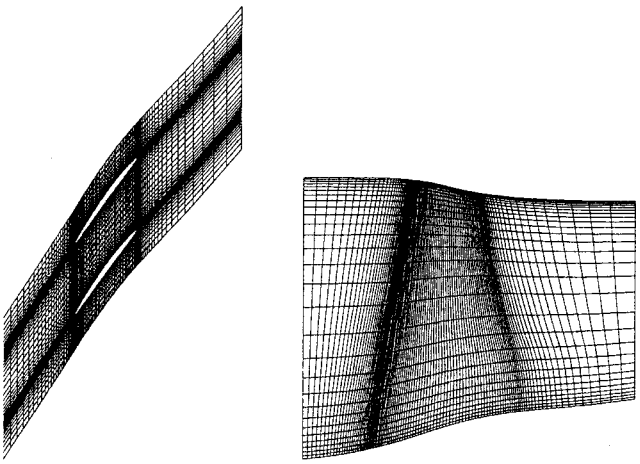

Fig. 1 Mesh (on pitchwise and spanwise section) of NASA rotor 67

During the transition from a steady state to a periodic unsteady state, an under-relaxation of the Fourier coefficients updating is essential for stability reason. The under-relaxation of the Fourier coefficients takes the following form:

$$A_{ni(stored)} = (1-\alpha)A_{ni(stored)} + \alpha A_{ni(new)} \tag{8}$$

where α is the under-relaxation factor between 0 and 1, a similar formula is also applied to B_{ni}. In addition, a numerical damping of variables on periodic boundaries is used to stabilize the solution procedure at the initial stage.

3 Code Validation

To validate the current viscous solver, a calculation of steady flow through a transonic fan rotor known as "NASA Rotor-67" has been carried out. The steady flow field had been extensively measured at the NASA Lewis Center by Strazisar et al. [17]. The test rotor has 22 blades with 0.8 percent of the span tip clearance operating at rotation speed 16043 rpm. A computational domain with $111\times25\times29$ mesh points shown in Fig. 1 is used in the calculation. This mesh has been subsequently used for the unsteady flow calculations both for single passage and multiple (up to 22) passages. A simplified one-cell tip-clearance model [18] is applied here to model leakage effects approximately.

The steady state adopted in this paper is at nondimensional mass flow rate 0.994. The calculation is performed assuming that the flow is fully turbulent. At the inlet, the measured flow angle, stagnation pressure and stagnation temperature are specified. The measured static pressure at outlet is specified. Figure 2 shows the comparison of the Mach number contours at blade-to-blade sections of 10, 30, and 70-percent span from the tip. Results from the current calculation agree well with the LDA measurement (Strazisar et al. [17]). Although the passage shock's position and width are slightly diverted from the experiment, the general flow

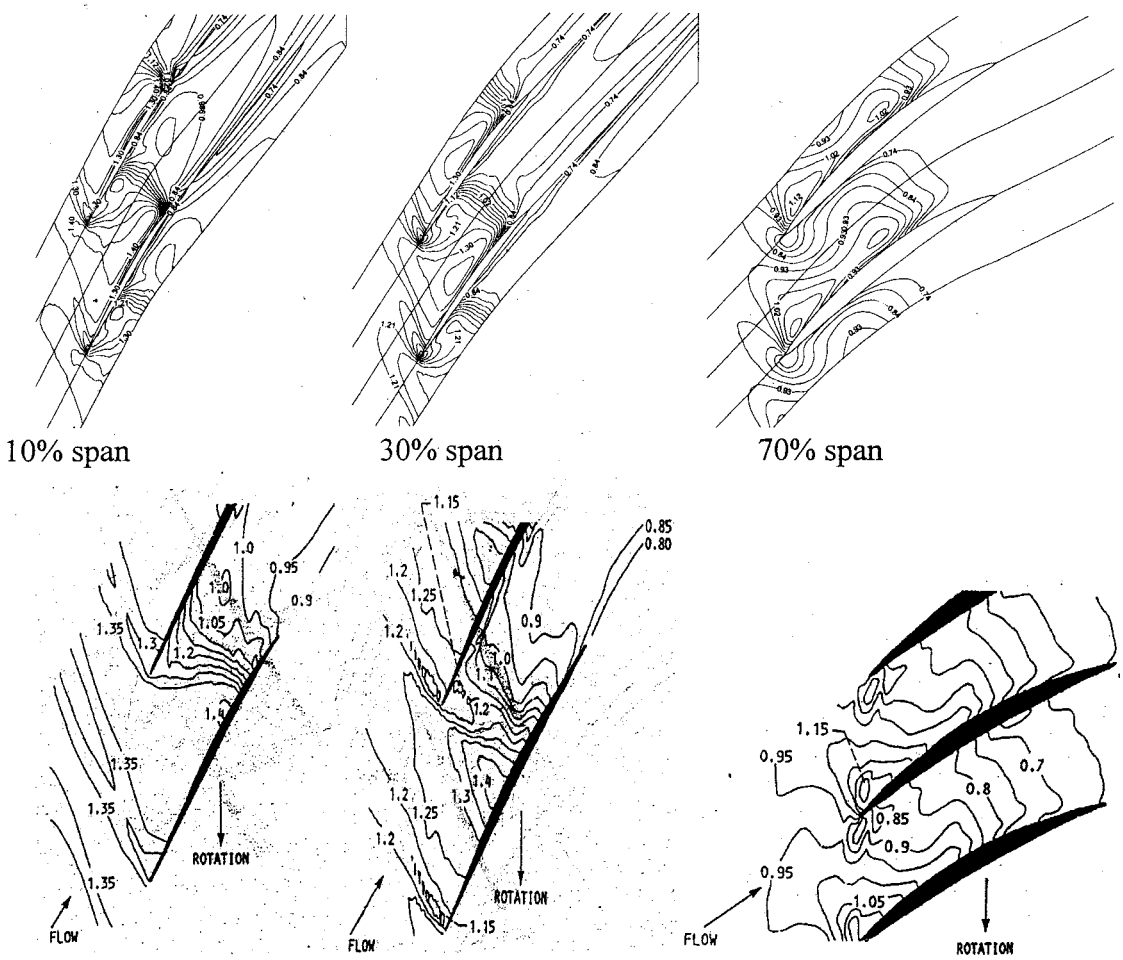

Fig. 2 Predicted (upper) and measured (lower) relative Mach number contours

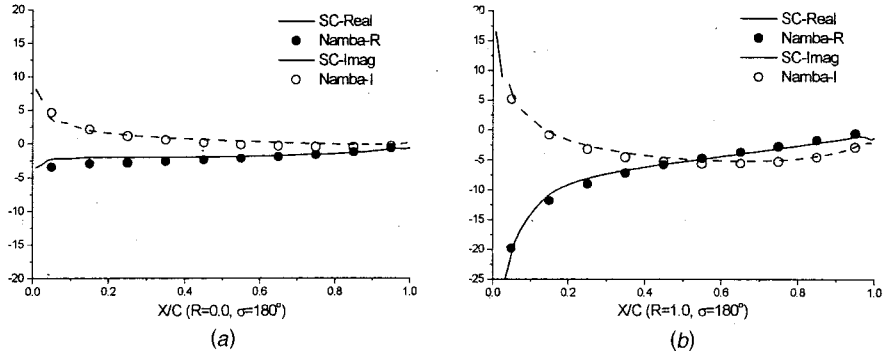

Fig. 3 Pressure jump coefficients ($\sigma=180$ deg)—(*a*) hub section, (*b*) tip section

patterns have been successfully predicted and the similar results were obtained by Jennions and Turner [19] and Arnone [20].

Validation of a 3-D unsteady flow code is much more difficult than its steady counterpart because of lack of published 3-D experimental data. Therefore, comparison between numerical methods and semi-analytical methods for simple inviscid flow cases play an essential part in code validations. A flat plate cascade test case, for which the semi-analytical solution of Namba [21] is available, is used here. This case has been previously adopted for validation purposes by others, e.g., He and Denton [18] and Gerolymos and Vallet [22]. The main difference between the present solver and that by He and Denton [15] is that the numerical scheme has been changed from a cell vertex scheme with direct time-marching to a cell centered scheme with the dual-time stepping. Also, the computational domain has been rearranged to a middle-blade domain for a convenient implementation of the phase-shifted periodic boundary conditions.

The flat plate cascade is placed between two parallel solid walls. It is oscillated in a three-dimensional torsion mode around the leading edge. The reduced frequency ($K=\omega C/u_\infty$) is 1 based on the inlet velocity and chord length. The same geometry and flow parameters as [18] are used in the current simulation with a grid density of $81\times25\times21$ in the streamwise, pitchwise and spanwise directions respectively.

Calculated unsteady pressure jumps at two spanwise sections, hub and tip, are presented in the form of $\Delta CP=\Delta P_1/0.5\rho_\infty u_\infty^2 A_m$, where ΔP_1 is the first harmonic pressure jump across the blade; A_m is the torsion amplitude at the tip in radians. Figure 3 shows comparisons of the chordwise distributions of the real and imaginary parts of the first harmonic pressure jump coefficient at an inter-blade phase angle $\sigma=180$ deg. Results from our single-passage calculation agree very well with the Namba's semi-analytic results.

4 Unsteady Flow Induced by Blade Oscillation and Inlet Distortion

4.1 Unsteady Flow due to Inlet Distortion. Here we first examine the unsteady flow response to an inlet distortion without blade vibration. A sinusoidal distortion pattern in a similar pattern to some experimental ones, e.g., [23], is chosen for its ease of implementation. The distribution of the stagnation pressure distortion can be expressed by the following formula:

$$P_T=P_T^{AV}+\Delta P\sin(\omega_p t+\theta_i+\varphi_k)$$

$$\Delta P=[0.1+0.05(R-R_{hub})/(R_{tip}-R_{hub})]P_T^{AV} \qquad (9)$$

where ΔP is linearly varying from 10 percent at the hub to 15 percent at the tip. Variation of amplitude in the circumferential direction is counted by phase angle θ_i and φ_k, where θ_i is the relative phase angle between the ith and the first pitchwise grid surface. And φ_k is the phase angle difference between the kth spanwise position and the hub on the first pitchwise grid surface. Note that Eq. (9) is the pattern seen in the rotor frame of reference, the distortion pattern is stationary in the absolute system.

Comparative calculations between a conventional multiple passage solver with a direct repeating (periodic) condition and the single-passage solver with the shape-correction method have been carried out here. The grid used for each passage is the same as that used in the previous steady calculation. Three cases with the same distortion amplitude but different circumferential length scales (wavelength) have been studied here, i.e., 11-node mode (wavelength corresponding to two passages), 2-node mode (wavelength corresponding to 11 passages) and 1-node mode (wavelength corresponding to 22 passages or whole annulus).

Figure 4 shows instantaneous total pressure contours on a near inlet section for three distortion modes. The upper side is for the computational results from the multiple-passage solutions, and the lower side is the results from the single-passage solutions with reconstruction base on the phase-shifted periodicity. The figures clearly indicate that the stagnation pressure distortion pattern is convected axially downstream as expected. The reconstructed results from the single-passage solutions are almost identical to the results directly obtained from the multiple-passage solutions.

The influence of the circumferential wavelength can be easily identified when we examine the passage shock wave movement. Figure 5 shows static pressure contours on a time-space plane at the three distortion wavelength conditions. The space coordinate here is a mesh line on the suction surface at 90 percent span, and the time is for two distortion periods. At the steady state, the passage shockwave foots on the suction surface at around 90 percent chord. For the shortest wavelength distortion, i.e., 11-node mode, there is hardly any appreciable oscillation of the shock, which is more or less the same as the steady one. But the shock oscillation is apparent in the middle wavelength distortion, i.e., two-node mode. And it is much more significant for the long wavelength one, where the shock oscillates over 50 percent of the chord, and its mean position is noticeably more upstream than the steady position. This long wavelength case is strongly nonlinear, and it is found that the nonlinear flow response can only be properly captured if higher order harmonics are included. In all the present computations, the first five order harmonics are included.

The strikingly different results from these three cases at the same distortion amplitude highlight the need to properly model the true circumferential wavelengths of unsteady distorted flows, where the most common one corresponds to a whole annulus.

4.2 Unsteady Flow due to Blade Oscillation. Before looking at a flow around oscillating blade under influence of an inlet distortion, we first consider the situation of a blade vibration in a clean flow. The blade vibration mode we choose here is a torsional mode with a vibrating frequency 1871.683 Hz (reduced frequency 1.086 based on tip parameters), which is very close to the first torsion frequency obtained from a structure analysis on the fan

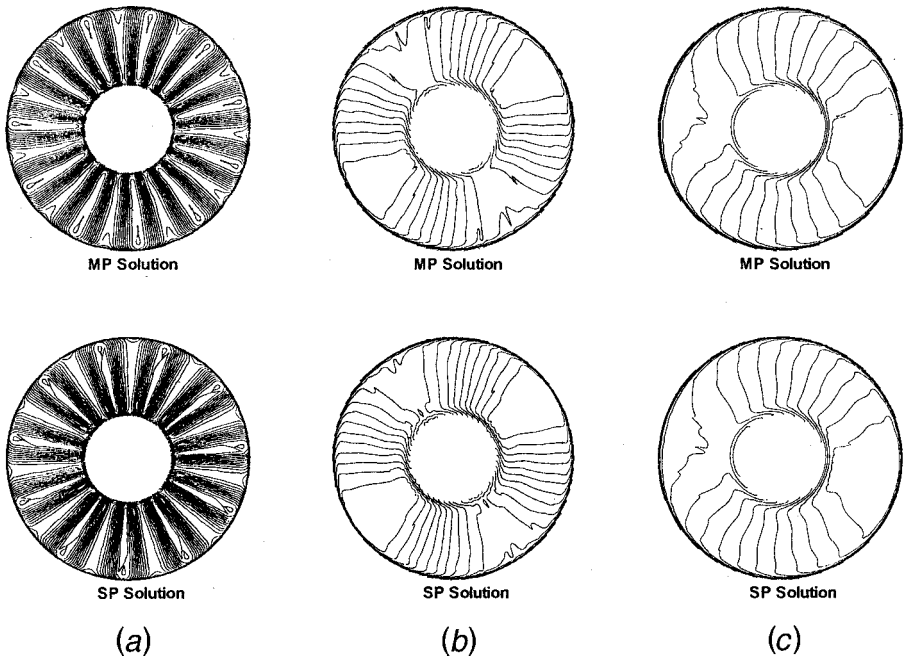

Fig. 4 Instantaneous total pressure contours at near inlet section—(*a*) 11-node mode, (*b*) 2-node mode, (*c*) 1-node mode

blade [24]. The inter-blade phase angle is taken as 32.727 deg, which corresponds to a forward traveling wave mode with two nodal-diameters. The torsion axis is a radial line through the midpoint of the chord on the hub section. For simplicity, the torsion amplitude was specified to linearly vary from 0 deg at the hub to a maximum at the tip. Three cases with different maximum torsion amplitudes, i.e. 0.25, 0.50, and 1.0 deg have been studied. Calculated unsteady pressure distribution on the blade surface is presented by the first harmonic pressure coefficient defined by $CP_1 = P_1/0.5\rho_\infty u_\infty^2 A_m$, where P_1 is the first harmonic static pressure on the blade surface in a complex form with its real and imaginary parts being the in-phase and out-phase components. If an unsteady flow behaves linearly, the unsteady pressure coefficient would be constant regardless of the torsion amplitudes used.

Figure 6 shows the CP_1 distributions on the suction side at 90 percent span section obtained from the single-passage calculation. The steep changes of the real and imaginary parts (and hence the amplitude and phase angle) around the mean shock position (90 percent chord) are typical of a ''shock impulse'' due to blade oscillation. The point to note is that the unsteady pressures induced by the blade vibration (hence the aerodynamic damping) are very much of a linear behavior, as shown by the close agreement among CP_1 distributions at the three amplitudes.

4.3 Blade Oscillation Subject to Inlet Distortion. In this section, we examine the unsteady flow fields around the vibrating blade under different inlet distortion modes. The blade vibration and inlet distortion modes adopted here are the same as described earlier, i.e., the blade is vibrating at the frequency of 1871.683 Hz with the inter-blade phase angle of 32.727 deg subject to an inlet distortion in either 11-node, 2-node, or 1-node mode. The frequen-

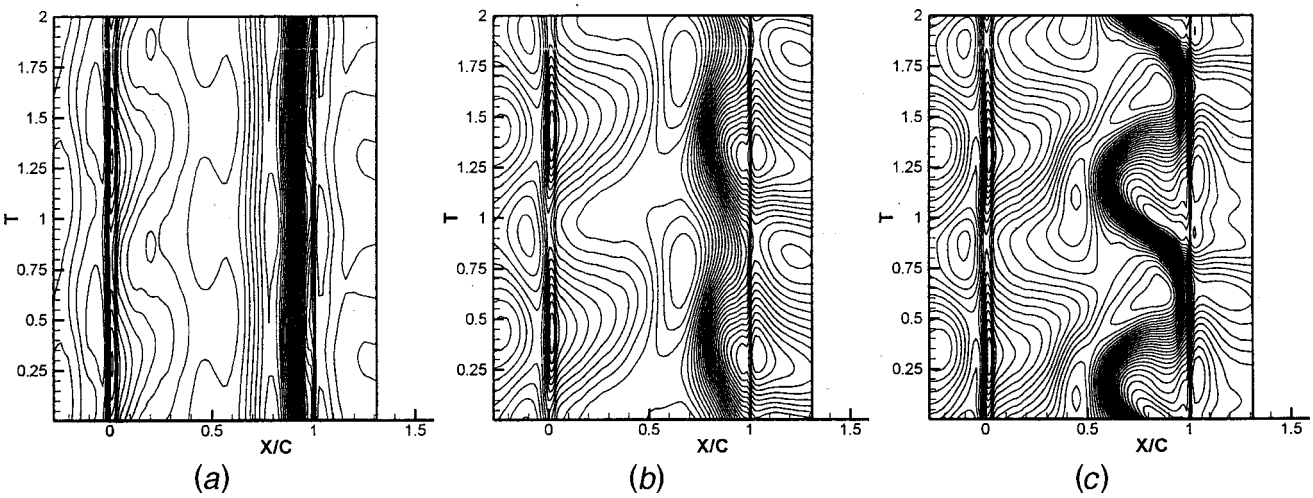

Fig. 5 Time-space pressure trace on the suction side at 90 percent span section (*T*: time period; *X*/*C*: nondimensional streamwise mesh line distance measured from blade leading edge)—(*a*) 11-node mode, (*b*) 2-node mode, (*c*) 1-node mode

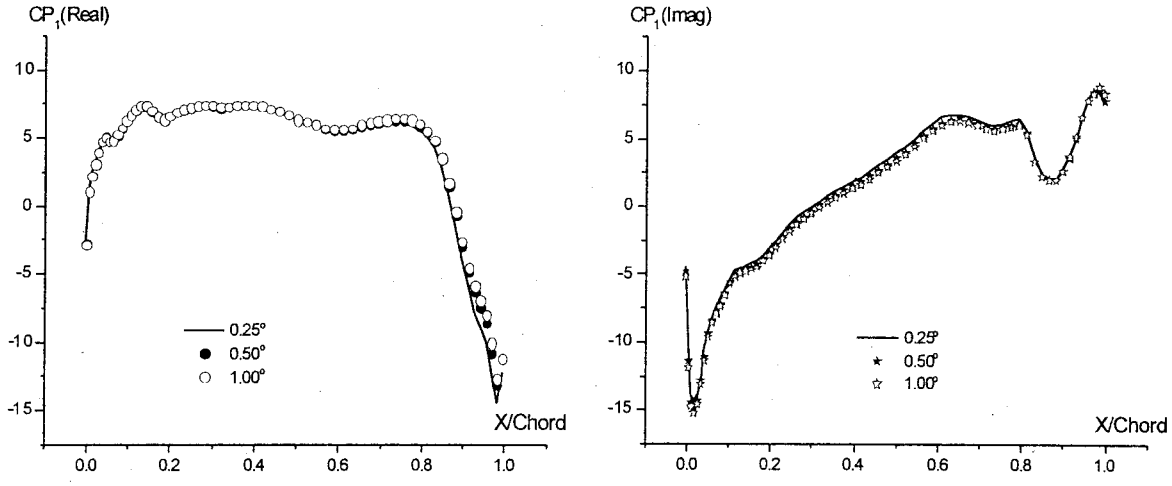

Fig. 6 First harmonic pressure coefficient distribution of torsion mode (clean inflow with different torsion amplitude)

cies of the three distortion modes are 2941.217, 534.7667, and 267.3833 Hz, respectively. All the cases are calculated by the single-passage approach.

For a validation purpose, an 11-passage calculation is also carried out for the case of the blade vibration under an inlet distortion in a two-node mode (wavelength corresponding to 11 passages). In this case, 210 physical time steps in each inlet distortion period and 60 time steps in each torsion period are applied in both the single-passage and the multi-passage calculations. The resultant number of time steps in each beating period is 420. The current choice of the physical time steps gives a relatively small number of time steps in each beating period, which is convenient for a validation purpose. Practical situations, on the other hand, might have much longer beating periods (and thus much larger numbers of time steps) which should not be a problem with the partial-substitution technique being used as described earlier. Comparisons between the two methods in terms of the calculated time-history of pressure jump at three different locations (at midchord with different spanwise position) are shown in Fig. 7(*a*). In general, the pressure variation is mainly influenced by the inlet total pressure distortion. Two main peaks are observed in each beating period, which correspond to the inlet distortion frequency (two periods of inlet distortion in each beating period). Noticeable influences from the torsion vibration are found at the outer part of blades (near the tip region), where the torsion amplitude is higher. Unsteady forces, as shown in Fig. 7(*b*), are also dominated by the inlet distortion effect, but with superposition of the vibration effects. We can see that the results from the single-passage calculation (SP) and the multi-passage one (MP) are in good agreement. This demonstrates that the periodic responses to multiple disturbances at a condition with noticeable nonlinear effects can be adequately predicted by the single-passage solver using the shape-correction method. It also confirms the validity of the phase-shifted periodicity for this transonic unsteady flow condition.

To examine the effects of different distortion modes on the unsteady flow due to the blade vibration, the total unsteady pressure is decomposed, and the part corresponding to the blade vibration is extracted by Fourier transform at the blade vibration frequency. For the given sinusoidal blade vibration mode, only would the first harmonic of this part of the unsteady pressure contribute toward the aerodynamic damping. The first harmonic pressure coefficients on the suction side at 90 percent span section are presented in Fig. 8. Compared with the results of the vibration under a clean flow condition (see Fig. 6), it is not surprising that

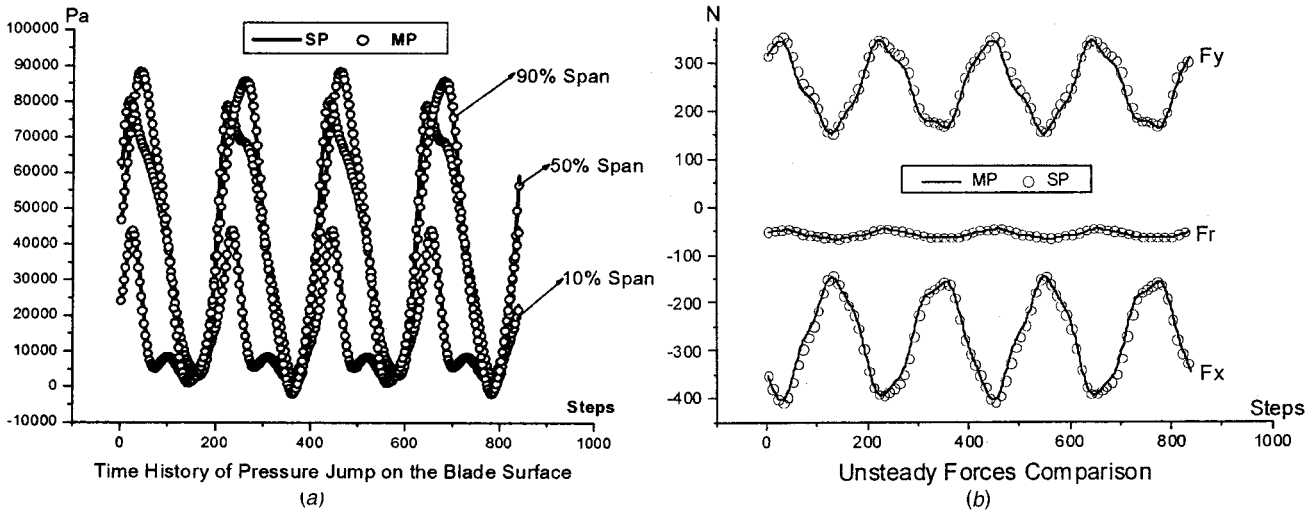

Fig. 7 Pressure jump and unsteady forces history (torsion and inlet distortion, SP: single passage solution, MP-11 passage solution)

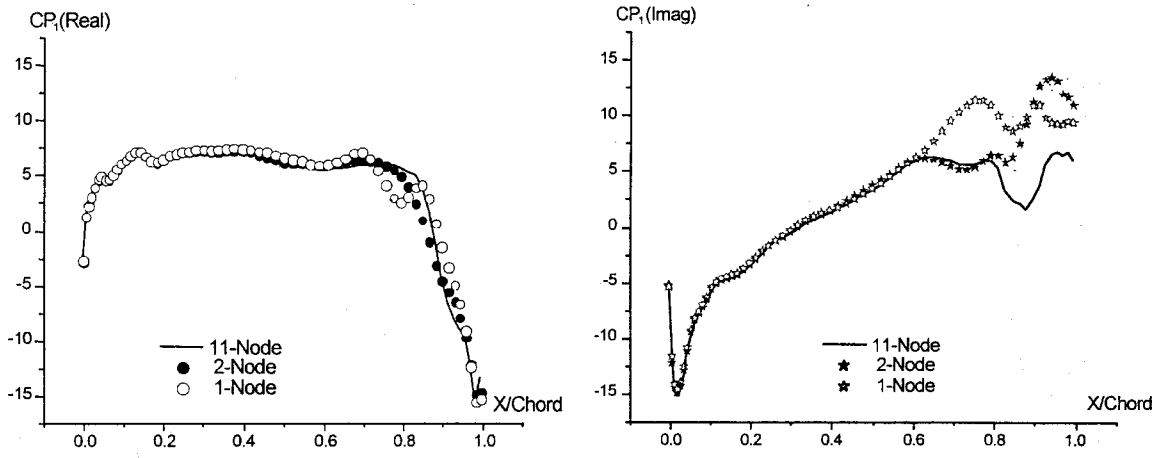

Fig. 8 First harmonic pressure coefficient distribution (torsion with different inlet distortion modes)

the shortest wavelength distortion (11-node mode) has minimal effects on the unsteady pressure due to the blade vibration. This is simply because the distorted flow itself at a short wavelength is shown to be predominantly linear; but the moderate and long wavelength distortions (2-node and 1-node modes) have stronger influences on the surface unsteady pressures shown by the deviation of the imaginary part of CP_1 in the rear blade region. This is the very area affected by the passage shock oscillation. The comparison of the unsteady pressures means that the aerodynamic damping will vary to an appreciable extent at the three different distortion conditions. This influence of inlet distortions on unsteady flow around oscillating blades will have to be taken into account when calculating blade aerodynamic damping in a distorted flow. The observation is relevant to both blade flutter characteristics in distorted flows and forced response predictions, where aerodynamic damping is often assumed to be completely decoupled from the forcing distortion and is evaluated at a clean flow condition.

In order to gain an insight into the interaction mechanism between the two disturbances, i.e., blade vibration and inlet distortion, two further calculations are conducted for the case subject to the distortion with the longest distortion wavelength (1-node mode) which has apparently a strong nonlinear effect. Given a linear aerodynamic damping characteristics in a clean flow condition (Fig. 6), one would ask whether or not the unsteady pressures due to the blade vibration would still behave in a linear manner in such a distorted flow condition. The linearity is checked by two more calculations with different blade vibration amplitudes. The CP_1 distributions at three blade torsional vibration amplitudes are shown on Fig. 9. The results generally agree very well with each other except for the imaginary part at the near the trailing edge region, where strong shock oscillation occurs. The difference among the results at different amplitudes is however much smaller than that at different inlet distortion length scales (shown on Fig. 8). This comparison suggests that the effect of the inlet distortion on the aerodynamic damping be dominated by the change of the time-averaged flow state, instead of a direct interaction (coupling) between the two modes. The results confirm the importance of a ''mean'' flow to aerodynamic damping prediction and implies that a pure linear perturbation method can be adequately used for predicting aerodynamic damping as long as we can provide a right ''mean'' flow state, on which the flow perturbation is based.

The overall effects of the two disturbances on the time-averaged flow can be seen from Fig. 10, where the time-averaged pressure distributions on the pressure surface at 90 percent span section of two cases (vibration in clean flow and vibration under two-node mode inlet distortion) are presented. There are two issues worth being noted here. The first is that results from single-passage solution agree very well with multiple-passage solution which again demonstrates the capability of the current shape-correction method in predicting unsteady time-mean flow under multiple disturbances. Secondly, the time mean flow under the inlet distortion is changed remarkably. As shown on Fig. 10(*b*), the location of the passage shock is moved forward about 10 percent of chord length. While in the pure torsion case, the time-averaged mean flow is very close to the steady state and the mean passage shock is almost at the original steady position, keeping with a linear behavior.

Finally regarding the consumption of the computing time of the present calculations, the shape-correction based single-passage solutions reduced CPU time by a factor of 5–10 times saving compared to the direct multi-passage solutions.

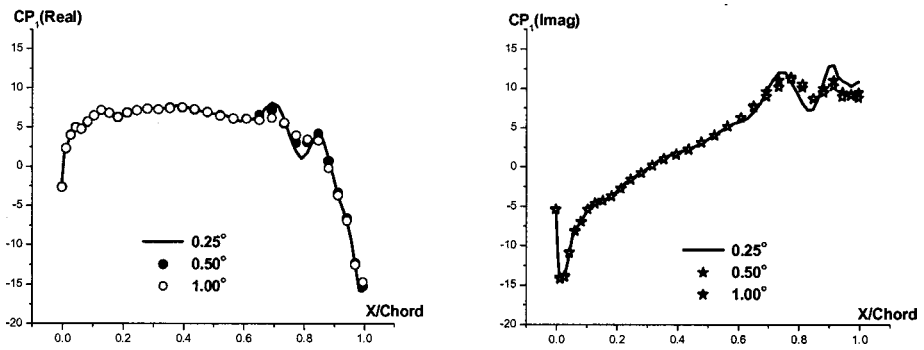

Fig. 9 First harmonic pressure coefficient distribution (1-node inlet distortion with different torsion amplitude)

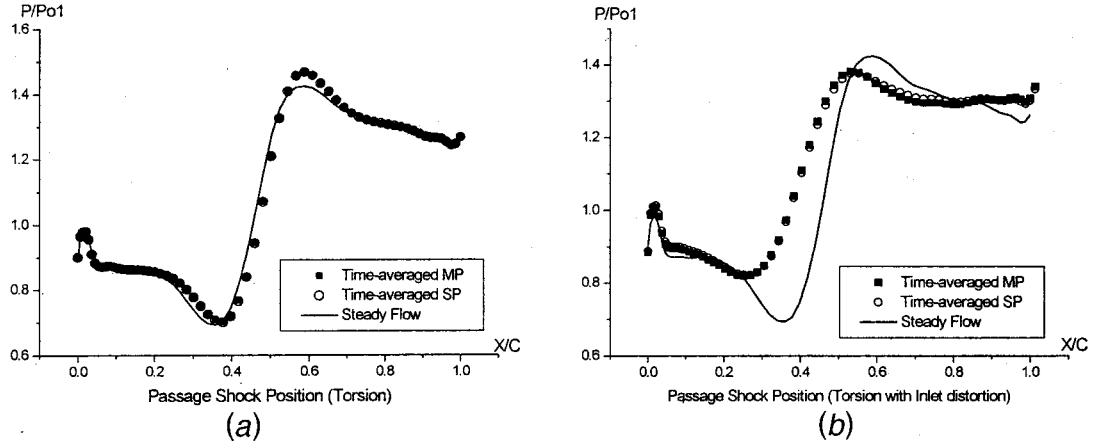

Fig. 10 Time-averaged and steady pressure distributions—(*a*) torsion, (*b*) torsion and 2-node inlet distortion

5 Concluding Remarks

A three-dimensional single-passage Navier-Stokes solver based on the shape-correction method has been developed for calculation of unsteady flows around vibrating blade under inlet distortion. Comparative studies for a transonic fan rotor (NASA Rotor-67) show that the present single-passage solution can capture both deterministic unsteadiness and time-averaged flows in good agreement with the direct multi-passage method. For all the transonic cases considered in the present study, the basic phase-shifted periodicity has been shown to be valid. The results clearly demonstrate the key capability of the present single-passage method in dealing with unsteady flows under influences of multiple disturbances.

A marked influence of distortion length scales is identified, confirming the importance of circumferential wavelength in propagation of unsteady disturbances. A flow response to a long wavelength distortion is shown to be strongly nonlinear with a large passage shock oscillation ranging over 50 percent chord. This is in contrast to that with a short wavelength at the same distortion amplitude.

The calculated results also reveal that for the case and conditions considered in the present work, the unsteady flow behavior due to blade oscillation in a torsion mode appears to be predominantly linear. Hence, there is negligible interaction between the blade vibration and the inlet distortion. The nonlinearity of the unsteady flow part due to the inlet distortion can only influence the aerodynamic damping by means of changing the time-averaged flow. Therefore, a pure linear perturbation method should be adequate in predicting aerodynamic damping as long as a right time-mean base flow can be provided.

Acknowledgment

The authors wish to thank Engineering and Physical Sciences Research Council (EPSRC) of U.K. for sponsoring this work under grant GR/M43821.

References

[1] Fleeter, S., Jay, R. L., and Bennett, W. A., 1978, "Rotor Wake Generated Unsteady Aerodynamic Response of a Compressor Stator," ASME J. Eng. Power, **100**, pp. 664–675.
[2] Manwaring, S. R., and Fleeter, S., 1990, "Inlet Distortion Generated Periodic Aerodynamic Rotor Response," ASME J. Turbomach., **112**, pp. 298–307.
[3] Monsarrat, N. T., 1969, "Design report: Single-Stage Evaluation of Highly-Loaded High-Mach-Number Compressor Stage," NASA CR 72565.
[4] Bowditch, D. N., and Coltrin, R. E., 1983, "A Survey of Engine Inlet Distortion Capability," NASA TM-83421.
[5] Hah, C., Rabe, D. C., et al., 1998, "Effects of Inlet Distortion on Flow Field in a Transonic Compressor Rotor," ASME J. Turbomach., **120**, pp. 233–246.
[6] Hirai, K., et al., 1997, "Unsteady Three-Dimensional Analysis of Inlet Distortion in Turbomachinery," AIAA Paper 97-2735.
[7] Marshall, J. G., Xu, L., Denton, J., and Chew, J. W., 2000, "Prediction of Low Engine Order Inlet Distortion Driven Response in a Low Aspect Ratio Fan," ASME Paper 2000-GT-0374.
[8] Breard, C., Vahdati, M., Sayma, A. I., and Imregun, M., 2000, "An Integrated Time-Domain Aeroelasticity Model for the Prediction of Fan Forced Response Due to Inlet Distortion," ASME Paper.
[9] He, L., 1992, "Method of Simulating Unsteady Turbomachinery Flows With Multiple Perturbations," AIAA J., **30**, No. 11, pp. 2730–2735.
[10] Erdos, J. I., Alzner, E., and McNally, W., 1977, "Numerical Solution of Periodic Transonic Flow Through a Fan Stage," AIAA J., **15**, No. 11, pp. 1559–1568.
[11] Giles, M. B., 1990, "Stator/rotor Interaction in a Transonic Turbine," J. Propul. Power, **6**, 5.
[12] Baldwin, B. S., and Lomax, H., 1978, "Thin Layer Approximation and Algebraic Model for Separated Turbulent Flows," AIAA Paper 78-0257.
[13] Jameson, A., Schmidt, W., and Turkel, E., 1981, "Numerical Solutions of the Euler Equations by Finite Volume Method Using Runge-Kutta Time-Stepping Scheme," AIAA Paper 81-1259.
[14] He, L., 2000, "Three-Dimensional Unsteady Navier-Stokes Analysis of Stator-Rotor Interaction in Axial Flow Turbine," IMechE, Part A, **214**, pp. 13–22.
[15] Jameson, A., 1991, "Time-Dependent Calculations Using Multi-Grid, With Applications to Unsteady Flows Past Airfoil and Wings," AIAA Paper 91-1596.
[16] Giles, M. B., 1990, "Nonreflecting Boundary Conditions for Euler Equation Calculations," AIAA J., **28**, No. 12, pp. 2050–2058.
[17] Strazisar, A. J., Wood, J. R., Hathaway, M. D., and Suder, K. L., 1989, "Laser Anemometer Measurement in a Transonic Axial-Flow Fan Rotor," NASA TR-2879.
[18] He, L., and Denton, J. D., 1994, "Three-Dimensional Time-Marching Inviscid and Viscous Solutions for Unsteady Flows Around Vibrating Blades," ASME J. Turbomach., **116**, pp. 469–476.
[19] Jennions, I. K., and Turner, M. G., 1993, "Three-Dimensional Navier-Stokes Computations of Transonic Fan Flow Using an Explicit Flow Solver and an Implicit k-e Solver," ASME J. Turbomach., **115**, pp. 261–272.
[20] Arnone, A., 1994, "Viscous Analysis of Three-Dimensional Rotor Flow Using a Multigrid Method," ASME J. Turbomach., **116**, pp. 435–445.
[21] Namba, M., 1991, Kyushu University, private communication.
[22] Gerolymos, G. A., and Vallet, I., 1996, "Validation of Three-Dimensional Euler Methods for Vibrating Cascade Aerodynamics," ASME J. Turbomach., **118**, pp. 771–782.
[23] Greg, M., and Patrick, P., 1998, "Unsteady Aerodynamics in Transonic Compressor Rotor Blade Passages," AIAA Paper 98-3897.
[24] Marshall, J. G., and Imregun, M., 1996, "An Analysis of the Aeroelastic Behavior of a Typical Fan-Blade," ASME Paper 96-GT-78.

Saim Dinc
e-mail: dinc@crd.ge.com

Mehmet Demiroglu

Norman Turnquist

Jason Mortzheim

GE Research and
Development Center,
Schenectady, NY 12309

Gayle Goetze

John Maupin

James Hopkins

GE Power Generation,
Greenville, SC 29602

Christopher Wolfe

Mark Florin

GE Power Generation,
Schenectady, NY 12345

Fundamental Design Issues of Brush Seals for Industrial Applications

Advanced seals have been applied to numerous turbine machines over the last decade to improve the performance and output. Industrial experiences have shown that significant benefits can be attained if the seals are designed and applied properly. On the other hand, penalties can be expected if brush seals are not designed correctly. In recent years, attempts have been made to apply brush seals to more challenging locations with high speed (>400 m/s), high temperature (>650 °C), and discontinuous contact surfaces, such as blade tips in a turbine. Various failure modes of a brush seal can be activated under these conditions. It becomes crucial to understand the physical behavior of a brush seal under the operating conditions, and to be capable of quantifying seal life and performance as functions of both operating parameters and seal design parameters. Design criteria are required for different failure modes such as stress, fatigue, creep, wear, oxidation etc. This paper illustrates some of the most important brush seal design criteria and the trade-off of different design approaches. [DOI: 10.1115/1.1451847]

Introduction

The GE Corporate Research and Development Center (CRD) has been involved extensively for several years in the development of advanced seals for turbo-machinery, focusing on applications in gas turbines, steam turbines, aircraft engines, industrial compressors, and generators. In particular, static seals have been developed for gas turbine hot gas path junctions and steam turbine packing ring segment end gaps. Brush seals have been developed for gas turbine compressor and interstage locations, steam turbine interstage and end packings, aircraft engine turbine locations, industrial compressor shaft seals, and generator seals. Abradable seals are currently being developed for numerous gas turbine applications. Also, an aspirating face seal has undergone extensive testing and analysis for potential application in aircraft engines (Turnquist et al. [1]).

In developing this array of seals for such a variety of applications, several design tools are used, including analytical equations, numerical methods (FEA and CFD), statistical methods, and empirical data obtained from several test rigs. In particular, a unique seal testing facility has three test rigs that are instrumental for quantifying the performance and behavior of advanced seals for turbomachinery. Following is a brief summary of the capabilities of each of the three test rigs:

Testing Capabilities

Static Seal Testing ("Shoebox" Rig)
Brush, cloth, labyrinth, and honeycomb Seals
3.10 MPa/600 °C air

Dynamic Seal Testing (90 cm/125 cm Rig)
Brush, aspirating, labyrinth, and honeycomb seals
90 and 125 cm diameter
150 m/s
0.69 MPa/ambient temperature air

Dynamic Seal Testing (125 mm Rig)
Brush, labyrinth seals
350 m/s
3.10 MPa/600 °C air
8.27 MPa/450 °C steam

Current Brush Seals Applications

Brush seals offer an opportunity for significant reduction in secondary leakage flows in rotating machinery. Brush seal development at GE Power Systems began in the early 1990s. Building on the GE aircraft engine development for the GE90 engine, initial work was focused on gas turbine applications. Technology development continues to leverage aircraft engine applications and power generation turbine applications, as well industrial compressor applications.

Typical brush seal designs for steam and gas turbine applications are shown in Figs. 1 and 3. The seal consists of a bristle pack, welded at the outer diameter to the side plates. The downstream plate is the backing plate, which provides structural support for the bristles. The forward plate protects the bristle pack from the incoming flow, and from handling damage during installation. Installation in a turbine on a retrofit basis typically requires the removal of a rotor land. This is necessary to maintain the axial clearance between the brush seal and the neighboring lands, because a brush seal that is capable of reliably sealing against the high pressures present in industrial steam and gas turbines typically requires more axial space than a simple labyrinth seal tooth.

Contributed by the International Gas Turbine Institute and presented at the International Gas Turbine and Aeroengine Congress and Exhibition, New Orleans, Louisiana, June 4–7, 2001. Manuscript received by the IGTI, February 27, 2001. Paper No. 2001-GT-400. Review Chair: R. A. Natole.

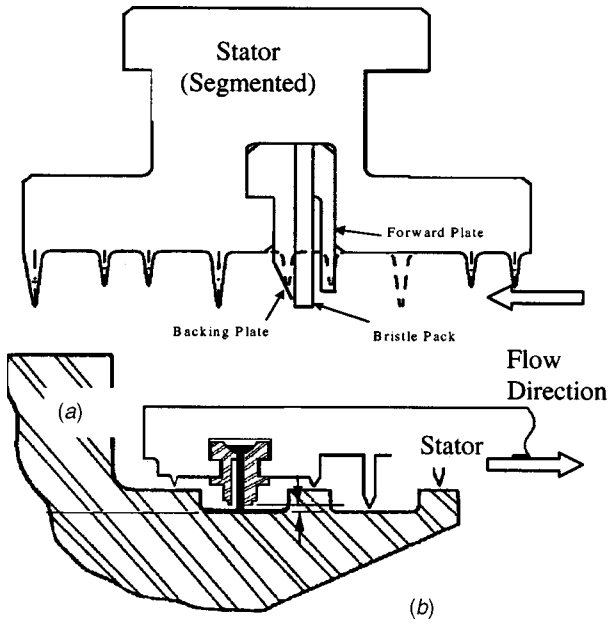

Fig. 1 Typical brush seal designs for (*a*) steam turbine, and (*b*) gas turbine applications

Steam Turbine Applications and Performance Benefits

Brush seals result in significantly reduced leakage when compared to typical labyrinth seals. Leakage rates for a variety of brush seal assembly clearances are shown in Fig. 2 compared to a typical labyrinth seal. This data comes from a number of test rigs with test capabilities that include pressures of 3.10 MPa (air) or 8.27 MPa (steam), 600 °C, and 350 m/s surface speeds. In addition to reduced leakages, the brush seals are not damaged by a rotor excursion such as would typically result in rubbed labyrinth teeth: the performance improvement is sustained in a way that is not possible with rigid labyrinth teeth. Typical performance benefits compared to new labyrinth seals are shown in Table 1.

Gas Turbine Applications and Performance Benefits

About 205 brush seals are currently operating in about 70 GE gas turbines, nine of which are instrumented for brush seal performance monitoring. Sixteen of these have been operating since 1996 and 52 others since 1997. With this wealth of field experience, the designers are able to validate their design work. The following are some examples from customer sites of the advantages that brush seals provide:

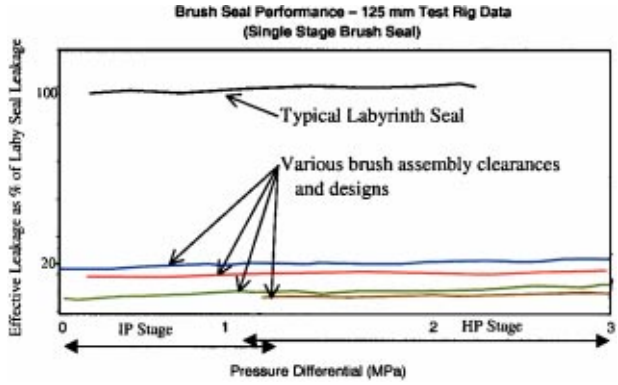

Fig. 2 Typical brush seal leakage data compared to a typical labyrinth seal

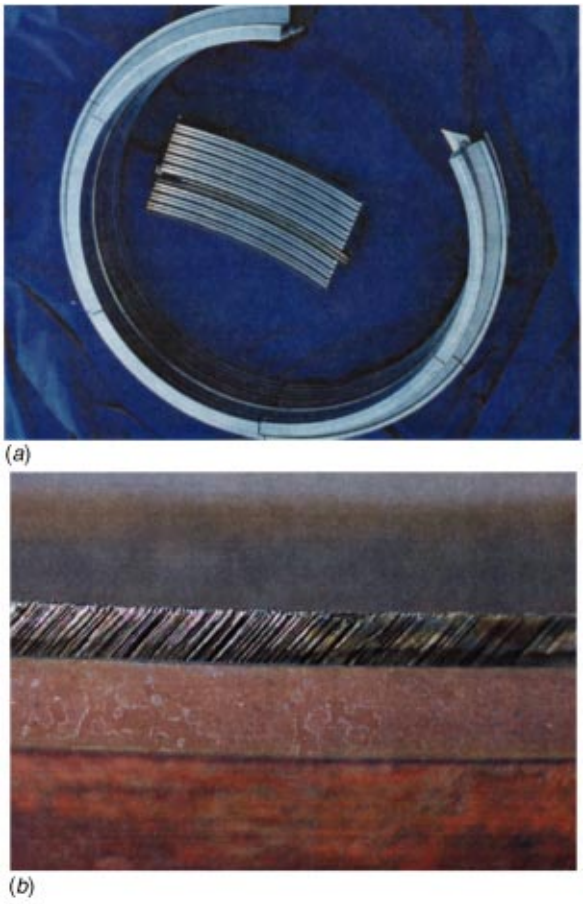

Fig. 3 (*a*) Typical steam turbine brush seal packing ring assembly. (*b*) 7EA gas turbine HPP brush seal after 22,000 h of operation.

- Current fleet leader: Frame 7EA high-pressure-packing (HPP) seal at 40,000 h.
- High-pressure-packing (HPP) and no. 2 bearing brush seals installed in a 9E in August 1996 provided 1.9 percent (2.5 MW) more power. The seals were inspected and reinstalled after three years of operation and have now provided 4 years of field data and monitoring.
- 7EA HPP brush seal resulted in 0.9 MW (1.1 percent MW) of additional power at installation and was still giving 0.6 MW after 22,000 h (3 yr). This seal is shown in Fig. 3(*b*) during engine overhaul and was returned into the engine for next 3 yr. 7EA 2nd stage turbine seal, which provides 0.4 percent MW output increase, has operated for 20,000 h with no significant degradation.

The current gas turbine brush seal installations have been performed on E and F class Frame 3, 5, 6, 7 and 9 machines at compressor discharge (HPP), bearing and turbine interstage locations. Figure 4 shows advanced seal locations on a Frame 7EA. Table 2 shows the percent MW and percent heat rate improvements of different frame size gas turbines due to brush seals. Aksit et al. [2] and Dinc et al. [3] give more details of the advanced seals currently applied. Chupp et al. [4] gives more insight into the developments at Siemens-Westinghouse.

Brush Seal Design Procedure and Analysis

The designer should be cognizant of the major mechanical design issues for brush seals. One of the key issues is the material selection for the bristles and the rotor rub surface. The materials must have enough wear resistance to meet engine durability re-

Table 1 Typical performance benefits for brush seals

Turbine Class and Location	Efficiency Benefit
Utility Steam Turbines (HP Section)	
End Packings (multiple locations)	0.1-0.2% unit heat rate
Interstage Packing (multiple stages)	0.5-1.2% HP section efficiency; 0.1-0.2% unit heat rate
Industrial Steam Turbines	
End Packings (multiple locations)	0.4 - 0.8% efficiency
Interstage Packing (multiple stages)	0.2 - 0.4% efficiency

quirements. The next key issue is the required radial gap between the backing plate and the rotor surface. The required gap is set by the transient growth characteristics of the rotor and stator (the typical secondary flow/heat transfer/mechanical analysis loop), as well as rotordynamic considerations. The rotor surface is not allowed to rub the backing plate. In this radial gap, the bristles are unsupported by the backing plate. For a given bristle density, diameter, and material, this sets the maximum ΔP the seal can withstand before the bristles begin to excessively deflect axially. Once the bristles deflect excessively, the sealing advantage of the brush seal is diminished. The ΔP requirement will determine seal bristle diameter, bristle density and even how many brush seals are required for a given application. Another major issue is frictional heating. The bristles rubbing on the rotor surface will create frictional heat, which must be properly dissipated through convection. The heat could lead to premature erosion of the bristles or in the worst case, the seal could become thermally unstable (i.e., the frictional heating causes the rotor to grow radially into the stator thereby increasing the frictional heating leading to additional rotor growth, etc., until the rotor rubs the backing plate and the seal fails). Some of these issues are addressed by Soditus [5]. These mechanical design issues significantly affect what applications are feasible for brush seals.

First, the seal design is developed to satisfy the engine operating conditions. The interaction of the seal with the engine flow system and its requirements are the second group of key issues to be addressed. The secondary flow analysis is performed around the sealing locations and the current flow requirements like wheel space temperature, purge flow, cooling flow, etc., are satisfied. Sub-scale endurance testing is done to validate the seal design and establish seal degradation rate in the engine. As soon as the seal design is completed, the next step is to integrate the seal into the engine which requires another set of development steps to address seal anti-rotation features, details of segmenting, stackup tolerances, engine vibrations, mechanical closures, etc.

The prototype seal field installation, instrumentation, data collection, performance testing and the secondary flow optimization using a by-pass piping system are the last steps before finalizing the seal design for production. During this process, design for six sigma (DFSS) methodology and transfer functions are used extensively to achieve overall critical to quality parameters (CTQs). Table 3 briefly describes the DFSS methodology.

Design Requirements and Criteria

Setting seal design requirements and criteria is important in the design process. For example, acceptable levels of seal leakage, seal design and operating stiffness, seal blowdown (deflection toward the rotor surface in the presence of flow), allowable level of seal heat generation, bristle tip temperatures, rotor thermal stability, seal oxidation and creep requires a deep understanding of brush seal dynamics and interaction with the engine system. Figure 5 shows how the seal design parameters interact with allowable seal design limits or engine limits. Each data point in this figure is a possible seal design, but the acceptable design limit of the seal or the engine eliminates some of the possible seal designs.

Establish Seal Operating Conditions

A good understanding of the operating conditions of the seal location is needed at the beginning of the design process. Some of the key operation conditions are pressure conditions, temperatures, surface speed, rotor material, rotor diameter, spacing, ther-

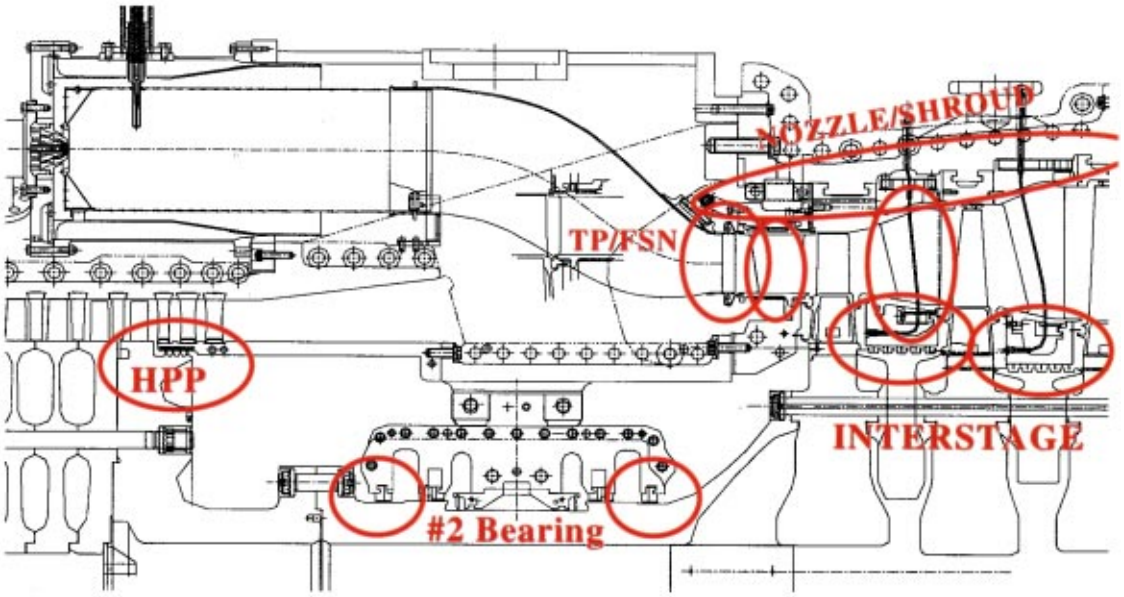

Fig. 4 Advanced seals locations on a Frame 7EA gas turbine

Table 2 Additional power and heat rate improvements of different frame size gas turbines

HPP	%MW & %Heat Rate
32G	+0.7%/-0.5%
32J	+0.7%/-0.5%
51P	+0.6%/-0.45%
61B	+1.0%/-0.5%
71E,EA	+1.0%/-0.5%
91E	+1.0%/-0.5%
ISTG	
51N	+1.0%/-0.5%
51P	+1.0%/-0.5%
61B	+1.0%/-0.5%
71E,EA	+1.0%/-0.5%
91E	+1.0%/-0.5%
BRG2*	**%MW & %Heat Rate**
71E	+0.3%/-0.2%
91E	+0.3%/-0.2%
HPP and BRG2**	
52C	+0.7%/-0.5%
52D	+0.9%/-0.6%
71B	+1.0%/-0.5%
91B	+1.0%/-0.5%

* Combination of forward and aft seals

** HPP and #2 bearing seals combination required for these machines

Table 3 A short description of the DFSS (design for six sigma) methodology

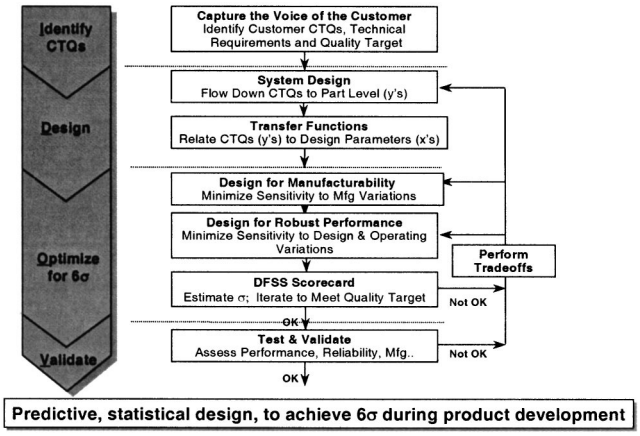

mal closures, etc. Figure 6 shows an example of a seal transient axial and radial closures on the engine. After establishing these conditions, the seal design process starts. During step-by-step seal design implementation and integration into the engine, more details of the operation conditions are needed like the complexity of the seal upstream flow, swirl, vibrations, and stack-up tolerances.

Seal Design Tools

A number of design tools have been developed to calculate brush seal characteristics such as pressure capability, leakage, radial stiffness, bristle blowdown, and bristle natural frequency. These design tools to evaluate the seal characteristics shown in Table 4 are based on a combination of analytical equations, numerical analyses (finite element analysis and computational Fluid dynamics), and empirical results. Where possible, tests are conducted using ambient temperature air as the working fluid; how-

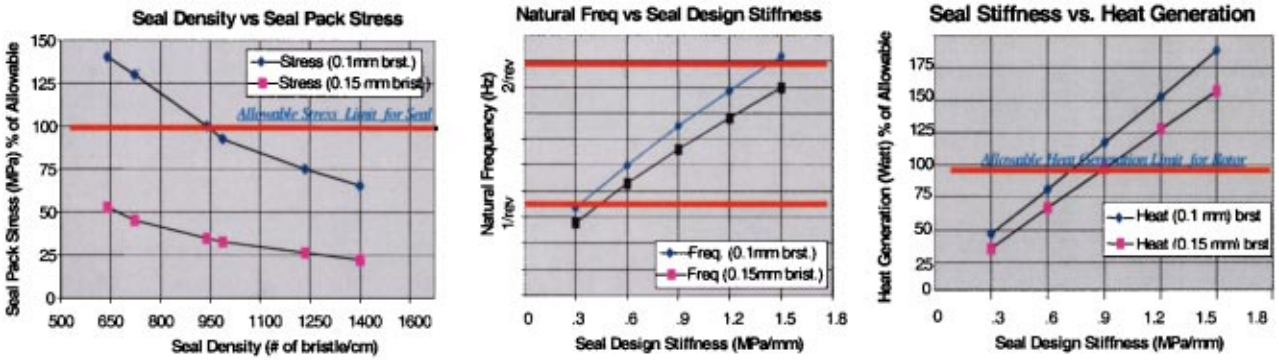

Fig. 5 Examples of allowable design limits and interaction with the seal design parameters

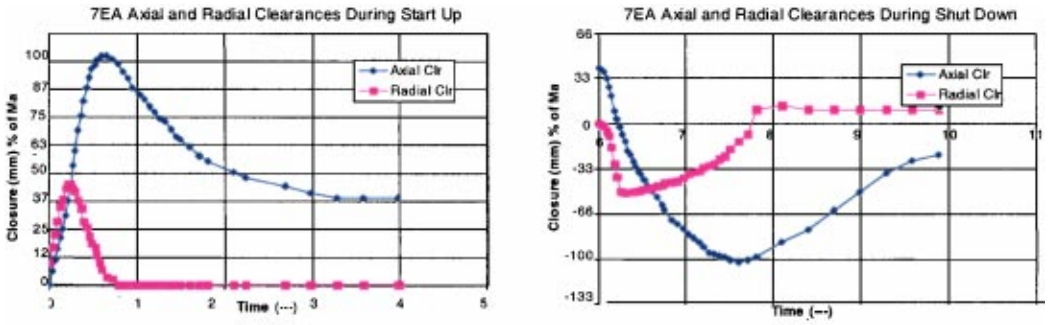

Fig. 6 Seal relative radial and axial transient closures

Table 4 Seal characteristics evaluated by design tools during the design process

Pressure capability
Frequency
Seal leakage
Seal stiffness
Seal blow-down
Bristle tip forces and pressure stiffening effect
Seal heat generation
Bristle tip temperature
Rotor dynamics
Rotor thermal stability
Secondary flow and cavity flow
Seal upstream protection
Seal HCF and LCF analysis
Seal oxidation
Seal creep
Seal wear
Solid particle erosion
Reverse rotation
Seal life/ Long term
Performance predictions
Oil sealing

ever, tests at elevated pressures (>3.10 MPa) are conducted in a superheated steam environment. In the 125-mm-rotary seals test rig, seal leakage has been measured at pressures as great as 8.27 MPa. Testing at pressure levels such as these is necessary to evaluate brush seal pressure capability, which is essentially established by the stress levels in the bristles themselves. The following section will describe more details of some of the design tools.

Seal Pressure Capability

Pressure capacity of a brush seal is one of the most important design parameters. In the bristle pack, all bristles are cantilever beams held at the bristle pinch point by a front plate and supported by the back plate. From a loading point of view, the bristles can be separated in to two portions (shown in Fig. 7): The lower part, *fence height*, between the rotor surface and the seal back plate inner diameter, and the upper part, from back plate ID to the bristle pinch point. The radially innermost portion carries the main pressure load, which is the main source of the seal stress (Chen [6]). Figure 8 shows a flow diagram of the seal stress and deflection analysis and the controllable and the noncontrollable design parameters.

As expected, tests at elevated pressures reveal the point of maximum bristle stress to be adjacent to the backplate corner, where the bending moment on the bristles is a maximum and where there exists a stress concentration at the point of bristle to backplate contact. Furthermore, this stress is a very strong function of the fence height, which is limited by the expected radial movement of the rotor relative to the seal during engine transients (such as during start up or shut down). Thus, the design of an effective brush seal hinges on thorough knowledge of the machine's behavior and operating conditions. The seal fence height must be selected to allow for expected transients, and the bristle pack design (diameter, pack thickness, free radial height) must then be designed to handle the expected pressure loading without having excessive radial stiffness and the resulting heat generation and rotor dynamics issues.

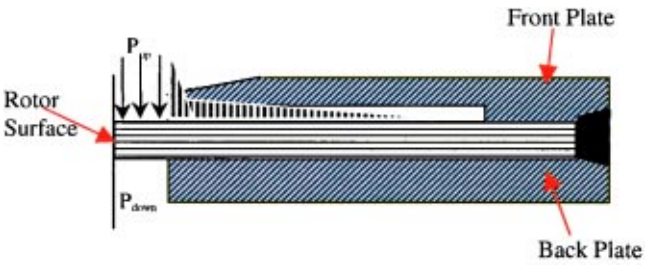

Fig. 7 Pressure forces acting on the seal bristle pack

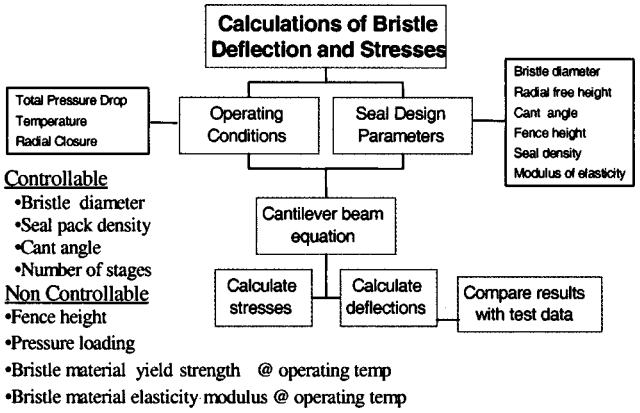

Fig. 8 Flow diagram for bristle stress and deflection analysis

As expected, tests at elevated pressures reveal the point of maximum bristle stress to be adjacent to the backplate corner, where the bending moment on the bristles is a maximum and where there exists a stress concentration at the point of bristle to backplate contact. Furthermore, this stress is a very strong function of the fence height, which is limited by the expected radial movement of the rotor relative to the seal during engine transients (such as during start-up or shut-down). Thus, the design of an effective brush seal hinges on thorough knowledge of the machine's behavior and operating conditions. The seal fence height must be selected to allow for expected transients, and the bristle pack design (diameter, pack thickness, free radial height) must then be designed to handle the expected pressure loading without having excessive radial stiffness and the resulting heat generation and rotor dynamics issues.

Tests run at various levels of bristle to rotor clearance allow bristle blowdown to be inferred. Additionally, tests using thermal imaging to measure seal and rotor temperature distributions in the 125-mm-test rig have allowed the validation of previously derived physical relationships for brush seal heat generation. Bristle natural frequency is significantly more difficult to measure. Currently, analytical equations are depended upon for estimates of bristle natural frequencies.

Leakage characterization of brush seals typically consists of a series of tests at varying levels of bristle to rotor interference or clearance; typical examples are shown in Figs. 9 and 10. While static (nonrotating) tests are run to obtain a general idea of seal leakage and pressure capability, dynamic (rotating) tests provide a truer measure of seal behavior. Rotating tests also reveal the effects of the seal on rotor dynamics, an important consideration for steam turbine rotors that can be sensitive to radial rubs due to potentially non-uniform heat generation. In both static and dynamic tests, mass flow is measured as a function of seal pressure differential, and seal effective clearance is then calculated based on the rotor diameter. By measuring baseline seal leakage in a line-to-line (zero) assembly clearance configuration, bristle blowdown for varying levels of assembly clearance can be inferred from the corresponding sets of leakage data.

As mentioned, steam turbine rotors can sometimes be particularly sensitive to rubs, owing to their solid shaft construction. By

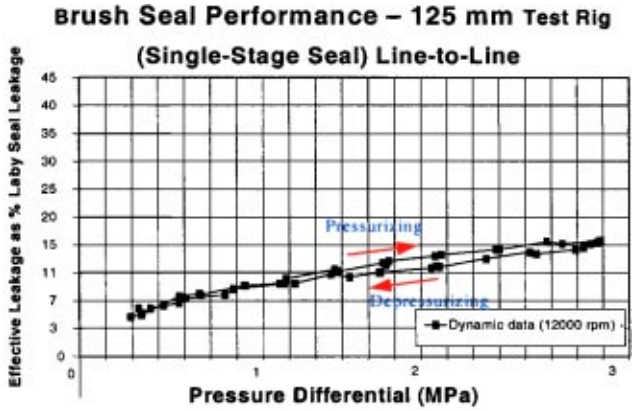

Fig. 9 Seal line to line leakage characteristics as a function of seal ΔP (y scale shows the ratio of brush seal leakage to laby seal leakage)

Table 5 Gas turbine system level secondary flow and performance analysis

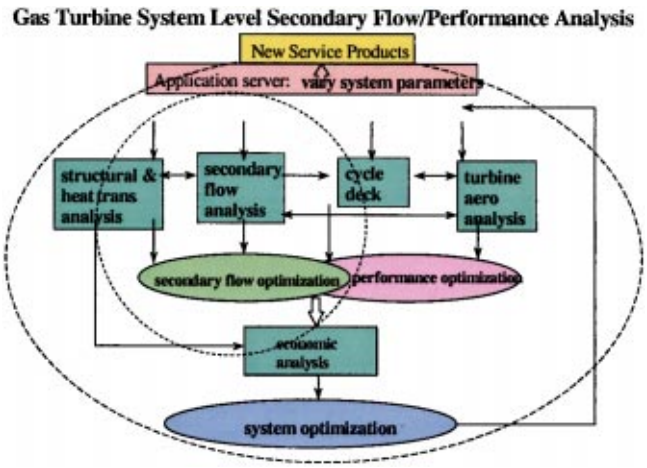

monitoring rotor vibrations at speeds close to the first and second critical speeds of the flexible rotor in the CRD test rig, the seal's effect on rotor behavior can be evaluated and the seal can be configured for the optimal balance between leakage performance and rotor dynamic behavior.

Finally, leakage, blowdown, and heat generation data obtained in rig tests are integrated into analytical tools used to design brush seals for new applications. Transfer Functions are either derived from the test data directly, or they are developed based on analytical equations and validated through testing.

Secondary Flow and Cavity Flow Analysis

By definition, the brush seal is designed to control the secondary flow system of a turbine machine in such a way as to reduce the chargeable flow and improve machine performance. As such, in order to effectively control the secondary flow system a seal designer must fully understand the secondary flow system and the concurrent effects of changing the flow balance. In Table 5, the level of integration of the secondary flow system is detailed. As the diagram shows, not only is the seal impact to the baseline turbine performance considered but the impacts over operating condition variation (cycle deck) as well as the effects on downstream turbine components (structural and heat transfer analysis, turbine aerodynamic analysis) are all maintained in an optimized environment. A brief description of the process is given in Table 5.

The point that this chart displays is the interaction of the seal design on the secondary flow system and the related components. In nearly all cases, one can not simply restrict the flow with brush seals as some leakage is required for part cooling, purge flow or some other useful and critical need. In many cases, the current machine sealing design provides excessive cooling; however, the brush seal is overly restrictive. The seal design must reflect this and/or the secondary flow system design must be altered to accept the advanced sealing of the brush seal but still maintain the required cooling/purge flow requirements. Failure to do so could result in decreased part life leading to part failure.

As an example consider a part downstream of a typical seal that requires 2.27 kg/s of cooling flow to maintain acceptable part life. Current sealing provides 4.54 kg/s of cooling, an excessive amount. A normal brush seal design could restrict the flow to 1.0 kg/s, an amount that would severely affect the part life. With the optimized secondary flow system analysis either a bypass flow of lower cost air or a seal design that would provide the required 2.27 kg/s could be utilized and still retain the performance benefit over the original sealing. Without in-depth knowledge of the actual machine needs and machine operation, one cannot simply design an acceptable seal to solve the dichotomy of stable part life and performance benefit.

The end point is that the brush seal design is not simply a separate design but a part of an integrated secondary flow analysis and optimization.

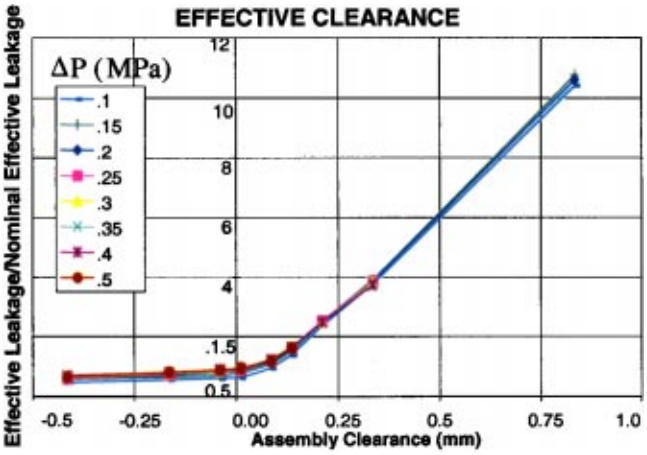

Fig. 10 Leakage characteristics of a typical seal under seal interference and clearance conditions (y scale shows the ratio of Brush seal leakage at a specified condition seal line-to-line leakage)

Seal Procurement and Functional Requirements

During seal manufacturing, the process capability of the seal vendor is important with respect to manufacturing variables such as the welding requirements and tolerances on key dimensions. For example, the seal stiffness (which effects bristle tip forces, seal heat generation, seal wear) is a cubic function of the bristle free length. A small change of the free length may double the seal stiffness. An understanding of design sensitivity to variables such as this is very important, as is the ability of the manufacturer to control them. Seal procurement details and functional requirements have to be very thorough to ensure quality parts.

Design Verification

After completing the design, the prototype engine installation, and pre and post-performance testing is the last and most important step of the design process to validate and tune the seal design before commercialization of the hardware. Figure 11 is an ex-

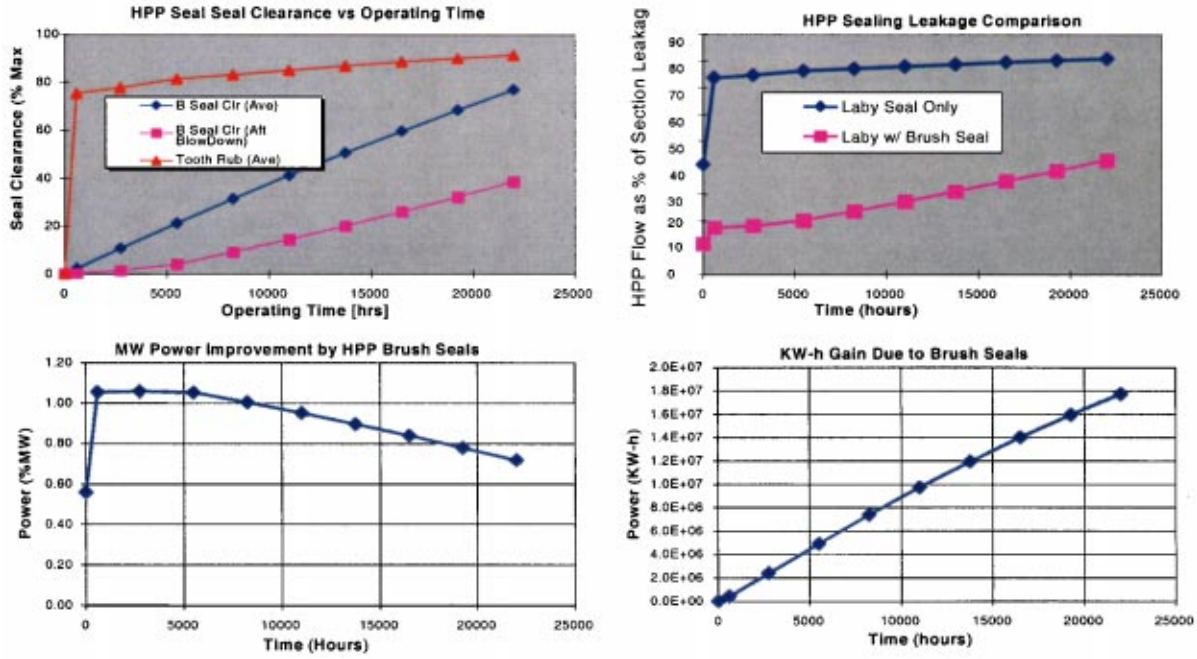

Fig. 11 7EA machine HPP brush seal field data during 22,000 h of operation: (from top left corner, clockwise) brush seal clearance due to wear versus labyrinth seal clearance due to rub, brush seal flow versus labyrinth seal flow, additional kW-h saving of the brush seal in the sealing system, brush seal performance degradation over 3 yr (as new seal provided additional 1.1 percent MW, after 3 yr provided 0.7 percent MW, seal returned to the machine after engine overhaul for additional 3 yr service the seal during overhaul is shown in Fig. 3(*b*))

ample of the field test data from a 7EA gas turbine high pressure packing (HPP) seal test showing seal performance over time.

Field Experience/Technology Maturation

More than 200 brush seals have been installed in gas turbines. The fleet leader has been in service for about 40,000 h. The first units had their 24,000 h inspections in 1999. In most of the cases, the brush seal wear was acceptable and the brush seals were returned to service. In all of the cases, the rotor wear was insignificant. The gas turbine brush seals have accumulated about 1.4 million h and 10,000 starts. Brush seals have been installed in seven commercial steam turbines to date. This includes two industrial units and five large steam turbines, with various combinations of interstage packing, end packing and bucket-tip brush seals. The fleet leader has been running successfully since early 1996. In addition, brush seals have been tested in the highly instrumented

Fig. 12 (*a*) Previous version of a seal from the engine after about 1000 cycles; (*b*) new and improved version of the seal after 2000 cycles at the same location on the similar engine

Table 6 Brush seal technology status/milestones

Transient Capability/Stable Brush Seals;
From current seals to 3-5 times dynamically more aggressive engine seals.
High Surface Speed;
From 120 m/s of AE seals to 244 m/s of GT seals, now moving to 500 m/s.
High Pressure Loading;
From 0.69 MPa two stage seals to 2.76 MPa single stage seal design, now moving to higher ΔP multi-stage seal designs.
High Swirl Flow Field;
Swirl ratios of current applications are 0.3, now moving to 0.6 – 1.2 region.
Air Temperature;
From 370 °C to 650 – 1000 °C temperatures.
Seal Life and Durability;
GT fleet leader w/40,000 field hrs w/minimum degradation.
ST fleet leader 28,000 hrs w/minimum degradation.
Rotor Surface;
Ceramic coated AE rotors to uncoated GT and ST applications.
Interrupted surface at bucket tip seals.

steam turbine test vehicle in both interstage and bucket-tip locations; tests in the end packing locations are planned for early 2001. Results of performance tests matched predictions, validating the system performance prediction tools.

Figure 12 shows brush seals from two similar engines after about 1000 and 2000 cycles of operation, respectively. Figure 12(*a*), which is version 1, shows significant bristle pack damage due to very turbulent upstream flow, and the other 12(*b*) is an improved and successful version at the same location from another similar engine. This example shows that brush seal technology is implemented and matured by many design, analysis, component test and instrumented engine tests. Every lesson learned from each is used in the next step.

Conclusion

Brush seals provide a significant performance improvement for industrial gas turbines. However, if they are not designed correctly or integrated properly into the engine, the engine will face two potential problems. First, it can loose the performance gain very quickly due to premature seal failure. Second, the main parts of the engine downstream of the seal can suffer due to insufficient cooling air. Particularly for the second case, expensive hardware like buckets, nozzles, and wheel space cavities will run hotter and will consume their design service life. Brush seal installations require a full understanding of the engine transient behavior, and cooling flow and temperature requirements. If this knowledge does not exist, long term engine performance benefit will not be achieved and major problems may be encountered.

Table 6 is a brief summary of where the brush seal technology is being driven. Brush seals offer significant performance benefits through leakage reduction, and these benefits have been shown to be sustainable. Information and experience from a broad range of applications, i.e., steam turbines, gas turbines, aircraft engines, and compressors, combined with development facilities aids significantly in design and implementation of brush seals for industrial turbines.

References

[1] Turnquist, A., Tseng, T., McNickle, A., and Steinetz, B., 1999, ''Full Scale Testing of an Aspirating Face Seal With Angular Misalignment,'' AIAA Paper No. Paper 99-2682.

[2] Aksit, M. F., Bagepalli, B. S., Demiroglu, M., Dinc, O., S., Kellock, I., and Farrell, T., 1999, ''Advanced Flexible Seals for Gas Turbine Shroud Applications,'' AIAA Paper No. 99–2827.

[3] Dinc, S., Turnquist, N. A., et al., 1998, ''Brush Seals in Industrial Gas Turbines—Turbine Section Interstage Sealing,'' AIAA Paper No. 98–3175

[4] Chupp, R. E., Prior, R. J., Loewenthal, R. G., Menendez, R. P., 1997, ''Advanced Seal Development for Large Industrial Gas Turbines,'' Paper No. AIAA 97-2731, presented at 33rd AIAA? ASME/SAE/ASEE Joint Propulsion Conference & Exhibit, Seattle, WA, July 6–9.

[5] Soditus, S. M., 1998, ''Commercial Aircraft Maintenance Experience Relating to Current Sealing Technology,'' AIAA Paper No. 98–3284.

[6] Chen, L. H., Wood, P. E., Jones, T. V., and Chew, J. W, 1999, ''Detailed Experimental Studies of Flow in Large Scale Brush Seal Model and A Comparison with CFD Predictions,'' AIAA Paper No. 99-GT-281

Compressor Discharge Brush Seal for Gas Turbine Model 7EA

Steve Ingistov
BP/WCC Los Angeles Refinery,
Carson, CA 90749
e-mail: ingissg@bp.com

Single-shaft, heavy-duty industrial gas turbines are extremely sensitive to compressed air bypassing at compressor discharge plane. This plane represents the highest pressure location in entire gas turbine unit (GTU). Standard method to minimize compressed air leakage is labyrinth seal that is integral part of the cylindrical element here called "inner barrel." The inner barrel is also the part of compressor discharge diffuser. This paper describes the efforts related to conversion of standard labyrinth seal into the hybrid seal that is combination of labyrinth and brush seals. [DOI: 10.1115/1.1457456]

Introduction

Watson Cogeneration Company (WCC) Plant is located in Los Angeles Refinery, Carson, California. The Plant is comprised of four GE-made gas turbines model 7EA. The steam generated in heat recovery steam generators (HRSG) is sent to refinery and also two Dresser Rand-made steam turbines generators (STG). The plant was started during the fall of 1987.

The first major inspection was performed on GTU No. 3, Mar. 1993. The inner barrel was replaced with a new, spare inner barrel because the labyrinth teeth were badly worn out. Initial calculations indicated that for measured labyrinth clearances the compressed air bypassing caused a power loss of approximately 2.50 MW. The original equipment manufacturer (OEM) was asked to provide removable labyrinth. OEM did not offer at the time removable labyrinth; however, they informed WCC that they were testing a prototype brush seal. The brush seal would be offered to Users in 18-mo period. WCC contacted Entity other than OEM. This entity never manufactured heavy-duty industrial gas turbines. WCC provided them with operating parameters required to design a rugged brush seal capable to take heavy compressor rotors excursion during planned start-ups, shutdowns, and unwanted shutdowns. Unwanted shutdowns are dangerous because compressor rotor having big mass is slow to cool and the portion of inner barrel around the compressor rotor is quick to cool having small mass. The result of sudden differential expansions and contractions is inevitable loss of fixed labyrinth teeth height.

Brush Seal Design and Manufacture

The entity, hereby called Seal Manufacturer, that accumulated remarkable experience in manufacturing the brush seals for their aircraft GTU type was contacted during Aug. 1995.

A feasibility study was initiated and the initial results of this study were quite encouraging. The Seal Manufacturer expressed concerns related to compressor rotor displacements, rotor-to-stator axial differential movements and the inner barrel diameters concentricity.

WCC had a spare inner barrel to send to the Seal Manufacturer for necessary measurements to accept the new brush seal. WCC prepared the guidelines and criteria for design of the brush seal:

- Re-use the old inner barrel
- Keep all existing labyrinth teeth
- Maintain integrity of inner barrel
- Design single brush seal
- Locate brush seal in front of labyrinth
- Keep rotor-to brush seal axial gap
- Provide cold brush clearance equal to new labyrinth seal radial clearance
- Minimize number of brush seal segments
- Ensure life expectancy of 40,000 h
- Optimize the cost and delivery time

In the following, the criteria and guidelines listed are described:

- **Re-use of the inner barrel**—typical brush seal design requires grooving of the wall. Stress calculations did not permit radial groove machining because the marginal integrity of the radial wall.
- **Keep all labyrinth teeth**—the philosophy behind this criterion was that in case of brush seal failure the labyrinth would take over the role of the brush seal.
- **Maintain the integrity of inner barrel**—drilling of the bolt holes or any machining of the end of shell must not compromise the strength of the wall.
- **Design single brush**—seal—this requirement was based on definite lack of available space. The air pressure ratio across the sealing elements exceeded 2.0. This high-pressure ratio indicates air sonic flow and its choking as a result. Single brush seal exposed to before-described air pressures and flows must be able to withstand the aerodynamic forces tending to ''sweep'' the bristles downstream in axial direction.
- **Locate brush seal in front of labyrinth**—this requirement resulted from requirement nos. 1, 2, and 3. The packaging of the seal in axial direction was challenging task. OEM-imposed axial clearance between the compressor rotor and the end of the inner barrel had to be maintained.
- **Keep rotor-to brush seal axial gap**—this requirement is in line with requirement no. 5 and it became obvious that the end of the inner barrel had to be machined to accept the brush seal holder. In addition a retaining ring or brush cover ring bolted to the brush holder had to fit within allowed axial space.
- **Provide cold brush clearance equal to new labyrinth seal radial clearance**—this criterion was of fundamental importance. WCC did not have enough time to harden the rotor area facing the proposed brush seal. In addition, significant rotor radial migrations precluded the ''aircraft approach'' that is the bristles of the brush seal contacting hardened rotor surface. If the contact brush bristle-to-the rotor surface is 0.001 to 0.002 in. interference generated friction heat will wear the bristle tips and the rotor contact area may be damaged.
- **Minimize number of brush segments**—this requirement was based on ease of installation and eventual removal. Two segments for the bottom half and one segment for the upper half of compressor casing.

Contributed by the International Gas Turbine Institute and presented at the International Gas Turbine and Aeroengine Congress and Exhibition, New Orleans, Louisiána, June 4–7, 2001. Manuscript received by the IGTI, January 24, 2001. Paper No. 2001-GT-410. Review Chair: R. A. Natole.

- **Optimize life expectancy of 40,000 h**—this predicted life expectancy is rather conservative keeping in mind that for steady-state conditions and under the full/base GTU load brush bristle barely touch the rotor surface. In other words the rotor surface facing the brush seal should be slightly burnished.
- **Optimize the cost and delivery time**—the cost to fabricate first, prototype brush seal involved complex engineering calculations and potential brush integrity tests. Later on it was decided to forgo the integrity tests because of lack of time. Delivery of the prototype brush seal became main concern to have the brush seal ready for October 1996 GTU Major Inspection.

Operating Constraints

The Seal Manufacturer that WCC selected to design and manufacture prototype brush seal needed sufficient amount of data and information to start engineering efforts. Compressed air temperatures and pressures typical variations during GTU controlled start up mode are shown in Fig. 1. Compressed air temperatures and pressures variations during the GTU controlled shut down mode are shown in Fig. 2.

Both Figs. 1 and 2 show the changes in compressor discharge parameters. The rate of change is noticeable in case of controlled GTU shut down. Note the steep temperature drop from 520 to 120°F during essentially 10 min period of time. The temperature drop is especially important because in that particular period of time the inner barrel having much smaller mass than the compressor rotor will cool fast and virtually pinch the rotor. The labyrinth teeth will contact the compressor rotor and the rub is therefore initiated. The labyrinth teeth rotor rubbing is especially significant during unscheduled GTU shutdown from the base load. Major loss of labyrinth teeth will happen during unscheduled shut down of GTU.

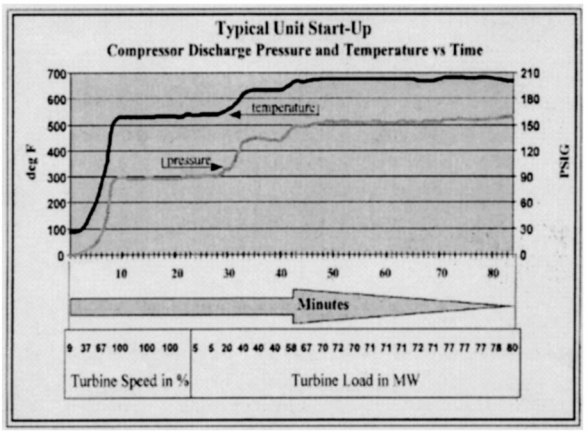

Fig. 1 Compressor discharge pressure and temperatures

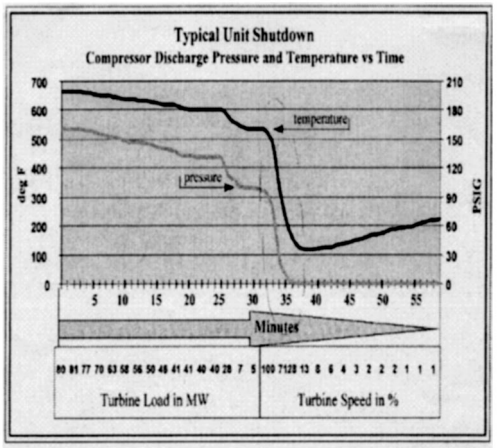

Fig. 2 Compressor discharge pressure and temperature during controlled shutdown

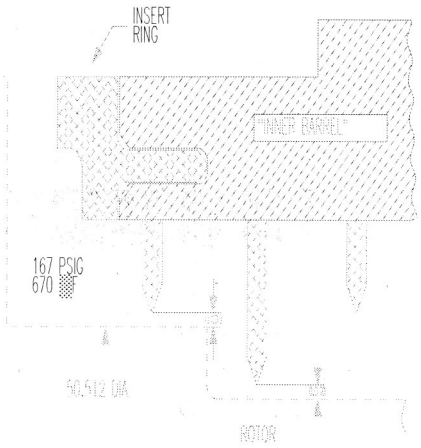

Fig. 3 Sketch of compressor discharge labyrinth and ''insert ring''

The sketch of the inner barrel labyrinth is shown in Fig. 3. Note the ''insert ring'' that was installed by OEM to extend the inner barrel. The extension was necessary to accept redesigned, shrouded 17th stage stator blades. The sketch also shows average pressures and temperatures of compressed air at compressor discharge plane. Typical labyrinth clearances are show in ''as-new-condition.''

The aforementioned operating constraints are accurate for controlled start-up and shut down. In case of electrical fault, when the breakers suddenly open the GTU is instantaneously unloaded and all elements inside the machine are exposed to some kind of the thermal shock. WCC could not provide the brush Seal Manufacturer with sufficient data reflecting the unwanted shutdown conditions. The conservative approach was therefore necessary in designing the brush seal with radial clearances matching the new labyrinth radial clearances.

Labyrinth Seal Performance

To assess the power loss due to parasitic airflows via the compressor discharge labyrinth seal the air leakage was computed using well-known equations shown in Appendix. OEM estimates for power loss were also used and compared by independent calculations. It is important to note that the calculations were done on the basis that the airflow in the last labyrinth tooth is essentially choking. This assumption is valid since the air pressure ratio across the existing labyrinth teeth is exceeding 2.0.

The compressed air leaking into the inner barrel cavity continues from there to leak into the turbine first stage. It cools the turbine forward wheel space and it also prevents hot gases backflow into the inner barrel cavity. The ''inner barrel'' air stream mixes with hot gasses. The enthalpy of the gas/air mixture is therefore slightly reduced. In the case when the inner barrel labyrinth is worn out, significant amount of relatively cold (680°F) air will mix with the gas stream lowering enthalpy of the mixture. The loss of the mixture enthalpy will negatively influence the heat rate (BTU/KW-h).

Figures 4–7 show that increased labyrinth radial clearances will:

- Increase air leakage into ''inner barrel''
- Reduce the power output

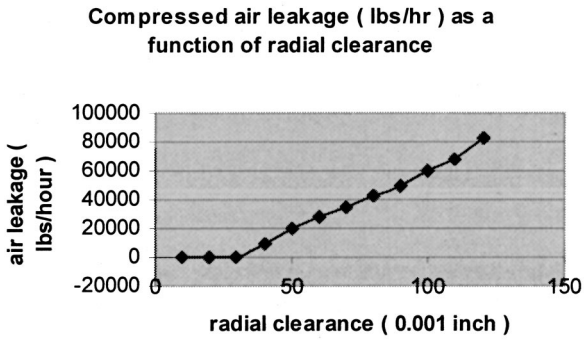

Fig. 4 Air leakage as a function of radial clearance

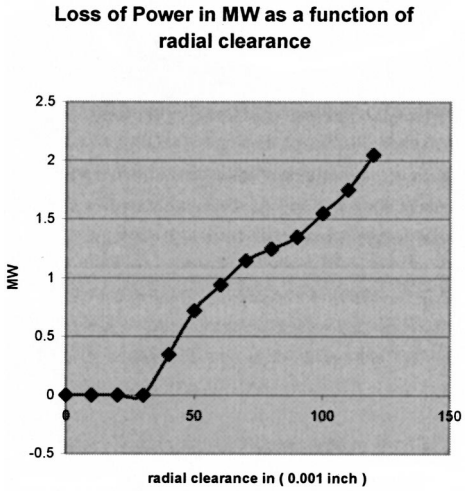

Fig. 5 Loss of power as a function of radial clearances

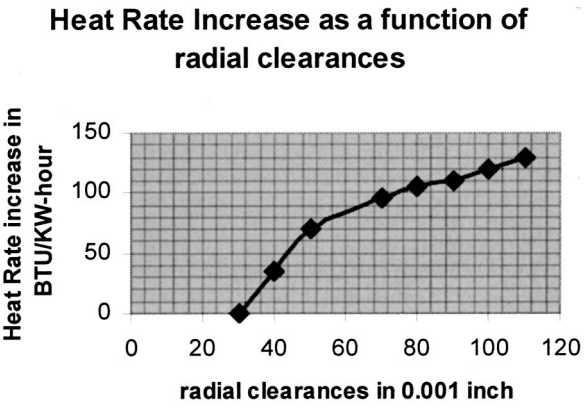

Fig. 6 Heat rate increase as a function of radial clearances

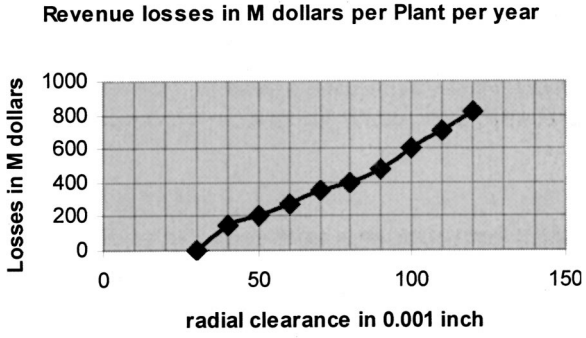

Fig. 7 Loss of revenues in dollars as a function of radial clearances

- Increase the heat rate
- Reduce the revenues

Increased air leakage is shown from as-new clearance of 0.030 in. to worn-out radial clearance of 0.120 in. Note that at 0.030 inches radial clearance there is definitely air leakage too, however for the purpose of comparison the air leakage into the ''inner barrel'' was labeled as ''zero'' or a reference point.

Increased radial clearances will have negative impact on GTU power output. OEM-published data indicate loss of approximately 1.0 MW in case if original radial clearances are increased from 0.030 to 0.060 in. Major Inspection of GTU revealed that the in some places (around horizontal split line) the labyrinth clearances were as large as 0.100 in. The excessive loss of labyrinth teeth around horizontal split line can be attributed to differential thermal expansion of inner barrel cylinder in x and y directions. This phenomenon was observed in all four GTU.

Increase of labyrinth radial clearances will have negative impact on GTU heat rate (BTU/KW-h). For example if the radial clearances are increased from design 0.030 in. to actual 0.060 in. the incremental heat rate will be 80 BTU/KW-h. It is important to remember that the heat rate is calculated for the fuel low heating value. If the fuel is natural gas the correction factor is 1.1 or 10 percent to obtain fuel high heating value.

The air that leaks form compressor discharge via the inner barrel splits into two streams:

- Bearing no. 3 stream
- 1st stage wheel space forward stream

Bearing no. 3 is situated between compressor and the turbine. It is protected by special heat shields. The bearing housing is also provided with a set of outboard shaft labyrinths that serve to retard ''inner barrel'' air leakage into the bearing cavity. The air pressure gradients allow some amount of ''inner barrel'' air to leak via labyrinths into the bearing cavity, mix there with the purge air (originating from 5th stage of compression) and exit into surrounding atmosphere via special coaxial pipes. The loss of the mixed air streams is therefore irreversible.

1st stage wheel space forward air stream is significantly bigger. It serves to purge and cool the wheel space. It also serves to maintain 1st-stage wheel/disk temperatures within recommended limits. This stream mixes with incoming gases and enters the first row of rotating blades/buckets. It cools the gas and it lowers the gas enthalpy. In case when the air flow, from the inner barrel, is excessive it may distort the gas temperature profiles affecting the life expectancy of the blades, nozzles and other turbine elements in the gas path. This air stream is however recaptured in the turbine 2nd and 3rd stage.

The loss in revenues in thousands of dollars is shown in Fig. 7. The losses of revenues were computed for all four GTU operating under base load for 8,000 h per yr. The price of natural gas was assumed 2.50 dollars per 1000 cu ft. Presently, the gas prices are significantly higher. The cost of project to fabricate and install the compressor discharge brush seals in front of existing labyrinths was spread out for the period of 10 yr. The rate of return was calculated close to 44 percent. Present, escalated natural gas prices will significantly increase the rate of return.

Operating Experiences and Results

First brush seal assembly was installed into GTU no. 3 during October 1996 scheduled Hot Gas Path Inspection. Finalized brush seal design is shown in Fig. 8. This particular design was result of intensive technical cooperation between WCC and brush Seal Manufacturer.

The first brush was in continuous operation until Mar. 1998 major inspection. The seal was removed from the inner barrel and examined for the following possible damages:

- Bristle wiring wear
- Bristle wiring bending

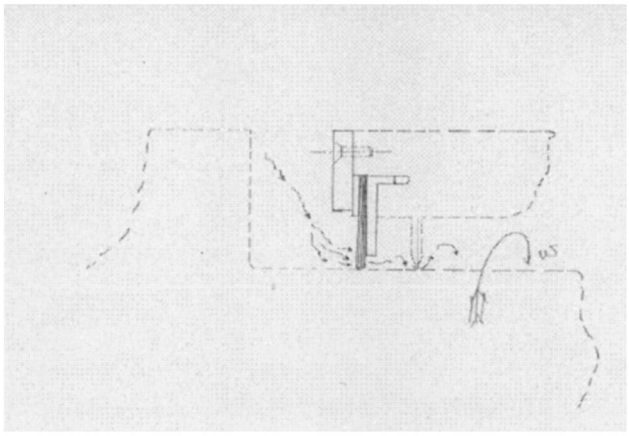

Fig. 8 Brush seal installed in front of inner barrel labyrinth

- Bristle wiring tapering
- Missing wires
- Stray wires
- Cover plate waviness
- Missing cover plate screws

The brush seal was found in satisfactory condition. The bristle loss due to wear was found in the vicinity of horizontal split line. This wear pattern is an indication that the inner barrel does not grow uniformly during GTU start up or shut down. Severe elliptical deformations can be expected during unwanted GTU shutdown when operating under full load.

To assess the performance of the brush seal when the GTU is under full/base load, the following parameters were monitored and recorded before and after installation of the brush seal:

- Ambient air pressure, temperature and relative humidity
- Compressor air discharge pressure and temperature
- Compressor air flow
- Air pressure and temperature inside inner barrel
- First wheel front space air pressure and temperature
- Thrust bearing metal temperature
- Bearing No. 3 metal temperature
- Fuel gas composition, pressure, temperature, and flow

The wheel space air temperatures were monitored and recorded for all three stages of expansion. In case if the brush seal working radial clearances are too tight the airflow from compressor discharge may be significantly reduced. The air pressure inside the inner barrel may then drop below the gas pressure in the turbine first stage of expansion. In the worst case hot, corrosive gas may back-flow into the inner barrel cavity. The back-flow of hot gas can inflict serious damage to mechanical integrity of bearing no. 3 and ultimately trigger catastrophic failure of GTU.

To prevent the phenomenon of ''inner barrel'' over-sealing WCC has installed a back-up system (US Patent No. 5,961,279) to ensure proper compressor discharge air flow into the inner barrel cavity.

Special pressure tap was introduced into the ''inner barrel'' cavity to monitor static pressure variations. This pressure is good indication weather the brush seal (in tandem with labyrinth) is sealing well or not. The pressure in the inner barrel is normally about 50 percent of compressor discharge pressure for ''as new'' labyrinth radial clearances. Introduction of brush seal in front of worn-out labyrinth caused further reductions of pressure. ''Inner barrel'' cavity pressure reduction was 3 to 5 lb per sq. in. as expected and predicted by relevant calculations.

Temperatures inside the ''inner barrel'' were not measured because the temperature elements were not installed. Complex heat and mass balance calculations were not performed because of the lack of data that only OEM may possess. The compressed air that leaks through the brush seal and the back-up worn-out labyrinth seal teeth essentially is at constant temperature because its flow is isothermal. The flow is at constant air enthalpy, though small temperature corrections can be made to account for Joule-Thompson effect.

Table 1

GTU No.	Date installed	Hours@ base load	Comments
3	10/1996	33,000	
4	1/1997	31,250	**Failure 11/2000**
2	3/1997	30,000	
1	5/1977	28,500	

Published data from OEM with their brush seal design indicated temperature drops up to 50°. This information was received much later after installation of first WCC brush seal.

The OEM-manufactured brush seals are installed between the labyrinth teeth. Special radial groove is machined in the wall to house the brush seal holder. The wall radial thickness is larger than original inner barrel wall thickness to compensate for the stress concentrations.

Table 1 shows the installation dates of compressor brush seals. The failure of the brush seal installed in GTU no. 4 was discovered during the routine GTU inspection. The failure was initiated by the failure of the cap screws holding the cover plate in the position. The cover plate is in the form of the ring with equally spaced screw holes. It serves to retain the seal in its slot. Once the bolts failed the cover plate/ring was pushed against the 17th-stage stator blades. Onrush of compressor discharge air forced the cover plate to fret and cut the stator blades.

There are 72 machine, flat head screws holding the cover plate firmly bolted to the ''inner barrel'' (refer to Fig. 8). The holding screws are aircraft type, they are American Standard Slotted Undercut Flat Head Machine Screws, ASA B18.6.3-1962, size no. 3 made from carbon steel. Size No. 3 machine screw diameter is 0.099 in. The carbon steel tensile strength is approximately 150,000 pounds per square inch. In order to fail each screw had to undergo average tensile force equal to 185 pounds (stress factor of 2.50 used). Or total tension force equally distributed around the retaining plate of 11,840 lb. Examination of the brush seal ''free body diagram'' indicates that the tension forces in the holding screws are the results of the moment caused by aerodynamic forces. The calculated moments are 7,460 in.-lb. The pressure differentials acting on the brush seal and the back-up plate are causing axial forces equal to approximately 3,240 lb. The foregoing abbreviated calculations indicate safety factor in original design of 11,840/3,240 or 3.65. It appears therefore that the original design was sufficient. The cause of the failure is either inadequate material or/and the high-cycle fatigue due to discharge air turbulence. Presently, WCC is working on redesigning the cover plate with larger holding screws. The material of the screws may be modified for high temperature applications.

The calculated power gain (1.0 to 1.50 MW) could not be verified due to the fact that the fuel burned in WCC GTU is mixture of natural gas and refinery gas. The molecular percentage of refinery gas is continuously changing. The back-up fuel butane gas was too valuable to burn, and therefore no rigorous performance tests could be conducted.

Conclusions

The compressor discharge air parasitic losses can be successfully controlled by installation of the brush seal in front of labyrinth seal.

The joint efforts between WCC and the brush Seal Manufacturer resulted in compact, highly efficient easy to install, remove and inspect brush seal.

The inner barrel was re-used.

The radial clearance between the rotor and the brush bristles tips should not be less than the brand-new labyrinth seal radial clearance in case the matching rotor surface is not hardened.

The power gains and heat rate reductions were calculated, however, could not be quantified during operation of GTU because of the fuel gas heating value fluctuations.

The pressure reduction of 3.0 to 5.0 lb per sq. in. was measured after installation of the brush seal in each GTU.

The inspection of the compressor rotor burnished area width indicates a differential axial movement between the rotor and the housing in the neighborhood of 0.25 to 0.38 in.

The unexpected failure of the brush seal retaining plate was due to material fatigue of the holding screws. Larger, improved material holding screws are being implemented.

Acknowledgment

Author wishes to express his gratitude to WCC Management for allowing design, manufacture and installation of the brush seals during the times when OEM was testing their brush seals.

Special thanks to WCC Chief Inspector J. Camburn for detailed borescope inspections of the brush seals and to Gary Hopkins for the help with drawings.

Appendix

Flows of gasses throughout labyrinth seals are well investigated and known. Numerous graphs are available showing parasitic internal gas flows as a function of labyrinth and matching shaft area geometry.

Several empirical equations are available to calculate the parasitic gas losses via the labyrinth. These equations are divided into two groups: for nonretarded gas flows, and for retarded/choked gas flows. Normally in the multi-teeth labyrinth, gas attains sonic speed; that is, the gas is virtually choking.

The pressurized gas that flows throughout the labyrinth is accelerated in the narrow passage formed by the labyrinth tooth and matching shaft area. The gas accelerates in this narrow passage and gains kinetic energy. The gas then enters the labyrinth chamber and it deaccelerates inside it. Deacceleration process is manifested in the gas kinetic energy reduction and its conversion into the heat energy. The conversion is not total because there is some heat energy loss due to inevitable heat exchange. The enthalpy of the gas drops from stage-to-stage of the labyrinth. The enthalpy drop is approximately equal from stage to stage, however it is biggest in the last stage.

Equation (1) neglects this small heat exchange

$$E = i + Ac^2 \frac{1}{2g} \tag{1}$$

where E is total gas energy in BTU/lb
$A = 778$ ftlbf is thermo-mechanical coefficient
$c =$ ft/s is gas velocity in the labyrinth gap
$g = 32.3$ ft/s^2 is gravitational constant

The gas velocity c in the labyrinth gap can be calculated from the continuity Eq. (2)

$$M\nu = Fc \tag{2}$$

where M lbs/s the mass flow of gas ν ft^3/lb specific volume of the gas and F ft^2 labyrinth cross section area

$$F \cong d_{\text{shaft}} \pi c_r \tag{3}$$

where d_{shaft}, c_r in ft, and c_r is labyrinth radial clearance.

Equation (1) can be now arranged

$$i = E - Ac^2 \frac{1}{g} = E - 12.081c^2 \tag{4}$$

Equation (4) can be plotted point-by-point into a Fanno line, a nonlinear curve. This curve represents the condition of gas being expanded inside the labyrinth seal. The expansion in each labyrinth chamber is presumed adiabatic. Normally in the last chamber the adiabatic expansion line is tangential to the Fanno line. This means that the gas has reached the sonic flow and that the flow is essentially choking.

The gas leakage throughout the labyrinth seal can be also calculated with reasonable accuracy as follows:

$$V = 100 \sqrt{\frac{\Delta p \, \nu_{av}}{\left(1.5 + \frac{1.5}{n-1}\right)}} \tag{5}$$

where V ft/s is average gas velocity in the annulus area,
Δp lb/in.^{2} is pressure difference across the labyrinth,
ν_{av} ft^3/lbm is average specific volume and n is number of labyrinth teeth.

Equation (5) must be corrected if the rotor/shaft is stepped; in this case the correction factor is approximately 0.60.

The gas leakage in cubic feet per second is now equal average gas velocity in the annulus area times the average velocity of gas calculated in Eq. (5).

The gas leakage from labyrinth chamber to next labyrinth chamber where the pressure ratios are less than 1.25 (except the last labyrinth chamber) can be calculated also as follows:

$$V = j_f 223.5 \sqrt{\Delta H_s} \tag{6}$$

where j_f an empirical factor approximately equal to 0.40
ΔH_s in BTU/lbm is an isentropic expansion head from labyrinth-to-labyrinth cavity

$$\Delta H_s = \frac{1.985 T_g \ln \frac{p_{n-1}}{p_n}}{M_w} \tag{7}$$

where T_g is absolute gas inlet temperature in degrees Rankine
R = °F + 460

p_n, p_{n-1} are pressures in two adjacent labyrinths in pounds per square inch absolute, and M_w molecular weight of the gas.

References

[1] Bartlett, R. L., and Hegetschweiler, H., 1957, "Predicting Performance of Large steam Turbine-Generator Units," Trans. ASME.
[2] Chinaeff, "Sydovye Gazovye Turbini" Transport, 1964, Moscow, Russia.
[3] Crane, 1942, "Flow of Fluids" Technical Paper No. 409, May.
[4] Gryzaya, L. L., 1965, "Sparavochnic Sudovogo Mechanika" Transport, Moscow, Russia.
[5] Ingistov, S., Meredith, G., and Sulda, E., 2000, "Brush Seals For the No. 3 Bearing of a Model 7EA Gas Turbine," IGTI, Munich 2000 ASME Paper No. 2000-GT-558.
[6] Ingistov, S., 1999, United States Patent No. 5,961,279 "TURBINE POWER PLANTS HAVING MINIMAL-CONTACT BRUSH SEAL AUGMENTED LABYRINTH SEAL" Oct.
[7] Marks, "Standard Handbook for Mechanical Engineers," 9th Edition.
[8] Scheel, L. F., 1969, "New Ideas on Centrifugal Compressors," Part No. 1, Compressor Handbook, Gulf Publishing Company Houston, TX.

Computational and Mathematical Modeling of Turbine Rim Seal Ingestion

Nicholas J. Hills
Thermo-Fluid Mechanics Research Centre, University of Sussex, Brighton, BN1 9QT, UK

John W. Chew
School of Mechanical and Materials Engineering, University of Surrey, Surrey, GU2 7XH, UK

Alan B. Turner
Thermo-Fluid Mechanics Research Center, University of Sussex, Brighton, BN1 9QT, UK

Understanding and modeling of main annulus gas ingestion through turbine rim seals is considered and advanced in this paper. Unsteady three-dimensional computational fluid dynamics (CFD) calculations and results from a more elementary model are presented and compared with experimental data previously published by Hills et al. (1997). The most complete CFD model presented includes both stator and rotor in the main annulus and the interdisk cavity. The k-ε model of turbulence with standard wall function approximations is assumed in the model which was constructed in a commercial CFD code employing a pressure correction solution algorithm. It is shown that considerable care is needed to ensure convergence of the CFD model to a periodic solution. Compared to previous models, results from the CFD model show encouraging agreement with pressure and gas concentration measurements. The annulus gas ingestion is shown to result from a combination of the stationary and rotating circumferential pressure asymmetries in the annulus. Inertial effects associated with the circumferential velocity component of the flow have an important effect on the degree of ingestion. The elementary model used is an extension of earlier models based on orifice theory applied locally around the rim seal circumference. The new model includes a term accounting for inertial effects. Some good qualitative and fair quantitative agreement with data is shown.
[DOI: 10.1115/1.1456461]

1 Introduction

In modern gas turbine engines ingestion of hot mainstream gas into the space between a rotating turbine disc and the stator can potentially lead to overheating and reduced life of the disk, and so must be controlled. To prevent or limit this effect, relatively cool air from the compressor may be channeled radially outwards through the cavity and ejected into the mainstream flow. To avoid excessive performance penalties associated with the secondary air system it is usually desirable to minimize the amount of sealing air used. This requires quantitative estimates for the relationship between sealing flow rate and hot gas ingestion. In the present contribution, computational fluid dynamics (CFD) and more elementary models are considered, and calculations from these models are compared to previously published experimental data. Particular attention is focused on the complex flow interactions in the rim seal region where the sealing and mainstream flows meet.

Early work on sealing of rotor-stator disk cavities centered on the effects of disk pumping which tends to draw flow into the cavity in order to satisfy the flow requirements of the boundary layer formed on the rotating disk. For example, Bayley and Owen [1] considered a simple axial seal in the absence of external flow and obtained a correlation for the minimum sealing flow required to prevent ingestion. With further experimental and analytical work from many workers, more general methods for estimating sealing requirements under these conditions are now available. As shown by Chew [2] and Chew et al. [3], semi-empirical methods can successfully correlate experimental data for a variety of different seal types. It may be noted that appropriate scaling parameters for this problem include a Reynolds number effect since viscosity has a direct influence on the strength of the disk pumping. These studies, in which the cavity is surrounded by a quiescent environment, are most relevant to ''inner seal'' arrangements where the direct effects of the mainstream annulus flow is negligible.

The influence of external flow on cavity rim sealing, and particularly the importance of circumferential pressure variations in the annulus flow, was noted by Campbell [4] and has been confirmed experimentally by several workers. For example, Abe et al. [5], Kobayashi et al. [6], Phadke and Owen [7], Dadkhah et al. [8], and Hamabe and Ishida [9] have performed experiments with various degrees of asymmetry in the annulus flow caused by guide vanes or other disturbances in the stationary reference frame. As suggested by Campbell, the presence of a circumferentially uniform external flow tends to improve sealing, while circumferential asymmetries tend to increase ingestion. Chew et al. [10] gave experimental results for ingestion with the rim seal located at various distances downstream of a row of guide vanes. The experimental measurements and order of magnitude arguments supported the conclusion that disk pumping had only a secondary effect on the degree of ingestion for conditions most representative of engine operation. In this case, the Reynolds number effects are weak and a more appropriate parameter is a seal-to-annulus flow velocity ratio. The densities of the sealing and annulus flows in these experiments were very close. At engine conditions, density differences are likely to be significant, so momentum or mass flux ratios may eventually prove more useful in correlating results. Some experiments, including both rotor and stator blade rows, have been reported by Green and Turner [11] and Bohn et al. [12]. Both sets of workers found evidence that the presence of rotor blades could improve sealing effectiveness, but Bohn et al. found the opposite trend for a different seal design, and their blades had a surprisingly large effect on the pressure asymmetry due to the vanes. As will be discussed further below there is also some doubt about Green and Turner's experimental conditions. Hence, the effect of rotor blades in engine conditions is still open to question.

A simple model of ingestion due to pressure asymmetries in the main flow may be constructed by assuming the length scale for circumferential variations to be much greater than the seal clear-

Contributed by the International Gas Turbine Institute and presented at the International Gas Turbine and Aeroengine Congress and Exhibition, New Orleans, Louisiana, June 4–7, 2001. Manuscript received by the IGTI, November 20, 2000. Paper No. 2001-GT-204. Review Chair: R. A. Natole.

ance so that the seal flow is treated as locally two-dimensional. With the cavity pressure assumed to be uniform, orifice theory is then applied at each circumferential location and the overall inflow and outflow obtained through integration. Hamabe and Ishida [9] published such a model and proprietary methods based on this approach have been available for some time (e.g., Campbell, unpublished work). However, Chew et al. [10] concluded that this method overpredicted the level of ingestion and attributed this to the neglect of inertial effects associated with the swirl component of velocity. This conclusion drew on experimental data and the results of CFD calculations which showed the influence of the inertial terms. The 3-D, steady CFD model also showed some encouraging agreement with ingestion measurements, particularly at low sealing flow rates.

Further combined experimental and CFD studies were reported by Hills et al. [13]. Comparison of 3-D, steady CFD solutions with pressure measurements showed good agreement at lower sealing flow rates. At higher flow rates the experimental and CFD results diverged, and this was attributed to interaction of the sealing and mainstream flows. Full details of this interaction could not be captured in the CFD model which did not include resolution of the flow through the vanes. Roy et al. [14] have also shown some agreement between steady CFD solutions and measurement from pressure tappings for a rim sealing rig including vanes and rotating blades. In another very recent paper, Bohn et al. [12] included 3-D, unsteady CFD calculations including both vanes and blades. They showed some differences in the calculated and measured levels of ingestion but obtained some qualitative agreement. It may be noted that most research has concentrated on the seal downstream of a row of stationary vanes. Arguably, more work is needed to clarify the flow mechanisms in seals downstream of a row of rotating blades.

In recent years there has been increasing interest in the influence of sealing flows on the aerodynamic efficiency of the main annulus flow. Denton [15] noted this effect, and likens the flow mixing process to that of leakage flow over a shroud. A first estimate of the mixing losses might be obtained from the formulas given by Denton [15] or Hartsel [16]. Denton notes that most of the entropy generation will be due to the difference in swirl velocity between the two flows and recommends preswirling the sealing flow where possible. Recent studies of turbine shroud leakage flows by Wallis et al. [17] and Pfau et al. [18] showed the importance of non-axisymmetric effects on the flow through the axial gaps upstream and downstream of the shroud. The flow fields identified are similar to those associated with the ingestion problem. Recent studies of stator shroud leakage in compressors are also of interest to the present study. For example, Wellborn and Okiishi [19] report both experimental and CFD results. These indicate that the effect of leakage flow on the blading aerodynamics can result in higher losses than would be expected from simple mixing. Demargne and Longley [20] conclude from experiments and computations for a linear cascade that pitchwise nonuniformities in the flow can lead to exchange of fluid across the axial gap upstream of a row of vanes, and that this contributed to loss generation.

CFD solutions for mainstream gas ingestion across a simple axial rim seal are presented in Section 3. These results are also compared to measurements from the experimental rig previously presented by Hills et al. [13]. For completeness a brief description of the rig is given in Section 2. Further discussion of the results and the flow physics are given in Section 4, which includes comparison with a more elementary model. The main conclusions from this study are summarized in Section 5.

2 Experimental Rig

The experimental rig has been fully described by Green [21]. A schematic diagram of the rig is given in Fig. 1. The rig consists of a rotor-stator system enclosed by an annular channel in which 29 nozzle guide vanes are positioned with the trailing edge 3 mm upstream of the rim seal gap. Mainstream flow is drawn through the annulus by a centrifugal fan, located well downstream of the cavity under investigation, and hence total pressure and temperature upstream of the vanes are atmospheric. The plain rotor was driven by 16 aluminum pegs attached to the periphery of the discs and located 18.5 mm downstream of the seal gap. The 16 equispaced pegs were manufactured from cylinders of 19 mm diameter and height 24 mm with a flat surface milled on them as shown in Fig. 2.

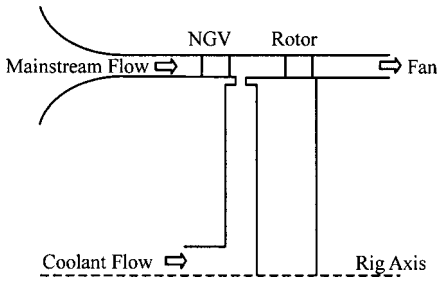

Fig. 1 Schematic of Experimental Rig

Some experiments were carried out with the rim seal gap blocked off, providing an unbroken annulus. In these cases static pressure measurements were made at five axial locations downstream of the vanes, as shown in Fig. 2. With the seal gap present annulus static pressure measurements were possible only at the first axial location. Pressure tappings in the cavity were located on the stator face at nine radial locations with the outermost location being at $r/r_0 = 0.95$. Mainstream flow ingestion was quantified through concentration measurements with the coolant seeded with about 450 ppm of nitrous oxide. Sampling of the air in the cavity was made at four radial positions on the stator.

For the measurements presented in this paper, the seal gap was 0.002 m, the radial extent of the seal gap was 0.003 m, the outer radius of the cavity was 0.2 m, the cavity width was 0.015 m, and the outer radius of the annulus was 0.23 m.

3 CFD Solutions

3.1 Description of the CFD Models. A commercially available CFD code (FLUENT5) [22] was used in these studies. This code allows use of unstructured meshes in solving the Reynolds-averaged compressible Navier-Stokes equations and has been preferred to the proprietary code used by Hills et al. [13] because of its capability for modeling complex geometries. The

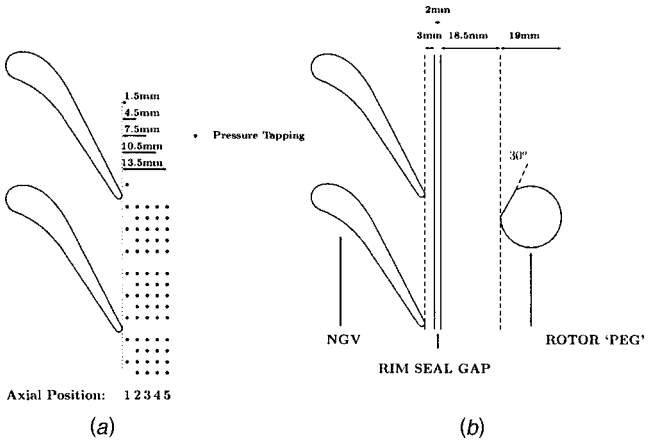

Fig. 2 Schematic showing guide vanes, pressure tappings, and rotor pegs—(*a*) pressure tappings in unbroken annulus, (*b*) positions of vanes and rotor pegs

Table 1 Summary of CFD models

Model No.	Steady / Unsteady	No. vanes	No. rotor pegs
1	Steady in stationary frame	1	0
2	Steady in rotating frame	0	1
3	Steady (with mixing plane)	2	1
4	Unsteady (with sliding plane)	2	1

numerical solutions were obtained using a pressure correction algorithm, and with the k-ε model of turbulence using standard wall functions at the near-wall mesh points. To quantify ingestion of mainstream gas into the disc cavity, a species concentration equation was solved. Thus, although a different code is used from earlier studies the numerical treatment and modeling assumptions are similar to those employed in earlier validation work on the disc cavity and rim sealing flows; see, for example, Virr et al. [23]. Although they are not reported here, several benchmark tests for disk cavity flows have been repeated using FLUENT. It may be noted, however, that the validation does not include examples of turbomachinery blading flows. This point, and some preliminary investigations into the use of alternative turbulence models, will be discussed further in the forthcoming.

Four different CFD models are used and these are summarized in Table 1. All models included the disc cavity and the same section of the annulus, but differ in treatment of the vanes and rotor pegs. All the models assumed 29 guide vanes (as were used in the experiment) and where rotor pegs were modeled, one rotor peg per two guide vanes was used. This corresponds to 14.5 rotor pegs as compared to 16 in the experiment. The most complete representation is given by model 4, for which the computational domain is illustrated in Fig. 3. This model calculates the unsteady flow with the solution for rotating and stationary parts of the domains being communicated across a sliding plane. Model 1 does not include the rotor pegs and assumes steady flow in the stationary frame (and models only one NGV passage compared to Fig. 3). Model 2 does not include the vanes and assumes steady flow in the rotating frame. Model 3 includes both vanes and pegs, but with a mixing plane (placed between the vane trailing edge and the rim seal gap) across which circumferentially averaged solutions are exchanged between the main steady (in the rotating reference frame) calculation for the rotor pegs and cavity and an auxiliary steady (in the stationary reference frame) calculation for the vanes. For the CFD calculations presented here, the conditions corresponded to a rotational Reynolds number $(\rho\Omega r_0^2/\mu)$ of 10^6, a mainstream Reynolds number $(\rho u_{ax} r_0/\mu)$ of 5.9×10^5, and a coolant flow rate such that the velocity ratio u_m/u_{ax} (the continuity-derived mean velocity through the seal divided by the axial component of the annulus velocity) was 4.8×10^{-2}.

Periodicity in the circumferential direction was assumed at the appropriate boundaries, and the usual no-slip conditions were applied on solid surfaces. At the sealing flow inlet, the normal velocity component was set to a uniform value so as to give the required mass flow, other velocity components were set to zero, and the species concentration was set to unity. In the annulus, total pressure, total temperature, flow angle and a species concentration of zero were specified at the inlet. For models including the vanes these inlet conditions were essentially atmospheric with allowance for boundary layers on the annulus walls. The boundary layer profile for a constant section annulus of the same length as the section of the rig upstream of the guide vanes was used. For model 2, the annulus inlet conditions were assumed to be uniform. Effectively the difference between models 2 and 3 is that model 3 uses the radial profiles from the vane exit instead of a uniform profile. At the flow exit, static pressure was specified at the hub, the pressure distribution was obtained from the radial equilibrium conditions, and zero axial gradient was assumed for other variables. While the unsteady solution did not include any special treatment to avoid reflections of waves at the boundaries, the boundaries were placed some distance from the blades and the solutions were found to show little unsteadiness at the inlet and exit.

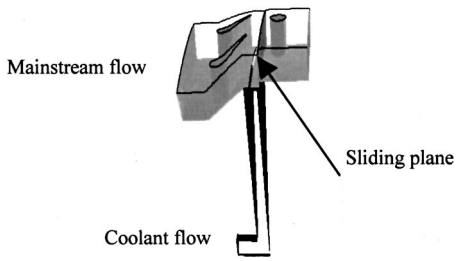

Fig. 3 Computational domain for model 4

Mesh generation was performed using the FLUENT mesh generator and unstructured quadrilateral meshes were used for all models. 5×10^5 mesh points were used for model 1; 7×10^5 mesh points were used for model 2; and 10^6 mesh points were used for models 3 and 4. In all the models, boundary layer meshes (using five layers of prisms) were grown away from the solid surfaces at a geometric growth rate of 1.2, and 30 mesh points were used to span the cavity in an axial direction to ensure that the cavity velocity gradients were resolved. The unsteady solution was obtained using implicit time stepping with a time step of 2×10^{-5} s (so approximately 30 time steps were used per pass of a rotor blade by a guide vane). Under-relaxation was used in the pressure correction algorithm for the solution of the steady flow solutions and for calculating the solution at each time step in the unsteady solution.

3.2 Convergence of Solutions. Convergence of the iterative steady state solutions was monitored using the residuals of the continuity, momentum, concentration and turbulence model equations. Typically, four to five orders of magnitude reduction was achieved after about 5000 iterations. These calculations took about 12 h CPU time on a cluster of 8 666MHz PCs.

Convergence of the unsteady solution was given careful consideration. Whereas in ''blading flow only'' calculations it is quite usual for convergence to periodicity to occur after about ten blade passing cycles, the solution in the disk cavity for the present model took considerably longer to converge. This may be attributed to the lower velocities within the disc cavity. Radial velocities in the cavity are typically 5 m/s or less. Thus, an element of fluid will take about 0.01 s (or about 200 blade passing cycles) to traverse the cavity. Convergence of the solution physically requires at a minimum for the ingested mainstream particles to recirculate the cavity, and hence the solution will require several times this amount of physical time to converge.

The convergence of the concentration in the cavity (at the measurement point $r/r_0=0.41$ on the stator) is shown in Fig. 4. As can be seen, after the unsteady simulation had proceeded for 780 periods the species concentration in the cavity was still observed to be changing significantly, although this is only obvious over a considerable number of periods. At this point the unsteady solution was suspended. A steady-state species concentration equation was then solved for the region of the cavity with $r\leqslant0.15$ m using fixed velocity and turbulence fields from the last time point of the unsteady solution. The boundary conditions specified at $r=0.15$ m were also taken from the unsteady solution. Since the flow in this inner region had been observed to be essentially steady, the steady concentration equation would be expected to show little change from a converged unsteady solution. However, the steady solution showed significant changes from the unsteady solution, which can be seen as the discontinuities in Fig. 4. Restarting the unsteady solution using the revised concentration in the region $r<0.15$ m produced further changes in the solution. Several repeats of this procedure gave a solution where the concentration remained approximately constant for some 80 periods.

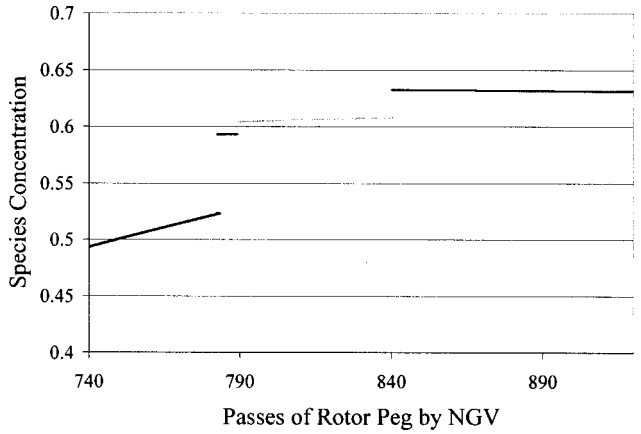

Fig. 4 Convergence of concentration at $r/r_0=0.41$ stator measurement point for unsteady solution

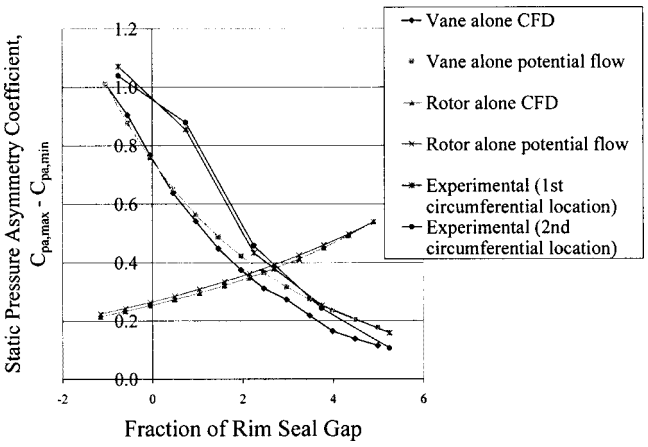

Fig. 6 Static pressure asymmetry due to vane alone and rotor peg alone

While it is accepted that this solution is not absolutely converged, it is believed that any further changes would be small in relation to the differences between the various models and the experimental data discussed in the forthcoming.

With the unsteady solution taking about 8 CPU min per time step (or 4 h per period) on 8 PCs, the calculation was halted after a total simulation time of about 920 periods. At this point, the solution appears to be close to convergence to periodic behavior. With dedicated use of eight processors of the PC cluster used it is estimated that this calculation would take about three mo if run continuously.

3.3 Comparison With Pressure Measurements. Pressures were measured using tappings in the inner annulus wall just downstream of the vanes, and on the stator in the disk cavity, as described in Section 2. Thus these measurements will not capture the unsteady variations at blade passing frequency. Comparisons of CFD results with these measurements are shown in Figs. 5 to 7. The mainstream pressures are plotted as an annular pressure coefficient, C_{pa}, defined as the difference between the mainstream pressure and the average mainstream pressure, nondimensionalized by the mainstream inlet dynamic head. The static pressure asymmetry coefficient in Fig. 6 is defined as the maximum annulus static pressure coefficient minus the minimum annulus static pressure coefficient. The cavity pressures in Fig. 7 are plotted as a cavity pressure coefficient, C_{pc}, defined as the difference between the cavity pressure and the cavity pressure at $r/r_0=1$, again nondimensionalized by the mainstream inlet dynamic head. In all the figures, where circumferential location is given as a fraction of NGV pitch, 0 represents a trailing edge position.

The annulus pressures are given in Fig. 5. For the unsteady solution the values plotted for the annulus represent time averages over a period. There is little difference between model 1 (modeling the vane only) and the time average of model 4. However, for the circumferential variation of pressure, agreement with the experimental data is only fair. Looking at the experimental data, it is clear that there is considerable scatter. Two sets of experimental data (measured at different circumferential locations) are plotted, and there are significant differences between these. Neither set repeats exactly over the guide vane period. Since the unsteady pressure variation due to the rotor blades is approximately ± 15 percent of the inlet mainstream dynamic head, it is possible that this variation in the experimental data is due to the unsteady effects.

Figure 6 shows the axial decay of the circumferential pressure asymmetries from CFD calculations (for both the guide vane alone and rotor peg alone) for an unbroken annulus. The experimental data for the guide vane alone with an unbroken annulus are included. Also included on this figure are the decay rates from a simple potential flow model discussed by Hills et al. [13]. The difference in decay rate between the vane alone and the rotor alone in the potential flow solution is simply due to the spacing between the blades, indicating that the number of blades and hence the rate at which the resulting pressure asymmetry will decay is important for their effect on ingestion. Agreement be-

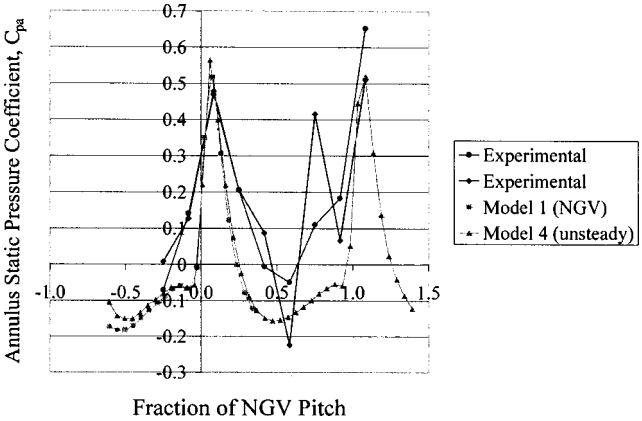

Fig. 5 Comparison of calculated and measured annulus pressures

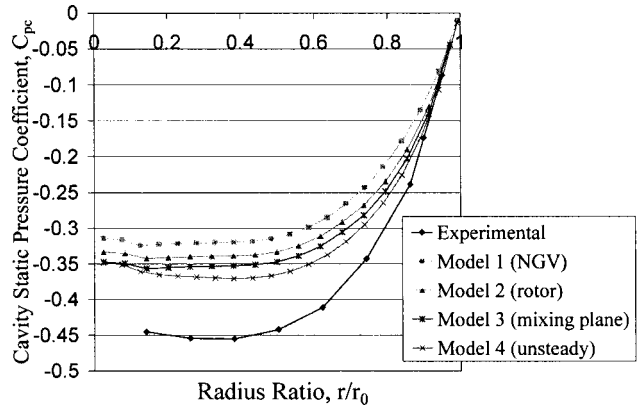

Fig. 7 Comparison of calculated and measured disc cavity pressures

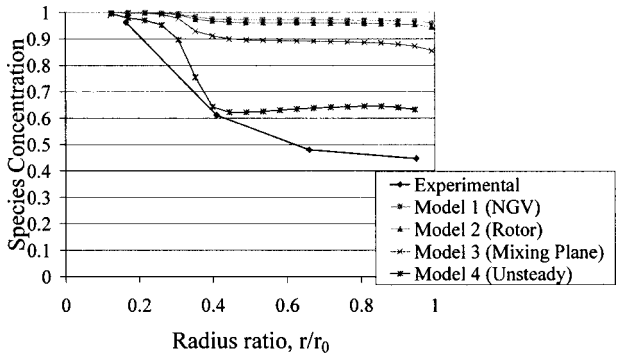

Fig. 8 Comparison of calculated and measured concentration in the cavity

tween CFD and measurement for the asymmetry due to the vanes is fair, with the CFD apparently under predicting the pressure variation. Earlier CFD calculations for this case by Hills et al. [13] showed slightly better agreement with the data. This is possibly because the earlier calculations were done using a CFD code that had been specifically developed and validated for turbomachinery applications.

Figure 7 shows the stator disc cavity pressures. The unsteady CFD solution at the cavity measurement positions showed negligible variation with time. All the models underpredict the pressure rise in the cavity, with the unsteady model being closest to the measured value. This is possibly because (as discussed in Section 3.4), all the models underpredict mainstream ingestion to some extent. The ingestion of highly swirled mainstream flow increases the core rotation rate in the cavity and leads to a higher pressure rise. Comparing with the concentration measurements shown in Fig. 8 and discussed below, the models show increasing pressure rise with increasing levels of ingestion. A further factor is the modeling assumptions for the cavity flow at inlet.

3.4 Comparison With Concentration Measurements. Figure 8 shows the measured and calculated species concentration in the disc cavity at the stator tapping positions. In contrast to the cavity pressures, there are very significant differences between the various CFD models. Note that according to the unsteady calculation the concentration at these positions is essentially constant.

All the models under-predict the level of ingestion, but agreement between the unsteady CFD model and the measurements is closest, and this calculation is considered very encouraging. Note that the underprediction of the annulus pressure asymmetry (as noted in the foregoing) may contribute to the underprediction of ingestion. It is clear from comparison of the CFD solutions that, for these conditions, the combined effect of the rotor asymmetries gives considerably more mainstream gas ingestion than either the rotor or stator acting alone. As could be seen from Fig. 6, the circumferential pressure asymmetry at the seal due to the vane alone was approximately twice that from the rotor alone. However, despite this, the rotor asymmetry can apparently cause greater ingestion than the stator asymmetry, depending on the inlet profile used. This is attributed to the near coincidence of annulus flow tangential velocity and rotor speed when the mixing plane model was used. The importance of tangential velocity will be discussed further in Section 4.

3.5 Further Discussion of Results. Contours of concentration in the rim seal gap (in a radial plane 1 mm inboard of the inner annulus wall) at two time instants from the unsteady solution are shown in Fig. 9. (The rim seal gap has been scaled to enable the detail to be seen. The bottom of the figure corresponds to the stator and the top to the rotor.) It can be seen that the ingestion occurs primarily in two regions close to the rotor driven

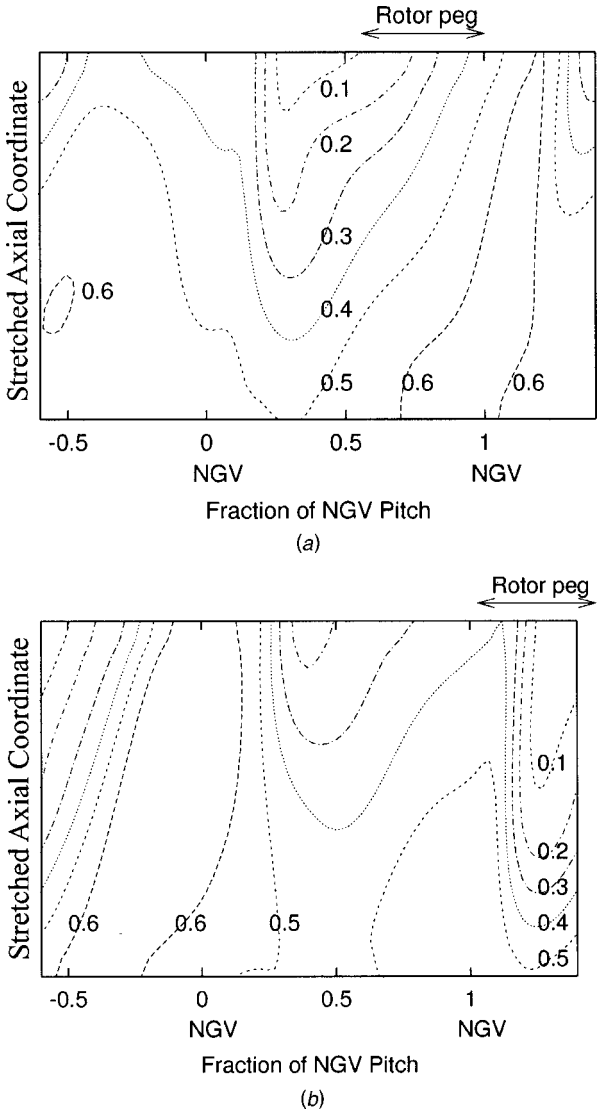

Fig. 9 Contours of instantaneous concentration on the radial plane in the seal gap 1 mm inboard of the inner annulus wall for two rotor peg positions—(*a*) time point A, (*b*) time point B

by the pressure maxima from the two guide vanes. The difference in ingestion levels in these two regions is due to the position of the rotor peg.

As has been shown in earlier studies, the flow in the rim seal region is quite complex. This is illustrated by the vector plots in the axial-radial plane in Fig. 10. These are from the unsteady solution at time point A. The vector plots are given for two circumferential positions: the trailing edge of one NGV (corresponding to the NGV pitch fraction of 0 in Fig. 9) and midway between the NGVs (corresponding to the NGV pitch fraction of 0.5). As can be seen from these plots (and also from Fig. 9), ingestion is mainly occurring midway between the NGVs, while the coolant flow is exiting at the NGV trailing edge position.

The static pressure, radial velocity, and concentration along a line 0.1 mm from the rotor in the plane of Fig. 9 are shown in Fig. 11. (The static pressure is again non-dimensionalised as the difference between the static pressure and the circumferentially averaged static pressure, divided by the mainstream inlet dynamic head. The radial velocity is non-dimensionalized by the rotor disc velocity.) The time-averaged values and the vane alone values are very similar. Also plotted are the values from the unsteady solution at two time instants to show the level of variation with time.

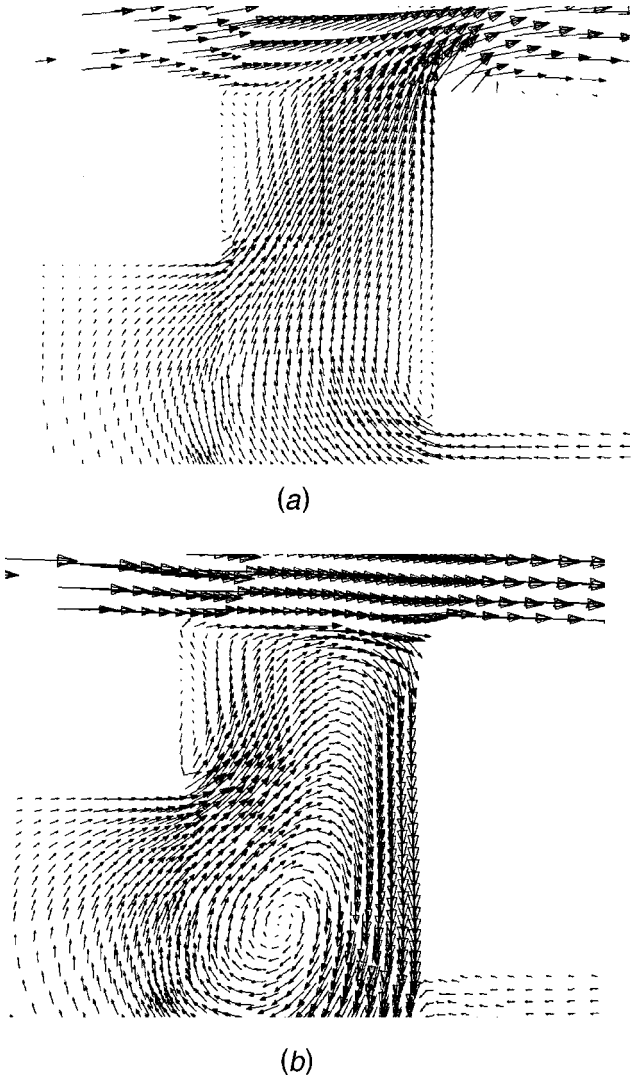

Fig. 10 Instantaneous velocity vector plots (axial-radial plane) at time position A—(*a*) fraction of NGV pitch=0, (*b*) fraction of NGV pitch=0.5

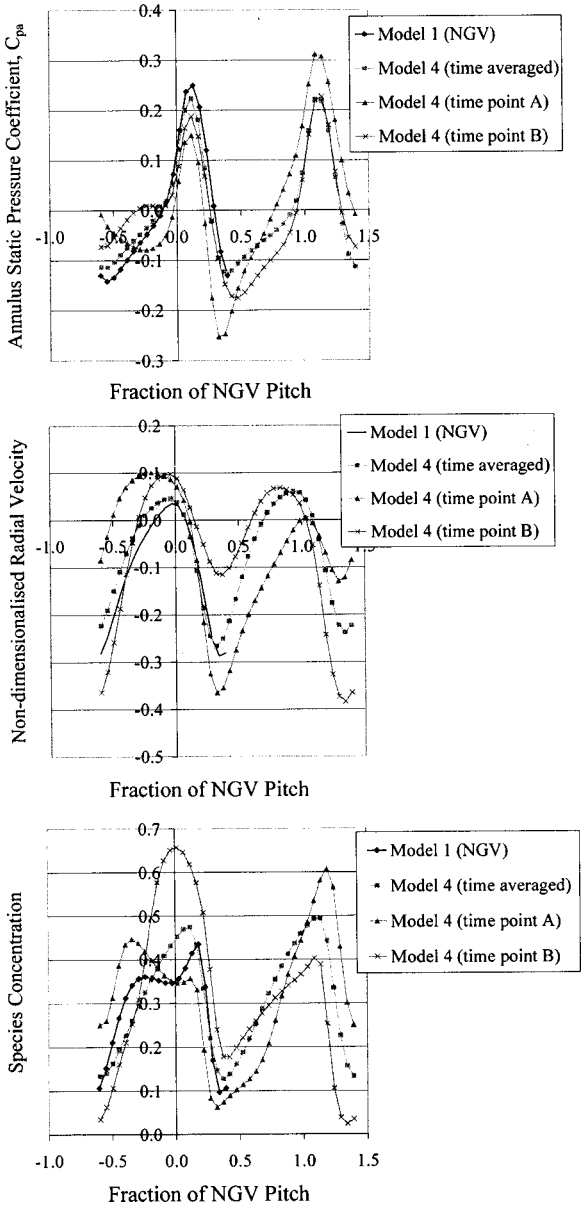

Fig. 11 Pressure, radial velocity and concentration in the rim seal gap on the line 0.1 mm from the rotor, and 1 mm radially inboard of the inner annulus wall

The increase in concentration in the cavity in the unsteady solution would appear to be due to the increase in mixing between the rim seal flow and the cavity recirculation due to the high frequency variation in radial velocity imposed by the rotor pegs. The level of unsteadiness in both concentration and radial velocity is clearly significant. Splitting the u and Φ into average and fluctuating components ($\mathbf{u}$, $\mathbf{\Phi}$ and u', Φ') the radial flux of the species will depend on the product $\mathbf{u\Phi}$ and the time mean of the fluctuating components $u'\Phi'$. Thus, a loose analogy may be drawn between the extra ingress due to the unsteadiness and turbulent mixing.

A further point that may be noted from Fig. 11 is the circumferential displacement of the positions of maximum and minimum radial velocity from the positions of minimum and maximum static pressure. This is due to the swirl component of the flow and confirms that inertial effects are significant.

The deterioration in sealing effectiveness in the CFD solutions due to the rotor blades is in contrast to Green and Turner's [11] conclusions. Reappraising Green and Turner's experimental results in the light of the present study it seems most likely that the presence of rotor blades in their experiment did contribute to ingestion measured, but that their estimate of the level of ingestion due to the guide vanes alone was in error. There is some uncertainty about the source of the "vanes-only" measurements reported by Green and Turner.

As noted in Section 3.1, the CFD model used was not validated for blading flow calculations. Examination of the steady solution for the vanes showed an unexpected loss of total pressure in the core of the flow. This solution was repeated (in FLUENT) using the Spalart-Allmaras turbulence model which is favored by some workers for blading aerodynamic calculations. The Spalart-Allmaras model showed significantly lower total pressure loss although the predicted pressure asymmetry was similar to that given by the k-ε model in Figs. 5 and 6 (although the Spalart-Allmaras model predicted approximately five percent greater pressure asymmetry). However, further testing of the Spalart-Allmaras model indicated some problems with this model in predicting flows in rotating disk cavities. Thus, at present, the choice of turbulence model depends on whether the primary interest is in

the disk cavity or blading flows. Further work is planned to arrive at a turbulence model which will give a good representation of both the blading and disk cavity flows.

4 The Simple Model

4.1 Description of the Model. Assuming inviscid flow, the equations expressing conservation of momentum in the radial and axial directions may be written

$$\frac{\partial u}{\partial t}+u\frac{\partial u}{\partial r}+\frac{v}{r}\frac{\partial u}{\partial \theta}+w\frac{\partial u}{\partial z}-\frac{v^2}{r}=-\frac{1}{\rho}\frac{\partial p}{\partial r} \tag{1}$$

$$\frac{\partial w}{\partial t}+u\frac{\partial w}{\partial r}+\frac{v}{r}\frac{\partial w}{\partial \theta}+w\frac{\partial w}{\partial z}=-\frac{1}{\rho}\frac{\partial p}{\partial z} \tag{2}$$

where (u,v,w) is the velocity in a cylindrical coordinate system (r,θ,z), t is time, ρ is density, and p is static pressure. Multiplying Eqs. (1) and (2) by u and w, respectively, summing the two equations, and performing some algebraic manipulation, gives

$$\frac{u}{\rho}\frac{\partial p}{\partial r}+\frac{w}{\rho}\frac{\partial p}{\partial z}+\frac{\partial(u_s^2/2)}{\partial t}+u\frac{\partial(u_s^2/2)}{\partial r}+w\frac{\partial(u_s^2/2)}{\partial z}+\frac{v}{r}\frac{\partial(u_s^2/2)}{\partial \theta}-\frac{uv^2}{r}=0 \tag{3}$$

where

$$u_s^2=u^2+w^2 \tag{4}$$

For the flow across the seal, it is reasonable to assume low Mach number or incompressible conditions. Equation (3) may then be expressed in vector notation as follows:

$$\underline{u}_s\cdot\underline{\nabla}(p/\rho+u_s^2/2)+u_s\left(\frac{\partial}{\partial t}+\frac{v}{r}\frac{\partial}{\partial \theta}\right)u_s-\frac{uv^2}{r}=0 \tag{5}$$

where

$$\underline{u}_s=(u,0,w) \tag{6}$$

It may be noted that for steady flow with v=0, Eq. (5) reduces to Bernoulli's theorem, giving conservation of total pressure along streamlines.

Some further approximation is needed to arrive at the simplified model for the seal. Changes in tangential velocity through the seal are assumed small relative to changes in the other velocity components. A characteristic value of $\underline{u}_s$ is then chosen as the velocity in the vena contracta, denoted U, and integrating in the r-z plane across the seal, the following result is deduced from Eq. (5).

$$\rho l\left(\frac{\partial}{\partial t}+\frac{v}{r_0}\frac{\partial}{\partial \theta}\right)U+\frac{\rho U^2}{2}C_h\,\mathrm{sgn}(U)=\Delta p \tag{7}$$

where C_h, is a loss coefficient, l is an appropriate length scale (in the r-z plane), r_o is the inner annulus wall radius which is taken to equal the seal radius, and Δp is the pressure in the cavity minus the annulus pressure. This equation was proposed by Cargill [24], who gives an alternative derivation based on Crocco's equation.

Equation (7) is relatively straightforward to represent in finite difference form and solve numerically. This was done using central differencing for derivatives with respect to θ, and backward differencing in time. Mass flows into and out of the cavity were calculated from the computed solutions for U, which required specification of seal clearance (s_c) and discharge coefficient (C_d). An estimate of the sealing effectiveness is then given by

$$\Phi=m/(m+m_{\mathrm{in}}) \tag{8}$$

where m is the net mass flow rate through the seal and m_{in} is the ingestion flow rate. This estimate is based on a fully mixed assumption for the flow in the cavity. It does not fully account for the unsteady effects shown in the CFD solution and discussed above. Derivation of the above equation involves the assumption that the concentration of outflow through the seal is at the mixed value for the cavity and inflow is at the annulus inlet concentration. Looking at Figs. 8 and 10 from the CFD solution suggests that this may be a reasonable approximation.

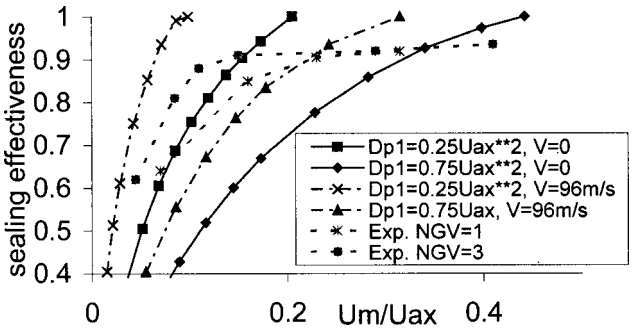

Fig. 12 Comparison of simple model with data from Chew et al. [10]

For the calculations described in the forthcoming C_h was taken as one and discharge coefficients were obtained from the correlations given by Chew et al. [10]. These give the discharge coefficient as a function of the ratio of mean seal velocity to the axial component of the annulus velocity (u_m/u_{ax}). Accuracy of the numerical solutions was tested by comparison with analytical integration of a sine function, by varying mesh spacing and time step, and by verifying that with appropriate coordinate transformation a transient solution with $v=0$ was equivalent to a steady solution with the appropriate value of v.

A shortcoming of the above model is the need to specify l and v. Here, l was set to $C_d.s_c$ and v was set to the estimated swirl velocity for the annulus flow above the seal. Note that effects arising from differences in tangential velocity between the cavity and annulus flows are not modeled. Sinusoidal variations of annulus static pressure are assumed with uniform and steady cavity pressure. The cavity pressure is varied to obtain results for a range of sealing mass flows.

4.2 Comparison With Measurements. Figure 12 shows a comparison of results from the simple model with the data given by Chew et al. [10]. In this case the pressure asymmetry in the annulus is caused by a row of 18 guide vanes at different axial positions (NGV=1 or 3) upstream of the seal. Predictions from the model are given with pressure asymmetries equal to 0.5 and 1.5 times the axial dynamic head for the annulus. These conditions are representative of the extremes of the experimental range. Calculations are also given for $v=0$ and $v=96$ m/s, which is an estimate of the experimental annulus swirl velocity. For $v=0$ (and no time dependency of Δp) the inertial term in Eq. (7) vanishes, and the model reverts to the straightforward orifice flow approximation used by other workers. As shown by Chew et al., without the inertial terms the model overpredicts the degree of mainstream ingestion. Inclusion of the inertial term gives much better quantitative agreement with the data at low sealing flow rates, although the model shows greater sensitivity to the level of pressure asymmetry than measured experimentally. At higher sealing flow rates, the experimental and calculated results show different trends, possibly due to complex interaction of the sealing and annulus flows.

Comparisons of model predictions of sealing effectiveness with data from the rig described in Section 2 are shown in Fig. 13. In these calculations Δp has been specified as follows:

$$\Delta p=p_c-[1+\sin(n_1\theta)]\frac{\Delta p_1}{2}-[1+\sin(n_2(\theta-\Omega t))]\frac{\Delta p_2}{2} \tag{9}$$

where n is the number of blades or vanes, and subscripts 1 and 2 refer to the stator and rotor, respectively. Estimating experimental conditions, the following values are assumed:

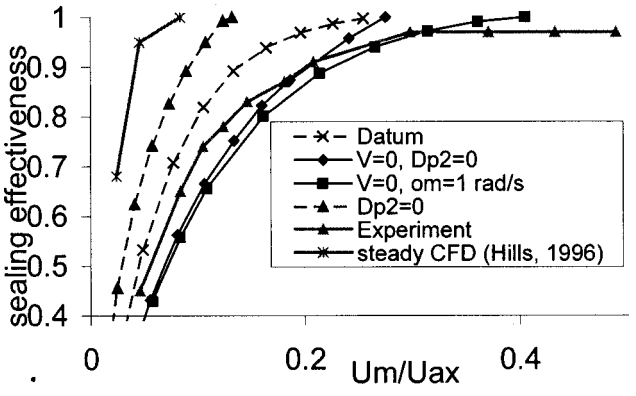

Fig. 13 Comparison of simple model with data from the present configuration

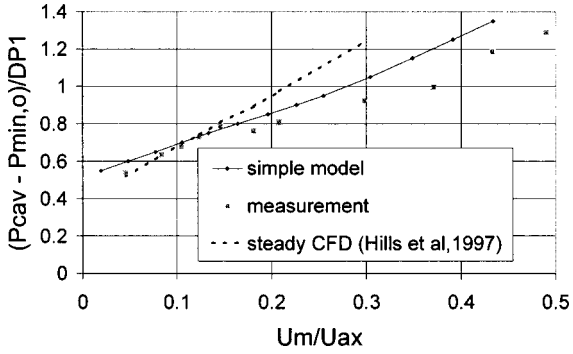

Fig. 14 Comparison of measured and calculated cavity pressure

$$v = 87 \text{ m/s}, \quad \Omega = 428 \text{ rad/s}, \quad n_1 = 29, \quad n_2 = 16, \quad \Delta p_1 = 1000 \text{ Pa}, \quad \Delta p_2 = 600 \text{ Pa} \tag{10}$$

where Ω is the angular velocity of the rotor, and Δp_2 has been estimated entirely from the CFD solution, no unsteady or rotating measurements being available. Values of some of these parameters were varied to show sensitivity of the model.

Looking first at the comparison between results for the base conditions given in the foregoing and the measurements shows some fair agreement at low sealing flows, but differences at higher flow rates. Again sealing/annulus flow interaction may account for some of this effect. Neglecting the pressure asymmetry due to the rotor and the inertial terms ($\Delta p_2 = v = 0$) leads to overprediction of ingestion at low flow rates. For $v = 0$, $\Omega = 1$ rad/s the inertial terms in Eq. (7) will be negligible but the computed solution will include a quasi-steady representation of the rotor pressure asymmetry. The calculated sealing effectiveness is close to that of the $\Delta p_2 = v = 0$ solution at low flows, but a higher flow rate is required to fully seal the cavity. Without the inertial terms, the model requires $\Delta p \geqslant 0$ in order to prevent ingestion. Thus, for the quasi-steady solution, a higher cavity pressure (and hence higher flow rate) is required for complete sealing.

The effect of the pressure asymmetry due to the rotor, as predicted by the model, is shown by comparing calculations for the base condition with those for $\Delta p_2 = 0$ in Fig. 13. As for the CFD solution in Section 3, without the rotor pressure asymmetry ingestion is significantly reduced. This figure also includes steady CFD results from Hills [25]. This CFD was based on the model presented by Hills et al. [13] and models the annulus flow asymmetry due to the vanes using a potential flow approximation. The underprediction of ingestion due to this model (despite some good agreement with pressure measurements) is in qualitative agreement with the simple model.

As mentioned in the introduction, and in Section 3, Green and Turner [11] concluded from their experimental studies that the presence of rotor blades may help reduce ingestion. Although based on a different configuration to that considered here, this seems to conflict with present results. Further studies with the simple model confirm that is does not predict any improvement in sealing due to rotating blades. The balance of evidence indicates that the presence of blades will usually tend to increase ingestion. Note, however, that the flow through the seal is complex with elements of fluid oscillating radially as they pass through regions of positive and negative pressure gradient. Thus, considerable uncertainty remains about the validity of the simple model. More measurements and CFD studies are needed to clarify this issue.

Calculated and measured values for the cavity pressure are compared in Fig. 14. Results from the steady CFD model of Hills et al. [13] are also included. The experimental values were obtained by extrapolating measurements from tappings at $r/r_0 = 0.90$ and $r/r_0 = 0.95$ to $r/r_0 = 1.0$. All values are normalized by subtracting the minimum annulus pressure at the lowest sealing flow rate and dividing by the peak-to-peak annulus pressure asymmetry. The simple model can be said to be in fair agreement with the measurements. The steady CFD results diverge from the measurements at higher sealing flows. Hills et al. considered that this might be due to the neglect of the effect of the sealing flow on the flow in the guide vanes in their CFD model. The better agreement between the simple model and measurement at high flow rates is consistent with this. Using a potential flow solution at inlet to model the annulus pressure asymmetry due to the vanes, the upstream extent of the CFD domain in the annulus was limited. Thus as the upstream influence of the flow ejected from the seal increased with flow rate this effect would not be captured. Although not shown on the figure, further results from the simple model show that the neglect of inertial terms in Eq. (7) have only a weak effect on the cavity pressure. This contrasts with a strong effect on sealing effectiveness shown in Fig. 12, and suggests that the relative pressures in the cavity and the annulus cannot, on their own, be used to give reliable estimates of ingestion levels.

4.3 Annulus Flow Losses. As mentioned in the introduction, the nonaxisymmetric nature of shroud leakage flows has been noted by workers concerned with the aerodynamic efficiency of the annulus flow. The 3-D nature of the flow is particularly clear from the velocity measurements of Pfau et al. [18] and Demargne and Longley [20]. As is consistent with the foregoing discussion of inertial effects, Demargne and Longley's velocity and concentration measurements also show that, in their configuration, increasing the tangential velocity of the sealing flow tends to reduce ingestion.

While loss generation in the annulus flow due to interaction with the blading flows can be very complex, ingestion and subsequent ejection of mainstream flow through the seal may be important at low sealing flow rates and large sealing gaps. This was noted by Wallis et al. [17]. Estimates of the ingestion flow rate when the net sealing flow is zero can be obtained from the simple model. Figure 15 gives results for the case of a sinusoidal pressure asymmetry for steady flow in which there are no rotor/stator interaction effects. For these conditions the nondimensional ingestion flow rate ($m^* = m_{in}/2\pi\rho s_c r_o u_{ax}$) is a function of just two parameters; the nondimensional peak-to-peak pressure asymmetry variation ($\Delta p^* = \Delta p/\rho u_{ax}^2$) and the group $n(l/r_o)(v/u_{ax})$. Direct comparison of these calculations with results from the references mentioned above is difficult. However, very roughly, for Demargne and Longley's case the simple model gives an inflow of about 0.1 percent of mainstream flow. This is consistent with the measurements. For Wallis et al.'s case there is little guidance as to the level of pressure asymmetry, but ingress flow rates of around 0.5 to 1 percent of annulus flow might be estimated for their seal exit cavity. Wallis et al. showed that fitting baffles in the seal cavity reduced turbine loss. This was attributed to better alignment of the

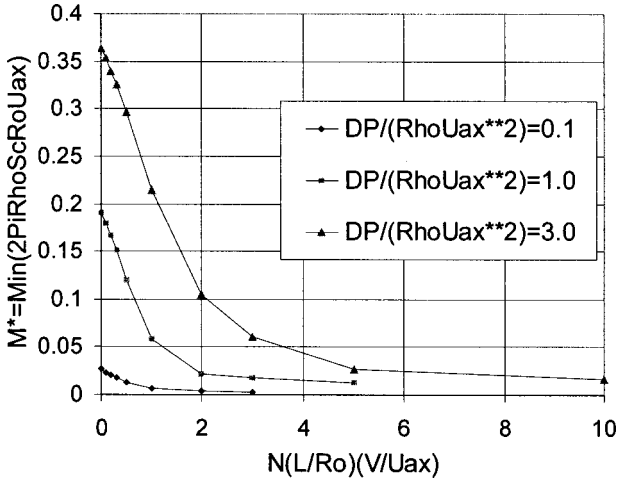

Fig. 15 Calculated mass inflow from simple model for steady conditions with no sealing flow

leakage flow with the annulus flow before it left the cavity. It is possible that the greater tangential velocity of the cavity flow (relative to the rotating blade) may have contributed to the improvement in loss with some suppression of ingestion.

5 Conclusions

Mainstream gas ingestion through a model turbine rim seal has been considered using experimental, CFD and more elementary modeling techniques. For the simple model considered reasonable agreement was found between CFD calculations and measurements when both the stator vanes and rotor pegs were included in a full 3-D, unsteady CFD simulation. The circumferential pressure asymmetry at the seal generated by the rotor pegs is considerably less than that due to the vanes, but the CFD results show the rotor pegs to have a disproportionately large effect on ingestion. The CFD calculations provide strong support for the view that unsteadiness due to the rotor blade will usually lead to more ingestion. Differences between measured and calculated levels of ingestion may be associated with differences between measured and calculated pressure asymmetries in the annulus. The experiments show some evidence of pressure asymmetry components at lower harmonics than those associated with the blades and vanes. These low harmonics could have slow axial decay rates and may be difficult to avoid both in experimental rigs and in engines.

Swirl velocity is found to be an important parameter in controlling the degree of ingestion. The relatively large effect of the rotor pegs in the CFD simulations is attributed to the swirl velocity in the annulus being close to rotor speed. An element of fluid traveling at the annulus flow swirl velocity will be subject to the radial pressure gradient arising from the rotor pegs which rotate at the same speed. This pressure force will tend to drive the fluid element either into or away from the disc cavity. The same fluid element is subject to a time varying radial force as it moves through the pressure field from the vanes. Since the radial force on the element due to the vanes will vary in direction with time it is less effective in driving flow into the disc cavity.

The simple orifice theory model for gas ingestion has been extended to include some inertial effects due to the swirl velocity. This extended model has had some success in reproducing experimental trends and correlating measurements. In addition to the swirl velocity, the numbers of blades and vanes are shown by the simple model to have a strong influence on ingestion. Considering experiments performed by Demargne and Longley [20] and Wallis et al. [17] it appears that the flow phenomena identified may also be significant in determining aerodynamic losses in the annulus flow.

While the present results provide encouragement for the application of CFD to turbomachinery rim sealing, there are also areas where further work would be useful. Convergence of the unsteady CFD solution to periodic behavior is slow due to different flow characteristics for the main annulus and disk cavity. This presently limits application of CFD to this problem, but improvements due to computing advances and improved numerical solution techniques are expected in the future. There is also a need for further work on turbulence models to identify or develop suitable models for both disk cavity and blading aerodynamic flows. Various models are established for use in either disc cavities or blading flows, but no model is yet established for use in both these areas. Further research into these areas and evaluation against experimental data are planned by the present authors.

Acknowledgments

Much of this work has been funded by Rolls-Royce plc. This is gratefully acknowledged by the authors who would also like to thank their colleague T. Green and P. Smout of Rolls-Royce plc for their help and interest.

Nomenclature

C_d = discharge coefficient
C_h = loss coefficient
l = length scale for seal flow
m = inlet mass flow to disk cavity
m_{in} = ingestion mass flow rate
m = nondimensional ingress flow rate $= m_{\text{in}}/2\pi\rho s_c r_o u_{\text{ax}}$
n = no. of blades or vanes
p = static pressure
p_c = static pressure in disc cavity
r = radial coordinate
r_o = inner annulus wall radius
s_c = seal clearance
u = radial component of velocity
U = representative velocity for seal flow
u_{ax} = axial component of mean annulus velocity
u_m = mean velocity through seal $= m/2\pi\rho s_c r_o$
$\underline{u}_s$ = $=(u,0,w)$
u_s = magnitude of $\underline{u}_s$
v = tangential component of velocity
w = axial component of velocity
z = axial coordinate
Δp = pressure difference across seal
Δp^* = $=\Delta p/\rho u_{\text{ax}}{}^2$
μ = viscosity
θ = angular coordinate in cylindrical system
ρ = density
Ω = angular velocity of rotor
Φ = sealing effectiveness or species concentration

Subscripts

1 = refers to stationary vanes
2 = refers to rotating blades or pegs

References

[1] Bayley, F. J., and Owen, J. M., 1970, "The Fluid Dynamics of a Shrouded Disk System With a Radial Outflow of Coolant," ASME J. Eng. Power, **92**, pp. 335–341.
[2] Chew, J. W., 1989, "A Theoretical Study of Ingress for Shrouded Rotating Disc Systems With Radial Outflow," ASME Paper 89-GT-187; also ASME J. Turbomach., **113**, pp. 91–97.
[3] Chew, J. W., Dadkhah, S., and Turner, A. B., 1991, "Rim Sealing of Rotor-Stator Wheelspaces in the Absence of External Flow," ASME Paper 91-GT-33; also ASME J. Turbomach., **114**, pp. 433–438.
[4] Campbell, D. A., 1978, "Gas Turbine Disc Sealing System Design," Proc., AGARD Conf. on Seal Technology in Gas Turbine Engines, AGARD-CP-237.
[5] Abe, T., Kikuchi, J., and Takeuchi, H., 1979. "An Investigation of Turbine Disc Cooling," Paper GT30, 3rd CIMAC Congress, Vienna.
[6] Kobayashi, N., Matsumato, M., and Shizuya, M., 1984, "An Experimental

Investigation of a Gas Turbine Disc Cooling System,'' ASME J. Eng. Gas Turbines Power, **106**, pp. 136–141.
[7] Phadke, U. P., and Owen, J. M., 1988. ''Aerodynamic Aspects of the Rim Sealing of Gas Turbine Rotor-Stator Systems, Parts 1–3,'' Int. J. Heat Fluid Flow, **9**, pp. 98–117.
[8] Dadkhah, S., Turner, A. B., and Chew, J. W., 1991, ''Performance of Radial Clearance Rim Seals in Upstream and Downstream Wheelspaces,'' ASME Paper 91-GT-32; also, ASME J. Turbomach., **114**, pp. 439–445.
[9] Hamabe, K., and Ishida, K., 1992, ''Rim Seal Experiments and Analysis of a Rotor-Stator System With Non-axisymmetric Main Flow,'' ASME Paper 92-GT-160.
[10] Chew, J. W., Green, T., and Turner, A. B., 1994, ''Rim Sealing of Rotor-Stator Wheelspaces in the Presence of External Flow,'' ASME Paper 94-GT-126.
[11] Green, T., and Turner, A. B., 1992, ''Ingestion Into the Upstream Wheelspaces of an Axial Turbine Stage,'' ASME Paper 92-GT-303.
[12] Bohn, D., Rudzihski, B., Sturken, N., and Gartner, W., 2000, ''Experimental and Numerical Investigation of the Influence of Rotor Blades on Hot Gas Ingestion Into the Upstream Cavity of an Axial Turbine Stage,'' ASME Paper 2000-GT-284.
[13] Hills, N. J., Chew, J. W., Green, T., and Turner, A. B., 1997, ''Aerodynamics of Turbine Rim-Seal Ingestion,'' ASME Paper 97-GT-268.
[14] Roy, R. P., Xu, G., and Feng, J., 2000, ''Study of Main-Stream Gas Ingestion in a Rotor-Stator Disk Cavity,'' Paper AIAA-2000-3372.
[15] Denton, J. D., 1993, ''Loss Mechanisms in Turbomachines,'' ASME Paper 93-GT-435.
[16] Hartsel, J. E., 1972, ''Prediction of Effects of Mass-Transfer Cooling on the Blade Row Efficiency of Turbine Airfoils,'' AIAA Paper 72-11, 10th Aerospace Sciences Meeting, CA.
[17] Wallis, A. M., Denton, J. D., and Demargne, A. A. J., 2000, ''The Control of Shroud Leakage Flows to Reduce Aerodynamic Losses in a Low Aspect Ratio, Shrouded Axial Flow Turbine,'' ASME Paper 2000-GT-475.
[18] Pfau, A., Treiber, M., Sell, M., and Gyarmarthy, G., 2000, ''Flow Interaction From the Exit Cavity of an Axial Turbine Blade Row Labyrinth Seal,'' ASME Paper 2000-GT-481.
[19] Wellborn, S. R., and Okiishi, T. H., 1998, ''The Influence of Shrouded Stator Cavity Flows on Multistage Compressor Performance,'' ASME Paper 98-GT-12.
[20] Demargne, A. A. J., and Longley, J. P., 2000, ''The Aerodynamic Interaction of Stator Shroud Leakage and Mainstream Flows in Compressors,'' ASME Paper 2000-GT-570.
[21] Green, T., 1994, ''Effect of External Flow on Sealing Performance of Rotor-Stator Rim Seals,'' D.Phil. thesis, University of Sussex, UK.
[22] FLUENT5, 1998. Users Guide, Fluent Inc.
[23] Virr, G. P., Chew, J. W., and Coupland, J., 1993, ''Application of Computational Fluid Dynamics to Turbine Disc Cavities,'' ASME Paper 93-GT-89; also, ASME J. Turbomach., **116**, pp. 701–708.
[24] Cargill, A. M., 1991, ''On Non-axisymmetric and Unsteady Effects on Rim Sealing,'' Rolls-Royce report.
[25] Hills, N. J., 1996, ''Development and Application of Multigrid Methods in CFD for Turbine Rim Sealing,'' D.Phil. thesis, University of Sussex, UK.